BRECCIA-HOSTED COPPER-MOLYBDENUM MINERALISATION AT RIO BLANCO, CHILE

by

Harmen
Peter H. Frikken B.Sc. (Hons)

University of Tasmania

CODES

Submitted in fulfilment of the requirements for
the degree of Doctor of Philosophy

University of Tasmania
Australia
March, 2003

DECLARATION

This thesis is not to be made available for loan or copying until January 2004. Following this time, this thesis may be made available for loan and limited copying in accordance with the *Copyright Act 1968*.

This thesis contains no material which has been accepted for the award of any other degree or diploma in any university and, to the best of my knowledge and belief, contains no material previously published or written by another person, except where due acknowledgement is made in the text of this thesis.

Peter Frikken

Date: 30-01-04

ABSTRACT

The Río Blanco-Los Bronces ore deposit is located at 33°15'S in the Principal Cordillera of central Chile. It lies midway between the Los Pelambres and El Teniente porphyry copper deposits, which together define one of Chile's most economically significant metallogenic belts. Río Batholith and surrounding Tertiary volcanic and volcaniclastic rocks at approximately 5-4 Ma. The bulk of the >50 million metric tonne copper resource is hosted by the Río Blanco Magmatic Breccia and the Sur-Sur Tourmaline Breccia.

The geometry of the Río Blanco-Los Bronces system is asymmetrical, and appears to have been controlled by three principal fracture orientations that trend N, NW and NE. Two N-trending faults terminate at the eastern and western boundaries of the Río Blanco-Los Bronces deposit and have acted as pull-apart structures that allowed hydrothermal fluids and felsic magmas to be emplaced within the ore deposit. The N-trending faults are the largest and most deeply eroded fault orientations in the district and at Sur-Sur are occupied by Tourmaline Breccia. The phyllic altered Tourmaline Breccia is marginal to the potassic altered Río Blanco Magmatic Breccia, which constitutes the core zone between the two N-trending fault terminations. Although the NW- and NE-trending faults crosscut the Tourmaline Breccia, their fracture intensities are highest where strongly mineralised zones occur along the strike length of the breccia body, indicating that these fracture trends were active during brecciation and helped to localise fluid flow.

Paragenetic studies indicate nine main stages of veins, breccia and porphyry emplacement in the Río Blanco and Sur-Sur sectors of the ore deposit. The stages are: (1) magnetite-actinolite alteration; (2) potassic stockwork veins; (3) Río Blanco Magmatic Breccia and Sur-Sur Tourmaline Breccia; (4) Feldspar Porphyry; (5) potassic stockwork veins; (6) Quartz Monzonite Porphyry and Don Luis Porphyry; (7) molybdenite stockwork veins; (8) chalcopyrite stockwork veins; and (9) D veins. Barren dacite and rhyolite intrusions cross-cut the ore deposit complex.

A change from potassic to phyllic alteration defines the contact between the Río Blanco Magmatic Breccia and Sur-Sur Tourmaline Breccia. The Río Blanco Magmatic Breccia occupies a large volume of rock within the Río Blanco, La Union, Don Luis and Sur-Sur sectors, and extends over a vertical interval of ~2 km. The Tourmaline Breccia lies transitionally outward from the Magmatic Breccia mainly in the Sur-Sur sector. There is a 100 m thick gradational contact between deep-level biotite breccia and shallow-level tourmaline breccia at Sur-Sur. Paragenetic studies of breccia cement minerals in the Río Blanco Magmatic Breccia and Sur-Sur Tourmaline Breccia reveal a similar cement infill sequence involving initial biotite and/or tourmaline precipitation at clast margins, followed by sulfate (anhydrite) and oxide (specularite) mineral phases, and in turn by chalcopyrite and magnetite.

Spatial zonation of breccia cement minerals occurs in the Río Blanco and Sur-Sur breccias. Zonation of biotite and tourmaline coincides with zonation of potassic and phyllic alteration, respectively. Chalcopyrite is spatially associated with stage 3 Magmatic Breccia and biotite alteration in the Río Blanco to Don Luis sectors, and with stage 3 Tourmaline Breccia and quartz-sericite alteration in the Sur-Sur sector. Outward from the potassic and phyllic altered zones; a propylitic assemblage occurs that is defined by chlorite alteration and pyrite-specularite breccia cement minerals.

New $^{40}Ar/^{39}Ar$ geochronology of hydrothermal biotite from the base of the Sur-Sur Tourmaline Breccia and whole rock sericite from the top of the Sur-Sur Tourmaline Breccia yielded ages of 4.78 ± 0.04 Ma and 5.42 ± 0.09 Ma, respectively. Both $^{87}Sr/^{86}Sr$ and $å_{Nd}$ analyses for tourmaline and anhydrite from the Río Blanco Magmatic Breccia and Sur-Sur Tourmaline Breccia range between 0.7040 and 0.7044, and +1.70 and +2.53, respectively. $^{206}Pb/^{204}Pb$ values for anhydrite cement in the Río Blanco Magmatic Breccia and the Sur-Sur Tourmaline Breccia ranged between 17.558 and 18.479, $^{207}Pb/^{204}Pb$ values ranged between 15.534 and 15.623, and $^{208}Pb/^{204}Pb$ values ranged between 37.341 and 38.412. The early-formed anhydrite cement has Pb isotopic compositions that are less radiogenic than the sulfide ores and host rocks, and also has elevated initial Sr ratios compared to the host rocks. Pb and Sr in anhydrite are interpreted to have been sourced from rocks and/or waters external to the main magmatic-hydrothermal system.

Oxygen/deuterium isotopes for tourmaline breccia cement minerals have 'magmatic' values, however recalculated values of propylitic-altered samples from previous workers indicate a meteoric water component of up to 25%. Zonation of sulfur isotope compositions occurs in the mineralised breccias, particularly at Sur-Sur. The Río Blanco sector is characterised by sulfides with $\delta^{34}S$ values between -3.94 and +3.34 and sulfates between +10.07 and +17.86 values. The Sur-Sur sector is characterised by sulfides with $\delta^{34}S$ values between -4.12 and +2.65 and sulfates between +11.15 and +13.39. These values are consistent with a magmatic-hydrothermal sulfur source. At Sur-Sur, the most negative $\delta^{34}S$ compositions ($\delta^{34}S < -3$ per mil) are spatially associated with the highest copper grades and specularite cement.

The Río Blanco Magmatic Breccia and Sur-Sur Tourmaline Breccia contain co-existing low salinity liquid-rich and vapour-rich fluid inclusions and localised zones containing co-existing vapour-rich and hypersaline fluid inclusions. Homogenisation temperatures from >600 to 131°C have been measured, but most are between 450° and 300°C. Complete salinity arrays from 0-69 wt.% NaCl equivalent were observed, and eutectic temperatures are commonly below -35°C. Minimum pressure estimates from fluid inclusions are between 48 and 368 bars. An average lithostatic formation depth of 200 m and a hydrostatic formation depth of 2300 m below the palaeo-surface have been calculated, indicating that up to approximately 1 km of erosion has occurred since breccia formation.

The mineralised breccias in the Río Blanco and Sur-Sur sectors are magmatic-hydrothermal in origin. They formed when magmatic-hydrothermal fluids (brine and gas) exsolved from deep-seated magma and potentially mixed with an external water. Hydrostatic pressures catastrophically exceeded lithostatic load plus the tensile strength of the confining rocks leading to brecciation. At Sur-Sur, fault rupture along the Río Blanco Fault may have been a trigger for magmatic-hydrothermal brecciation. Phase separation of magmatically-derived aqueous fluid occurred at the onset of brecciation, with a low density gas phase (carrying H_2O, SO_2, HCl and B_2O_3) separating physically from the dense copper-bearing brine. The gas phase fluxed through the breccia column first, where it condensed into exotic groundwaters of uncertain derivation, resulting in the deposition of oxide-stage cements (anhydrite, specularite, tourmaline) from a hybrid low salinity water. Subsequent upwelling of the magmatic-hydrothermal brine resulted in main stage sulfide deposition, possibly in part due to fluid mixing with the hybrid water.

ACKNOWLEDGEMENTS

I wish to thank my principal supervisors, Dr John Walshe and Dr David Cooke for initiating the research project and providing guidance, support and encouragement throughout the period of study. John Walshe is thanked for inspirational discussions, good stories and supervision outside the porphyrocentric box. Dave Cooke is thanked for his tireless effort and patience, for beating my manuscripts into shape and bringing welcomed rays of objectivity to cloudy days. Thanks are also extended to Dr Peter Hollings and Dr Ron Berry who have also provided unlimited scientific support over the years.

CODELCO is thanked for providing logistical support for fieldwork at the Río Blanco mine. Specifically, I would like to thank Francisco Camus, Jorge Skarmeta, Enrique Tidy, Luis Serrano, Ricardo Vargas, Juan Carlos Castelli, Juan Carlos Zamora, Andrew Hodgkin, Gloria Lopez, Nestor Alvarez, Alberto Adriasola, Augosto Mont and all the people at the mine who helped in one way or another during my field seasons. I would also like to thank AMIRA and the fifteen participating mining companies associated with the GODS project for providing financial assistance.

I would like to extend a special thanks to Professor Ross Large for providing us lucky few the opportunities to study at CODES. Thanks to CODES and Earth Sciences academic staff; Dr Mike Solomon, Professor Tony Crawford, Dr Garry Davidson, Walter Herrmann, Dr Andrew Rae, Dr Robina Sharpe, Dr Cathryn Gifkins, Dr Catherine Reid, Dr Jocelyn McPhie and Dr Dima Kamenetsky. Thanks also to CODES and Earth Sciences general staff; Loreto Lazcano-Frikken, June Pongratz, Dianne Steffens, Cristine Higgins, Nilar Hlaing, Simon Stevens, Peter Cornish, Alistair Chilcott, Fernando Della-Pasqua, Mike Blake, Katie McGoldrick and Lyn Starr.

Thanks to my colleagues past and present, who have always provided good laughs, good discussions and good times; Karin, Rohan, the Andrews, the Mike's, Kate, James, Dene, Daryl, Owen, Sarah, Vanessa, David, Peter, Mawson, Rick, Nicky, Russell, Wallace, Alan, Neil, Greg, Lee, Ben and Paul. A special thankyou is extended to my officemate of four years, Glen Masterman who I shared many discussions and proved to be a brilliant source of knowledge.

Finally, I'd like to thank my family, especially my wife Loreto who has supported me, not only mentally but also financially over the final 6 months of my research. Her unconditional love and encouragement is greatly appreciated.

TABLE OF CONTENTS

LIST OF TABLES

LIST OF FIGURES

Preamble

Porphyry copper deposits are commonly thought to be one of the best-understood classes of hydrothermal ore deposits. The prevailing view is that they are essentially closed, orthomagmatic hydrothermal systems operating above a crystallising magma chamber which may have intruded its own coeval stratovolcano (e.g. Fig. P1a; Hedenquist and Richards, 1998). Many of the key aspects of the genetic model for porphyry ore formation were generated in the 1970's (e.g. Lowell and Guilbert, 1970; Sillitoe, 1973; Gustafson and Hunt, 1975; Henley and McNabb, 1978; Burnham, 1979). Since that time, researchers have refined and updated the orthomagmatic model, mostly with insights gained from new technologies (e.g. Bodnar et al., 1985; Hedenquist and Richards, 1998; Audetat et al., 1998).

Despite current widespread acceptance of the porphyry copper model, certain aspects continue to be dabated. Some workers have documented geochemical evidence for the involvment of fluids other than those directly sourced from the magma chamber (e.g. Bowman et al., 1987; Hedenquist et al., 1998; Mathur et al., 2000a; Mathur et al., 2000b). These external fluids may be from shallow crustal sources (e.g. meteoric waters), evaporitic sources (Barton and Johnson, 1996) or they may be sourced from the deeper crust or mantle (e.g. Kay et al., 1999). They are not detected in all porphyry deposits, either because their geochemical signatures can be subtle and difficult to detect, or because in some deposits external waters play no role in the processes of alteration and mineralisation.

The schematic models for porphyry systems that were developed in the 70's show no structural constraints on the localisation of magmatism and mineralisation. In many of these models, alteration assemblages are portrayed as occurring in concentric zones (Fig. P1a), although Gustafson and Hunt (1975) highlighted the complexities caused by overprinting. In recent times, the structural architecture and geodynamic settings of porphyry systems is being given more careful consideration. The question of coeval volcanism at the time of porphyry ore formation has begun to be debated widely (e.g. Keith, 2000). The roles of arc-parallel strike-slip and arc-normal basement faults in localising porphyry deposits is also now being discussed, largely due to work in northern Chile (e.g. Lindsay et al, 1995; Richards et al., 2001; Dilles et al., 1997. Camus (2002) and McClay et al. (2002) have discussed the architecture and geodynamics of the Chilean porphyries, noting that the prevailing tectonic regime involved shortening, termination of volcanic activity and the emplacement of syn-tectonic intrusions (Fig. P1b), a setting vastly different to the stratovolcano environment, first proposed by Sillitoe (1973; compare Fig. P1a and b).

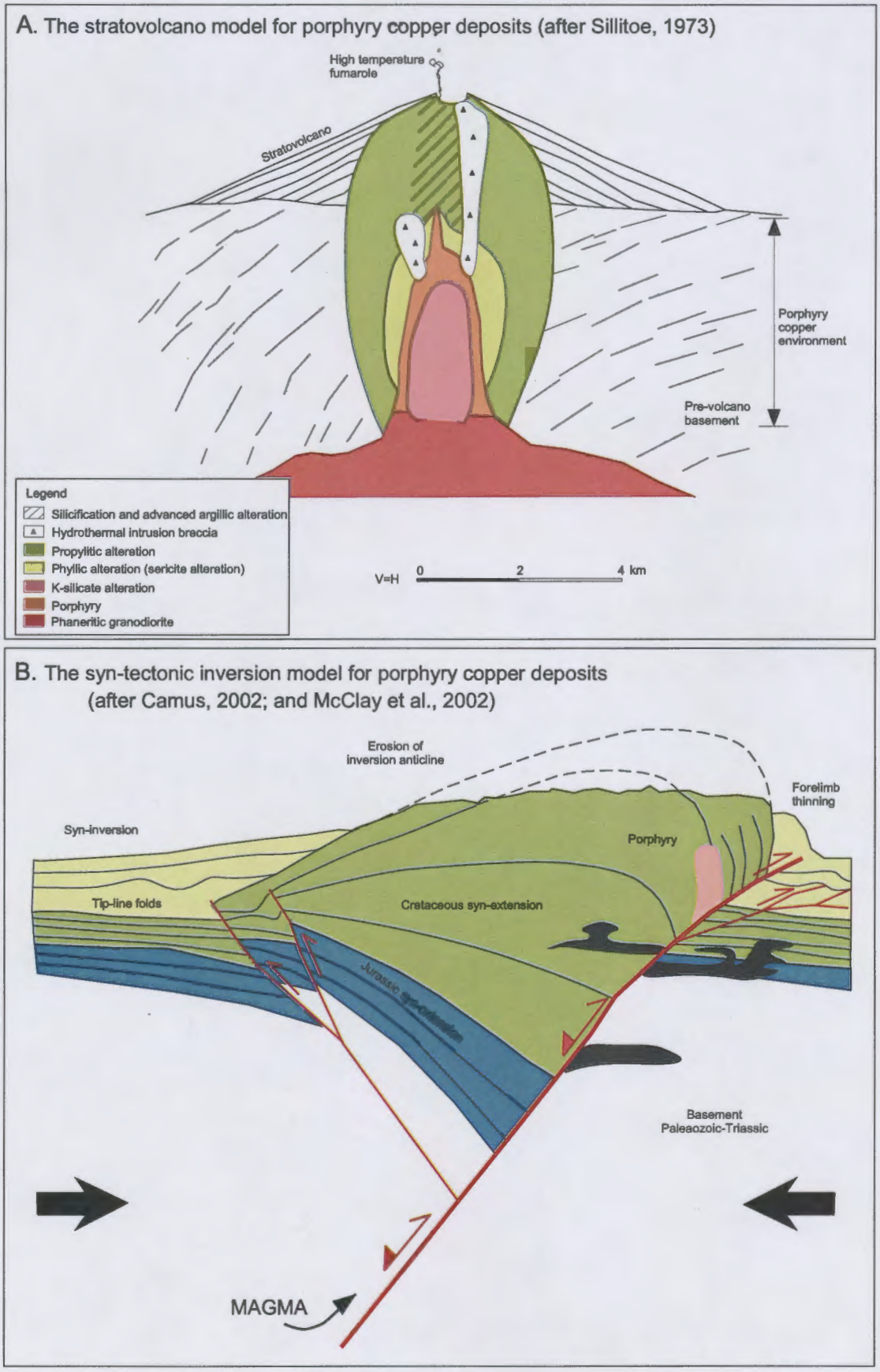

Figure P1. a. Porphyry copper ore formation in a coeval stratovolcano, modified from Sillitoe (1973). b. Formation of porphyry copper deposits in Chile with a contractional tectonic regime, modified from Camus (2002), and McClay et al. (2002). Note the absence of coeval volcanism in (b). The two-way arrows on the main fault in (b) represent reactivated normal faults.

Río Blanco-Los Bronces

The Río Blanco-Los Bronces ore deposit, located in V region, central Chile, is the third largest porphyry copper deposit in the world in terms of contained copper metal (Camus, 2002). Two separate mining companies, CODELCO (Río Blanco) and Anglo American (Los Bronces) are currently exploiting the resource (Fig. P2). The Río Blanco-Los Bronces deposit is a distinct end-member of the continuum of porphyry style ore systems, because the copper resource occurs almost entirely as cement within large magmatic-hydrothermal breccia complexes (e.g. Warnaars et al., 1985; Vargas et al., 1999), rather than as stocwork veins.

Previous workers, including Warnaars et al. (1985), Stambuk et al. (1993), Serrano et al. (1996), Vargas et al. (1999) and Skarmeta et al. (2000), have described aspects of the geology, structure, mineralisation and alteration at Río Blanco and Los Bronces. Previous sulfur isotope and fluid inclusion studies at Río Blanco and Los Bronces have been concluded by Kusakabe et al. (1984, 1990), Holmgren et al. (1988), Skewes and Holmgren (1993), Skewes (1996) and Skewes et al. (2002). These workers found that the fluids that formed the Río Blanco-Los Bronces ore deposit were magmatic-hydrothermal fluids typical of porphyry copper deposits (Holmgren et al., 1988; Vargas et al., 1999).

AMIRA P511

The current PhD research study of the Río Blanco ore deposit was initiated as part of the Australian Minerals Industry Research Association's (AMIRA) project P511 entitled Giant Ore Deposit Systems (GODS). This collaborative research effort involved staff and students from the Centre for Ore Deposit Research (CODES) at the University of Tasmania, together with staff of the Commonwealth Scientific and Industrial Research Organisation (CSIRO) Division of Exploration and Mining. Access to Río Blanco and full logistical support for this project was provided by Corporación Nacional del Cobre (CODELCO-Central and Division-Andina). The PhD scholarship was provided by the Australian Postgraduate Award – Industry scheme over 3.5 years. Additional financial support for P511 was provided by:

- Anglo American Exploration Australia Pty Ltd
- AngloGold Ltd
- AurionGold Ltd
- Barrick Gold of Australia
- BHP Billiton
- Centaur Mining and Exploration
- Falconbridge Ltd
- Gold Fields Ltd
- Newcrest Mining Ltd
- Newmont Exploration Pty Ltd
- Phelps Dodge Australasia, Inc
- Placer Dome
- Sons of Gwalia Ltd
- Teck Cominco Ltd
- WMC Resources Ltd

Figure P.2. Oblique aerial photograph of the Rio Blanco-Los Bronces ore deposit. Ore sectors to the left of the Los Bronces mine are owned by CODELCO. Los Bronces mine is owned by Anglo American. Photograph is oriented to the south.

Project Aims and Objectives

The ultimate question for P511 was "*Where and how does nature create giant, high-grade mineral deposits?*" In response to this question, the P511 team endeavoured to understand the following five aspects of specific ore deposits:

- What is the system?
- What is the pressure-temperature and geodynamic history?
- What is the nature of fluid reservoirs in the system?
- What mechanisms advect/convect/focus fluids?
- What are the metal transport/depositional mechanisms for ore formation?

Research collaboration with Codelco drew attention to the giant porphyry copper deposits of Chile, and particularly to those deposits with an inherent lack of research data previously generated. Through a rigorous process, the giant breccia-related porphyry copper deposit at Río Blanco was chosen for study. The specific aim of the PhD research project at Río Blanco has been to determine the chemistry, evolution and origins of mineralising fluids within the context of the regional architecture and geodynamic setting, and what that implies for ore genesis. To achieve this aim, core logging and petrographic studies have been combined with isotopic and fluid inclusion investigations. In order to determine how the mineralising fluids evolved both temporally and spatially, analytical data have been integrated with the mine's database of mineralogical information, allowing comparisons to be made between mineralogical zonation and geochemical analyses. These data are integrated into a new genetic model for ore formation at Río Blanco.

This thesis is divided into five main sections:

Section 1 - Literature Review: A summary of findings from previous workers with regards the regional geology, structure and tectonic setting of Río Blanco-Los Bronces.

Section 2 – Geological Evolution of Río Blanco: Outlines the geological evolution of Río Blanco by describing the geological components of the ore deposit complex. Structural and geochemical characteristics are also described.

Section 3 – The Mineralised Río Blanco and Sur-Sur Breccia Complexes: Presents detailed descriptions of the mineralisation and alteration assemblages based on drillcore and petrographic observations. New paragenetic stages have been identified, leading to a clarification of the sequence of hydrothermal events at Río Blanco. The spatial distributions of hydrothermal minerals are presented, and their implications for fluid evolution are discussed.

Section 4 – Fluid Chemistry and Fluid Evolution: This section presents the results of new geochemical investigations including mineral chemistry, fluid inclusions, oxygen, sulfur and radiogenic isotopes. Two new Ar-Ar age determinations are also presented. These data are used to evaluate fluid evolution and sources.

Section 5 – Synthesis and Genetic Model: The final section of the thesis combines the observations and results from the preceding sections into a general discussion on breccia formation and a specific genetic model for ore formation at Río Blanco. Ideas regarding the deposition of discrete high-grade zones within the orebody are discussed, specifically with regards physical and chemical gradients that may have been critical in the formation of this high-grade, large tonnage ore deposit.

SECTION 1 – LITERATURE REVIEW

1.1 Regional Geology of Central Chile

1.1.1 Location

The Río Blanco-Los Bronces ore deposit is located approximately 60 km north east of Santiago (Fig. 1.1). It is situated at altitude between 2700-4100 m above sea level and has been subject to recent glacial erosion. Logistical problems for mining are common at these high altitudes, and can result in complete disruption of open pit excavations during the winter months due to heavy snowfall and avalanches.

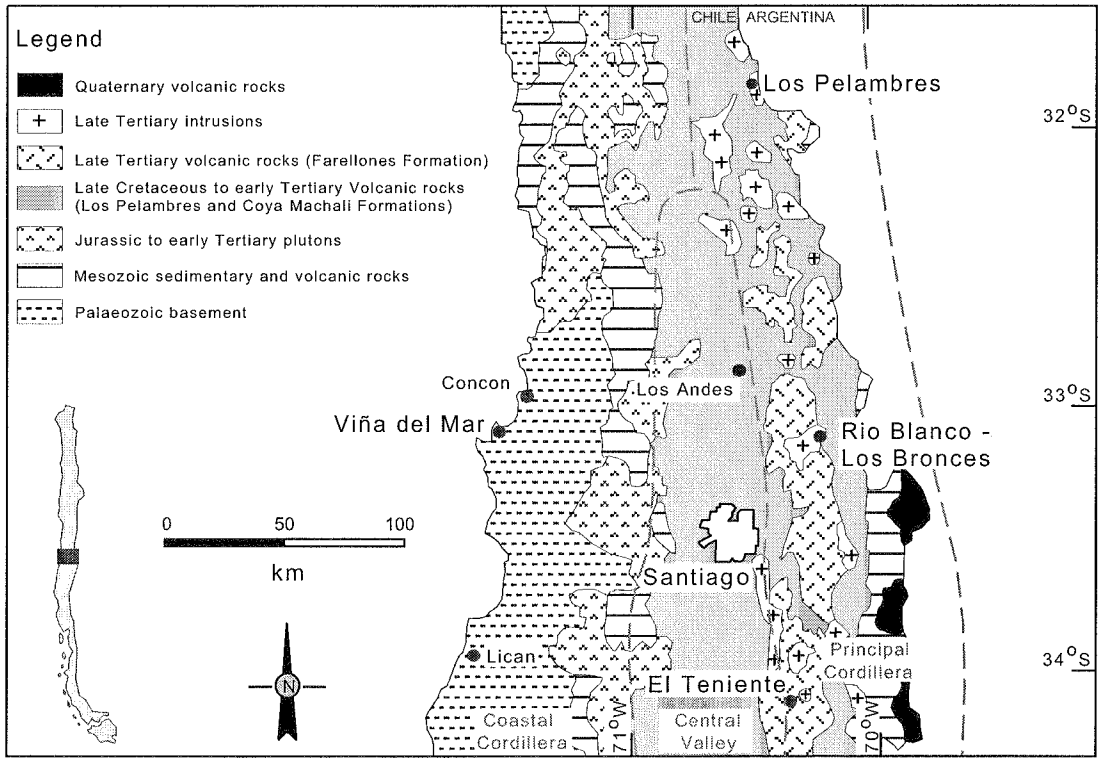

Figure 1.1. Regional geology map of central Chile (adapted from Serrano et al., 1996).

1.1.2 Overview

The Andes of central Chile from Los Pelambres (32°S) to El Teniente porphyry Cu-Mo deposits (34°S) contain a variety of late Palaeozoic to recent sedimentary, volcanic and intrusive rocks (Fig. 1.1). The Principal Cordillera encompasses the high Andes of central Chile (Ramos, 1995), and is bound to the east by the border with Argentina and to the west by the Central Valley (Fig. 1.1). The Principal Cordillera consists of Palaeozoic basement and Mesozoic to Tertiary sedimentary/volcanic rocks of the Southern Volcanic Zone (SVZ). It has been intruded by Miocene-Pliocene batholiths, stocks, dykes and breccias (Fig. 1.2).

The SVZ extends from 32°S in the north to approximately 45°S latitude in the south (Fig. 1.1; Stern, 1989). The northern end of the SVZ consists of the Los Pelambres, Las Chilcas and Salamanca Formations north of Río Blanco, and the Coya-Machali Formation in the vicinity of El Teniente. All of these formations are overlain unconformably by the Farellones Formation (Rivano, 1995). Stratigraphic relationships are complex due to the intimate relationships between volcanism and tectonism in central Chile (Drake et al., 1982). The volcanic units are broadly elongate in a north-south orientation, and occurs a trough-shaped basin within the intra-arc of the Principal Cordillera (Fig. 1.1).

Volcanic activity in central Chile occurred through the Mesozoic and Tertiary periods. It ended with the cessation of deposition of the Farellones Formation 7.4 m.y. ago. During this time, broadening of the magmatic arc occurred as the volcanic front migrated over 40 km to the east (Kay et al., 1987, 1988, 1991; Stern and Skewes, 1995). The termination of volcanic activity and arc migration is considered to be associated with the relative quiescence in sub-crustal conditions below the Principal Cordillera as a result of slab flattening in central Chile (Stern and Skewes, 1995).

Magmatism occurred in four main phases through the Mesozoic and Cainozoic eras (Rivano, 1995): i) Jurassic; ii) early to late Cretaceous; iii) late Cretaceous to Palaeogene; and iv) Neogene (Rivano, 1995). The intrusions that crop out in the vicinity of the Río Blanco-Los Bronces ore deposit were emplaced from late Cretaceous to Neogene (Miocene to Pliocene). These include the Chalinga Intrusives, San Francisco Batholith and the Tambillos Intrusives (Fig. 1.2). The cessation of major Neogene volcanic activity in central Chile occurred when the newly evolved continental crust of the Principal Cordillera entered a compressive phase of deformation coinciding with the onset of major intrusive activity. Batholiths and plutons in central Chile were emplaced during the episodic eastward migration of the arc across the region.

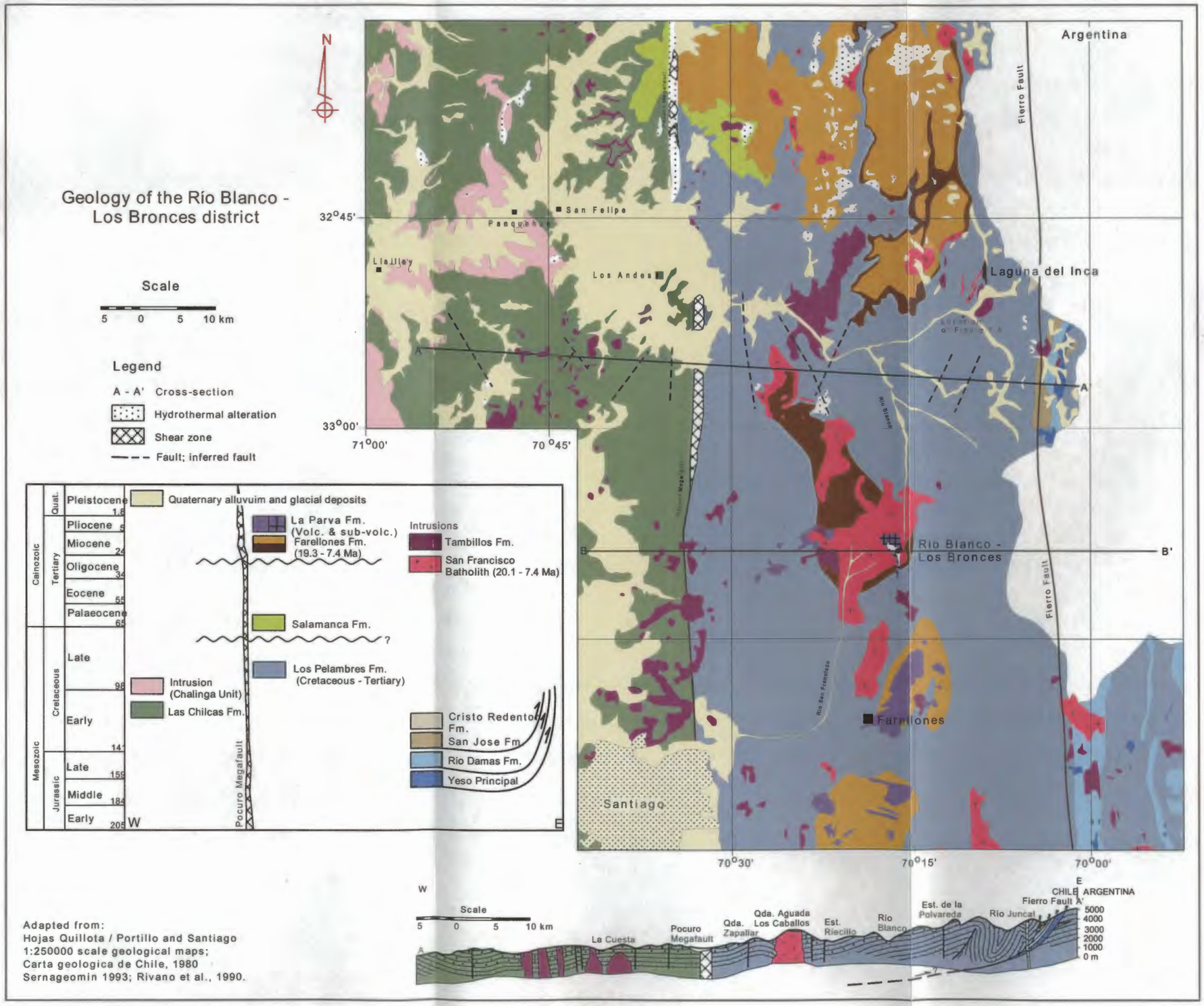

Figure 1.2. Local geology map, stratigraphic section and cross-section (A-A') of the Río Blanco-Los Bronces district. Quat. = Quaternary, Volc. = volcanics, sub-volc. = sub volcanics.

1.1.3 Rock Units

Palaeozoic

Palaeozoic basement crops out as the Cochoa Unit in the western part of the Coastal Cordillera (Fig. 1.1; Rivano, 1995). The Cochoa Unit consists predominantly of granodiorites, granites and gniessic tonalites that contain a NW-trending structural fabric (Rivano, 1995). The intrusions were emplaced between 299 and 153 Ma (using Rb-Sr and K-Ar; Rivano, 1995). The intrusions are interpreted to be the products of melting in the accretionary prism of the Frontal Cordillera, related to the subduction of the Nazca Plate beneath the South American plate (Rivano, 1995; Ramos, 1995).

Mesozoic

The Palaeozoic basement is overlain by Mesozoic successions of marine and terrestrial volcanic rocks and associated volcaniclastic and clastic sedimentary rocks (Rivano, 1995). These successions occur in two main areas; (1) within the Coastal Cordillera, and (2) the eastern side of the Principal Cordillera near the border with Argentina (Fig. 1.1).

The Jurassic and Cretaceous sedimentary successions in the Principal Cordillera are exposed as an elongate belt within the Andes along the border with Argentina (Stambuk et al., 1993). They are unconformably overlain by volcanic and volcaniclastic rocks of the Cretaceous - Tertiary SVZ.

The Jurassic sediments in the Principal Cordillera comprise Yeso Principal and the Río Damas Formation (Fig. 1.2; Ramos, 1995). Yeso Principal is the lowest member of the sequence and is composed of laminated coarse gypsum beds that were probably stratiform evaporite deposits (Rivano, 1995). Yeso Principal is overlain by the Río Damas Formation, a predominantly terrestrial sequence that consists of fine to coarse clastic sedimentary rocks (lutites, arenites and conglomerates), gypsum beds and minor volcanic intercalations (Rivano, 1995). Andesite clasts are predominant in the arenites and conglomerates. These clasts typically have a red colour due to iron-oxide alteration.

The Río Damas Formation is overlain by the San José Formation, an early Cretaceous marine sedimentary sequence with intercalated andesites (Fig. 1.2; Rivano, 1995). The sedimentary facies consist of fossiliferous limestone, calcilutite, calcarenite, lutite, conglomerate and subordinate

gypsum (Rivano, 1995; Stambuk et al., 1993). The fossils preserved in the strata include ammonites, pelecypods, cephalopods and gastropods indicating a shallow water marine depositional environment. The San José Formation is overlain by the Cristo Redentor Formation (Fig. 1.2), which consists of transitional continental facies composed of red calcareous arenites, conglomerates and lenses containing gypsum and/or stromatolites (Rivano, 1995).

Cretaceous to Tertiary

Los Pelambres and Coya-Machali Formation

The Los Pelambres and Coya-Machali Formations are lithologically similar and at least in part, time-equivalent (Fig. 1.2) and are treated here as broadly coeval (e.g. Drake et al., 1982). Characteristics of the Los Pelambres and Coya-Machali Formations are summarised in Table 1.1. The Coya-Machali Formation crops out to the south of, and is considered stratigraphically coeval with the Los Pelambres Formation in the Principal Cordillera (Drake et al., 1982). This sequence was originally referred to as the Chilense Formation but was re-named the "Coya-Machali" by Klohn (1960).

Table 1.1. A summary of the character and age of the Los Pelambres and Coya Machali Formations (from Drake et al., 1982; Kay and Kurtz, 1995; Rivano, 1995; Castelli, 1999; Vergara and Drake, 1978).

	Los Pelambres Formation		**Coya Machali Formation**	
	western belt	eastern belt	western belt	eastern belt
Character	*upper*: high K, calc-alkaline terrestrial volcanic (andesite to rhyolite) and volcaniclastic rocks (fine-grained arenites to coarse conglomerates). *lower*: Intercalated calcarenites and limestones deposited during early to mid Cretaceous		terrestrial volcanic (basalt to dacite), volcaniclastic and lacustrine sedimentary rocks. The volcanic rocks range in composition from basalt to dacite with aphanitic, porphyritic and microphaneritic textures	
Age	62.3 - 16.4 Ma Palaeocene to early Miocene (nb: fossil ages at base indicate an age >100 Ma)	40.9 - 25.2 Ma late Eocene to early Miocene	62.3 - 16.4 Ma Palaeocene to early Miocene	27.7 - 20.5 Ma late Oligocene to early Miocene

The Las Chilcas Formation crops out west of, and adjacent to, the Los Pelambres Formation. It is lithologically and stratigraphically similar to the Los Pelambres Formation (Rivano, 1995), but the two formations are separated by a large shear zone (the Pocuro Megafault; Fig. 1.2). The Las Chilcas Formation and the Los Pelambres Formation are here described together as the Los Pelambres Formation. Prior to the work by Rivano (1995), the Los Pelambres Formation was formerly known as the Abanico Formation. However, some authors still use "Abanico Formation" for the sequence south of 32°30'S until it reaches the Coya Machali Formation (e.g. Charrier et al., 2002).

Los Pelambres Formation overlies the San José Formation locally near the border with Argentina (Rivano, 1995). The base of the Los Pelambres Formation contains intercalated calcarenites and limestones that were deposited during the early to middle Cretaceous. The intercalated volcanics have undergone intense chlorite and sericite alteration (Rivano, 1995). The bulk of Los Pelambres Formation is composed of clastic sedimentary rocks, with fine to medium-grained tuffaceous clasts. These are intercalated with andesites and dacites. Lavas have large phenocrysts of sericitised plagioclase (1-4 mm), chloritised amphibole and rare phenocrysts of pyroxene (Rivano, 1995).

Geochemical analyses of the Los Pelambres volcanic rocks have revealed high Al_2O_3 and low TiO_2 concentrations (Kay and Kurtz, 1995). Increasing FeO/MgO ratios with increasing SiO_2 concentrations are consistent with the Coya-Machali volcanics being tholeiitic, having formed in an extensional environment and erupted through thin, non-radiogenic continental crust (Kay and Kurtz, 1995). Based on geochemical studies, Kay and Kurtz (1995) suggest that the Los Pelambres Formation was deposited between 28 and 20 Ma.

Palaeocene to Miocene

Salamanca Formation

The Salamanca Formation is exposed in the region between Los Andes and the Los Pelambres porphyry copper deposit (Fig. 1.2). Erosional surfaces separate the Salamanca Formation from the underlying Pelambres Formation and the overlying Farellones Formation (Rivano, 1995). A schematic representation of stratigraphic relationships between the Pelambres, Salamanca and Farellones Formations is shown on Figure 1.3 (Rivano, 1995). The unconformable stratigraphic surfaces in Figure 1.3 mark breaks in volcanism and volcaniclastic deposition some of which can be correlated to episodes of active tectonism and magmatism (e.g. Charrier et al, 2002).

The Salamanca Formation consists of terrestrial andesitic lavas and andesite to dacite volcaniclastic rocks with intercalations of rhyolite (Rivano, 1995). The sequence has been sub-divided into two members: (1) "Santa Virginia", the lower member, which crops out mostly to the west and consists primarily of conglomerates and arenites and; (2) "Río Manque", the upper member, which has a greater areal extent than the Santa Virginia member and consists mainly of andesites and dacites (Rivano, 1995).

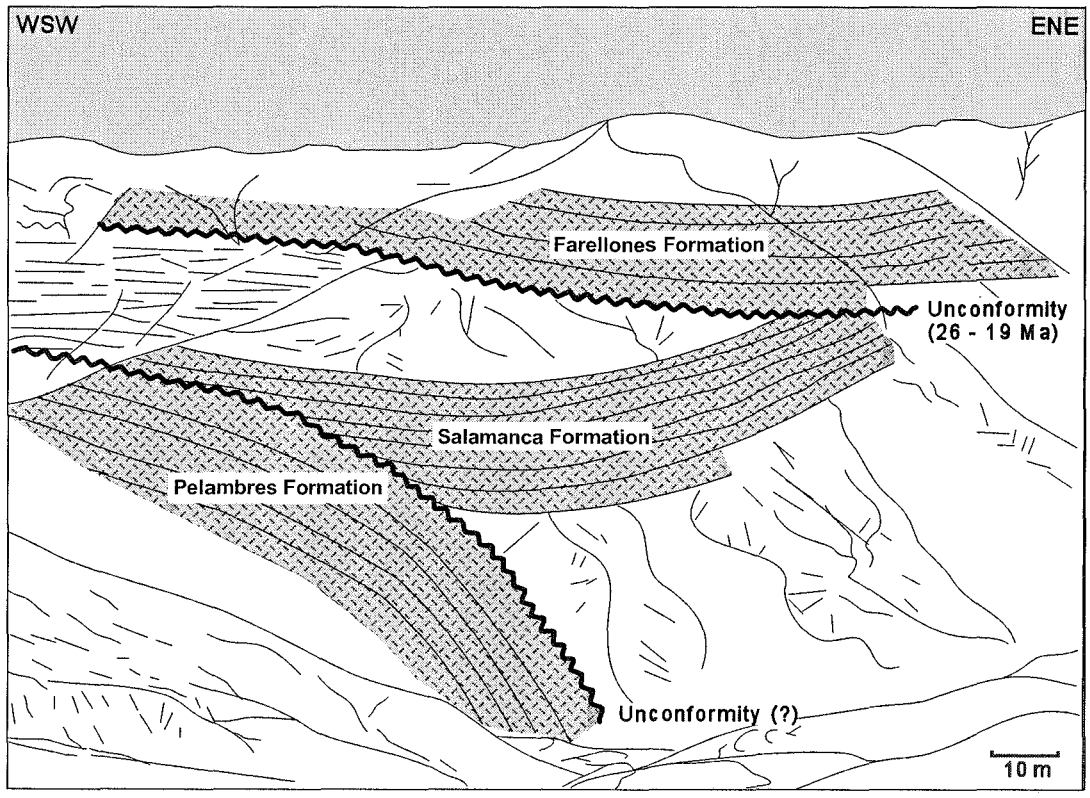

Figure 1.3. Sketch of a mountainside illustrating the unconformable stratigraphic relationships between the Los Pelambres, Salamanca and Farellones Formations located at the junction between Río Hidalgo and Río Rocin, central Chile (from Rivano, 1995). This location is approximately 2 km north of the map in Figure 1.2 and can be seen on the Quillota y Portillo 1:250000 scale geology map (Rivano et al., 1993).

The Salamanca Formation is estimated to have a maximum thickness of 2000-2500 m, with an average thickness of 1300 m (Rivano, 1995). Plagioclase and whole rock K-Ar radiometric age determinations constrain the Salamanca Formation between 128 Ma and 56 Ma, respectively (Rivano, 1995).

Chalinga Unit

The Chalinga Unit comprises intrusive bodies that occupy a large (40-50 km wide) north-trending belt within the Las Chilcas Formation (Fig. 1.2; Rivano, 1995). The Chalinga Unit makes up approximately 95% of the large magmatic chain known as the Illapel Group in central Chile (Rivano, 1995). The unit consists predominantly of leucocratic granodiorite to tonalite with a minor proportion of monzonites, quartz monzodiorites and monzogranites. The rocks are texturally variable and typically display hypidiomorphic and porphyritic textures (Rivano, 1995). K-Ar dates from the Chalinga Unit range from 139 Ma to 79 Ma, indicating emplacement between the early to mid Cretaceous (Rivano, 1995).

Miocene

Farellones Formation

The Farellones Formation crops out in the Principal Cordillera as a north-trending belt approximately 400 km long and 26-65 km wide (Fig. 1.1; Vergara et al., 1988). The formation is best exposed east of the Oligocene – Miocene magmatic belt and west of the present-day volcanic arc (Vergara et al., 1988). The Farellones Formation consists of continental volcanic and volcaniclastic units varying in composition from intermediate to felsic and, in lesser proportion, from mafic to intermediate (Vergara et al., 1988). Based on major element geochemistry, the Farellones Formation is calc-alkaline and K-Ar dating indicate eruptions occurred between 19 and 5 Ma (Vergara et al., 1988; Kay and Kurtz, 1995).

The Farellones Formation has been separated into lower and upper members (Rivano et al., 1990; Table 1.2). The lower Farellones Formation consists of tuffs, ignimbrites and rhyolites with thin intercalated volcanic units (Rivano et al., 1990). This lower sequence has a maximum thickness of 300 m and crops out at approximately 33°S latitude (Rivano et al., 1990). The basal part of this sequence unconformably overlies the Los Pelambres Formation and Salamanca Formation and has been dated at 15-18 Ma (Rivano et al., 1990).

Table 1.2. Geometry, lithology, structure, age and intrusions of the Farellones Formation between 31°S and 34°45'S latitudes in central Chile. Summarised from Kay and Kurtz (1995) and Rivano et al. (1990).

Farellones Formation		31°S - 33°S	33°15'S - 33°30'S	34°S - 34°45'S
Geometry	Width	35 km	25 km	24 km and terminating southwards
	Thickness	1200 m (between 32°S - 32°50'S)	3500 m	2400 m
Lithology (members)	Lower	200 m of pyroclastics (tuffaceous rocks, ignimbrites and rhyolites) & interlayered sediments	2000 m of volcaniclastics (tuffs, pyroclastics, epiclastic breccias & clastic sediments - shale & turbidites) unconformably overlie Pelambres Fm.	2400 m of porphyritic & aphanitic flows & pyroclastic flows of varied colours. They are generally andesitic but some are dacitic. This sequence unconformably overlies the Coya-Machali Fm.
	Upper	1000 m of thickly bedded andesitic lavas & volcaniclastic conglomerates/breccias	1500 m of andesitic & basaltic lava flows	
Structure		sub-horizontal stratigraphy, thrust faults (compressional tectonics)	slightly deformed to open folds	concentric folds with 5000 - 8000 m wavelengths. Buckling mechanism involving flexural slip
Age (K/Ar)		19.3 - 8.4 Ma	18.6 - 16.6 Ma	14 - 7.4 Ma
Intrusives		dacitic sills & dykes, rhyolite domes & andesitic necks	domes & rhyolitic sills	none

The upper sequence of the Farellones Formation consists predominantly of andesite and basalt lavas with intercalations of andesitic volcaniclastic rocks (Rivano et al., 1990). The thickness of the upper sequence is estimated to be 1500 m (Rivano et al., 1990). Based on K-Ar geochronology, the upper Farellones Formation sequence ranges in age from 14.4 to 7.4 Ma (Kay and Kurtz, 1995; Rivano et al., 1990; Table 1.2).

Thiele et al. (1991) suggested that the Farellones Formation erupted in a volcano-tectonic graben which had formed through a series of caldera collapses. Their supporting evidence includes: a) the outer limits of the Farellones Formation are typically bounded by normal faults, at which point the stratigraphy also tapers out and is upraised, indicating deposition during subsidence; and b) the large volume of erupted acid magma (Thiele et al., 1991).

The Farellones Formation is horizontal to gently dipping (< 15°) and is separated from all underlying units by an angular unconformity (Vergara et al., 1988; Fig. 1.3). The position of this unconformity in the stratigraphy has been debated for many years due to the presence of many local unconformities within both the underlying lavas and volcaniclastic rocks, and internally within the Farellones Formation. The basal Farellones Formation unconformity marks a major break between the underlying strongly deformed units and the flat-lying, broadly folded Farellones Formation (Fig. 1.3). This unconformity marks the end of a period of deformation, uplift, and erosion throughout the region that probably occurred during the late Oligocene to early Miocene (Warnaars et al., 1985).

The Farellones Formation has been affected by burial metamorphism, which produced zeolite, calcite, chlorite and clay-bearing mineral assemblages (Vergara et al., 1988; Levi et al., 1988). The spatial distribution and intensity of regional metamorphism is variable, but overall is less intense than in the Los Pelambres Formation (Vergara et al., 1988). The regional alteration assemblage is considered to be a product of burial metamorphism because (a) original rock fabrics are preserved; (b) metamorphic grade increases with stratigraphic depth; (c) increases in metamorphic grade are generally unrelated spatially to the location of granitoid intrusions; and (d) thermal gradients are estimated to have been less than 50°C/km (Levi et al., 1988).

San Francisco Batholith

A belt of Miocene calc-alkaline batholiths, plutons and dykes intruded the lavas and volcaniclastics of the SVZ in the Principal Cordillera. The north trending belt is approximately 350 km long and averages 25 km wide (Stambuk et al., 1993; Fig. 1.2). Individual intrusions range in composition from quartz monzonites and monzogranites to microgranodiorites, dacite porphyries and dacites (Castelli, 1999). The San Francisco Batholith (SFB), which hosts the Río Blanco-Los Bronces ore deposit, is part of this Miocene intrusive suite.

The SFB has an aerial extent of 200 km^2 in the vicinity of the Río Blanco-Los Bronces ore deposit (Serrano et al., 1996). It consists of multiple plutons that are elongated along north-south axes, and have intruded the Los Pelambres and Farellones Formations (Stambuk et al., 1993; Warnaars

et al., 1985). The SFB contains diorite, quartz diorite, quartz monzodiorite, quartz monzonite and granodiorite plutons as well as minor quartz syenite and aplitic dykes (Stern and Skewes, 1993).

The Río Blanco intrusive complex is part of the SFB. It was emplaced in a compressive tectonic regime between 20.1 and 5.2 Ma. (Vergara and Drake, 1978; Kay and Kurtz, 1995; Serrano et al., 1996; Lopez and Vergara, 1982). Three discrete intrusive events have been identified: 13-12 Ma, 8.5-8.3 Ma and 5.2 Ma. (Lopez and Vergara, 1982).

Whole-rock analyses show that the Al_2O_3 / CaO + K_2O + Na_2O ratio of individual intrusions varies between 1.37 and 1.57, indicating that the SFB is strongly peraluminous (Warnaars et al., 1985). Major element chemical analysis of the lavas and plutons of the SFB reveal medium to high K_2O calc-alkaline rocks, similar to other Andean volcanic and plutonic rocks in central Chile (Serrano et al., 1996). Trace element ratios (Ba/La; La/Yb) and relatively primitive mantle-like Sr, Nd, Pb, S and O isotopic compositions together indicate that these igneous rocks were derived by melting of sub-Andean mantle modified by the addition of a small proportion of components (<2%) from subducted oceanic crust (Serrano et al., 1996).

Tambillos Intrusions

The Tambillos Intrusions are exposed in a belt that is bound by the Chalinga Intrusions to the west and the San Francisco Batholith to the east (Fig. 1.2). The Tambillos Intrusion consist predominantly of leucocratic dacite porphyries that have a distinctive white colour in outcrop (Rivano, 1995). Based on K-Ar dating, the Tambillos Intrusions were emplaced during the late Miocene (9.8 to 6.5 Ma; Rivano, 1995).

Pliocene

La Parva Formation

La Parva Formation crops out as numerous discrete volcanic and sub-volcanic centres that have intruded into and erupted onto the Farellones Formation (Fig. 1.2). Although some authors have proposed that the Parva Formation is part of the Farellones Formation (e.g. Thiele et al., 1991), the two formations are separated here on the basis of the subvolcanic nature and the restricted areal extent of the former. In the vicinity of the Río Blanco-Los Bronces mine, a sub-volcanic sequence, considered part of La Parva Formation has crosscut rocks younger than the Farellones Formation (Thiele, 1980). The volcanic rocks within La Parva Formation are dominantly andesites with minor dacites, whereas the subvolcanic units consist of rhyolites and quartz porphyries (Thiele, 1980).

Subvolcanic Complex - Río Blanco

Volumetrically minor components of the SFB were emplaced during the Pliocene. These included monzodiorites, monzonites, quartz feldspar porphyries, dacite porphyries, dacites, rhyodacites and rhyolites (Rivano 1995). These are intimately associated with Cu-Mo mineralisation at the Río Blanco-Los Bronces mine.

The Río Blanco subvolcanic complex was emplaced between 5.2 Ma and 3.9 Ma (K/Ar age dates; Serrano et al., 1996). In chronological order, the complex consists of Feldspar Porphyry (PF), Quartz Monzonite Porphyry (PQM), Dacite Porphyry (PDL), a dacite 'chimney' (CHDAC) and a rhyodacite 'diatreme' (CHRÍOL; Serrano et al., 1996). These intrusions were emplaced after the main phase of Cu-Mo mineralisation at Río Blanco. They are characterised by high silica and low Ca, Mg contents (Vergara and Latorre, 1984).

Quaternary glaciation

River valleys in the vicinity of the Río Blanco mine are filled with glacio-fluvial debris sourced from steep scree slopes along U-shaped valley walls. Coarse, clastic materials (volcanic and volcaniclastic debris) in streams are poorly sorted and angular to sub-rounded. Sub-vertical to vertical valley walls contain sub-horizontal striations and smoothed surfaces that have resulted from large masses of ice and rock moving down the valley during summer months.

1.2 Ore deposits of central Chile

Central Chile is characterised by a variety of ore deposit types, ranging from breccia-related porphyry copper deposits in the Principal Cordillera to manto- and iron-oxide copper-gold deposits proximal to the Coastal Cordillera in the west. Río Blanco-Los Bronces is one of three giant breccia-related porphyry copper deposits that define the Late Miocene-Pliocene metallogenic belt of central Chile. The Los Pelambres and El Pachón deposit, located 200 km north of Santiago contain >25 million tonnes of contained copper (Fig. 1.1; Atkinson et al., 1996; Skewes and Stern, 1996). The bulk of the resource is hosted in biotite cemented breccias and in cross-cutting sulfide veins hosted within a quartz diorite stock and surrounding volcanic rocks (Skewes and Stern, 1996; Atkinson et al., 1996). South of Río Blanco-Los Bronces, also in the Principal Cordillera is the El Teniente porphyry copper deposit, located 100 km south of Santiago (Fig. 1.1). The El Teniente deposit is host to >70 million tonnes of contained copper, making it the single largest known deposit of copper on the planet. The copper resource at El Teniente is hosted mainly in a stockwork of cross-cutting veinlets, although recent publications (e.g. Skewes et al., 2002) suggest a substantial

resource of copper hosted in biotite-cemented breccias. In addition to copper, these three giant porphyry copper deposits are also host to substantial molybdenum resources.

The feature that separates the central Chilean porphyry copper deposits from their northern Chilean counterparts is the ubiquitous presence of large breccia bodies, and their associations with the mineralization process, particularly at Río Blanco-Los Bronces. Previous studies suggest that the formation of these three giant ore deposits are the result of complicated subcrustal processes related to the oblique subduction of the Juan Fernandez Ridge under central Chile (e.g., Stern and Skewes, 1995; Kay et al, 1999). The oblique nature of the ridge subduction has resulted in the southward migration of the locus, a convective front that when tapped by active fault systems in the upper crust released the necessary fluids involved in ore genesis. The decreasing age of the three giant ore deposits southwards from Los Pelambres (10 to 8.9 Ma) in the north, to Río Blanco-Los Bronces (7.3 to 4.2 Ma), and then El Teniente (4.8 to 4.0 Ma) in the south agrees with this notion (Skewes and Stern, 1996). However, without the generation of more robust datasets, these ideas remain nothing more than speculation.

In addition to the three giant porphyry copper-molybdenum deposits, extensive areas of apparently barren hydrothermal alteration and associated brecciation have been recognised in the Principal Cordillera (Fig. 1.2).

1.3 Regional Alteration and Brecciation

1.3.1 Alteration

Most of the Tertiary and older rocks throughout central Chile have been affected to some degree by hydrothermal alteration and/or metamorphism. Intense metasomatism however, is generally constrained to areas generally no more than 3 km^2 (Fig. 1.2). A spatial and temporal association with porphyry dykes and breccia bodies is apparent in the most intensely altered zones, particularly in the vicinity of the Río Blanco-Los Bronces ore deposit. Intense hydrothermal alteration is also focussed along fault zones such as the Pocuro Megafault.

Alteration assemblages in the region are propylitic or phyllic in character. They locally contain pyrite, quartz, tourmaline, jarosite, hematite, geothite and in some cases copper sulfides (Gana and Wall, 1996). Although some hydrothermally altered zones in the region contain copper ore, none are comparable to the amount of copper concentrated at the three giant porphyry deposits in the central Chile region (Los Pelambres, Río Blanco-Los Bronces and El Teniente; Fig. 1.1).

In the Río Blanco district, potassic alteration is restricted to the Río Blanco-Los Bronces mine

area. It is characterised by hydrothermal biotite and orthoclase (Serrano et al., 1996). A moderately developed halo of quartz-sericite alteration occurs in and up to 1 km around the Río Blanco-Los Bronces mine (Antoine, 1976). A transitional zone containing quartz-sericite and propylitic alteration in turn surrounds it. Propylitic alteration extends up to 5 km from the Río Blanco mineralised centre (Antoine, 1976).

1.3.2 Brecciation

The Cu-Mo ore deposits of central Chile are characterised by the presence of magmatic-hydrothermal breccia bodies. These bodies are small in plan, covering areas up to 500 m^2. The largest of these occurs at Río Blanco-Los Bronces, where several breccia bodies have coalesced within an area of approximately 3 km^2. Diamond drilling and underground mining has shown that the breccia bodies at Río Blanco extend to depths of greater than 1200 m below the present-day surface.

The breccias in central Chile generally consist of host rock clasts in a rock flour matrix and/or hydrothermal cement. The clasts are of volcanic or plutonic origin, and are derived primarily from the local wall rocks. The matrix cement is variable and locally consists of tourmaline, biotite, quartz, anhydrite and/or rock flour (Skewes and Stern, 1994). Clasts in the breccias are typically hydrothermally altered to silicic and/or phyllic mineral assemblages that contain pyrite, jarosite and copper sulfides in some areas.

1.4 Regional Structure of Central Chile

The crust in central Chile is divided into three main structural domains: 1) coastal; 2) central; and 3) cordilleran (Fig. 1.1; Rivano, 1995). The coastal domain occupies an area from the coast inland to the longitude of 71°00'W (Fig. 1.1). The central domain extends from 71°00'W eastward to the Pocuro Megafault at 70°30'W, east of the Los Andes township (Fig. 1.1). The cordilleran domain (host to the Río Blanco-Los Bronces ore deposit) lies between the Pocuro Megafault and the Chile-Argentina border (Fig. 1.1; Rivano, 1995). The structural evolution of central Chile in all domains has involved periods of both extension and shortening resulting in the development of normal, reverse and thrust faults as well as broad-scale open folds.

1.4.1 Coastal Domain

The coastal domain contains the oldest rocks exposed in the region. Consequently, it preserves the longest record of deformation, spanning from late Palaeozoic to the present. This terrane has undergone a complicated history of shortening involving sinistral transpression, resulting in the

clockwise rotation of isolated crustal blocks into their present NNW orientation (Rivano, 1995). Block rotation is expressed by strong, sub-parallel foliations within volcanic and sedimentary strata in the Jurassic Ajial Formation (Rivano, 1995). In addition, clasts within the La Ligua Formation (Triassic) and fossils in the Los Molles Formation (early Jurassic) have been reported as stretched and deformed by a probable clockwise rotation to their present orientation (Rivano, 1995). In the Los Molles Formation, broad foliated zones (up to 700 m wide) are most intensely developed proximal to high angle reverse faults (Rivano, 1995). Mylonites and porphyroblasts are also preserved locally, suggesting exhumation of relatively deep crust within the coastal domain (Rivano, 1995).

1.4.2 Central Domain

The central domain is composed mainly of Cretaceous volcanic and volcaniclastic units intruded by Cretaceous and Tertiary batholiths. These units are weakly deformed into broad, open folds, most of which are constrained to areas where horst and graben structures pre-dominate (Rivano, 1995). In the western part of this domain, the most prominent features are east directed monoclines that decrease in amplitude towards the east into mainly sub-horizontal strata (Rivano, 1995). The lack of deformation in the central domain is attributed to a combination of: i) abundant intrusive units that acted as buttresses to deformation and; ii) the relative competency of thick stratigraphic units, both of which are thought to have strengthened this belt considerably (Rivano, 1995).

1.4.3 Cordilleran Domain

The cordilleran domain forms the western flank of the Principal Cordillera. It is composed mainly of Cretaceous and Tertiary volcanic/volcaniclastic units that have been intruded by Tertiary batholiths. This domain has undergone considerable shortening, resulting in significant reverse faulting, folding, thickening and uplift (Rivano, 1995). The western part of this domain (near the Pocuro Megafault; Fig. 1.2) is characterised by normal faults with only minor displacement (Rivano, 1995). In the eastern sector, greater shortening has resulted in the development of macroscopic disharmonic folds with an overall vergence to the east , together with north-trending high angle reverse faults with significant displacement (Rivano, 1995). Shortening has also produced a lower angle reverse fault system with an eastward vergence, characteristically developed within the Farellones Formation (Rivano, 1995).

Open folding around a north-south trending fold axis has produced a large trough-shaped synclinorium in the central and cordilleran domains of the SVZ. Macroscopic folds within the cordilleran domain correspond to the prevailing thickness of the crust. At the time of deformation, the crust in this zone reached a potential maximum thickness of 65 km (Kay et al., 1991). Such a considerable thickness

of competent continental crust buckles at much greater wavelengths producing very large-scale folds usually unrecognisable at any one point in the field. Thick crust is also the likely precursor to the development of high angle faults with the current erosional surface potentially representing the upper extent of large listric fault zones at depth. Alternatively, the high angle nature of these reverse faults may have been produced from the reactivation of normal faults during basin inversion (Skarmeta et al., 2000).

1.4.4 Structural characteristics of the geological formations

Yeso Principal and Río Damas Formation

The Jurassic and Cretaceous successions in the Principal Cordillera have a spectacular outcrop pattern. They have a north-trending strike and dips ranging from sub-vertical to vertical (Fig. 1.2). Duplex thrusting on high angle reverse faults has placed these units over the younger volcanic and volcaniclastic rocks of the Los Pelambres Formation to the east of Rio Blanco (Fig. 1.2, cross-section A-A').

Los Pelambres, Las Chilcas and Coya-Machali Formations

Within the intra-arc of the Principal Cordillera and Central Valley, the Los Pelambres Formation and Las Chilcas Formation form the base of the northern SVZ within a broad basin-like syncline with a north-trending fold axis (Fig. 1.2, cross-section A-A'). The Los Pelambres Formation occupies the eastern limb, where vergence is to the east. The Las Chilcas Formation occupies the western limb, which has west-directed vergence. The axis of this basin has been sheared by the north trending Pocuro Megafault, which separates the Los Pelambres and Las Chilcas Formations (Fig. 1.2; Rivano, 1995).

The Los Pelambres Formation attains an average thickness of 3600 m and has mostly undergone thick-skinned deformation in the western part of the sequence. The formation thins towards the east, where thin-skinned deformation predominates (Sergio Iriarte, pers. comm., 2000). The transition in deformation style from west to east is a function of the crustal thickness and the lithological elements involved. Shortening is expressed generally as large, open folds (wavelength > 100 m) formed by a buckling mechanism involving flexural slip (Stambuk et al., 1993; Ramsey, 1967).

In the vicinity of the Río Blanco-Los Bronces ore deposit, the Los Pelambres Formation attains a potential thickness of up to 4-5 km (Skarmeta et al., 2000). Within the sequence there are marked changes in facies shape that have resulted from active horst and graben style structures during deposition (Skarmeta et al., 2000). In some areas, the dips are up to 80°, but the beds are so thick

that the entire folds are not observable at the mesoscopic scale. This broad scale folding of a thick stratigraphic sequence led to limited cleavage development. Furthermore, where cleavage has been developed it is generally weak, spaced, discontinuous and are only preserved near the hinges of folds.

Small-scale brittle faults are common in the Los Pelambres Formation with shear sense indicating periods of extension and compression. Extension generally produced N to NE striking normal faults. Compression generated high angle reverse faults with west over east shear sense indicators (Fig. 1.4), together with rollover angular unconformities in fault-bend folds (Fig. 1.4).

As for the Los Pelambres Formation, the Coya Machali Formation is moderately deformed (Drake et al., 1982). The western sector has been shortened by approximately 35% and contains west directed vergence indicators. The eastern sector has been shortened 45% and verges to the east (Drake et al., 1982). The irregular folding style of the Los Pelambres Formation, with its variable amplitude, longitude, tightness and vergence suggests that deformation is attributable to the inversion of faults associated with basin development (Charrier et al., 2002). The collective geometry of the Los Pelambres, Las Chilcas and Coya Machali Formations represent a trough-shaped, basin-like architecture for the intra-arc basin into which the rocks of the northern SVZ were deposited within the Principal Cordillera.

Salamanca Formation

Deformation endured by the Salamanca Formation has resulted in broad, open folds with limbs dipping no more than 20° and fold axes that strike NNW (Rivano, 1995).

Farellones Formation

In the southern (34°S - 34°45'S) and mid (33°15'S - 33°30'S) sectors of the SVZ, the Farellones Formation is thickest, deformation is characterised by thick-skinned tectonics which produced large, open, concentric style folds with wavelengths up to 8000 m and amplitudes up to 500 m (Vergara et al., 1988). However, in the northern sector (31°S - 33°S) the sequence tapers out and is characterised by thin-skinned tectonics involving low angle reverse faults (Vergara et al., 1988; Table 1.2). Geochemical studies by Kay and Kurtz (1995) indicate that the Farellones Formation was deposited in a tectonic regime involving lateral shortening and crustal thickening.

In the vicinity of the Río Blanco-Los Bronces ore deposit, the Farellones Formation contains broad synclines and anticlines bound by sub vertical NE striking normal faults with eastern blocks downthrown (Skarmeta et al., 2000). The traces of these faults reach up to 5-6 km in length. Both hydrothermal alteration and copper mineralisation are present, indicating that these faults were probably active during the mineralisation event (6-4 Ma).

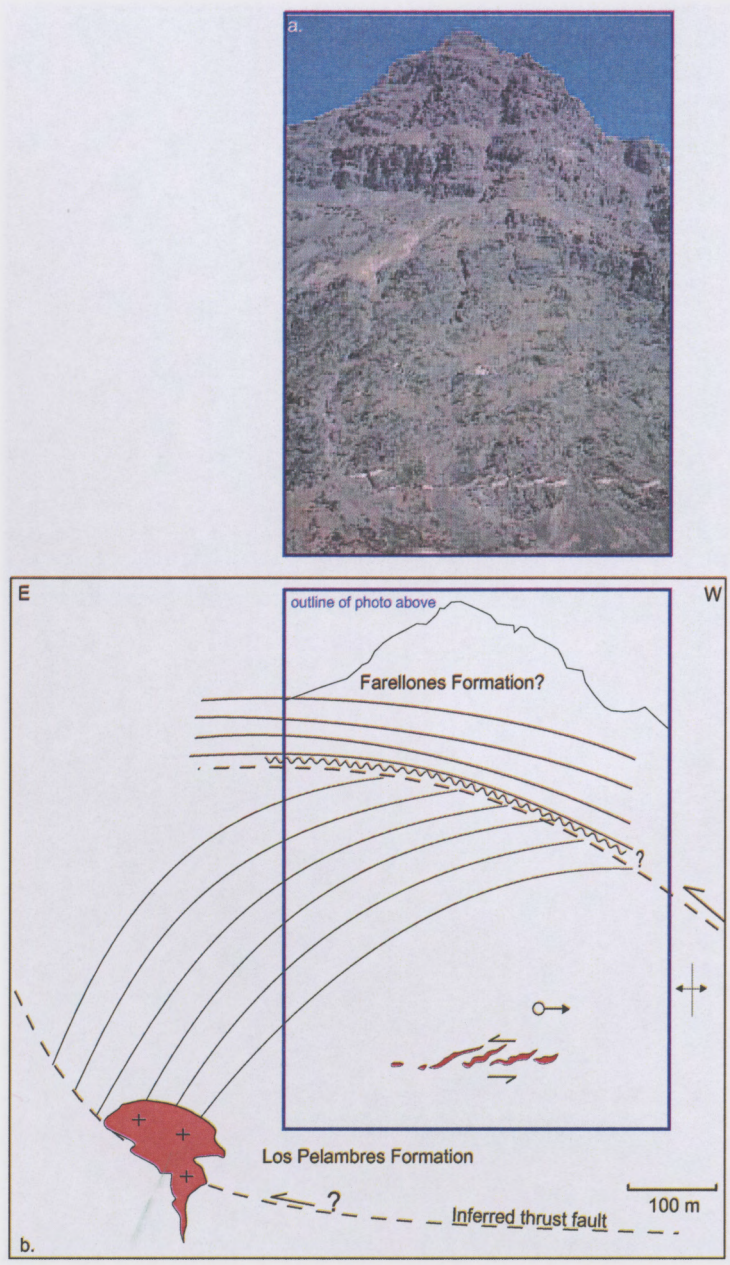

Figure 1.4. a. Photograph showing stratigraphic relationships of the Los Pelambres and Farellones Formations including west over east shear sense indicators (felsic dykes) and roll-over angular unconformities, Río Juncal, central Chile (location is shown in Fig. 1.2), b. Schematic interpretation of the stratigraphy from the photograph shown in 1.4a. Felsic intrusions are shown in red. (NB: the photo and cross section are viewed from the north).

1.4.5 Regional to ore deposit scale fault patterns

Evaluation of fault orientations in central Chile has involved the collation of data from the regional, district and ore deposit scales. The same fracture orientations are preserved at each scale of observation. All three structural domains contain the same three major fault sets: i) north-south; ii) north-east and; iii) north-west trending sets. These three fault sets are illustrated on a rose diagram (Fig. 1.5), which portrays the strike of each fault with appended length values from the Quillota y Portillo 1:250000 geology map.

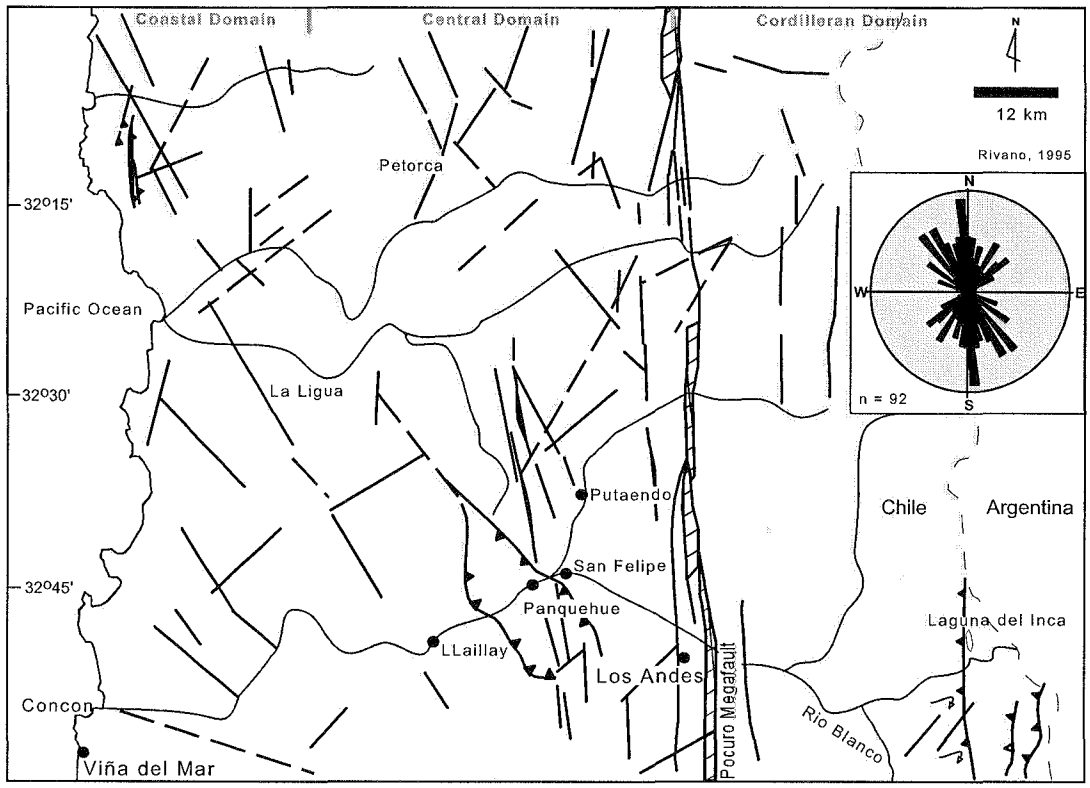

Figure 1.5. Faults in the Río Blanco region from the Quillota y Portillo 1:250000 geology map. The Rose diagram (inset) shows orientations and appended length value of the faults marked on the map.

The regional characteristics of each fracture set are as follows;

1. *North-trending faults:* These faults are most prevalent in the central and cordilleran domains, especially close to the Pocuro Megafault, a major N-trending, vertically dipping suture zone that separates the Central (Las Chilcas Formation) and Cordilleran domains (Los Pelambres Formation; Rivano, 1995). The fault zone is characterised by variable shear sense indicators, a highly sheared matrix and zones of hydrothermal alteration. These features indicate that this fault zone has been re-activated through a number of deformation events. Approximately 10 km north-east of the Los Andes township, the shear zone contains contorted blocks of Los Pelambres Formation within a strongly altered, light coloured, friable, iron oxide stained matrix. The Pocuro Megafault is exposed as many small, sub-parallel shear zones ranging up to 40 m wide separated by unsheared rock over an E-W width of approximately 250 m. The megafault may be an analogue (or southward continuation) of the West Fissure Fault in northern Chile.

   The Pocuro Megafault is surrounded by parallel subsidiary faults. In many cases, these smaller N-trending faults have been preferentially eroded, forming prominent north-trending lineaments preserved within the topography. A major north-trending fault to the east of the Pocuro Megafault is known as the Fierro Fault. It is a high angle, east-vergent

fault (Fig. 1.2). The Fierro Fault is interpreted to be an inverted normal fault that was active during initial basin development and deposition of the Abanico Formation (Skarmeta et al., 2000).

The Río Blanco-Los Bronces ore deposit is located along strike of a north trending fault zone (Río Blanco Fault; Skarmeta et al., 2000). This fault defines the Río Blanco valley north of the mine. Skarmeta et al. (2000) interpret this fault as high angle, east-dipping and with reverse shear sense. The Río Blanco and other N-S faults are considered to be basin accommodation structures (normal faults) that have been reactivated by shortening into high angle reverse faults upon basin inversion (Juan Carlos Castelli, pers. comm., 1999).

2. *Northwest-trending faults:* This fault set occurs throughout the Quillota y Portillo 1:250000 geology map and is prominent on the 1:10000 scale geology map of the Río Blanco-Los Bronces ore deposit produced by Alvarez (1999). Variable shear sense indicators (normal, thrust and strike/slip faults) occur and are attributed to reactivation through discrete deformation events (Rivano, 1995).

   In the central domain, ongoing shortening of structurally competent crust has resulted in the development of a major northwest trending fault system between San Felipe and Llaillay (Fig. 1.5). This fault system surrounds exposure of the Chalinga Unit, part of the Illapel Group, which is bound to the west by the Carbón Fault and to the east by the Giganta Fault (Rivano, 1995). Both major NW faults dip inward at high angle with respect to each other and with continued shortening, the Chalinga Unit was exhumed between the two faults to its presently exposed crustal level (Fig. 1.2 and 1.5; Rivano, 1995).

   The frequency of the NW fracture set intensifies in the same areas where the NE-trending fault set prevails, indicating an association between them. In conjunction with the NE fracture trend described below, the NW trend cuts all rock units in the Río Blanco ore deposit up to and including the Don Luis Porphyry (4.9-3.9 Ma; Serrano et al., 1996), an intrusive event that formed after the main-stage mineralisation event in the ore deposit.

3. *Northeast-trending faults:* These faults are preserved throughout the Quillota y Portillo 1:250000 geology map, the 1:10000 geology map surrounding the Río Blanco-Los Bronces ore deposit produced by Alvarez (1999) and within the ore deposit. No field data have been obtained from most of these structures, however where sense is observable on the regional and district scale maps, the faults display a normal sense of displacement. This fault set has cut all rock units up to and including the Don Luis Porphyry in the Río Blanco-Los Bronces ore deposit.

1.4.6 Regional Stress Fields

Lavenu and Cembrano (1999) carried out kinematic analysis of fault slip data on Miocene to Quaternary rocks in Chile between latitudes 33° and 46°S. Their results indicate well-defined s_1 orientations during the Pliocene to Quaternary periods. Unfortunately, late Miocene stress fields were not easily determinable for rocks in central Chile, however mid-Miocene coastal rocks at Lican (34°S latitude; Fig. 1.1) contain NE-striking normal faults, indicating an extensional regime (Lavenu and Cembrano, 1999). Kinematic indicators from Pliocene age faults delineate a s_1 orientation in an E-W direction. Consequently, the Pliocene represents a period of arc-normal shortening in central Chile (Lavenu and Cembrano, 1999).

Kinematic indicators in the Quaternary rocks of central Chile preserve two distinctive and coeval stress states. In the fore-arc zone, shortening occurred, with s_1 striking N-S to NNE-SSW (Lavenu and Cembrano, 1999). However, in the intra-arc zone the state of stress was transpressional, with s_1 striking NE-SW. This N-S style of shortening is only preserved in rocks south of 33°S latitude, i.e. south of the flat slab zone (Lavenu and Cembrano, 1999).

1.5 Tectonics of Central Chile

The tectonic evolution of western South America has been governed by subduction of first the Pacific Plate, and currently by the Nazca Plate, beneath the South American Plate since the Proterozoic (Frutos, 1990). This has involved the descent of oceanic crust beneath evolving continental crust above an east-dipping subduction zone. The result has been the development of the Andes mountain range, a linear mountain belt 8000 km long and 1000 km wide that extends from Venezuela in the north to southern Chile in the south (Frutos, 1990).

Central Chile was dominated by marine and marginal marine conditions in an oceanic fore-arc basin until the Mesozoic, when terrestrial influences began. However, the landmass of central Chile did not emerge above sea level until the early Cretaceous when the Pelambres Formation and its coeval equivalents began erupting in the active volcanic arc (SVZ) of the Principal Cordillera (Stern, 1989; Ramos, 1995).

The subduction rate in central Chile increased dramatically 25 m.y. ago, from 50 mm/year to 150-200 mm/year, when the Farellon Plate split into the Nazca and Cocos Plates (Pardo-Casas and Molnar, 1987; Ramos, 1995; Yañez et al, 2002). The increase in subduction rate was subsequently followed by the initiation of Farellones Formation volcanism in central Chile. Towards the late Tertiary, this active volcanic arc was interrupted by quiescent sub-crustal conditions initiated by a

reduced angle of the descending oceanic slab and subsequent waning of Farellones Formation volcanism (Stern, 1989).

Subduction rate along the western margin of South America has never been consistent due to variation in crustal thickness of the descending oceanic slab (Frutos, 1990). Variation in the thickness of oceanic crust arose from the development of oceanic ridges, large oceanic fracture zones or intra-plate volcanic activity such as hot-spot magmatism within the oceanic plate (Frutos, 1990). When these structures are subducted, they may produce changes in: (a) crustal architecture; (b) volcanic activity; (c) subduction rate; (d) seismic activity; (e) deformation; (f) thickness of the crust (uplift); (g) magma chemistry; and (h) style of ore deposits (Jordan et al., 1983; Frutos 1990; Kay et al., 1991; Stern and Skewes, 1995). A summary of the Tertiary tectonic evolution of central Chile is shown on Table 1.3.

Table 1.3. Summary of tectonic events in central Chile during the Tertiary (Ramos, 1995; Yañez et al, 2002; Kay and Mpodozis, 2002).

Time (Ma)	Tectonic events (27-34°S)	Far-field stress
~27-20	relatively steep subduction relates to distinct magmatic episodes, break-up of Farallon Plate at 25 Ma	extension
~20-16	frontal arc migration associated with forearc subduction erosion, changes in magmatic style and chemical signature reflect a transition from extensional to compressional tectonics	extension/shortening
~15-9	compressional deformation and andesitic volcanism, southward migration of the subducted Juan Fernandez Ridge and extreme slab flattening	shortening
~8-4	slab shallowing associated with frontal arc migration and arc broadening	shortening
~5	termination of volcanism over the flat slab	shortening

On the latitude of central Chile, the Nazca plate contains an elongate chain of volcanoes referred to as the Juan Fernandez Ridge (JFR). The ridge has an oblique orientation to the trench with a NE to ENE strike (Fig. 1.6). The subduction of the JFR began approximately 26 m.y. ago (Fig. 1.6; Kay et al., 1999; Pardo-Casas and Molnar, 1987). Seismic profiles through the Andes indicate a reduction in angle of the Wadati-Benioff zone at 28°-33° S in central Chile (Frutos, 1990). This flat slab zone in central Chile corresponds to the location where the JFR has been subducted beneath the South American Plate. The flat slab zone maintains a dip of approximately 5°-10° at about 100 km depth below the Andes and is flanked to the north and south by dips of 30° where no ridge subduction has occurred (Fig. 1.6; Ramos, 1995). This decrease in slab angle could be due to the buoyant nature of the descending ridge (Kay et al., 1991), which is hotter and thicker than the adjacent oceanic plate rocks.

The plate tectonic vector of the Nazca Plate during the past 5 -10 Ma has remained consistent, with an orientation of ~N79° at a velocity of 7.9 cm/year (Levanu and Cembrano, 1999). The

evolution of the subducting ridge beneath the overriding South American Plate is considered to have changed through time due to changes in the orientation of the JFR on the Nazca Plate. Von Huene et al. (1997) postulated that the rapid southward migration of the flat slab during the late Miocene proposed by Kay et al. (1991) is due to subduction of a NE striking segment of the JFR at that time. Subduction of an ENE striking segment has been ongoing since 8 Ma, causing the amount of southward migration to decrease significantly (Von Huene et al., 1997).

During the late Miocene to early Pliocene, dextral shearing along the western margin of South America in the vicinity of central Chile is thought to have buttressed the westernmost continental terrane against the southward migrating flat slab zone. This mechanism is thought to have produced the array of NE striking normal faults in the Principal Cordillera and Central Valley areas in central Chile (Levanu and Cembrano, 1999). The timing of this event broadly correlates with the cessation of volcanism, arc migration and emplacement of the three giant breccia-related porphyry Cu-Mo deposits in central Chile. The termination of volcanic activity and arc migration is considered to be associated with the relative quiescence in sub-crustal conditions below the Principal Cordillera as a result of slab underplating in central Chile (Kay et al., 1987, 1988, 1991; Stern and Skewes, 1995).

As well as a decrease in volcanic activity, Bonatti et al. (1977) demonstrated that where oceanic ridges, large oceanic fracture zones or hot-spot type volcanic alignments have been subducted beneath an overriding plate, there is a clear decrease in seismic activity. This phenomenon has been demonstrated at various locations under the Andes mountain chain where these structures have been subducted, including the latitude of central Chile where a paucity of slab earthquakes occur (Frutos, 1990; Cahill and Isacks, 1985; Kay et al., 1991).

The Benioff zone under the Andes of Peru and Chile is characterised by an aseismic gap that appears at 100 and 200 km depth, which exactly corresponds, in its normal projection, towards the surface to recent volcanic activity (Frutos, 1990). Hanus and Vanek (1978) proposed that this represents the partially melted zone, which is the source of primary magma for active volcanoes in the Andes. The exception is that no aseismic gap appears at 100-200 km in any of the zones where structures such as the JFR have been subducted, indicating the significant effects that ridge subduction has on the overriding continental crust (Frutos, 1990).

1.6 Regional Geochemistry

Central Chile has been a focus for research by several geochemists in recent years due to the geochemical affinities of volcanic and plutonic rocks that formed above and surrounding the flat

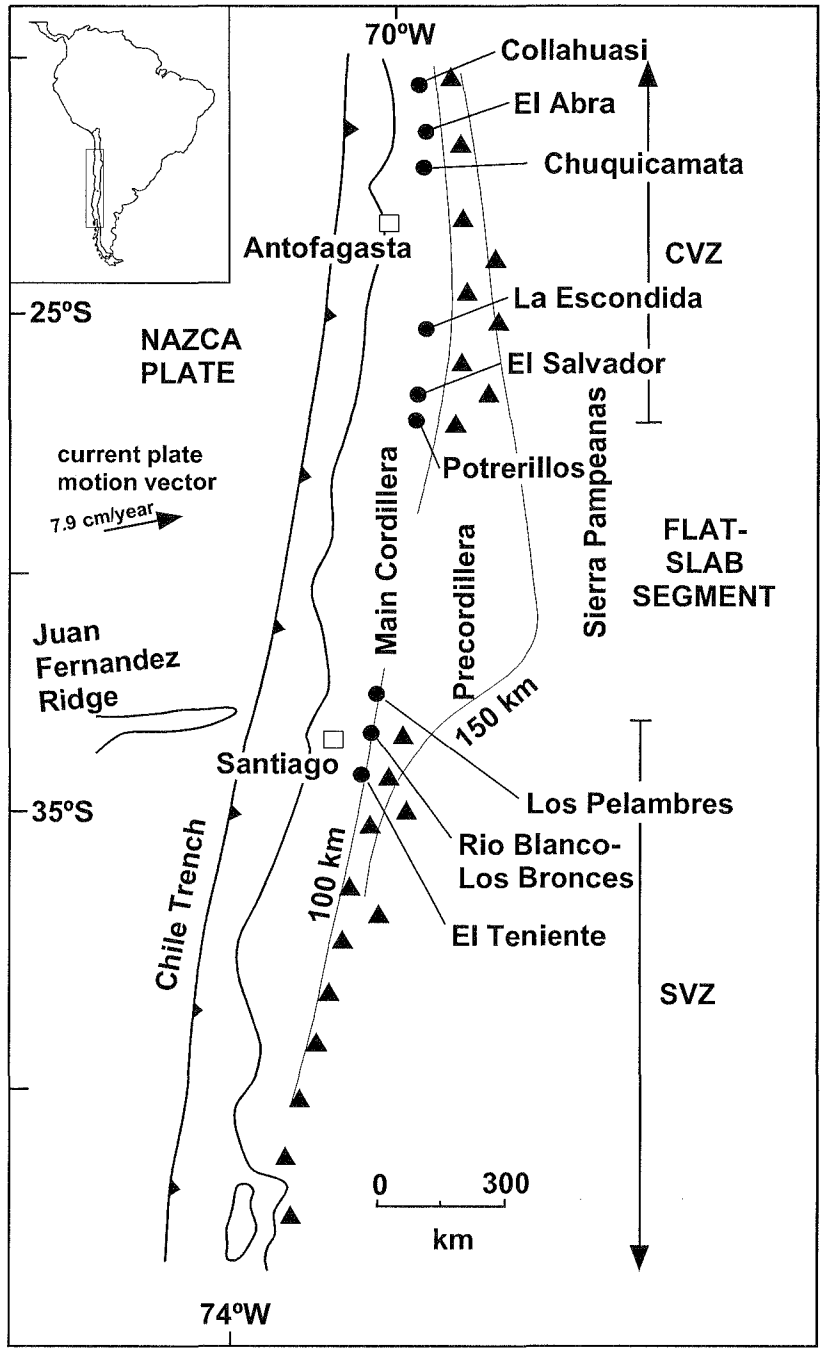

Figure 1.6. Flat slab segment and Juan Fernandez Ridge in central Chile (Serrano et al., 1996). Triangles = active volcanoes, circles = ore deposits, CVZ = Central Volcanic Zone, SVZ = Southern Volcanic Zone.

slab subduction zone (Fig. 1.6; Gutscher et al., 2000). Studies by Kusakabe et al. (1984), Vergara et al. (1988), Kay et al. (1991) and Stern and Skewes (1995) have provided some important insight into the evolution of the subduction zone with the recent and ongoing descent of an aseismic ridge. These studies have incorporated various geochemical analyses including major element, rare earth element, incompatible trace element, La/Yb ratios, fluid inclusion and isotopic data including strontium, neodymium, oxygen, hydrogen and sulfur.

The major element chemistry of the volcanic and intrusive rocks in central Chile indicates medium-K calc-alkaline to mildly tholeiitic continental-arc affinities (Kay et al., 1991). Late Oligocene to early Miocene volcanic rocks (Los Pelambres and Farellones Formations) of the northern and central flat slab region (Fig. 1.6) show broad ranges in SiO_2 (52-76%), this is also reflected in volcanic rocks south of the flat slab at approximately 35°S (51-69%; Kay et al., 1991). However, samples analysed from the central flat slab are more potassic compared to the northern and southern flat slab (Kay et al., 1991). By the mid-late Miocene, the volcanic rocks from the flat slab region developed a more restricted compositional range (56-68% SiO_2, but mostly 60-64% SiO_2; Fig. 1.6; Kay et al., 1991).

The evolving characteristics of the flat slab magmatic rocks from north (28°-30°S) to south (33°S) in central Chile suggests that crustal thickening occurred earlier in the north and central regions compared to the south. Kay et al. (1991) approximated crustal thickening in the flat slab zone mainly by La/Yb ratios applied to similar rocks along the belt. They speculated that the crust thickened from ~35–40 km in the late Oligocene to ~55-65 km in the late Miocene in the northern and central flat slab zone. These relatively rapid increases in crustal thickness are considered to be attributable to ductile deformation in the lower crust accompanying magmatism under a shortening tectonic regime (Stern, 1989; Kay et al., 1991).

Kay et al. (1991) found that the mineralogy of crustal residues (calculated from parental basalt compositions) for the flat slab volcanic rocks changed from a hydrous amphibole-garnet-plagioclase assemblage to an almost anhydrous plagioclase-poor garnet granulite assemblage as the crust thickened. These changes are reflected by increasing La/Yb ratios and Sr contents associated with decreasing Eu anomalies (Kay et al., 1991).

Kay et al. (1999) attribute the increases in the La/Yb ratio of magmatic rocks in central Chile to the changes in pressure driven by crustal shortening, ridge subduction, underthrusting of older basement and subsequent crustal thickening. Alternatively, the increases in the La/Yb ratios may simply be product of fractionation and not in any way related to crustal thickening. Analogous to temporal increases in La/Yb ratios, Kay et al. (1999) also documented higher Sm/Yb ratios in successively younger magmas, which is explained by changes from clinopyroxene to amphibole to garnet in the mafic mineral residue.

Evidence from Sr isotopes also supports crustal thickening in the flat slab zone, where early Miocene (~20 Ma) back-arc alkaline basalts have relatively low $^{87}Sr/^{86}Sr$ ratios (~0.7036) and high epsilon Nd (+4.5) compared to the flat slab calc-alkaline magmatic rocks (Kay et al., 1991). This fact in combination with evidence for increasing crustal thickness corresponds to increasing crustal contamination through time. However, recent regional geochemical studies by Hollings et al. (submitted) do not support gradual crustal thickening, but rather they suggest that anomalously high

La/Yb ratios and Sr in subvolcanic rocks from the Río Blanco-Los Bronces ore deposit relates to rapid crustal thickening associated with the subduction of the Juan Fernandez Ridge.

1.7 Summary

Important background information relevant to this study;

- The Principal Cordillera in central Chile emerged above sea level during the Cretaceous with the eruption and deposition of volcanic and volcaniclastic rocks associated with the Southern Volcanic Zone (SVZ).
- The volcanic and volcaniclastic rocks of the SVZ (Los Pelambres, Las Chilcas and Coya Machali Formations) formed a trough-shaped intra-arc synclinorium consisting of horst and graben structures (Fig. 1.7).
- The break-up of the Farallon Plate into the Nazca and Cocos Plates 25 m.y. ago resulted in an increased convergence rate, resulting in shallowing of the subduction zone.
- Subduction of the Juan Fernandez Ridge occurred at approximately 26 Ma but did not begin to affect the crustal architecture in the Principal Cordillera until between 15 and 9 m.y. ago where andesitic volcanism, southward migration of the subducted Juan Fernandez Ridge and extreme slab flattening occurred. Andesitic volcanism produced the relatively flat lying Farellones Formation along the axis of the trough-shaped SVZ.
- The extensional tectonic regime changed to shortening between 20 and 16 m.y. ago. This resulted in the onset of plutonism in the Principal Cordillera and the emplacement of the San Francisco Batholith, host to the Río Blanco-Los Bronces ore deposit.
- Southward migration of the flat slab zone slowed down at approximately 8 Ma when the orientation of the Juan Fernandez Ridge changed to ENE. Subsequently, Farellones Formation volcanism waned.
- By late Miocene the San Francisco Batholith had cooled, the crust had thickened up to 65 km in the Principal Cordillera and continued magmatism focussed fluids necessary for ore deposit formation at Río Blanco between 7.4 and 4.2 Ma (Fig. 1.7; Kay et al., 1991; Serrano et al., 1996).
- At 5 Ma, volcanism terminated over the flat slab zone.

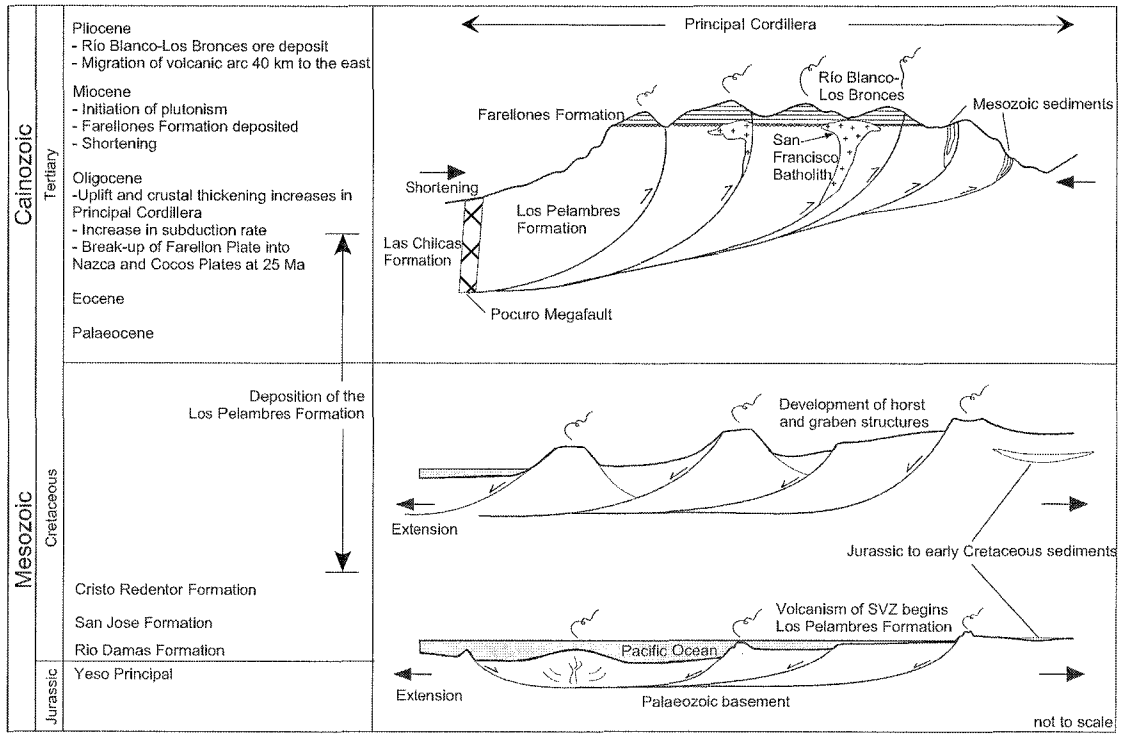

Figure 1.7. A schematic summary diagram featuring the evolution of the Principal Cordillera that the Río Blanco-Los Bronces ore deposit was emplaced within.

SECTION 2 - GEOLOGICAL EVOLUTION OF RIO BLANCO

2.1 Introduction to Río Blanco

This section discusses the geological evolution of Río Blanco using a combination of available public domain literature, CODELCO data and new information generated in this study. The interpretations given in this section are those of the author, except where otherwise cited.

2.1.1 Resource, reserves and mining

Although Río Blanco and Los Bronces are parts of the same hydrothermal system (Fig. 2.1), they are mined separately by different companies. The Los Bronces sector of the ore deposit has been mined since 1864. Early mining extracted high-grade ore (10-20% Cu) intermittently up until 1921 when Compañia Minera Disputada de las Condes established a larger operation. This continued between 1978 and 2002 when Exxon Corporation owned and operated the mine. Current production is on the order of 37,000 metric tonnes per day at 1.2% copper (Serrano et al., 1996). Reserves have been estimated at 457Mt @1.03% Cu plus 741Mt @ 0.47% Cu leach ore (31/12/00). Production in 2001 was 171,000 tonnes of copper in concentrate and 12,000 tonnes of copper cathode (Website: Anglo American). Anglo American purchased the Los Bronces mine in 2002.

East of the Los Bronces mine, the Río Blanco (Andina) orebody (Fig. 2.1) was discovered by Cerro Corporation in the early 1970's, however the operation was annexed to CODELCO (the state owned Chilean mining company) in 1976. Río Blanco contains four main centres of mining:

1) The Río Blanco underground mine with a current production of 15,000 metric tonnes per day at 1.0% copper;
2) The Sur-Sur open pit mine, with a current production of 20,000 metric tonnes per day at 1.5 % copper (Serrano et al., 1996).
3) Don Luis sector, resource for future production; and
4) La Union sector, resource for future production.

The current overall, combined resource of Río Blanco and Los Bronces is 7 billion metric tonnes at 0.75% copper and 0.02% molybdenum (Camus, 2002). This equates to 52.43 million metric tonnes of copper metal and 1.26 million metric tonnes of molybdenum (Camus, 2002).

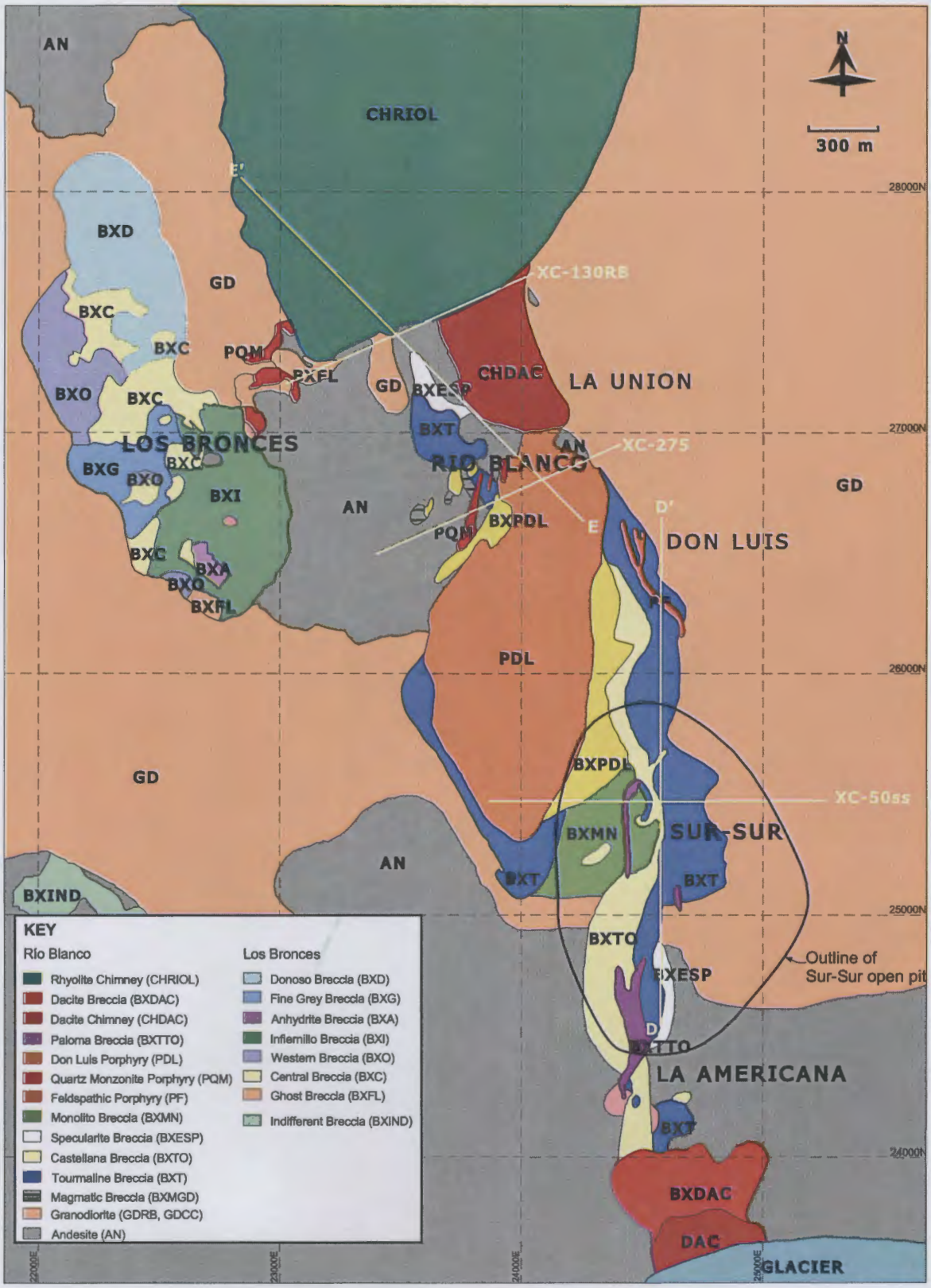

Figure 2.1. Geology map of the Río Blanco-Los Bronces ore deposit complex (modified after Contreras and Vargas et al., 1994). The host granodiorite (GDRB, GDCC) represent facies of the San Francisco Batholith. Cross sections used in this study are shown in yellow.

2.2 Ore Deposit Geology

2.2.1 Host Rocks

In the mine area, the Los Pelambres and Farellones Formations comprise late Cretaceous to late Tertiary volcanic and volcaniclastic rocks (Figs. 1.2 and 2.1). The Los Pelambres and Farellones Formations consist of basaltic andesite, trachyandesite, dacite lavas and volcaniclastic rocks that crop out as a 700-1200 m thick flat-lying sequence at Cerro Negro, 2.4 km to the east of the mine (Stambuk et al., 1985, 1988; Serrano et al., 1996). Samples from the Farellones Formation close to the ore deposit have been dated at 18.5 Ma (K/Ar, plagioclase; Table 2.1, Fig. 2.2). Andesite from within the ore deposit has not been dated due to the pervasive biotite alteration associated with mineralisation (Fig. 2.3a). The volcanic rocks in the mine area host approximately two percent of the total ore reserve (Stambuk et al., 1985).

The volcanic and volcaniclastic rocks of the Los Pelambres and Farellones Formations were intruded by the San Francisco Batholith (SFB; Fig. 2.3b). The location of the contact zone between the overlying volcanic and volcaniclastic rocks and the underlying granodiorite is shown in longitudinal section E-E' in Figure 2.4. The SFB comprises many different phases of granitoid across its 200 km^2 areal extent. The Río Blanco-Los Bronces ore deposit is hosted mainly in two phases (Fig. 2.1): the Río Blanco Granodiorite (GDRB) in the northern sector and the Cascada Granodiorite (GDCC) in the southern sector. Both of these rock units consist mainly of granodiorite, quartz monzonite, tonalite and diorite (Stambuk et al., 1988). The GDRB is characterised by a coarser grainsize, greater abundance of orthoclase feldspar and plagioclase with albite-andesine compositions compared to the GDCC. The GDCC has a finer grain-size and is enriched in Ca-plagioclase (oligoclase-andesine; Stambuk et al., 1988).

Cooling ages of unaltered hornblende, biotite and plagioclase feldspar (K/Ar and Ar/Ar geochronology) for the SFB are between 20.1 and 7.4 Ma (Table 2.1, Fig. 2.2; Serrano et al., 1996). In addition, two Ar/Ar ages have been obtained but they are considered to be reset by hydrothermal activity associated with the ore deposit (5.4 and 5.2 Ma, whole-rock and sericite ages respectively; Serrano et al., 1996, Table 2.1).

Table 2.1. K/Ar and Ar/Ar ages (Ma) for igneous rocks and breccias associated with the Río Blanco-Los Bronces ore deposit. rock, Sernageomin = Servicio National de Geologia y Minera - unpublished data (adapted from Stambuk et al., 1993; Serrano e

Geologic Unit	Rock Type	Material analysed	K-Ar age	Ar-Ar age	Reference
Farellones Formation	Andesite	Plagioclase	18.5 ±0.2		Vergara and Drak
	Rhyolitc tuff	Plagioclase	17.3 ±0.3		Vergara and Drak
San Francisco Pluton	Quartz monzonite	Hornblende	20.1±2.0		Warnaars et al., 19
	Hornblende diorite	Hornblende		18.5 ±1.7	Warnaars et al., 19
	Quartz monzonite	Biotite	15.9 ±0.6		Warnaars et al., 19
	Quartz monzonite	Biotite		14.9 ±0.07	Sernageomin, 199
	Granodiorite	Plagioclase	13.6 ±0.2		Vergara and Drak
	Hornblende diorite	Biotite		12 ±0.5	Warnaars et al., 19
	Granodiorite	Biotite		11.7 ±0.9	Stambuk et al., 19
	Quartz monzonite	Biotite	11.3 ±0.4		Warnaars et al., 19
	Granodiorite	Biotite	10		Ruiz et al., 1965
	Granodiorite	Hornblende	8.6 ±0.9		Warnaars et al., 19
	Granodiorite	Plagioclase		8.6 ±0.1	Vergara and Drak
	Granodiorite	Plagioclase		8.4 ±0.2	Vergara and Drak
	Granodiorite	Biotite	7.9 ±0.4		Warnaars et al., 19
	Granodiorite	Biotite		7.4 ±0.1	Warnaars et al., 19
	Biotised Granodiorite	WR		5.4 ± 0.3	Sernageomin, 199
	Sericitised quartz monzonite	Ser		5.2 ± 0.3	Warnaars et al., 19
Rio Blanco breccia complex	Magmatic Breccia	WR-cement	7.3 ±0.7		Sernageomin, 199
	Tourmaline Breccia	WR	7.1±0.8		Sernageomin, 199
	Magmatic Breccia	Biotite		4.6 ±0.1	Munizaga, 1994
	Magmatic Breccia	K-feldspar		4.2 ±0.1	Munizaga, 1994
La Americana breccia complex	Tourmaline Breccia	WR	5.9 ±0.2		Spröhnle, 1988
Sur-Sur breccia complex	Tourmaline Breccia	WR	5.3 ±0.2		Spröhnle, 1988
	Tourmaline Breccia	WR	5.1±0.2		Spröhnle, 1988
	Paloma Breccia (BXTTO)	WR	5.2 ±0.2		Spröhnle, 1988
	Monolito Breccia	WR	5.2 ±0.4		Sernageomin, 199
Late porphyries	Quartz Monzonite Porphyry	K-feldspar	5.2 ±0.3		Blondel, 1980
	Quartz Monzonite Porphyry	K-feldspar		5.2 ±0.01	Munizaga, 1994
	Don Luis Porphyry	K-feldspar	4.9 ±0.1		Munizaga, 1994
	Don Luis Porphyry	Biotite	4.6 ±0.8		Quirt et al., 1971
	Don Luis Porphyry	WR	4.5 ±0.4		Rojas, 1985
	Don Luis Porphyry	Biotite	3.9 ±0.7		Sernageomin, 199
Rio Blanco subvolcanic complex	Dacite porphyry dyke	Biotite	4.9 ±0.2		Warnaars et al., 19
	Rhyolite porphyry	Plagioclase	4.9 ±0.2		Vergara and Drake
	Dacite porphyry	Biotite	4.8 ±0.2		Warnaars et al., 19
	Rhyolite porphyry	Biotite	4.6 ±0.1		Quirt et al., 1971
	Rhyolite porphyry	Biotite	4.3 ±0.4		Toro, 1986
	Rhyolite porphyry	Biotite	4.1±0.1		Vergara and Drake
	Rhyolite porphyry	Biotite	3.9 ±0.1		Quirt et al., 1971

Whole
996).

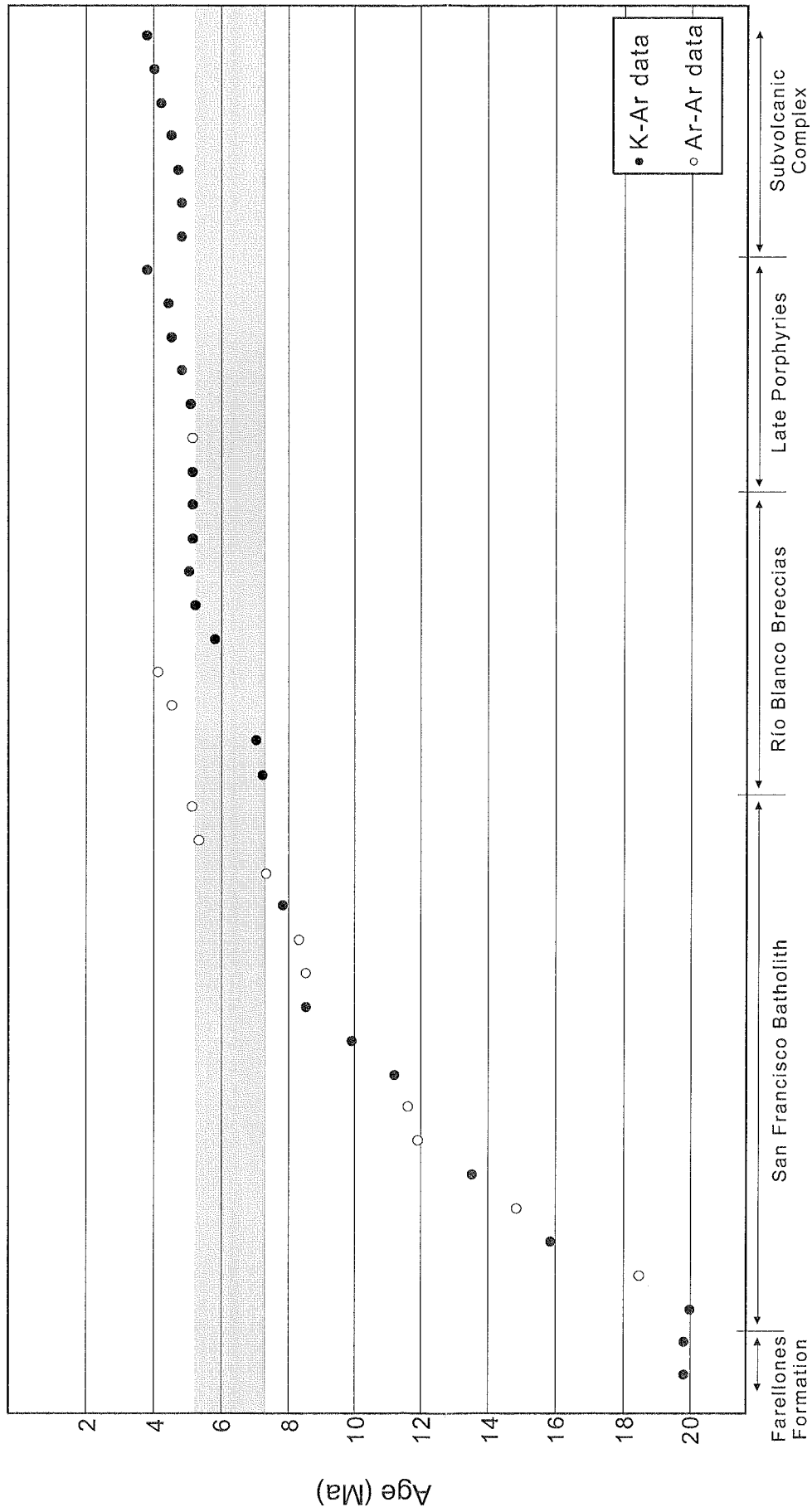

Figure 2.2. Graphical representation of ages plotted from data in Table 2.1.

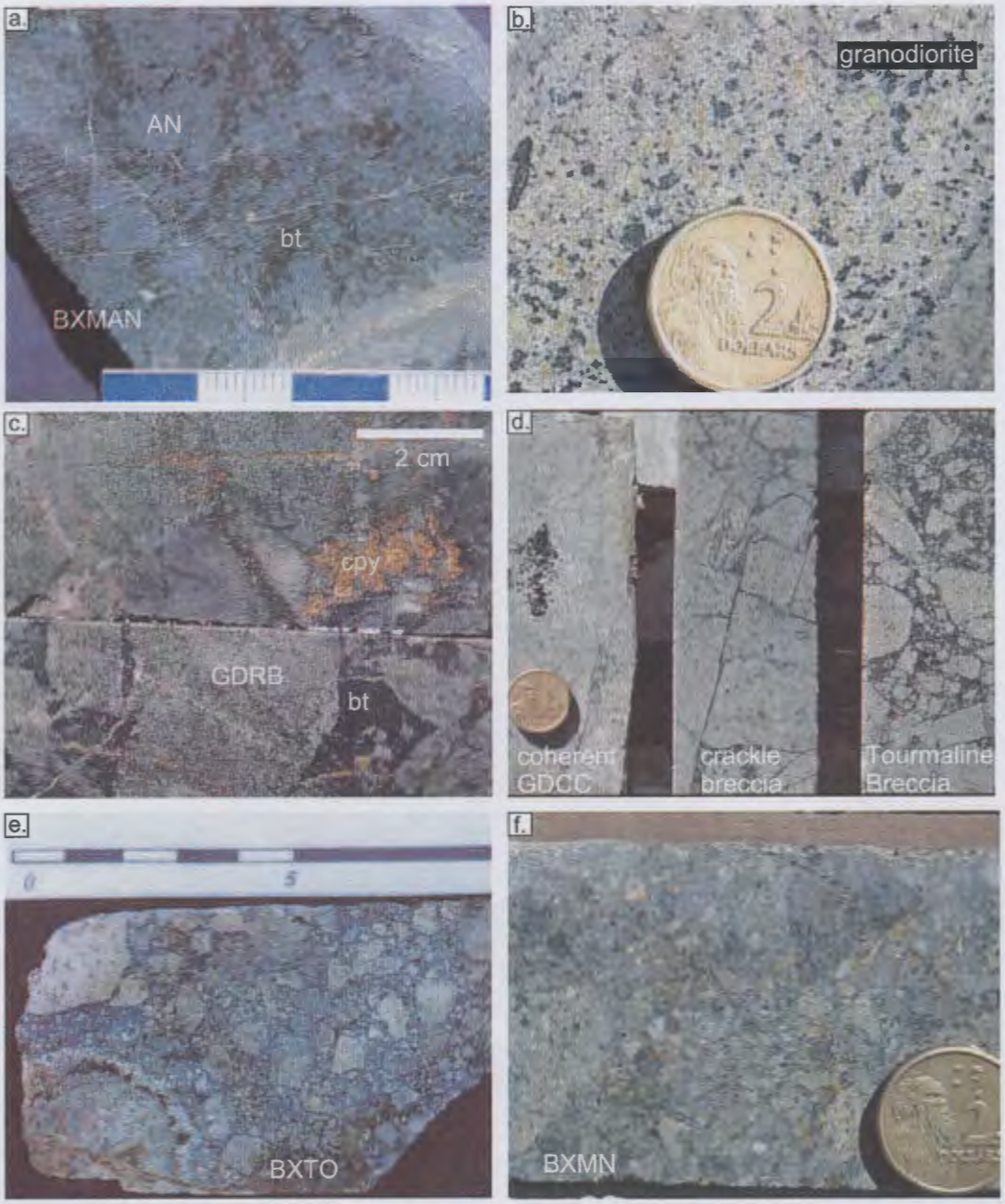

Figure 2.3.
a. Andesite host rock with pervasive biotite alteration (BXMAN, DDH-352, sample 251d);
b. Representative sample of granodiorite (GDCC) part of the San Francisco Batholith host rock in Sur-Sur, commonly contains quartz-sericite alteration (section XC 50);
c. Magmatic Breccia (BXMGD) from the Río Blanco sector, contains GDRB clasts and biotite cement (section XC 125, DDH-450, sample 239e);
d. Representative samples of Tourmaline Breccia (BXT) in the Sur-Sur sector, commonly transitional from tourmaline cemented breccia, through zones of crackle breccia to zones of coherent host granodiorite (section XC 50);
e. Castellana Breccia (BXTO) contains a variety of fragments including host andesite and granodiorite (GDCC), BXT, PDL and BXMN in a quartz-sericite altered rock flour matrix (section XC 130, DL-138, sample 85);
f. Monolito Breccia (BXMN) contains a variety of clast types including host andesite and granodiorite (GDCC), BXT, PF and PDL in a chlorite altered rock flour matrix (section XC 50, TSS-04).
Note scale: Australian $2 coin is 1.5cm in diameter.

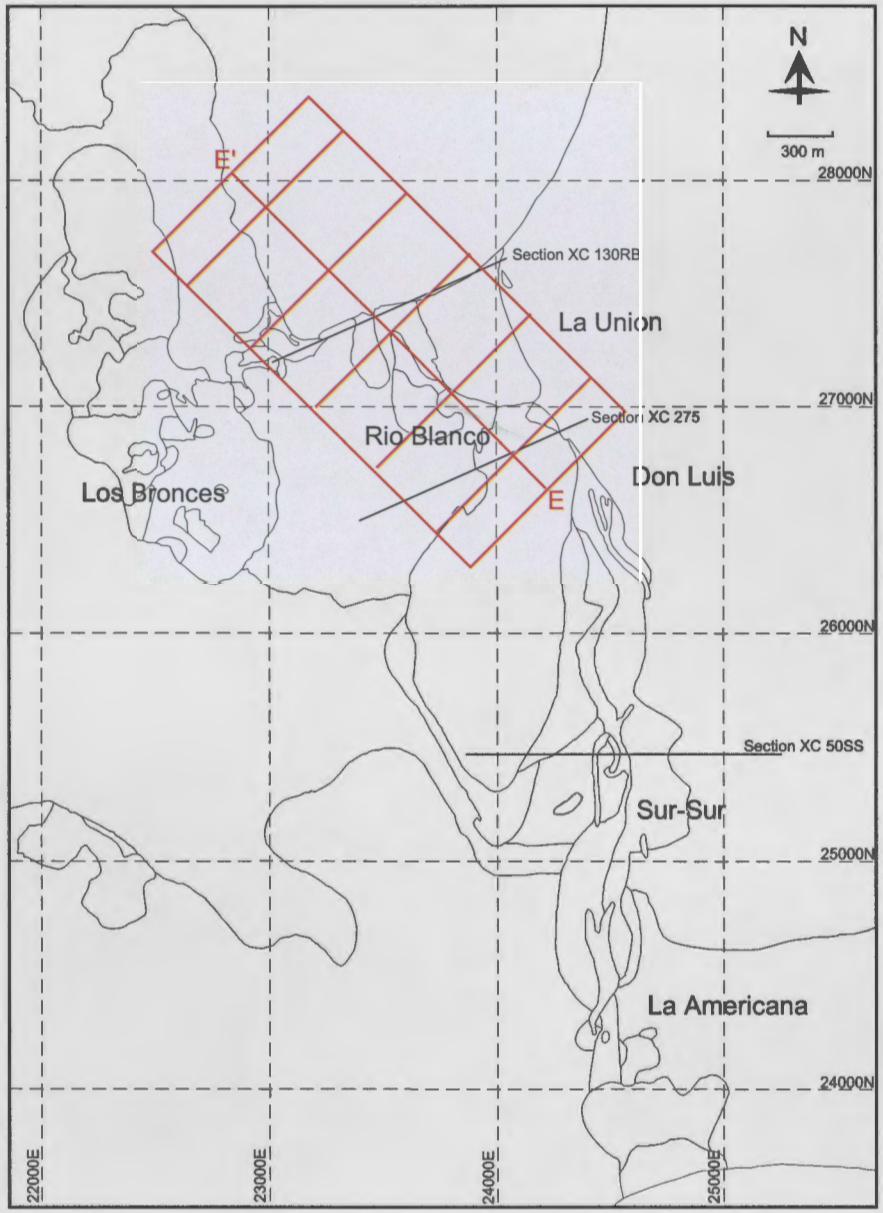

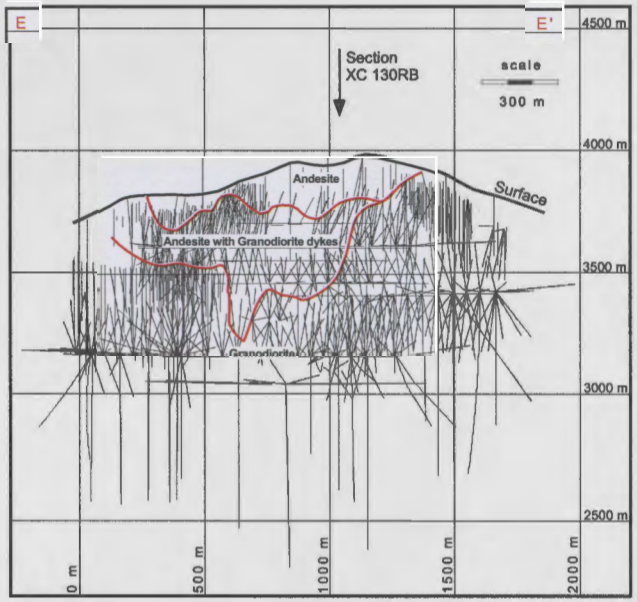

Figure 2.4. Longitudinal section E-E' through the Río Blanco sector showing the contact between overlying volcanic and volcaniclastic rocks and the granodiorite of the San Francisco Batholith. Red rectangle in map plan is the extent of drillcore coverage.

2.2.2 Río Blanco Breccia complex

Geology

In the Río Blanco sector, ore is hosted in a 'magmatic breccia' unit (mine terminology) within the Río Blanco Granodiorite and overlying volcanic rocks where clasts of either granodiorite or andesite are supported within a biotite-cemented matrix (Figs. 2.1 and 2.3c). Some contention exists as to whether the overlying andesites are part of the Los Pelambres or the Farellones Formation, with most workers preferring the Farellones Formation (e.g. Hollings and Frikken, 2001).

The conventional definition of a magmatic breccia is any rock with a crystalline, igneous cement (igneous-cemented breccia, e.g. Davies et al., 2000). However, the "magmatic breccia" at Río Blanco contains clasts that are supported by an interstitial material that ranges from a fine-grained, partially recrystallised microgranular hydrothermal cement to a rock flour matrix composed of altered, broken mineral and clast fragments. The matrix of the breccia has been either partly or wholly replaced by hydrothermal minerals that include biotite ± sulfides ± sulfates ± quartz ± magnetite ± specularite ± tourmaline. Anhydrite, chalcopyrite, magnetite, tourmaline or quartz are the predominant hydrothermal cements locally.

Heterogenous brecciation has caused the degree of attrition to vary spatially resulting in variable proportions of rock flour matrix and clasts across the Magmatic Breccia. The clasts are also variable in size (2 mm to >5 m wide). As a general rule, smaller clasts are more rounded.Throughout the breccia, angular to sub-angular clasts predominate. The clasts of andesite and granodiorite have been altered, with primary igneous minerals replaced by secondary biotite ± magnetite ± sulfides ± K-feldspar (Fig. 2.3c, d). In general, the intensity of alteration of the clasts has been much less than that of rock flour contained in the breccia matrix (Fig. 2.3d, e, f).

Figure 2.5 is a geological cross-section through section XC-130RB. It has been compiled by combining data from cross sections XC-125 and -135, which are spaced 30 m apart in the Río Blanco sector (Fig. 2.1). It shows the approximate margins of the Magmatic Breccia, which are generally defined by a gradual decrease in brecciation and alteration over tens of metres. In some areas, sharp contacts with coherent granodiorite have been recognised. The bottom of the Magmatic Breccia is poorly defined. However, it occurs at least 800 m below the contact of the granodiorite and the overlying andesite at 2600 m elevation (Fig. 2.4).

One of the deepest drill holes into the Magmatic Breccia is located in the Don Luis sector (section XC-275, DDH-734, between the Río Blanco and Sur-Sur sectors; Fig. 2.1). This drillhole intercepted deformed zones within the Magmatic Breccia, which are characterised by a contorted fabric composed of elongate (sheared) granodiorite clasts and broken crystals. These clasts are sup-

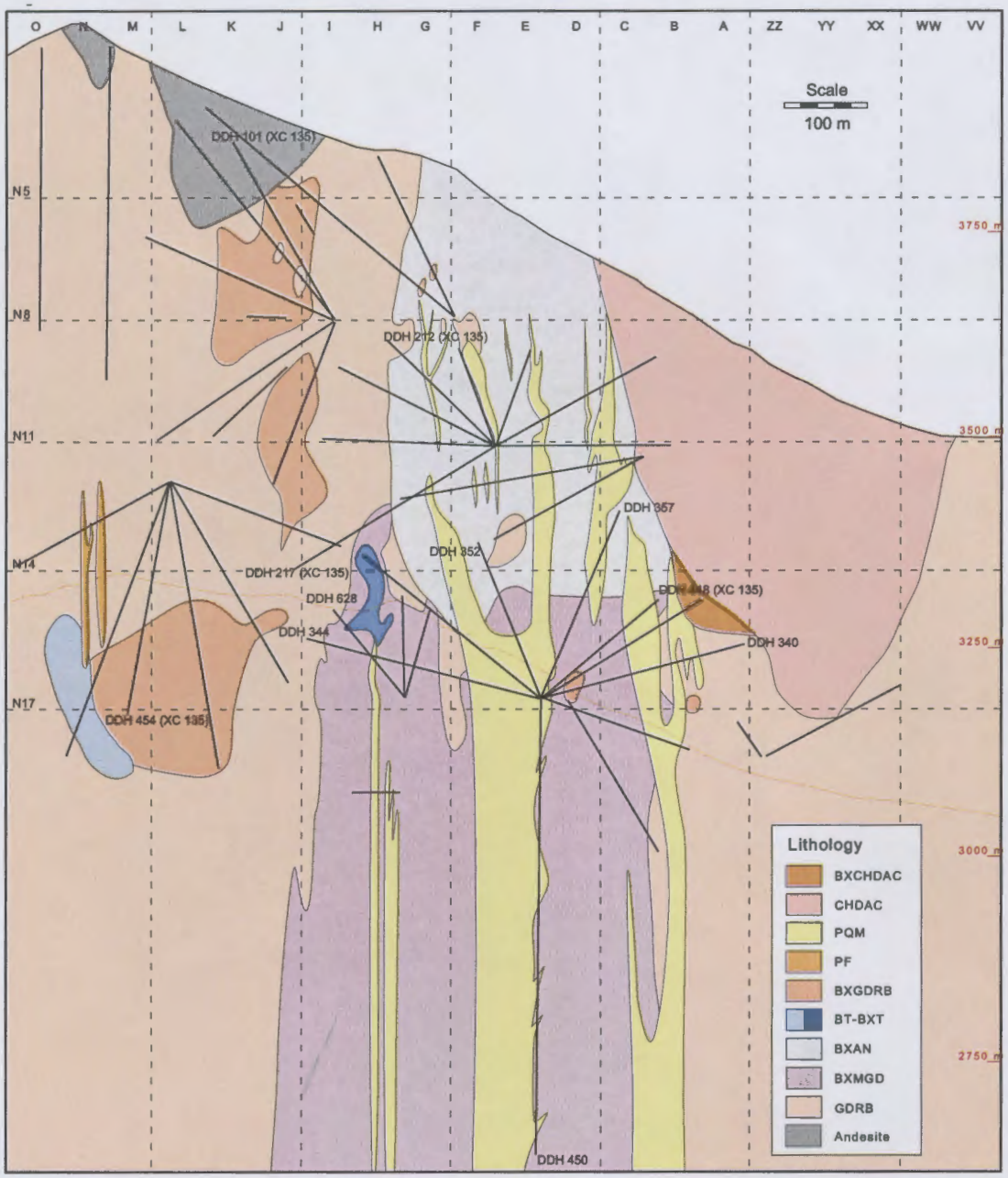

Figure 2.5. Cross-section XC-130RB showing the rock units through the Río Blanco sector. GDRB = Río Blanco granodiorite; BXMGD = Magmatic Breccia; BXAN = brecciated andesite; BT = tourmaline breccia with <5% tourmaline; BXT = Tourmaline Breccia with 5-15% tourmaline; BXGDRB = brecciated Río Blanco granodiorite; PF = Feldspar Porphyry; PQM = quartz monzonite porphyry; CHDAC = dacite chimney; BXCHDAC = brecciated dacite chimney. Location of section XC-130RB shown in Figure 2.1.

ported in a matrix of finer-grained crystal fragments with preferred alignment and hydrothermal biotite, which has grown along clast boundaries and replaced some of the crystal fragments. This indicates that at least some ductile deformation of the granodiorite pre-dated hydrothermal biotite deposition.

The Magmatic Breccia was emplaced between the late Miocene and early Pliocene based on K/Ar and $^{40}Ar/^{39}Ar$ radiometric age determinations between 7.3-4.2 Ma (Table 2.1; Fig. 2.2; Serrano et al., 1996).

2.2.3 Sur-Sur breccia complex

Geology

The Sur-Sur sector is characterised by the presence of four distinct breccia bodies that crop out over a >5 km long belt striking N10° to 30°W (Fig. 2.1). They generally have sharply defined and steeply dipping contacts with the surrounding host rocks, and the breccias have a known vertical extent of >1000 m below the present surface (Serrano et al., 1996). The Tourmaline Breccia (BXT) is truncated along its western boundary by the Castellana breccia (BXTO; Fig. 2.1). The contact between the two breccias is typically abrupt and clasts of BXT in BXTO are common (Vargas et al., 1999). Westward, BXTO grades into Monolito Breccia (BXMN) with a coalescent, indistinct contact between them (Vargas et al., 1999). The Paloma Breccia (BXTTO) forms well-defined and narrow dykes that cut the other breccias (Vargas et al., 1999). These four main breccia facies are shown on Figure 2.6 and are described in detail below.

Tourmaline Breccia (BXT)

The Tourmaline Breccia is monolithic and hosted in the Cascada Granodiorite. It consists of variable sized granodiorite clasts supported by a milled rock flour matrix that has been almost completely replaced by secondary tourmaline cement. In addition, the cement also contains variable amounts of sulfide, sulfate (anhydrite, gypsum), quartz, magnetite, specular hematite and biotite. Open spaces in the breccia have been filled by tourmaline-quartz-sulfide cement. Cement varieties include coarse tourmaline, specular hematite (at higher elevations), sulfides and quartz. Tourmaline cement throughout the BXT matrix is typically fine-grained and anhedral, however in some cases tourmaline is acicular and has grown into both clasts and matrix from the clast margins. BXT has been subdivided on the basis of its tourmaline content by Serrano et al. (1996) as shown in Table 2.2. Where matrix content is low (BT-BXT; Table 2.2; Fig. 2.3d), clasts are generally angular to sub-angular, but with increasing matrix content (BXTT) they are more rounded due to milling during breccia formation. Clast size ranges from fragments less than a millimetre in size

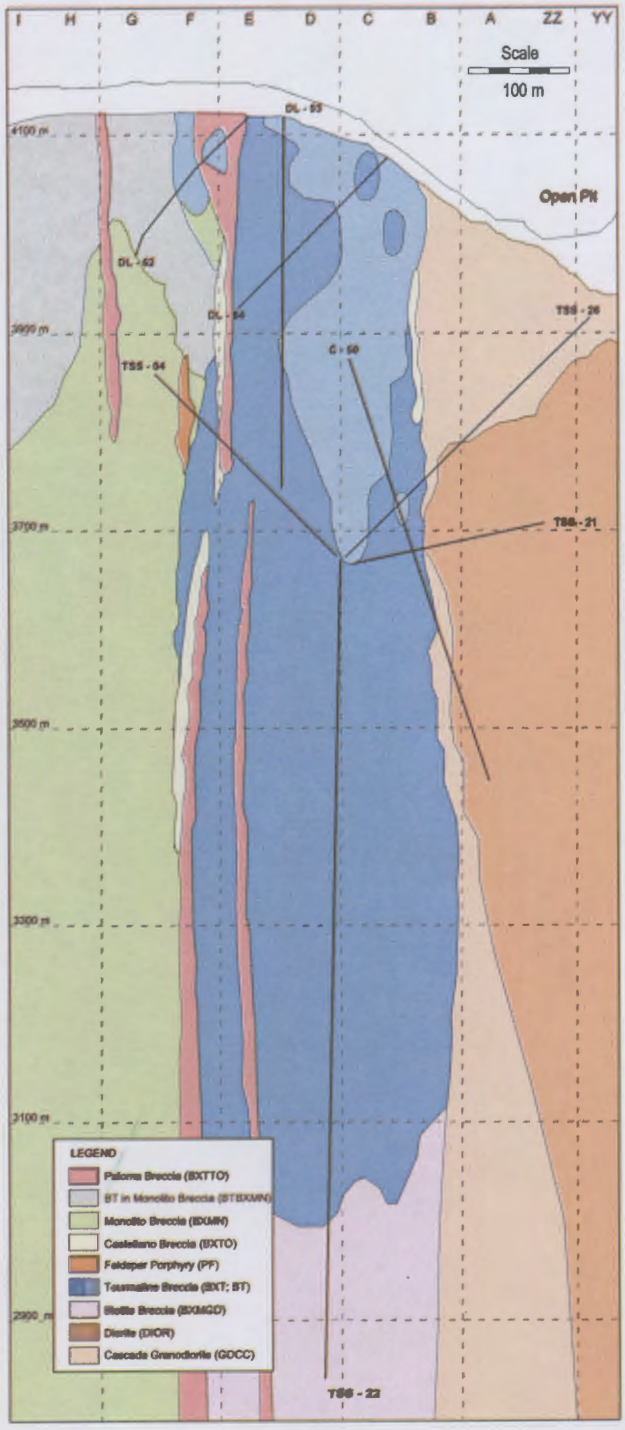

Figure 2.6. Geology of cross-section XC-50, Sur-Sur. Location of section XC-50 shown in Figure 2.1.

Table 2.2. Descriptions of breccia units in the Sur-Sur sector (modified from Serrano et al., 1996).

Breccias, Sur Sur			
Name	**Symbol**	**Characteristics**	**Form**
Paloma	BXTTO	50-80% tourmaline rock-flour matrix	N-S trending dykes cut all other breccias
Monolito	BXMN	50-80% rock-flour and chlorite-biotite matrix, transitional to BXTO where the chlorite content is low	Gradational west margin of BXTO, east of breccia margin of Don Luis porphyry
Castellana	BXTO	50-90% rock-flour matrix, rounded clasts, <10% tourmaline	N-S elongate body, truncates west part of Tourmaline breccia
Tourmaline	BT	<5% tourmaline, angular clasts	Transitional outer margin NW-elongated core zones in BXT
	BXT	5-15% tourmaline, increasingly rounded	
	BXTT	>15% tourmaline	
Magmatic	BXMGDCC	Biotite, anhydrite and sulfides have replaced a rock flour matrix, not magmatic genesis as the name implies	Unknown, occurs at depth in Sur Sur

up to metres in size. At higher elevations, the Tourmaline Breccia contains abundant vugs within the matrix, which are attributable to either the leaching of anhydrite and carbonates (Vargas et al., 1999) or residual voids that were never filled by mineral precipitation.

The BXT was emplaced southeast of the Río Blanco Magmatic Breccia orebody between the late Miocene and early Pliocene based on whole-rock K/Ar radiometric age determinations that range from 7.1 to 5.1 Ma (Fig. 2.1; Table 2.1; Serrano et al., 1996).

Castellana Breccia (BXTO)

The Castellana Breccia is a north-south elongate body that crops out between the BXT and BXMN (Fig. 2.1). The breccia is heterolithic (fragments of AN, GDCC, BXT, PDL and BXMN are present; acronyms in Fig. 2.1), and consist of rounded clasts in a grey coloured rock flour matrix that contains little or no tourmaline (Fig. 2.3e; Vargas et al., 1999). Ore grades in the BXTO are low (<0.5% Cu), even though it has been affected by quartz-sericite alteration similar to the BXT breccia (Stambuk et al., 1988). At the contact with the BXT, the abundances of tourmaline, sulfide and specular hematite increase, possibly due to assimilation from the older BXT. No radiometric age determinations have been performed on BXTO.

Monolito Breccia (BXMN)

The BXMN crops out with no defined orientation to the west of the BXTO (Fig. 2.1). The BXMN contains a rock flour matrix similar to the BXTO, however the clasts and matrix have been strongly altered to a chlorite assemblage (Vargas et al., 1999). The Monolito Breccia, despite its name, is heterolithologic, containing clasts of AN, GDCC, BXT, PF and PDL. It has uniformly low copper grades (<0.5%; Fig. 2.3f). Clasts in the matrix are variably altered to chlorite, with alteration intensity ranging from incipient to almost complete textural obliteration. One K/Ar whole-rock age of 5.2 Ma has been determined for BXMN (Table 2.1; Serrano et al., 1996). However, as with

BXTO, this breccia must have formed after BXT, PF and PDL based on the contained clasts.

Paloma breccia (BXTTO)

The Paloma Breccia crops out with a north-south orientation to the south of the Sur-Sur open pit (Figs. 2.1 and 2.4), and also occurs as numerous dykes cutting the other breccia units. It is characterised by typically small, well-rounded clasts in a strongly tourmalinised matrix (Fig. 2.7a; Vargas et al., 1999). In addition to tourmaline, the matrix also contains rock flour and chalcopyrite, pyrite, quartz, magnetite and minor amounts of chlorite and siderite cement (Stambuk et al., 1988). Clasts are moderately to intensely altered (texturally obliterated) due to multiple re-working through successive breccia events. BXTTO contains clasts of AN, GDCC, BXT, BXTO, BXMN and PDL. One K/Ar, whole-rock age determined for BXTTO resulted in an age of 5.2 Ma (Table 2.1; Serrano et al., 1996). However, based on the contained wallrock clasts, this breccia formed after BXTO, BXMN and PDL.

Los Bronces Breccias (summary from Warnaars et al., 1985)

The Los Bronces breccia system was superimposed on the western side of the Río Blanco Breccia Complex. Los Bronces is composed of at least seven different mineralised tourmaline and rock flour breccias. They form one large NNW-trending contiguous breccia complex with surface dimensions of 2 km long and 0.7 km wide at the present erosional surface. The breccia bodies crop out at elevations between 3450 and 4150 m asl.

The different breccias have been characterised based on their locations, matrix cement, clasts, shapes, types and degree of mineralisation and alteration. The seven different breccia units from oldest to youngest are Ghost, Central, Western, Infiernillo, Anhydrite, Fine Gray and Donoso (Warnaars et al., 1985). The breccia complex maintains sharp contacts with the surrounding intrusive rocks and andesites and dip inwards on the north, west and south margins. The eastern contact is almost vertical, suggesting a 15° westward tilt of the breccia complex after emplacement. The internal breccia contacts are sharp locally but elsewhere individual breccias coalesce, interfinger or have gradational contacts with each other.

The breccias are commonly monolithic, but in some cases are bilithic or heterolithic. Most of the clasts consist of quartz monzonite or andesite with minor amounts of quartz latite porphyry, monzodiorite and vein quartz locally. The breccia matrices consist of variable amounts of tourmaline, quartz, specularite, anhydrite, pyrite, chalcopyrite, bornite, molybdenite, sericite, chlorite and altered rock flour.

The Donoso Breccia contains the highest hypogene copper grades compared to any of the other Los Bronces breccias, except for local high-grade zones in the Infiernillo Breccia. The Donoso Breccia is the youngest and the northernmost breccia body (5 Ma; Warnaars et al., 1985). It shares similar textural and mineralogical characteristics with the Sur-Sur Tourmaline Breccia (Serrano et al., 1996). The ore is generally confined to the breccia matrix and occurs as coarse aggregates or irregular patches of pyrite, chalcopyrite and rare bornite. Minor stockwork and disseminated mineralisation occurs in clasts on the southwestern side of the breccia. The chronological order of mineral deposition in the breccia matrix is quartz, black tourmaline (dravite), pyrite, chalcopyrite and specularite.

2.2.4 Porphyries

Both the potassic zone, containing the Magmatic Breccia, and some of the younger mineralised tourmaline breccia bodies are cut by late Miocene porphyritic intrusions (5.2 Ma; K/Ar dating of K-feldspar; Serrano et al., 1996). These porphyry dykes are typically narrow (<10 m wide) and are generally oriented in a N27°W trend (Serrano et al., 1996).

Feldspar Porphyry (PF)

The Feldspar Porphyry dykes at Río Blanco are poorly documented. Prior to the current study, they have been the subject of only limited research (Vargas et al., 1999). The PF dykes have not been dated, and no temporal relationships have been determined for this unit. The PF has a porphyritic texture and contains phenocrysts of plagioclase feldspar, quartz, K-feldspar (coarse grained, up to 2 cm long), and primary biotite within a fine-grained aplitic groundmass characteristic of mineralising porphyries that have become saturated with water, and have exsolved an aqueous phase (Fig. 2.7b). The PF also contains zones of biotite alteration that contain chalcopyrite (generally low-grade) and magnetite. Contacts with the Magmatic Breccia are typically sharp and the Magmatic Breccia shows minor biotite alteration adjacent to the PF contact. In appearance, the PF generally has a darker grey colour than the other porphyries (described below). The PF generally is only found in the deeper drillcore intersections and underground exposures. It is volumetrically the least abundant porphyry in the system.

Quartz Monzonite Porphyry (PQM)

PQM dykes, generally oriented N27°W, cut biotite altered rocks and the high-grade zone of the Río Blanco Magmatic Breccia, where they truncate grade (Serrano et al., 1996). The porphyry dykes increase in thickness downward and are believed to coalesce into a quartz monzonite stock

at depth (<2000 m asl; Serrano et al., 1996). Where the PQM cuts the Magmatic Breccia, quartz-sericite alteration haloes occur peripheral to the dykes. The PQM is characterised by quartz-sericite and silicic alteration assemblages, and contains no hydrothermal biotite (Serrano et al., 1996). The PQM is composed of plagioclase feldspar, quartz, K-feldspar and biotite phenocrysts in a fine-grained groundmass equal to that of the PF (Fig. 2.7c). As with PF, this phase also contains large (2cm long), euhedral megacrysts of K-feldspar. The PQM has been dated at 5.2 Ma based on K/Ar and Ar/Ar radiometric age determinations (Table 2.1; Serrano et al., 1996).

2.2.5 Sub-volcanic complex

A late to post-mineralisation igneous complex intruded the Río Blanco system. The complex consists of three main late-stage intrusions, which are essentially barren with respect to copper and molybdenite mineralisation. The three intrusions are co-magmatic and intruded successively northward as the complex evolved (Stambuk et al., 1988) They are characterised by high silica and low Ca and Mg contents (Vergara and Latorre, 1984) and contain metal-enriched melt inclusions (Davidson and Kamenetsky, 2001). Based on K/Ar age determinations, the sub-volcanic intrusions were emplaced between 4.9 Ma and 3.9 Ma (Table 2.1; Serrano et al., 1996).

Don Luis Porphyry (PDL)

The PDL is a large, elongate porphyry body that crops out in the centre of the ore deposit complex, parallel to the PQM dykes (Fig. 2.1; Serrano et al., 1996). The PDL is partly enclosed by zones of magmatic brecciation that are considered to have formed during emplacement of the porphyry body ('emplacement breccia'; Serrano et al., 1996). Where the emplacement breccia is absent, contacts of the PDL with other rock units are sharp and typically unaltered. However, there has been quartz-sericite alteration of some PDL contacts locally. PDL contains phenocrysts of plagioclase feldspar, quartz, K-feldspar (up to 2 cm long) and minor (<10%) fine-grained biotite phenocrysts in a groundmass equal to the PF described above (Fig. 2.7d). The relatively low biotite content of this unit compared to the previous two porphyries (20-25%) is interpreted here to indicate lower water contents, possibly due to fluid exsolution at depth before it reached the site of final crystallisation. This is consistent with the weakly developed alteration assemblages and generally low copper grades (<0.5%) within, and surrounding the porphyry. The PDL is cut by quartz ± sericite ± anhydrite ± sulfide veins and K-feldspar veins, indicating that minor hydrothermal activity continued after emplacement of the PDL (Serrano et al., 1996). Based on K/Ar age determinations, the PDL was emplaced between 4.9 Ma and 3.9 Ma (Table 2.1; Serrano et al., 1996).

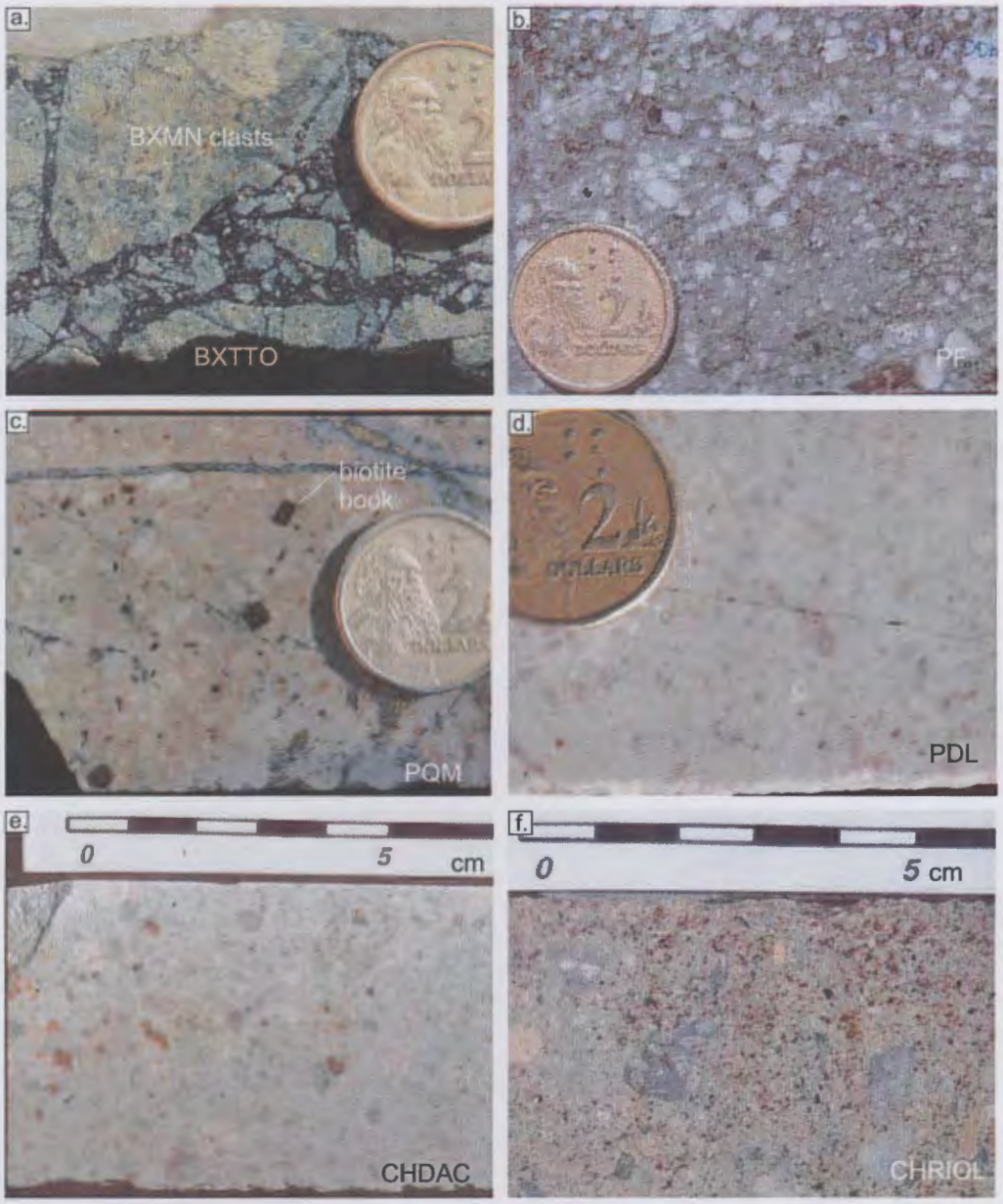

Figure 2.7.
a. Paloma Breccia (BXTTO) contains a variety of clasts including host andesite and granodiorite (GDCC), BXT, BXTO, BXMN and PDL within a quartz-sericite altered rock flour matrix and variable degrees of tourmaline cementation. This photo demonstrates the existence of BXMN clasts in BXTTO (section XC-50, DL-62);
b. Feldspar Porphyry (PF) has a darker colouration compared to the other porphyries in the ore deposit and contains phenocrysts of feldspars, quartz and books of biotite (section XC-235, DDH-576, sample st1-d);
c. Typical sample of Quartz Monzonite Porphyry (PQM) with quartz-sericite alteration, contains phenocrysts of feldspars, quartz and books of biotite (section XC-125RB);
d. Typical sample of Don Luis Porphyry (PDL), contains phenocrysts feldspars and quartz but only small flecks of biotite (section XC 295RB, DDH-638);
e. Typical sample of Dacite Chimney (CHDAC), contains quartz and feldspar phenocrysts with minor biotite (section XC-155, DDH-555, sample MiD9907);
f. La Copa Rhyolite (CHRIOL) contains fragments from surrounding rock units due to assimilation upon ascent (section XC-035, DDH-513, sample MiR9901).

Dacite Chimney (CHDAC)

The CHDAC crops out between the PDL and the CHRIOL (Fig. 2.1) and has the shape of an inverted cone. As with the PDL, CHDAC is surrounded by zones of emplacement breccia. The CHDAC contains phenocrysts of quartz and plagioclase feldspar with minor biotite in a fine-grained quartz/feldspar matrix (Fig. 2.7e) and autobrecciated fragments are also present, generally at contact zones. The matrix of the emplacement breccia generally contains secondary biotite, specularite, chlorite and minor chalcopyrite. Although grades are low (<0.3% Cu) in the emplacement breccia, it appears to have been a focus for late-stage fluid flow and minor copper deposition (Serrano et al., 1996).

La Copa Rhyolite (CHRIOL)

La Copa Rhyolite (CHRIOL) crops out as a large, circular body containing multiple felsic intrusive phases and an extrusive phase. The CHRIOL was the final intrusive complex to be emplaced into the ore deposit and resulted in the destruction of mineralised zones in the Río Blanco sector (Fig. 2.7f; Serrano et al., 1996). Although the CHRIOL consists dominantly of various intusive phases, there is evidence of coeval eruptive facies at high elevations on the Los Bronces side of the ore deposit (Table 2.3; Warnaars et al., 1985). K/Ar age determinations of biotite and plagioclase from the intrusive phases in the La Copa Rhyolite range between 4.9 and 3.9 Ma (Serrano et al., 1996). An ignimbrite unit at the top of the present-day surface overlies a volcaniclastic, mass-flow unit with a brown-coloured soil horizon developed at its upper contact. This contact is irregular, indicating erosion before deposition of the ignimbrite. Flow structures within the ignimbrite follow this contact. This contact reveals important information about the erosional history of the deposit and indicates that the ore deposit had been unroofed and exhumed by the time of eruption of the ignimbrite.

Table 2.3. Intrusive phases of the La Copa Rhyolite (Modified from Toro, 1986).

A Vuggy rhyolite
B Intrusive units
- B1: Intrusive sub-unit I
  - B1.1 Dense siliceous rhyolite porphyry
  - B1.2 Moderately sericitised rhyolite porphyry
- B2: Intrusive sub-unit II
  - B2.1 Rhyolite
  - B2.2 Rhyolite porphyry with elongate, zoned feldspars
- B3: Intrusive sub-unit III
  - B3.1 Phaneritc rhyolite to porphyry series
  - B3.2 Granular rhyolite
  - B3.3 Rhyolite porphyry with white aphanitic masses

C Contact breccia (fluidised)
- C1: Lapilli Unit
- C2: Lapillistone Unit
- C3: Agglomeritic Unit

D Subaerial Sub-volcanic Unit
- D1: Amygdoidal tuffaceous rhyolite
- D2: Tuffaceous rhyolite with oriented glass
- D3: Rhyolite porphyry with siliceous masses and few amygdales

E Lithic unit (fluidised)
- E1: Green lithic tuff
- E2: Tuff agglomerate

F Sub-volcanic unit
- F1: Indifferent rhyolite porphyry
- F2: rhyolite porphyry with oxidised, red siliceous masses

G Ridgeform unit
- G1: Banded rhyolite bodies
- G2: Andesite, dacite veins

H Ignimbite* (plagioclase/quartz phyric) flow banded over surface of upper soil horizon, andesite fragments preserved

* Documented by Frikken (2001)

2.3 Structure

2.3.1 Introduction

The formation of giant porphyry copper ore deposits requires effective fluid pathways to transport large quantities of magma and fluid into the upper crust. As part of the current study, analysis of faults has revealed distinct similarities between regional, district and ore deposit architecture in central Chile. However, assertions generated in this study are the result of literature reviews by the author and it is apparent that a rigorous structural study is needed in the vicinity of the Río Blanco ore deposit. The architecture at each scale is defined by three principal fault orientations as described in Section 1 of this thesis. In response to E-W crustal shortening, the collective interaction of these three fault sets at different scales are considered to have been responsible for focussing magmatism and hydrothermal fluids at Río Blanco-Los Bronces.

The Río Blanco-Los Bronces ore deposit is located between two north trending basement faults and is crosscut by late Miocene to Pliocene NW and NE trending faults (Skarmeta et al., 2000).

Fracture frequency of the NW and NE fault arrays has been plotted in plan view in the ore deposit complex (Fig. 2.8) and described in Section 1. It should be noted that most of this section is based on the data gathered from various Codelco workers, however the interpretations superimposed on the data are those from the author of this thesis. In addition, the fractures measured by company geologists are in most cases joints, but faults have been compiled together with joints in the dataset. Hence, they are described here together as 'fractures'. The fractures crosscut the Tourmaline Breccia. No information about fracture dips has been provided by CODELCO and the fracture information cannot be confidently related to the paragenesis.

2.3.2 District scale

Linear features are apparent in the district scale topography, surrounding Río Blanco-Los Bronces within the Cordilleran Domain, with three principal orientations recognised (N, NE and NW). This is consistent with the district scale geology mapped at the 1:10000 scale by Alvarez (1999; Fig. 2.8).

2.3.3 Ore deposit scale

CODELCO-Chile, Division Andina, provided data of fracture frequency versus orientation from the Sur-Sur and La Union open pit mines to this study. Analysis of the data set has revealed a predominance of NW and NE striking fracture sets and an absence of N striking fractures (Fig. 2.9). The landsat image (Fig. 2.8) reveals a N trending fault that extends northward from the ore deposit complex in the Río Blanco valley. This N trending fracture set is inferred to have become inactive at some stage after crystallisation of the host San Francisco Batholith at 7.4 Ma due to the absence of this fracture set in the younger rocks.

2.3.4 Structural characteristics of the Tourmaline Breccia

The mineralised Tourmaline Breccia in the Sur-Sur sector is elongate with a N- to NW- trend. In combination with variable width along its strike, the Tourmaline Breccia also shows variability in its grade, frequency of crosscutting fractures, frequency of crosscutting veins and abundance of hydrothermal minerals (Fig. 2.9).

In the Sur-Sur open pit, high frequency of crosscutting fractures and veins and an abundance of hydrothermal cement (5 to >15%) coincide with high copper grades. The fractures preserved in the open pit have a penetrative NE trend, with only a minor frequency of NW trending fractures (Fig. 2.9). However, a zone north of the Sur-Sur open pit is low grade, contains a low frequency of fractures and crosscutting veins and a low abundance of tourmaline cement and other hydrother-

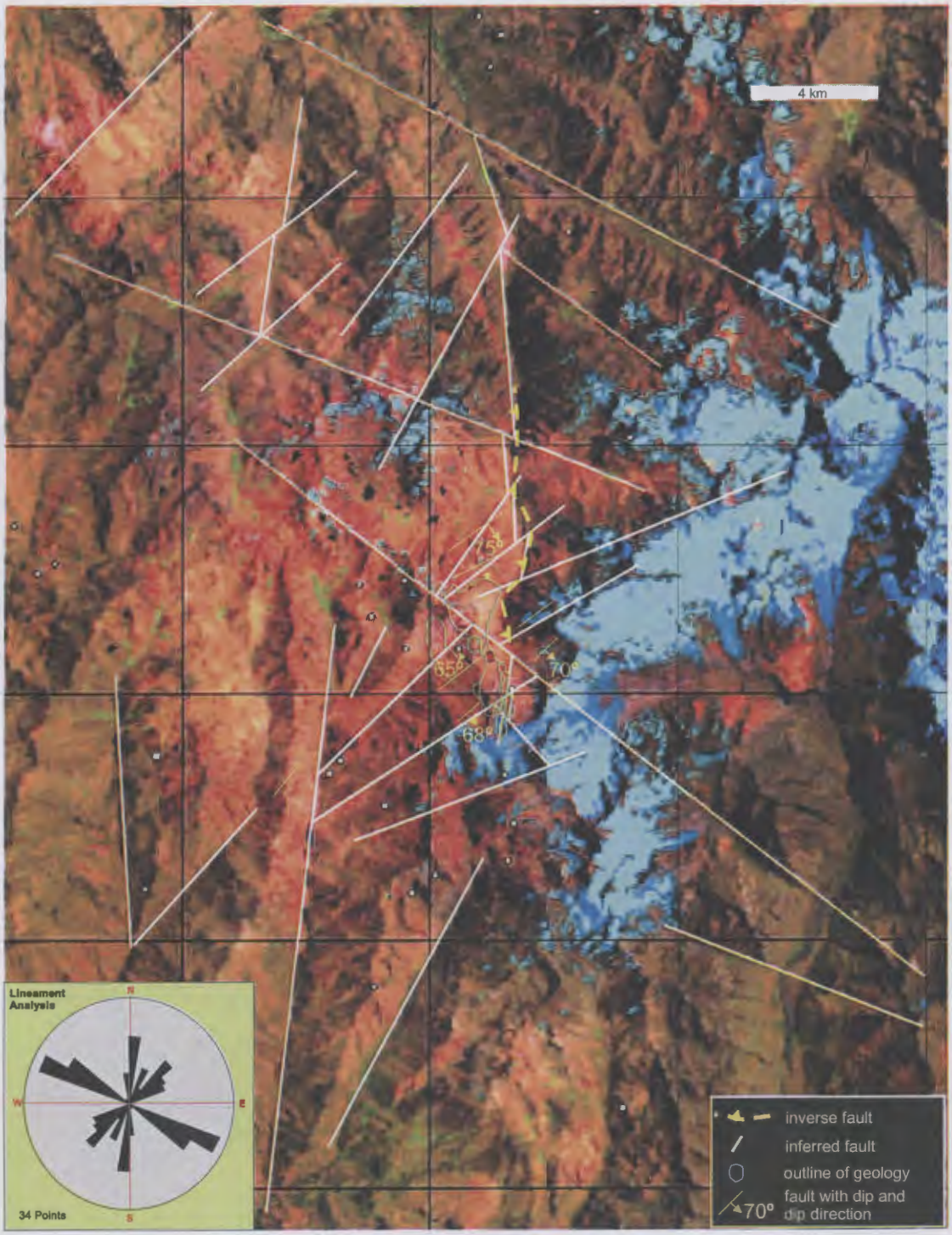

Figure 2.8. Landsat image with the outline of Río Blanco-Los Bronces geology, lines in the place of linear topographic features and district scale rose diagram indicating orientation of lineaments versus length on the image. Structural data from Alvarez (1999) is shown in yellow. Landsat image provided by CODELCO-Division Andina.

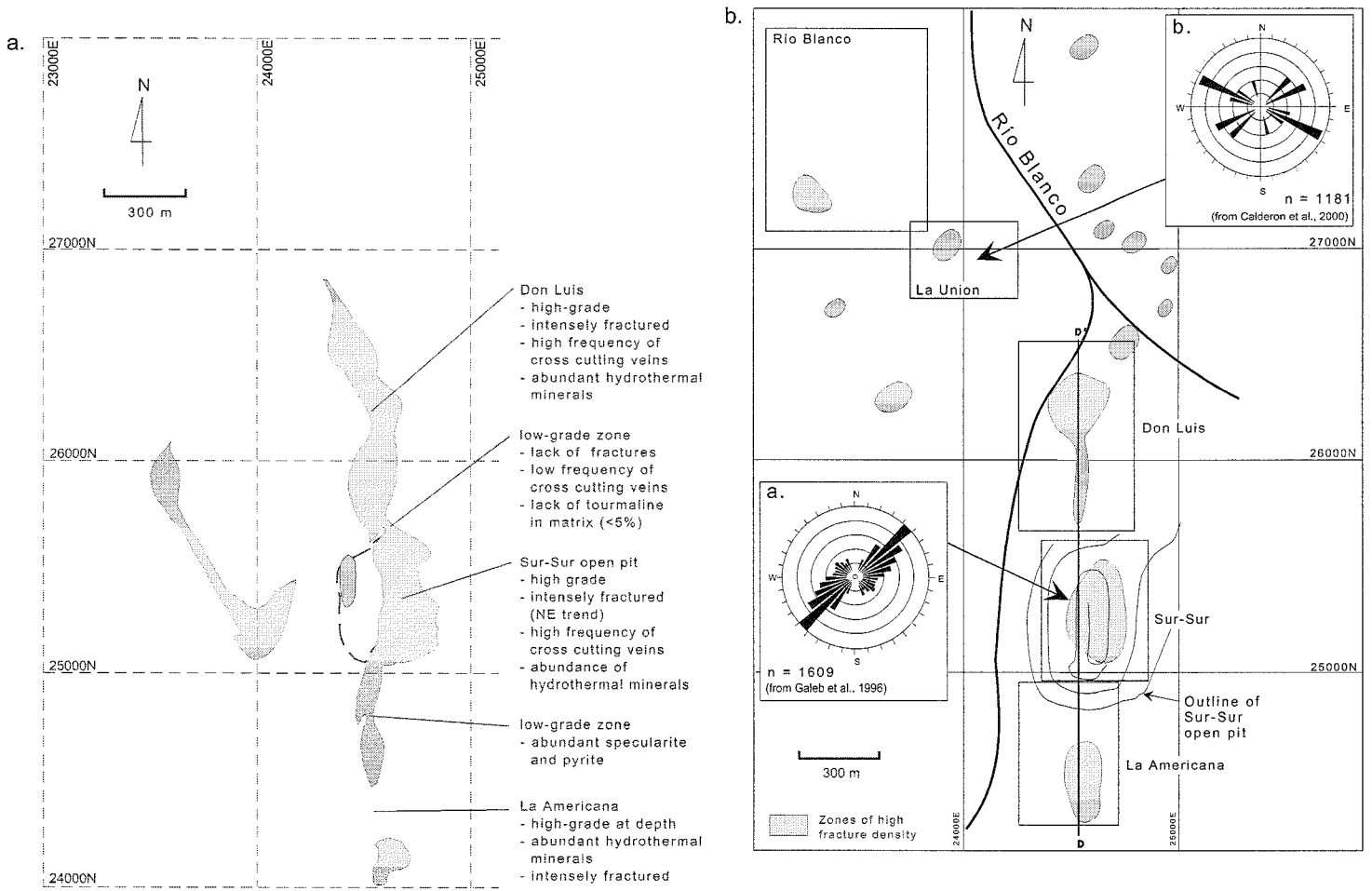

Figure 2.9. a. Along-strike characteristics of the Sur-Sur mineralised Tourmaline Breccia, b. Fracture orientation and density in the Río Blanco ore deposit complex (Galeb et al., 1996; Calderon et al., 2000; Skarmeta et al., 2000). Both maps are drawn to the same scale.

mal minerals in the matrix (<5%). In addition, the geometry of the breccia body changes orientation, and the width significantly narrows in this zone. Further north, in the Don Luis sector the tourmaline breccia contains high copper grades, a high frequency of crosscutting fractures and veins and abundant hydrothermal mineral cement (Fig. 2.9). The same features are preserved at La Americana to the south, along strike of the Tourmaline Breccia (Fig. 2.9). The crosscutting fractures, measured by Codelco geologists, are considered to have been active during breccia formation as well as after due to their close correlation to the abundance of hydrothermal minerals.

2.3.5 Architecture

Skarmeta et al. (2000) interpreted the district-scale architecture surrounding Río Blanco-Los Bronces. Mapping was carried out from the district to the ore deposit scale by Jorge Skarmeta (aeromagnetic interpretation at 1:50000), Juan Carlos Castelli (1:50000 mapping), Nestor Alvarez (1:10000 mapping), Alberto Adriasola (1:5000 mapping) and Gloria Lopez (drillcore mapping and aeromagnetic interpretation at 1:50000). Their interpretation is as follows:

- The Río Blanco intrusive complex is considered to have formed as a laccolith within the Los Pelambres Formation under a shortening tectonic regime (Fig. 2.10).
- Under this shortening regime, the original basement faults that formed during the deposition of the Los Pelambres Formation were inverted to high angle reverse faults. The faults in compression became locked-up, preventing fluid flow to the surface in many areas at the same time that plutonism was initiated. This enabled the hydrothermal system to develop without destruction of the system by volcanism (Juan Carlos Castelli, pers. comm., 2000).
- Two systems of north-trending basement faults occur in the Río Blanco-Los Bronces district. These are the San Francisco Fault, located in the San Francisco River, and the Río Blanco Fault, located in the Blanco River (Río Blanco; Fig. 2.11). Displacement on the San Francisco Fault is west over east and increases from north to south. Displacement on the Río Blanco Fault is east over west and increases from south to north (Fig. 2.12). The result of this displacement is illustrated on Figure 2.13 (Skarmeta et al., 2000). Both of these north-trending faults terminate within the Río Blanco intrusive complex and are inferred to have collectively acted as a pull-apart structure, increasing the porosity and permeability of the zone between the fault terminations significantly.
- The fact that the Farellones Formation crops out in the vicinity of the Río Blanco - Los Bronces ore deposit can be explained by the architecture observable in Figure 2.13, where erosion has removed all Farellones Formation in the zones of upthrow along the north trending basement faults and preserved it where displacement is near-zero.
- The NE- and NW- trending fault arrays observed within the Río Blanco deposit can be attributable to the prevailing stresses during the late Miocene to Pliocene in combination with the interaction between the two north-trending basement faults (interpretation from this study).

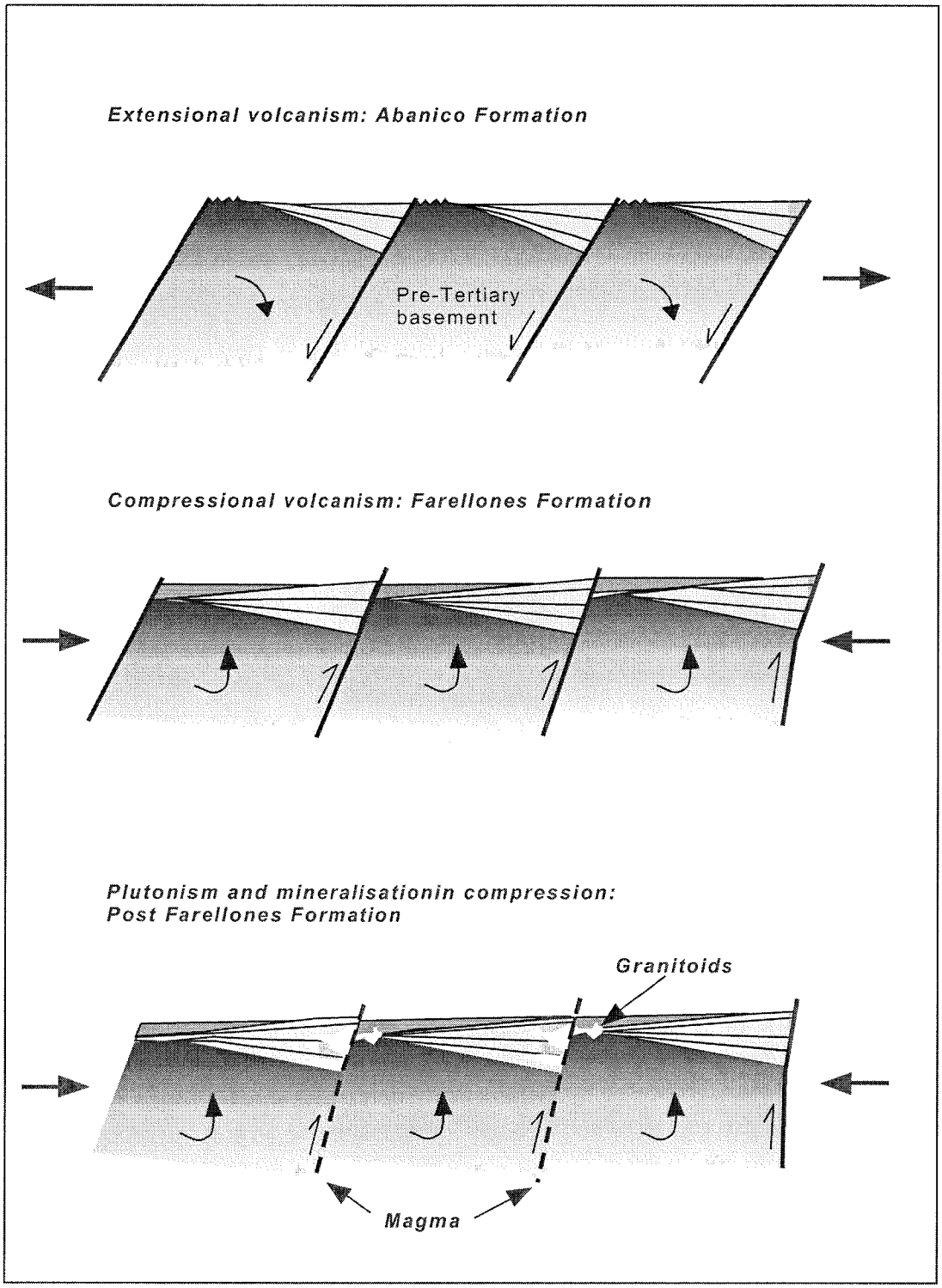

Figure 2.10. Schematic model for the tectono-stratigraphic evolution of the Los Pelambres (Abanico), Farellones and granotoids during the Tertiary in central Chile, latitude Río Blanco-Los Bronces (from Skarmeta et al., 2000).

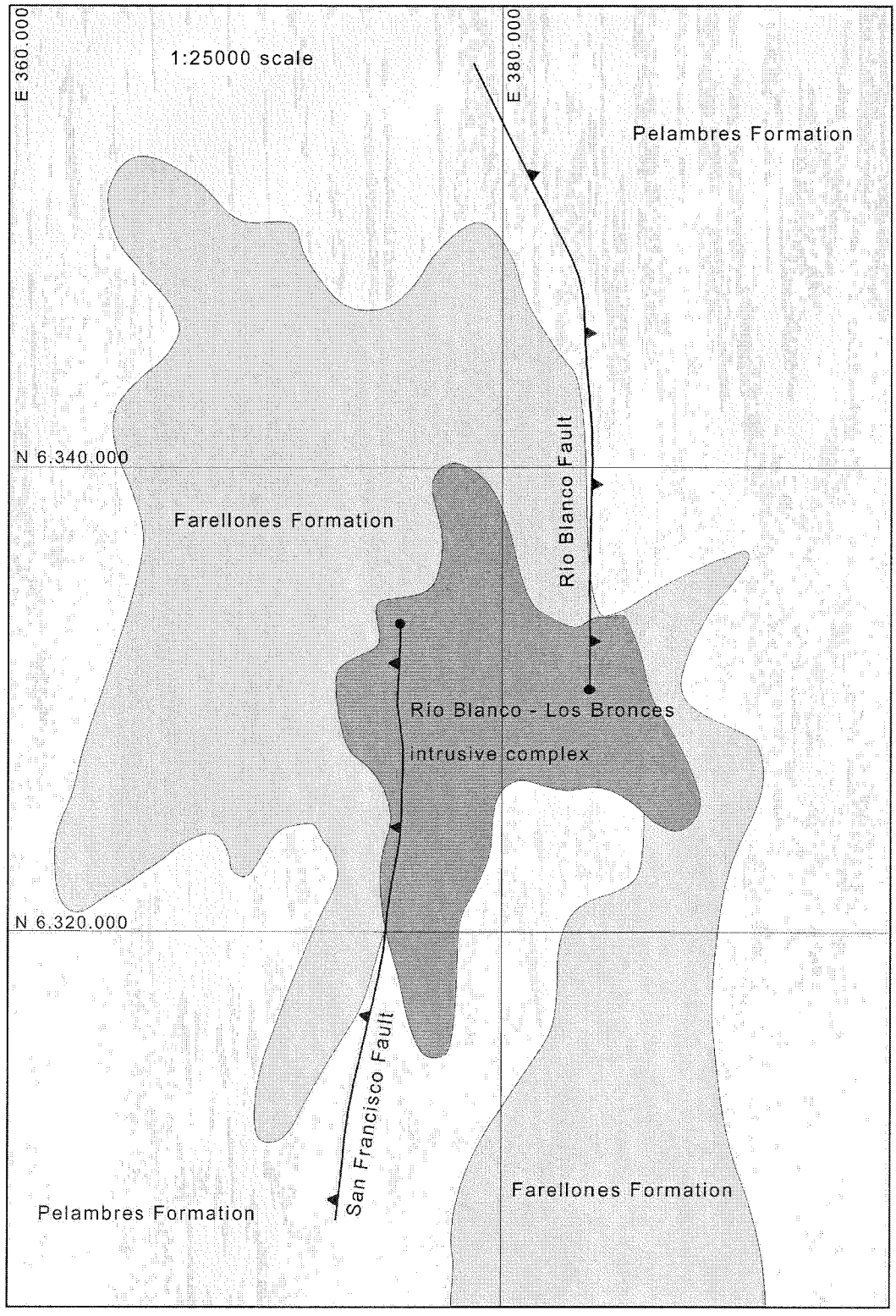

Figure 2.11. Attitude and dip of north trending basement faults in the Río Blanco-Los Bronces district (from Skarmeta et al., 2000).

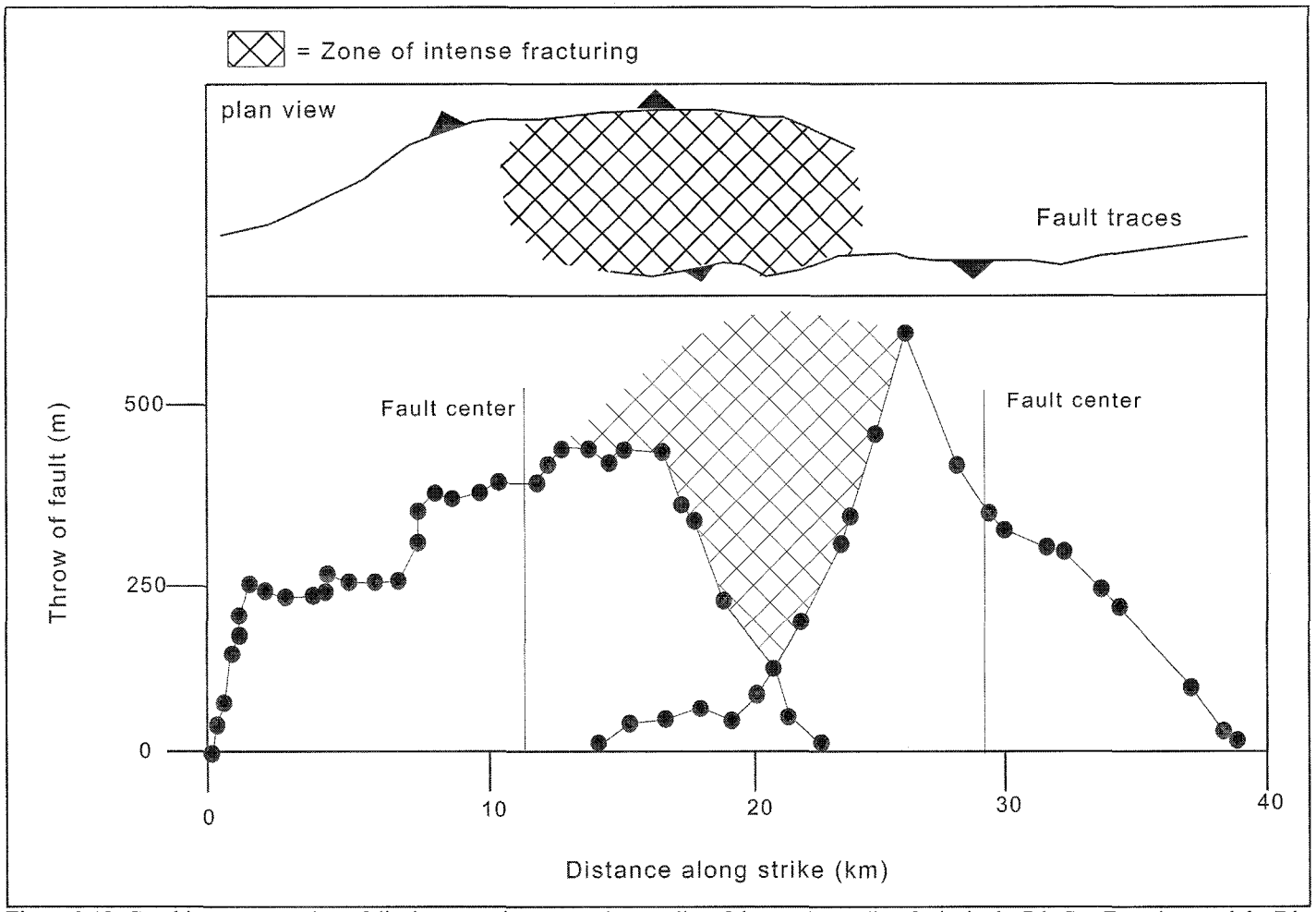

Figure 2.12. Graphic representation of displacement in metres along strike of the north trending faults in the Río San Francisco and the Río Blanco (from Skarmeta et al., 2000).

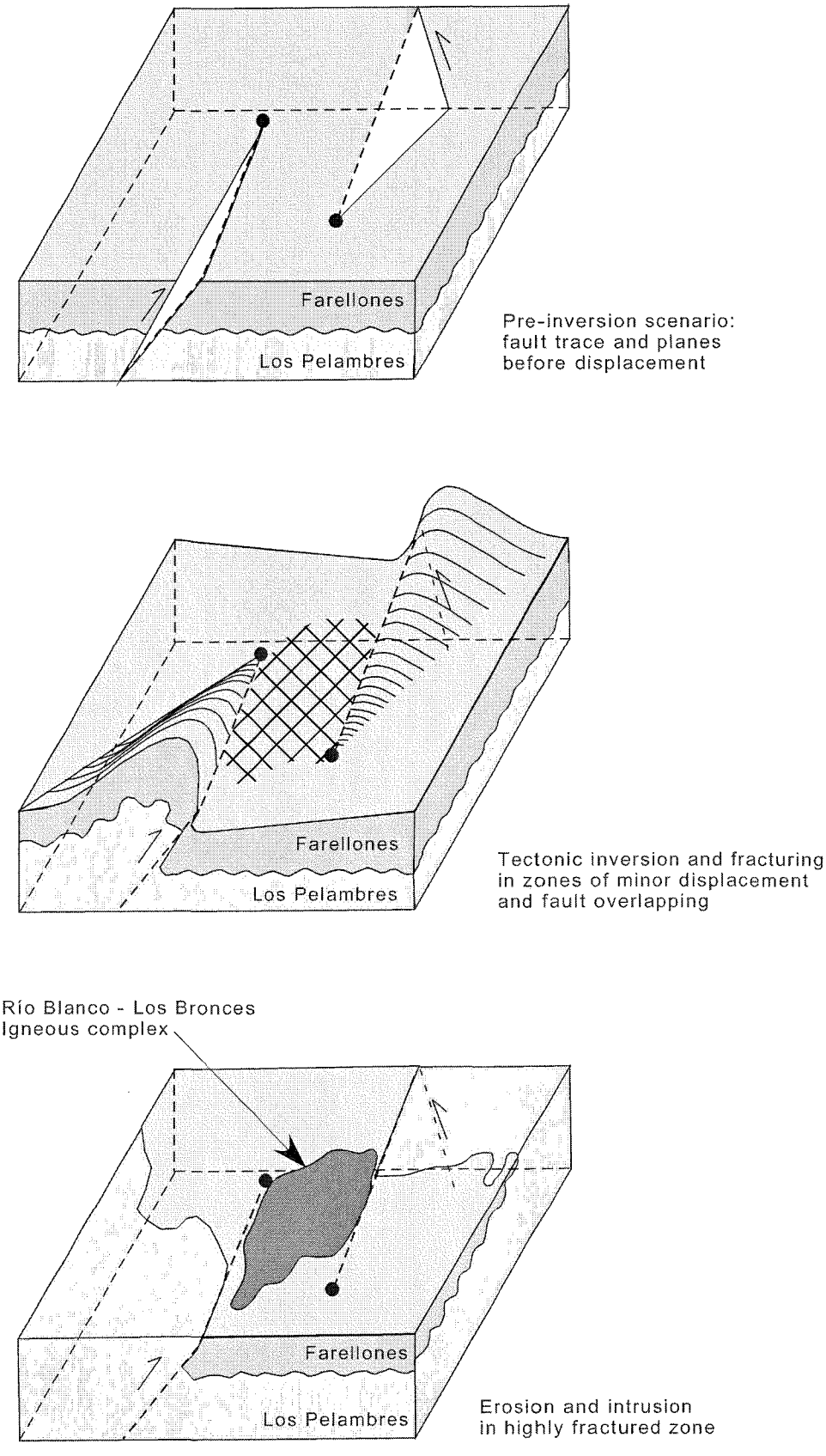

Figure 2.13. Schematic model for the consequences of displacement along the north trending basement faults, erosion and intrusion of the Río Blanco-Los Bronces igneous complex (from Skarmeta et al., 2000).

2.4 Whole-rock geochemistry

A database containing analyses of major and trace element geochemical data and isotopic compositions from Río Blanco-Los Bronces has been compiled from Serrano et al. (1996), Warnaars et al. (1985) and Skewes and Stern (1994). An additional nineteen samples have been analysed as part of the current study for major and some trace elements at the University of Tasmania by X-ray fluorescence spectrometry using a Philips PW1480 X-ray spectrometer. Trace element and rare earth element analyses were undertaken at the University of Tasmania using an Agilent HP4500 quadrupole ICP-MS and the methodology of Yu et al. (2001). Preliminary interpretations of these results were provided by Hollings and Frikken (2001). This data, rock sample descriptions and previous data are shown in Appendices B1 and B2, respectively. The data display the geochemical characteristics of the major geology units at Río Blanco in terms of major, trace and REE and will be compared with regional geochemical datasets.

In addition, an investigation into the geochemical properties of the roof pendant andesite, Don Luis Porphyry and the Feldspar Porphyry was undertaken. Contention exists whether the roof pendant is a separate intrusive body or is a roof pendant of Farellones Formation. The Don Luis Porphyry is poorly understood and geochemical data was generated through a depth section to investigate whether any spatial variations in igneous compositions occur within the large body. The Feldspar Porphyry is also poorly understood in terms of its geochemistry and data was generated to better constrain its characteristics.

2.4.1 Major element geochemistry

Major element geochemistry suggests a high K_2O calc-alkaline affinity for the intrusions of the Río Blanco-Los Bronces ore deposit. These are similar to other Tertiary Andean volcanic and plutonic rocks in central Chile (Skewes and Stern, 1994; Serrano et al., 1996). In addition, Warnaars et al. (1985) documented molecular ratios of $Al_2O_3/CaO + Na_2O + K_2O$ greater than 1.1, indicating that the igneous rocks in the vicinity of the Río Blanco-Los Bronces mine are peraluminous. There is an apparent fractionation trend of SiO_2 vs time (where age constraint is available; Fig. 2.14a) and SiO_2 vs Al_2O_3 for andesite host rocks, Don Luis Porphyry and Feldspar Porphyry in Figure 2.14b. However, the ore deposit rocks are strongly affected by alteration resulting in low MgO, CaO and Na_2O and high K_2O values compared to regional samples of Los Pelambres (Abanico) and Farellones Formation (Hollings and Cooke, 2002; Skewes and Stern, 1994). Due to the effect of alteration, Skewes and Stern (1994) do not consider major element geochemistry to be a reliable means of classifying the different igneous rock types within the Río Blanco ore deposit.

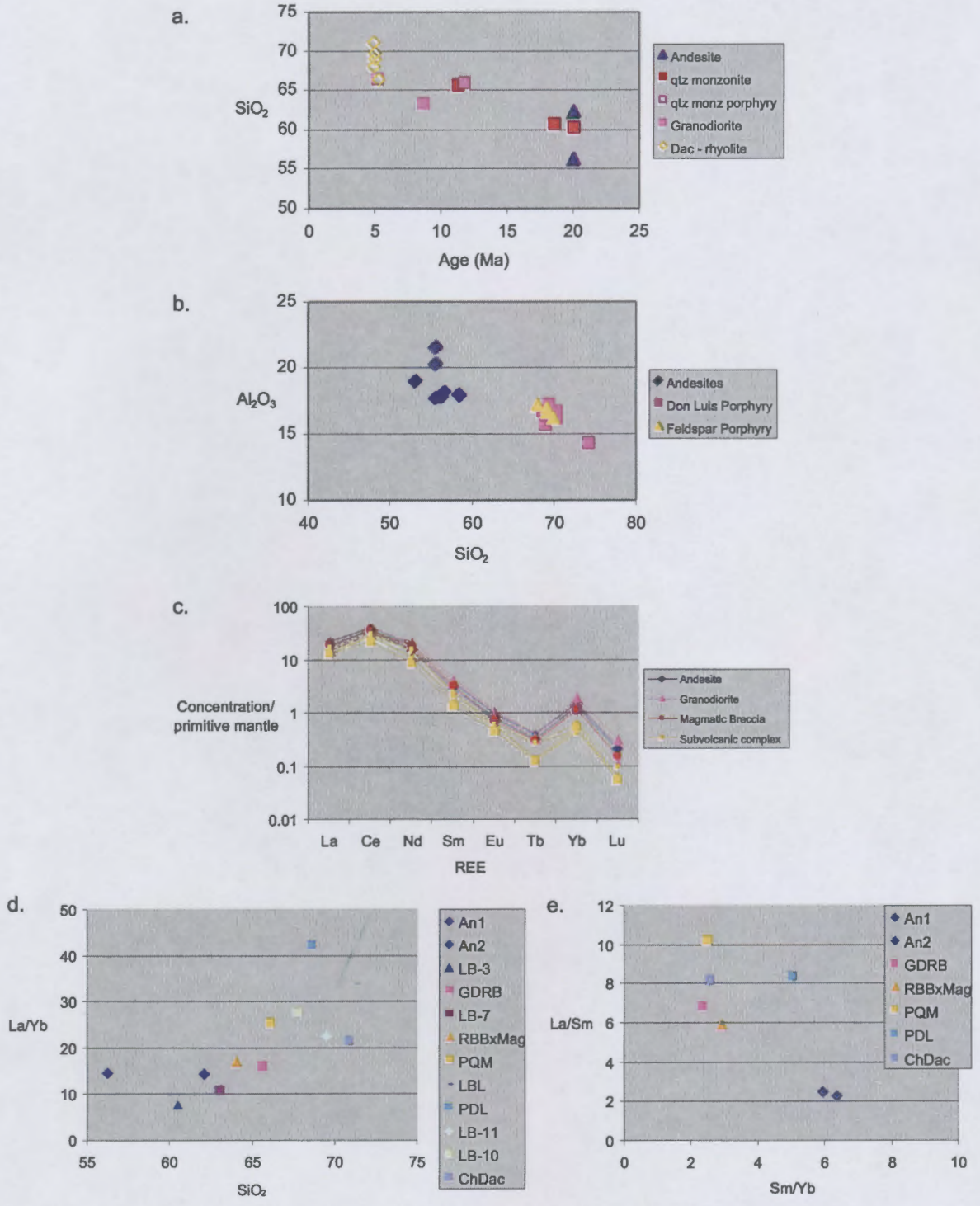

Figure 2.14.

a. SiO_2 versus age for host rocks and post-mineral porhyries at Río Blanco;

b. SiO_2 versus Al_2O_3 for host rocks and post-mineral porhyries at Río Blanco;

c. REE element plot for samples collected within the ore deposit (data from Skewes and Stern, 1994);

d. SiO_2 and La/Yb plot; and

e. La/Sm and Sm/Yb plot for rocks collected within the Río Blanco-Los Bronces ore deposit (data sourced from Serrano et al, 1996; Warnaars et al., 1985; Skewes and Stern, 1994).

Data are in Appendix B2.

2.4.2 Trace element geochemistry

Large ion lithophile elements (LILE) such as Rb, Cs, Sr and Ba can readily be remobilised due to the effects of secondary alteration, however other elements such as rare-earth elements (La, Ce, Nd, Sm, Eu, Tb, Yb, Lu) and the high field strength elements (Hf, Ti) are considered to be relatively immobile even during high temperature potassic alteration (Rollinson, 1993). Skewes and Stern (1994) documented three main conclusions from their central Chile trace element dataset:

1) The samples are enriched in light REE relative to heavy REE (La/Yb>>1), this is typical of all Andean igneous rocks;
2) The Ba/La ratio of all the samples (except LBL – a highly altered sample) is greater than 18, another feature of Andean igneous rocks which has been interpreted to imply the addition of alkali elements from the subducted slab into the mantle source of these magmas; and
3) The older pre-mineralisation host rocks (e.g. An1, An2 and GDRB) have higher REE contents and lower La/Yb ratios than the younger, post-mineral magmatic rocks (PQM, PDL, LBL and CHDAC; Fig. 2.14c).

Kay et al. (1991) reported similar higher La/Yb ratios in progressively younger igneous rocks in central Chile and in the Maricunga Belt (Kay et al, 1999). The sequence from low to high La/Yb ratios plotted against SiO_2 is interpreted as the result of the progression from relatively thin to thicker continental crust (Kay et al., 1999). In the Maricunga Belt, crustal thickening is attributed to crustal shortening at the northern end of the Chilean flat slab region (Kay et al., 1999). Figure 2.14d and e illustrates the relationships between SiO_2 and La/Yb, and Sm/Yb and La/Sm at Río Blanco-Los Bronces.

Experiments by Kay and Kay (1993) suggest that amphibole breaks down at pressures near 12-15 kb, which would correspond to depths of about 40-50 km, however exact amphibole breakdown pressures are controlled by bulk composition and ambient temperatures, and can only be approximately inferred from REE data (Kay et al., 1999). Comparison of fields for mineralised units in the Maricunga, El Indio and El Teniente belts by Kay et al. (1999) shows that porphyry mineralisation was likely to have occurred as the residual mafic mineral assemblage was changing from hornblende to garnet. A significant aspect of this reaction is that the breakdown of amphibole releases low-salinity aqueous fluids that may contribute to the mineralisation process (Fig. 2.15; Kay et al., 1999). REE and other chemical signatures in lavas erupted near the time of mineralisation indicate a switch from hydrous, intermediate-pressure, amphibole-bearing residual mineral assemblages to anhydrous, high pressure, garnet-bearing residual mineral assemblages in equilibrium with the magmas (Kay et al., 1999).

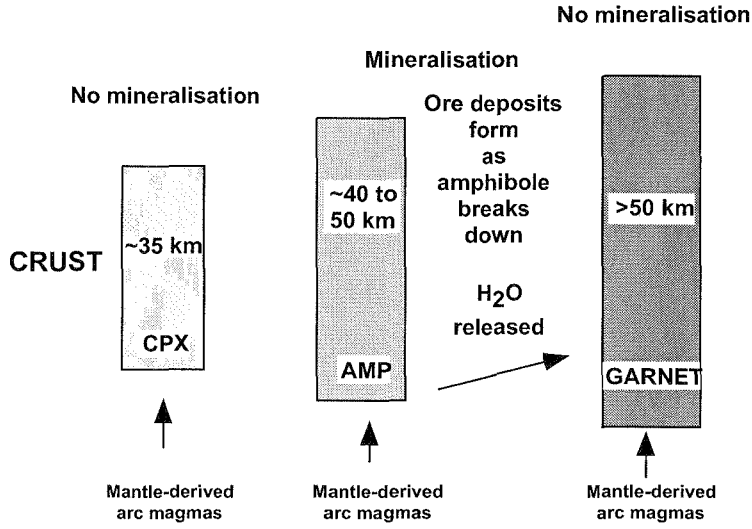

Figure 2.15. Summary diagram speculating on the correlations between crustal thickening, the principal mafic residual mineral assemblage, and formation of Andean mineral deposits (from Kay et al., 1999).

The accumulation of intrusions in the deep crust promotes crustal melting and increases the ductility of the lower crust, making it more susceptible to failure under compression (Kay et al., 1999). Horizontal failure of ductile crust can result in dramatic lower crustal shortening and subsequent thickening with increase in pressure promoting the breakdown of amphibole (Kay et al., 1999). Skewes and Stern (1994) speculated that this rapid crustal thickening could also cause overpressured fluids to be expelled from plutons at a high rate. In the case of Río Blanco, multiphase breccia formation suggests accumulation, release and re-accumulation of overpressured fluids. These overpressured fluids may be sourced from the wholesale breakdown of amphibole to garnet.

2.4.3 Comparison of Roof Pendant andesite and Farellones Formation

Contention exists between Río Blanco geologists as to whether the large body of andesite (roof pendant) in the Río Blanco sector represents a downfaulted block of Farellones Formation or an andesitic intrusion. Five samples from the andesite roof pendant and four samples of andesite from La Americana were analysed by XRF for major and trace element geochemistry and ICP for REE concentrations. The localities of samples collected by Hollings and Frikken (2001) for whole rock geochemistry are shown in Figure 2.16 with sample descriptions and results listed in Appendix B1.

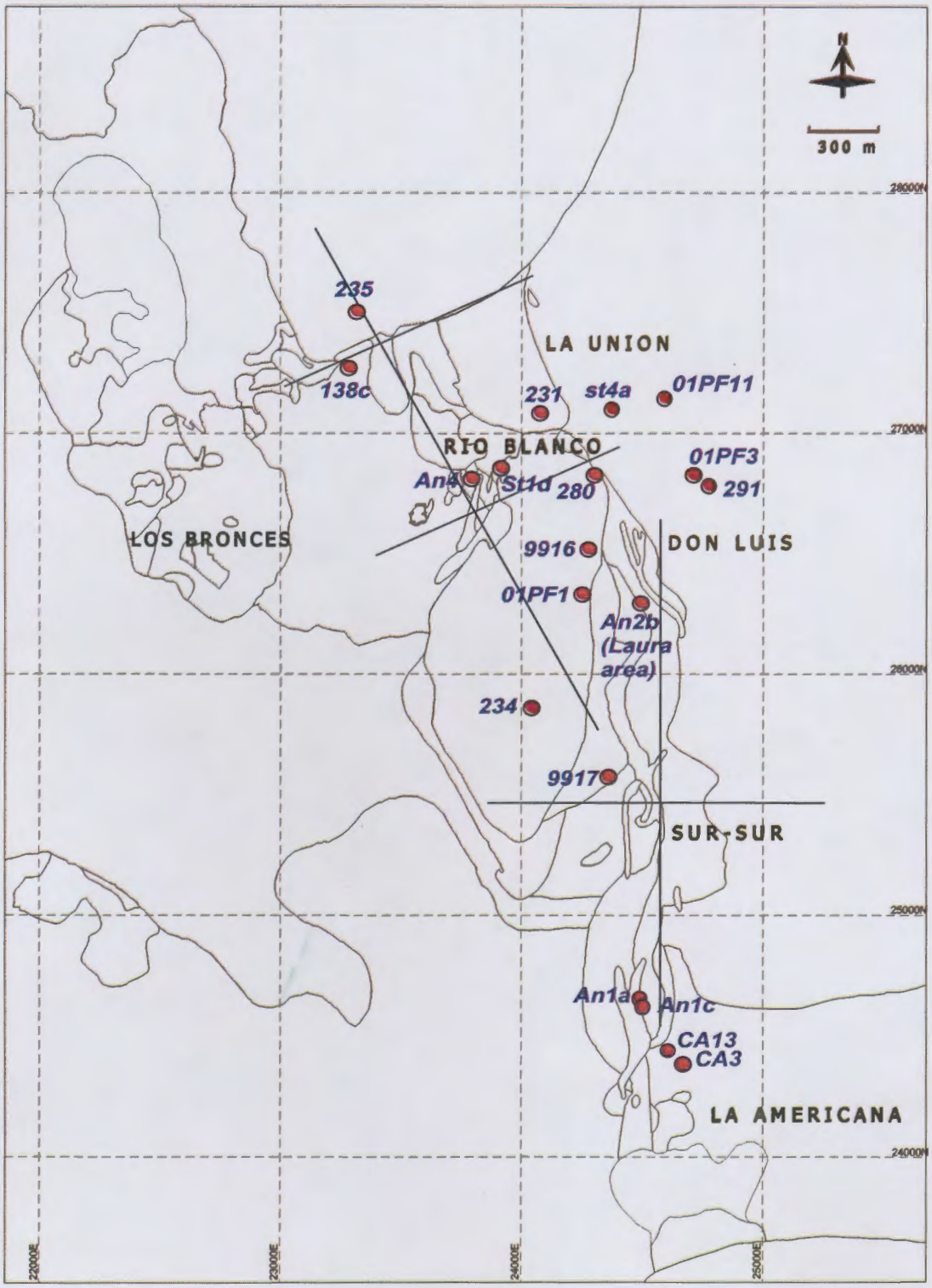

Figure 2.16. Sample localities for whole rock geochemistry from Hollings and Frikken (2001).

The nine samples of andesite chosen for analysis are all moderately to intensely altered with pervasive chlorite, biotite and carbonate alteration. In most of the samples, hydrothermal alteration has destroyed any primary igneous textures (Fig. 2.17), however relict textures containing fresh primary minerals are preserved in two samples. An2b, a surface sample from the Laura area (Fig. 2.16), displays an intrusive texture with large interlocking crystals of plagioclase and relict mafic minerals (now altered to chlorite and biotite). In contrast, sample 235 (Fig. 2.16) contains large plagioclase phenocrysts in a fine-grained groundmass typical of rapid cooling, either as a shallow intrusion or possibly a thick flow. Because primary textures are only preserved in two samples, petrography cannot be used to resolve the origin of the andesite roof pendant (Hollings and Frikken, 2001).

The five samples from the roof pendant, the two samples from deep in La Americana and the two samples from high in La Americana are all andesitic in composition (SiO_2 = 55-58 wt%) and, with one exception, display broadly similar trace element characteristics (Fig. 2.17). The anomalous sample has elevated K_2O (9 wt% versus 1 to 4 wt% for other samples) and Ba contents (1300 ppm), which are likely to be an alteration product. Given the degree of biotite and chlorite alteration in the nine samples, the remarkably coherent primitive mantle normalised patterns (Fig. 2.17) indicate that most of the trace elements remained immobile during hydrothermal alteration (Hollings and Frikken, 2001).

When compared with regional samples of the Farellones Formation from high altitude in La Americana (south of Sur-Sur sector; Fig. 2.16) and andesite samples from deep in La Americana, the roof pendant samples are characterised by higher Rb, and Th but generally lower Sr (Fig. 2.17). In terms of the other trace elements, the roof pendant and La Americana samples are indistinguishable from the regional Farellones Formation data set. Although the roof pendant is geochemically similar to Farellones Formation andesites at La Americana, this fact alone cannot be used to preclude an intrusive origin. Shallow level intrusions emplaced at the same time as the Farellones Formations can be expected to have tapped the same magma sources, and consequently have similar geochemical properties (Hollings and Frikken, 2001).

Copper contents for the andesite roof pendant samples and one of the deep La Americana samples (AN4) are significantly higher than the range of values for the regional Farellones Formation, which includes CA3 and CA13 from the top of La Americana (1300-5400 ppm versus 35-850 ppm for the regional Farellones samples; Hollings, 2001). These copper contents are unlikely to be primary given the generally low copper abundances in fresh andesites (Hollings, 2001). This implies that the hydrothermal fluids responsible for much of the alteration in the roof pendant samples were copper-rich and possibly related to ore formation (Hollings and Frikken, 2001).

The geochemical data are permissive of either model for the origin of the downfaulted block or

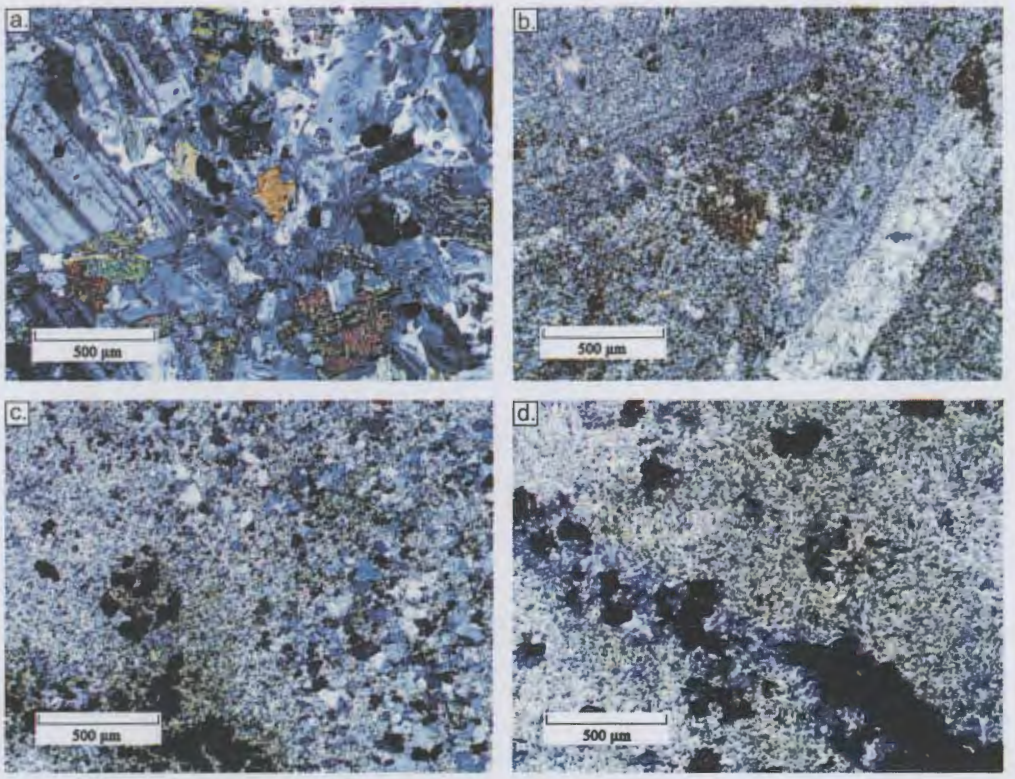

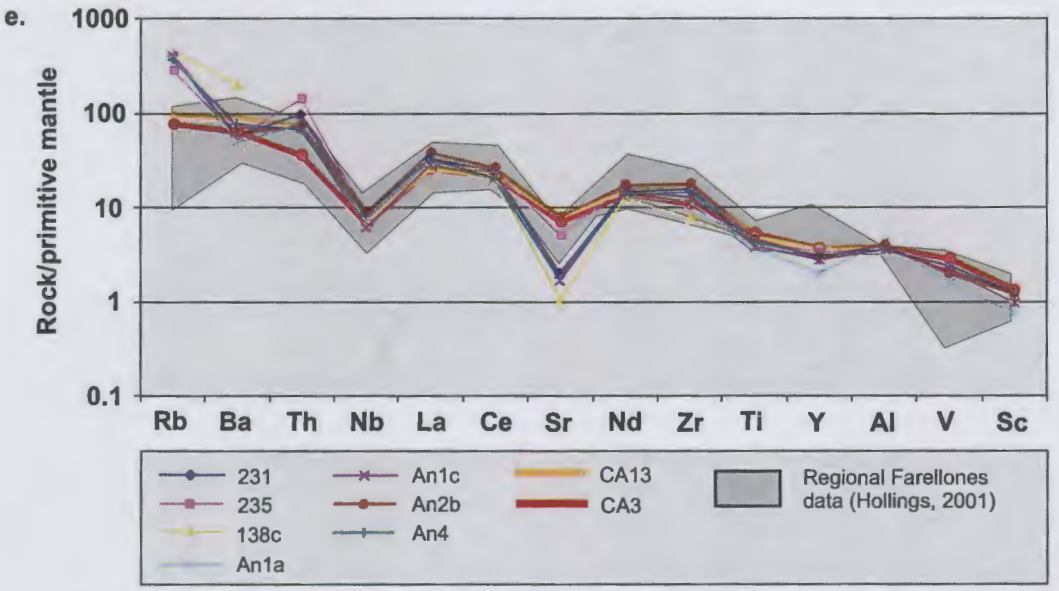

Figure 2.17. Photomicrographs of andesite samples;
a. 235 - least altered roof pendant sample (section XC-195, level 16);
b. An2b - altered surface sample from Laura sector;
c. 231 - biotite altered roof pendant sample (La Union sector);
d. An1c - andesite from deep in La Americana sector (TSS-23, 609 m); and
e. Trace element plot of andesite samples collected within the Río Blanco ore deposit compared with regional Farellones Formation samples from Hollings (2001).

andesite intrusion. Based on geochemical similarities between the roof pendant andesites and the Farellones Formation, I interpret that the roof pendant formed prior to ore formation probably as part of the Farellones Formation, as the andesites are compositionally distinct from the later porphyries.

2.4.4 Comparison between Don Luis Porphyry and Feldspar Porphyry

An investigation of chemical differences between late-stage porphyries at Río Blanco was undertaken using six samples from the Don Luis Porphyry and four samples from the Feldspar Porphyry to assess possible petrogenetic relationships (Fig. 2.16; Appendix B1). In addition, samples of the Don Luis Porphyry were collected through a vertical section to detect whether any changes in composition occur spatially through zones of moderate and low copper grades.

Samples of the Feldspar Porphyry display similar major element abundances to samples from the Don Luis Porphyry. Elevated MgO contents in the Feldspar Porphyry are not coincident with high Ni contents and therefore are probably a product of biotite alteration. Primitive mantle normalised trace element abundances for the Feldspar Porphyry are coherent for all four samples, suggesting they have not been remobilised during alteration (Figs. 2.18, 2.19). When compared with data from the Don Luis Porphyry obtained during this study, the Feldspar Porphyry samples can be seen to overlap the Don Luis Porphyry compositionally (Figs. 2.18, 2.19; Hollings and Frikken, 2001). This is consistent with the work of Serrano et al. (1996) who demonstrated that the majority of late porphyries from Río Blanco had similar whole rock geochemistry and therefore cannot be distinguished geochemically. This suggests that the Feldspar Porphyry and Don Luis Porphyry are co-magmatic.

In order to investigate variations between the deep and shallow Don Luis porphyry, two samples from the deeper levels of the mine and four surface/near surface samples were analysed. All six samples are characterised by broadly similar major element abundances comparable to values reported in Serrano et al. (1996) with SiO_2 from 69 to 74 wt% and Al_2O_3 from 14 to 17 wt% (Appendix B1 and B2). Figure 2.19 shows the trace element abundances of the six samples. Apart from minor variations in LILE (Rb, Ba and Sr) the six samples are geochemically indistinguishable. Consequently, within the limitations of the existing geochemical data set, there are no apparent compositional differences between deep (280 and 291) and shallow (9916, 9917, 234 and St4a) portions of the Don Luis porphyry that would indicate distinct intrusive phases (Hollings and Frikken, 2001). Consequently, the Don Luis Porphyry is interpreted to have intruded as one body rather than as two discrete phases.

Copper contents for the six Don Luis Porphyry samples vary considerably (15-6025 ppm; Appen-

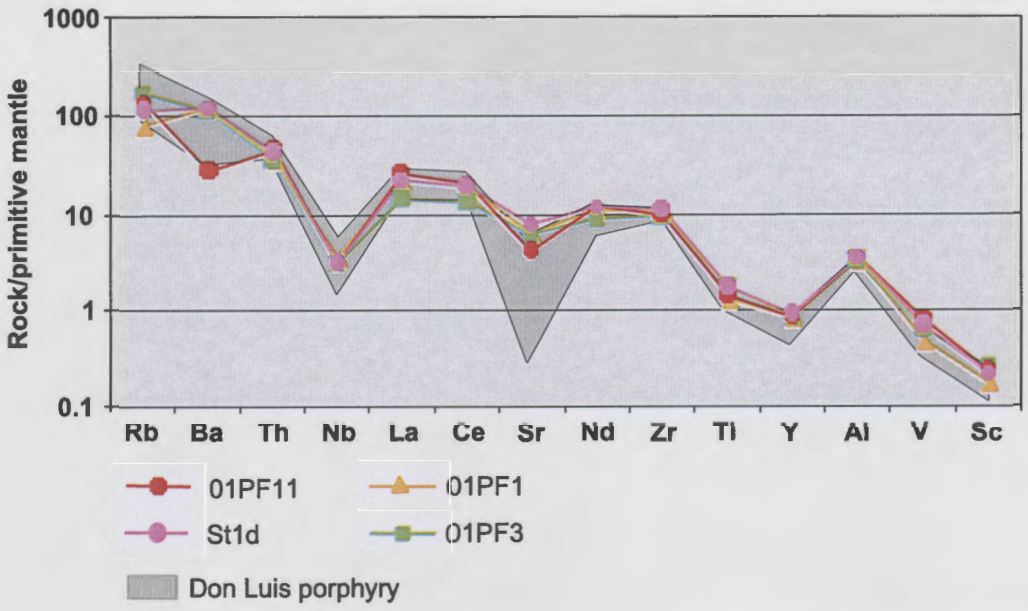

Figure 2.18. Trace element plot of Feldspar Porphyry (PF) collected in the Río Blanco ore deposit. A photograph showing typical PF can be seen in Figure 2.7b. Sample 01PF11 = DDH-738, 276.5 m; 01PF1 = DDH-733, 343.5 m; st1d = DDH-576, 109 m; and 01PF3 = DDH-734, 465 m.

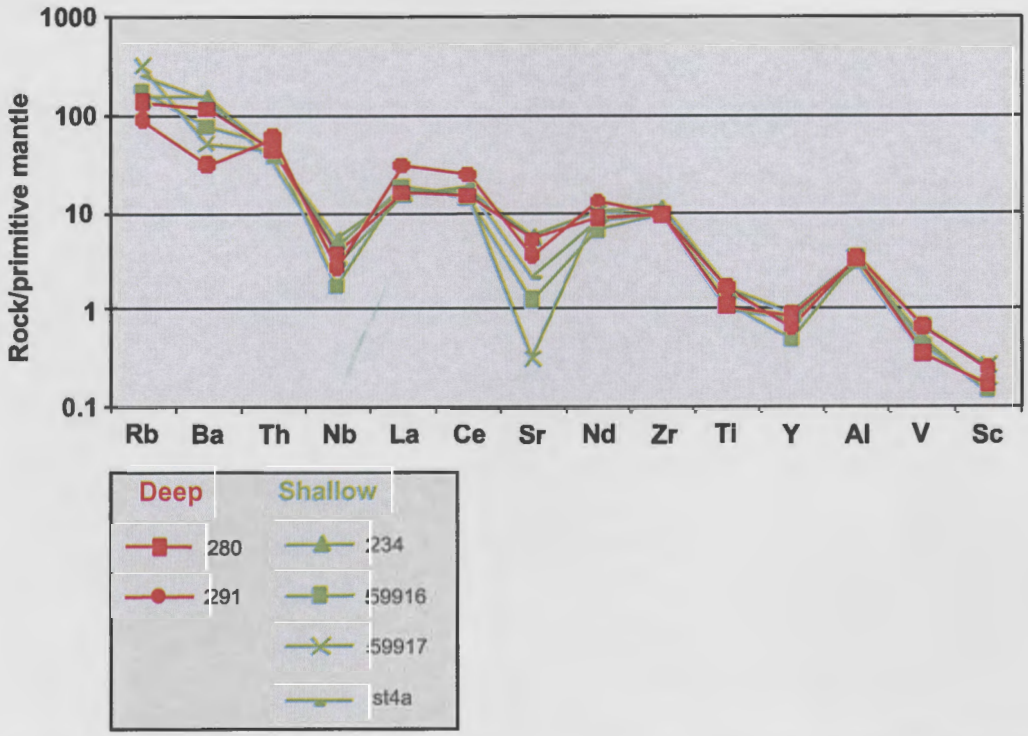

Figure 2.19. Trace element plot of deep and shallow Don Luis Porphyry (PDL) collected in the Río Blanco ore deposit. A photograph showing typical PF can be seen in Figure 2.7d. Sample 280 = DDH-734, 392 m; 291 = DDH-734, 470.4 m; 234 = surface sample from Monolito Mountain; 59916 = DL-94, 221 m; 59917 = DDH-560, 258 m; and st4a = DDH-380, 320 m.

dix B1) but not systematically in a spatial sense (Figs. 2.16 and 2.19). Similarly there are no significant correlations between trace element abundances and copper contents (Hollings and Frikken, 2001). It is concluded that the Don Luis Porphyry is variably mineralised with copper up to 0.6 wt%. It is a post-mineral, weakly mineralised intrusion, as is observed in many other porphyry deposits (e.g. El Salvador, Grasberg etc, Gustafson and Hunt, 1975; McMahon, 1994).

2.5 Summary

- The Río Blanco-Los Bronces deposit is hosted within Miocene granodiorite of the San Francisco Batholith and overlying rocks of the Farellones Formation.
- The Río Blanco sector is host to the 7.3-4.2 Ma biotite-cemented Magmatic Breccia. The Magmatic Breccia is not igneous-cemented as its name suggests. Instead, it contains igneous clasts that are supported by an interstitial material that ranges from fine-grained, partially recrystallised microgranular hydrothermal cement to a rock flour matrix composed of broken mineral and clast fragments. The breccia has been cemented and clasts and matrix altered by hydrothermal minerals that include biotite ± sulfides ± sulfates ± quartz ± magnetite ± specularite ± tourmaline.
- The Sur-Sur sector is host to four distinct breccia bodies, the Tourmaline Breccia, Castellana Breccia, Monolito Breccia and the Paloma Breccia. The Tourmaline Breccia is host to the Sur-Sur orebody, is monolithologic and consists of variably shaped clasts supported by a milled rock flour matrix that has been almost completely replaced by secondary tourmaline cement. In addition, the cement also contains variable amounts of sulfides ± sulfates ± quartz ± magnetite ± specularite ± biotite. The Castellana, Monolito and Paloma breccias are rock flour breccias.
- Three major fault orientations occur at the district and ore deposit scales that are N-, NW- and NE-trending. The Sur-Sur Tourmaline Breccia is aligned along a N-S trending fault (Río Blanco Fault) and is cross cut by the NW- and NE-tending faults. The fracture frequency the NW and NE faults in the Tourmaline Breccia is variable along strike. The zones of highest fracture frequency correspond to zones of high copper grade, high frequency of cross cutting veins and an abundance of hydrothermal mineral cement in the breccia. In contrast, zones of low fracture frequency are low grade; contain a low frequency of fractures and crosscutting veins; and a low abundance of tourmaline cement and other hydrothermal minerals in the matrix (<5%).
- The results of geochemical studies of the roof pendant andesite, Don Luis porphyry and Feldspar Porphyry at Río Blanco are consistent with the findings of Serrano et al. (1996). Samples from deep and shallow portions of the Don Luis Porphyry are geochemically indistinguishable and comparable to the Feldspar Porphyry. Although the roof pendant

samples are geochemically indistinguishable from regional samples of the Farellones Formation, this cannot conclusively demonstrate an extrusive or shallow intrusive origin for these rocks. Deeper intrusions emplaced coevally with the Farellones Formation could be expected to have tapped the same sources and hence have the same geochemistry as the Farellones Formation. However, the data does demonstrate that the andesite roof pendant is not a separate intrusion with geochemical affinities to the later porphyries.

- Detailed mapping of contact zones and further petrographic studies are required to conclusively resolve the origin of the roof pendant but will be difficult given the high degree of pervasive alteration. If the roof-pendant is a downfaulted block of Farellones Formation, then it may be that more detailed mapping of contact relationships and small-scale mapping will provide evidence to confirm or refute the down-faulting model.

Section 3 - The Mineralised Río Blanco and Sur-Sur Breccia Complexes

3.1 Introduction

This section describes the mineralised breccias in the Río Blanco and Sur-Sur sectors of the ore deposit complex. In comparison to classic porphyry stockwork mineralisation (e.g. El Teniente; Camus, 1975), stockwork mineralisation at Río Blanco is weakly developed. Instead, approximately three-quarters of the >50 million metric tonnes of copper and >1.26 million metric tonnes of molybdenum contained in the system (Camus, 2002) occurs as cement to the Río Blanco 'Magmatic Breccia' and Sur-Sur Tourmaline Breccia. Part of the resource is hosted within the various potassic and phyllic altered wallrocks, breccia clasts and related veins.

The orebody in the Río Blanco sector constitutes 50% of the resource in the Río Blanco-Los Bronces ore deposit (Serrano et al., 1996). The Río Blanco orebody extends from the Río Blanco sector through La Union and the Don Luis sectors, and is associated with biotite (potassic) alteration. The Sur-Sur orebody has an elongate north-trending geometry and occurs to the southeast of the Río Blanco orebody associated with quartz-sericite alteration. Ore grades decrease to the east and west of the Río Blanco and Sur-Sur orebodies, as does the chalcopyrite/pyrite ratio, and ore is hosted increasingly by stockwork veins (Serrano et al., 1996). The paragenesis at Río Blanco has so far been poorly documented, however Serrano et al. (1996) argue that the mineralised breccias are cut by the porphyries, while Vargas et al. (1999) argue for mutually cross cutting relationships between the mineralised breccias and the porphyries. Overall, they both provide no substantial data on the paragenesis at Río Blanco.

Results of core logging and thin section petrography of ore and gangue minerals are described within a paragenetic framework defined on the basis of observed cross cutting and overprinting relationships. Ore and gangue minerals are also plotted spatially to assess spatial zonation patterns.

3.2 Paragenesis

This section describes the breccias, veins, porphyries and associated mineralisation and alteration assemblages in the Río Blanco and Sur-Sur sectors. They are described sequentially from oldest to

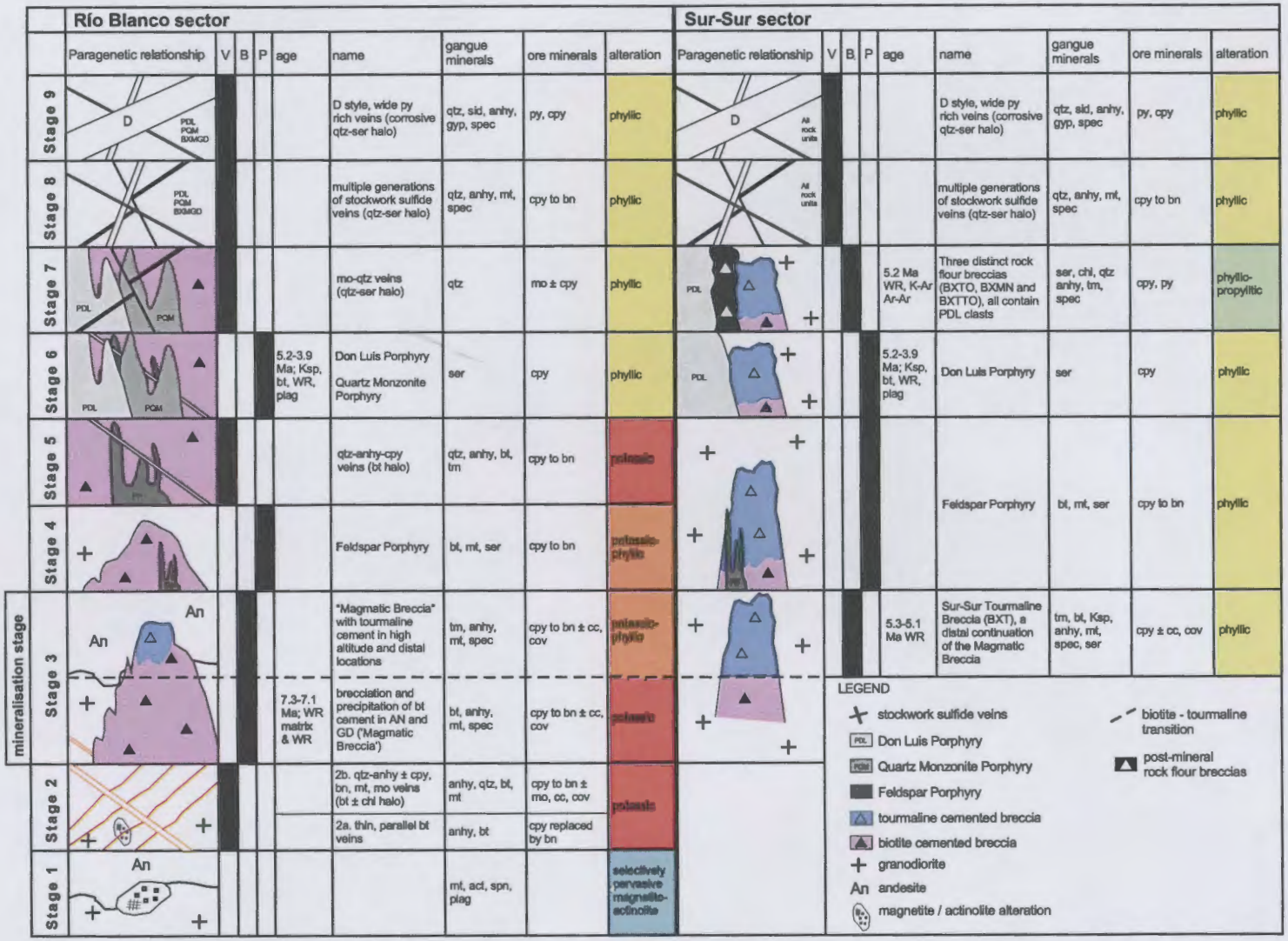

Figure 3.1. Paragenetic sequence of veins, breccias, porphyritic intrusions and alteration with associated ore/mineral assemblages for Río Blanco and Sur-Sur sectors. Abbreviations: act = actinolite; An = andesite; anhy = anhydrite; B = breccia; bn = bornite; bt = biotite; BXMGD = Magmatic Breccia; BXT = Tourmaline Breccia; cpy = chalcopyrite; chl = chlorite; D = D vein; dig = digenite; gal = galena; gd = granodiorite; gyp = gypsum; hbl = hornblende; Ksp = K-feldspar; mo = molybdenite; mt = magnetite; PDL = Don Luis Porphyry; P = porphyry; plag = plagioclase; PQM = Quartz Monzonite Porphyry; py = pyrite; qtz = quartz; sid = siderite; spec = specularite; spn = sphene; tenn = tennantite; tm = tourmaline; V = vein; WR = whole-rock.

youngest with the paragenesis determined from observations made through detailed core logging and petrographic studies of samples from Río Blanco, Don Luis and Sur-Sur sectors in the ore deposit complex (Fig. 3.1). The paragenesis is based specifically on cross-cutting relationships and some minerals preserved in events may be have been deposited by later events. The paragenetic sequence, illustrated in Figure 3.1 has been divided into two main periods on the basis of alteration assemblages:

i) early vein sets and breccias associated with potassic alteration, and characterised by hydrothermal biotite; and

ii) late stage intrusions, rock flour breccias and stockwork veins associated with quartz-sericite alteration.

3.2.1 Stage 1: magnetite-actinolite alteration

Initial hydrothermal activity in the Río Blanco system resulted in magnetite-actinolite alteration of the Río Blanco Granodiorite and Cascada Granodiorite (Fig. 3.1). Serrano et al. (1996) described magnetite-actinolite as the most widely distributed alteration assemblage at Río Blanco. It has affected all of the plutons of the San Francisco Batholith that surround the potassically-altered core of the deposit. This alteration assemblage is characterised by disseminated hydrothermal actinolite ± magnetite ± sphene with halos containing secondary actinolite ± magnetite ± sphene that has replaced primary igneous minerals such as biotite and hornblende (Figs. 3.2a; 3.3a; Serrano et al., 1996). The stage 1 alteration assemblage is not associated with any particular vein generation. It appears to be a pervasive metasomatic precursor to later fracture- and breccia-controlled hydrothermal activity.

3.2.2 Stage 2: early potassic veins

The stage 1 magnetite-actinolite alteration assemblage has been crosscut by a set of thin (0.1-0.2 cm), typically sub-parallel biotite veins (Stage 2a) with variable spacing from 0.5 cm to 5 cm (Figs. 3.1; 3.2a; 3.3a, b). Stage 2a veins also contain anhydrite and chalcopyrite, the latter of which has in many cases been partially replaced by bornite, covellite and chalcocite (Fig. 3.3c, d). Outside the vein walls, these veins have thin (<1 mm) alteration halos of hydrothermal biotite.

Stage 2a veins are crosscut by stage 2b, which are predominantly quartz-anhydrite veins with biotite halos that have random ('stockwork') distribution (Fig. 3.2b). The minor chalcopyrite in these veins has been partially replaced by bornite. Magnetite, molybdenite, chalcocite and covellite are also present (Fig. 3.3e, f). Stage 2b veins are wider than the stage 2a veins, ranging up to 4 cm, but generally are 0.5 to 1 cm wide. Biotite-chlorite alteration halos around stage 2b veins extend for up to 3 cm laterally from the vein walls. Chlorite typically occurs near the vein walls with biotite

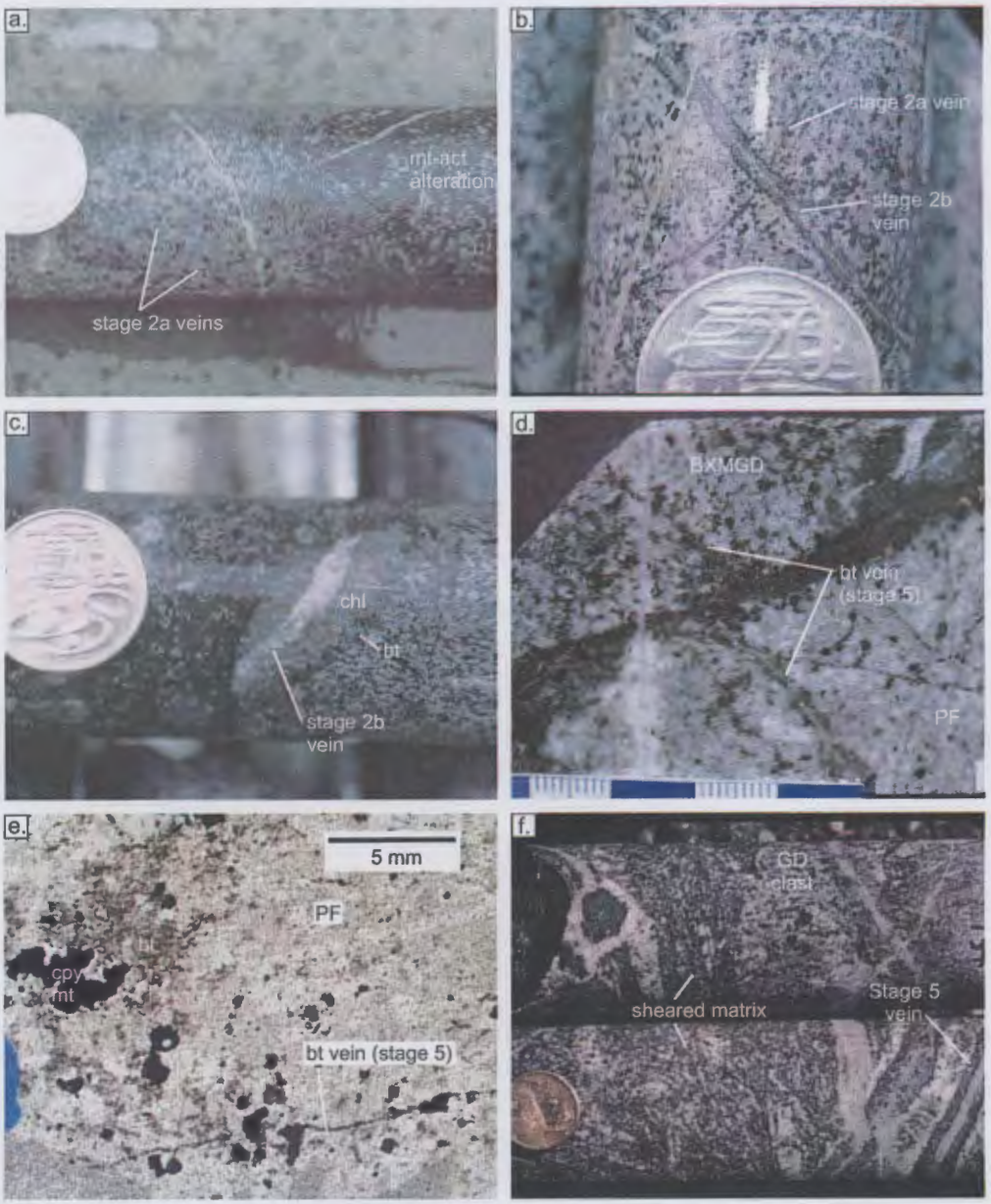

Figure 3.2. Cross-cutting relationships that define the paragenesis of potassic events at Río Blanco. All samples from DDH-734 in the Don Luis sector, abbreviations shown on Figure 3.1, scale bar in cm, Australian 20c piece is 2.5 cm in diameter:
a. Stage 1 magnetite-actinolite alteration in Río Blanco Granodiorite cut by thin stage 2a biotite veins (sample 272, 350 m downhole);
b. Stage 2a thin parallel biotite vein cut by stage 2b quartz-anhydrite ± chalcopyrite, bornite, magnetite, molybdenite veins (biotite-chlorite halo) in Río Blanco Granodiorite (sample 282, 411 m downhole);
c. Stage 2b quartz-anhydrite ± chalcopyrite, bornite, magnetite, molybdenite veins (biotite-chlorite halo) cut by stage 3 Magmatic Breccia (sample 324, 616 m downhole);
d. Stage 3 Magmatic Breccia (BXMGD) cut by stage 4 Feldspar Porphyry (PF) that is in turn cut by stage 5 quartz-anhydrite-chalcopyrite veins (biotite halo; sample 321, 596.5 m downhole);
e. Photomicrograph of stage 4 Feldspar Porphyry cut by stage 5 quartz-anhydrite-chalcopyrite veins (biotite halo) and hydrothermal biotite alteration (sample 301, 508 m downhole); and
f. Deformed stage 3 Magmatic Breccia deep in the Don Luis sector (628 m downhole, 2730 m elevation). Granodiorite clasts occur as elongate, rectangular splinters and are randomly oriented except where shear bands have caused realignment of clasts. Stage 5 veins are cut by the sheared Magmatic Breccia and are unaffected by the deformation.

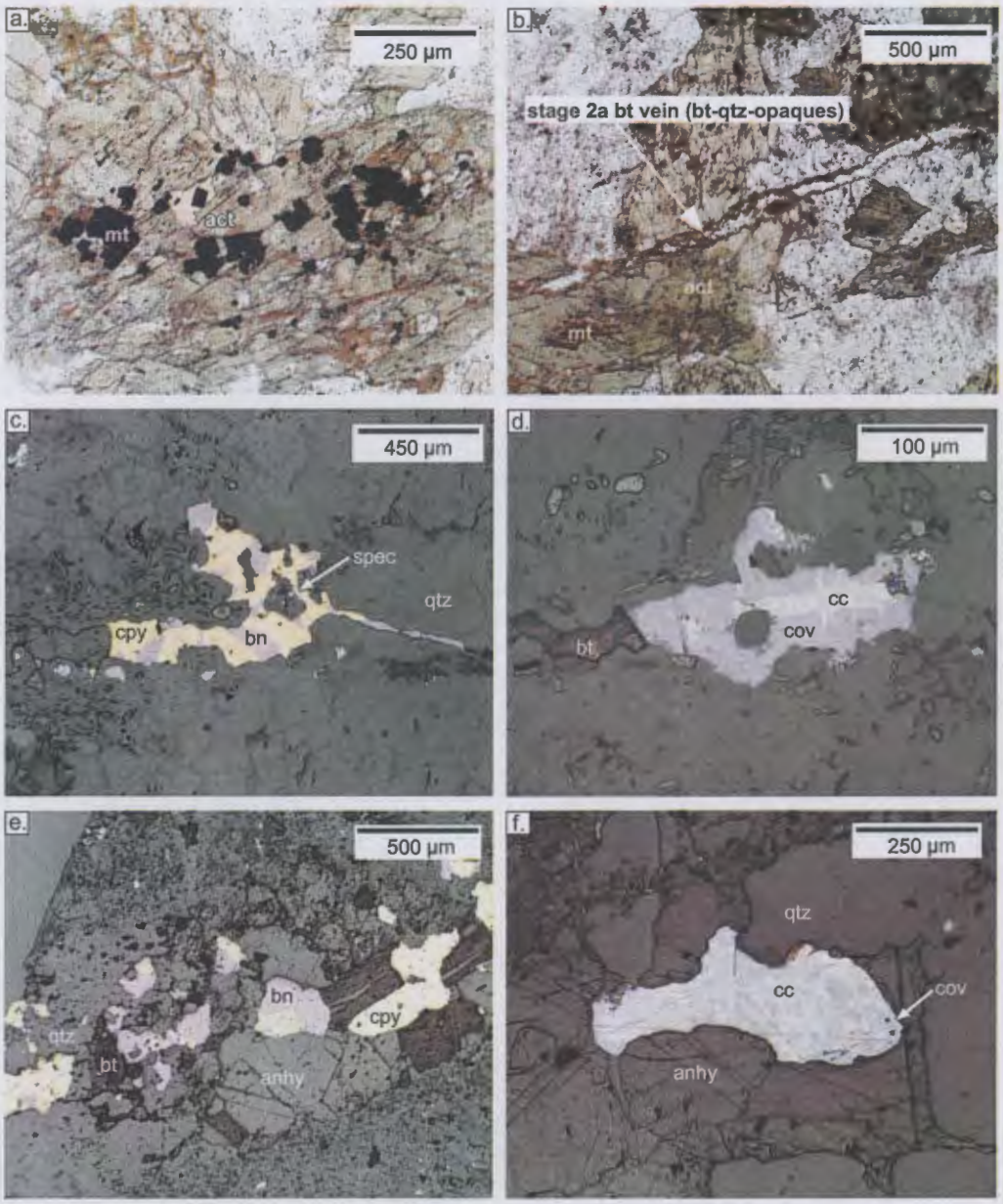

Figure 3.3. Photomicrographs showing pre-mineralisation magnetite-actinolite alteration (stage 1) and potassic vein events (stage 2). All samples from DDH-734.
a. Stage 1 magnetite-actinolite alteration of primary hornblende in Cascada Granodiorite. The magnetite-actinolite-biotite assemblage are in textural equilibrium (sample 272, 350 m down hole);
b. Stage 1 magnetite-actinolite altered Cascada Granodiorite cross cut by stage 2a biotite veinlets (with visable quartz and opaques; sample 272, 350 m down hole);
c. Stage 2a biotite veinlets. Bornite is intergrown with chalcopyrite, specularite and quartz. Host rock is Cascada Granodiorite (sample 272, 350 m down hole);
d. Stage 2a thin, parallel biotite veinlets with chalcocite, covellite and biotite in Cascada Granodiorite (sample 272, 350 m down hole);
e. Stage 2b quartz-anhydrite vein with chalcopyrite and bornite in Cascada Granodiorite (sample 270, 347.9 m downhole) and;
f. Stage 2b quartz-anhydrite vein with chalcocite and covellite that appears to have partially replaced anhydrite in Cascada Granodiorite (sample 272, 350 m down hole).

more abundant towards the outer edge of the halo. This is interpreted to be a product of vein reopening, which has caused retrogression of stage 2 biotite to chlorite (Fig. 3.2b, c).

Stage 2 veins are abundant locally in the core of the Río Blanco and Don Luis sectors. These early veins invariably have biotite-bearing vein selvages and alteration halos.

3.2.3 Stage 3: mineralised breccias

Río Blanco Magmatic Breccia

Stage 2 veins were disrupted and segmented by a major brecciation event, which produced the mineralised Río Blanco 'Magmatic Breccia' complex (Fig. 3.2c). The Magmatic Breccia is characterised by a potassic alteration assemblage where hydrothermal biotite and K-feldspar are the main alteration minerals. The breccias contain both rock flour matrix (altered to biotite) and hydrothermal cements, including tourmaline, anhydrite, specularite, chalcopyrite, magnetite, pyrite and quartz (Fig. 3.4). Clasts of andesite and granodiorite occur in the breccia (Fig. 3.5a). The deposition of hydrothermal cement minerals in the Tourmaline Breccia occurred in two main stages; 1) a pre-ore oxide stage, which is overgrown by 2) a mineralisation stage (Fig. 3.4).

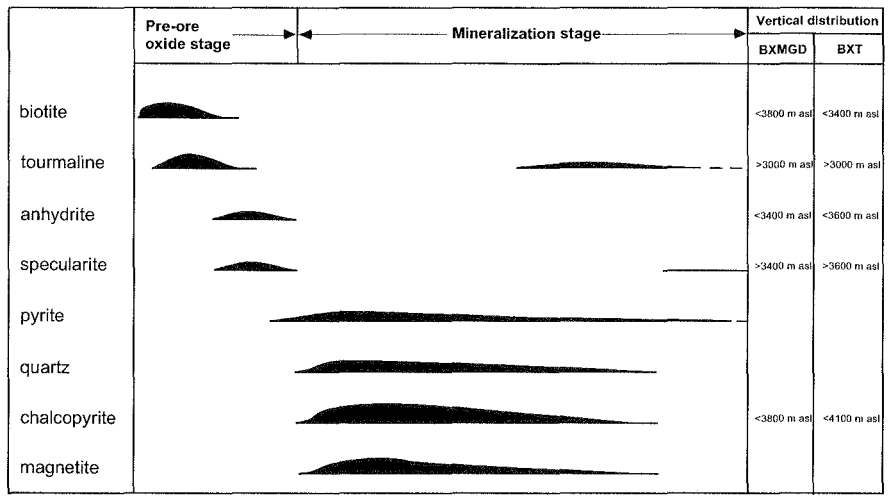

Figure 3.4. Paragenesis of the Río Blanco Magmatic Breccia (BXMGD) and Sur-Sur Tourmaline Breccia (BXT). This scheme encompasses hydrothermal cements deposited during and/or after breccia formation, together with their spatial distribution.

The infill sequence for the Magmatic Breccia cement is biotite and tourmaline, then anhydrite, specularite, chalcopyrite and magnetite (Figs. 3.4-3.7). Relationships between hydrothermal biotite and tourmaline remains unresolved due to their fine-grained nature. No textural evidence has been observed that eliminates the possibility of co-precipitation. Conversely, no unambiguous evidence of simultaneous deposition of biotite and tourmaline can be shown. There is a spatial zonation in the breccia cement from biotite in the core of the system, outward to tourmaline cement in both Río Blanco and Sur-Sur. Bornite has replaced chalcopyrite and specularite is commonly associated with the bornite, probably accommodating the iron liberated by chalcopyrite destruction.

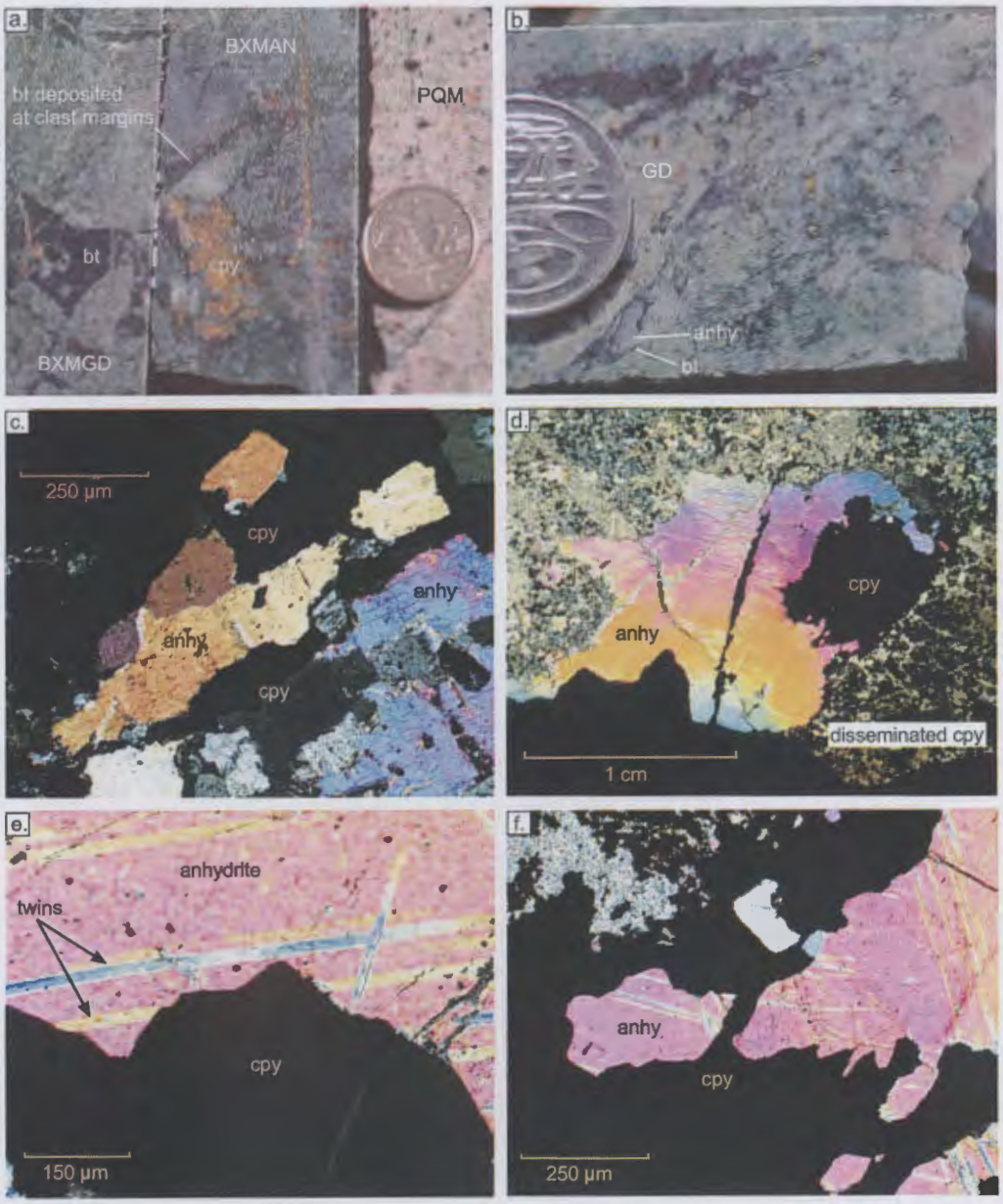

Figure 3.5. Photographs and photomicrographs showing stage 3 - Magmatic Breccia cement in the RíoBlanco sector:
a. Typical Magmatic Breccia with granodiorite clasts (BXMGD; far left) and andesite clasts (BXMAN; middle). Hydrothermal biotite has replaced clast margins and was the first cement to form within the Magmatic Breccia (DDH-450);
b. Cement infill relationship between biotite and anhydrite. Biotite has replaced clast margins and is overgrown by anhydrite (DDH-454);
c. Large, euhedral anhydrite crystals partially replaced by chalcopyrite (sample 241b, DDH-450, 3044 m asl), cross polarised light;
d. Anhydrite cement at depth, replaced by chalcopyrite (sample 335, DDH-628, 3261 m asl);
e. Higher magnification of textural relationship shown in 3.5d., chalcopyrite crosscuts anhydrite twins; and
f. Anhydrite cut by chalcopyrite (sample 335, DDH-628, 3261 m asl).

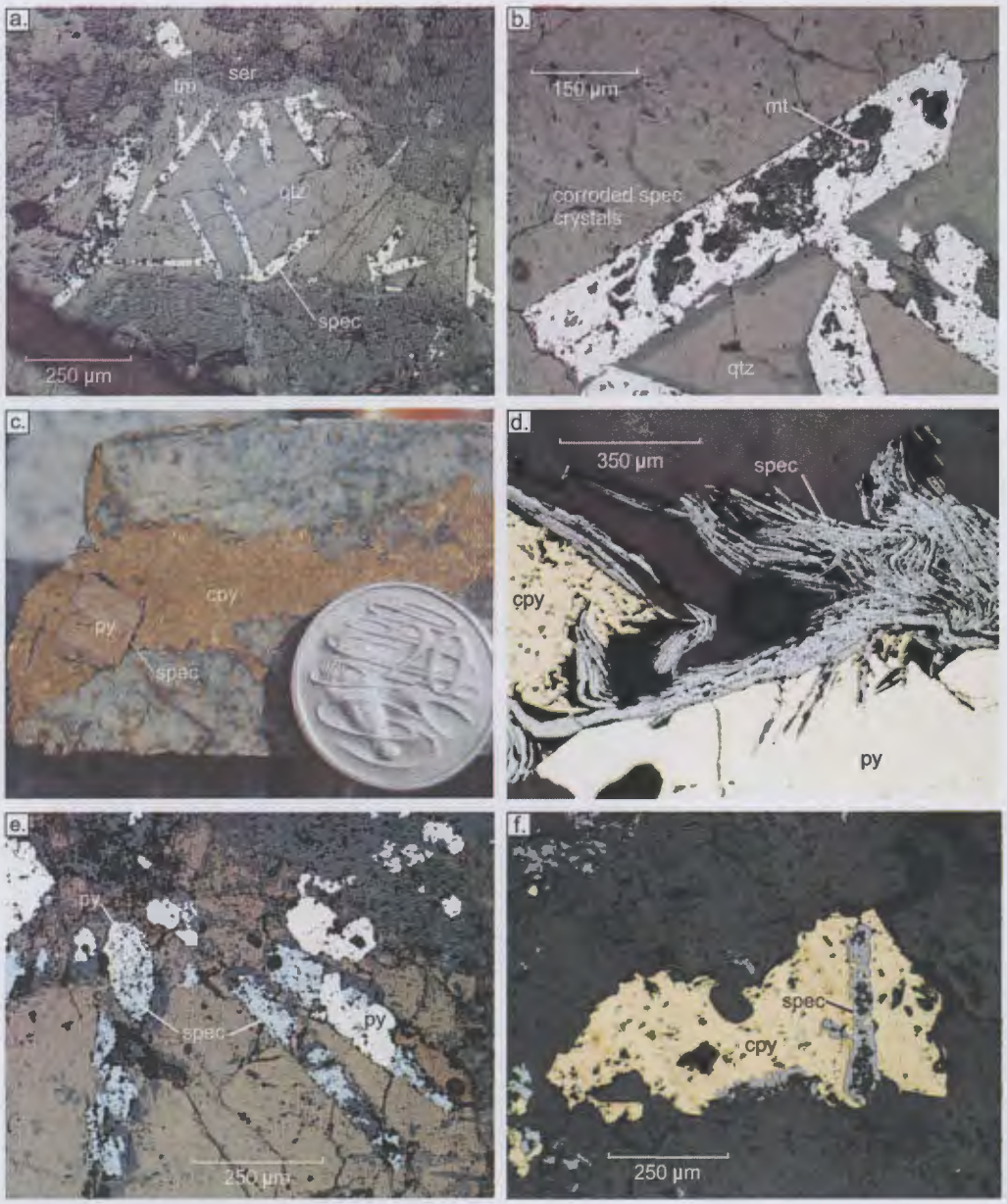

Figure 3.6. Photomicrographs of Magmatic Breccia cement in the Río Blanco sector:
a. Specularite is an abundant early oxide-stage mineral at high elevation in the breccia column. In this example it has overgrown a thin rind of tourmaline at the clast margins and subhedral quartz crystals have grown perpendicular to clasts margins with (or after) the specularite. Sericite alteration occurs in clasts associated with the tourmaline (sample 354, DDH-101, 3862 m asl);
b. Enlargement of part of Figure 3.7a. The specularite crystals display internal corrosion and replacement by main-stage magnetite;
c. Large, euhedral pyrite crystal grown in chalcopyrite-cemented Magmatic Breccia. Specularite crystals occur on the rim of the pyrite crystal (sample 376, DDH-454, 116 m downhole);
d. Photomicrograph of the edge of a large, euhedral pyrite crystal. Deformed specularite crystals occur on the rim of the pyrite crystal. This sample was collected from the outer margins of the orebody (sample 376, DDH-454, 116 m);
e. Early, euhedral specularite crystals replaced by pyrite, again surrounded by subhedral quartz crystals (sample 354, DDH-101, 3862 m asl); and
f. Early, relict specularite crystal corroded and partially replaced by chalcopyrite and rutile (sample 241b, DDH-450, 136 m).

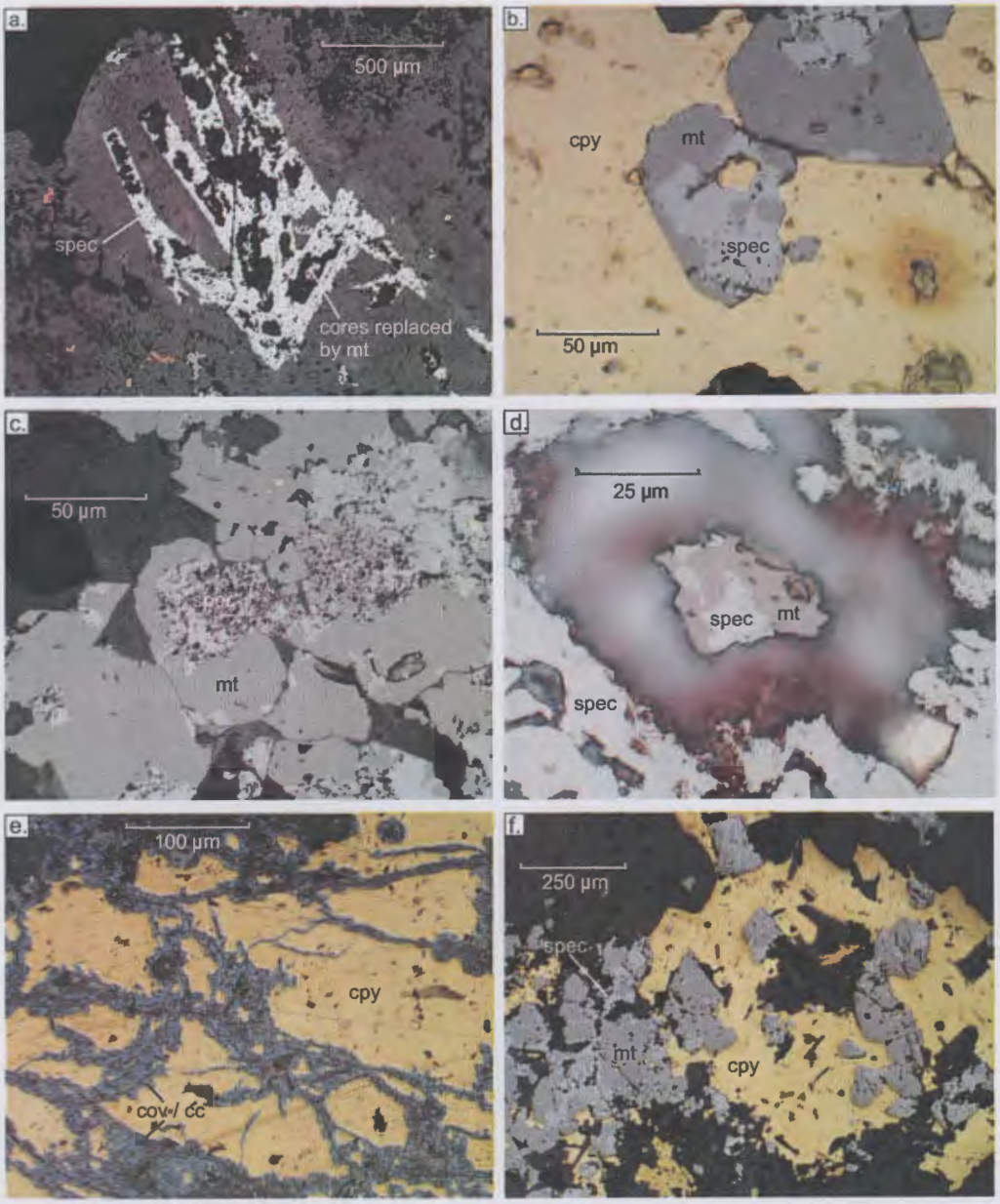

Figure 3.7. Photomicrographs of Magmatic Breccia cement in the Río Blanco sector:
a. Specularite crystals with corroded cores that have been replaced by magnetite (sample 354, DDH-101, 3862 m asl);
b. Residual specularite replaced by magnetite, which in turn has been partially altered to hematite (sample 241b, DDH-450, 3044 m asl);
c. Residual specularite replaced by magnetite at crystal margins (sample 241b, DDH-450, 3044 m asl);
d. Corroded core of a specularite crystal that has been partially replaced by magnetite (sample 354, DDH-101, 3862 m asl);
e. Sample from high altitude in the Río Blanco orebody. Chalcopyrite has been partially replaced by chalcocite and covellite, which are inferred to be supergene in origin (sample 350, DDH-101, 3860 m asl); and
f. Typical main-stage cement in the Magmatic Breccia orebody. Chalcopyrite is interpreted to have co-precipitated with magnetite based on the well-formed nature of chalcopyrite and magnetite crystals and the non-destructive textures between them. Magnetite has been altered to hematite along fractures and around grain margins (sample 239f, DDH-450, 3104 m asl).

Anhydrite and specularite cement in the Magmatic Breccia have overgrown early biotite and tourmaline, respectively (Figs. 3.5b and 3.6a). Where biotite and anhydrite occur together as cements, biotite has replaced the clast margins and anhydrite has grown into space outwards from the clast margins and the thin layer of biotite (Fig. 3.5b). Anhydrite crystals are euhedral and range up to 1 cm long and 3 mm wide. Anhydrite has been partially replaced by chalcopyrite (e.g. Fig. 3.5c, d, e, f). No textural relationships between anhydrite and specularite have been observed because early anhydrite occurs only at depth (<3400 m) and early specularite occurs only at high elevations (>3400 m) in the orebody. No spatial overlap of these two early stage 3 cement phases has been observed in the Río Blanco sector during the current study.

Euhedral specularite crystals are 0.5 mm long and 150 ìm wide (Figs. 3.6a, b, f and 3.7a). Specularite crystals have been replaced by magnetite on their outer margins (Fig. 3.7b, c) and internally (Figs. 3.6b, 3.7a, d). The degree of internal corrosion of specularite varies with spatial location, with specularite in the deeper parts of the deposit less corroded compared to that preserved at higher altitudes (Fig. 3.7a, b). Oxide cement replacement textures in the Río Blanco Magmatic Breccia indicate an important change in the redox conditions of the fluid from oxidised to relatively reduced mineral assemblages.

On the lateral fringes and upper levels of the orebody, large, euhedral pyrite crystals occur that are surrounded by fine-grained deformed specularite (Fig. 3.6c, d). The specularite has in turn been overgrown by chalcopyrite. Specularite has overgrown pyrite (Fig. 3.6d) and also has been replaced by pyrite (Fig. 3.6e). These contradictory replacement textures are interpreted to indicate that the pyrite was deposited either after specularite, or at the same time.

The predominant sulfide cement in the Magmatic Breccia is chalcopyrite (85 vol.%) and bornite (15 vol.%). The sulfides have partially cemented the biotite-altered rock flour matrix. Chalcopyrite also occurs as disseminations within the altered granodiorite and andesite clasts. Chalcopyrite-bornite and chalcopyrite-pyrite were observed as stable mineral assemblages. Bornite has replaced chalcopyrite at grain margins and along internal fractures. Bornite is most abundant within stage 2 veins that have been crosscut by the stage 3 Magmatic Breccia, and in stage 4 veins that crosscut the Magmatic Breccia. At high elevations within the Río Blanco Magmatic Breccia, chalcopyrite has been partially replaced by covellite and chalcocite, probably as a result of supergene processes (Fig. 3.7e). This minor supergene upgrading has not increased the grade of the copper resource significantly. This is evident from its limited (approximately 100 m) vertical extent in Río Blanco and Sur-Sur and its incipient nature, based on the abundance of chalcopyrite relative to the supergene sulfides. The photomicrograph in Figure 3.7e shows the greatest abundance of chalcocite relative to chalcopyrite observed in the current study.

Magnetite is a stable cement phase in the stage 3 breccias. Textural relationships between chalcopyrite and magnetite cement are interpreted to indicate co-precipitation rather than replacement (Fig. 3.7f). Stage 3 magnetite is most abundant towards the top of the Río Blanco system. At these high elevations, it has consistently been replaced by hematite around grain boundaries (Fig. 3.7f). Rutile is one of the most common minerals observed in all samples analysed and has commonly replaced magnetite, biotite and specularite. Minor late-stage specularite has overgrown all earlier-formed stage 3 minerals within the Magmatic Breccia (Fig. 3.4).

The abundance of chalcopyrite and other sulfide minerals is variable throughout the Río Blanco orebody, particularly where stage 4 and 6 porphyries (average grades <0.5% Cu) have crosscut the Magmatic Breccia (average grades ~1.0%, locally up to 5% Cu) resulting in significant dilution of copper grade.

Biotite alteration gives way laterally to the east and west of the Río Blanco orebody, outwards to a propylitic assemblage characterised by chlorite and epidote (Serrano et al., 1996). This alteration assemblage also occurs in the highest levels of the Magmatic Breccia in the andesite above its contact with the granodiorite, where a chlorite, epidote, specularite, pyrite and siderite alteration assemblage has destroyed primary igneous textures (Serrano et al., 1996).

The Magmatic Breccia is deformed in the deeper levels of the Don Luis sector. Figure 3.2f shows Magmatic Breccia with both brittle and ductile deformation fabrics. The granodiorite clasts occur as elongate, rectangular splinters, a process best explained by brittle deformation. Locally, the elongate clasts are preferentially aligned parallel to shear bands and a cleavage is defined by the biotite-altered rock flour matrix. This zone of sheared Magmatic Breccia breccia is located north of the Sur-Sur Tourmaline Breccia, along strike of the Río Blanco Fault at 2730 m elevation. It has only been observed in one exploration drill hole (DDH-734) in the current study, and its full extent is unknown.

Sur-Sur Tourmaline Breccia

The Sur-Sur Tourmaline Breccia (BXT) complex extends over a 3 km strike length to the southeast of the Río Blanco Magmatic Breccia (Fig. 2.1). The cement infill sequence of the Sur-Sur breccia cement is identical to that in the Río Blanco Magmatic Breccia (Fig. 3.4). However, the abundance of key minerals such as biotite and tourmaline varies dramatically between the two breccia bodies. As for the Río Blanco Magmatic Breccia, the deposition of hydrothermal cements in the Tourmaline Breccia occurred in two main stages; 1) a pre-ore oxide stage and; 2) a mineralisation stage (Fig. 3.4). One major difference between the two breccia bodies is the associated hydrothermal alteration minerals. Biotite is predominant in the Magmatic Breccia, whereas a quartz-sericite (phyllic) alteration assemblage characterises the Tourmaline Breccia.

Stage 2 biotite veins have not been observed in the Sur-Sur sector. However, stage 3 biotite cement is preserved at the deepest levels of the Tourmaline Breccia complex (<3000 m elevation). Deep-level biotite and high-level tourmaline (dravite) were consistently the first silicate gangue minerals precipitated in the oxide stage (Fig. 3.4). In most cases, hydrothermal biotite or tourmaline needles have grown outward from the clast margins (Fig 3.8a, b). In some areas, these minerals have also replaced clast margins. There is a transitional zone where the dominant cement changes from hydrothermal biotite upwards to tourmaline. Textural relationships between the two phases in the transitional zone are non-destructive, with several domains containing the two minerals in apparent textural equilibrium (Fig. 3.8c). Above the transitional zone, there is a higher degree of brecciation, tourmaline is the dominant hydrothermal mineral and sericite alteration is more intense. The tourmaline needles range in length from 0.1 mm to 1 cm and are generally a translucent blue to yellow and green colour in plane-polarized light. Tourmaline also occurs as fine-grained, equigranular blue/black masses and sinuous trails in the cement. These are interpreted to be a second phase of tourmaline deposition, because the tourmaline needles crosscut pre-existing finer grained tourmaline (Fig. 3.4).

At deeper levels (<3600 m) in the Tourmaline Breccia body, the sequence of cementation is early hydrothermal biotite cement followed by anhydrite. This cement occurs in what is termed as a 'potassic', biotite-cemented domain in the granodiorite (Fig. 3.8a; Vargas et al., 1999). The crystals of anhydrite are up to 2 cm long and 5 mm wide and have been partially replaced by chalcopyrite and sericite (Figs. 3.8b, d, e, f and 3.9a, b).

Tourmaline and specularite are the only oxide stage cements that occur above 3600 m elevation (Fig. 3.4). The coarse specularite cement precipitated after tourmaline and before sulfide mineralisation (Fig. 3.9c). This early specularite only occurs in high altitude zones in the Tourmaline Breccia (>3600 m asl). The specularite is euhedral and has grown into void space outwards from a thin rind of tourmaline that has replaced clast margins. Early void-fill specularite crystals are up to 3 mm long and 1 mm wide (Fig. 3.9c). This zone coincides with an increased abundance of vuggy textures in the Tourmaline Breccia, possibly due to the dissolution of anhydrite by modern-day groundwater (Vargas et al., 1999).

Main-stage mineralisation has overgrown the oxide stage cements at Sur-Sur and is associated with quartz-sericite alteration of the clasts. Main-stage cements of quartz, pyrite, chalcopyrite, magnetite, and tourmaline were deposited within open spaces (Fig. 3.4). The zone between 3600 m and 4000 m contains the highest copper grades. Above this zone pyrite gradually becomes the dominant sulfide mineral. Chalcopyrite and magnetite appear to have been co-precipitated based on consistent, non-destructive textural relationships between these minerals (e.g. Fig. 3.9d). At mid

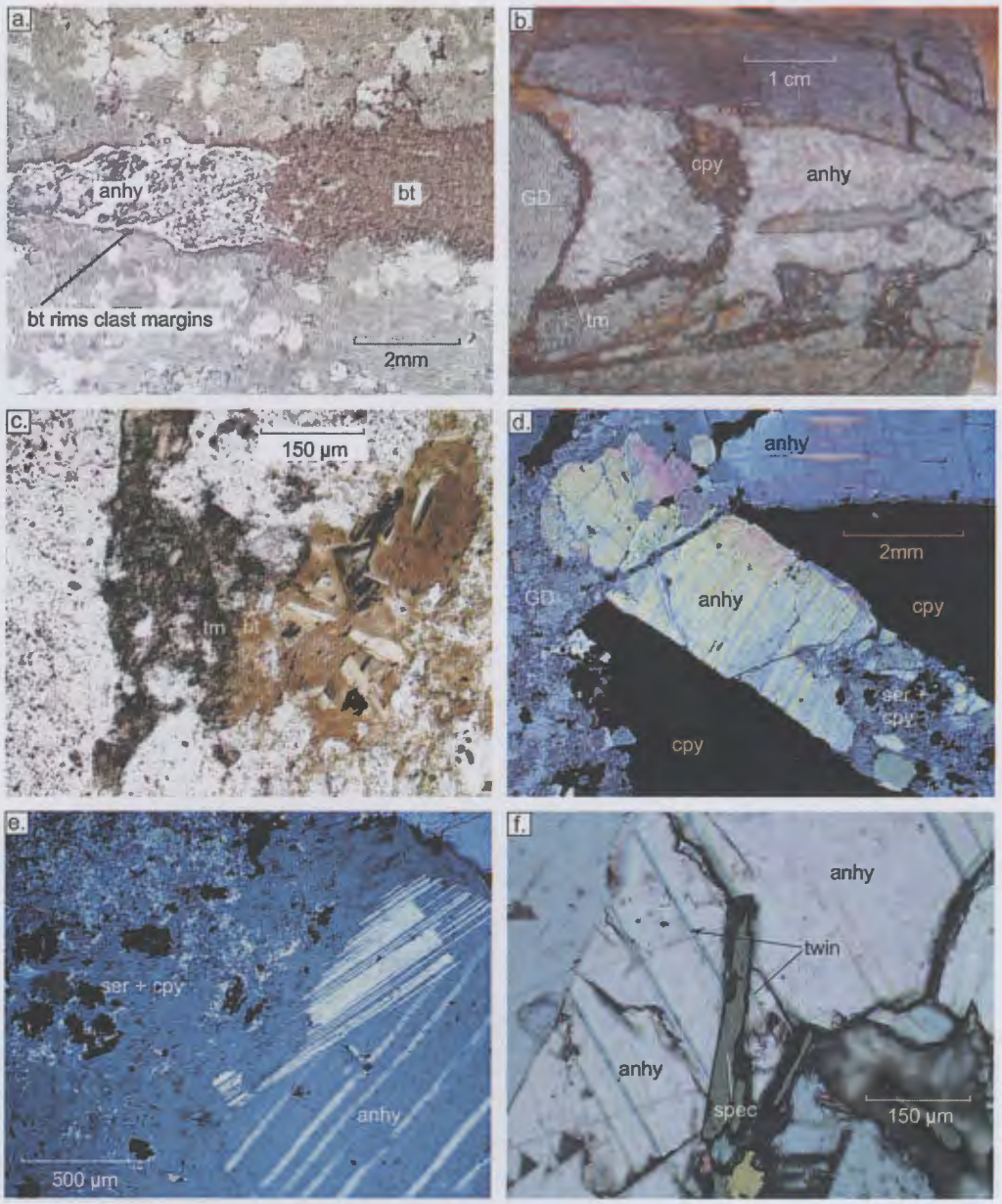

Figure 3.8. Sequence of cement deposition in the Sur-Sur Tourmaline Breccia:
a. In the deepest intersections of the Sur-Sur breccia, biotite occurs as rims around clast margins. Anhydrite has partially cemented the central void space (sample 215a, TSS-22, 2873 m asl);
b. At higher elevations, tourmaline occurs as rims around clast margins and has been overgrown by anhydrite (sample 500, TSS-12, 3539 m asl);
c. A transitional zone occurs between 3000 and 3100 m in the Sur-Sur Tourmaline Breccia, where the main silicate mineral cement phase changes from biotite to tourmaline. There is a 100 m vertical interval where the two minerals coexist locally. Temporal relationships are difficult to resolve based on the fine grained textures (sample 546, DDH-737, 3248 m asl);
d. Anhydrite crystal cut by chalcopyrite and sericite (sample 01BXT12, TSS-12, 3541 m asl);
e. Anhydrite has been partially replaced by chalcopyrite and sericite in the breccia cement (sample 01BXT12, TSS-12, 3541 m asl); and
f. Co-existing anhydrite and specularite crystals, difficult to determine temporal relationships between these two minerals (sample 500, TSS-12, 3539 m asl).

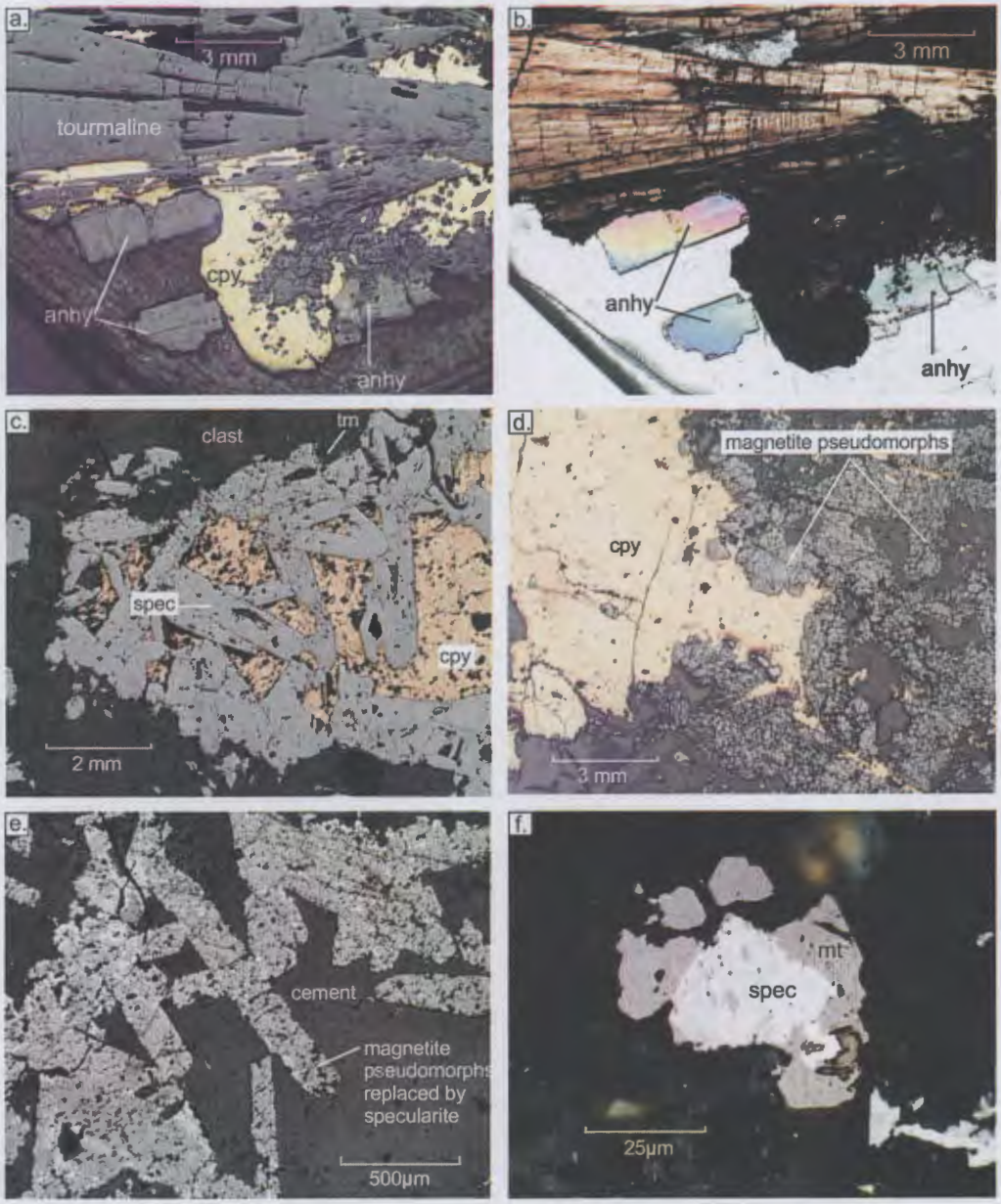

Figure 3.9. Sequence of cement deposition in the Sur-Sur Tourmaline Breccia:
a. Reflected light photomicrograph showing early tourmaline and anhydrite crystals cut and partially replaced by chalcopyrite (sample 62b, TSS-22, 2919 m asl);
b. Same as 3.9a in cross polarised light. Long axis of tourmaline and anhydrite crystals have grown parallel, chalcopyrite cuts through anhydrite;
c. Pre-ore oxide stage specularite has grown into space from a thin selvage of tourmaline at clast margins and has been overgrown by chalcopyrite (4000 m elevation), nb. specularite is stable in the presence of mineralisation stage chalcopyrite, and no magnetite is present (sample 492, DL-57, 4021 m asl);
d. Early specularite pseudomorphed by magnetite associated with the mineralization event (high grade interval; 3500-4000 m elevation; sample 523, DL-71, 4033 m asl);
e. Magnetite pseudomorphs after specularite have been replaced on their outer margins and internal fractures by late-stage hematite (sample 523, DL-71, 4033 m asl); and
f. Early specularite replaced by magnetite (sample 7, TSS-4, 3708 m asl).

to high altitude locations (3600 to 4000 m asl), early specularite has been almost completely pseudomorphed by magnetite (Fig. 3.9d, e, f), whereas at greater depths, main-stage magnetite contains no relict specularite. Specularite below ~4000 m elevation is weakly magnetic due to partial magnetite alteration. Specularite samples above ~4000 m are non-magnetic. In the southern part of the orebody, at an elevation of 3541 m, only minor replacement of specularite by main-stage magnetite has occurred (Fig. 3.10a, b, c). Above 4000 m elevation, magnetite alteration of the specularite crystals has not been observed, even though specularite coexists with chalcopyrite (Fig. 3.9c). Internal corrosion of specularite cores and partial replacement by magnetite has resulted in cavity textures at high elevations (>4000 m; e.g. Fig. 3.10d, e, f), whereas specularite has apparently resisted corrosion at mid levels (3500 m; e.g. Fig. 3.10c). Specularite has also been replaced by pyrite (~4000 m; Fig. 3.11a).

Typical high-grade mineralisation in the Sur-Sur Tourmaline Breccia is shown in Figure 3.11b. Chalcopyrite is dominant, having almost completely cemented cavities within the breccia column. Bornite is absent from the Tourmaline Breccia cement, however it is present in cross-cutting stage 8 sulfide veins. High copper grades also occur at high elevations (between 3950 and 4100 m elevation) in the Tourmaline Breccia body. The high-grade zones are spatially associated with early specularite cement and where supergene chalcocite, covellite and digenite have partly upgraded the chalcopyrite resource (Fig. 3.11c). The supergene minerals occur mainly as rinds around and along internal fractures within chalcopyrite grains. The chalcocite maintains a black and sooty colour in hand specimen indicating a supergene origin. No hypogene chalcocite has been observed at Río Blanco or Sur-Sur. In rare examples, chalcopyrite has been replaced by molybdenite in the Tourmaline Breccia cement (Fig. 3.11d). The molybdenite may be associated with stage 7 molybdenite stockwork veins (Fig. 3.1), or with the stage 3 mineralising fluids.

Primary and hydrothermal biotites in the granodiorite clasts have been altered to chlorite, rutile and in some cases epidote in many of the samples analysed. In some areas, magnetite and specularite have been altered to rutile, and colouration changes to yellow in tourmaline proximal to iron oxide minerals suggest that iron has been leached from tourmaline (Fig. 3.11c, e).

The granodiorite clasts in the Sur-Sur Tourmaline Breccia have been altered to a quartz-sericite (phyllic) alteration or quartz dominant (silicic) assemblage. In some cases, the clasts preserve relicts of the primary minerals. In most examples, however, plagioclase and orthoclase feldspar have been almost completely replaced by sericite and/or albite, with only the phenocryst shapes preserved. Quartz is abundant both as a primary phase and an alteration product, such that quartz locally comprises up to 30% of the rock. Phyllic alteration is most intensely developed in open framework samples of the Tourmaline Breccia (i.e. clasts isolated within abundant cement). The intensity of phyllic alteration decreases outwards through the closed framework crackle breccia to the coherent host granodiorite.

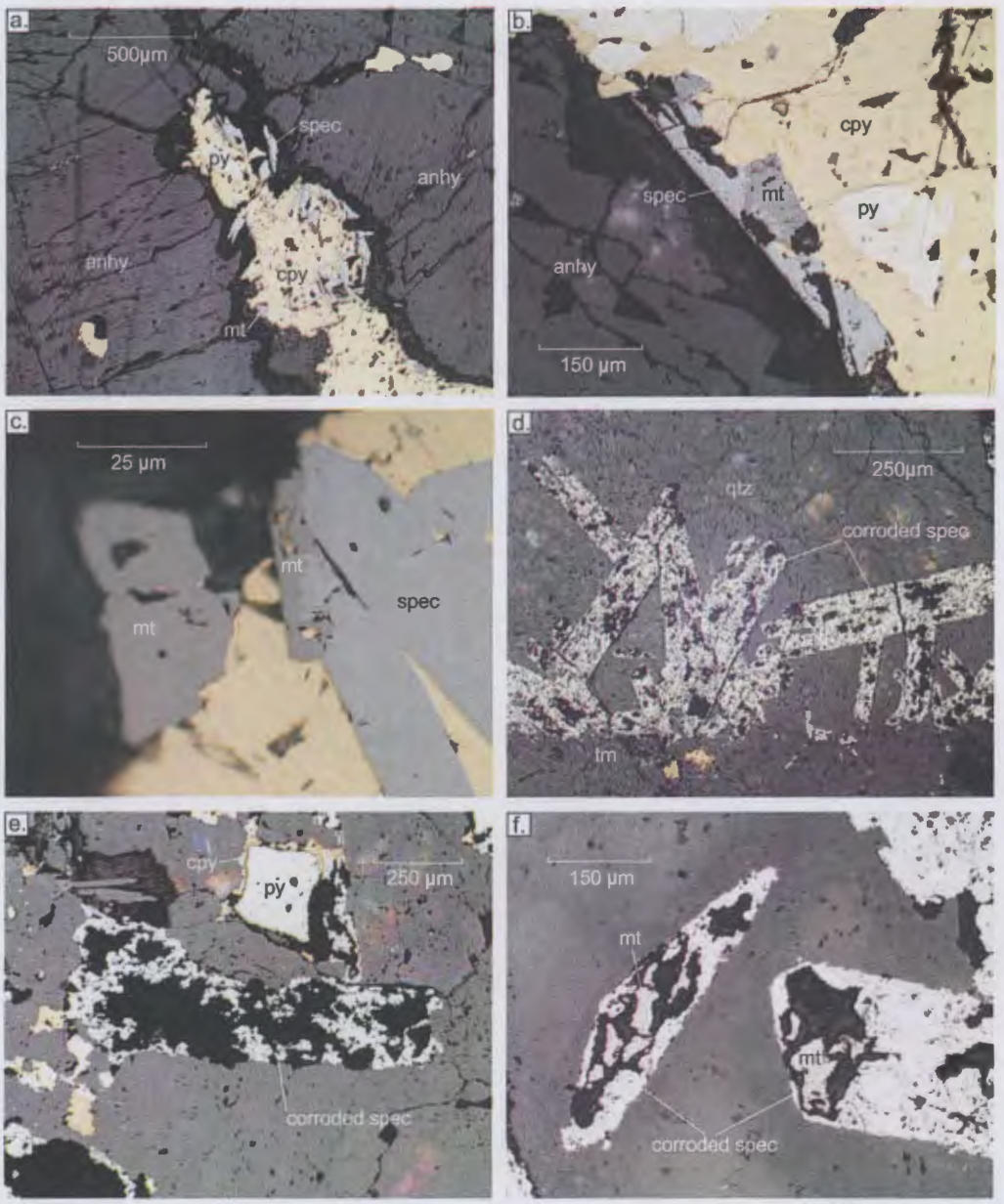

Figure 3.10. Sequence of cement deposition in the Sur-Sur Tourmaline Breccia:
a. Sulfide and oxide cement has infilled voids between anhydrite crystals. Specularite occurs at the edge of the anhydrite crystal, and has been overgrown by chalcopyrite, pyrite and magnetite (sample 01BXT12, TSS-12, 3541 m asl);
b. Specularite in contact with anhydrite and chalcopyrite. The specularite has been partially replaced by magnetite. Chalcopyrite contains pyrite inclusions (sample 01BXT12, TSS-12, 3541 m asl);
c. Higher magnification photomicrograph of specularite replaced by magnetite as shown in Figure 3.11b (sample 01BXT12, TSS-12, 3541 m asl);
d. Specularite crystals grown out from a thin tourmaline-altered rim at clasts margin. Later fluids have caused partial dissolution of the specularite. Subhedral quartz has grown in the space around the specularite (sample 524, DL-71, 4032 m asl);
e. Specularite crystal that has been intensely corroded and replaced by void space (sample 524, DL-71, 4032 m asl); and
f. Corroded specularite partially replaced by magnetite (sample 524, DL-71, 4032 m asl).

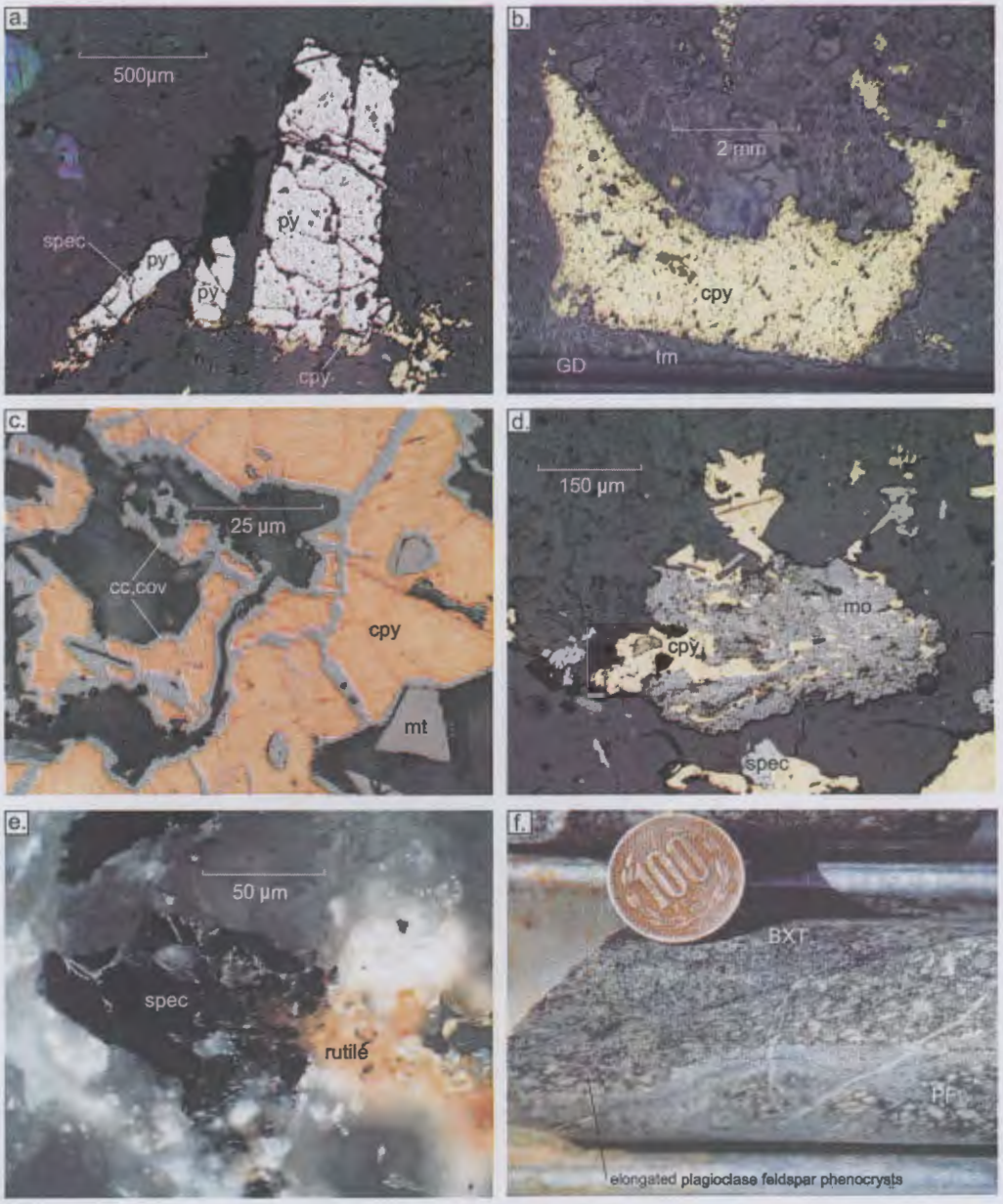

Figure 3.11. Sequence of cement deposition in the Sur-Sur mineralised Tourmaline Breccia and relationship with Feldspar Porphyry:
a. Pyrite has almost entirely replaced early specularite crystals in this sample, preserving the specularite crystal shape and appearance. Unaltered specularite crystals are located a few millimeters out of the field of view - see Figure 3.10d (sample 524, DL-71, 4032 m asl);
b. Typical chalcopyrite filled void has overgrown a thin selvage of tourmaline (sample 94, DL-139.1, 4031 m asl);
c. Partial replacement of chalcopyrite cement by chalcocite and covellite at high altitudes is interpreted to be the result of supergene processes (sample 523, DL-71, 4033 m asl);
d. Chalcopyrite cement intergrown with molybdenite. Molybdenite is not common in the Sur-Sur breccia (sample 01BXT12, TSS-12, 3541 m asl);
e. Specularite partially replaced by rutile in quartz cement (sample 491, DL-57, 4021 m asl); and
f. Sheared contact between the stage 3 Tourmaline Breccia and the stage 4 Feldspar Porphyry. Crystallisation of the Feldspar Porphyry appears to have been incomplete at the time these two rocks were brought into contact based on the ductile deformation fabrics at the apparently chilled margin of the porphyry. If emplacement of the Tourmaline Breccia post-dated the Feldspar Porphyry, Feldspar Porphyry clasts should occur in the Tourmaline Breccia, a relationship that has not been observed (section XC-325, DDH-737 at 126.8 m, Don Luis sector). 100 peso coin is 2.5 cm in diameter.

Locally, clasts in the Tourmaline Breccia have undergone silicic alteration. This alteration assemblage is inferred to be a mineralogical variant of the phyllic assemblage, defined by the anomalous local accumulations of secondary quartz. Many of the clasts also contain remnant secondary biotite, approximately 100 m above the biotite/tourmaline transitional zone (altered to chlorite). To the west and east of the Sur-Sur Tourmaline Breccia, a propylitic alteration assemblage occurs that is characterised by the presence of chlorite, epidote, pyrite and specularite.

3.2.4 Stage 4: Feldspar Porphyry

The Río Blanco Magmatic Breccia has been intruded by a dyke swarm collectively referred to as the Feldspar Porphyry (PF; Fig. 3.2d). This rock unit was described in Section 2. Plagioclase feldspar in the PF has been partially or wholly replaced by fine sericite. In places, primary biotite occurs as books up to 5 mm across, and has been partially altered to chlorite.

Contact relationships between PF and Magmatic Breccia are generally characterised by minor sericitisation of the Magmatic Breccia and entrainment of biotite altered Magmatic Breccia clasts within the PF. Contacts with the Sur-Sur Tourmaline Breccia have only been observed in one drill hole beneath the Don Luis sector. The contacts are sheared or obscured by cross-cutting veins (e.g. Fig 3.11f). Ductile deformation and decreasing grain size of plagioclase feldspar in the Feldspar Porphyry (chilled margin?) imply that crystallisation of the PF was incomplete at the time these two rocks were brought into contact, based on the ductile deformation fabrics at the apparently chilled margin of the porphyry. No contact relationships between PF and the stage 6 porphyries have been observed in this study. The PF dykes have mostly been intersected in the deep, potassic altered zones of the Río Blanco and Don Luis sectors.

Of all the late-stage porphyries at Río Blanco, the PF is the only that has undergone stage 5 biotite alteration. It is crosscut by rare biotite-bearing stage 5 veins (Fig. 3.2d, e). The PF is therefore interpreted to be the first porphyry to have intruded the system after the formation of the mineralised Magmatic Breccia and Tourmaline Breccia complexes, even though contact relationships with only relatively small volumes of PF are exposed at Río Blanco in contrast to the stage 6 Quartz Monzonite and Don Luis porphyries.

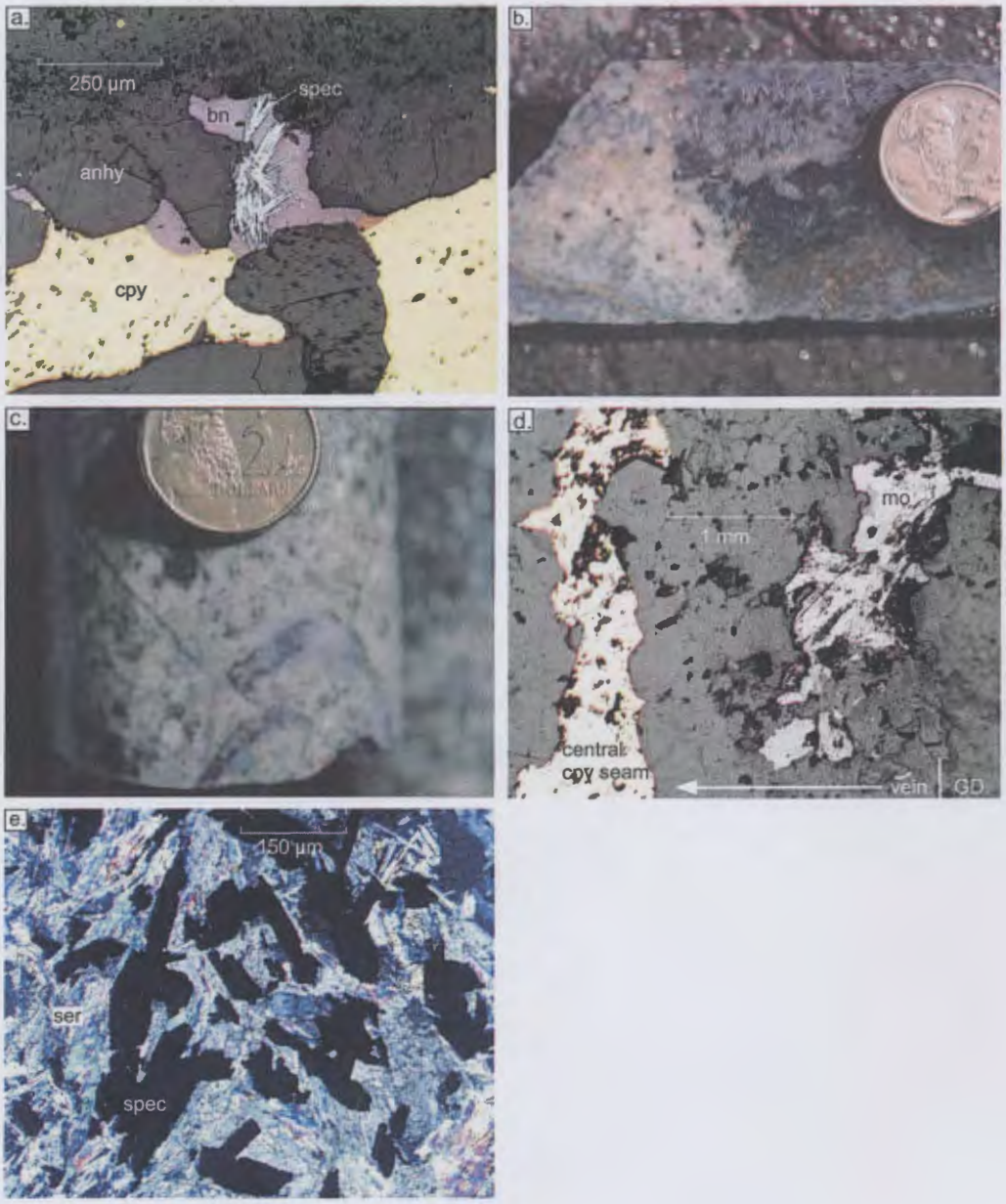

Figure 3.12. Paragenetic stages 5 to 8:
a. Photomicrograph of chalcopyrite deposited in stage 5 quartz-anhydrite-chalcopyrite veins with a biotite halo. Although the chalcopyrite appears in equilibrium with bornite in the this sample, in many other samples the bornite clearly replaces the margins of chalcopyrite grains. Specularite is commonly observed associated with bornite in the presence of chalcopyrite in these veins (sample 270, DDH-734, 2929 m asl);
b. Contact zone, where the Magmatic Breccia has been crosscut by the PQM (XC-125);
c. Stage 4 Feldspar Porphyry cut by stage 7 molybdenite rimmed quartz veins (quartz-sericite) which has in turn been cut by stage 7 molybdenite veins (quartz-sericite; sample 257, DDH-734, 491 m);
d. Stage 7 quartz-molybdenite vein with a central seam of chalcopyrite. Molybdenite occurs on the vein margin adjacent to the granodiorite wallrock (sample 320, DDH-734, 2762 m asl); and
e. Photomicrograph of sericite alteration and specularite blades associated with halos of stages 7 and 8 stockwork sulfide veins (sample 390, DDH-566, 3079 m asl).

3.2.5 Stage 5: late potassic veins

The PF is crosscut by stage 5 - quartz-anhydrite-chalcopyrite veins that have biotite halos (Figs. 3.2d, e and 3.12a). This is the final potassic alteration event recognised at Río Blanco, and is confined to the Río Blanco and Don Luis sectors. Stage 5 veins contain quartz, anhydrite, chalcopyrite, biotite, tourmaline, bornite and specularite (Fig. 3.12a). Texturally, the specularite and bornite are late, and probably formed by replacement of chalcopyrite.

Stage 5 veins are generally 1 mm wide and have hydrothermal biotite halos that extend outward from the vein wall up to 2 mm. Where stage 5 veins have crosscut the contact between Stage 4 Feldspar porphyry and stage 3 Magmatic Breccia, the veins are invariably displaced over the contact, implying post-stage 5 movements on the lithological contacts (Fig. 3.2d). Stage 5 veins have only been recognised at depth in the Don Luis sector (<3000 m elevation), along strike and to the north of the Sur-Sur Tourmaline Breccia. The paragenetic relationship between Stages 4 and 5 with the Sur-Sur Tourmaline Breccia is unknown.

3.2.6 Stage 6: monzonite porphyries

The Quartz Monzonite Porphyry (PQM; Fig. 3.12b) and the Don Luis Porphyry (PDL) were described in Section 2. The PQM and PDL contain stage 6 quartz-sericite alteration assemblages with plagioclase feldspar ubiquitously partially or wholly replaced by sericite and primary biotite partially altered to chlorite. Quartz-sericite alteration has also affected country rocks and breccias adjacent to PQM and PDL contacts. The PQM and PDL are weakly mineralised with grades that range up to 0.5% Cu. Visual estimates suggest that approximately 50% of this copper is associated with cross-cutting stage 7 and 8 veins (described below). Chalcopyrite contained within the PQM has been interpreted to be remobilised from previous mineralisation events (Serrano et al., 1996).

3.2.7 Stage 7: molybdenite stockwork veins and rock flour breccias

Stage 7 quartz-sulfide veins with quartz-sericite alteration halos have crosscut the breccias, PQM and PDL stocks and dykes. There are two recognisable molybdenite-bearing vein types (Fig. 3.12c). The first has molybdenite on the vein walls and the central seam is filled with quartz. These relatively thick (up to 1 cm wide) molybdenite-rimmed quartz veins have been cut by thin (up to 1 mm wide) molybdenite veinlets that contain minor quartz. The molybdenite rimmed quartz veins also have a central chalcopyrite seam, suggesting these veins have been reopened by stage 8 veins. The quartz-sericite alteration halos have a white to blue colour and mainly contain sericite and quartz that have replaced wallrock minerals. Stage 7 comprises the bulk of molybdenite ore in the Río Blanco system.

Three distinct rock flour breccias (BXTO, BXMN and BXTTO) located adjacent to the Tourmaline Breccia all contain clasts of the Tourmaline Breccia and Don Luis Porphyry. The BXTO and BXTTO have clasts and rock flour that is quartz-sericite altered. BXMN has chlorite altered clasts and rock flour. Stage 7 molybdenite veins were not observed to cross cut the breccias. The breccias and stage 7 veins are therefore inferred to be broadly of the same paragenetic stage. More research is required to establish the exact timing relationships between stage 7 veins and the rock flour breccias.

3.2.8 Stage 8: chalcopyrite stockwork veins

Stage 7 veins and the rock flour breccias have been crosscut by stage 8 chalcopyrite-anhydrite-quartz-bearing veins that also contain minor magnetite and specularite and have quartz-sericite alteration halos (Figs. 3.12d, e, 3.13a, b, c). In addition to chalcopyrite, these veins also contain bornite, molybdenite, pyrite and rare chalcocite, covellite and digenite. They have produced locally elevated copper grades based on drillcore assays and visual observations of vein assemblages. The stage 8 veins have locally reopened and infilled stage 7 veins (Fig. 3.12d). The quartz-sericite alteration halos are a white-grey to blue colour (Fig. 3.13a, b) and extend outward from vein walls up to 5 mm where quartz and sericite have replaced wallrock minerals.

Stage 8 veins occur as a weak, randomly oriented stockwork throughout the ore deposit. In some locations deeper in the Magmatic Breccia body, stage 8 appears to have caused chalcopyrite cement to be altered to bornite proximal to stage 8 vein selvages. Also, hematite has replaced magnetite and fine blades of specularite were deposited within and surrounding the stage 8 veins (Fig. 3.12e). It is not clear whether the copper in stage 8 veins has been remobilised from the breccias, or whether it was a new phase of metal introduced into the system.

3.2.9 Stage 9: D veins

All preceding veins, breccias and stage 4 and 6 intrusions have been crosscut stage 9 veins. These are comparable to the 'D' veins described from El Salvdor by Gustafson and Hunt (1975). They are pyrite-rich and have texturally destructive quartz-sericite alteration halos (Fig. 3.13d, e). The veins contain variable abundances of quartz, chalcopyrite, specularite, siderite, and gypsum with rare galena and tennantite (Fig. 3.13f). Stage 9 veins are up to 1.5 cm wide and their alteration halos extend up to 4 cm from vein walls. They occur throughout the ore deposit complex. In the Sur-Sur sector, stage 9 veins commonly have near-vertical dip angles.

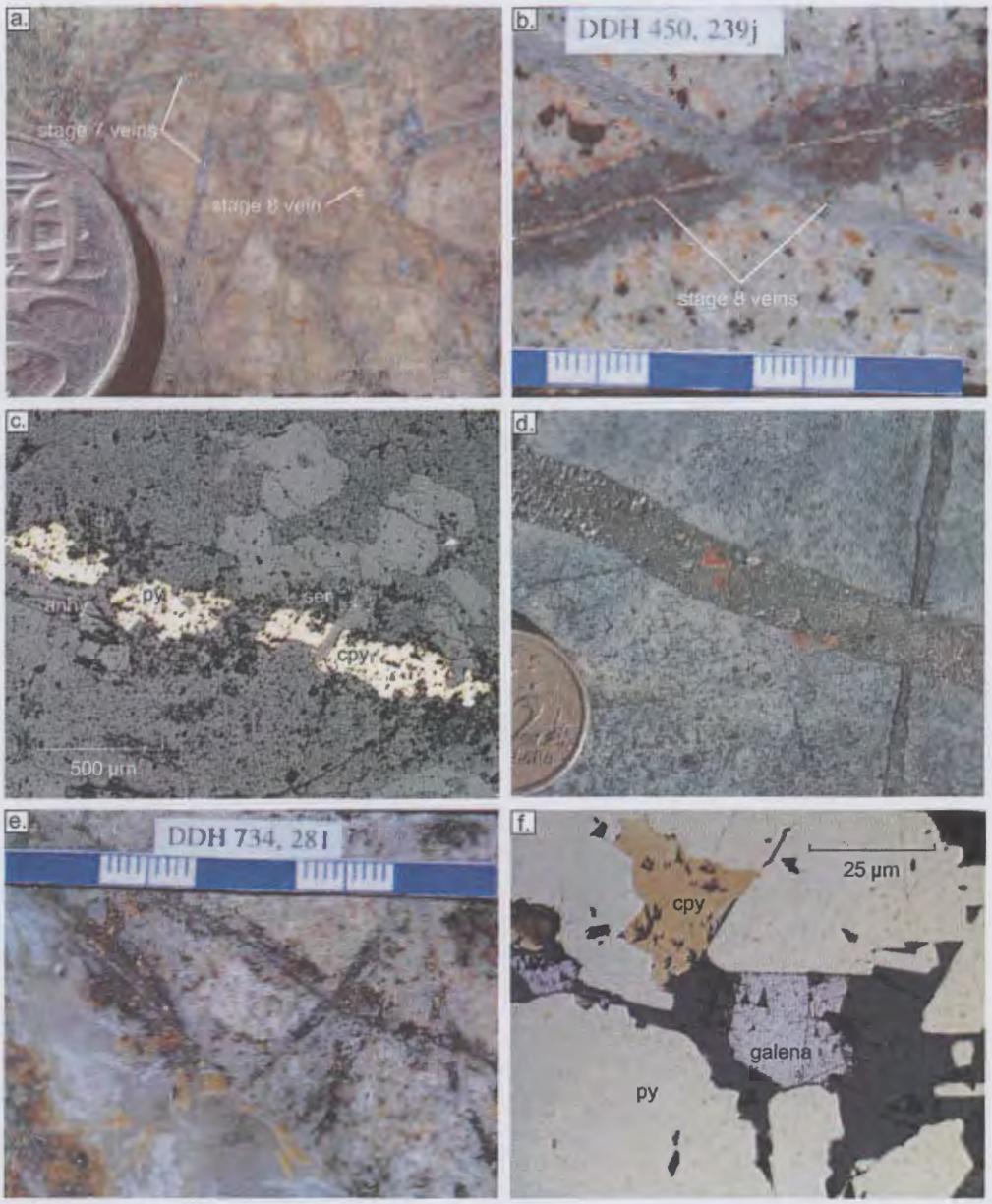

Figure 3.13. Paragenetic stages 8 to 9. Abbreviations shown in Figure 3.1 caption, scale bar in cm:

a. Stage 7 molybdenite veins (quartz-sericite) cut by stage 8 sulfide veins that contain chalcopyrite, quartz and anhydrite with quartz-sericite alteration halos (sample 393, DDH-566, 163.8 m);

b. Stage 8 sulfide veins - chalcopyrite, quartz, anhydrite (quartz-sericite) overprinting another stage 8 sulfide vein in phyllic altered Río Blanco Granodiorite . The dark coloured alteration halos have greater proportions of quartz compared to the white stage 8 halos (sample 239j, DDH-450, 80 m);

c. Photomicrograph of typical stage 8 stockwork chalcopyrite and pyrite vein with quartz-sericite alteration halo (sample 61b, TSS-22, 3020 m asl);

d. Stage 8 sulfide veins with chalcopyrite, quartz and anhydrite with a quartz-sericite alteration halo cut by stage 9 D style, cm-wide pyrite-rich veins ± siderite, gypsum, chalcopyrite in Cascada Granodiotite host (sample 21, TSS-26, 36 m);

e. Stage 9 D style, pyrite-rich veins ± siderite, gypsum, chalcopyrite and minor specularite in phyllic altered Cascada Granodiotite host (sample 281, DDH-734, 395 m); and

f. Galena between grains of pyrite and chalcopyrite in a stage 9 vein (sample 43c, TSS-22, 3650 m asl).

3.2.10 Stage 10: late stage intrusions

The final components to be emplaced in the ore deposit were the weakly altered and non-mineralised Dacite Chimney and La Copa Rhyolite. The emplacement of these rock units removed part of the copper resource to the north and east of the Río Blanco Magmatic Breccia. These intrusions are unmineralised with the exception of some minor upgrading that has occurred in a mechanically-formed 'contact breccia' on the southern flank of the La Copa Rhyolite (Vargas pers. comm., 2001)

3.3 Spatial distribution of breccia cements and alteration assemblages

Mineralogical zonation in the Río Blanco and Sur-Sur breccia complexes has been determined using digital data of down hole mineral occurrences provided by CODELCO – Division Andina. This dataset is based on drill core observations by mine geologists over more than 20 years of drill core logging. These data were processed using MapInfo-Discovery software in order to plot the spatial distribution of hydrothermal minerals on longitudinal sections E-E' and D-D' (Fig. 3.14). The drill holes cover an area that encompass La Americana sector in the south through the Sur-Sur and Don Luis sectors to the north, then northwest through the Río Blanco sector (Fig. 3.14). Drill holes have been projected from distances of up to 250 m laterally onto section plane E-E' and up to 225 m onto section plane D-D' from either side of the sections.

Sections E-E' and D-D' are shown at the same scale to allow easy comparison of the two mineralised centres. Individual cross-sections through the Río Blanco and Sur-Sur sectors show the distribution of biotite, phyllic alteration, chlorite alteration, chalcopyrite:pyrite ratio, tourmaline, anhydrite, specularite, and magnetite.

The longitudinal section and cross-sections have been generated in MapInfo by extracting three-dimensional information from the digital database and plotting them in two-dimensions. This has led to some local distortion of mineral abundances. Overall, however, projection from up to 225 m off section has been found to have little effect on the overall mineral distribution patterns presented here.

The distribution of specularite has been disrupted by the post-mineral intrusions. Consequently, specularite distribution has been projected through post-mineral intrusions, to provide an indication

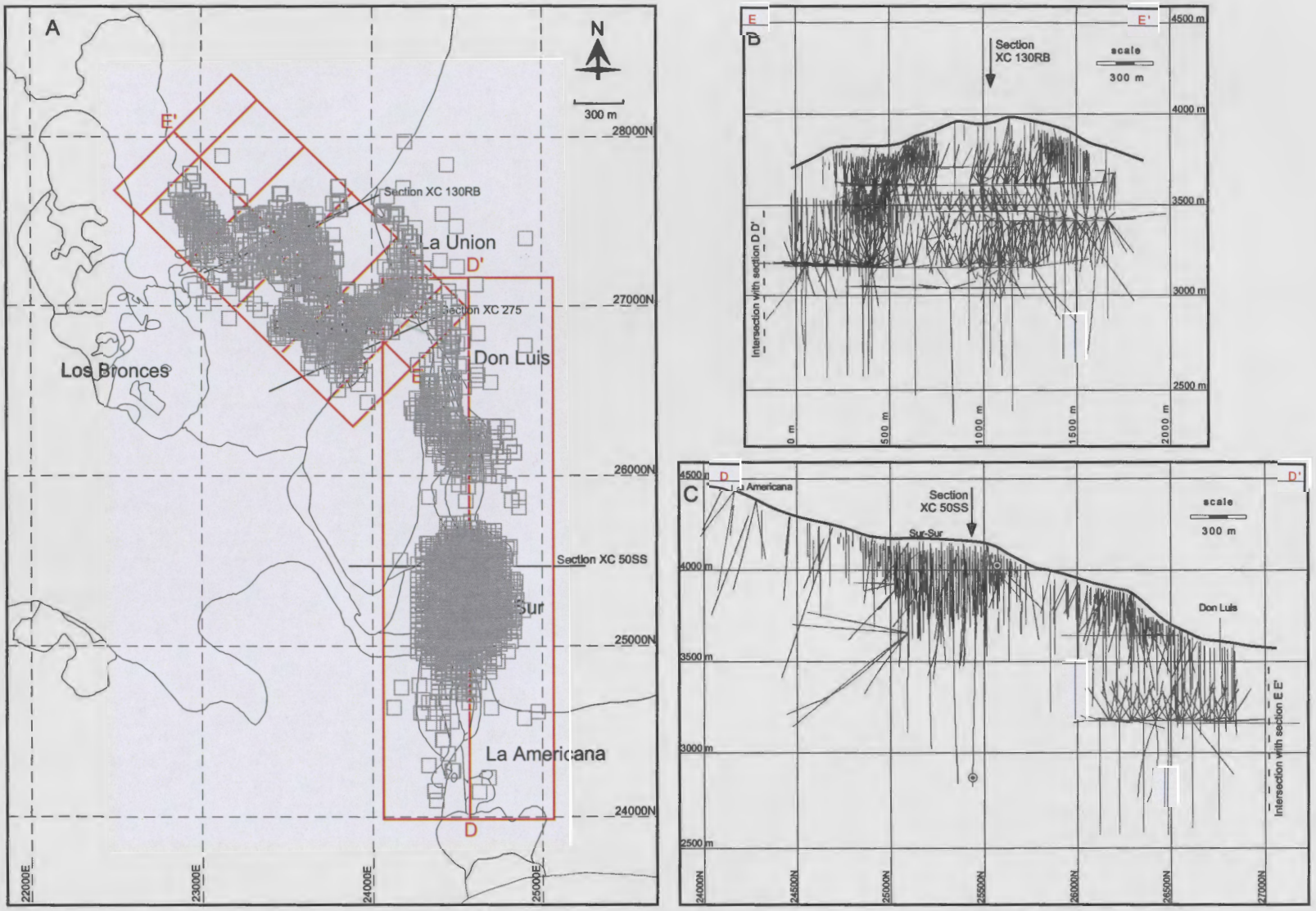

Figure 3.14. a. Location of longitudinal sections D-D', E-E', and cross-sections XC-130RB, XC-50SS and XC-275 in the ore deposit complex. Drill holes (grey squares) have been projected to the land surface that has an elevation between 3500 and 4500 m. b. Section E-E', showing drill hole traces and cross-section XC-130RB. c. Section D-D' showing drill hole traces and cross-section XC-50SS. ⊙ = locations of samples collected for $^{40}Ar/^{39}Ar$ age determinations.

of stage 3 specularite distribution in the Río Blanco sector. None of the other minerals presented in Figures 3.15 to 3.18 were significantly affected by the problems encountered with specularite, and so extrapolation of data was not required for these phases.

One other problem with the data is that there was no discrimination between primary and secondary biotite, magnetite or K-feldspar by Andina geologists. Problems caused by this are discussed below. In addition, Andina geologists over the years used qualitative scales such as "abundant, moderate, weak and very weak". Such scales are subjective and vary from one observer to another, and for one observer, from one day to the next, or even in one day, as his fatigue grows stronger towards the end of the day. It is also based on contrast, with "abundant" alteration applied to a drillcore interval next to a zone with none, but next to "moderate", it might not appear abundant at all.

3.3.1 Potassic alteration

Alteration minerals in the Río Blanco sector have a clear but asymmetrical zonation. The biotite-altered potassic core at depth in the Río Blanco and Don Luis sectors zones outwards to a complex halo of quartz-sericite and propylitic alteration assemblages. The distribution of these alteration assemblages is mapped by the abundances of biotite (Fig. 3.15a, b), sericite (Fig. 3.15c, d) and chlorite (Fig. 3.16a, b), respectively.

As documented previously, the Magmatic Breccia is cemented by hydrothermal biotite. This is illustrated on Figure 3.15a by the biotite-rich domains (orange zones) in the Río Blanco to Don Luis sectors. The Magmatic Breccia in the Río Blanco and Don Luis sectors have elevated cpy:py ratios (Fig. 3.16c, d; orange zones) that correlate to high hypogene copper grades (0.75 to >1% Cu). In contrast, the biotite breccia that occurs at the base of the Sur-Sur Tourmaline Breccia (Fig. below 3500 m elevation; 3.15a) is associated with low cpy:py ratios (Fig. 3.16c; blue/yellow zones) and is only weakly mineralised (0.2-0.3% Cu).

Cross-section XC-130RB contains the biotite-altered core to the Río Blanco sector (Fig. 3.17a). This zone is characterised by abundant bornite and chalcopyrite at depth, and abundant chalcocite and covellite at higher elevations (Fig. 3.18a,b). Cross-sections XC-50SS shows the domain of biotite alteration in the deepest parts of the Tourmaline Breccia in the Sur-Sur sector (Fig. 3.19a, b). The biotite abundances illustrated on cross-section XC-50SS (Fig. 3.19a) highlight the extent of the potassic alteration assemblage (up to 3600 m elevation) in the mineralised system, and also highlight the change from deep level potassic (biotite) to shallow phyllic (quartz-sericite) assemblages in the Sur-Sur sector. Note that elevated biotite abundances also occur in the adjacent Cascada Granodiorite in Figure 3.19a, which relates to the presence of primary biotite. This high-

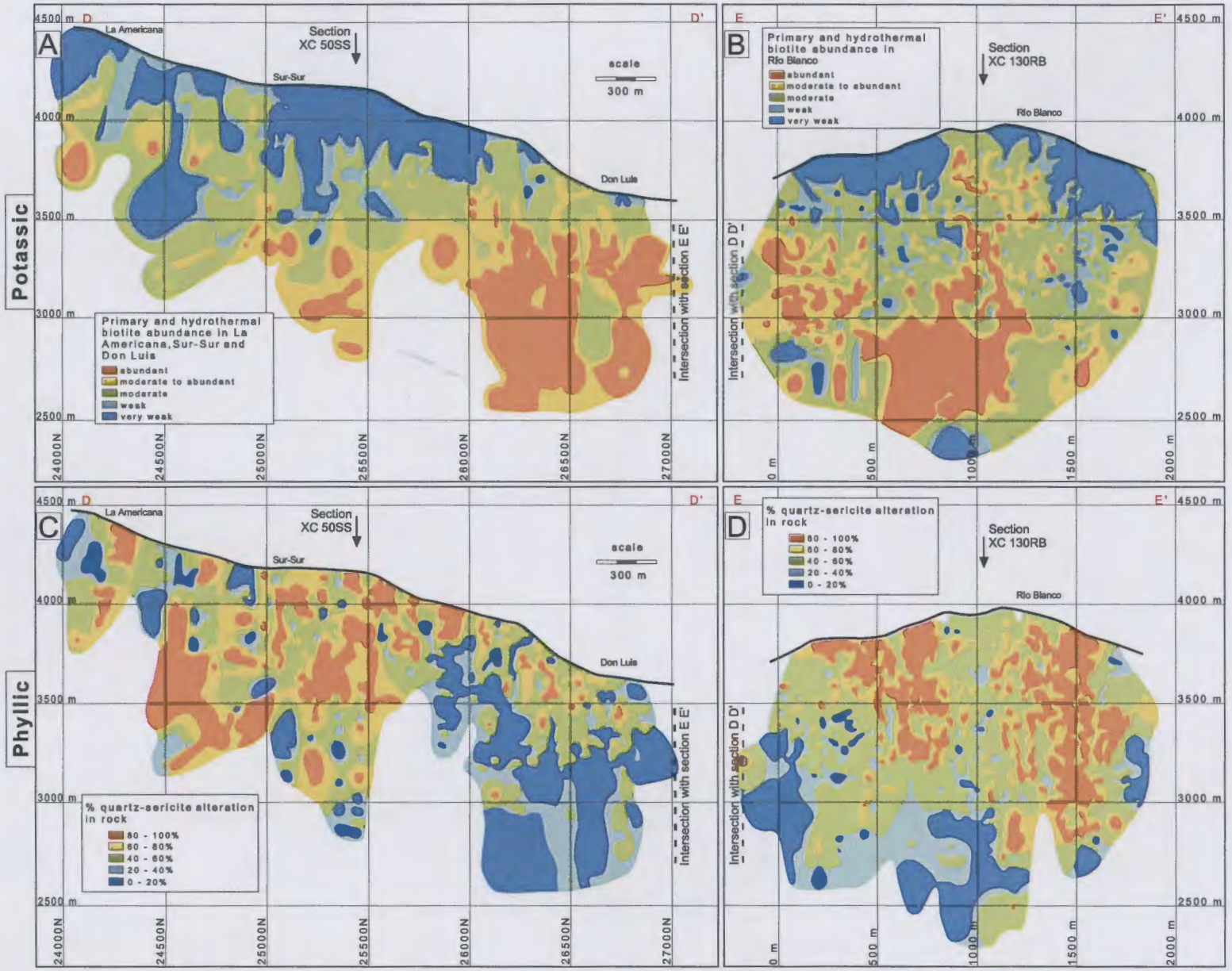

Figure 3.15. a. Distribution of primary and secondary biotite in longitudinal section D-D'; b. Distribution of primary and secondary biotite in longitudinal section E-E'; c. Distribution of phyllic alteration in longitudinal section D-D'; and d. Distribution of phyllic alteration in longitudinal section E-E'. Location of these sections shown on Figure 3.14.

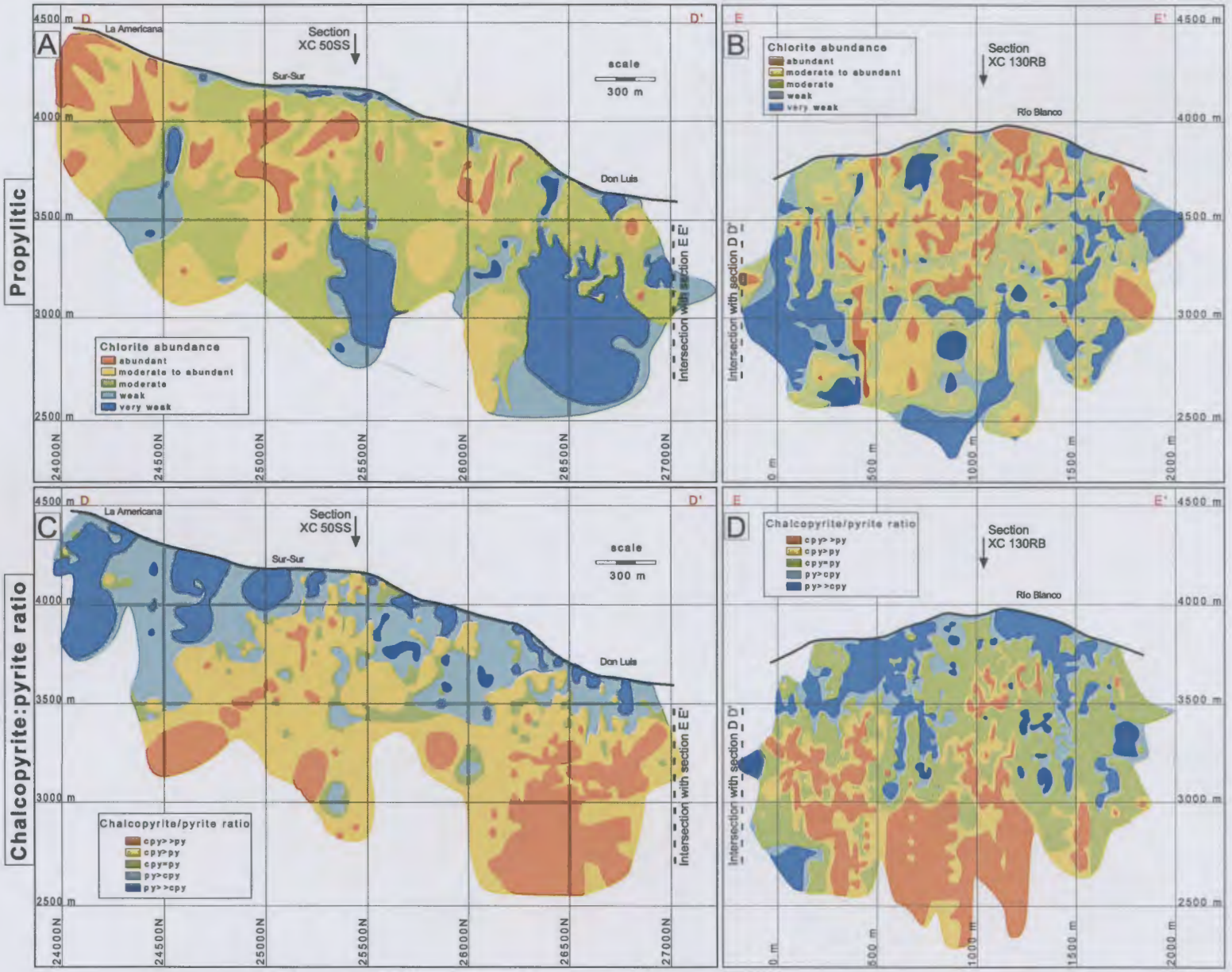

Figure 3.16. a. Distribution of chlorite in longitudinal section D-D'; b. Distribution of chlorite in longitudinal section E-E'; c. Chalcopyrite/pyrite ratios in longitudinal section D-D'; and d. Chalcopyrite/pyrite ratios in longitudinal section E-E'. Location of these sections shown on Figure 3.14.

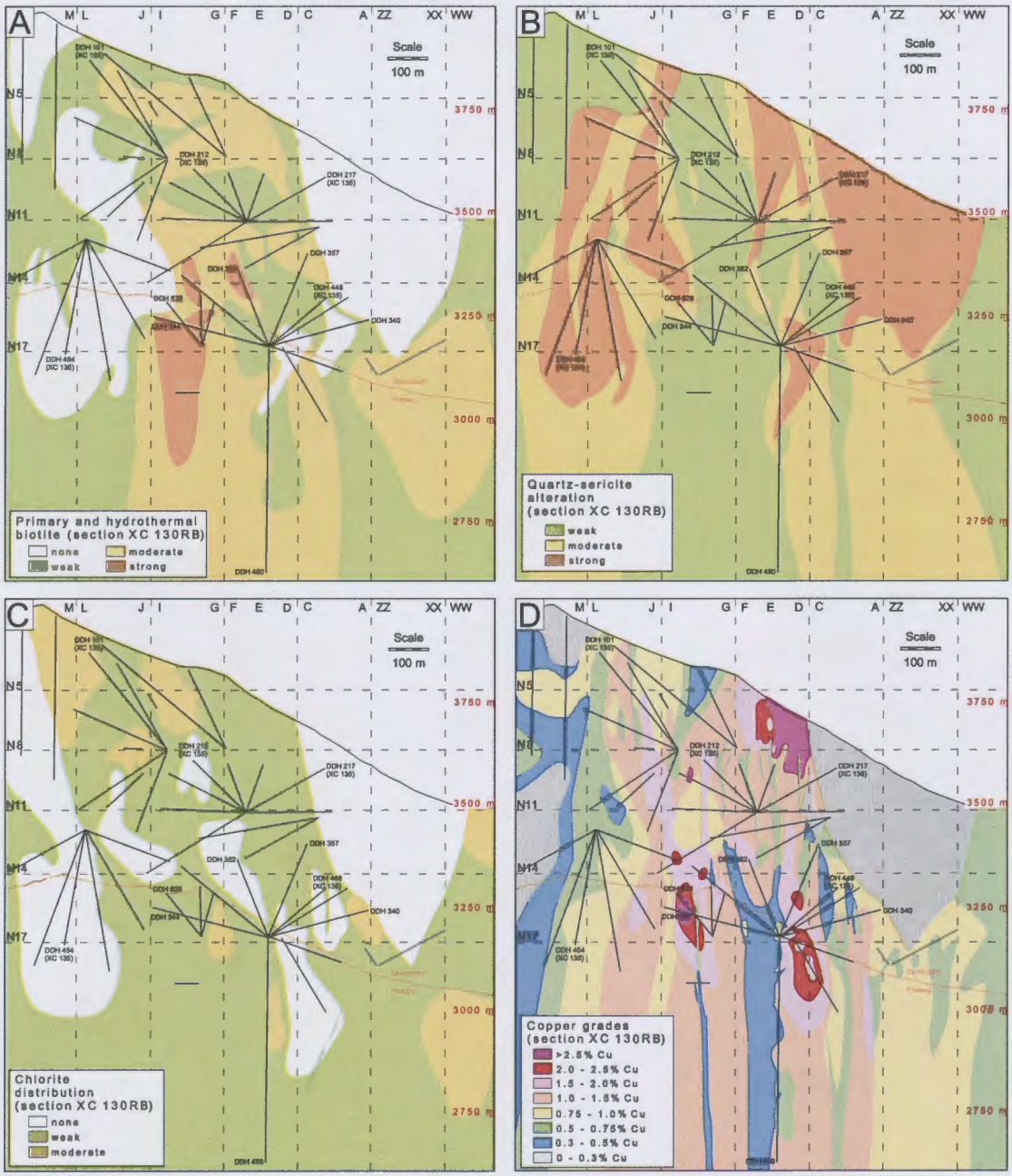

Figure 3.17. a. Distribution of potassic alteration; b. Distribution of phyllic alteration; c. Distribution of propylitic alteration; and d. Distribution of copper grades in section XC-130RB in the Río Blanco sector. The orange line separates secondary and primary zones. 'Secondary' represents the zone in the rock column that has been affected by weathering, no anhydrite occurs above this line, only gypsum. Location of these sections shown on Figure 3.14 and geology shown on Figure 2.5.

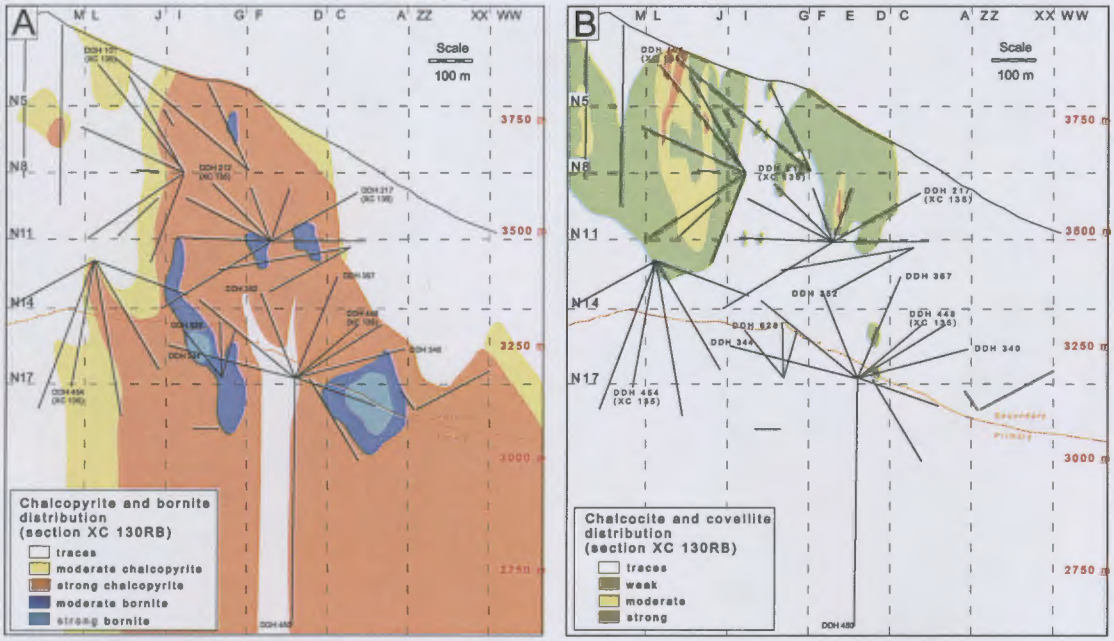

Figure 3.18. Distribution of copper minerals in cross-section XC-130RB; a. chalcopyrite and bornite; b. chalcocite and covellite. The orange line separates secondary and primary zones. 'Secondary' represents the zone in the rock column that has been affected by weathering, no anhydrite occurs above this line, only gypsum. Location of these sections shown on Figure 3.14 and geology shown on Figure 2.5.

lights the problem with the biotite dataset, which does not discriminate between primary and secondary biotite. The most biotite-rich zone in section XC-50 is confirmed by drillcore logging in the current study to be secondary.

3.3.2 Phyllic alteration

The quartz-sericite alteration assemblage forms an outer halo to the potassic-altered domain in the Río Blanco and Don Luis sectors (Figs. 3.15c, d and 3.17b). From the Don Luis sector southwards to the Sur-Sur sector along section D-D' a transition from the potassic to phyllic alteration assemblages occurs (Fig. 3.15a, c). Phyllic alteration is associated with high cpy:py ratios and locally elevated hypogene copper grades (~1% Cu) in the Sur-Sur sector (Figs. 3.15c, d and 3.16c, d). However, low cpy:py ratios correlate with abundant phyllic alteration in the upper/marginal zones of the Río Blanco and Don Luis sectors (Figs. 3.15c, d and 3.16c, d).

Phyllic alteration is predominant in the Tourmaline Breccia body above 3100 m elevation on section XC-50SS (Fig. 3.19a, b). Phyllic alteration is most intense in the upper parts of the Tourmaline Breccia where copper grades are also highest (>1.5% Cu; Fig. 3.19d).

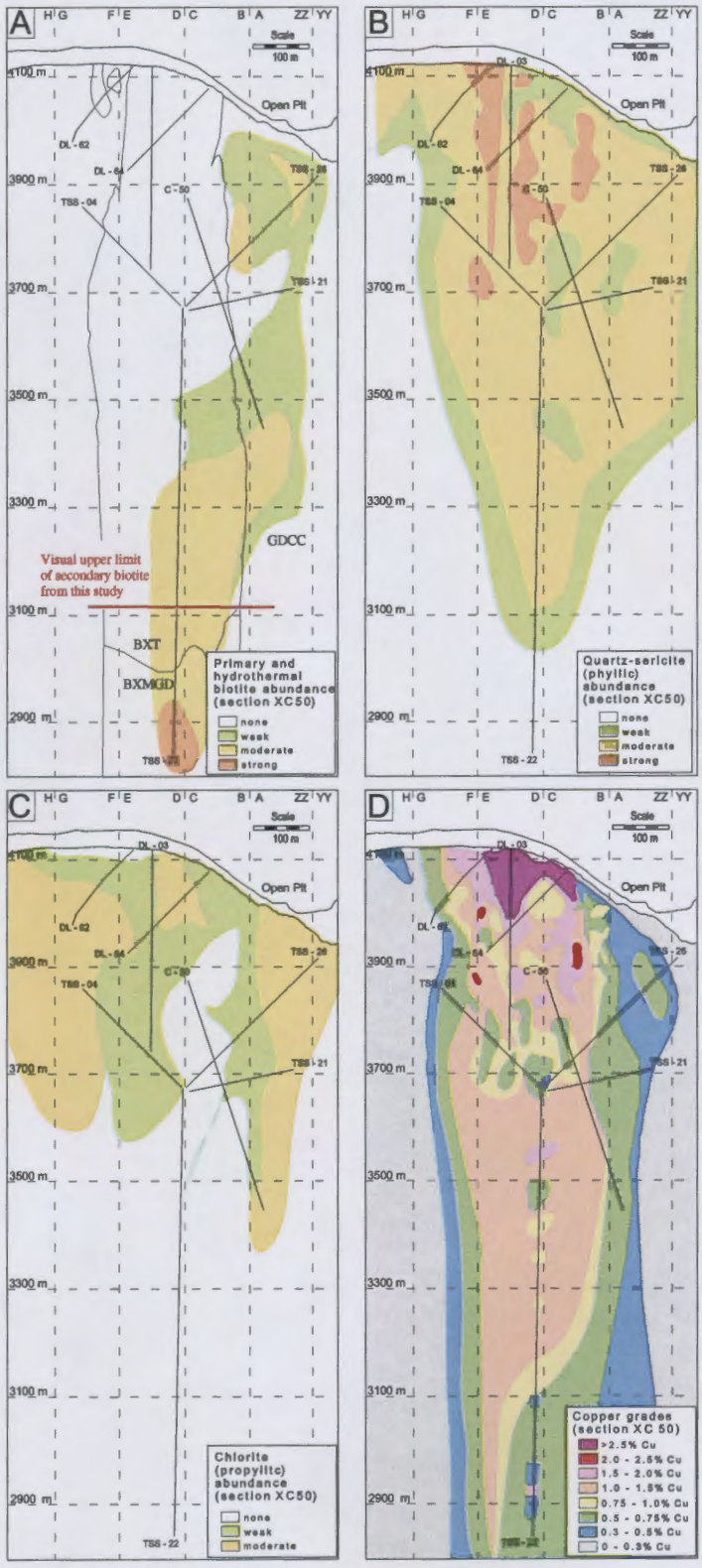

Figure 3.19. a. Distribution of potassic alteration; b. Distribution of phyllic alteration; c. Distribution of propylitic alteration; and d. Distribution of copper grades in section XC-50SS in the Sur-Sur sector. Note the distribution of biotite suggests a biotite alteration zone in the Cascada Granodiorite, however this actually reflects the primary biotite contained in this rock, the upper limit of secondary biotite based on observations in the current study are shown. Location of these sections shown on Figure 3.14 and geology shown on Figure 2.6.

3.3.3 Propylitic alteration

The spatial distribution of the propylitic alteration assemblage is mapped by chlorite distribution (Figs. 3.16a, b; 3.17c and 3.19c). Chlorite is the most abundant propylitic alteration mineral, occurring together with minor epidote, pyrite and specularite. In the Río Blanco and Sur-Sur sectors, chlorite broadly forms an outer halo to potassic alteration (Fig. 3.16a, b) with patchy distribution in the mid to upper parts of the Río Blanco and Sur-Sur orebodies mainly on the margins of the sections (Figs. 3.17c and 3.19c). Propylitic alteration is only weakly developed on cross-section XC-130RB and a weak propylitic alteration assemblage also characterises cross-section XC-50SS. Chlorite is best developed in the upper portion of section XC-50 and laterally outward from the well-developed phyllic alteration zone (Fig. 3.19c).

3.3.4 Chalcopyrite/pyrite distribution and copper grades

Visual estimates of the chalcopyrite/pyrite ratios for sections D-D' and E-E' are shown on Figure 3.16c, d. Copper assays for cross-sections XC-130RB and XC-50SS are shown on Figures 3.17d and 3.19d, respectively. In the Río Blanco and Don Luis sectors on sections D-D' and E-E', chalcopyrite is predominant in the biotite-altered domains (Figs. 3.15a, b and 3.16c, d). However, in Sur-Sur, chalcopyrite is also abundant in the phyllic alteration domain within the Tourmaline Breccia body (Figs. 3.15c and 3.16c). Pyrite is predominant over chalcopyrite in the upper and peripheral domains of the ore deposit (Fig. 3.16c, d). The Tourmaline Breccia at Sur-Sur has a complex interfingering of high-grade (chalcopyrite rich) and low-grade (pyrite-rich) domains associated with phyllic alteration (Figs. 3.15c and 3.16c).

High copper grades in cross-section XC-130RB occur within the biotite-altered domains and upwards into the phyllic altered zones (Fig. 3.17d). Copper grades have been disrupted and possibly in some areas redistributed and concentrated on the margins of the phyllic altered Quartz Monzonite Porphyry dykes (compare blue zones in centre of XC-130RB on Fig. 3.17d to the geology shown on Fig. 2.5). Bornite occurs as a halo to the PQM dyke in the centre of this section (Fig. 3.18a). Based on this spatial association, local bornite upgrading of chalcopyrite is inferred to be related to the intrusion of the PQM. Chalcocite and covellite in cross-section XC-130RB are constrained to the upper parts of the section, where supergene processes are inferred to have caused partial replacement and upgrading of hypogene chalcopyrite (Fig. 3.18b)

In cross-section XC-50SS, copper is concentrated within the phyllic altered Tourmaline Breccia body, but the highest copper grades are located between 3800 and 4100 m asl (Fig. 3.19d). This high-grade zone corresponds to intense phyllic alteration, and also to a zone where magnetite has pseudomorphed specularite crystals. The biotite-altered zone at the base of the Tourmaline Breccia is only weakly mineralised with copper (Fig. 3.19a, d).

3.4 Hydrothermal Mineral Zonation

This section describes the spatial zonation of hydrothermal minerals that occur in veins and as breccia cements in the Río Blanco ore system. The minerals discussed here include specularite, magnetite, tourmaline, anhydrite, K-feldspar, bornite, chalcocite and covellite. Their distributions are portrayed on sections D-D', E-E', XC-130RB and XC-50SS (Figs. 3.18-3.24).

3.4.1 Tourmaline

Tourmaline correlates with phyllic alteration on sections D-D' and E-E' (compare Fig. 3.20a, b and Fig. 3.15c, d). This supports the field and petrographic observations of the correlation between tourmaline-cemented breccia and phyllic-altered clasts in the Río Blanco and Sur-Sur sectors. Tourmaline occurs as upper halos to the domains of biotite alteration and cementation. In the Río Blanco sector on section E-E', zones of tourmaline enrichment and phyllic alteration correspond to zones where pyrite is the dominant sulfide mineral (compare Figs. 3.20b; 3.15d and 3.16d).

The biotite-tourmaline transition is best exposed on cross-section XC-50SS and shown schematically in Figure 3.21a. The transitional zone between the biotite-cemented breccia at the base of the Tourmaline Breccia and the tourmaline-cemented breccia is approximately 100 m thick between 3000 and 3100 m elevation. The gradational nature of this contact is shown in Figure 3.21b, by comparing drill core samples collected at regular (10 m) intervals through the transitional zone. Textural relationships between hydrothermal biotite and tourmaline in this zone are non-destructive (Fig. 3.8c).

3.4.2 Anhydrite

The distribution of anhydrite is strongly controlled by the 'gypsum line' (Vargas et al., 1999), a weathered interface located at approximately 3400 m elevation in section E-E' and 3600 m elevation in section D-D' (Fig. 3.20c, d). Above the weathered interface, anhydrite has either been removed by weathering or hydrated to gypsum. However, below the interface the original distribution of anhydrite is preserved. Anhydrite distribution is concentrated towards the edges of the Río Blanco and Sur-Sur orebodies as defined by the distribution of biotite and chalcopyrite in section E-E' (Figs. 3.15b and 3.16d). The zone of high anhydrite abundance at the top left hand corner of section D-D' is a late-stage anhydrite cemented breccia, unrelated to the Tourmaline Breccia (Fig. 3.20c).Unfortunately, no data were obtained on this breccia.

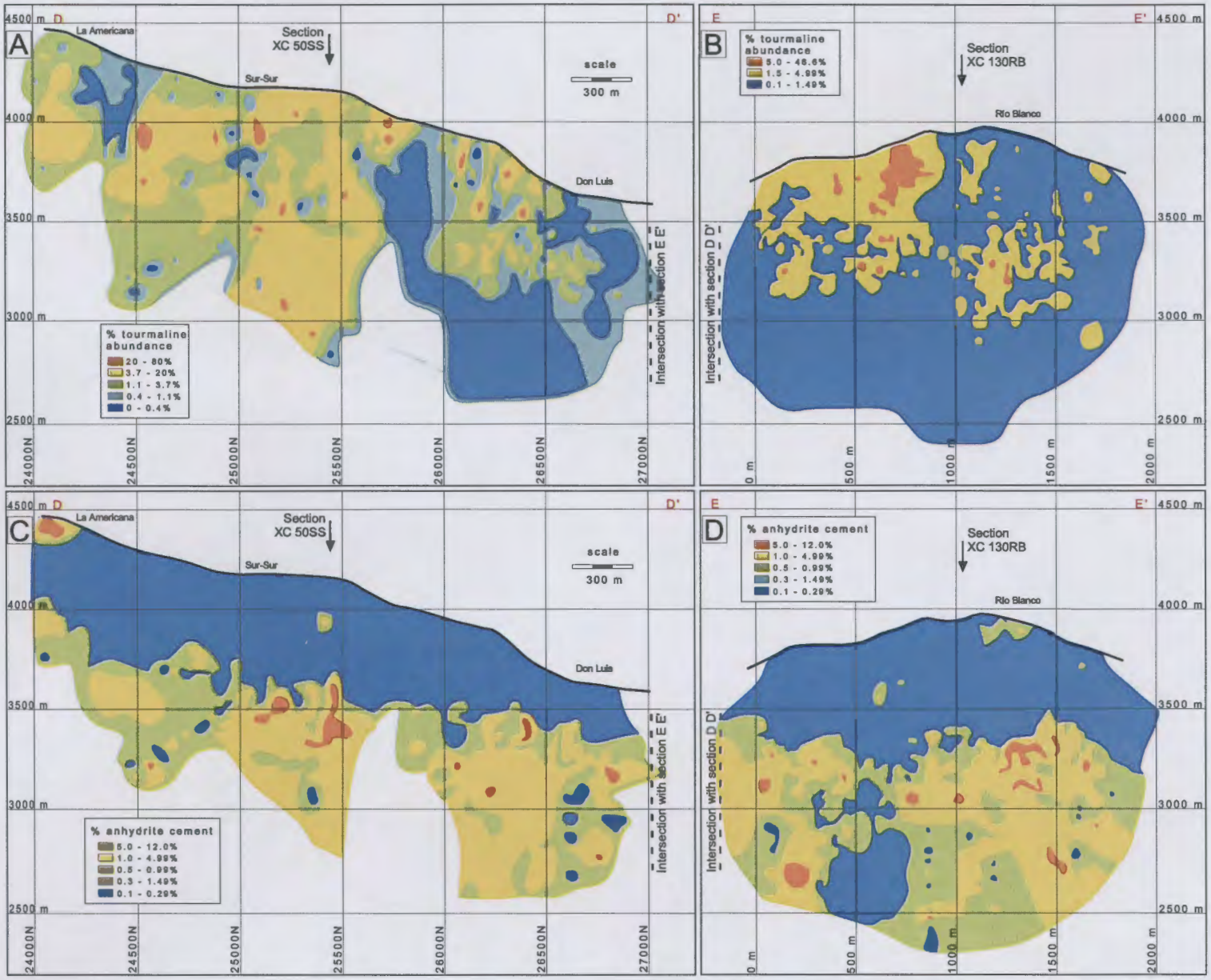

Figure 3.20. a. Tourmaline distribution on longitudinal section D-D'; b. Tourmaline distribution on longitudinal section E-E'; c. Anhydrite distribution on longitudinal section D-D'; and d. Anhydrite distribution on longitudinal section E-E'. Location of these sections shown on Figure 3.14.

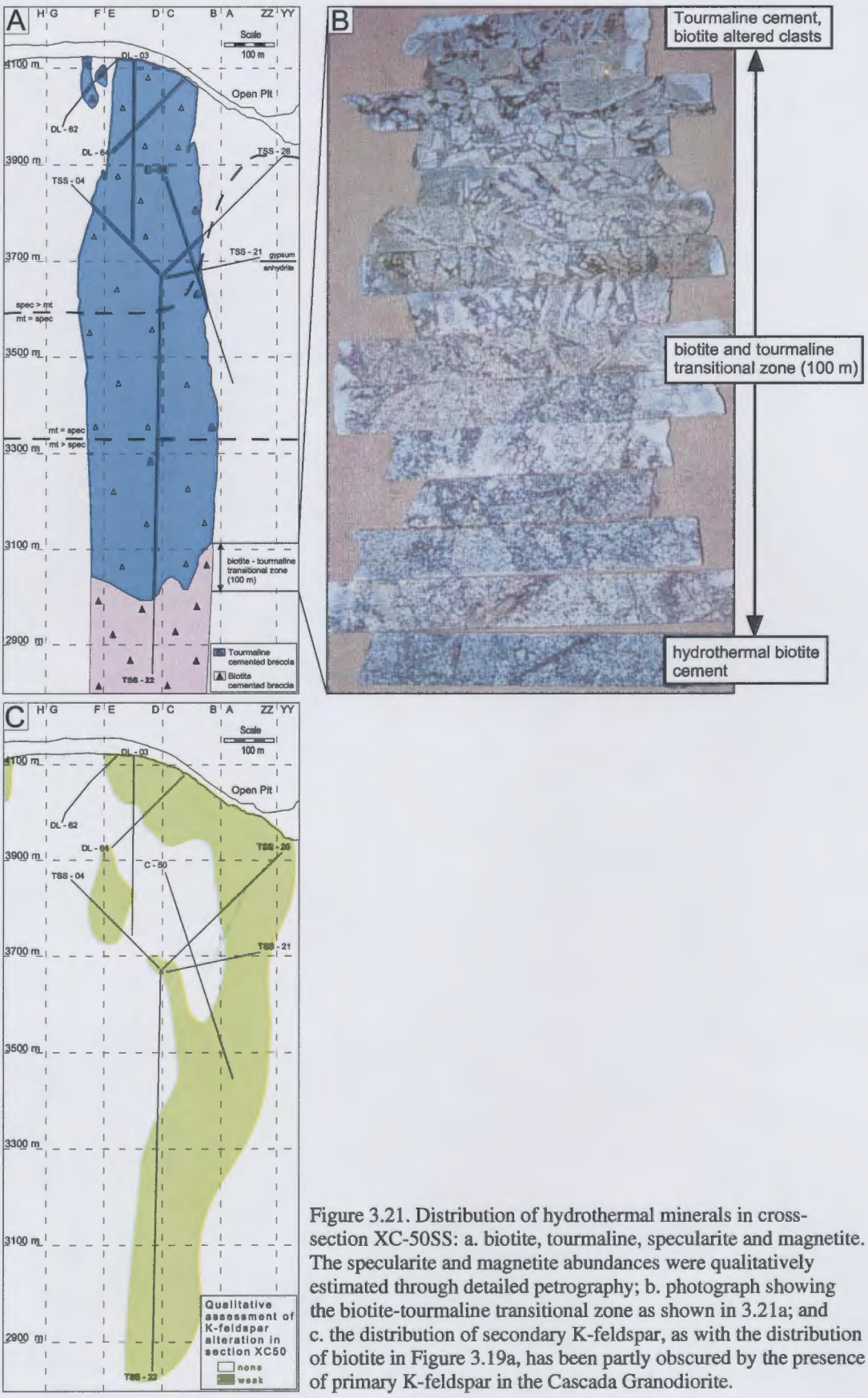

Figure 3.21. Distribution of hydrothermal minerals in cross-section XC-50SS: a. biotite, tourmaline, specularite and magnetite. The specularite and magnetite abundances were qualitatively estimated through detailed petrography; b. photograph showing the biotite-tourmaline transitional zone as shown in 3.21a; and c. the distribution of secondary K-feldspar, as with the distribution of biotite in Figure 3.19a, has been partly obscured by the presence of primary K-feldspar in the Cascada Granodiorite.

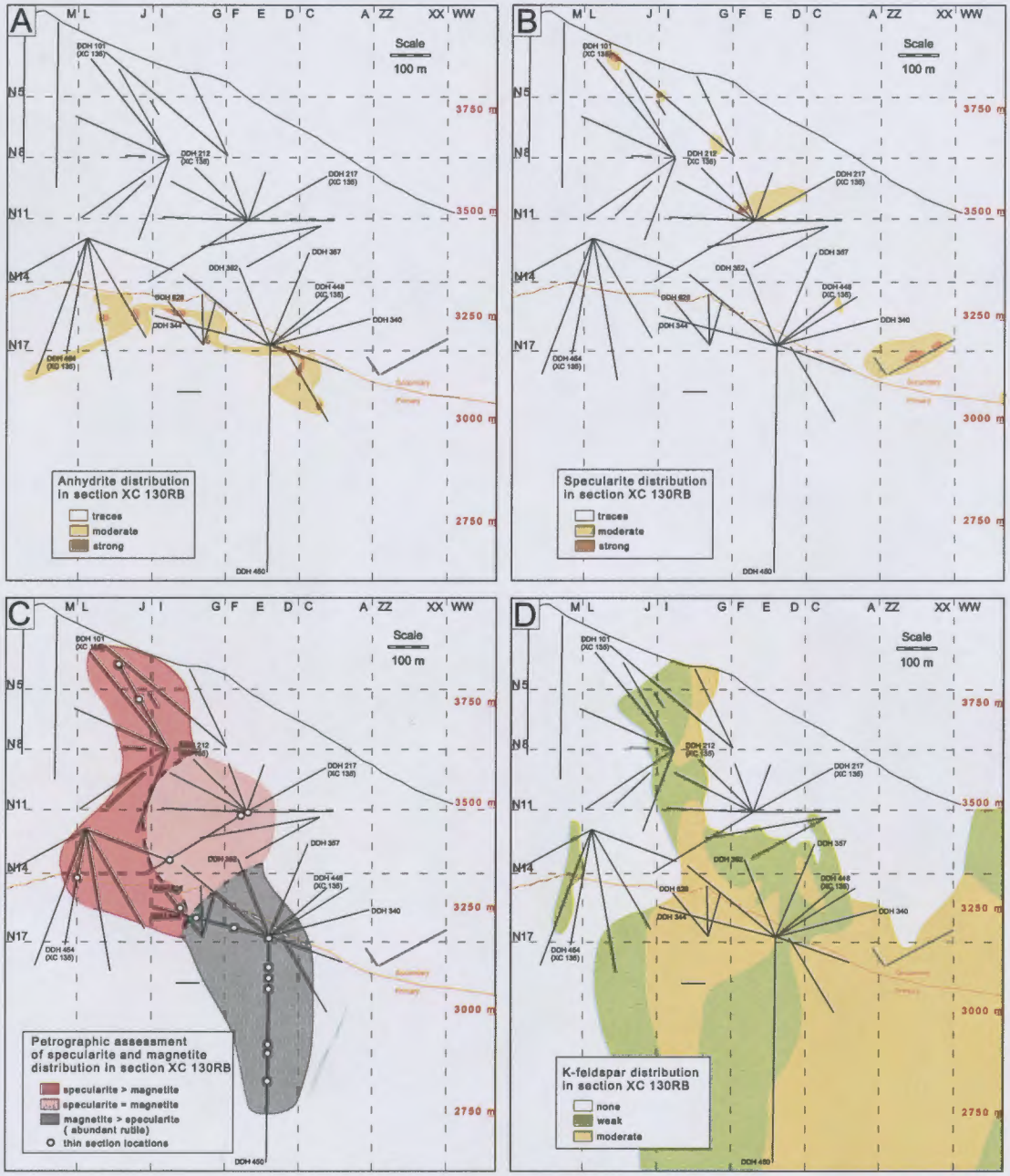

Figure 3.22. Distribution of hydrothermal minerals in cross-section XC-130RB: a. anhydrite; b. specularite; c. petrographic assessment of specularite and magnetite distribution; and d. K-feldspar. The orange line separates secondary and primary zones. 'Secondary' represents the zone in the rock column that has been affected by incipient weathering, no anhydrite occurs above this line, only gypsum.

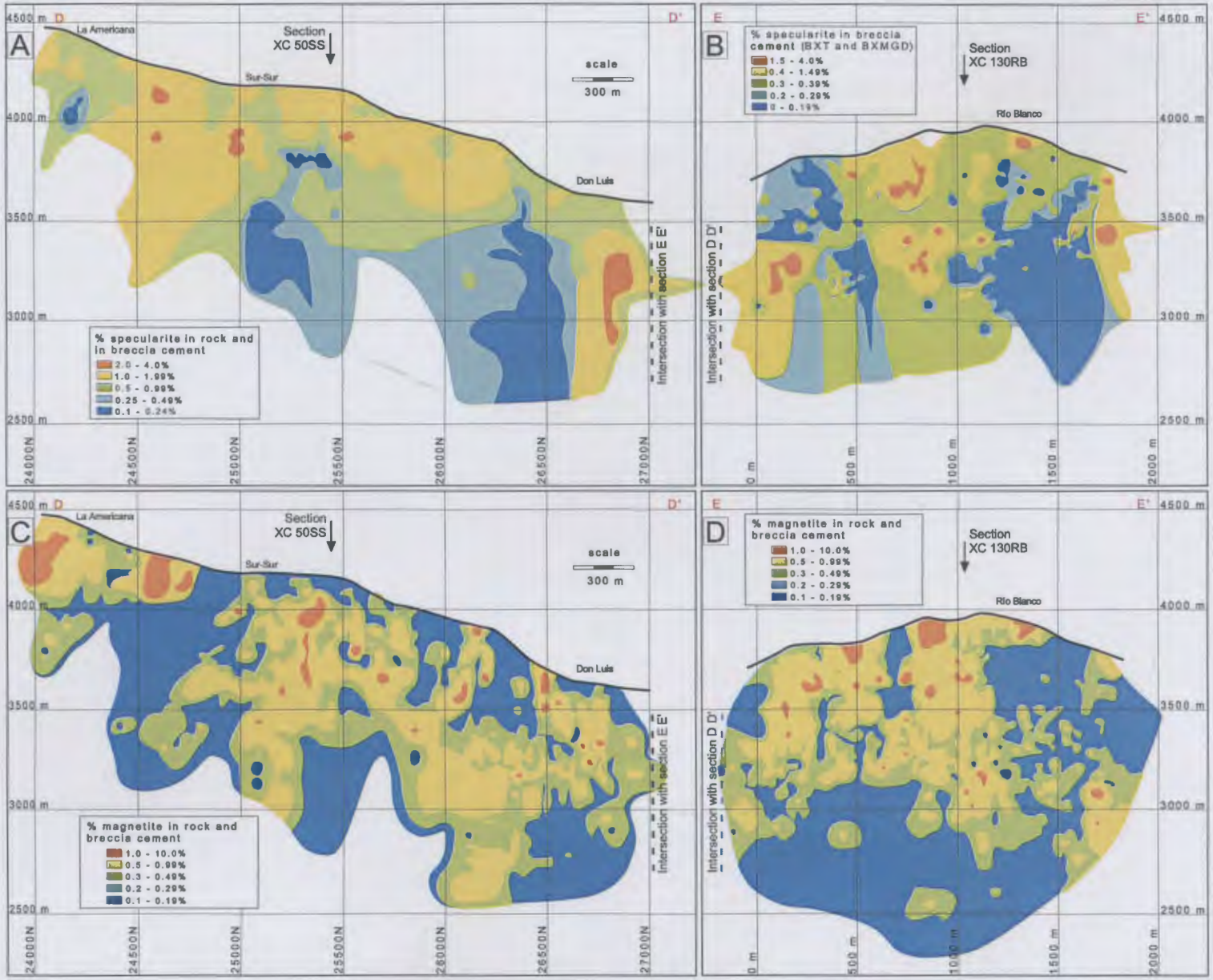

Figure 3.23. a. Distribution of specularite alteration in longitudinal section D-D'; b. Distribution of specularite alteration in longitudinal section E-E'; c. Distribution of magnetite alteration in longitudinal section D-D'; and d. Distribution of magnetite alteration in longitudinal section E-E'. The abundance's of magnetite are potentially obscured by primary magnetite in the granodirite, stage 1 magnetite-actinolite alteration and from magnetite precipitated in the breccia cement. Location of these sections shown on Figure 3.14.

Cross-section XC-130RB has the shallowest weathered zone of any of the sections considered here (Fig. 3.22). Unfortunately a lack of drill core coverage below the anhydrite line prevents any detailed discussion of spatial relationships between anhydrite and other hydrothermal minerals (Fig. 3.22a).

3.4.3 Specularite

Vargas et al. (1999) documented specularite on the fringes of the Sur-Sur orebody. Their findings are confirmed by the specularite distribution shown in Figures 3.23a, b. The greatest abundance of specularite occurs as halos about the Río Blanco, Don Luis and Sur-Sur mineralised centers, where large, oxide stage specularite crystals have been observed petrographically (e.g. Fig. 3.6a, b and 3.9c). There is overall a good correlation between abundant pyrite and specularite on the upper and outer fringes of the orebody (compare Figs. 3.16c, d with 3.23a, b).

In section E-E', while specularite occurs at the outer margins of the section, there is also a central zone of enrichment that correlates to the Magmatic Breccia (Fig. 3.23b). Here, specularite occurs as a late stage mineral that has replaced the margins of magnetite crystals in stage 8 chalcopyrite veins. The distribution of specularite in section XC-130RB is constrained to the outer and upper margins of the mineralised system (Fig. 3.22b, c).

The distribution of specularite correlates to the distribution of pyrite and chlorite on the fringes of the orebody in section D-D' (compare Figs. 3.16a, c and 3.23a). At Sur-Sur, specularite is least abundant in the deeper parts of the Tourmaline Breccia body.

To better assess the distribution of specularite in section XC-50SS, thirty-three polished thin sections were analysed to determine the mineral abundance throughout the section. Specularite abundance intensifies toward the highest altitudes on this section (Fig. 3.21a). Above 3600 m altitude, the Tourmaline Breccia body is dominated by specularite. Petrographic information from twenty-one polished thin sections has also been superimposed on a schematic of section D-D' along strike of the Tourmaline Breccia to further constrain specularite distribution (Fig. 3.24). In this section, specularite was found to be most abundant above 3500 m elevation. However, between 3500 m and 4000 m elevation, the early specularite crystals deposited in breccia matrix have been pseudomorphed by magnetite associated with the mineralising fluid (Figs. 3.24 and 3.9d, e). This and may have affected the visual estimates of specularite distribution by CODELCO geologists, in that the actual distribution of specularite may have been greater than implied by Figure 3.23a.

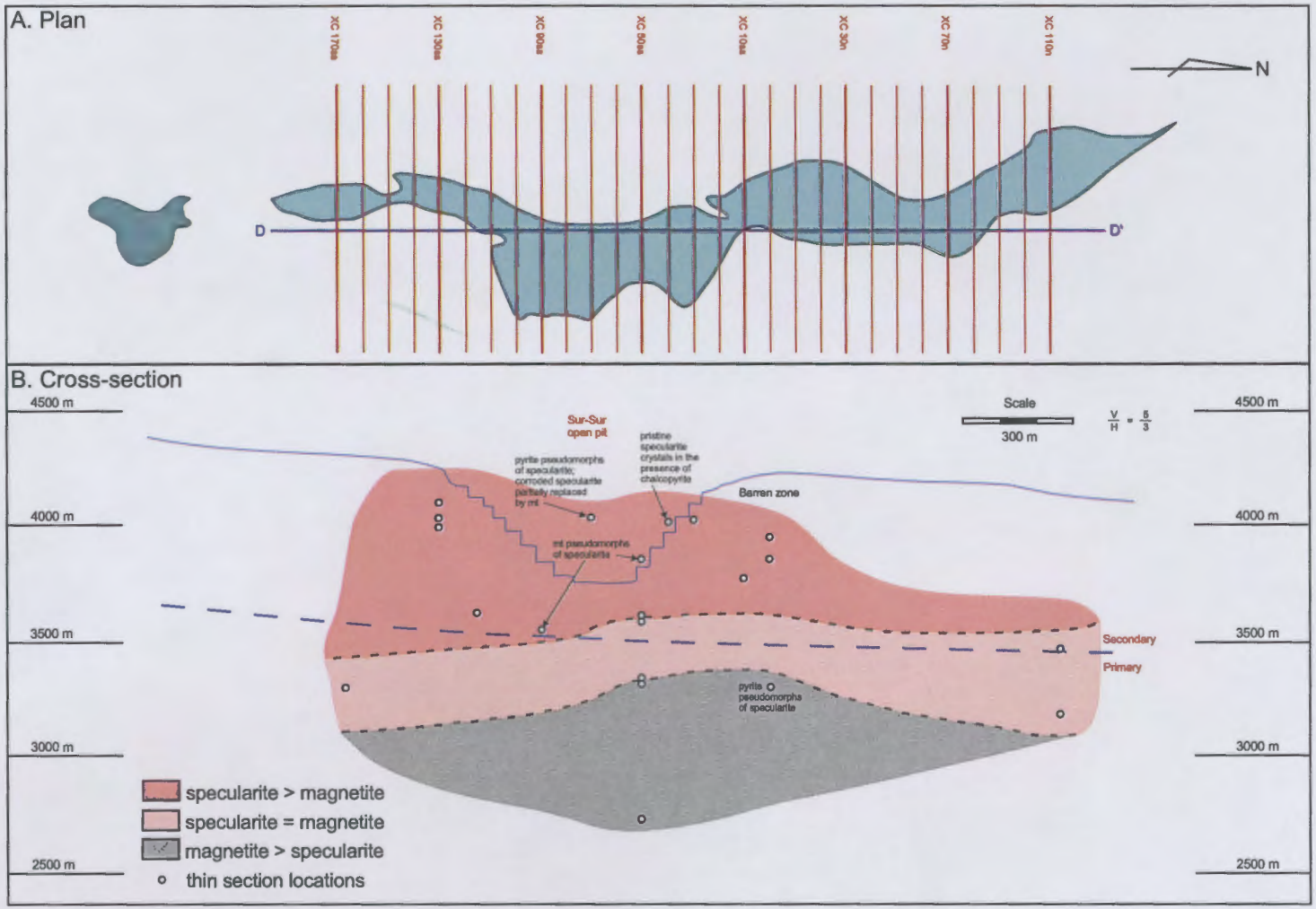

Figure 3.24. a. Plan view of Sur-Sur Tourmaline Breccia and location of longitudinal section D-D'; and b. Petrographic assessment of specularite and magnetite distribution in section D-D'.

3.4.4 Magnetite

Hydrothermal magnetite is distributed mainly on the outer margins of the mineralised zones in sections D-D' and E-E' (Fig. 3.23c, d). However, magnetite is also abundant in the deeper, mineralised zones along section D-D'. In section E-E', magnetite is concentrated in the mid to upper parts of the section, upwards and outwards from the orebody. Paragenetically, magnetite occurs as a primary mineral in the granodiorite, and a secondary mineral in both stages 1 and 3. Magnetite in stage 3 is synchronous with chalcopyrite, however most of the magnetite lies above the chalcopyrite-rich zones in section E-E', possibly due to remobilisation of magnetite during porphyry emplacement (compare Figs. 3.16d and 3.23d). In contrast, in section D-D', zones of chalcopyrite abundance are magnetite-enriched (compare Figs. 3.16c and 3.23c). However, as for biotite there is no discrimination of primary and secondary magnetite in the database.

In section XC-50SS, magnetite is predominant at elevations below 3330 m depth (magnetite > specularite; Fig. 3.21a). There is a transitional zone between 3330 m and 3600 m where magnetite and specularite coexist in equal proportions. These same features are also present on Section D-D' in Figure 3.24.

In section XC-130RB, magnetite is more abundant than specularite at depth. Magnetite has been almost completely replaced by rutile in the grey zone in Figure 3.22c. The rutile is associated with pervasive sericite alteration.

3.4.5 K-feldspar

K-feldspar is not an abundant alteration mineral in the Río Blanco complex. Primary K-feldspar is not abundant in the granodiorite wallrocks at the eastern margin of the Sur-Sur Tourmaline Breccia (Fig. 3.21c). Secondary K-feldspar is more abundant in the Río Blanco orebody, occurring in the deep to mid zones of section XC-130RB and broadly corresponding to the distribution of hydrothermal biotite (Figs. 3.17a and 3.22d).

3.5 Summary

- The sequence of mineralisation and alteration in the Río Blanco ore system began with early magnetite-actinolite alteration (stage 1). This was followed by development of weak sheeted biotite veins and a stockwork of mineralised quartz-anhydrite veins localised mainly in the Don Luis sector (stage 2).

- The early calcic and potassic alteration and vein assemblages were crosscut by mineralised biotite-cemented breccia (Magmatic Breccia) and mineralised tourmaline breccia associated with phyllic alteration. The contact between the biotite-cemented breccia and tourmaline-cemented breccia appears to be gradational, and occurs over a depth of approximately 100 m in section XC-50. The Magmatic Breccia and Tourmaline Breccia host the bulk of ore at Río Blanco (stage 3).
- The breccia cement infill sequence of the Magmatic Breccia and the Tourmaline Breccia is identical, and is characterised by early biotite (deep levels) or tourmaline (shallow levels), followed by anhydrite (at depth) and specularite (higher elevation) and finally by chalcopyrite and magnetite.
- The phyllic-altered Tourmaline Breccia is surrounded by a domain of propylitic alteration characterised by a chlorite, pyrite and specularite mineral assemblage.
- The mineralised breccias are then cut by a sequence of post-mineral porphyries, rock flour breccias, minor veins and phyllic alteration (stages 4-7). The porphyries are associated with a stockwork of molybdenite and chalcopyrite veins (stages 7-8). Compared to the earlier breccias, stage 8 chalcopyrite veins contributed only minor quantities of ore to the system.
- Stage 9 is defined by D veins that cross cut the stage 7-8 stockwork veins. These veins are in turn cross cut by late-stage, weakly altered and unmineralised felsic subvolcanic units (Dacite Chimney and La Copa Rhyolite).
- Mineral and alteration zoning is apparent in both the Río Blanco and Sur-Sur sectors. The implications for fluid evolution are discussed in Section 4 of this thesis.

SECTION 4 - FLUID CHEMISTRY AND FLUID EVOLUTION

This section presents new geochemical data for ore and gangue minerals and fluid inclusions from the Río Blanco and Sur-Sur sectors of the ore deposit. The aims are to determine the chemistry and sources of the ore forming fluids and to evaluate possible processes of ore formation.

4.1 Biotite and Tourmaline Mineral Chemistry

4.1.1 Introduction

The aim of this section is to describe the chemical composition of biotite and tourmaline mineral cements in the Sur-Sur Tourmaline Breccia. The chemistry of the two minerals will be compared to establish how the precursor fluid evolved spatially. The transition from biotite cement at depth in the Sur-Sur sector upward and outward to tourmaline (>3100 m elevation in Sur-Sur) is the most distinctive mineralogical zonation in the ore deposit. Biotite-altered rocks contain the high copper grades in the Río Blanco sector, whereas quartz-sericite altered rock contains the high copper grades in the Sur-Sur sector. As described in Section 3, textural relationships between biotite and tourmaline cement in the transitional zone are non-destructive, and are inferred (in part) to indicate coeval deposition of these two minerals. Chemical compositions of biotite and tourmaline cement from the Sur-Sur sector (section XC-50) have been analysed at the Central Science Laboratory, University of Tasmania, using a Cameca SX50 Electron Microprobe.

4.1.2 Biotite cement

A total of fourteen biotite analyses were obtained from three polished thin sections containing biotite cement from the base of the Sur-Sur Tourmaline Breccia. One sample comes from the biotite breccia (BXMGD) at a depth of 2850 m elevation, one from the biotite/tourmaline transitional zone (3350 m elevation) and one from the highest level of biotite occurrence, where tourmaline is more abundant (3520 m elevation; Fig. 4.1). Analytical results are listed in Appendix C1. Cations for biotite have been calculated on the basis of 22 (O, OH, F).

The chemical composition of biotite is dependant on the relative abundance of iron and magne-

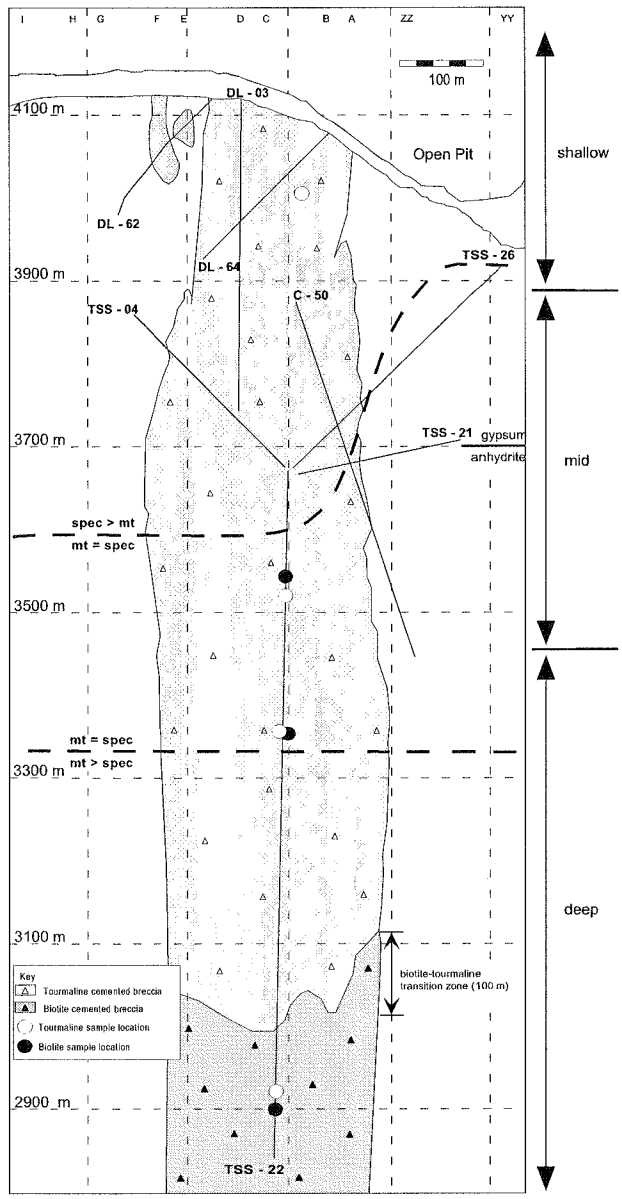

Figure 4.1. Cross-section XC-50, depth and sample locations for biotite and tourmaline cement.

sium (Deer et al., 1992) and lies between two end members;

$K_2Fe_4Al_2Si_4Al_4O_{20}(OH)_4$ (Fe-rich end member, annite)

$K_2Mg_4Al_2Si_4Al_4O_{20}(OH)_4$ (Mg-rich end member, phlogopite)

The chemical composition of the biotite cement analysed from Sur-Sur indicates a Mg# (100*Mg/ Mg + Fe) of approximately 60 (Fig. 4.2). All analyses are enriched in magnesium relative to iron, however this ratio is greatest in the deep-level biotite-cemented breccia (Mg#=65). Based on the limited data available, it appears that magnesium concentrations in biotite decrease upward through the Sur-Sur Tourmaline Breccia (Fig. 4.2a). Interestingly, there is little change in the total abundance of iron in biotite upwards through the Tourmaline Breccia (Fig. 4.2a). The decrease in mag-

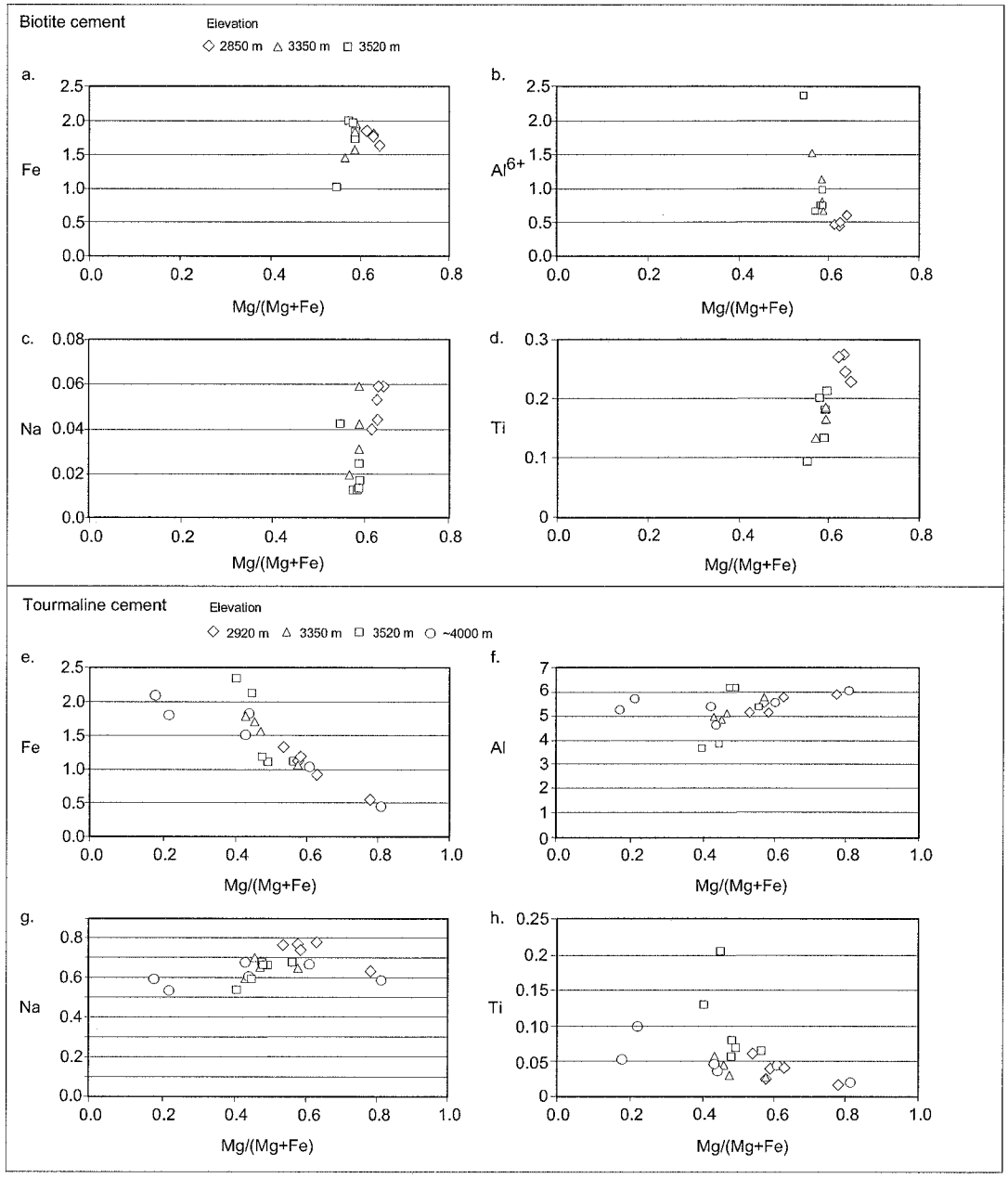

Figure 4.2. Cation plots for biotite and tourmaline cement from the Sur-Sur Tourmaline Breccia:
a. Mg/(Mg+Fe) versus Fe plot for biotite cement;
b. Mg/(Mg+Fe) versus Al^{6+} plot for biotite cement;
c. Mg/(Mg+Fe) versus Na plot for biotite cement;
d. Mg/(Mg+Fe) versus Ti plot for biotite cement;
e. Mg/(Mg+Fe) versus Fe plot for tourmaline cement;
f. Mg/(Mg+Fe) versus Al plot for tourmaline cement;
g. Mg/(Mg+Fe) versus Na plot for tourmaline cement; and
h. Mg/(Mg+Fe) versus Ti plot for tourmaline cement. Sample locations shown in Figure 4.1.

nesium is matched by an increase in the concentration of Al^{6+} in biotite upwards in the Tourmaline Breccia (Fig. 4.2b). Sodium concentrations are either at or below detection limits for biotite cement (Fig. 4.2c). In concordance to magnesium, titanium also decreases upward through the Sur-Sur Tourmaline Breccia (Fig. 4.2d). Although the titanium content of biotite can be a very good indicator of temperature (c.f. Henry and Guidotti, 2002), there is not enough data available to directly calibrate the temperature in Sur-Sur. Instead, the titanium content of biotite appears to reflect the mineralogical zonation in Sur-Sur (Fig. 4.1).

4.1.3 Tourmaline cement

A total of twenty-one analyses of tourmaline cements were obtained from four polished thin sections. One sample is from the base of the Tourmaline Breccia (2920 m elevation), one from the biotite-tourmaline transitional zone (3350 m elevation), one from a mid level in the Tourmaline Breccia (3520 m elevation) and one from high altitude (~4000 m elevation) in the Tourmaline Breccia (Fig. 4.1). Analytical results are listed in Appendix C2. Cations have been calculated on the basis of 27 (O, OH, F).

The chemical composition of tourmaline is considerably more complex than biotite. The three relevant end member species of tourmaline are (Deer et al., 1992);

$NaMg_3Al_6B_3Si_6(O,OH)_{30}(OH,F)$ (Dravite)

$Na(Fe,Mn)_3Al_6B_3Si_6(O,OH)_{30}(OH,F)$ (Schorl)

$Na(Li,Al)_3Al_6B_3Si_6(O,OH)_{30}(OH,F)$ (Elbaite)

In general, compositional differences in tourmaline occur as a result of variations in the abundance of magnesium, manganese, aluminium, lithium and iron.

In the Sur-Sur Tourmaline Breccia, tourmaline compositions vary with depth in terms of the aluminium, iron, magnesium and sodium concentrations. The stoichiometry are presented in Appendix C2 and illustrated in Figure 4.3. Tourmalines in the Tourmaline Breccia are dravitic at depth, however enrichment in iron at higher elevations shifts compositions toward schorl.

There is no obvious systematic trend in the Mg# (100*Mg/Mg + Fe) for tourmaline, apart from relatively depleted iron concentrations at depth increasing to higher concentrations in the mid to shallow levels in the Tourmaline Breccia (Fig. 4.2e; Appendix C2). The Mg# versus iron field for biotite cement located within the biotite-tourmaline transitional zone in the Tourmaline Breccia

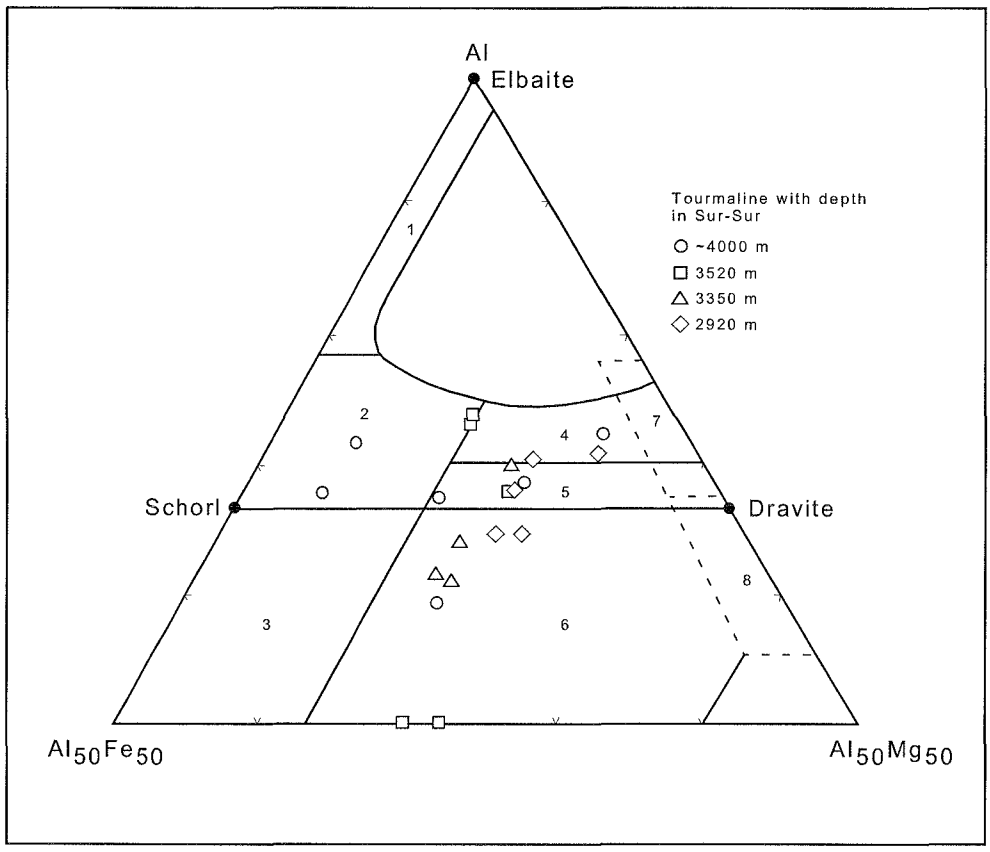

Figure 4.3. Triplot showing tourmaline compositions in terms of aluminium, iron and magnesium (in cation proportions) from different elevations in the Sur-Sur Tourmaline Breccia. Fields: 1 = Li-rich granitoid pegmatites and aplites; 2 = Li-poor granotoids and their associated pegmatites and aplites; 3 = Fe^{3+} -rich quartz-tourmaline rocks (hydrothermally altered granites); 4 = Metapelites and metapsammites coexisting with an Al-saturating phase; 5 = Metapelites and metapsammites not coexisting with an Al-saturating phase; 6 = Fe^{3+} -rich quartz-tourmaline rocks, calc-silicate rocks, and metapelites; 7 = Low Ca metaultramafics and Cr, V-rich metasediments; and 8 = Metacarbonates and meta-pyroxenites (adapted from Henry and Guidotti, 1985).

trends towards the Mg# versus iron field for tourmaline cement (Fig. 4.2a, e). The anomalous sample in this dataset is the mid level sample (3520 m elevation), which is iron enriched (between 1.0 to 2.5) and aluminium depleted (between 3.8 and 6.0; Fig. 4.2e, f). In terms of the contents of aluminium, magnesium and iron, this anomalous sample has two distinct compositions, one with high aluminium and one with almost no aluminium (Fig. 4.3). In contrast to the other samples, this sample contains abundant magnetite within the breccia cement suggesting that high iron concentrations derived from the wallrocks substituted for aluminium in the tourmaline crystal structure. The highest aluminium concentrations occur in the deepest (2920 m) and the shallowest samples (~4000 m), both of which have coarse (up to 2 cm long) tourmaline crystals (e.g. Fig. 3.9b). In contrast, tourmaline analysed in the two mid-level samples (3350 m and 3520 m) are fine-grained.

The deepest level tourmaline sample had an average value of 0.736 cations of sodium. This decreases upwards to 0.650 cations (3350 m elevation), 0.634 cations (3520 m elevation) and 0.588 cations (~4000 m; Fig. 4.2g). Titanium is mostly below detection limits (Fig. 4.2h).

4.1.4 Discussion

Based on the limited dataset generated in this study, there appear to be systematic changes in biotite and tourmaline mineral chemistry in the Sur-Sur Tourmaline Breccia, however it is clear that more data are needed. These appear to track changes that occurred in the parent fluid composition upwards through the breccia column, although more data are needed to confirm this. Goerne et al. (2001) investigated sodium concentrations in tourmaline as a function of temperature. As fluids cool, they found that the sodium content of tourmaline decreases. This may relate to a decrease in the solubility of sodium-bearing minerals, e.g. albite, resulting in their precipitation and the activity of sodium ions greatly reduced. At Sur-Sur, progressive cooling up through the breccia column may have resulted in a greater abundance of sodium-rich feldspars and a subsequent descrease in the sodium content of tourmaline. Decreasing titanium with increasing elevation in biotite cement also represents decreasing temperature. Consequently, aluminium enrichment and sodium depletion in tourmaline with increasing elevation is interpreted to reflect increasing acidity and decreasing temperature.

Across the biotite-tourmaline transition zone at Sur-Sur, there are subtle changes in mineral chemistry between the two minerals. In their study of granitic magmas, Wolf and London (1997) found that during magma crystallisation, the magnesium and iron content of the melt decreases due to the precipitation of ferromagnesian minerals, and B_2O_3 contents increase until the tourmaline equilibria are attained. Because the magnesium and iron contents of biotite cements appear to decrease upwards through the Tourmaline Breccia, it appears that the fluid was becoming depleted in magnesium and iron as it reached saturation in aluminium and B_2O_3 which may have been a factor in causing the transition from biotite to tourmaline. It would have also been a function of decreasing temperatures and increasing acidity of the fluids (Morgan and London, 1989; Wolf and London, 1997).

Aluminium-bearing minerals such as feldspars and micas are more soluble in acidic rather than alkaline fluids, and tourmaline stability is favoured by an increase in aluminium availability in the fluid (Morgan and London, 1989). Tourmaline is therefore more likely to have precipitated from acidic fluids (pH < 6.0; Morgan and London, 1989). This notion is supported by the spatial correlation of tourmaline with quartz-sericite alteration in the Sur-Sur sector. The majority of the samples analysed in this study contained almost the limit of six cations of aluminium, however, one sample, the mid level sample (3520 m elevation) is enriched in iron and depleted in aluminium. The iron enrichment and aluminium depletion in this sample is possibly due to the incorporation of Fe^{3+} into the Z site of the tourmaline crystal structure (Henry and Guidotti, 1985). This potentially reflects local iron enrichment in the rock demonstrated by a high abundance of magnetite in the breccia cement, a feature that discriminates this sample from all the other samples analysed. The two discrete aluminium, magnesium and iron compositions at 3520 m (Fig. 4.3) may indicate

deposition from two different fluids, or from one fluid that evolved compositionally during tourmaline growth. The low aluminium concentrations at 3520 m indicate that the tourmaline crystallised directly from the fluid with no rock interaction, whereas the compositions with higher proportions of aluminium have interacted to a much larger degree with wallrocks. In the highest elevation sample, the large spread of data indicates highly variable fluid compositions.

4.2 Radiogenic isotopes

4.2.1 Introduction

Radiogenic isotopes can be used to gain information about:

- the age of rocks and minerals;
- the source(s) of igneous rocks and hydrothermal minerals;
- source(s) of metals
- mixing trends between different sources, and
- host rock and mineralisation ages.

This subsection provides a review of argon, strontium, neodymium and Pb isotope data from central Chile and presents new $^{40}Ar/^{39}Ar$, $^{87}Sr/^{86}Sr$, $^{143}Nd/^{144}Nd$, $^{207}Pb/^{204}Pb$, $^{206}Pb/^{204}Pb$ and $^{208}Pb/^{204}Pb$ data obtained during this study from the Río Blanco mineralised breccias. Mineral separation and $^{40}Ar/^{39}Ar$ radiometric analyses were performed at the Department of Geological Sciences, Queens University in Ontario, Canada by Doug Archibald, using the technique outlined in Appendix D1. Sr, Nd and Pb isotope compositions were analysed on a Finnigan MAT 261 TIMS housed at the Department of Geology and Geophysics at the University of Adelaide by John Foden. Analytical methods are described in Appendix D2 and D3.

4.2.2 $^{40}Ar/^{39}Ar$ results for the Sur-Sur Tourmaline Breccia

Introduction

Previous geochronological studies on the Sur-Sur Tourmaline Breccia have been performed on altered whole-rock samples (e.g. Warnaars et al., 1985; Serrano et al., 1996). They have yielded an age range between 7.1 ± 0.8 and 5.1 ± 0.2 Ma (Table 4.1; Serrano et al., 1996). The Río Blanco Magmatic Breccia has been dated previously using whole-rock samples and mineral separates (biotite, K-feldspar) with ages between 7.3 ± 0.7 and 4.2 ± 0.1 Ma determined (Table 2.1; Serrano

et al., 1996). In both cases, the older ages were obtained from whole-rock samples using the K-Ar technique; whereas younger ages were obtained from pure mineral separates of biotite and K-feldspar using the $^{40}Ar/^{39}Ar$ technique. Based on this previous work, this study attempts to resolve the uncertainty and controversy of age between the Río Blanco Magmatic Breccia and the Sur-Sur Tourmaline Breccia.

Table 4.1. Step heating Ar isotopic data, apparent ages and plateau ages for hydrothermal biotite cement (sample 215a) and sericite whole rock (sample 530).

Sample 215a - mass = 0.9 mg, J value = 0.002451 ± 0.000018

DDH	**section**	**metres**	**altitude**	**lithology**	**material**	**method**	**39Ar released**	**plateau age (Ma)**
TSS 22	XC-50	782 m	2873 m	BXMGD	hydrothermal biotite	Ar/Ar	86%	4.78 ± 0.04 Ma

Power	$^{36}Ar/^{40}Ar$	$^{39}Ar/^{40}Ar$	r	Ca/K	%40Atm	$\%^{39}Ar$	$^{39}Ar/^{40}Ar^*$	Age
0.5	0.0034	0.0343	0.049	0.697	100.53	0.14	-0.183	-0.81± 5.44
1	0.0031	0.1786	0.243	0.392	91.74	0.48	0.435	1.92 ± 1.64
1.5	0.0015	0.5174	0.068	0.21	44.62	2.44	1.057	4.67 ± 0.29
1.75	0.0006	0.7598	0.007	0.065	17.69	6.65	1.078	4.76 ± 0.12
2	0.0004	0.8335	0.009	0.044	12.74	4.81	1.043	4.61 ± 0.10
<2.25>	0.0003	0.8314	0.002	0.078	10.41	3.77	1.074	4.74 ± 0.16
<2.75>	0.0004	0.8155	0.002	0.109	11.42	4.14	1.083	4.78 ± 0.16
<3.50>	0.0003	0.8154	0.006	0.27	11.22	4.93	1.085	4.79 ± 0.11
<4.50>	0.0002	0.8551	0.002	0.406	6.37	6.4	1.093	4.83 ± 0.08
<7.00>	0.0001	0.8796	0.013	0.268	4.62	66.22	1.083	4.78 ± 0.02

notes:
Volume 39K: 61.53 x 1E-10 cm^3 NTP
Integrated age: 4.75 ± 0.04 Ma
Initial 40/36: 320.54 ± 98.19 (MSWD = 0.55, isochron between 0.18 and 2.63)
Correlation age: 4.76 ± 0.09 Ma (85.5% of 39Ar, steps marked by >)
Plateau age: 4.78 ± 0.04 Ma (85.5% of 39 Ar, steps marked by <)
All errors are 2 X standard error

Sample 530 - mass = 0.9 mg, J value = 0.002449 ± 0.000018

DDH	**section**	**metres**	**altitude**	**lithology**	**material**	**method**	**39Ar released**	**plateau age**
DL-53	XC-30	50 m	4021 m	BXT	WR-sericite	Ar/Ar	81%	5.42 ± 0.09 Ma

Power	$^{36}Ar/^{40}Ar$	$^{39}Ar/^{40}Ar$	**r**	**Ca/K**	**%40Atm**	$\%^{39}Ar$	$^{39}Ar/^{40}Ar^*$	**Age**
0.5>	0.0034	0.0003	0.151	0.064	102.01	0.46	-54.75	-259.73 ± 213.55
0.75>	0.0033	0.0016	0.013	0.033	99.45	0.55	3.421	15.05 ± 38.88
1>	0.0033	0.0065	0.003	0.012	99.32	0.87	1.003	4.42 ± 9.54
1.25>	0.0032	0.0229	0.005	0.005	96.85	1.24	1.348	5.94 ± 3.05
1.5>	0.0031	0.0621	0.007	0.005	91.76	1.76	1.297	5.72 ± 1.42
1.75>	0.0025	0.1915	0.011	0.003	74.93	3.31	1.286	5.67 ± 0.44
2.25>	0.0026	0.1559	0.01	0.003	78.61	4.12	1.348	5.95 ± 0.48
<2.75>	0.0026	0.1649	0.009	0.003	79.07	6.71	1.245	5.49 ± 0.39
<3.25>	0.0023	0.257	0.007	0.004	68.01	9.24	1.224	5.40 ± 0.25
<3.75>	0.0022	0.2836	0.008	0.004	64.95	13.05	1.216	5.37 ± 0.19
<4.25>	0.0021	0.3042	0.012	0.003	62.11	17.2	1.227	5.41 ± 0.16
<4.75>	0.0016	0.4062	0.012	0.004	49.34	14.54	1.232	5.44 ± 0.13
<5.50>	0.0018	0.3746	0.008	0.008	53.43	12.28	1.227	5.41 ± 0.15
<6.50>	0.0016	0.4168	0.01	0.01	48.01	7.83	1.233	5.44 ± 0.16
7	0.0025	0.1847	0.014	0.053	73.96	6.86	1.387	6.12 ± 0.37

notes:
Volume 39K: 43.51 x 1E-10 cm^3 NTP
Integrated age: 4.42 ± 0.91 Ma
Initial 40/36: 295.17 ± 6.8 (MSWD = 1.23, isochron between 0.59 and 1.82)
Correlation age: 5.43 ± 0.08 Ma (93.1% of 39Ar, steps marked by >)
Plateau age: 5.42 ± 0.09 Ma (80.8% of 39 Ar, steps marked by <)
All errors are 2 X standard error

This study

This study aims to determine whether the Magmatic Breccia and Tourmaline Breccia are the same age by analysing a biotite mineral separate and a sericite-altered whole rock sample from the Sur-Sur breccia using $^{40}Ar/^{39}Ar$ geochronology. The biotite was handpicked from fine-grained hydrothermal biotite cement collected from the base of the Sur-Sur Tourmaline Breccia. Pervasive sericite-altered granodiorite clasts were collected from high elevation in the Tourmaline Breccia. The clasts were separated from the cement and powdered prior to analysis.

The sample locations, elevations and results for the Ar-Ar study are listed on Table 4.1 and Figure 3.14, and stepwise release spectra are illustrated on Figure 4.4. From these, an age is determined by recognition of a 'plateau' that was defined by Fleck et al. (1977) as: "that part of the spectrum diagram composed of contiguous gas fractions that together represent more than 50% of the total ^{39}Ar released from the sample and for which no difference in age can be detected between any two fractions at the 95% confidence level".

The plateau age for hydrothermal biotite (4.78 ± 0.04 Ma) from the Sur-Sur Tourmaline breccia is illustrated on Figure 4.4. It correlates well with $^{40}Ar/^{39}Ar$ age determinations for biotite (4.6 ± 0.1 Ma) and K-feldspar (4.2 ± 0.1 Ma) from the Magmatic Breccia in the Río Blanco sector (Table 2.1).

The plateau age for the sericite-altered whole rock sample is 5.42 ± 0.09 Ma (Table 4.1; Fig. 4.4). It is similar to whole rock age determinations previously documented for the Tourmaline Breccia (Table 2.1).

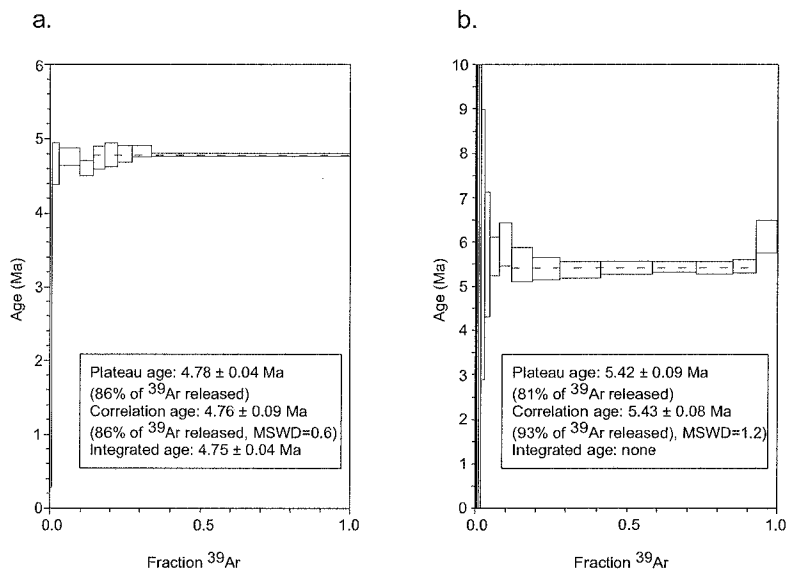

Figure 4.4. $^{40}Ar/^{39}Ar$ apparent age spectra for (a) hydrothermal biotite, and (b) sericite-altered whole rock from the Sur-Sur mineralised Tourmaline Breccia.

Discussion

One problem with whole rock age determinations on breccias is the potential contamination by relict primary minerals in the wall rock clasts. The youngest cooling age for the granodiorite host rock is 7.4 ± 0.1 Ma (Serrano et al., 1996). The mineralised whole rock breccia samples analysed in previous studies and in this study span the range of ages between the youngest age of the granodiorite and the Ar-Ar ages determined from pure breccia cement mineral separates. Therefore, the most reliable ages for the brecciation events are considered here to be those determined on the hydrothermal cements.

Without a pure sericite mineral separate, it has not been possible to confirm the age of the Sur-Sur Tourmaline Breccia. The older age of the sericite whole rock sample compared to the biotite is probably from contamination by residual plagioclase from the granodiorite clasts, similar to previous whole rock age determinations on the Tourmaline Breccia (e.g. Serrano et al., 1996). Alternatively, the difference in the older whole-rock sericite and the younger biotite cement ages may reflect cooling (Fig. 3.14). The older whole rock sericite occurs at 4021 m elevation and the biotite cement occurs at 2873 m elevation. Final cooling of the hydrothermal system will have progressed downwards from higher to lower elevations. If temperatures were above the closure temperatures for both sericite (~350°C) and biotite (~300-325°C), cooling to lower temperatures should produce an older age for the near-surface sericite-altered whole rock sample than for the deeper level biotite-cement if they actually formed at the same time (McDougall and Harrison, 1988). To add further complexity, the intrusion of post-breccia events (stages 6-9) may have reset the biotite and sericite isotopic compositions, and so the ages determined here may reflect post-brecciation intrusive activity, rather than the mineralising event.

The biotite cement at the base of the Tourmaline Breccia has a similar age to the biotite cement in the Río Blanco sector (Magmatic Breccia; 4.6 ± 0.1 Ma, Table 2.1). This is interpreted to indicate that the Magmatic Breccia is one spatially continuous breccia body that extends from the Río Blanco to Sur-Sur sectors. Alternatively, the Río Blanco and Sur-Sur breccias may have both been reset by the same thermal event. The age for hydrothermal biotite cement is also younger than the oldest age determinations for the stage 6 porphyries (5.2 ± 0.3 Ma) that cross cut the mineralised breccias, but are older than the youngest age (3.9 ± 0.7 Ma; Table 2.1). The age determinations for the porphyries were undertaken using primary biotite and K-feldspar by Serrano et al. (1996). These dates are enigmatic because the mineralised breccias are cross cut by these porphyries.

In summary, the new Ar-Ar dates for biotite breccia cement and sericite wholerock from the Tourmaline Breccia are either the result of cooling, thermal resetting or inherited from wall rocks. A comprehensive study is needed using geochronological methods other than Ar-Ar to solve the problems encountered in this study.

4.2.3 Strontium and Neodymium Isotopes

Introduction

Isotopes of strontium and neodymium have been used for decades to identify the sources of igneous rocks (Wilson, 1989; Rollinson, 1993). These tracers have also been applied to host intrusions and minerals associated with porphyry copper mineralisation to determine if these materials are in some way isotopically distinct (Hedenquist and Richards, 1998). Early workers (e.g. Kesler et al, 1975; Titley and Beane, 1981) studied the initial Sr isotope compositions of island arc and continental arc porphyry Cu systems and found that the island arc rocks consistently displayed low ratios ($^{87}Sr/^{86}Sr < 0.705$) whereas the continental rocks ranged up to 0.709. Kesler et al. (1975) interpreted these data as an indication for a depleted mantle source for the island arc magmas with little upper crustal involvement, thereby precluding a crustal source for Cu in porphyry deposits in general. However, many continental porphyry copper systems display isotopic evidence for extensive involvement of crustal materials in magma genesis, and the search for a crustal source of metals continues today (Hedenquist and Richards, 1998).

Previous work

The nature of the mantle source region of central Andean Neogene mafic magmas has been the subject of debate for many years, as all lavas erupting through thickened crust in the main Andean Cordillera have enriched isotope signatures ($^{87}Sr/^{86}Sr > 0.705$, $\varepsilon_{Nd} < 0$) relative to mid ocean ridge basalts (MORB) and most oceanic arc lavas (Kay et al., 1999). The question is whether this enrichment is due to contamination within the crust of mantle-derived magmas that have initally-depleted compositions, or whether the enriched signature is present in the mafic magmas when they enter the crust (Kay et al., 1999). If the $^{87}Sr/^{86}Sr$ ratio of magmas is already enriched upon entering the crust, there may be a number of different possible sources for this enrichment:

1. old enriched lithospheric mantle;
2. intraplate (hot-spot) asthenospheric mantle;
3. subducted sediment and fluids from the slab;
4. recycled continental crust incorporated into the mantle from the fore-arc or the base of the crust; and /or
5. a complex combination of all these sources (Kay et al., 1999).

In central Chile, the $^{87}Sr/^{86}Sr$ datasets (e.g. Skewes and Stern, 1996, Kay and Abruzzi, 1996, Kay et al., 1999, Hashke et al., 2002, Hollings et al., submitted) generally display a trend to higher values in younger rocks. The ε_{Nd} data show a contrasting trend to lower values in younger rocks (Fig. 4.5). However, Nyström et al (1993) identified a reversal in $^{87}Sr/^{86}Sr$ values towards MORB from the Jurassic to the Cretaceous period and then back to a crustal contamination trend during

the Miocene (Fig. 4.5). This reversal has been demonstrated to occur earlier in the north (in the so-called flat slab zone; Kay et al., 1991) and the trend towards MORB coincided with an observed shift in geochemistry from high calc-alkaline-shoshonitic to calc-alkaline with features transitional to tholeiitic (Nyström et al., 1993; Hollings et al., submitted). Rocks of tholeiitic affinity appear to be confined to an area south of 33°S (Hollings et al., submitted). The eruption and deposition of the Los Pelambres (Abanico) Formation is thought to represent the point of reversal towards MORB. Nyström et al. (1993) suggested that the Los Pelambres Formation has isotopic characteristics indicative of the lowest amounts of crustal contamination of any known igneous rock emplaced in the Andean cycle. Their data is consistent with an extensional model for the Cretaceous suites followed by crustal thickening in the Miocene during emplacement of the Los Pelambres (Abanico) and Farellones Formations as proposed by Vergara et al. (1995).

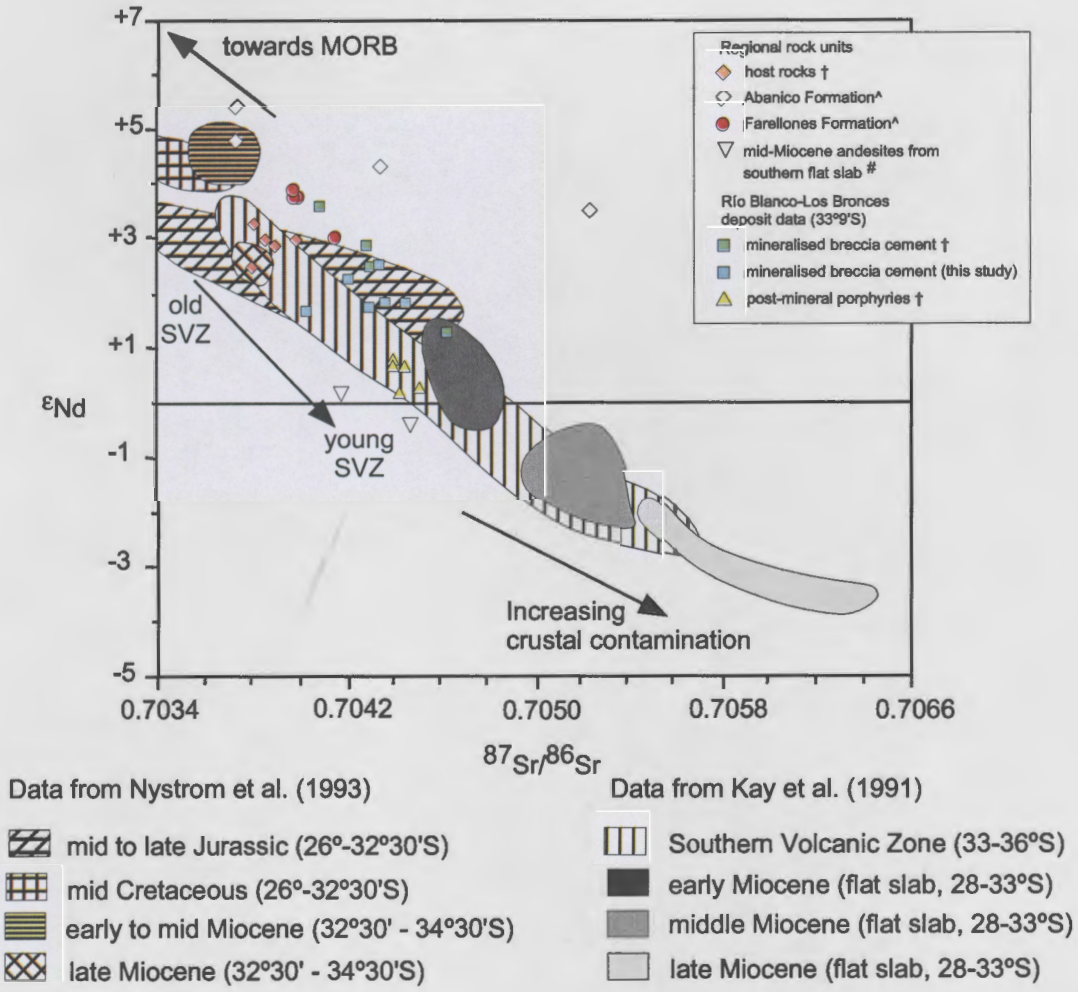

Figure 4.5. Initial $^{87}Sr/^{86}Sr$ and ε_{Nd} datasets for Tertiary samples collected from the "flat slab" region (28-33°S) compared to modern northern SVZ volcanic rocks in central Chile and data from and the Río Blanco-Los Bronces ore deposit (33°09'S; includes previous data and data from this study. Farellones Formation data from Hollings et al., 2002. Young and old SVZ data from Kay et al. (1999), * = Skewes and Stern, + = Hollings et al., 2002, ^ = Kay et al., 1991. Adapted from Kay et al. (1991).

A compilation of chemical and radiogenic isotope data for the northern portion of the SVZ between 33° and 38°30'S (Hildreth and Moorbath, 1988) shows a striking correlation between the degree of inferred crustal contamination and increasing crustal thickness and age from south to north. This supports the notion that the nature of the overriding lithosphere controls the compositions of the erupted magmas (Davidson et al., 1991). This premise is sustained when considering the volcanoes in the southern part of the SVZ between 36 and 40°S that have lower $^{87}Sr/^{86}Sr$ and higher $^{143}Nd/^{144}Nd$ isotope signatures (0.7036 and 0.5129, respectively) that are coincident with thinner crust (30-40 km). In contrast, the volcanoes from the northern part of the SVZ (33 - 34°S) are built on thicker crust (45-60 km) and have higher $^{87}Sr/^{86}Sr$ and lower $^{143}Nd/^{144}Nd$ isotopic signatures (0.7057 and 0.5125, respectively; Hildreth and Moorbath, 1988; Davidson et al., 1991). Hildreth and Moorbath (1988) discussed different mechanisms that may have resulted in the observed isotopic compositions, including contributions from the subducted plate (sediments and basalts), mantle and lower versus upper crustal contamination. They concluded that intracrustal processes and contributions from the lowermost crust control the observed gradient in $^{87}Sr/^{86}Sr$ and ε_{Nd} values of SVZ rocks from south to north.

Kay and Abruzzi (1996) concluded that the Sr isotope ratios of the Main Cordilleran, Precordilleran and Pampean magmas north of 33°S were sourced from the mantle and contaminated by the crust. They proposed a scenario involving the incorporation of substantial amounts of continental lithosphere into the circulating asthenosphere by delamination, lithospheric boundary erosion and subduction erosion processes. These processes are considered to have accompanied slab shallowing due to subduction of the Juan Fernandez Ridge, crustal thickening and shortening in central Chile during the Miocene (28-33°S; Kay et al., 1991; Kay and Abruzzi, 1996).

Data generated on Tertiary igneous rocks between 22° and 33°S by Kay et al. (1999) display systematic increases in $^{87}Sr/^{86}Sr$ and decreases in ε_{Nd} values with time (Fig. 4.5). Kay et al. (1999) interpreted the increasing $^{87}Sr/^{86}Sr$ ratios as being caused by increasing amounts of crustal contamination as mantle-derived magmas pass through a progressively thicker crust. They interpreted the trends to be the result of mixing between mantle-derived melts with variable, but low $^{87}Sr/^{86}Sr$ ratios that reflect their mantle sources, and silicic crustal end-member contaminants with a broad range of $^{87}Sr/^{86}Sr$ ratios reflecting their composition and age. In addition, they postulated that southward younging of ore deposits reflects a southward progression of crustal thickening, which is considered responsible for delamination of the lower crust during the Pliocene.

Skewes and Stern (1996) analysed rock and mineral samples from the Río Blanco-Los Bronces ore deposit for their $^{87}Sr/^{86}Sr$ and $^{143}Nd/^{144}Nd$ compositions. Their work focussed on the host rocks, mineralised breccias and post-mineral porphyries (Table 4.2, Fig. 4.5). Their data plot in the field for the regional SVZ dataset and show a broadly linear enrichment trend in $^{87}Sr/^{86}Sr$ and gradual

decrease in ε_{Nd} through time. However, the mineral and rock data from mineralised breccia samples plot slightly to the right of the trend for the host rocks and post-mineral porphyries with no change in ε_{Nd} values and a shift towards increased $^{87}Sr/^{86}Sr$. The lowest $^{87}Sr/^{86}Sr$ sample is anhydrite cement from the Río Blanco Magmatic Breccia (7.3 Ma) and the highest $^{87}Sr/^{86}Sr$ sample is anhydrite cement from the Los Bronces Anhydrite Breccia (5 Ma; Fig. 4.4; Skewes and Stern, 1996). The two intermediate samples between the anhydrite outliers are whole rock and tourmaline samples (Table 4.1, Fig. 4.4).

Table 4.2. Previous $^{87}Sr/^{86}Sr$ and ε_{Nd} datasets for the Río Blanco-Los Bronces ore deposit.

Sample	Age (Ma)	Rock type	Material analysed	$(^{87/86}Sr)_i$	$(^{143/144}Nd)_i$	εNd_i
An1*	>16	andesite	whole rock	0.70381	0.51274	2.5
An2*	>16	andesite	whole rock	0.70382	0.51279	3.3
LB-3*	18.5	granodiorite	whole rock	0.70387	0.51277	3
GDRB*	11.7	granodiorite	whole rock	0.704	0.51278	3
LB-7*	8.6	granodiorite	whole rock	0.70391	0.51278	2.9
CN18^	20	Abanico Formation	whole rock	0.70411	0.512847	4.3
CA60^	20	Abanico Formation	whole rock	0.70528	0.512801	3.4
CN37^	21.9	Abanico Formation	whole rock	0.70379	0.512875	4.9
CN41^	22	Abanico Formation	whole rock	0.70379	0.512909	5.4
CA13^	11.6	Farellones Formation	whole rock	0.70399	0.512824	3.7
CE45^	11.6	Farellones Formation	whole rock	0.70414	0.512789	3
CE21^	12.4	Farellones Formation	whole rock	0.70397	0.512829	3.8
CE44^	10.9	Farellones Formation	whole rock	0.70397	0.512824	3.7
whole rock†	7.3	Magmatic Breccia (RB)	whole rock	0.7043	0.5128	2.9
anhydrite#1†	7.3	Anhydrite Breccia (RB)	anhydrite	0.7041	0.512811	3.6
anhydrite#2†	5	Anhydrite Breccia (LB)	anhydrite	0.70463	0.512696	1.3
tourmaline†	5	Donoso Breccia (LB)	tourmaline	0.70431	0.512762	2.5
PQM*	5.2	Quartz Monzonite Porphyry	whole rock	0.70441	0.51267	0.8
PDL*	4.9	Don Luis Porphyry	whole rock	0.70441	0.51267	0.7
LB-11*	4.9	dacite porphyry	whole rock	0.70444	0.51264	0.2
LB-10*	4.8	dacite porphyry	whole rock	0.70452	0.51265	0.3
ChDac*	4.8	Dacite Chimney	whole rock	0.70446	0.51268	0.7

* = Serrano et al. (1996), ^ = Hollings et al. (2002), † = Skewes and Stern (1996)

LB = Los Bronces, RB = Rio Blanco, GDRB Rio Blanco Granodiorite

This study

Six samples were chosen for $^{87}Sr/^{86}Sr$ and $^{143}Nd/^{144}Nd$ analysis. Two of these samples are anhydrite cement from the Río Blanco Magmatic Breccia, two are anhydrite cement from the Sur-Sur Tourmaline Breccia and two are tourmaline cement from the Sur-Sur Tourmaline Breccia (Table 4.3). All of these breccia cement minerals were precipitated as breccia cement prior to sulfide deposition. The results for $^{87}Sr/^{86}Sr$ range between 0.704049 and 0.704464, and ε_{Nd} analyses range between +1.70 and +2.53. Epsilon Nd values were calculated using a present-day CHUR (Chondritic Uniform Reservoir) reference value of 0.512638 (Skewes and Stern, 1996). The data generated in this study are plotted in Figure 4.5, superimposed on the previous datasets.

The results from this study follow the trend defined by the data of Skewes and Stern (1996).

Furthermore, the anhydrite data from the mineralised breccias displays a temporal trend from low $^{87}Sr/^{86}Sr$ and high ε_{Nd} in the Río Blanco Magmatic Breccia, intermediate values for anhydrite in the Sur-Sur Tourmaline Breccia and the most enriched $^{87}Sr/^{86}Sr$ and most negative ε_{Nd} values for anhydrite cement in the late Anhydrite Breccia from Los Bronces (Table 4.3, Fig. 4.5).

Table 4.3. $^{87}Sr/^{86}Sr$ and ε_{Nd} results generated in this study. RB = Río Blanco sector, SS = Sur-Sur sector of ore deposit, BXMGD = Río Blanco Magmatic Breccia, BXT = Tourmaline Breccia, ages shown are whole rock K-Ar. The 4.5 Ma age used for the epsilon Nd calculation is based on the average of the three pure mineral ages 4.6, 4.2 (Table 2.1) and 4.78 Ma (this study) of biotite and k-feldspar from the breccia cements at RB and SS.

Sample	Age (Ma)	Rock type	Material analysed	$(^{87/86}Sr)_i$	$(^{143/144}Nd)_i$	εNd_i
RB246h	4.5	BXMGD	anhydrite	0.704215	0.512750	2.29
RB240b	4.5	BXMGD	anhydrite	0.704348	0.512764	2.56
SS01BXT12	4.5	BXTGDCC	anhydrite	0.704374	0.512730	1.91
SS60c	4.5	BXTGDCC	anhydrite	0.704307	0.512726	1.83
SS225c	4.5	BXTGDCC	tourmaline	0.704464	0.512728	1.87
SS open pit	4.5	BXTGDCC	tourmaline	0.704049	0.512722	1.76

Discussion

The fact that the breccia cement minerals plot with increased $^{87}Sr/^{86}Sr$ and unchanged ε_{Nd} from the linear trend between the host rocks and post-mineral porphyries presents a perplexing challenge for data interpretation. The $^{87}Sr/^{86}Sr$ compositions for the mineralised breccias are more similar to the post-mineral porphyries but the ε_{Nd} values plot closer to the host rocks. Given the greater solubility of Sr compared to Nd in high temperature fluids (Farmer and DePaolo, 1987), exchange between fluids and host rock clasts would cause the Sr isotope composition of the fluids to approach that of the host rocks (Skewes and Stern, 1996). In the early anhydrite sample collected from the Río Blanco Magmatic Breccia, this is certainly the case, but in the later anhydrite samples associated with Los Bronces Anhydrite Breccia the $^{87}Sr/^{86}Sr$ composition is closer to the post-mineral porphyries. Skewes and Stern (1996) concluded that the observed isotopic compositions of the mineralised breccias may be explained by the exsolution of the breccia-forming fluids from magmas produced by admixture of older magmas that suffered little interaction with continental crust and variable amounts of younger, more contaminated magmas.

The samples of post-mineral porphyry with high $^{87}Sr/^{86}Sr$ and low ε_{Nd} from Río Blanco-Los Bronces are best interpreted as the result of increased crustal contamination associated with extended crustal residence times due to crustal thickening (Skewes and Stern, 1996). In addition, the high SiO_2 content of the rhyolite indicates extensive fractionation and is consistent with long residence times (Hollings et al., submitted). This data supports the notion that fractionation of crustal components continued throughout the evolution of the ore deposit. Skewes and Stern (1996) conclude that the incorporation of progressively greater proportions of crustal material through time is the result of either crustal thickening or increased subduction erosion of the lower crust into the mantle source regions due to slab flattening in central Chile.

4.2.4 Lead Isotopes

Introduction

Pb isotopes in ore deposit studies can be used to determine

- the source(s) of Pb and other metals using sulfide minerals;
- the interaction between hydrothermal fluids and wall-rocks;
- the influence of basement rocks and tectonic setting on Pb sources in magmatic arcs;
- regional controls on ore deposition and fluid pathways; and
- model age(s) of ore formation. (Tosdal et al., 1999)

Pb isotope data are typically presented on two covariation diagrams, the thorogenic and uranogenic diagrams. The thorogenic diagram plots $^{208}Pb/^{204}Pb$ versus $^{206}Pb/^{204}Pb$, or the radiogenic daughter of thorium versus the radiogenic daughter of the most abundant uranium isotope (Tosdal et al., 1999). The uranogenic diagram plots $^{207}Pb/^{204}Pb$ versus $^{206}Pb/^{204}Pb$, or the radiogenic daughter nuclide of least abundant isotope of uranium versus the most abundant (Tosdal et al., 1999).

Doe and Zartman (1979) utilised the distinct U/Pb and Th/U characteristic of different parts of the evolving Earth to suggest that Pb isotopes can be traced from three idealised reservoirs, the mantle, lower crust and upper crust. These reservoirs mix in what is known as the orogene, where crustal deformation, magmatism, sedimentation and metamorphism occur (Tosdal et al., 1999). Model curves for each of these major sources are known and many Pb isotope studies discuss data with respect to these model reservoirs (Tosdal et al., 1999).

On the uranogenic diagram, measured Pb isotope compositions that plot at $^{207}Pb/^{204}Pb$ indicate that the Pb evolved in environments with U/Pb values higher than that of the average crust and vice versa for lower $^{207}Pb/^{204}Pb$ values (Tosdal et al., 1999). According to Doe and Zartman (1979), elevated $^{207}Pb/^{204}Pb$ values are indicative of crustal regions where radiogenic Pb evolved in Archaean rocks because of the relative abundance of ^{235}U at that time. In addition, the Pb was not reworked or diluted by material with lower $^{207}Pb/^{204}Pb$ values. Conversely, lower $^{207}Pb/^{204}Pb$ values indicate a lack of old radiogenic Pb, suggesting evolution of that Pb in an environment such as the mantle that was isolated from old radiogenic crust. This Pb could have been derived in recent times from mantle or oceanic crust and then incorporated into the rock or mineral analysed (Tosdal et al., 1999). Hence, variation in Pb isotope composition is mainly a function of the relative input of primitive versus old crustal Pb as recorded by $^{207}Pb/^{204}Pb$ (Tosdal et al., 1999).

On the thorogenic diagram, elevated $^{208}Pb/^{204}Pb$ (high Th/U) and low $^{206}Pb/^{204}Pb$ compositions indicate a lower crustal source. A good example of this composition is the basement in Peru (Kay et al., 1999; see below). Low $^{208}Pb/^{204}Pb$ and $^{206}Pb/^{204}Pb$ compositions in a given terrane indicate a

non-radiogenic, depleted source. In contrast, high $^{208}Pb/^{204}Pb$ and $^{206}Pb/^{204}Pb$ compositions will indicate a radiogenic, upper crustal source (Tosdal et al., 1999).

Magmas derived from the mantle have intrinsically low Pb concentrations (1-2 ppm) relative to feldspar-rich crustal rocks that typically have relatively high Pb concentrations (10-30 ppm; Tosdal et al., 1999). Due to this strong contrast in Pb concentration, the incorporation of small amounts of crustal Pb can significantly modify the composition of mantle-derived basaltic magmas (Tosdal et al., 1999). Hence, the Pb isotope composition of most granitic rocks reflects that of the crust that it has intruded, even if the magma had a significant mantle contribution to its formation (Farmer and DePaolo, 1983; Davidson, 1996; Tosdal et al, 1999). Tosdal et al. (1999) suggest that a similar line of reasoning can be applied to hydrothermal fluids when tracing Pb sources.

Previous work

Recent contributions to the Pb isotope database for central Chile have been made by Tilton (1979), Hildreth and Moorbath (1988), Puig (1988), Zentilli et al. (1988), Davidson et al. (1991), Kay and Abruzzi (1996), Tosdal (1996) and Kay et al. (1999). These datasets cover the CVZ and SVZ between 22° and 38°30'S, incorporating crust associated with the flat slab zone from 28° to 33°S (Fig. 4.6). The data generated in the studies by these authors are plotted in Figure 4.6. Locations are illustrated in Figure 1.6.

Pb isotope compositions in Miocene magmas from the Main Cordillera, Chilean flat slab or southern CVZ are characterised by more radiogenic, upper crustal-like signatures (Kay and Abruzzi, 1996). The Pb isotope data for flat slab Main Cordilleran arc and back-arc rocks falls within a relatively narrow range that overlaps the fields for recent southern (SVZ), south central (CVZ) and northern (NVZ) volcanic zone Andean lavas (Fig. 4.6; Kay and Abruzzi, 1996). Such Pb isotope ratios are commonly attributed to mixing of subducted sediments into the wedge above a subducting slab (e.g. Zartman and Haines, 1988). The alternative, as suggested by Kay and Abruzzi (1996), is for this Pb signature to be inherited largely from the underlying crust. However this origin is difficult to prove on the basis of Pb isotopes alone, as subducted sediment eroded from the continental margin would have a similar Pb signature to that of the underlying crust.

In contrast, the Precordilleran basement rocks and Precordilleran, metaluminous Miocene volcanic rocks of the central Chilean flat slab back arc region have the least radiogenic Pb isotope ratios among all central Andean magmatic rocks of Tertiary age and approach those of middle Proterozoic North American Precordilleran basement (Kay and Abruzzi, 1996; Kay et al., 1999). Kay and Abruzzi (1996) suggested that the low concentrations of Pb in the Precordilleran basement rocks are inherited from a depleted source region, such as the mantle. Furthermore, the Precordilleran basement rocks were an important contaminant for the Precordilleran and Sierras Pampeanas

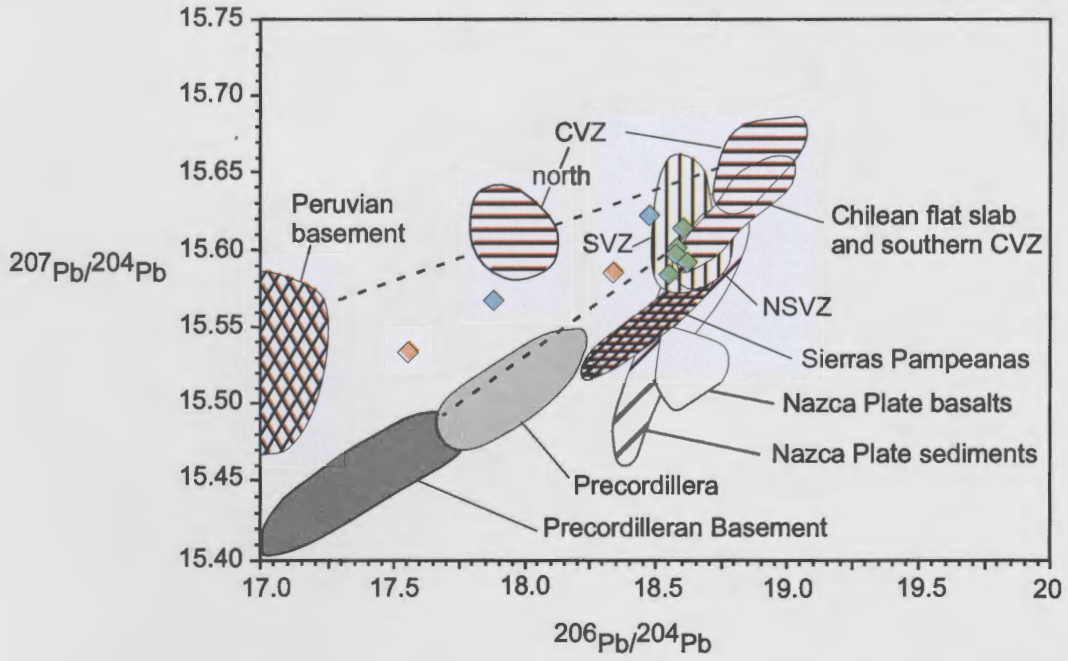

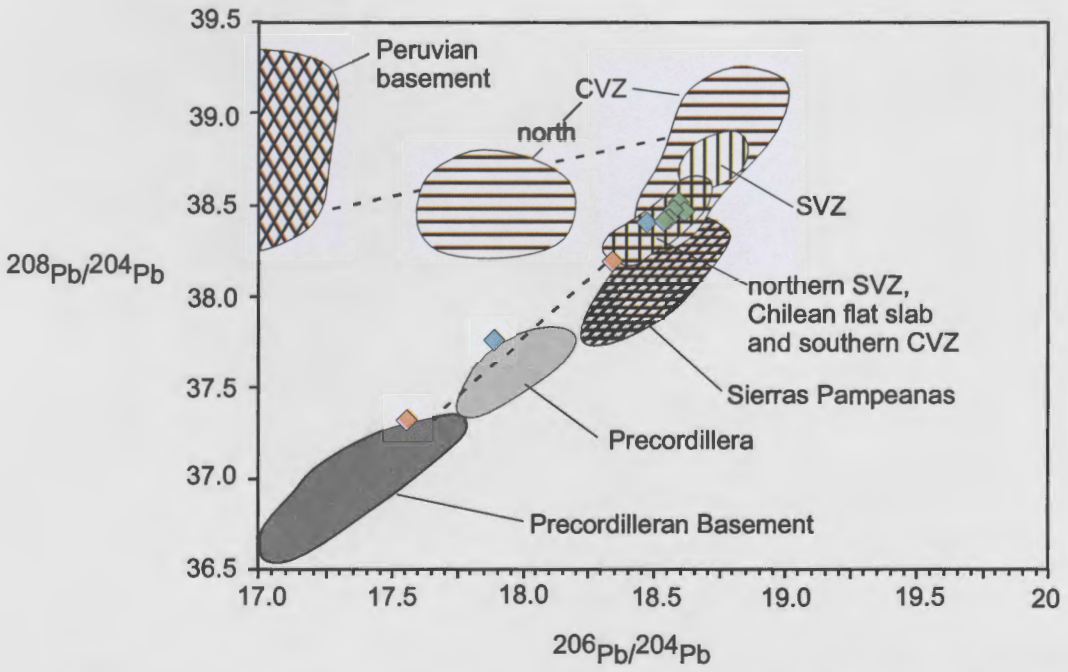

◆ Previous Pb compositions from sulfides collected in the Río Blanco-Los Bronces ore deposit

This study - Pb compositions

◆ Pre-sulfide anhydrite cement from mineralised Río Blanco Magmatic Breccia (7.3 Ma)

◆ Pre-sulfide anhydrite cement from mineralised Sur-Sur Tourmaline Breccia (5.2 Ma)

- - - - Mixing line (Kay and Ambruzzi, 1996)

Figure 4.6. Uranogenic and thorogenic diagrams showing Pb isotope compositions for regional volcanic rocks in central Chile, sulfides from the Río Blanco-Los Bronces ore deposit and anhydrite cement from the Río Blanco-Los Bronces ore deposit (this study). Regional rocks from Kay et al. (1999).

magmas, which can be modelled as mixtures between basement and Main Cordilleran magmas (Fig. 4.6). Kay and Abruzzi (1996) argued that ancient Pb signatures in these mantle components can be explained by storage in old continental lithosphere.

In an analogous situation, Barreiro (1984) modelled Pb isotope ratios in northern CVZ lavas as mixtures between Peruvian basement Pb and a subducted component with Pb similar to that in southern CVZ lavas (Fig. 4.6). In the Precordilleran case, the more radiogenic Pb should have a crustal component with Pb similar to that in the Main Cordilleran magmas (Fig. 4.6; Kay and Abruzzi, 1996).

Kay and Abruzzi (1996) suggested that crustal architecture may have also played a role in channelling the less radiogenic basement melts to the surface due to the inherent proximity of Precordilleran eruptive centres to fault zones. This may lend credence to a genetic relation between magmatism and the generally eastward-younging Precordilleran fault system described by Jordan et al. (1993). Tosdal (1995) was driving at the same issue by pointing out that the Eocene-Oligocene porphyry copper deposits on the West Fissure Fault have mantle Pb signals, whereas the adjacent Miocene Maricunga Belt porphyry copper deposits have crustally contaminated magmas in terms of their Pb isotope systematics.

It is widely recognised that the lack of accreted material at the trench along the margin of central Chile indicates that an enormous volume of sediments have been subducted beneath the entire arc segment (e.g. Stern, 1989). Hildreth and Moorbath (1988) plotted the Pb isotope data for Nazca Plate sediments and for Nazca Plate basalts in general to determine if the subducted component had an influence on arc magmas (Fig. 4.6). They concluded that although the water-rich slab initiates mantle melting to drive the system, the Pb isotope data suggest that the subducted sediments and basalt played no major role in influencing the isotopic composition of the arc magmas.

There are only a limited number of Pb isotope analyses of sulfides from the Río Blanco–Los Bronces ore deposit collected to date (Tilton, 1979; Puig, 1988; Zentilli et al., 1988; and Tosdal, 1996). They plot as a well-homogenised, closely spaced cluster within the field for the regional volcanic rocks of the SVZ within which the ore deposit is hosted (Table 4.4; Fig. 4.6).

Table 4.4. Previous Pb isotope compositions of sulfides from Río Blanco-Los Bronces.

Sample no.	Minerals	$^{206}Pb/^{204}Pb$	$^{207}Pb/^{204}Pb$	$^{208}Pb/^{204}Pb$
Rio Blanco-Los Bronces				
A-S-2^	Pyrite ± chalcopyrite	18.561	15.584	38.412
A-U-4B^	Cpy-pyrite-bornite	18.552	15.584	38.408
A-U-5^	Chalcopyrite + pyrite	18.585	15.602	38.478
A-O-6^	Pyrite-bornite	18.589	15.596	38.468
A-O-7^	Chalcopyrite	18.56	15.586	38.427
Z-AA-1‡	Galena	18.627	15.593	38.458
Disputada*	Galena	18.582	15.598	38.47
Disputada#	Pyrite	18.611	15.615	38.51
Los Piches*	Galena	18.582	15.598	

‡denotes sample from Zentilli et al. (1988)
*denotes samples from Puig (1988)
#denotes sample from Tilton (1979).
^ denotes samples from Tosdal (1996)

This study

Four samples of anhydrite were analysed for their Pb isotope compositions in this study. Two samples were anhydrite cement from the Río Blanco Magmatic Breccia and two were anhydrite cement from the Sur-Sur Tourmaline Breccia. In all four samples, textures indicate that the anhydrite had precipitated prior to sulfide deposition. Analytical results of anhydrite from Río Blanco-Los Bronces, are listed in Tables 4.5.

Table 4.5. Pb isotope compositions of pre-ore anhydrite for Río Blanco-Los Bronces generated in this study.

Sample no.	Mineral analysed	$^{206}Pb/^{204}Pb$	$^{207}Pb/^{204}Pb$	$^{208}Pb/^{204}Pb$
RB246h	Anhydrite	17.558	15.534	37.341
RB240b	Anhydrite	18.345	15.586	38.205
SS01BXT12	Anhydrite	17.892	15.567	37.774
SS60c	Anhydrite	18.479	15.623	38.412

The $^{207}Pb/^{204}Pb$ isotope compositions (uranogenic) for the anhydrite cement plot along a linear trend towards less radiogenic values, the least radiogenic value measured in the anhydrite cement from Río Blanco and the most radiogenic value measured from anhydrite cement in the Sur-Sur Tourmaline Breccia (Fig. 4.6). These Pb isotope compositions provide a broad spatial zonation among these samples from depleted Río Blanco anhydrite cement to more enriched values from Sur-Sur anhydrite cement (Fig. 4.6; Serrano et al., 1996). However, the trend for $^{207}Pb/^{204}Pb$ data does not extend to any other data field for regional rocks on the diagram, but lies between the trend for Precordilleran rocks in central Chile and the basement rocks from Peru (Fig. 4.6). In contrast, the $^{208}Pb/^{204}Pb$ isotope compositions (thorogenic) for anhydrite cement also form a linear trend, that extends from the Chilean flat slab field (+ Río Blanco sulfides) towards the least radiogenic field for the Precordilleran Basement and Precordillera (Fig. 4.6). Furthermore this linear trend

intersects the cluster defining Pb isotope compositions for sulfides in the Río Blanco-Los Bronces ore deposit.

An additional plot, produced by Doe and Zartman (1979) and referred to as the 'Plumbotectonics' model can be used to determine the source and possible mixing trends of fluids. Published sulfide Pb isotope compositions and new anhydrite Pb isotope compositions plotted on the diagram of Doe and Zartman (1979) in Figure 4.7 plot along the orogene growth curve. The sulfide data are tightly constrained; however the data from anhydrite straddle the curve towards less radiogenic values associated with older rocks (Fig. 4.7).

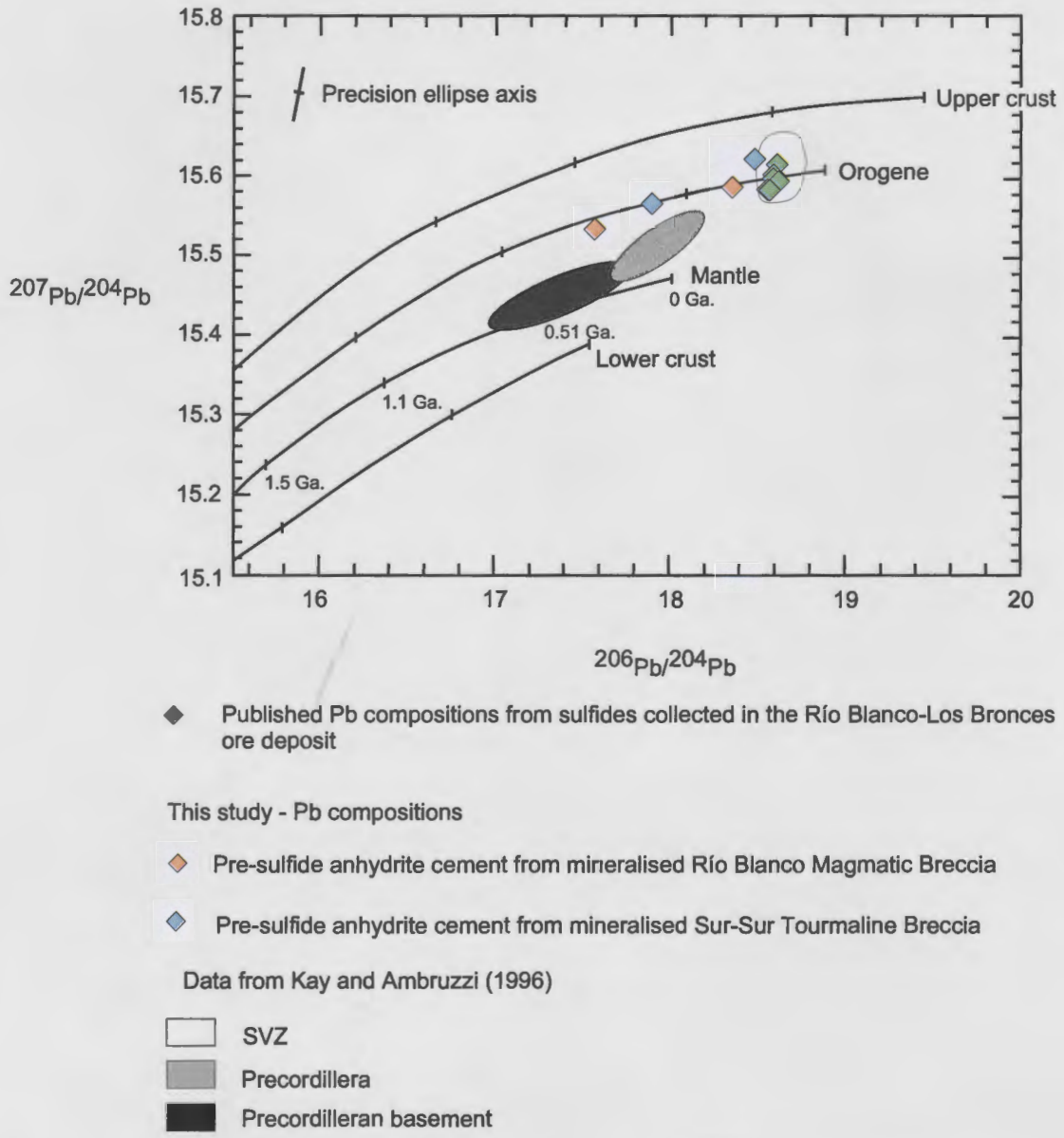

Figure 4.7. Published and new data from the Río Blanco-Los Bronces ore deposit plotted on the "Plumbotectonics" model of Doe and Zartman (1979) with four growth curves that define three Pb reservoirs: mantle, lower and upper crust, and a fourth growth curve, the orogene curve, that results from the mixing of the three Pb reservoirs.

4.2.5 Discussion

The $^{87}Sr/^{86}Sr$ and ε_{Nd} results summarised and presented here indicate a systematic trend with time from an originally depleted source similar to MORB toward increasing crustally contaminated magmas. The source of the rock material analysed in this study is a mixture of mantle, lower and upper crust, with the greatest proportions characterised by a crustal source. The fluids involved in ore genesis at Río Blanco-Los Bronces have a similar composition to the rocks that host them and to the late-stage intrusions that crosscut the breccias.

Anhydrite from the mineralised breccias at Río Blanco-Los Bronces (datasets of Skewes and Stern, 1996; and this study) provides evidence for mixed source material in the hydrothermal precipitates. Anhydrite from the Río Blanco Magmatic Breccia has the most depleted $^{87}Sr/^{86}Sr$ and the most enriched ε_{Nd} isotope composition, however anhydrite deposited in the Los Bronces Anhydrite Breccia (5 Ma) has the most enriched $^{87}Sr/^{86}Sr$ and the most depleted ε_{Nd} isotope composition (Fig. 4.5). Intermediate to these values is anhydrite from the Sur-Sur Tourmaline Breccia. These results indicate that the fluid responsible for anhydrite deposition associated with the potassic alteration zone had isotopic compositions similar to the host rocks (including Farellones Formation), and the fluid that deposited anhydrite in the Sur-Sur Tourmaline Breccia and anhydrite in the Los Bronces Anhydrite Breccia gradually mixed to a greater extent with late-stage magmas that were to intrude the mineralised system. The late stage magmas had sufficient residence times in the upper crust to evolve, Pb to enrichment in $^{87}Sr/^{86}Sr$ and depletion in ε_{Nd}. These late-stage magmas are inferred to be the likely heat source that formed the mineralised breccias.

Based on the Sr and Nd data, the Río Blanco ore body (Magmatic Breccia) is interpreted to have formed from fluids that either interacted with and/or were in part sourced from andesite (Los Pelambres and Farellones Formations) and granodiorite (GDRB) host rocks. These monzonite intrusions were most likely the dominant sources of mineralising fluid. Less radiogenic fluids were sourced from the post-mineral porphyries.

It is not clear why the pre-ore breccia cement minerals in Río Blanco and Sur-Sur have isotopic compositions that are enriched in $^{87}Sr/^{86}Sr$ and ε_{Nd} compared to the host rocks and the post-mineral porphyries. Previous studies have suggested that when basalts such as those erupted at mid ocean ridges are exposed to seawater, the $^{87}Sr/^{86}Sr$ isotope composition increases dramatically. In contrast, Nd isotopes are insensitive to seawater contamination resulting in constant $^{143}Nd/^{144}Nd$ composition relative to the dramatic increases in $^{87}Sr/^{86}Sr$ (Rollinson, 1993). This may imply that the fluid that precipitated anhydrite interacted with another, crustally sourced fluid or continental basement rocks along its path. One possibility is fluid interaction with the Jurassic sedimentary succession, an oxidised, marine package of clastic sediments, evaporites and volcanic rocks that crop out

to the east of the ore deposit and are inferred to underlie the volcanic pile (Section 1; Fig 1.2). One $^{87}Sr/^{86}Sr$ isotope analysis of gypsum from this sequence has been undertaken, giving a value of 0.70681 (Hollings et al., submitted). Interaction of hydrothermal fluids with this Jurassic package (e.g. Yeso Principal) may have shifted the isotope composition to more enriched $^{87}Sr/^{86}Sr$, while no change occurred in ε_{Nd}. The Sr and Nd dataset supports this hypothesis, but unfortunately no Pb isotope data are available for the Jurassic rocks.

Another possibility that could explain the anhydrite Sr and Nd data is by mineralising fluids interacting with the Cretaceous San José Formation, Cristo Redentor Formation and/or the base of the Los Pelambres Formation. Based on their major, trace and REE geochemistry, these units were erupted from a depleted source that coincided with a period of intra-arc and back-arc rifting of relatively thin crust in the early Cretaceous and ended in the earliest late Cretaceous (Table 1.1; Jordan et al., 1993; Tosdal et al., 1999). These three formations contain intercalated calcarenites and limestones deposited during the early to mid Cretaceous. Because andesitic volcanism occurred in a marine setting at this time, enrichment in $^{87}Sr/^{86}Sr$ by seawater could have occurred while ε_{Nd} values remained unchanged. The Sr and Nd isotope dataset support this possibility; however no Pb isotope data has been generated specifically on these formations (Figs. 4.5 and 4.6). The Sr and Nd data for the Los Pelambres Formation are consistent with the shift from enriched to depleted isotope compositions from the Jurassic to the Cretaceous as proposed by Nyström et al. (1993). The Los Pelambres Formation data in Figure 4.5 form a depleted end member for the region, and interaction of hydrothermal fluids with the rocks of the Los Pelambres Formation could have produced the measured Sr and Nd isotope compositions of anhydrite.

Less radiogenic signatures are also recorded in the Pb isotope data for the pre-ore anhydrite breccia cements. These signatures are not distinct from the sulfide Pb data, indicating that the fluid that precipitated the sulfides was isotopically distinct from the anhydrite-forming fluid. Figure 4.6 illustrates that the anhydrite from Río Blanco is the least radiogenic, whereas anhydrite from Sur-Sur is the most radiogenic. The line of best fit through the anhydrite data ends with intersection of the sulfide data, suggestive of mixing of two sources, with the sulfide Pb being the most radiogenic end-member.

The sensitivity of Pb with regards to external sources in the anhydrite is probably a function of the considerably smaller concentration contained in the mineral structure compared to the larger amounts of Pb contained in the sulfides. The Pb associated with the sulfide will have been in contact with the same Pb that contaminated the anhydrite, however the overall mass of Pb associated with the sulfide would have been too great to be modified by the external source. The fluid that deposited anhydrite may have had comparably low concentrations of Pb and therefore may have been easily modified by interaction with the depleted source.

The observed Pb isotopic compositions from the regional dataset and the data for Río Blanco-Los Bronces are consistent with crustal contamination of a depleted mantle source. The Río Blanco-Los Bronces deposit is located in the upper part of extremely thickened crust (up to 65 km; Kay et al., 1999). One explanation to account for the measured isotopic compositions is that the processes that caused crustal thickening may also have caused mixing of Pb from less radiogenic upper crust and more radiogenic lower crust (Kay and Abruzzi, 1996), consistent with the array of Pb isotope data from Río Blanco-Los Bronces.

The notion that subducted sediments and basalts affect the isotopic composition of arc magmas is not consistent with the isotopic compositions shown in Figure 4.6. The Pb isotope compositions of Nazca Plate sediments and basalts plot in a field distinct from the ore fluids, the Precordilleran basement and the Precordilleran rocks. If the isotopic compositions of the arc magmas are not reflecting simple crustal contamination of a depleted mantle source, then an alternative model is required to explain the observed isotope compositions in central Chile and the Río Blanco-Los Bronces ore deposit. It is possible that continental crust (sediments?) was incorporated into the mantle wedge from the fore-arc and base of the crust. In this scenario, enriched crustal rocks are delaminated and incorporated into the mantle and re-melted as the crust thickens, locally changing the mantle isotope composition to more radiogenic signatures.

Hildreth and Moorbath (1988) demonstrated a northward gradient towards thicker crust from 38.5° to 33°S with a parallel change to more enriched isotopic compositions. Similarly, Kay et al. (1999) concluded that thicker crust in the flat slab zone, due to the subduction of the Juan Fernandez Ridge, has resulted in the progression to more radiogenic isotope compositions. Furthermore, the locus of crustal thickening in the Chilean flat slab region has migrated southward due to the oblique nature of ridge subduction, resulting in less radiogenic crust in the CVZ compared to the southern CVZ. This suggests that crustal thickening occurred earlier in the northern flat slab zone compared to the south. The effect of crustal thickening results in the wholesale break down of amphibole to garnet potentially releasing large quantities of dilute aqueous fluid (Kay et al., 1999) that may have been the early, oxidised fluid that precipitated the least radiogenic anhydrite at Río Blanco.

The Río Blanco-Los Bronces ore deposit occurs within the most recently thickened crust at around 33°S (Hildreth and Moorbath, 1988; Kay et al., 1999). The observed isotopic compositions from Río Blanco-Los Bronces reflect a combination of both rocks that formed within relatively thin crust (less radiogenic host rocks) and late-stage magmas that formed in thickened crust (more radiogenic signatures). The Los Pelambres Formation began erupting over the San José and Cristo Redentor Formations through relatively thin oceanic crust in the Tertiary resulting in a relatively less radiogenic isotopic signature (Fig. 4.5). Through time, continued eruption of this sequence

and increased shortening thickened the crust of central Chile significantly. When the tectonics regime switched to shortening at the beginning of the Miocene, the crust of central Chile continued to thicken and uplift substantially until the emplacement and crystallisation of the San Francisco Batholith, host to Río Blanco-Los Bronces ore deposit. Continued melting in the lower crust drove magmas up through the pre-existing, depleted crust, eventually incorporating a combination of depleted and crustal enriched radiogenic isotope signatures.

To account for the observed isotope compositions at Río Blanco-Los Bronces, the fluids that formed the early anhydrite cement in the mineralised breccias carried depleted signatures, probably owing to fluid interaction with rocks of the Los Pelambres Formation at deeper levels in the crust. The early anhydrite-forming fluid may have been a separate entity migrating ahead of, and driven upwards by magma from deep levels in the crust. As this early fluid reached the brittle crust it underwent isotopic exchange, becoming more crustal and radiogenic probably through interaction with the relatively more radiogenic and evolved late-stage magmas and/or their brines. The brine that produced copper mineralisation was homogenised isotopically in the crustally contaminated magma. At high levels in the crust, brine eventually exsolved from the magmas and mineralised the breccia matrices. After brine exsolution, additional magmas were emplaced at depth. They had prolonged residence times (reflected by more radiogenic isotope signatures) before intruding and crosscutting the copper ore and crystallising as a succession of post-mineral porphyries.

4.3 Fluid Inclusions

4.3.1 Introduction

This section presents the results of fluid inclusion microthermometry of samples from the Río Blanco and Sur-Sur sectors. The aim of this investigation is to use fluid inclusion data from the various paragenetic stages to determine if there were any temperature and/or salinity zonation in the mineralised system. The microthermometric data are used to evaluate any temporal and spatial evolution of mineralising fluids responsible for copper mineralisation, and to assess their likely source(s).

4.3.2 Previous work

Previous fluid inclusion investigations have focussed on breccia cements from the Río Blanco, Sur-Sur and La Americana sectors (Kusakabe et al., 1990; Vargas et al. 1999) and from Los Bronces (Holmgren et al., 1988; Skewes and Holmgren 1993).

Kusakabe et al. (1990) analysed fluid inclusions from what they described as the potassic to propylitic transitional alteration zone; and from the potassic zone with quartz-sericite alteration in the Río Blanco sector (Fig. 4.8). They documented homogenisation temperatures between 430° and 320°C at Río Blanco. No differences in temperatures were found for fluids associated with the different alteration assemblages. Kusakabe et al. (1990) reported that the inclusions were so poorly transparent that only a few freezing point determinations were carried out on relatively large inclusions, and were not documented in their results.

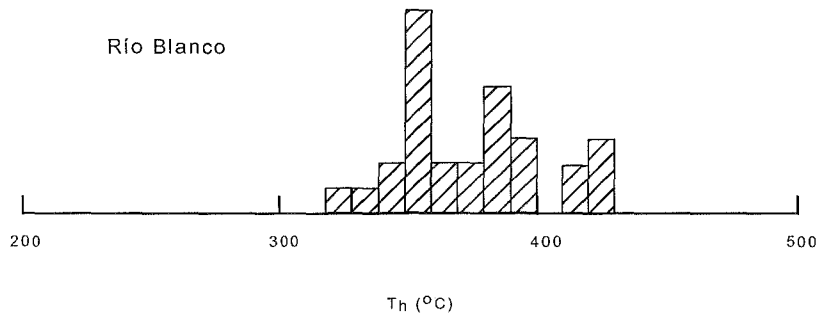

Figure 4.8. Histogram showing homogenisation temperatures of fluid inclusions in quartz from Río Blanco. Adapted from Kusakabe et al. (1990).

Vargas et al. (1999) reported on analytical results from nineteen fluid inclusion samples, which were selected to span a range in elevation and copper grades in the Sur-Sur and La Americana sectors (Fig. 4.9). Hypersaline, liquid and vapour-rich fluid inclusions were found to coexist in the samples, but proportions of the individual types varied widely. They identified liquid CO_2-bearing inclusions in one sample adjacent to hypersaline liquid-rich and vapour-rich fluid inclusions (Vargas et al., 1999). Many of their hypersaline and liquid-rich fluid inclusions had first melting (eutectic) temperatures below -35°C. This was interpreted to indicate probable Ca, Mg, or Fe as well as Na and K chloride in solution (Vargas et al., 1999).

Fluid inclusions from La Americana and Sur-Sur were found by Vargas et al. (1999) to have similar salinities and homogenisation temperatures (Fig. 4.9). The hypersaline inclusions contain 30 to 55 wt.% NaCl equivalent and were trapped at temperatures of 225° to 500°C. The liquid-rich fluid inclusions range from low salinity to nearly 30 wt.% NaCl equivalent, trapped at temperatures of 150° to nearly 450°C (Vargas et al., 1999).

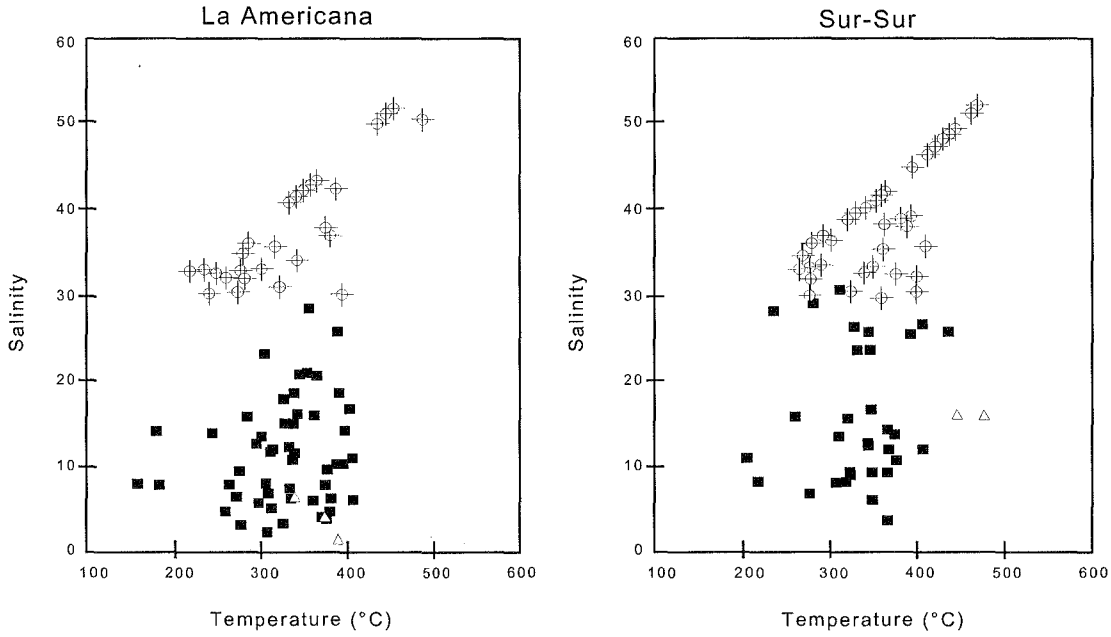

Figure 4.9. Data from Vargas et al. (1999) showing homogenisation temperatures versus salinities (wt.% NaCl equivalent) of fluid inclusions from quartz cement in Tourmaline Breccia at La Americana and Sur-Sur. Diamonds represent hypersaline fluid inclusions, black filled squares represent liquid-rich two-phase fluid inclusions and triangles represent low-density, vapour-rich fluid inclusions. Seventeen of these fluid inclusions are from quartz cement and two samples are from veinlets cutting the breccia cement. Modified from Vargas et al. (1999).

Vargas et al. (1999) recognised a vertical zonation of fluid inclusion types in the La Americana breccia. Hypersaline inclusions were observed only at deep elevations and diminished in abundance upward, being absent in many samples with low copper grades (Vargas et al., 1999). Hypersaline inclusions are also more abundant where copper grade is high in Sur-Sur, however the vertical zonation observed in La Americana is much less apparent. Vargas et al. (1999) speculated that this is because the breccia in Sur-Sur does not extend to such high elevations and is mostly higher grade than La Americana.

Skewes (1996) undertook a study of Tourmaline Breccia cement in the La Americana sector. Coexisting liquid and vapour-rich fluid inclusions are common at high altitudes in the La Americana sector, suggesting that boiling occurred during breccia formation. However, there is no relationship between vapour-rich and liquid-rich inclusions at depth in La Americana, which Skewes (1996) interpreted to indicate that no boiling occurred at that location. Skewes (1996) also recognised that hypersaline inclusions at La Americana have a large range of dissolution temperatures. Furthermore, in some fluid inclusions, salt dissolution occurred before disappearance of the vapour bubble, but in others salt dissolution after disappearance of the vapour bubble upon heating. Skewes (1996) suggests that these characteristics reflect large fluctuations in the pressure during entrapment of the fluid. Fournier (1999) maintains that decompression processes that induce the massive formation of steam would probably be accompanied by mineral deposition in veins and cavities and the

formation of primary and secondary fluid inclusions. In this situation, single fluid inclusions would be expected to exhibit widely ranging salinities in association with abundant vapour-rich fluid inclusions.

Holmgren et al. (1988) reported cogenetic hypersaline and vapour-rich fluid inclusions in quartz-cemented breccia from Los Bronces. They suggested that this represents phase separation (boiling) of the mineralising fluid and possible mixing of meteoric fluids with magmatic-hydrothermal fluids (Holmgren et al., 1988). They also describe liquid-rich fluid inclusions that appear to be in textural equilibrium with the previous two types petrographically but are not in thermal equilibrium based on their divergent homogenisation temperatures (Holmgren et al., 1988).

Hypersaline fluid inclusions in quartz collected from the breccia cement at Los Bronces have homogenisation temperatures between 245° and 600°C and salinities between 34 and 56 wt.% NaCl equivalent (Holmgren et al., 1988). Vapour-rich fluid inclusions have homogenisation temperatures between 364° and 534°C with a salinity of 7.4 wt.% NaCl equivalent (Holmgren et al., 1988). Liquid-rich fluid inclusions have homogenisation temperatures between 240° and 380°C and salinities between 3 and 21 wt.% NaCl equivalent (Holmgren et al., 1988). The large range of salinities in the breccia cement at Los Bronces have been interpreted to represent mixing of high salinity brine with a cooler, dilute fluid (e.g. meteoric water?).

Pressures of trapping calculated by Vargas et al. (1999) for the Sur-Sur and La Americana sectors were between 85 and 135 bars and imply a depth of formation (and erosion) between 1000 and 1800 m at hydrostatic pressure or between 320 and 510 m at lithostatic pressure. These data correlate well to the inferred depths of formation from fluid inclusion data for the Los Bronces breccias between 425 and 1113 m (hydrostatic) or 0 to 382 m (lithostatic; Holmgren et al., 1988).

4.3.3 This study

Fluid inclusion microthermometry was undertaken on samples from several paragenetic stages in the Río Blanco and Sur-Sur sectors. Samples were collected from section XC-130RB in Río Blanco, section XC-275 in Don Luis and section XC-50SS in Sur-Sur. In most samples, the host medium for the fluid inclusions is quartz. However, a small number of analyses were also undertaken on fluid inclusions in anhydrite and tourmaline.

This fluid inclusion investigation aims to provide the following information;

- Temperatures, compositions and salinities of the hydrothermal fluids
- Type and frequency of fluid inclusions present with respect to copper grade and depth.
- Physicochemical conditions of the hydrothermal fluids (e.g. phase separation)

- Changes in fluid compositions in time and/or space (e.g. mixing arrays)
- Pressure/depth estimates
- Infer fluid source(s)

4.3.4 Methods

Forty-six doubly polished fluid inclusion thick sections were prepared from samples collected from Río Blanco (includes Don Luis sector; n = 24) and Sur-Sur (n = 22). Petrographic study of fluid inclusion populations resulted in data acquisition regarding;

- The relative abundance of each fluid inclusion type
- Daughter mineral types and abundance
- Relative size of fluid inclusions; and
- Identification of mineral assemblages proximal to quartz.

Glue used to bind the rock wafers to glass slides was dissolved by immersion in acetone over a twenty-four hour period. Heating and freezing experiments were then carried out on fluid inclusions wafers.

Microthermometric measurements were performed at the University of Tasmania using a Linkam MDS600 heating/freezing stage manufactured by Linkam Scientific Instruments Ltd. The Linkam stage has an upper temperature limit of 600°C and was calibrated using synthetic fluid inclusions supplied by Synflinc Inc. The precision of measured temperatures is ±1.0°C for heating and ±0.3°C for freezing (Rae, 2002).

Salinities were calculated as weight percent NaCl equivalent or (in the case of hypersaline fluid inclusions with halite and sylvite daughter crystals) NaCl + KCl equivalent weight percent. The salinity of halite-undersaturated inclusions was calculated from measured freezing point depression temperatures and applying a linear least squares regression method (Potter et al., 1978). The salinity of halite-saturated inclusions was calculated from the halite dissolution temperature using the SALTY algorithm of Bodnar et al. (1989).

4.3.5 Fluid Inclusion Types

Based on petrographic observations made at room temperature, the following six fluid inclusion types were recognised (Figs. 4.10, 4.11 and 4.12);

Type ia: two-phase (liquid + vapour), liquid-rich fluid inclusions that homogenise to a liquid (Figs. 4.10 and 4.11c).

Type ib: three-phase (liquid + vapour + non-ionic solid), liquid-rich fluid inclusions that contain an unknown insoluble opaque mineral. These inclusions homogenise to a liquid (Figs. 4.10 and 4.11d).

Type iia: three-phase hypersaline inclusions with a halite daughter salt and vapour bubble in a liquid. These inclusions homogenise either by vapour disappearance or halite dissolution (Figs. 4.10 and 4.11e).

Type iib: three-phase hypersaline inclusions with a sylvite daughter salt and vapour bubble in a liquid (Figs. 4.10 and 4.11f).

Type iic: multi-phase (at least four phases) hypersaline inclusions with a variety of daughter minerals present in addition to vapour and liquid. These may include halite, sylvite, anhydrite, hematite and/or opaque (Figs. 4.10 and 4.12a).

Type iii: two-phase (vapour + liquid) vapour-rich inclusions that either homogenise to vapour or decrepitate before homogenisation (Figs. 4.10 and 4.12b).

Only secondary fluid inclusions were observed. They range in size up to 40μm but those analysed were typically between 10 and 20μm. The criteria used for distinguishing primary and secondary fluid inclusions are from Roedder (1984). Specifically, primary fluid inclusions are those in crystal growth zones, as isolated, solitary inclusions or those with negative crystal shapes. Secondary fluid inclusions occur along planes or healed fractures, and have lower homogenisation temperatures than adjacent primary fluid inclusions. Unequivocal evidence of primary origins for fluid inclusions have not been observed in the samples analysed due in part to the high abundance of fluid inclusions in any given sample. Consequently, the data in this study has been obtained on secondary fluid inclusions.

Inclusion type	Phases at 25°C	Homogenisation behaviour
Type i		
a 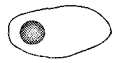	Liquid > vapour	Vapour disappears
b 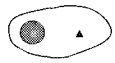	Liquid > vapour + opaque	Vapour disappears, solid phase does not dissolve on heating
Type ii		
a 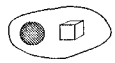	Liquid-vapour-halite	Vapour + halite disappear
b 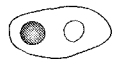	Liquid-vapour-sylvite	Vapour + sylvite disappear
c 	Liquid-vapour-halite-sylvite hematite-anhydrite-opaque	Vapour + halite + sylvite + anhydrite disappear, non-soluble solids remain upon heating
Type iii		
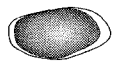	Vapour > liquid	Liquid disappears

Figure 4.10. Summary of fluid inclusion types, phase(s) at 25°C and homogenisation behaviour.

4.3.6 Fluid Inclusion Petrography

Fluid Inclusions in Quartz

Hydrothermal quartz crystals that occur in the breccia cements and in veins host most of the workable fluid inclusions at Río Blanco and Sur-Sur. Quartz is preserved in variable proportions through all paragenetic stages, and therefore provides the most complete record of fluid evolution in the ore deposit. The fluid inclusions in quartz are either preserved as isolated inclusions or along healed fractures (Fig. 4.11a, b).

Type ia are the most common fluid inclusion type observed in most of the paragenetic stages analysed, except for the Sur-Sur Tourmaline Breccia cement. Type ia inclusions are preserved most commonly along secondary trails or healed fractures but also occur in many samples as isolated secondary inclusions (Fig. 4.11c). Type ia vary in size from small (0.5-10μm) inclusions hosted within secondary trails to large (5-40μm) isolated inclusions that occur randomly distributed in the quartz. Type ib inclusions are less common, with only minor quantities present in all paragenetic stages (Fig. 4.11d).

Of the three sub types of hypersaline fluid inclusions, type iia are the most common in most paragenetic stages. Furthermore, they are consistently the most abundant type ii fluid inclusion

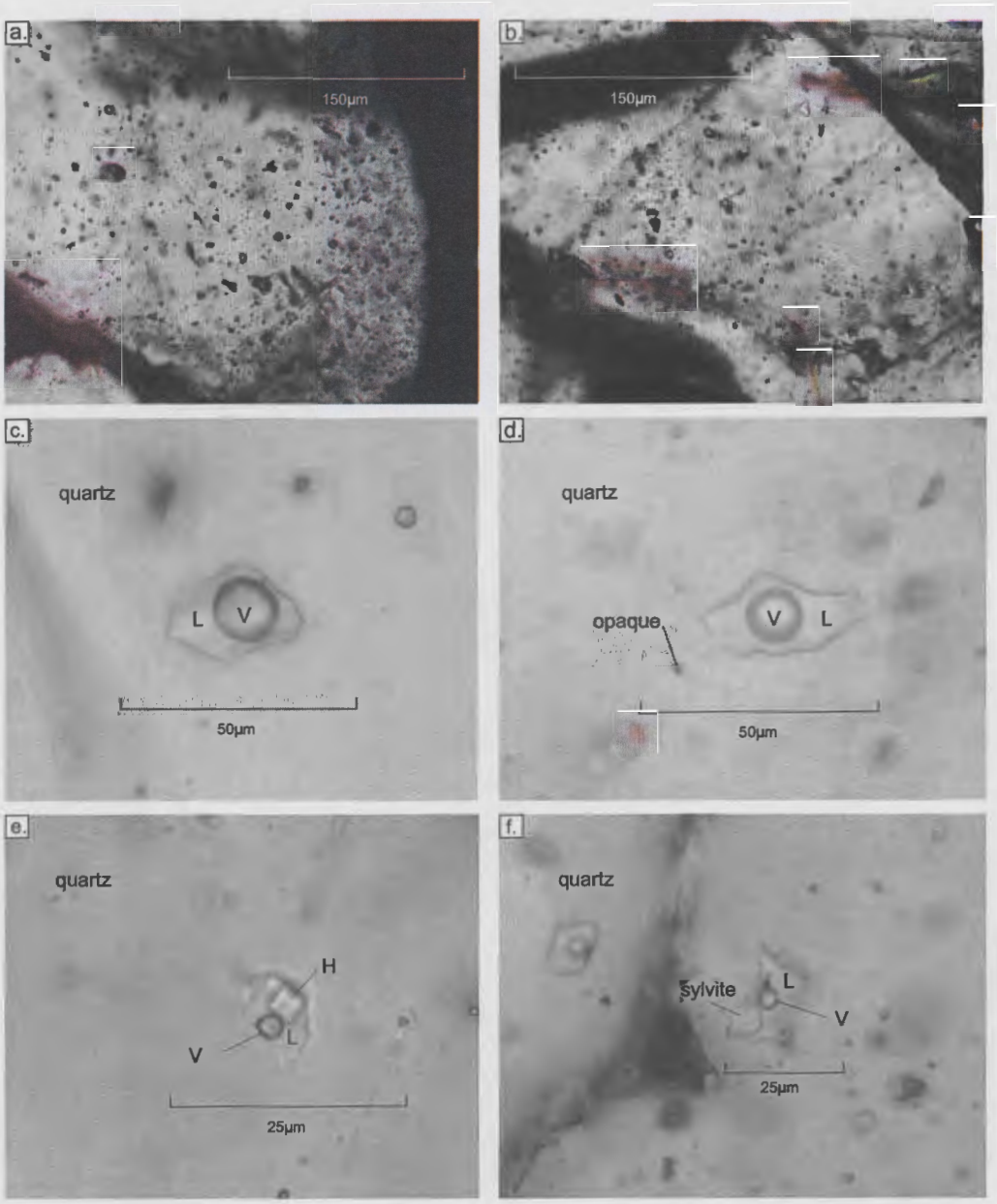

Figure 4.11. Fluid inclusion photomicrographs:
a. typical quartz grain containing abundant fluid inclusions, making unambiguous identification of primary fluid inclusions impossible;
b. typical quartz grain containing secondary fluid inclusions along healed fractures;
c. type ia - liquid-rich fluid inclusion in quartz host;
d. type ib - liquid-rich fluid inclusion with opaque in quartz host;
e. type iia - halite and vapour hypersaline fluid inclusion in quartz host; and
f. type iib - sylvite and vapour hypersaline fluid inclusion in quartz host.
V = vapour, L = Liquid and H = halite.

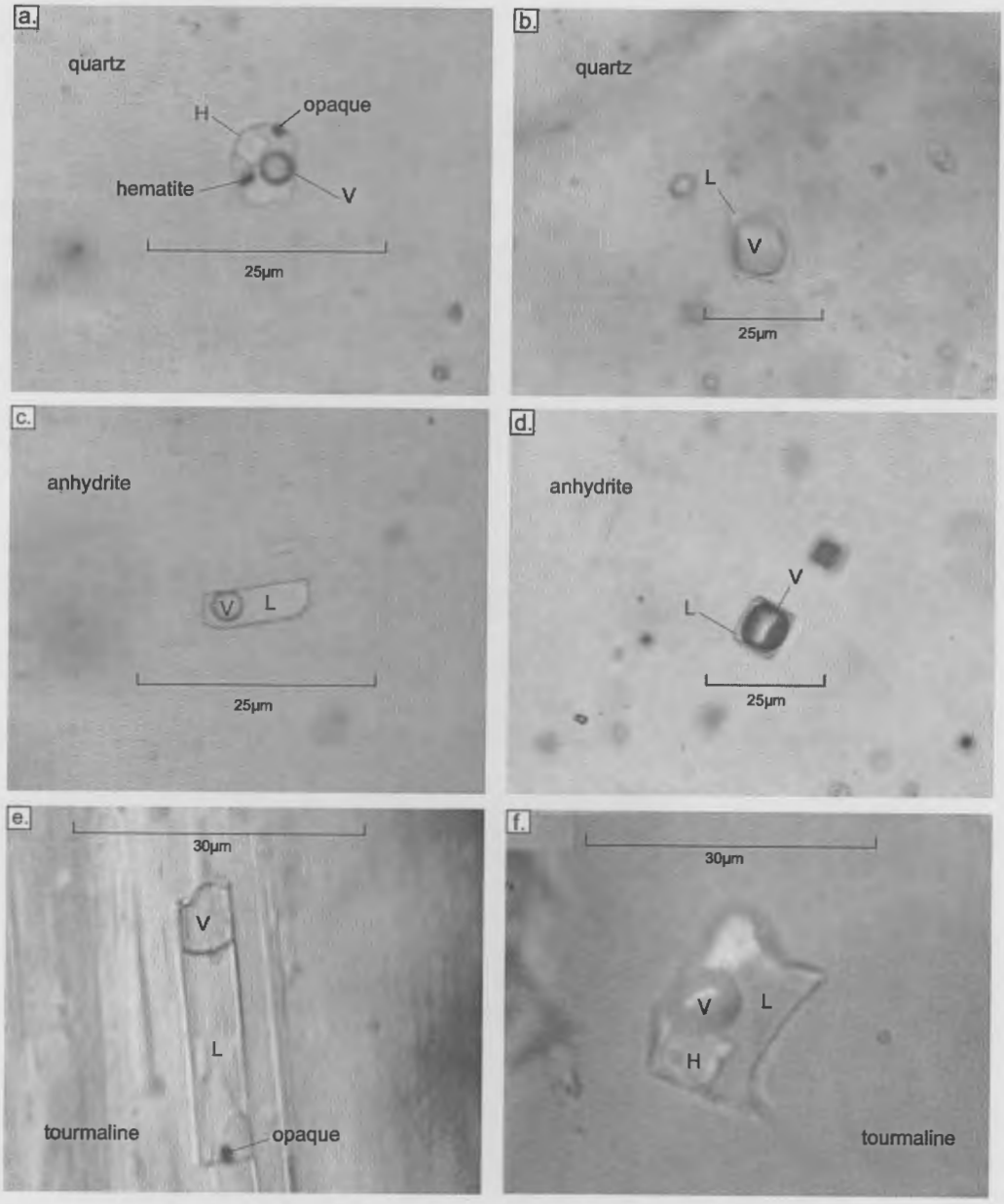

Figure 4.12. Fluid inclusion photomicrographs:
a. type iic - halite, hematite, opaque and vapour polyphase hypersaline inclusions in quartz host;
b. type iii - vapour-rich inclusions in quartz host;
c. type ia - liquid-rich inclusion in anhydrite host;
d. type iii - vapour-rich inclusion in anhydrite host;
e. type ib - liquid-rich inclusion with an opaque in tourmaline host; and
f. type iia - halite and vapour hypersaline inclusion in tourmaline host.
V = vapour, L = liquid and H = halite.

type observed in quartz from the breccia cements. Type iia hypersaline inclusions occur both in healed fractures and as isolated, secondary inclusions (Fig. 4.11e). Type iia inclusions vary in size between 5 and 30μm.

Type iib sylvite-bearing fluid inclusions are significantly less abundant than type iia. It can be difficult to clearly identify the salt crystals unambiguously in small inclusions. Where salt is consistently irregular in shape and is not birefringent, they have been identified as sylvite (Fig. 4.11f).

Type iic inclusions occur mostly within quartz in both stage 2 veins and in stage 3 mineralised breccia cement. Type iic are the most common hypersaline fluid inclusion type in the Río Blanco stage 3 Magmatic Breccia quartz cement. Type iic inclusions contain a variety of daughter minerals, including any of halite, sylvite, unknown opaque minerals, rare hematite or anhydrite (Fig. 4.12a). Hematite is easily recognisable as a blood-red coloured daughter mineral. Anhydrite is distinguished by its low birefringence and elongate shape. Type iic inclusions most commonly occur in healed fractures, but have also been observed as isolated inclusions in quartz. The inclusions range in size from <10 to 30μm.

Type iii vapour-rich fluid inclusions are the second most abundant type preserved in all paragenetic stages, except in the Sur-Sur stage 3 breccia cement and Sur-Sur stage 8 veins where they are the most abundant. Type iii inclusions occur most commonly in healed fractures but also as isolated secondary inclusions (Fig. 4.12d). In rare cases, type iii inclusions contain an opaque daughter mineral. The inclusions vary in size between 0.5 and 50μm, with an average diameter of 15μm.

Fluid inclusions in anhydrite

Anhydrite crystals observed in this study contain fluid inclusion types ia and iii. These inclusions commonly have a cubic shape and occur in secondary trails or along cleavage planes. They generally have small (5-15μm) diameters (Fig 4.12c, d). Some type ia and iii inclusions contain opaque daughter minerals. Hematite has also been observed as separate solid inclusions in trails that contain type iii fluid inclusions.

Fluid inclusions in tourmaline

Tourmaline crystals in the Sur-Sur Tourmaline Breccia cement host rare type ia, ib and iic fluid inclusions along their cleavage planes. The inclusions have elongate shapes, trapped along negative crystal faces (Fig. 4.12e). Most of the fluid inclusions are type i and were too small to analyse (<5μm). Hypersaline fluid inclusions were recognised in two samples, but analyses were only possible on one of these samples. Daughter minerals in these type iic inclusions include halite, hematite and opaques (Fig. 4.12e, f).

4.3.7 Fluid inclusion microthermometry

Fluid inclusion microthermometric analyses were performed on 739 individual, paragenetically constrained fluid inclusions from the Río Blanco (n = 299) and Sur-Sur (n = 440) sectors of the ore deposit. Samples were chosen to provide maximum spatial coverage within sections XC-130RB, XC-275 and XC-50SS. The majority of the data come from quartz in the Río Blanco Magmatic Breccia and the Sur-Sur Tourmaline Breccia.

Río Blanco sector

A total of twenty-four samples from Río Blanco and Don Luis sectors were used in fluid inclusion microthermometric experiments. Of these twenty-four samples, fluid inclusions were analysed from quartz in stage 2 quartz veins, stage 3 Magmatic Breccia quartz cement, stage 4 Feldspar Porphyry, stage 6 Quartz Monzonite Porphyry, stage 7 quartz-molybdenite veins, stage 8 quartz-chalcopyrite veins, and a stage 9 D vein. Fluid inclusions in the porphyries were contained within quartz phenocrysts.

Stage 2: Pre-breccia quartz veins

Stage 2 veins were only observed and collected at depth in the Don Luis sector (section XC-275) between 2743 and 2943 m elevation. Microthermometric analyses were performed on thirty-one fluid inclusions from two samples of quartz veins with biotite alteration halos that occurred in clasts of the Magmatic Breccia. The following types were analysed: type ia (n = 12), type ib (n = 3), type iia (n = 11), type iic (n = 3) and type iii (n = 1; Fig. 4.13a-d). Vapour homogenisation temperatures (T_hV), liquid homogenisation temperatures (T_hL), salt dissolution temperatures (T_hD), salinities (wt.% NaCl equivalent), freezing temperatures (T_f), temperatures of first melting (T_e) and temperatures of final melting (T_m) are illustrated on Table 4.6, Figure 4.13a-d and listed in Appendix E1.

Type i, liquid-rich fluid inclusions are the largest and most abundant, occurring together with type ii hypersaline inclusions and rare type iii inclusions. Daughter minerals in type ii fluid inclusions include halite, opaque, hematite and anhydrite. The fluid inclusions are secondary occurring either as isolated inclusions or along healed fractures. Fluid inclusions of unambiguous primary origin were not found.

T_hV of types i and ii fluid inclusions are low to moderate with a range from 156° to 405°C (Table 4.6). T_hD of salts had a similar range to the vapours, extending up to 500°C (Fig. 4.13a). Two groups of data are apparent on a plot of T_h versus salinity for stage 2 veins. One group is defined by

Table 4.6. Minimum to maximum homogenisation temperatures of vapour (T_hV), liquid (T_hL) and salts (T_hD) in °C, salinities (wt.% NaCl equivalent), freezing temperatures (T_f), temperature of first ice melting (Te) and temperatures of final ice melting (T_m) for the different paragenetic stages at Río Blanco and Sur-Sur.

Paragenetic stage	Host mineral	T_hV		T_hL	T_hD_{halite}	$T_hD_{sylvite}$	Salinity (NaCl equiv. wt %)			T_f		T_e		T_m	
		type i	type ii	type iii	type ii	type ii	type i	type ii	type iii	type i	type iii	type i	type iii	type i	type iii
Rio Blanco															
Stage 2	quartz	213-405	156-373	304	210-500		1-22	32-56	8.3	-69 to -42	-38			-19 to -1	-5
Stage 3	quartz	191-534	227-600	328-600	176->600	222	0-23	31-69	0-23	-89 to -28	-95 to -36	-46 to -19	-70 to -22	-25 to 21	-55 to 11
Stage 4	quartz	191-389	256-364		348-443		3-11	41-50		-57 to -36		-38 to -21		-8 to -1	
Stage 6	quartz	422-498	328-428	459	261-352	248	3-21	35-42	9	-72 to -53	-54	-32 to -23	-33	-18 to 2	-6
Stage 7	quartz	281-429	268-369	389-473	208-343		0-22	32-41	0-15	-60 to -34	-58 to -40	-52 to -14	-28 to -21	-19 to 0	-11 to 1
Stage 8	quartz	266-435	246-459	373-500	155-383		0-23	30-45	1-10	-84 to -31	-69 to -27	-50 to -25		-23 to 2	-7 to 7
Stage 9	quartz	185-348	160	418	211		4-11	32	1	-52 to -36	-35	-39 to -11		-7 to -2	-1
Sur-Sur															
Stage 2	quartz	191-376	153-311	431-522	183-437		1-23	23-50	7-23	-75 to -34	-62 to -37	-45 to -25		-49 to 2	-20 to -4
Stage 3	quartz	195-446	135->600	353->600	131->600	180-194	0-23	25-69	0-59	-89 to -33	-75 to -35	-59 to 3	-49 to -24	-25 to 20	-23 to 1
Stage 3	tourmaline	141-445	148-403		217-304		1-23	33-38		-64 to -46		-62 to -31		-23 to 13	
Stage 8	quartz	236-459	215-263	393-407	170-484		0-23	31-56	3-10	-58 to -36	-37	-39 to -16		-23 to 19	-7 to 2

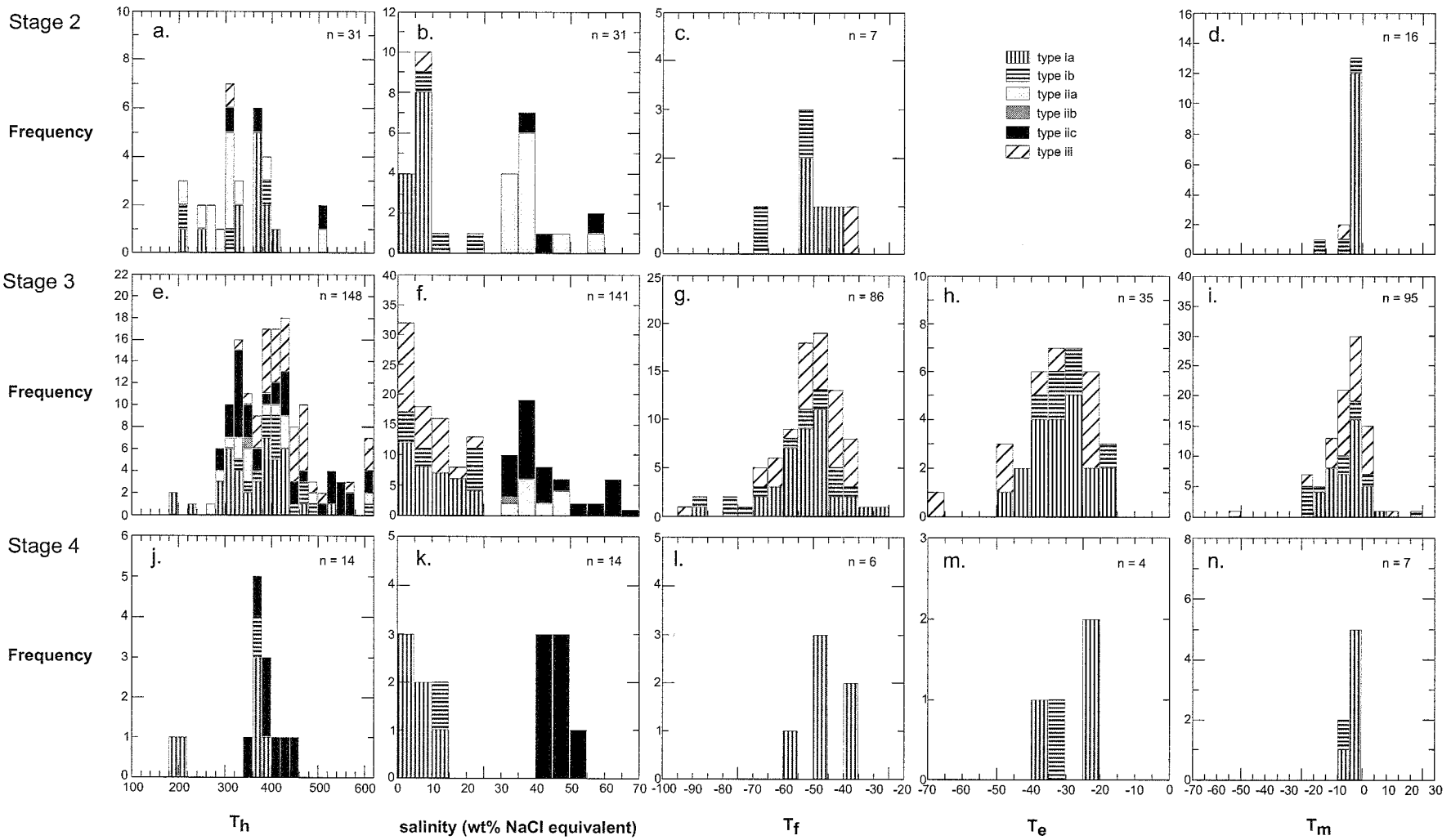

Figure 4.13. Frequency histograms of homogenisation temperatures, salinities (wt.% NaCl equivalent), freezing temperatures (T_f), eutectic temperatures (T_e) and final melting temperatures (T_m) for stages 2 (a-d), 3 (e-i) and 4 (j-n) in the Río Blanco mineralised system.

type i and iii fluid inclusions, and the other by type ii hypersaline fluid inclusions (Figs. 4.13b and 4.14a). The clusters are distinct in terms of their salinities. Most of the type i inclusions have salinities below 10 wt.% NaCl equivalent. Type ii inclusions have salinities greater than 30 wt.% NaCl equivalent. Both clusters have the same range of homogenisation temperatures (Fig. 4.13a). T_f for type i fluid inclusions were as low as -69°C and the T_m most commonly between -10° and -1°C (Table 4.6; Figs. 4.13c, d)

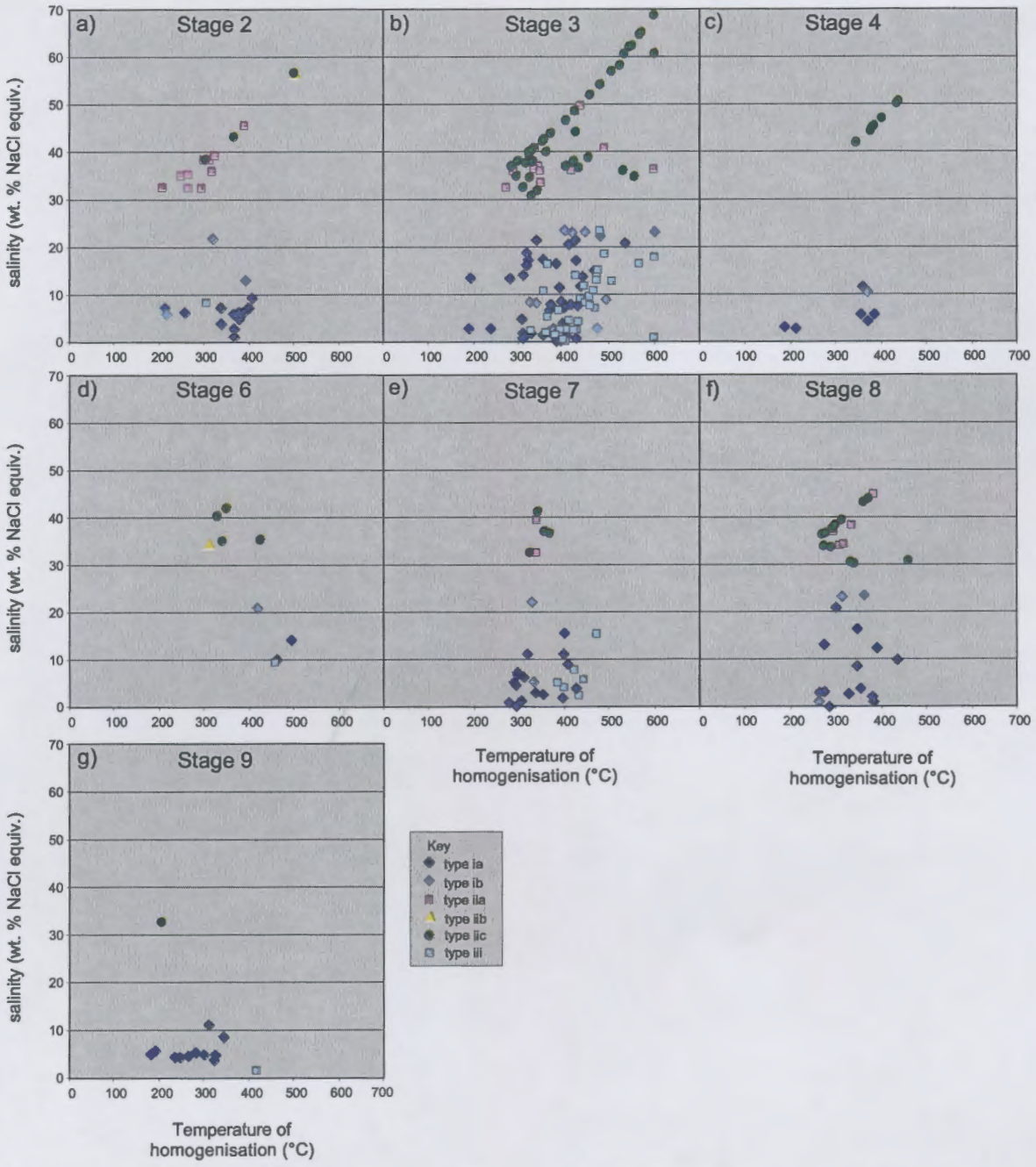

Figure 4.14. Homogenisation temperatures versus salinity for paragenetically constrained samples collected in the Río Blanco sector: a. stage 2; b. stage 3; c. stage 4; d. stage 5; e. stage 7; f. stage 8; and g. stage 9.

Magmatic Breccia quartz cement

Microthermometric analyses were performed on one hundred and fifty-three fluid inclusions from eleven samples of Magmatic Breccia. These were: type ia (n = 42), type ib (n = 16), type iia (n = 15), type iib (n = 1), type iic (n = 39) and type iii (n = 40; Table 4.6; Fig. 4.13e-i).

Most of the fluid inclusions from the Magmatic Breccia were collected from section XC-130RB with the exception of one sample from section XC-275. In all samples, there is a predominance of type i, liquid-rich secondary fluid inclusions and lesser amounts of secondary type ii and iii fluid inclusions. Coexisting type i and iii fluid inclusions are common in many of the samples throughout the breccia column. There is no obvious spatial distinction between these inclusions and type ii inclusions, which are most commonly preserved in trails that crosscut quartz crystals as healed fractures. The type iii fluid inclusions commonly contain an opaque daughter mineral (e.g. chalcopyrite) and/or hematite together with halite, sylvite and anhydrite. Type ii inclusions occur most commonly as secondary trails and are most commonly type iic, polyphase fluid inclusions. The size of fluid inclusions was generally between 10 and 30 microns, with type ii generally the largest.

T_hV and T_hD_{halite} of type i and ii fluid inclusions have large ranges from <200° to >600°C. (Table 4.6; Fig. 4.13e). Type iii T_hL also homogenise up to 600°C, but have a lesser range with a lower limit of 328°C (Fig. 4.13e). Salinity data shows a complete spectrum from type i and iii fluid inclusions to type ii hypersaline fluid inclusions (Figs. 4.13f and 4.14b). The type i data plot between 0 and 23 wt.% NaCl equivalent and the type ii data plots between 30 and 69 wt.% NaCl equivalent, with both clusters showing no difference in homogenisation temperatures (Fig. 4.13b). The 6.5 wt.% NaCl equivalent gap between type i, iii and type ii fluid inclusions is a function of the two distinct methods of calculation of the salinities for undersaturated and saturated fluid inclusions. The large range in homogenisation temperatures and salinities indicates the presence of a hot, saline brine fluid and a cooler, low salinity fluid. T_f of type i and iii fluid inclusions were as low as -89°C, however most fluid inclusions froze at approximately -50°C (Fig. 4.13g). Lower limit T_e for types i and iii fluid inclusions were as low as -70°C (Table 4.6; Fig. 4.13h) suggesting the presence of other cations in addition to Na and K in solution. T_m for types i and iii fluid inclusions most commonly occurred between -15° and 0°C (Fig. 4.13i).

Stage 4: Feldspar Porphyry

Microthermometric analyses were performed on fourteen secondary fluid inclusions in primary quartz phenocrysts from one sample of Feldspar Porphyry. Fourteen fluid inclusions were analysed: type ia (n = 6), type ib (n = 1) and type iic (n = 7; Table 4.6; Fig. 4.13j-n). The Feldspar Porphyry sample was collected from section XC-275 in the Don Luis sector at an elevation of 2831 m. The inclusions occur on secondary trails. The type iic inclusions contain halite, hematite, opaque and

anhydrite daughter minerals. All of the fluid inclusions have diameters between 10 and 30 microns.

Lower T_hV and T_hD_{halite} for types i and ii fluid inclusions were measured in the Feldspar porphyry compared to stage 3 (Table 4.6), and two distinct peaks in Figure 4.13j indicate two distinct fluids. This is reflected in the salinity data where two peaks (Fig. 4.13k) or clusters (Fig. 4.14c) illustrate the occurrence of a low salinity and a high salinity fluid. In contrast to the Magmatic Breccia, there are no salinities transitional between the two end-member fluids. T_f and T_e for type i fluid inclusions have a shorter range compared to stage 3 (Fig. 4.13l, m), and T_m has a narrow range between -8° and -1°C (Table 4.6; Fig. 4.13n).

Stage 6: Quartz Monzonite Porphyry

Microthermometric analyses were performed on ten secondary fluid inclusions in primary quartz phenocrysts from two samples containing Quartz Monzonite Porphyry. Ten fluid inclusions were analysed: type ia (n = 3), type ib (n = 1), type iib (n = 1), type iic (n = 4) and type iii (n = 1; Fig. 4.15a-e).

The samples were collected from section XC-130RB at elevations of 3100 to 3205m. Proportions of fluid inclusion types were variable, however type i inclusions are the most abundant, with lesser amounts of type iii. Type ii fluid inclusions are uncommon. The type i, ii and iii fluid inclusions occur along secondary trails. The fluid inclusions are relatively small (<30 microns in diameter) and no obvious relationship can be observed between the different inclusion types.

T_hV and T_hL for type i and ii fluid inclusions, respectively have moderate to high temperatures (Table 4.6; Fig. 4.15a). Whereas the T_hV for type ii fluids are moderate with a range from 328° to 428°C (Table 4.6). T_hD_{halite} for type ii fluid inclusions are low to moderate with a range from 261° to 352°C, and the one $T_hD_{sylvite}$ measurement for a type ii fluid inclusion was 248°C (Table 4.6).

Salinities of types i, ii and iii fluid inclusions, as with stage 4 predominantly form two separate peaks (Fig. 4.15b) and distinct clusters (Fig. 4.14d), however data are limited for this stage. T_f and T_e of type i fluid inclusions are similar to that measured in stage 4 (Figs. 4.15c, d), however the stage 6 T_m values have a larger range (-18° to 2°C) for type i inclusions (Fig. 4.15e).

Stage 7: Quartz-molybdenite veins

Microthermometric analyses were performed on thirty-two fluid inclusions in quartz-molybdenite veins from two samples. Thirty-two fluid inclusions were analysed: type ia (n = 16), type ib (n =

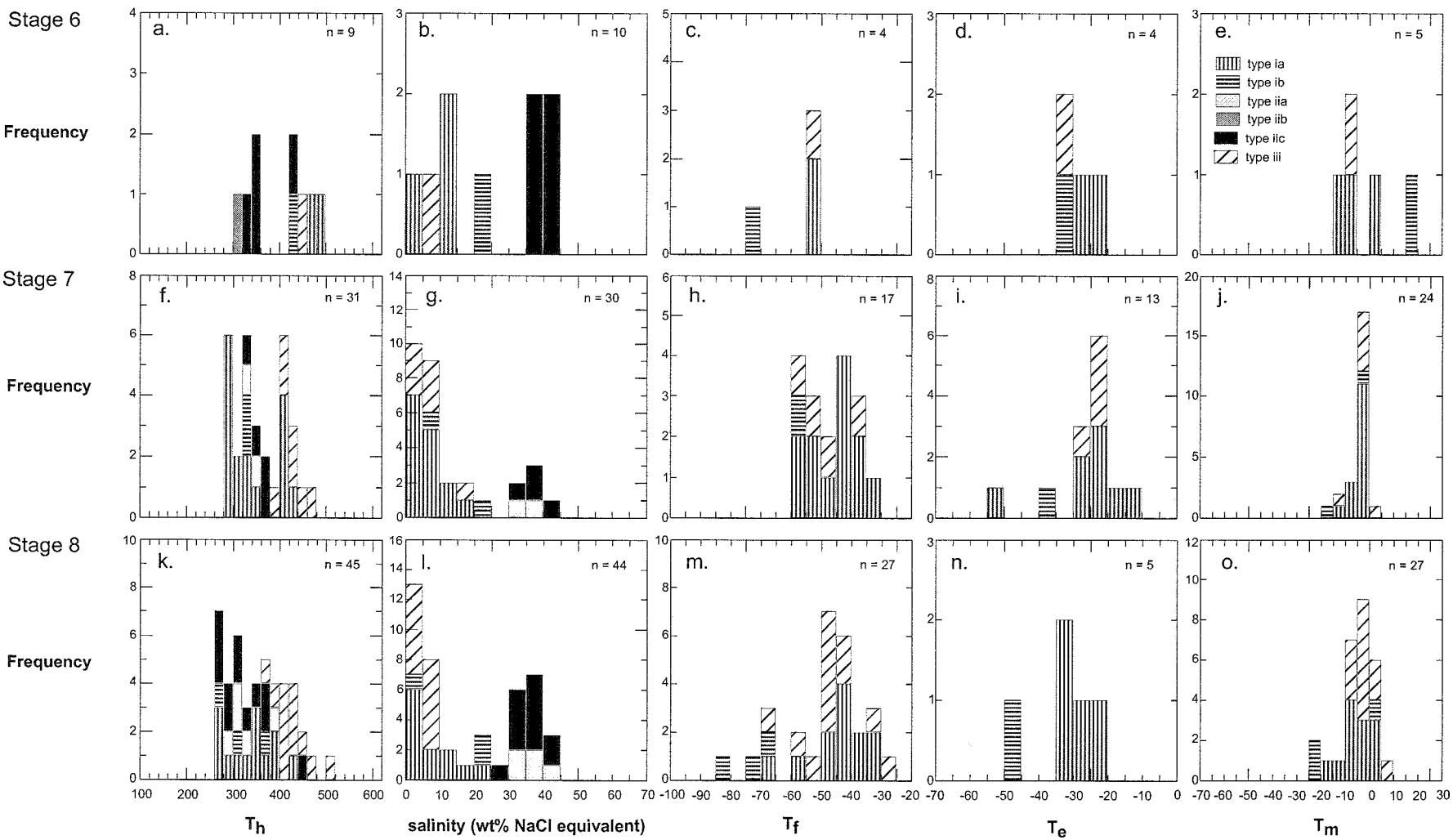

Figure 4.15. Frequency histograms of homogenisation temperatures (T_h), salinities (wt.% NaCl equivalent), freezing temperatures (T_f), eutectic temperatures (T_e) and final melting temperatures (T_m) for stages 6 (a-e), 7 (f-j) and 8 (k-o) in the Río Blanco mineralised system.

2), type iia (n = 2), type iic (n = 4) and type iii (n = 8; Fig. 4.15f-j). One sample was collected from section XC-130RB at an elevation of 2903 m. It contains type i and type iii fluid inclusions with no hypersaline inclusions. The other sample was from section XC-275 (2934 m elevation) and it contains the full range of fluid inclusion types.

Type i fluid inclusions are by far the most abundant in both samples. They have generally been trapped along trails and range in size up to 40 microns. Type iii fluid inclusions are a similar size to the type i inclusions, however type ii fluid inclusions are generally smaller (10-20 microns). Type ii fluid inclusions range up to 30 microns in size and contain halite, opaque and hematite daughter minerals.

T_hV for type i and ii fluid inclusions have a moderate temperature range between 268° and 429°C. T_hL for type iii fluid inclusions have a higher range from 389° to 473°C (Table 4.6; Fig. 4.15f). T_hD_{halite} for type ii fluid inclusions is low to moderate at 208° to 343°C (Table 4.6). Salinities for types i, ii, and iii fluid inclusions have a full range of values between 0 and 41 wt.% NaCl equivalent, but without the high upper limit as measured in stage 3 fluid inclusions (Fig. 4.15g and 4.14e). T_f for types i and iii fluid inclusions ranges between -60° and -34°C (Fig. 4.15h). T_e for types i and iii fluid inclusions ranges between -52° and -14°C (Fig. 4.15i). T_m for most of the types i and iii fluid inclusions ranged between -10° and 0°C (Fig. 4.15j).

Stage 8: Quartz-chalcopyrite veins

Microthermometric analyses were performed on forty-five fluid inclusions in quartz-chalcopyrite veins from five samples. Forty-five fluid inclusions were analysed: type ia (n = 13), type ib (n = 3), type iia (n = 5), type iic (n = 12) and type iii (n = 12; Fig. 4.15k-o).

The samples were collected from section XC-130RB between 3100 and 3860 m elevation. The proportions of fluid inclusion types were variable, with no dominant inclusion type. Secondary trails are abundant. Type i and iii fluid inclusions range in size between 10 and 20 microns. Type ii fluid inclusions are generally smaller, typically around 10 microns in diameter. They contain halite, hematite and opaque daughter minerals.

T_hV for types i and ii fluid inclusions are moderate, from 266° to 435°C and 246° to 459°C, respectively (Table 4.6). T_hL for type iii fluid inclusions have a higher temperature range from 373 to 500°C (Table 4.6; Fig. 4.15k). T_hD_{halite} for type ii fluid inclusions have a low to moderate temperature range with the most inclusions homogenising from 250° to 300°C (Table 4.6; Fig. 4.15k). Salinities for type i and iii fluid inclusions are between 0 and 23 wt.% equivalent NaCl, but predominantly less than 5 wt.% NaCl equivalent (Table 4.6; Fig. 4.15l). Salinities for type ii fluid

inclusions are from 30 to 45 wt.% NaCl equivalent (Table 4.6; Fig. 4.15l). The types i and iii and type ii salinities form separate peaks (Fig. 4.15l) and distinct clusters (Fig. 4.14f), however the data are joined by intermediate values. T_f for types i and iii fluid inclusions range from -84° to -27°C, with the lowest value measured from a type ib fluid inclusion (Table 4.6; Fig. 4.15m). T_e for type i and iii fluid inclusions has a range predominantly between -35° and -20°C, however one type ib inclusion had a T_e of -50°C (Table 4.6; Fig. 4.15n). T_m for type i fluid inclusions are between -23° and 2°C, but type iii fluid inclusions have a tighter range of final melting temperatures, between -7° and 7°C (Table 4.6; Fig. 4.15o).

Stage 9: D veins

Microthermometric analyses were performed on fourteen fluid inclusions in one sample of late stage D veins. Fourteen fluid inclusions were analysed: type ia (n = 12), type iic (n = 1) and type iii (n = 1; Fig. 4.16a-e). The sample was collected from section XC-275 (2920 m elevation). This vein contained few workable fluid inclusions, with most less than 10 microns in diameter. Type i fluid inclusions are abundant, but rare type iii and type ii inclusions were also observed. The type ii fluid inclusions contain halite and an opaque phase.

T_hV for type i and ii fluid inclusions in D veins are the lowest of all stages analysed, ranging from 160° to 348°C (Table 4.6; Fig. 4.16a). One higher T_hL value was obtained for a type iii fluid inclusion (418°C). The one T_hD_{halite} value obtained from a type ii fluid inclusion was 211°C (Table 4.6). Salinities of type i and iii and type ii fluid inclusions form separate peaks (Fig. 4.16b) and distinct clusters (Fig. 4.14g), however the data are limited by a small number of results for type ii fluid inclusions. The salinity calculated for the type ii fluid inclusion was at the lowest limit of all type ii inclusions analysed for the previous stages described (~30 wt.%). T_f for types i and iii fluid inclusions range from -52° to -36°C (Fig. 4.16c). T_e for type i fluid inclusions have two end-members between -39° and -11°C (Fig. 4.16d). T_m for type i and iii fluid inclusions range between -10° and 0°C (Fig. 4.16e).

Sur-Sur sector

A total of twenty-two samples from Sur-Sur were used in fluid inclusion microthermometric experiments. Of these twenty-two samples, fluid inclusions were analysed from quartz in stage 2 veins, stage 3 quartz cement, and stage 8 veins. Microthermometric results for Sur-Sur are listed in Appendix E2.

Stage 2: Pre-breccia quartz veins

Microthermometric analyses were performed on thirty-five fluid inclusions from two samples of

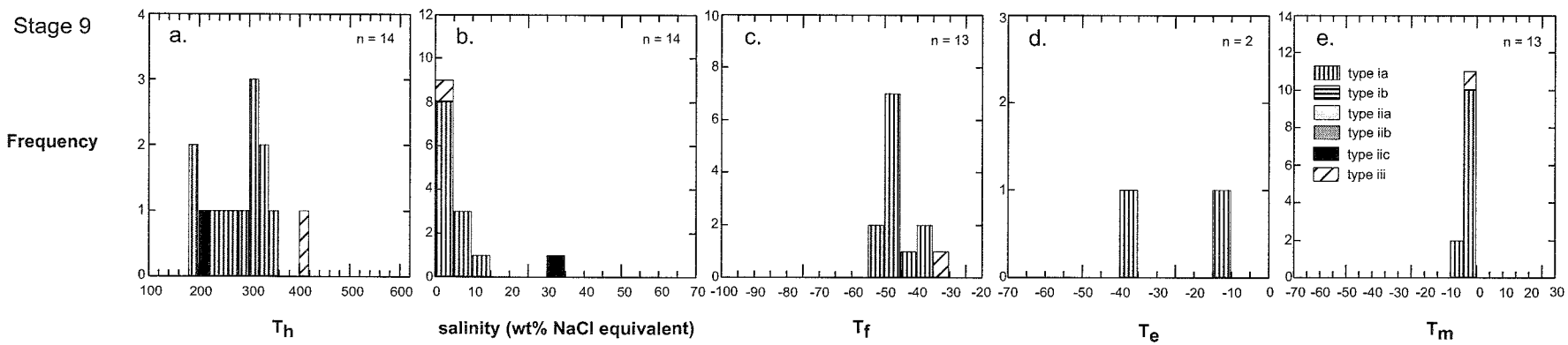

Figure 4.16. Frequency histograms of homogenisation temperatures (T_h), salinities (wt.% NaCl equivalent), freezing temperatures (T_f), eutectic temperatures (T_e) and final melting temperatures (T_m) for stage 9 (a-e) in the Río Blanco mineralised system.

quartz veins with biotite alteration halos that occur in clasts of the Tourmaline Breccia. Thirty-five secondary fluid inclusions were analysed: type ia (n = 13), type ib (n = 1), type iia (n = 8), type iic (n = 6) and type iii (n = 7; Fig. 4.17a-e).

The samples were collected from section XC-50 at elevations from 2854 to 3989 m. Type i fluid inclusions are most abundant in the sample from 2854 m elevation. In the sample from 3989 m, type iii fluid inclusions are the most abundant. Generally, type i inclusions are small (<10μm), type ii are medium sized (10-15μm) and type iii are the largest inclusions (10-20μm). The daughter minerals contained in type ii fluid inclusions are halite and opaques.

T_hV for type i and ii fluid inclusions are low to moderate and range between 191° to 376°C and 153° to 311°C, respectively (Table 4.6, Fig. 4.17a). In contrast, T_hL for type iii fluid inclusions are of moderate to high temperature (431°-522°C; Table 4.6). T_hD_{halite} for type ii fluid inclusions are low to moderate between 183° and 437°C (Fig. 4.17a). Salinities for type i and iii fluid inclusions range from 1 to 23 wt.% NaCl equivalent and type ii fluid inclusions from 32 to 50 wt.% NaCl equivalent (Table 4.6; Fig. 4.17b). There is a consistent array of salinity data with no separate peaks (Fig. 4.17b) or discrete clusters (Fig. 4.18a) for this stage. T_f for types i and iii fluid inclusions range from -75° to -34°C (Fig. 4.17c). T_e for type i fluid inclusions ranges from -45° to -25°C (Fig. 4.17d). T_m for type i fluid inclusions have a lower limit of -49°C that ranges up to 2°C (Fig. 4.17e). The T_m lower limit is lower than any sample described from the Río Blanco sector.

Stage 3: Tourmaline Breccia - quartz cement

Microthermometric analyses were performed on three hundred and five fluid inclusions in fifteen samples of quartz cement from the mineralised Tourmaline Breccia. The fluid inclusions analysed were: type ia (n = 100), type ib (n = 2), type iia (n = 152), type iib (n = 2), type iic (n = 23) and type iii (n = 26; Fig. 4.17f-j)

Most of the samples were collected from section XC-50. Individual samples were also taken from sections XC-000, XC-40 and XC-70. The samples were collected at elevations from 2919 to 4066 m. Type iii fluid inclusions are most common in the Tourmaline Breccia quartz cement, commonly comprising 50% of all inclusions present. Generally, type i and type ii inclusions are smaller (5-15μm) than coexisting type iii inclusions (10-20μm). Daughter minerals in type ii fluid inclusions include halite, sylvite, opaque, anhydrite, tourmaline and hematite.

T_hV for type i fluid inclusions range from low to moderate temperature (195-446°C), with most data at 300° to 440°C (Table 1; Fig. 4.17f). T_hV for type ii fluid inclusions range from 135° to >600°C. T_hL for type iii fluid inclusions also have a moderate to high temperature range, from

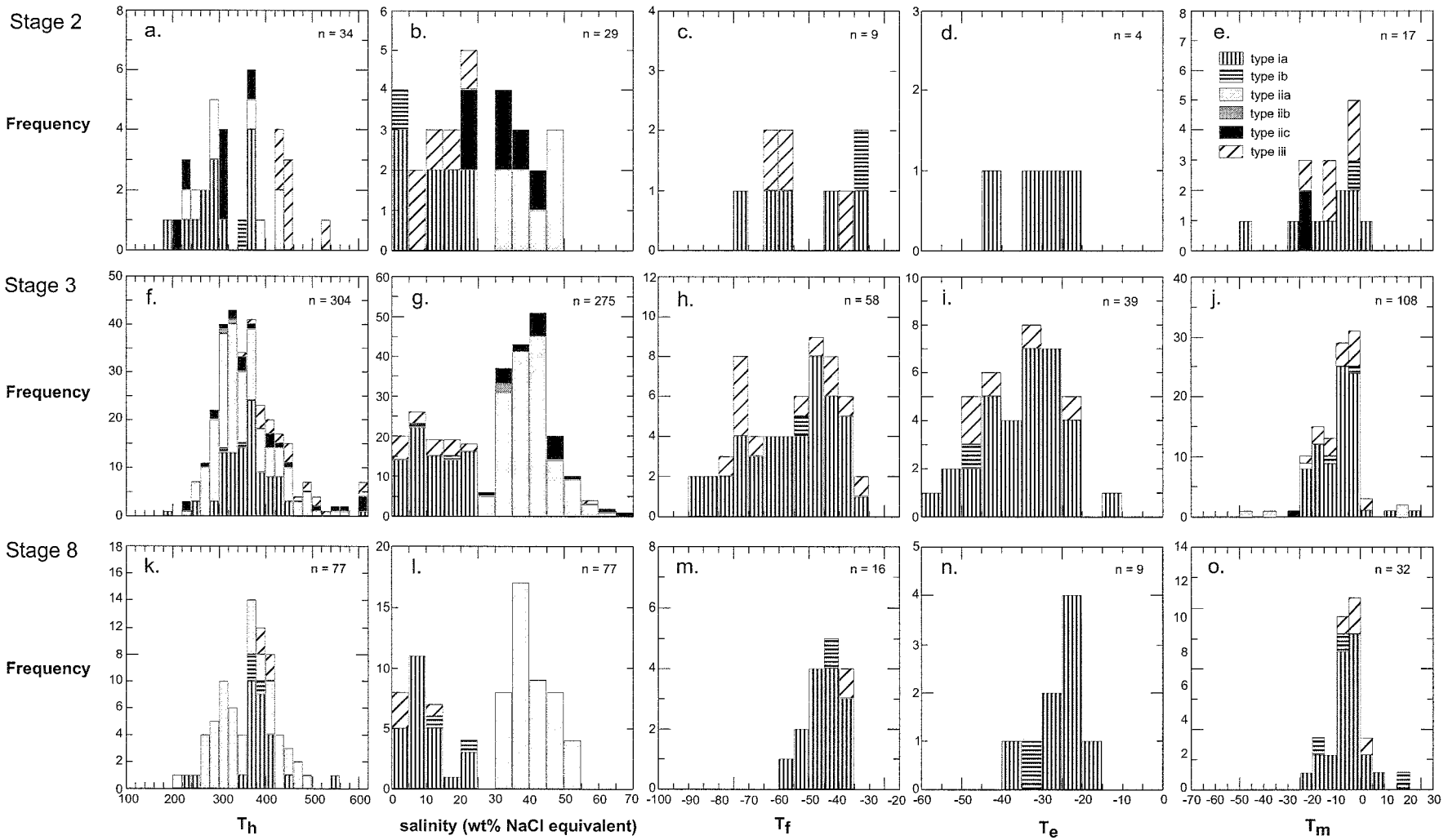

Figure 4.17. Frequency histograms of homogenisation temperatures (T_h), salinities (wt.% NaCl equivalent), freezing temperatures (T_f), eutectic temperatures (T_e) and final melting temperatures (T_m) for stages 2 (a-e), 3 (f-j) and 8 (k-o) in the Sur-Sur mineralised system.

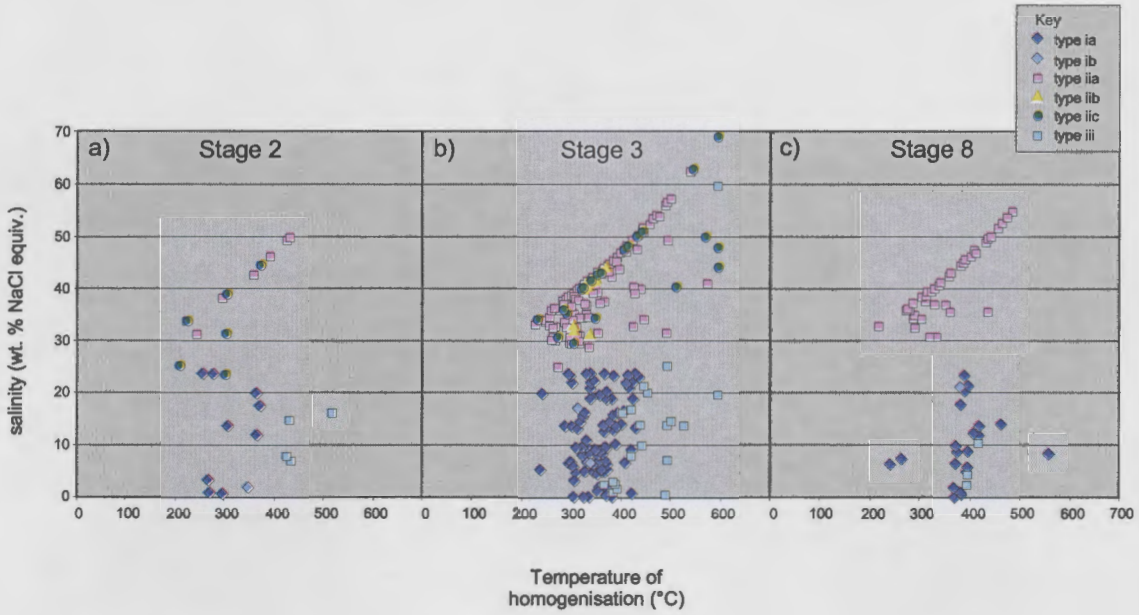

Figure 4.18. Homogenisation temperatures versus salinity for paragenetically constrained samples collected in the Sur-Sur sector. a. stage 2, b. stage 3, and c. stage 8.

353° to >600°C (Table 4.6). T_hD_{halite} for type ii fluid inclusions are between 131° and >600°C, however $T_hD_{sylvite}$ for type ii fluid inclusions have a low temperature range (180° to 194°C; Table 4.6).

An array of salinities from type i and iii to type ii fluid inclusions occurs in this stage (Fig. 4.17g and 4.18b). Most salinities for type ii fluid inclusions are between 30 and 50 wt.% NaCl equivalent, however they range up to 69 wt.% NaCl equivalent (Fig. 4.17g). As was the case in the Río Blanco Magmatic Breccia, T_f for this stage varies widely, in this case between -89°C and -33°C (Table 4.6; Fig. 4.17h). T_f for type iii fluid inclusions also has a large range, between -75° and -35°C. T_e for type i fluid inclusions range from -59° to 3°C, however T_e for type iii fluid inclusions have a narrow range between -49° and -24°C (Table 4.6; Fig. 4.17i). Similar again to the Río Blanco Magmatic Breccia, this stage has T_m for type i fluid inclusions between -25° to -20°C (Table 4.6; Fig. 4.17j). T_m for type iii fluid inclusions are from -23° to 1°C (Fig. 4.17j).

The Tourmaline Breccia contains coexisting type i and iii fluid inclusions in secondary trails in quartz cement (Fig. 4.19a, b). T_hV and T_hL have a range mostly between 350° and 400°C for these inclusions. In addition, the Tourmaline Breccia contains coexisting vapour-rich and hypersaline inclusion populations in samples from the highest altitudes sampled in this study (>4000 m elevation; Fig. 4.19c, d, e). The inclusions in these samples had consistently high homogenisation temperatures (>500°C) for both halite and vapour (Table 4.6).

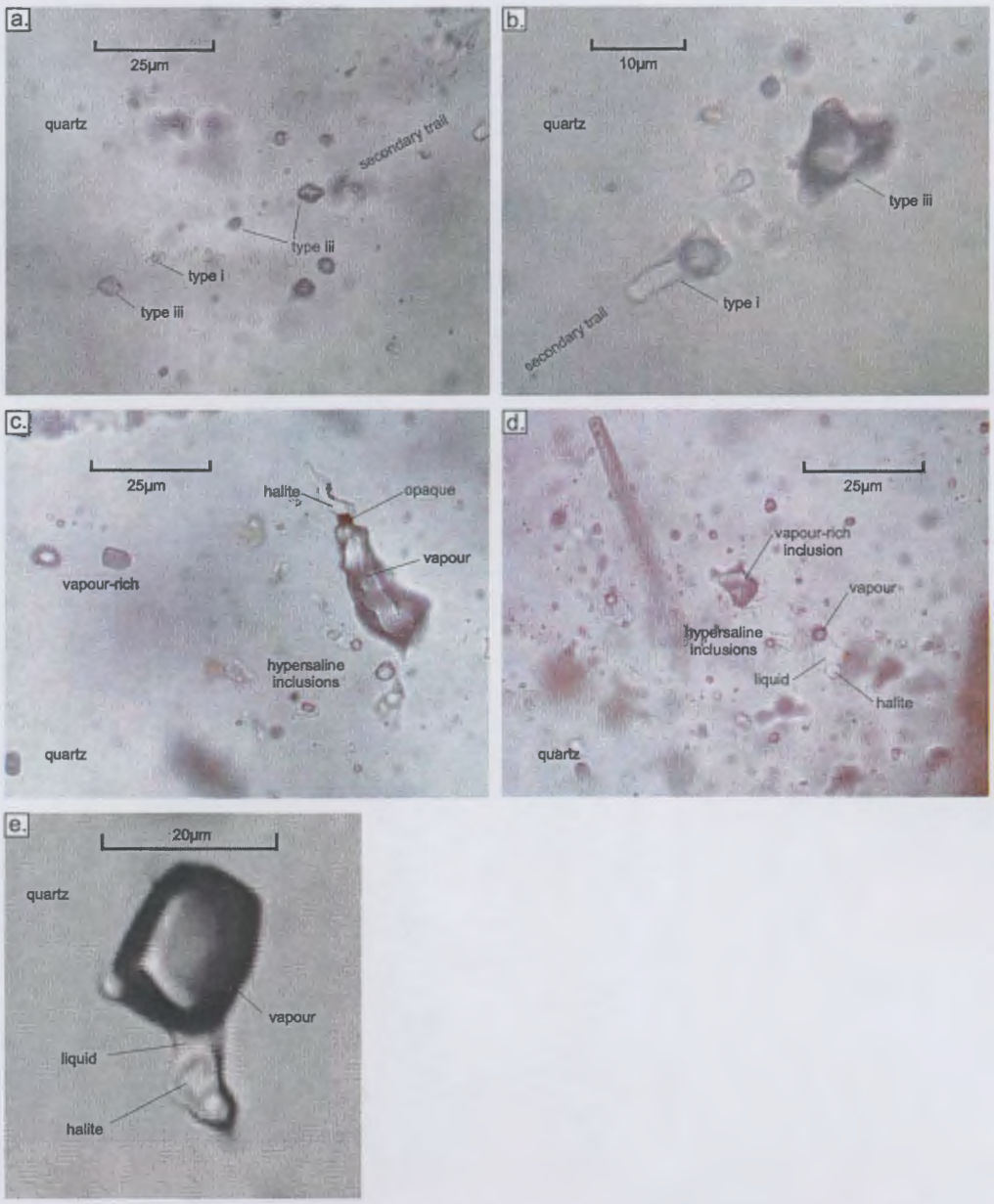

Figure 4.19. Coexisting type i and type ii fluid inclusions (a, b) and coexisting type ii and type iii fluid inclusions (c, d, e) from the Sur-Sur Tourmaline Breccia.
a. Secondary trail containing coexisting type i, liquid-rich and type iii, vapour-rich fluid inclusions (sample 190);
b. Secondary trail containing coexisting type i, liquid-rich and type iii, vapour-rich fluid inclusions (sample 190);
c. Coexisting type ii, hypersaline and type iii, vapour-rich fluid inclusions, the vapour-rich inclusion also contains a halite daughter crystal and an opaque (sample 490);
d. Coexisting type ii, hypersaline and type iii, vapour-rich fluid inclusions within the same population (sample 490); and
e. A vapour-rich inclusion containing a halite daughter crystal, $T_{h\ (halite)}$ = 527°C, T_h (vapour) = >600°C (sample 524).

Stage 3: Tourmaline Breccia – tourmaline cement

Microthermometric analyses were performed on twenty-three fluid inclusions in tourmaline from five samples of Tourmaline Breccia. The twenty-three fluid inclusions analysed were: type ia (n = 14), type ib (n = 5) and type iic (n = 4; Fig. 4.20a-f).

Samples were collected from section XC-50 between 2919 and 4064 m elevation. Type i are the most abundant, but rare type ii inclusions are also present. The fluid inclusions are generally small with elongate shapes due to their growth along cleavage planes. The inclusions analysed are between 5 and 40 microns long. Daughter minerals in type ii fluid inclusions include halite, hematite and opaques.

T_hV for type i and ii fluid inclusions range from 141° to 445°C (Table 4.6; Fig. 4.20a). T_hD_{halite} for type ii fluid inclusions are moderate (217°-304°C). Salinities for type i fluid inclusions range from 1 to 23 wt.% NaCl equivalent with most values between 1 and 15 wt.% NaCl equivalent, and type ii fluid inclusions have a narrow range between 33 and 38 wt.% NaCl equivalent (Table 4.6; Fig. 4.20b, f). T_f for type i fluid inclusions are from -64° to -46°C (Fig. 4.20c), T_e for type i fluid inclusions are from -62° to -31°C (Fig. 4.20d), and T_m for type i fluid inclusions are from -23° to 13°C (Fig. 4.20e).

Stage 8: Quartz- chalcopyrite veins

Microthermometric analyses were performed on seventy-eight fluid inclusions in five samples of stage 8 veins in the Sur-Sur sector. Seventy-eight secondary fluid inclusions were analysed: type ia (n = 25), type ib (n = 3), type iia (n = 46) and type iii (n = 4) inclusions (Fig. 4.17k-o; Fig. 4.18).

The samples for this vein stage were collected from section XC-50 between 2854 and 3902m elevation. Type iii fluid inclusions are the most common occurring with type i inclusions and rare type ii inclusions. Generally, type i and type ii inclusions are smaller in size (5-15μm diameter) than type iii (10-20μm diameter). Daughter minerals in type ii inclusions include halite, sylvite, hematite and opaques.

Most T_hV for type i fluid inclusions are between 350° and 400°C (Table 4.6; Fig. 4.17k). T_hV for type ii fluid inclusions are low (215°-263°C), with corresponding T_hD_{halite} values typically higher (170°-484°C; Table 4.6). T_hL for type iii fluid inclusions are tightly constrained between 393° and 407°C. Calculated salinities for type i fluid inclusions range from 0 to 23 wt.% NaCl equivalent, whereas type iii salinities are between 3 and 10 wt.% NaCl equivalent (Table 4.6; Fig. 4.17l).

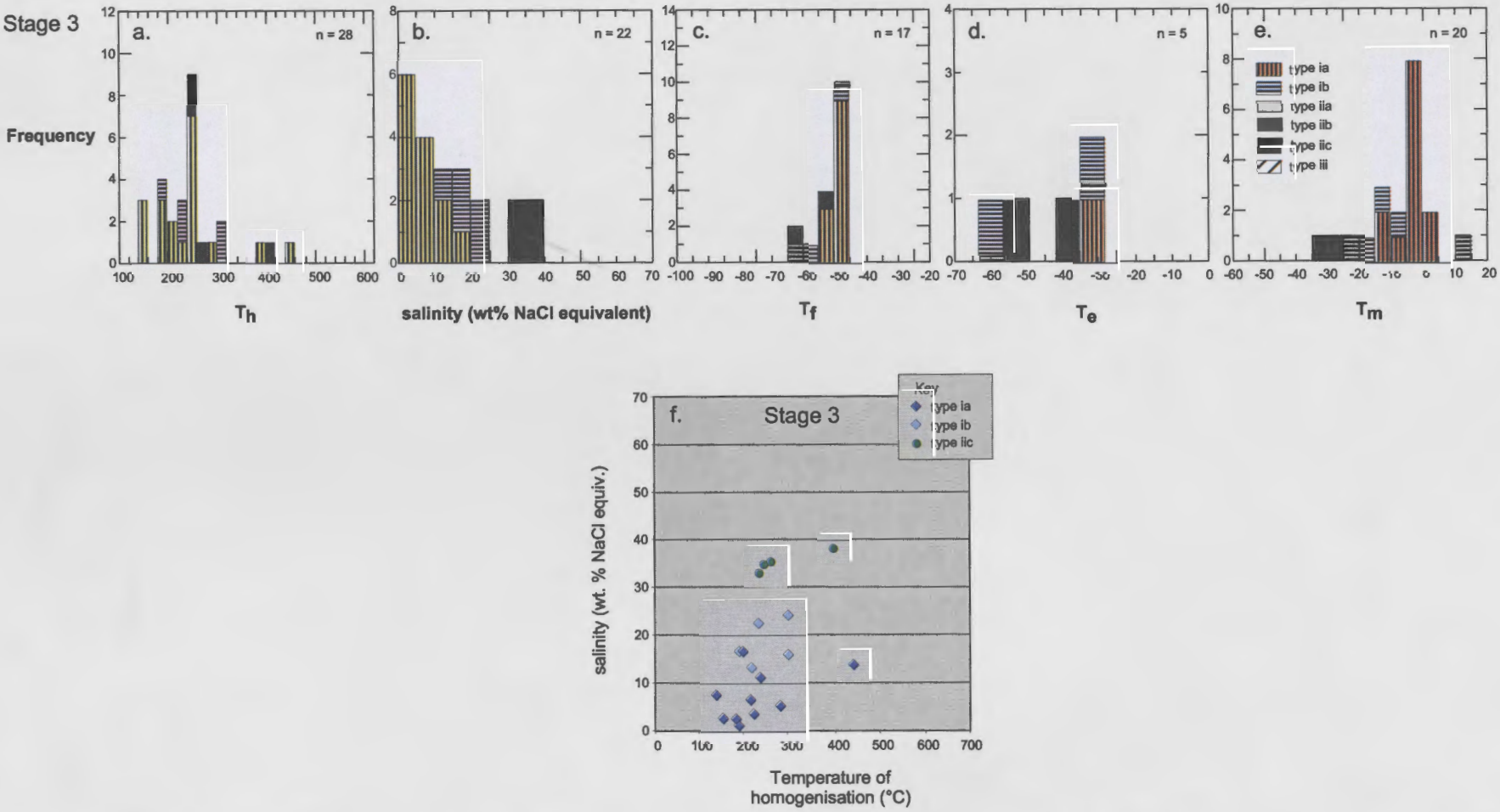

Figure 4.20. Frequency histograms of homogenisation temperatures (T_h), salinities (wt.% NaCl equivalent) freezing temperatures, eutectic temperatures (T_e) and final melting temperatures (T_m) for stage 3 (a-e) tourmaline cement in the Sur-Sur Tourmaline Breccia. f. Homogenisation temperatures versus salinities for stage 3 - tourmaline cement.

Salinities for type ii fluid inclusions range from 31 to 56 wt.% NaCl equivalent. The salinity data for types i and ii fluid inclusions form two separate peaks (Fig. 4.17l) and distinct clusters (Fig. 4.18c) indicating that high and low salinity fluids were present. T_f for type i fluid inclusions are higher than for the previous paragenetic stages in Sur-Sur (Table 4.6; Fig. 4.17m), but have similar upper limits (Fig. 4.17n). T_e for type i fluid inclusions is higher compared to the previous two stages (Fig. 4.17o), while T_m for type i inclusions is similar to the stage 3 data (Fig. 4.17p). T_m for type iii fluid inclusions had a narrower range, between -7° and 2°C (Table 4.6).

4.3.8 Spatial variations

To test whether any spatial variations occur in fluid inclusion data from the mineralised breccia cements, samples from the two main sections through Río Blanco and Sur-Sur (XC-130RB and XC-50, respectively) have been grouped into deep, mid and shallow locations and plotted on Figures 4.21 and 4.22. The relative proportions of type i, ii and iii inclusions are also plotted on these diagrams to test whether domains dominated by gas, brine or lower salinity water can be identified.

Río Blanco (section XC-130RB)

In the Río Blanco Magmatic Breccia, most of the data are clustered between 300 and 500°C. Homogenisation temperatures of fluid inclusions hosted by quartz cement do not change from the deep to the mid levels (Fig. 4.21). Surprisingly, at shallow levels, distinctly higher homogenisation temperatures and salinities are preserved in addition to the main range of temperatures.

Salinities of types i and iii fluid inclusions for the deep to mid levels are predominantly less than 10 wt.% NaCl equivalent, however in the shallow level samples, types i and iii fluid inclusions are predominantly above 10 wt.% NaCl equivalent. Salinities for type ii fluid inclusions mostly range between 30 and 50 wt.% NaCl equivalent through all depth levels, however in the shallow level there is a separate high salinity peak between 60 and 70 wt % NaCl equivalent which is distinct from the deeper levels (Fig. 4.21)

Sur-Sur (section XC-50)

A similar scenario to Río Blanco is recorded in the Tourmaline Breccia quartz cement in the Sur-Sur sector. The greatest range in homogenisation temperatures is observed at the shallowest levels, with the range of T_h values becoming tighter with greater depth (Fig. 4.22). There is a complete spectrum of salinity data defined by the type i, iii and ii fluid inclusions which is interpreted to indicate that mixing between low and high salinity fluids occurred throughout the entire breccia

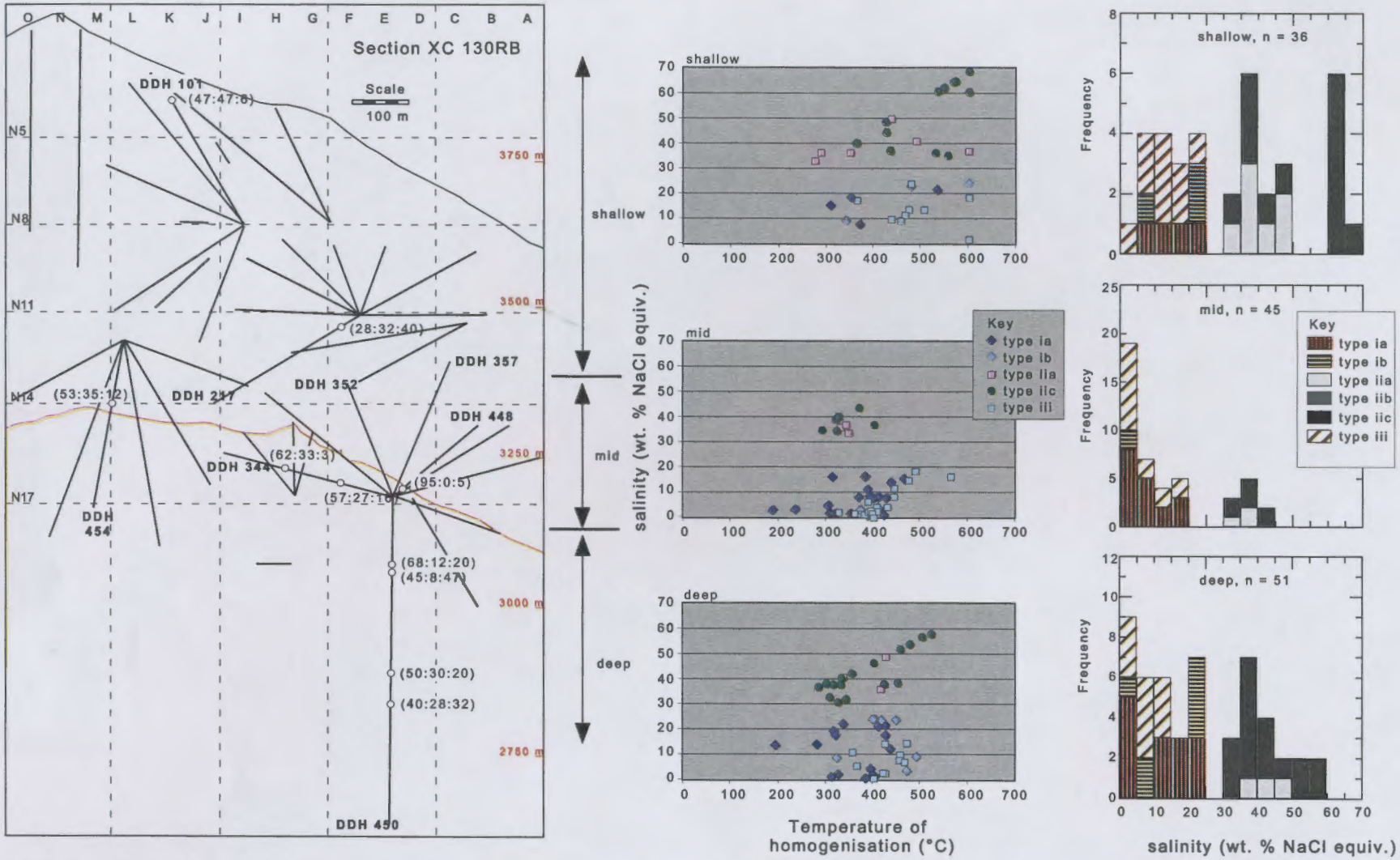

Figure 4.21. Spatial variation in homogenisation temperatures and salinity in quartz cement from the Río Blanco Magmatic Breccia (section XC-130RB). Samples collected from deep, mid and shallow levels within the breccia. (x:y:z) = proportions of type i, type ii and type iii respectively.

column. Type iic, polyphase fluid inclusions are most abundant at shallow levels in the breccia column, and are absent at depth (Fig. 4.22). Type iii, vapour-rich fluid inclusions commonly have higher homogenisation temperatures than type i, liquid-rich inclusions, but the overlap in homogenisation temperature is where type i and iii fluid inclusions coexist spatially (Fig. 4.22). The highest homogenisation temperatures from type iii fluid inclusions are also located at shallow levels.

The salinity histograms show two groupings at depth indicating the presence of low salinity water and high salinity brine (Fig. 4.22). A third grouping of type i fluid inclusions with salinities around 20 wt.% NaCl equivalent may be the product of mixing between the two end members. At mid and shallow levels, these groups converge, suggesting that mixing has occurred to produce the observed salinity array. As with the Río Blanco Magmatic Breccia, type iic fluid inclusions dominate the high temperature data at shallow levels (Fig. 4.22)

4.3.9 PIXE data

Proton Induced X-Ray Emission (PIXE) analysis is a non-destructive analytical technique that can provide quantitative information about the composition of fluid inclusions (Heinrich et al., 1992). Individual fluid inclusions were chosen within 10μm of the host grain surface to minimise attenuation of X-Ray signals from S, Cl and K as they pass through quartz. Na is not detectable by PIXE analysis.

The PIXE technique was employed to analyse nine fluid inclusions from four samples at CSIRO, Canberra. The four samples were collected from the Sur-Sur Tourmaline Breccia in section XC-50. Sample locations and microthermometric data are shown in Table 4.7, and element concentrations from the PIXE analysis shown in Table 4.8. Two of the samples are stage 3 quartz-hosted fluid inclusions from the Tourmaline Breccia and the other two samples are stage 8 veins that have crosscut the Tourmaline Breccia cement. The concentrations of various elements in the inclusions analysed are shown in Figure 4.23. Photographs showing the distribution of elements in individual fluid inclusions can be observed in Figure 4.24. The data for these images is presented in Appendix E3.

Table 4.7. Sample locations, fluid inclusion types, and microthermometry of PIXE fluid inclusions.

sample	stage	section	DDH	metres	lithology	Cu (%)	Type	T_m	T_hV	T_hD_{salt}	T_d	salinity
PF221B-1A	3	XC-50	TSS-22	28 m	BXTGDCC	0.59	ia	-6.7	331.8			40.28
PF221B-1B	3	XC-50	TSS-22	28 m	BXTGDCC	0.59	ia	-4.2	413.5			6.72
PF221B-1C	3	XC-50	TSS-22	28 m	BXTGDCC	0.59	iia		436.4			
PF230B-1A	3	XC-50	DL-64	25 m	BT-BXTGDCC	0.28	iia		339.8			40.90
PF230B-2A	3	XC-50	DL-64	25 m	BT-BXTGDCC	0.28	ia				572.1	
PF218B-1A	8	XC-50	TSS-22	802 m	BXMGDCC	0.3	ia	-8.2	417			11.95
PF218B-1B	8	XC-50	TSS-22	802 m	BXMGDCC	0.3	iia	-14.5	409.4			46.90
PF218B-1C	8	XC-50	TSS-22	802 m	BXMGDCC	0.3	ia	-14.5	409.9			18.36
PF46-1A	8	XC-50	TSS-22	37 m	BXTGDCC	0.86	iia	-25	325.2	248.4		34.55

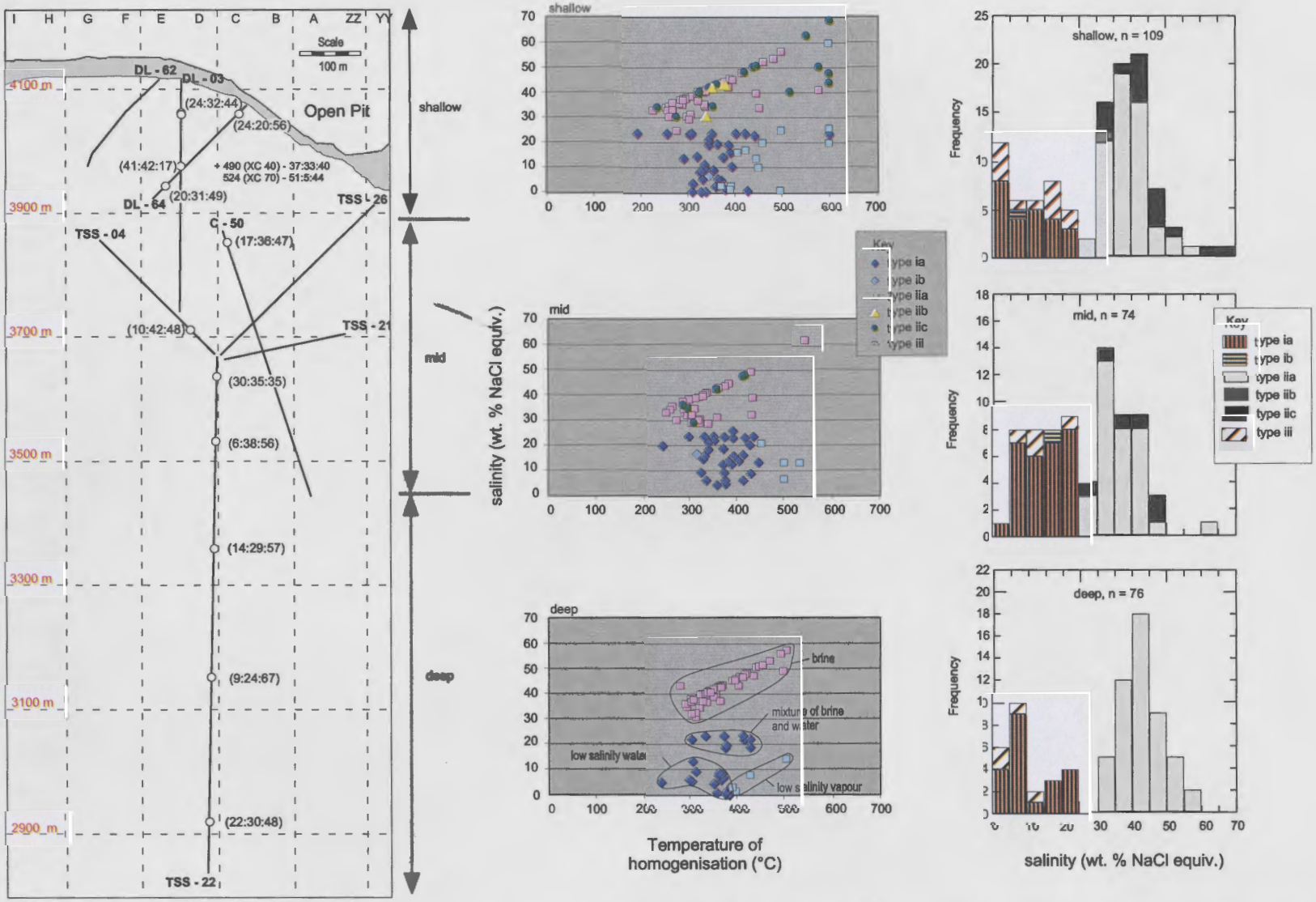

Figure 4.22. Spatial variation in homogenisation temperatures and salinity in quartz cement from the Sur-Sur mineralised Tourmaline Breccia (sections XC-40 to XC-70). Samples are collected from deep, mid and shallow levels within the breccia. (x:y:z) = proportions of type i, type ii and type iii respectively. The deep level homogenisation temperature versus salinity plot shows the different fluid fields that can be recognised from the data.

Table 4.8. Element concentrations (ppm) from fluid inclusions analysed by PIXE.

Sample	K	Ca	Ti	Mn	Fe	Cu	Zn	As	Br	Rb	Sr	Pb	salinity
	ppm	ppm	ppm	ppm	ppm	ppm	ppm	ppm	ppm	ppm	ppm	ppm	wt% NaCl
PF221B-1A	9382.7	1214.8	0	574.9	105.97	21.353	104.94	67.476	40.249	44.542	36.781	2.235	40.28
PF221B-1B	2811	1020.1	0	1231.4	1453.7	53.613	467.02	92.525	68.08	0	0	52.482	6.72
PF221B-1C	9857.8	1193.1	107.5	1144.2	10916	2382.3	397.02	809.79	486.42	211.05	90.08	234.54	
PF230B-1A	35381	8910.7	588.79	3762.3	52561	1551.3	1115.9	1101.6	588.82	597.7	616.26	397.96	40.90
PF230B-2A	2442.7	178.15	0	2311.6	1669.3	57.92	331.26	55.796	61.68	0	0	358.4	
PF218B-1A	12651	2706	3304.6	854.19	6478.1	1105.3	364.3	49.214	75.136	73.538	8.9573	179.81	11.95
PF218B-1B	18105	3610.3	3024.7	1484.2	10434	170.5	452.14	143.31	88.286	154.53	27.984	54.023	46.90
PF218B-1C	12597	3873.1	6775.2	2828.3	18683	57.572	547.26	300.28	6.7518	0	0	0	18.36
PF46-1A	13239	1703.7	76.401	1593.4	29238	100.2	669.89	621.56	432.02	128.56	81.409	295.61	34.55

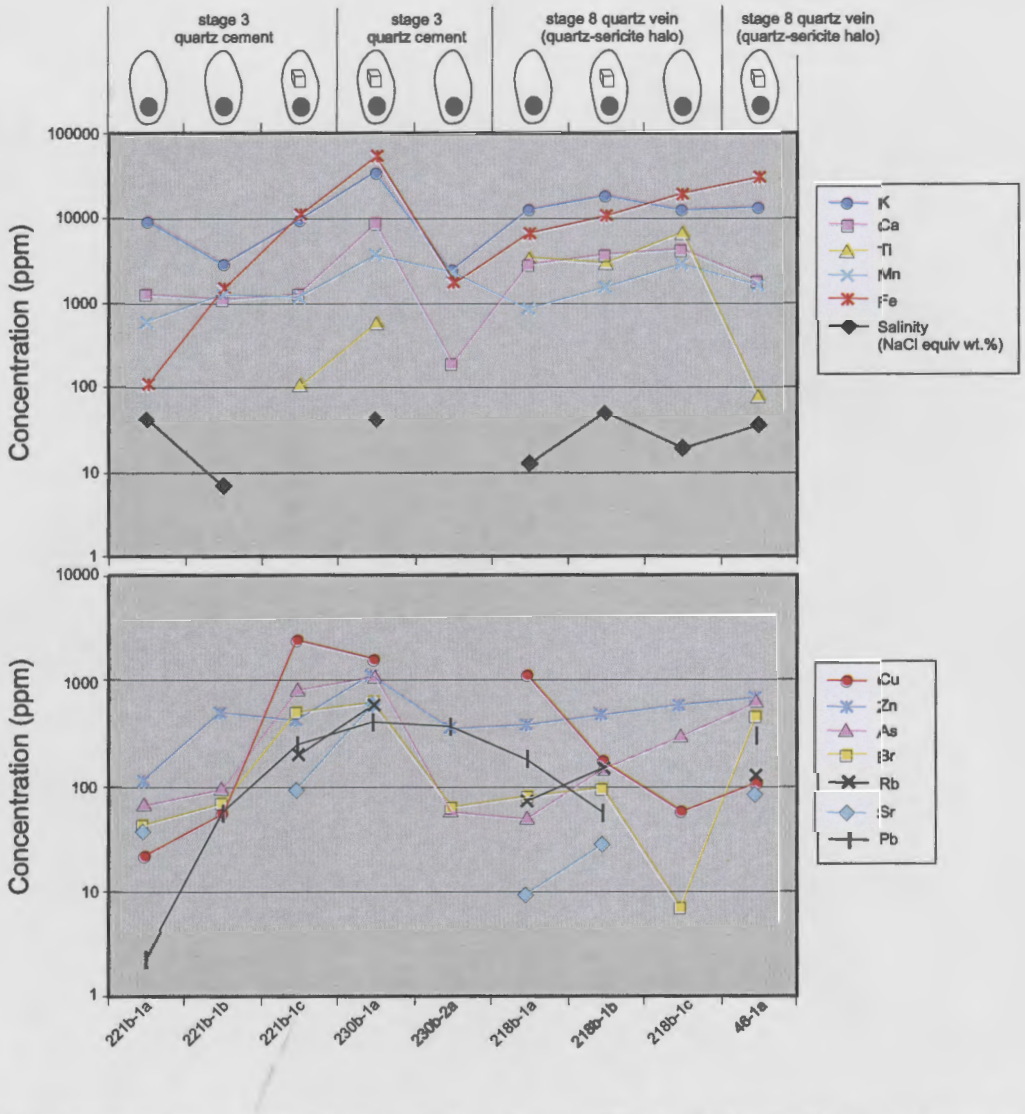

Figure 4.23. Graphical representation of concentrations in ppm of K, Ca, Ti, Mn, Fe, NaCl, Cu, Zn, As, Br, Rb, Sr and Pb for fluid inclusions analysed by PIXE.

The results for PIXE analysis in the stage 3 Tourmaline Breccia quartz cement show high (100-1000 ppm) concentrations of K, Fe, Ca, Cu, As and Br in the hypersaline inclusions and relatively low concentrations of these elements in liquid-rich fluid inclusions (Fig. 4.23). In contrast, the element concentrations in the stage 8 veins show no systematic variation between type i and type ii fluid inclusions with the exception of Cl and Br (Fig. 4.23). Elevated concentrations of Mn and Zn in addition to K, Fe, Ca and Br are particularly evident in the PIXE photographs in Figures 4.24-4.28. The concentrations of Cu are highest in 221b-1c (type ii), 230-1a (type ii) and 218-1a (type i). High concentrations of Fe, K and Mn can be explained by the high solubility of these elements in hydrothermal fluids, so rather than precipitate, they become trapped in fluid inclusions and form daughter minerals. Type ii fluid inclusions from the mid to shallow levels in stage 3 quartz cement have elevated K, Ca, Ti, Mn, Fe, Pb, Rb, Sr, As and Zn (Fig. 4.23).

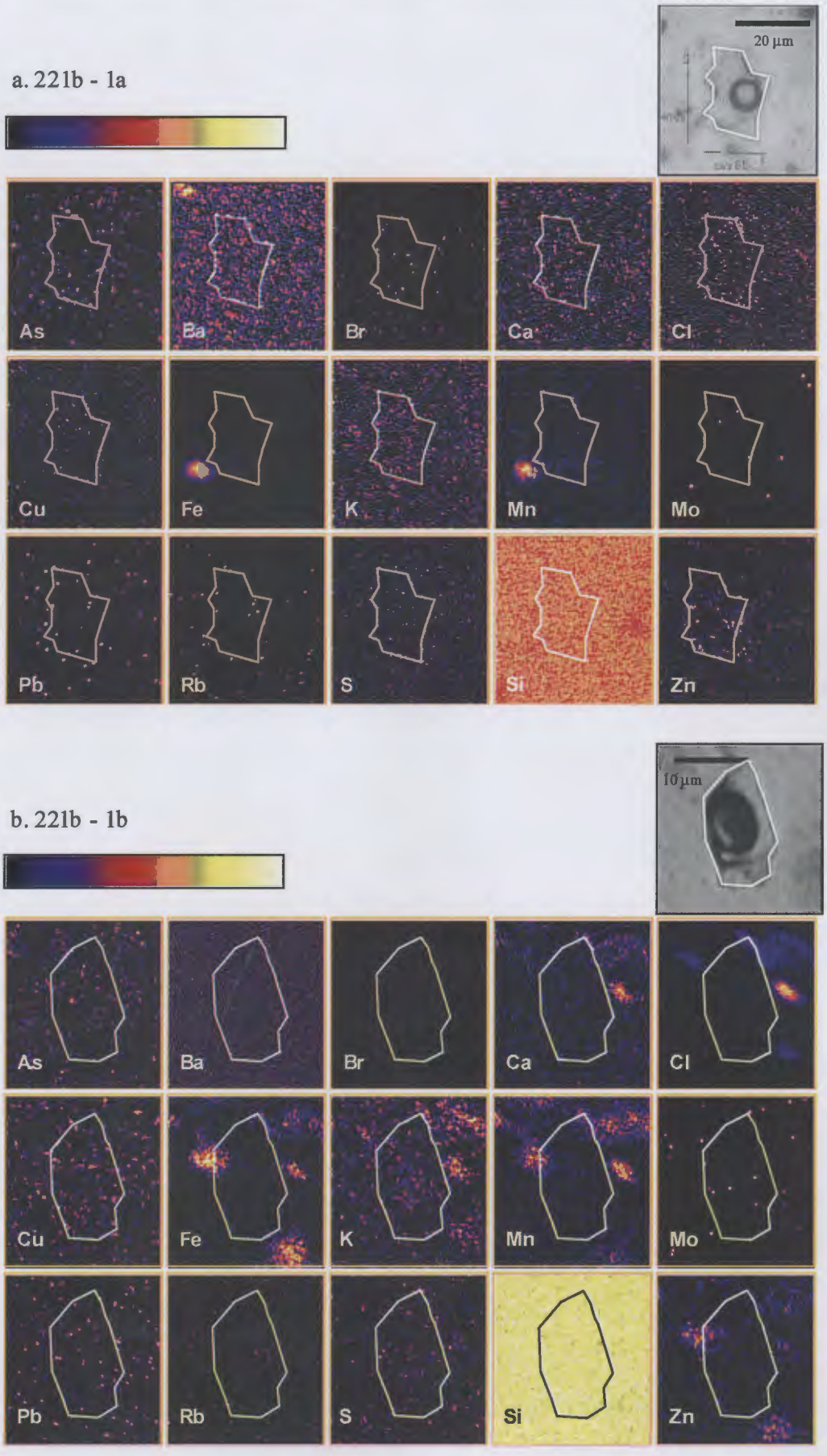

Figure 4.24. PIXE photographs showing the distribution of elements (ppm) in quartz hosted fluid inclusions: a. 221b-1a = liquid-rich fluid inclusion in stage 3 quartz cement from a mid level in the Sur-Sur Tourmaline Breccia; and b. 221b-1b = liquid-rich fluid inclusion from stage 3 quartz cement.

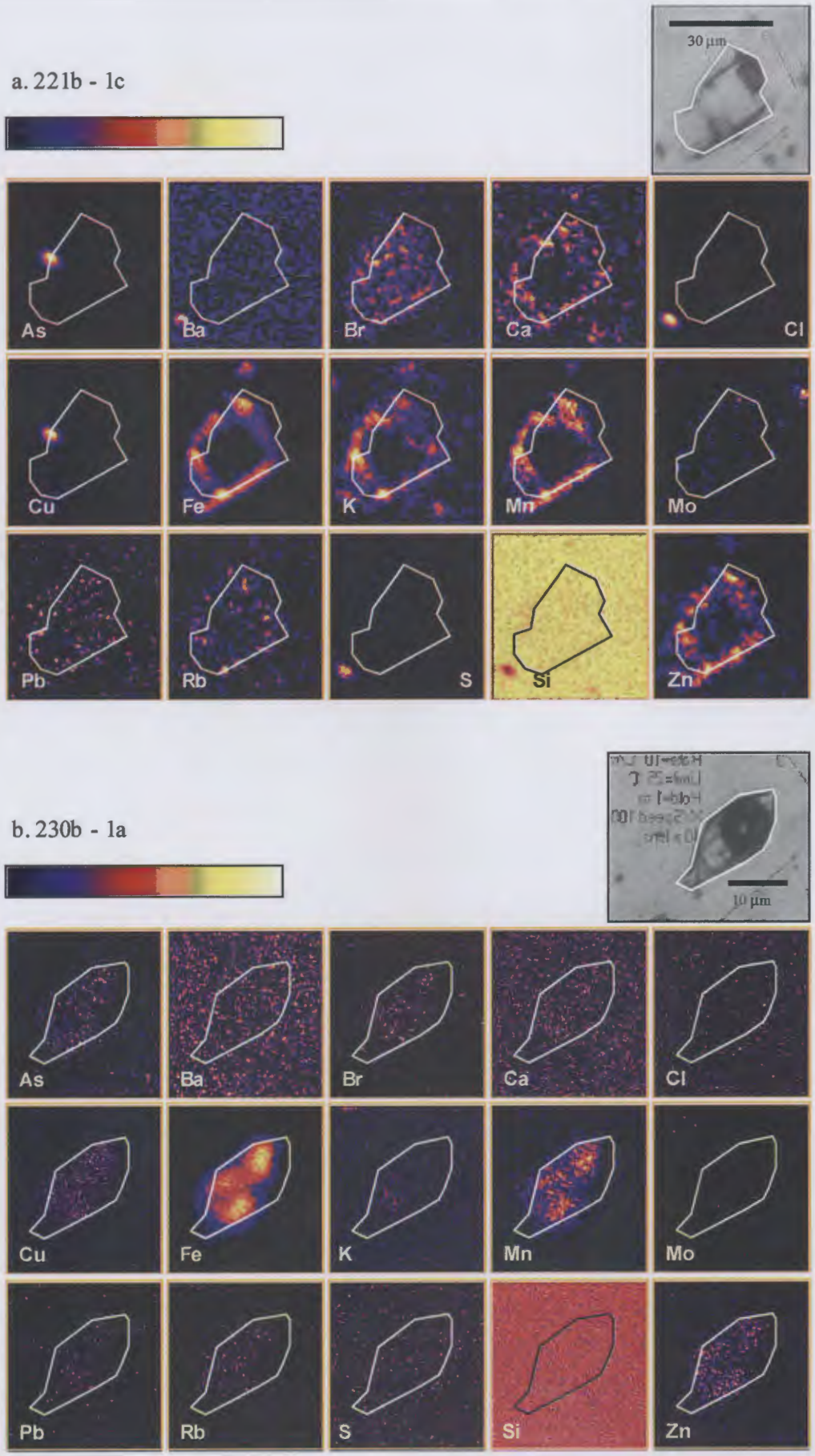

Figure 4.25. PIXE photographs showing the distribution of elements (ppm) in quartz hosted fluid inclusions: a. 221b-1c = hypersaline from stage 3 quartz cement; and b. 230b-1a = hypersaline fluid inclusion in stage 3 quartz cement from a shallow level in the Sur-Sur Tourmaline Breccia.

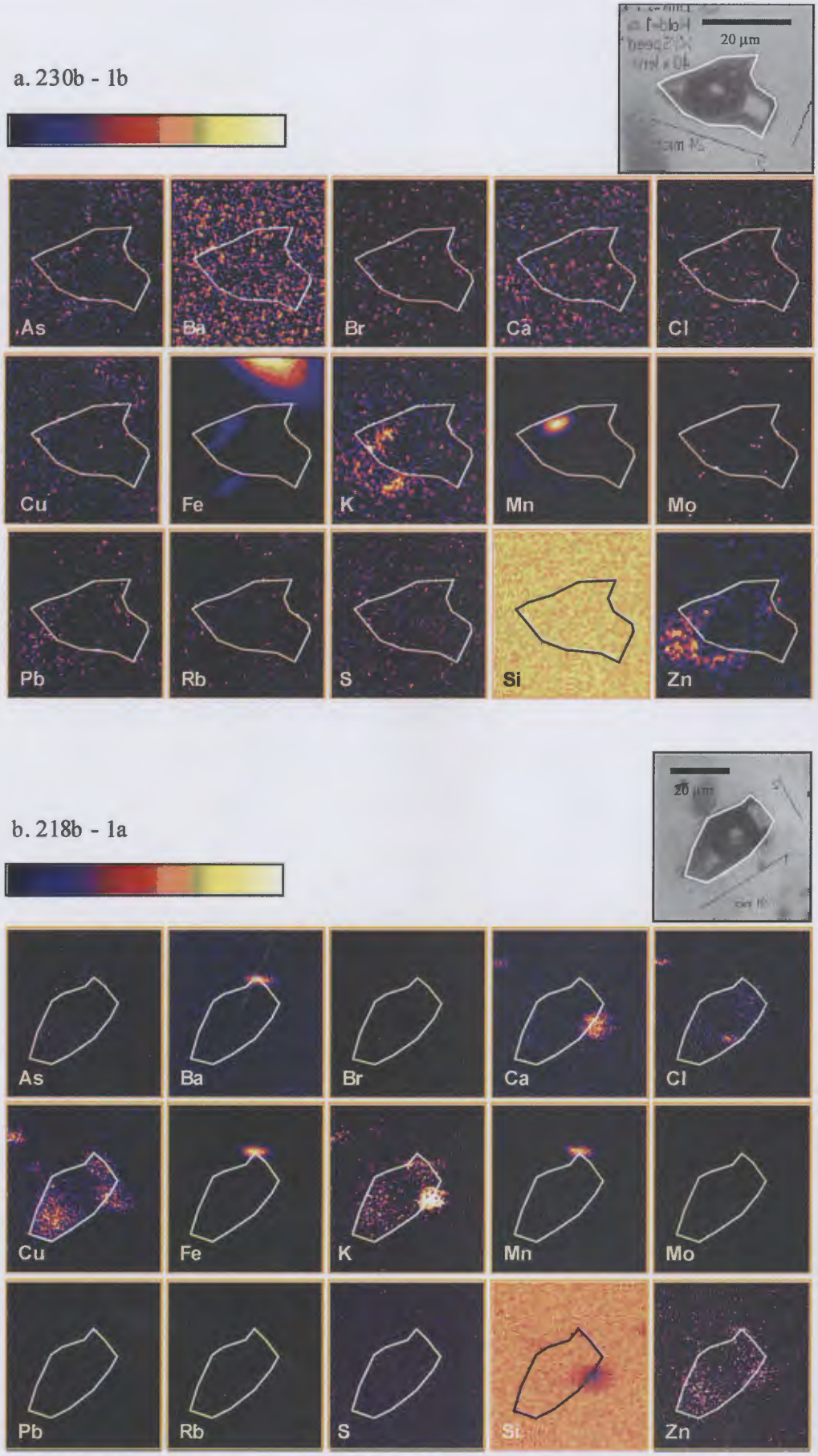

Figure 4.26. PIXE photographs showing the distribution of elements (ppm) in quartz hosted fluid inclusions: a. 230b-1b = liquid-rich fluid inclusion from stage 3 quartz cement; and b. 218b-1a = a liquid-rich fluid inclusion in a stage 8 vein from the base of the Sur-Sur Tourmaline Breccia.

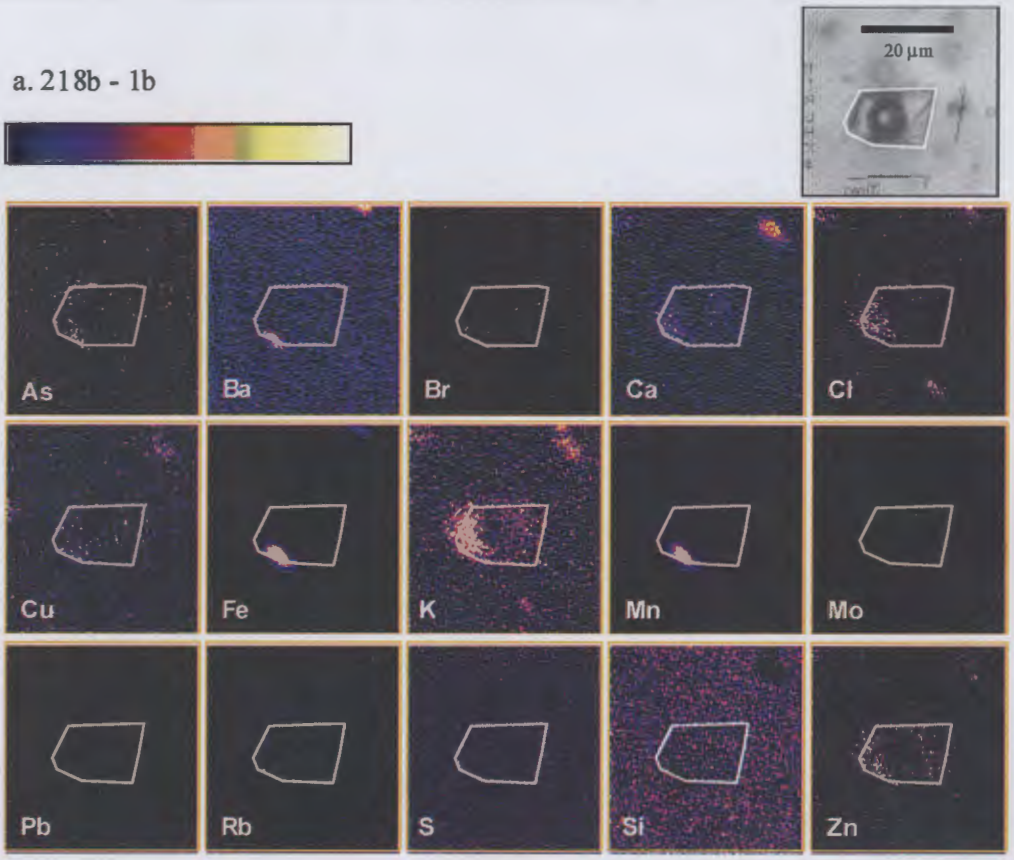

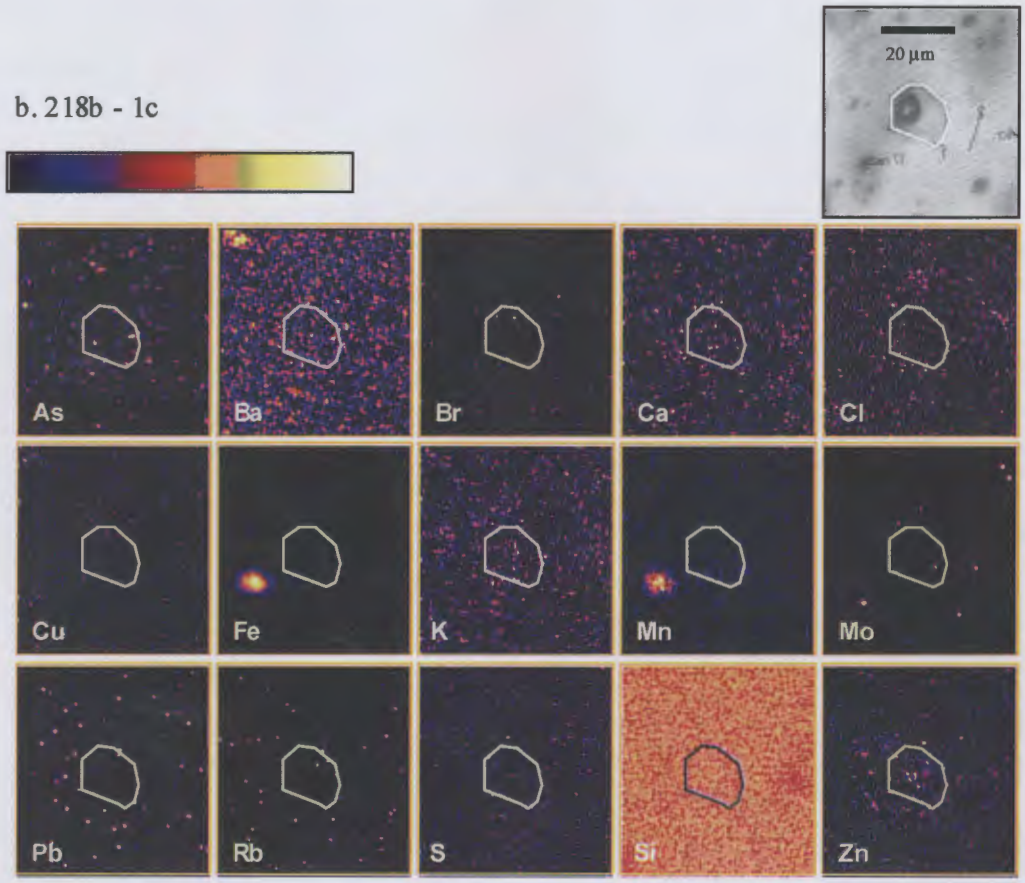

Figure 4.27. PIXE photographs showing the distribution of elements (ppm) in quartz hosted fluid inclusions: a. 218b-1b = a hypersaline fluid inclusion from a stage 8; and b. 218b-1c = liquid-rich fluid inclusion from a stage 8 vein.

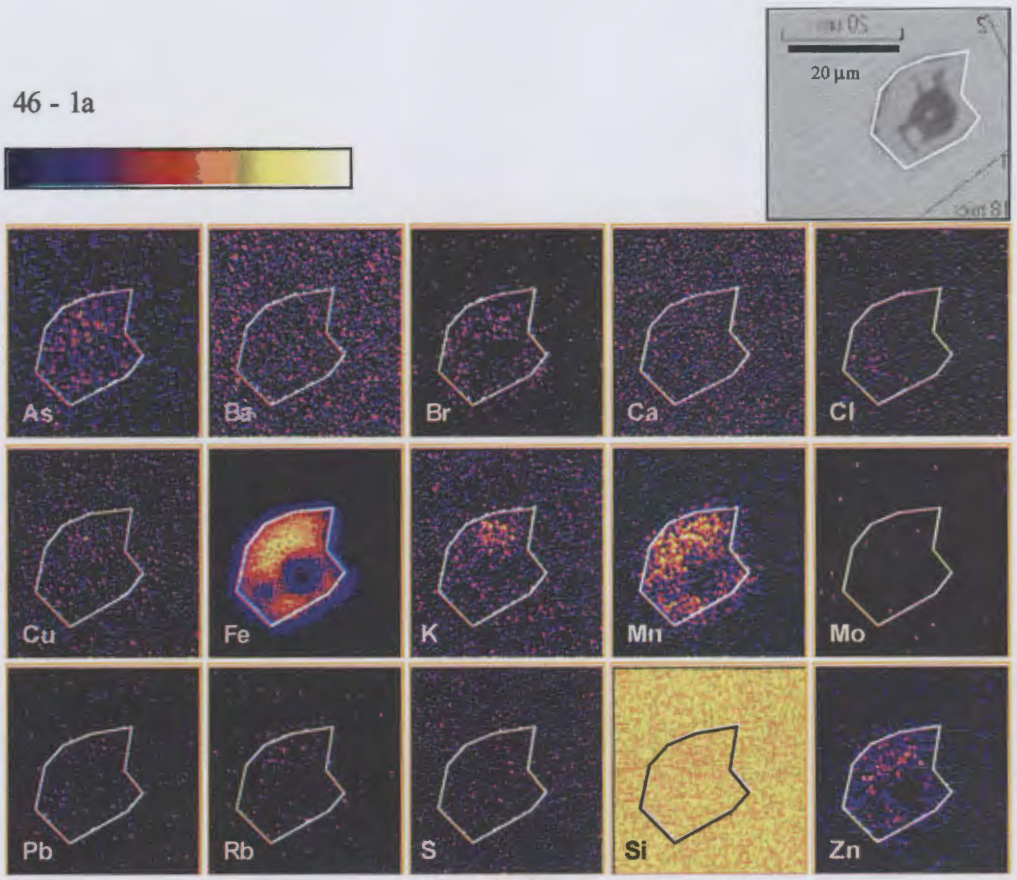

Figure 4.28. PIXE photographs showing the distribution of elements (ppm) in quartz hosted fluid inclusions: 46-1a = hypersaline fluid inclusion in a stage 8 vein from a mid level in the Sur-Sur Tourmaline Breccia.

4.3.10 Discussion

The new fluid inclusion data generated from the Río Blanco and Sur-Sur sectors confirm the findings of Vargas et al. (1999) in La Americana and Sur-Sur with regards the homogenisation temperatures and salinity of fluids that precipitated quartz in the breccia cement (Figs. 4.9, 4.13b and 4.15b). This study has expanded on the previous findings with more detailed temporal and spatial constraints on fluid compositions.

For all paragenetic stages analysed in this study, the homogenisation temperatures (T_h), salinities, freezing temperatures (T_f), eutectic temperatures (T_e) and final ice melting temperatures (T_m) are similar. The greatest variation of values was measured in the quartz breccia cement (131->600°C; 0-69 wt.% NaCl equivalent), where copper grades are highest. Type i, liquid-rich fluid inclusions generally homogenise at moderate temperatures (200-450°C) and occur in secondary trails. There were no liquid-rich fluid inclusions that could be identified confidently as primary. Homogenisation temperatures for type iii, vapour-rich fluid inclusions were generally above 380°C, and in some cases did not homogenise at 600°C in breccia cements. Breccia cement type ii fluid inclusions have similar homogenisation temperatures to the vapour-rich fluid inclusions. Coexisting high temperature vapour-rich and hypersaline inclusions were only trapped in the breccia cement. In contrast, type i inclusions represent the entrapment of low-density waters within the breccia column. These waters could be magmatically derived, or alternatively, could be from an influx of external (meteoric?) water. Source(s) of water will be tested further in Section 4.4 using O/D isotopes.

Pressure/depth estimates

Fluid inclusions with similar (within 15°C) homogenisation temperatures of halite and vapour can be used to estimate confining pressures from the H_2O-NaCl phase diagram (Bodnar et al, 1985; Fournier, 1999). In the temperature versus pressure diagram in Figure 4.29, modified from Muntean and Einaudi (2001), depths are shown assuming densities of 1 g/cm^3 hydrostatic pressure and 2.5 g/cm^3 for lithostatic pressures. The brittle-ductile transition is plotted at 400°C with a strain rate assumed to be 10^{-14} sec^{-1} (Fournier, 1987; Muntean and Einaudi, 2001). Within the two-phase gas + liquid (G + L) field, contours of constant NaCl wt.% dissolved in the gas and liquid are shown. To determine an estimate of pressure, and therefore depth of formation, homogenisation temperatures and salinities have been plotted (Fig. 4.29). The data table showing estimated pressures and depths of formation are shown in Table 4.9. The uncertainty of this method is approximately 100-200 bars (Muntean and Einaudi, 2001). The validity of the pressure/depth data is challenged by the 100-200 bar error placed on individual pressure estimates. The data field on Figure 4.29 below 200 bars is placed in doubt when the error is considered.

Table 4.9. Quartz-hosted, type ii fluid inclusions used for minimum pressure/depth estimates in the Río Blanco and Sur-Sur sectors. Depth below present surface, paragenetic stage, fluid inclusions type, vapour and salt dissolution temperatures, salinity, estimated pressure (bars) and the estimated minimum lithostatic and hydrostatic depths are shown. The estimated pressures are derived from Figure 4.29.

Fi sample	depth below surface (m)	stage	Fi type	T_hV	T_hD_{halite}	salinity	Δ in T_h	mean T_h	P (bars)	$Depth_{lith}$ (m)	$Depth_{hyd}$ (m)
Rio Blanco											
259iib	856	2	iia	242.8	252	34.8	9.2	247.4	31	120	300
259iic	856	2	iia	265.8	258.1	35.1	7.7	261.95	44	180	400
246kiic	1067	3	iic	523.4	514.8	58	8.6	519.1	368	1500	3600
354iik	454	3	iic	551.5	568.1	64.5	16.6	559.8	355	1490	3500
240eiia	835	3	iia	421.2	427.3	48.6	6.1	424.25	223	950	2250
155iid	690	3	iic	323.4	315.9	39.1	7.5	319.65	86	350	900
377iic	573	8	iic	279.6	273.5	36.1	6.1	276.55	56	220	550
239jiib	800	8	iia	294.4	287.1	37	7.3	290.75	59	260	620
Sur-Sur											
123aiig	200	3	iia	479	477.3	53.8	1.7	478.15	305	1300	3050
62biic	1282	3	iia	310.1	297.8	37.8	12.3	303.95	74	310	790
224biid	1051	3	iia	323.2	328.1	40	4.9	325.65	96	390	950
224biim	1051	3	iia	324.8	328.1	40	3.3	326.45	97	395	975
lgs50iik	275	3	iia	380.1	371	43.5	9.1	375.55	140	600	1400
190iic	217	3	iia	269.8	268.6	35.8	1.2	269.2	48	200	420
190iir	217	3	iia	330.4	328.7	40	1.7	329.55	100	400	1000
490iig	177	3	iia	298.8	288.4	37.1	10.4	293.6	67	270	690
218biib	1346	8	iia	214.6	211.5	32.5	3.1	213.05	9	50	100
218biic	1346	8	iia	311.8	316.2	39.1	4.4	314	80	320	820
7iig	425	8	iia	270.6	274.4	36.2	3.8	272.5	47	200	420
7iik	425	8	iia	442.4	439.2	49.8	3.2	440.8	242	1000	2400

Stage 2 quartz veins in the Don Luis sector yielded minimum pressure estimates of 31 to 44 bars corresponding to minimum lithostatic depths between 180 m and 120 m, and minimum hydrostatic depths of 400 m to 300 m (Table 4.9). The inclusions used for this analysis were secondary and if 100-200 bars of error are placed on the data, these depths are most likely not representative of the original depths at which these veins formed given the sample was collected at a present-day depth of 856 m.

Fluid inclusions from stage 3 (Río Blanco Magmatic Breccia and Sur-Sur Tourmaline Breccia) quartz cement yielded minimum pressure estimates between 48 and 368 bars corresponding to minimum lithostatic depths between 1500 m and 200 m, and minimum hydrostatic depths from 3600 m to 420 m (Table 4.9). This wide pressure and depth range may relate to dramatic pressure fluctuations during and after catastrophic brecciation. The average depth estimates for the Río Blanco Magmatic Breccia (lithostatic = 1073 m and hydrostatic = 2563 m) are deeper than those for the Sur-Sur Tourmaline Breccia (lithostatic = 483 m and hydrostatic = 1159 m). The depth estimates in the current study for the Sur-Sur Tourmaline Breccia correlate well to the minimum depth estimates of Vargas et al. (1999) and Holmgren et al. (1988) for the Tourmaline Breccia and Donoso Breccia, respectively. However, the minimum depth estimate of the potassic-altered Río Blanco Magmatic Breccia was approximately 1 km deeper than the Sur-Sur Tourmaline Breccia. Present-day depths are up to 1282 m and 1067 m for the Río Blanco Magmatic Breccia and Sur-Sur Tourmaline Breccia, respectively (Table 4.9). This suggests a lithostatic formation depth of 200 m and a hydrostatic formation depth of 2300 m below the palaeo-surface. This indicates that

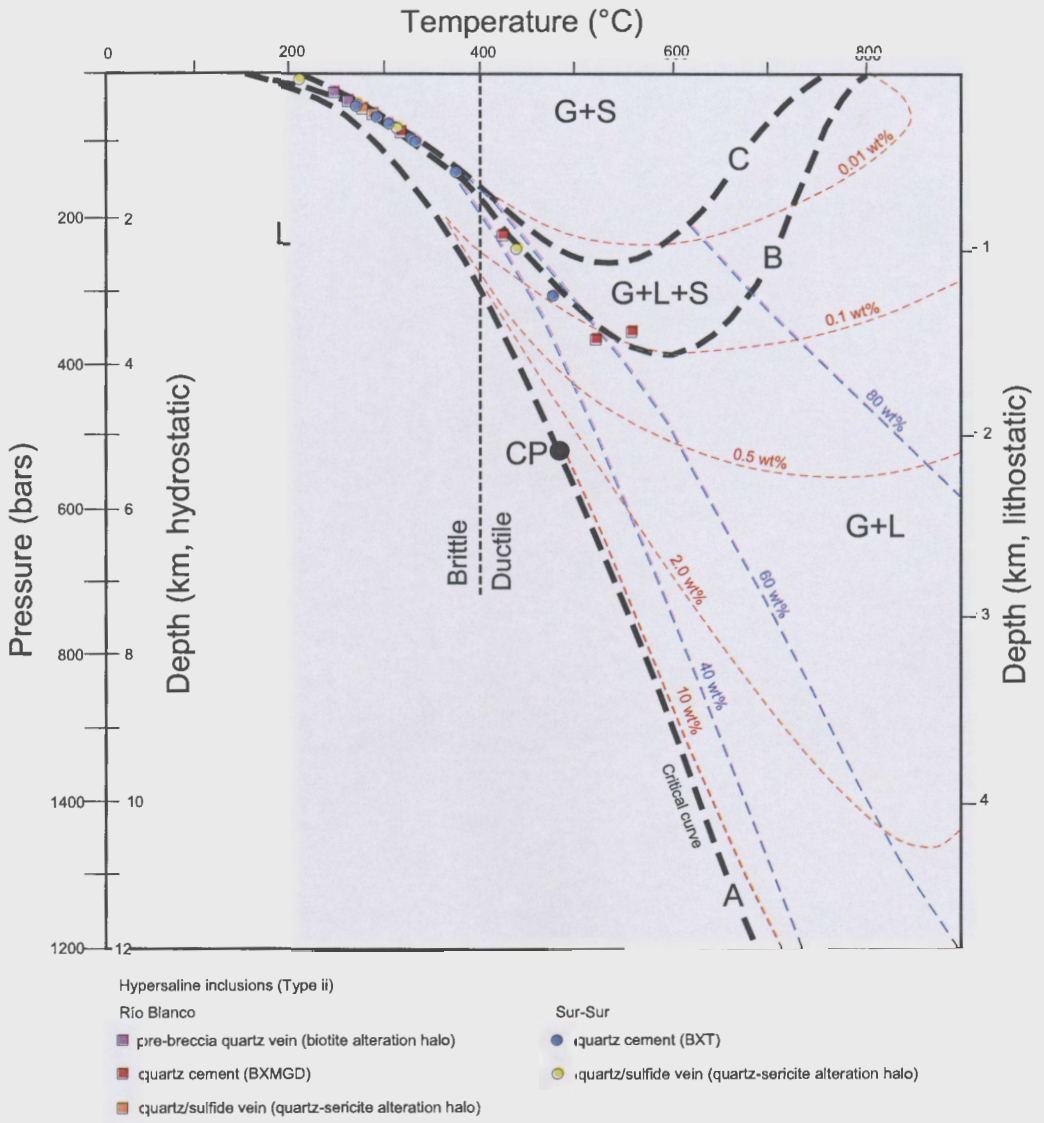

Figure 4.29. Temperature versus depth diagram in the NaCl-H_2O system, based on Bodnar et al. (1985), Fournier (1999) and modified from Muntean and Einaudi (2001). The diagram shows the predominance fields for liquid (L), gas + liquid (G+L) and gas + halite (G+S). Curve A represents the boiling point curve for 10 wt.% NaCl, with the critical point at CP. Curve B separates the G+L field from a three phase transitional field (G+L+S) for the system NaCl-H_2O. Curve C is the liquid saturation curve for the NaCl-KCl-H_2O system, where Na/K ratios are in equilibrium with albite and K-feldspar. Contours of constant NaCl (wt.%) in the G+L field are shown for liquid (blue dash lines) and gas (red dash lines). The vertical dashed line at 400°C is the approximate temperature of the brittle-ductile boundary. The diagram shows the estimated minimum depths of trapping for fluid inclusions in the Río Blanco and Sur-Sur sectors. See Table 4.9 for sample locations and paragenetic stage.

up to approximately 1 km of erosion has occurred since breccia formation.

Fluid inclusions from stage 8 veins collected from the Río Blanco sector yielded minimum pressure estimates between 56 and 59 bars corresponding to minimum lithostatic depths between 260 m and 220 m, and minimum hydrostatic depths from 620 m to 550 m (Table 4.9). If 100-200 bars of error are placed on the data, these depths are most likely not representative of the original depths at which these veins formed given the sample was collected at a present-day depth of 1346 m.

Fluid inclusions from stage 8 veins collected from the Sur-Sur sector yielded minimum pressure estimates between 9 and 242 bars corresponding to minimum lithostatic depths between 1000 m and 50 m, and minimum hydrostatic depths from 2400 m to 100 m (Table 4.9). This large pressure difference in stage 8 veins at Sur-Sur compared to Río Blanco may reflect greater pressure fluctuations during quartz deposition at Sur-Sur. Furthermore, the large pressure differences between stage 2 and 8 veins and the breccias may be a reflection of the process for vein formation as opposed to breccia formation, where much larger changes in fluid pressure are required.

Fluid compositions

Vargas et al. (1999) documented that many hypersaline and liquid-rich fluid inclusions had eutectic temperatures below -35°C, suggesting the presence of abundant Ca, Mg, or Fe as well as Na and K chloride in solution. Their inference is supported by the eutectic temperatures and PIXE data generated in the current study. Eutectic temperatures below -35°C are common in quartz from the mineralised breccia cements in Río Blanco and Sur-Sur, suggesting that salts other than those containing Na and K chlorides also occur. The PIXE data reveal high concentrations of Fe and Mn in addition to K.

Fluid mixing

Paragenetic stages that contain complete salinity arrays, permissive of fluid mixing, are stages 2, 3, 7 and 8 (Figs. 4.13b, 4.13f, 4.14b, 4.14e, 4.14f, 4.15g, 4.15l, 4.17b, 4.17g, 4.17l, 4.18a, 4.18b and 4.18c). Those stages where data are clustered with two separate populations, and do not appear to have mixed are 4, 6 and 9 (Figs. 4.13k, 4.14c, 4.14d, 4.14g, 4.15b and 4.16b,). The range of salinities from fluids in the Tourmaline Breccia quartz cement are inferred to relate to mixing of brines and low salinity water from deep to shallow levels (Fig. 4.22). At depth, the two end member fluids have distinct compositions in terms of salinity. At mid levels, there is a complete salinity spectrum, interpreted here to indicate that mixing has occurred between these two fluids. At shallow levels, the fluids are also mixed and the hypersaline brine is well represented in terms of abundance, coincident with the zone of highest hypogene copper grade in the breccia column.

Walshe et al. (1996) reported that dilution of brine in the Mt Bischoff Sn deposit resulted from vapour phase condensation, generally in the deeper parts of the system. This type of dilution may have also occurred in the deep to mid parts of the Río Blanco system, where liquid-rich fluid inclusions dominate and salinities are low (Fig. 4.21). Furthermore, at higher levels in the two-phase part of the system, mixing with shallow groundwaters can also cause dilution (Walshe et al. 1996). This may have occurred at Sur-Sur, where a relatively larger population of low salinity, liquid-rich fluid inclusions occur at high elevations in the Tourmaline Breccia quartz cement (Fig. 4.22).

Evidence for phase separation and implications for ore formation

Phase separation (boiling) is a commonly reported feature when fluids circulate at high temperature in a low-pressure environment (Bodnar et al., 1985). Furthermore, because phase separation is a potential mechanism for mineral deposition, fluid inclusion evidence for phase separation has been proposed as an exploration tool (Bodnar et al., 1985). The single most common evidence for the entrapment of phase-separated fluids is the co-existence of liquid and vapour-rich fluid inclusions (Burnham, 1979; Roedder, 1984, Bodnar et al, 1985). Coexisting hypersaline and vapour-rich fluid inclusions are also textural evidence for phase separation from a supercritical fluid (Bodnar et al., 1985). Such transitions may occur if pressure conditions changed from lithostatic to hydrostatic, which may be caused by fault rupture and/or catastrophic brecciation (e.g. Fournier, 1999). Besides faulting, rapid uplift and erosion and/or glacial retreat may have caused pressure fluctuations sufficient to trigger phase separation.

Type ii inclusions are high salinity brines most likely of magmatic-hydrothermal origin. Type iii inclusions are gases, indicating phase separation has occurred in the breccia bodies. Henley and McNabb (1978) and Bodnar et al. (1985) agree that brines and vapour form when a supercritical magmatic-hydrothermal fluid splits into two phases when confining pressures and/or temperatures decrease. Alternatively, co-existing brines and gases can be released directly from a crystallising magma if it is emplaced at shallow crustal depths (Bodnar et al., 1985). Either way it is likely that the type iii fluid inclusions are of magmatic-hydrothermal origin.

Type i, liquid-rich and type iii, vapour-rich fluid inclusions in secondary trails coexist in the Río Blanco and Sur-Sur systems (Fig. 4.19a, b). This is interpreted to indicate the separation of a low-density gas from a low salinity liquid within the rock column. Evidence for coexisting hypersaline and vapour-rich fluid inclusions were preserved only at high elevation in the Río Blanco and Sur-Sur systems (Fig. 4.19c, d, e). This scenario may be explained by phase separation of a moderately saline supercritical fluid into a low-density vapour and small proportions of brine (e.g. Henley and McNabb, 1978). Initial phase separation of a moderately saline aqueous liquid at depth would have produced large volumes of low-density vapour and small volumes of dense brine. This gas

phase fluid would have migrated upwards through the breccia column, whereas the dense brine would have been more recalcitrant, and may have at least in part been carried as aerosol particles. Continued input of magma at may have helped to drive larger volumes of brine up through the breccias. Alternatively, dilution via mixing with low salinity water may have changed the density of the brine to the point where it could buoyantly ascend through the breccia.

4.4 Oxygen Isotopes

4.4.1 Introduction

Oxygen/hydrogen (O/H) isotope geochemistry allows us to evaluate fluid sources (e.g. magmatic versus meteoric water) for hydrothermal minerals. Specifically, in porphyry copper environments, these data are used to evaluate whether meteoric water played a role in ore genesis and associated alteration. Controversy surrounds this issue (e.g. Taylor, 1974; Sheppard et al., 1971; Sheppard and Gustafson, 1976; Taylor, 1997; Hedenquist et al., 1998; Watanabe and Hedenquist, 2001), with early workers advocating an important component of meteoric convection, and later workers favouring an orthomagmatic model for ore formation.

Previous investigations of O/H isotope systematics have revealed contradictory results among different porphyry deposits, even by different workers on the same deposit. Sheppard et al. (1969, 1971) and Taylor (1974, 1997) concluded that the fluids responsible for phyllic alteration are dominated by meteoric water, based on O/H isotope data from North American porphyry copper deposits. In contrast, Kusakabe et al. (1984, 1990) suggested that phyllic alteration assemblages at the El Teniente and Río Blanco deposits in Chile are magmatic in origin.

At El Salvador, Gustafson and Hunt (1975) concluded that the evolution from early K-silicate to late sericite alteration stages correlated with a transition from magmatic fluid at lithostatic pressure to a dominance of meteoric water at hydrostatic pressure. Sheppard and Gustafson (1976) supported this conclusion with their interpretation of O/H isotope compositions. Kusakabe et al. (1990) contradicted their conclusions arguing for a magmatic origin for the fluids that formed late sericite at El Salvador. Watanabe and Hedenquist (2001) supported the magmatic fluid model with their study of the andalusite-muscovite-diaspore assemblage at El Salvador.

Several O/D isotopic studies of porphyry copper deposits have shown that sericite formed from a water with a 25-50 percent meteoric component, in contrast to the end-member magmatic water

responsible for hydrothermal biotite alteration (e.g. Hedenquist et al., 1998). Based on O/D data and geochronology, Hedenquist et al. (1998) concluded from the Lepanto-Far South East deposit that K-silicate and advanced argillic alteration formed at the same time, with the latter originating from magmatic vapour condensing into meteoric water.

4.4.2 Previous work

Kusakabe et al. (1984; 1990) documented non-paragenetically constrained oxygen and hydrogen isotope data from various alteration zones within the Río Blanco orebody (Table 4.10). Oxygen isotope ($\delta^{18}O$ SMOW) compositions at Río Blanco were found to be between +5 and +10.7‰ for quartz and anhydrite in veins from potassic, quartz-sericite and propylitic alteration zones. Hydrogen isotope (δD) compositions have a range from -55 to -32‰ for biotite and sericite from potassic, quartz-sericite and propylitic alteration zones at Río Blanco (Table 4.10). Kusakabe et al. (1984; 1990) calculated fluid compositions using fractionation factors from Matsuhisa et al. (1979), Chiba et al. (1981) and Suzuoki and Epstein (1976) for quartz, anhydrite and biotite (+sericite), respectively based on the above data in combination with temperature estimates derived from invalid sulfate-sulfide geothermometry.

Because the temperature estimate used by Kusakabe et al. (1984; 1990) are considered to be inadequate, based on non co-precipitated sulfur-bearing mineral phases, anhydrite and biotite O/D data from them were recalculated using the anhydrite-H_2O, biotite-H_2O and muscovite-illite-H_2O fractionation factors of Chiba et al. (1981), Bottinga and Javoy (1973) and Sheppard and Gilg (1996), A range of compositions have been calculated, allowing for a ±100°C error in temperature estimates from the data of Kusakabe et al. (1984;1990). The re-calculated $\delta^{18}O_{fluid}$ values resulted in a range between -0.12 and 8.18 for quartz and anhydrite, and δD_{fluid} values between -61.42 and -83.36 for biotite and sericite mineral separates.

The recalculated fluid values have been plotted in Figure 4.30. The samples associated with potassic and quartz-sericite alteration plot within the magmatic water box defined by Taylor (1974). The propylitic-altered sample plots to the left of the magmatic water box toward the meteoric water line.

Table 4.10. $\delta^{18}O_{fluid}$ values calculated from temperature estimates by Kusakabe et al. (1984) based on sulfur isotopes of co-existing sulfide and sulfate minerals and recalculated fractionation factors. The current study precludes the use of geothermometry from sulfide and sulfate data due to precipitation of these sulfur-bearing mineral species at different stages of breccia infill. The Kusakabe et al. (1984; 1990) hydrogen isotope fluid compositions are for OH-water (OH-bearing sericite and biotite) from fractionation factors documented in Suzuoki and Epstein (1976). The recalculated fractionation factors for anhydrite, biotite and sericite are from Chiba et al. (1981), Bottinga and Javoy (1973) and Sheppard and Gilg

Sample information			Altitude	Temp.	$d^{18}O$ (‰)			Recalculated $\delta^{18}O_{fluid}$ using H_2O, ±100°C		anhy-	dD (‰)			Recalculated δD_{fluid} using bt-H_2O and musc-illite (sericite), ±100°C		
No.	DDH	Site (m)	(m)	(°C)	qtz	anhy	$\delta^{18}O_{fluid}$	373°C	473°C	573°C	mineral	$\delta D_{mineral}$	δD_{fluid}	373°C	473°C	573°C
potassic zone								373°C	473°C	573°C				373°C	473°C	573°C
1	228	99.85	3073			7.7	6.65	4.73	6.65	7.94	biotite	-81	-51	-78.86	-78.62	-78.46
2	228	478.05	3075	473		7.2	6.15	4.23	6.15	7.44	biotite	-85.5	-55	-83.36	-83.12	-82.96
11	230	502.5	3081			7.5	6.45	4.53	6.45	7.74	biotite	-84.1	-54	-81.96	-81.72	-81.56
potassic-propylitic transitional zone								298°C	398°C	498°C				298°C	398°C	498°C
4	235	161				5	2.59	-0.12	2.59	4.32						
12	225	499.4	3083	398							biotite	-83.7	-44	-81.83	-81.49	-81.27
17	233	450.1	3076		9.5		5.4									
potassic-zone with quartz-sericite alteration								325°C	425°C	525°C				325°C	425°C	525°C
8	230	387	3079			7.7	5.83	3.45	5.83	7.38						
9	230	375.1	3079			8.1	6.23	3.85	6.23	7.78	sericite	-58.5	-32	-61.42	-59.64	-58.49
10	230	371.9	3079	425		7.8	5.93	3.55	5.93	7.48						
22	166A	361.2	3098								biotite	-70.8	-35	-68.82	-68.52	-68.33
23	166A	150.1	3083			8.5	6.23	4.25	6.63	8.18						
Quartz-sericite alteration zone																
5	234	353.2	3085	424		8.1	6.22									
5	234	353.2	3085		10.7		7.14									
Brecciated zone																
13	189	9.9	3072			0.6										
19	231	54.4	3072			5.5										
45					9.9											

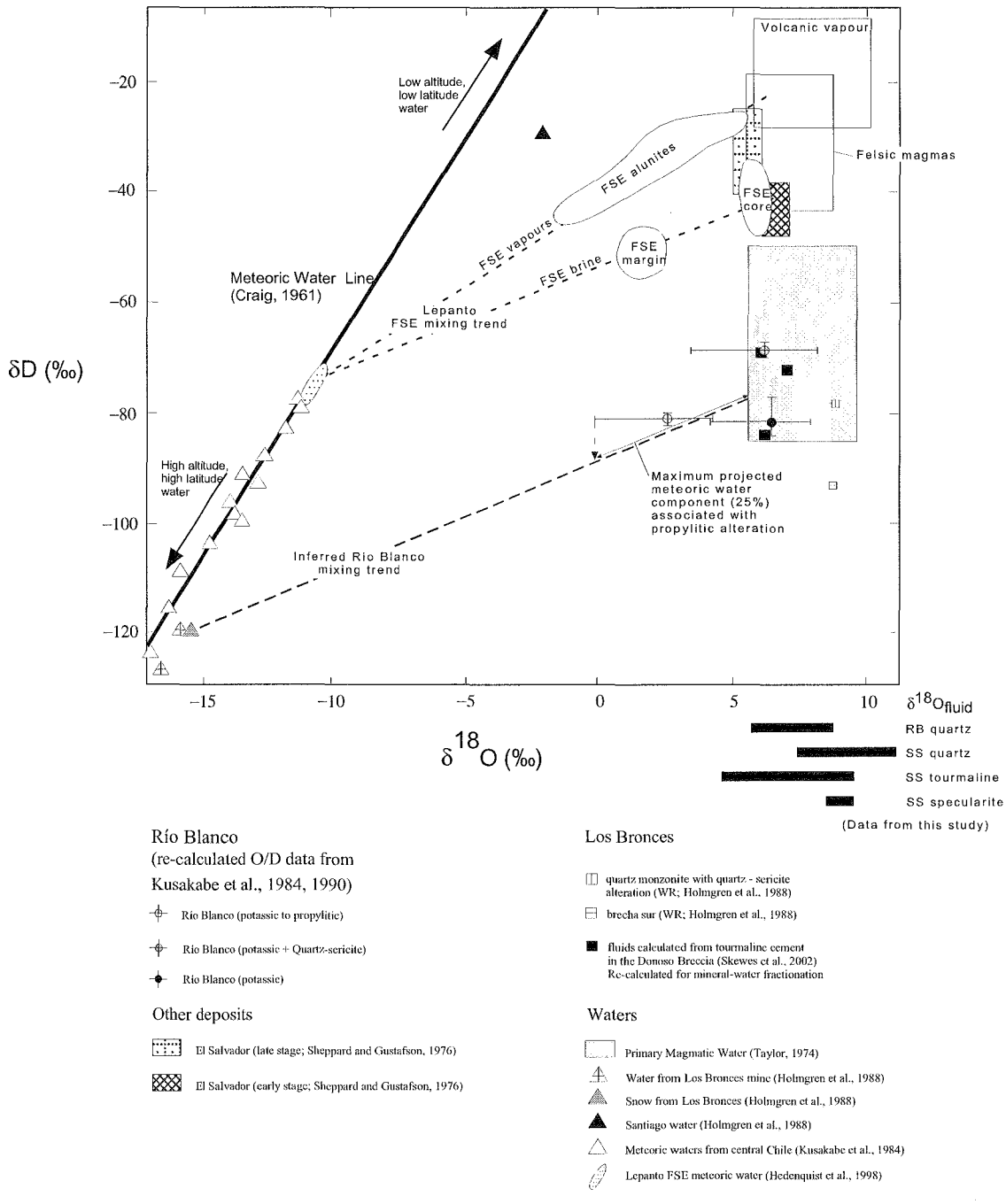

Figure 4.30. Pre-existing $\delta^{18}O$ and δD calculated fluid compositions (in per mil) from Río Blanco-Los Bronces, Lepanto Far South East, El Salvador and various meteoric waters collected proximal to the Río Blanco-Los Bronces deposit and localities in central Chile. The tourmaline data from Skewes et al. (2002) was re-calculated using the tourmaline-water fractionation equation of Kotzer et al. (1993). Río Blanco anhydrite and biotite data from Kusakabe et al. (1984; 1990) has been re-calculated using anhydrite-H_2O and biotite-H_2O fractionation factors from Chiba et al. (1981) and Bottinga and Javoy (1973), respectively. In addition, ±100°C error bars have been superimposed on the Río Blanco data points due to poor temperature constraints. Volcanic vapour, felsic magma boxes and Lepanto-Far South East data from Hedenquist et al. (1998). RB = Río Blanco, SS = Sur-Sur.

Kusakabe et al. (1984) proposed that hydrothermal fluids at Río Blanco were of magmatic origin throughout the evolution of the hydrothermal system. They suggested that their elevated δD_{fluid} values were produced by incursion of meteoric waters in the deposit periphery. However, deuterium enrichment cannot be explained by groundwater incursion, since meteoric waters of the studied area at the time of mineralisation-alteration had probably already been depleted in deuterium due to the uplift of the Andes (Kusakabe et al., 1990). Kusakabe et al. (1990) concluded that the progressive enrichment in deuterium toward the later stages might best be interpreted in terms of closed system evolution of the hydrothermal fluids exsolved from the emplaced porphyry stocks. An alternative is that the ~20 per mil range in δD values between the quartz-sericite altered sample and the potassic altered sample represents the separated vapour and the hypersaline liquid, respectively. Horita et al. (1995) documented experimental data that defines an ~20 per mil range between a phase separated vapour and a hypersaline liquid, and this was demonstrated by Hedenquist et al. (1998) for the Lepanto-Far South East deposit in the Philippines.

At Los Bronces, oxygen isotope ($\delta^{18}O_{mineral}$) compositions of quartz and tourmaline cement from the quartz-sericite altered Donoso Breccia at different elevations range from +6.9 to +12.0‰ (Skewes et al., 2002; Table 4.11). Hydrogen isotope ($\delta D_{mineral}$) compositions measured in tourmaline cement ranges between -73 and -95‰ (Table 4.11). These data were combined with the highest measured homogenisation temperatures of hypersaline fluid inclusions by Skewes et al. (2002) to calculate the O/D isotopic composition of the aqueous fluid that precipitated quartz and tourmaline. The calculated $\delta^{18}O_{fluid}$ composition is between +5.6 and +9.1‰, and the δD_{fluid} composition for tourmaline has a range between -68.3 and -84‰ (Table 4.11; Fig. 4.30). This data falls within the magmatic range depicted by Taylor (1974) and precludes the participation of a significant amount of meteoric water in the formation of the phyllic-altered Donoso Breccia (Skewes et al., 2002). They also concluded that magmatic fluids caused sericite alteration of clasts within the breccia column.

4.4.3 This study

The aim of this study is to determine if a component of meteoric water was present during quartz, tourmaline and/or specularite cementation in the Sur-Sur Tourmaline Breccia and quartz cementation in the Río Blanco Magmatic Breccia. Furthermore, it aims to determine if there is any spatial zonation in $\delta^{18}O_{fluid}$ in the Sur-Sur Tourmaline Breccia that can be related to copper grades and/or mineral and sulfur isotope zonation.

Quartz, tourmaline and specularite minerals were separated from the mineralised Sur-Sur Tourmaline Breccia and the Río Blanco Magmatic Breccia. The separates were submitted for $\delta^{18}O$ and δD analyses at the Commonwealth Scientific and Industrial Research Organisation (CSIRO) facility

Table 4.11. Measured $\delta^{18}O_{mineral}$, $\delta D_{mineral}$ and calculated $\delta^{18}O_{fluid}$, δD_{fluid} values for different vertical depths in the Los Bronces Donoso Breccia (cement and vein) from Skewes et al. (2002). Fluid values have been re-calculated for quartz-water, specularite-water and tourmaline-water for consistency with this study and because these minerals are not equilibrium with the breccia cement. Temperatures are from maximum homogenisation temperatures of liquid-rich fluid inclusions (T°C). Fractionation equations are listed in Appendix F2.

Sample information	Measured: $\delta^{18}O$ in minerals (per mil)			δD in minerals (per mil)	Ta	$\delta^{18}O_{fluid}$	δD_{fluid}
	Quartz	Tourmaline	Specularite	Tourmaline	(°C)	(calculated, per mil)	
Current surface							
	10.8				400 (inclusions)	6.74	
I.5-9.7 m (breccia matrix; ~3,674 m a.s.l.)			0.4		450 (qtz-hematite)	9.2	
		8.9		-81	400 (qtz-tourmaline)	6.02	-68.3
I.5-11.3 m (breccia matrix; ~3,672 m)	8.3				500 (inclusions)	6.02	
~210 m below the surface							
H5.5-194 m (breccia matrix; ~3,462 m)	10.6				560 (inclusions)	9.1	
H5.5-199.5 m (breccia matrix; ~3,465.5 m)	10.6				560 (inclusions)	9.1	
I.5-210 m (breccia matrix; ~3,467.3 m)	7.1				560 (inclusions)	5.6	
		7.9		-95	560 (inclusions)	6.22	-84
~410 m below the surface							
I.5-419.3 m (breccia matrix; ~3,264 m)	6.9				690 (inclusions)	6.61	
		8.3		-73	690 (inclusions)	6.89	-71.9
I.5-418.4 m (vein; ~3,265 m)	12				400 (inclusions)	7.94	

located in North Ryde. Analytical methods and standards used for oxygen isotope analyses are in Appendix F1. Unfortunately, logistical problems at the North Ryde laboratory prevented any deuterium analyses being completed. Consequently, only oxygen isotope data were received (Table 4.12). Furthermore, no Fe-oxides were observed in textural equilibrium with quartz and so no mineral pairs were available for oxygen isotope geothermometry.

4.4.4 Results

Río Blanco

Two samples of quartz cement from the Río Blanco Magmatic Breccia were separated for oxygen isotope analysis. The two samples chosen, 246k and 240e, were collected from DDH-450 (section XC-125), deep in the Río Blanco Magmatic Breccia at elevations of 2833 m and 3065 m, respectively (Table 4.12). The two samples also have contrasting copper grade, allowing a superficial assessment of the relationship between grade and oxygen isotope composition (Table 4.12). Measured $\delta^{18}O_{mineral}$ values for sample 240e (high-grade) range between 9.26 and 9.88‰ (n=3). Sample 246k (low-

Table 4.12. Oxygen isotope data for breccia cement minerals collected from the Río Blanco Magmatic Breccia and the Sur-Sur Tourmaline Breccia. Minerals analysed include quartz, tourmaline and specularite.Fluid compositions have been calculated by using mineral-water fractionation equations. Fractionation equations for fluid values are listed in Appendix F2.

sample	DDH	section	downhole	altitude	lithology	% Cu	mineral	fluid inclusion data (°C)	$\delta^{18}O_{mineral}$	$\delta^{18}O_{fluid}$
Rio Blanco										
240e	DDH-450	XC-125	115 m	3065 m	BXMGD	2.0% Cu	quartz	427.3	9.38	5.88
							quartz		9.88	6.38
							quartz		9.26	5.76
246k	DDH-450	XC-125	347 m	2833 m	BXMGD	0.39% Cu	quartz	523.4	10.72	8.77
							quartz		10.65	8.7
Sur-Sur										
VHG50a	DL-03	XC-50	56 m	4066 m	BXTGDCC	13.85% Cu	tourmaline	400	9.02	6.14
							tourmaline		8.24	5.36
							tourmaline		8.02	5.14
225c	TSS-22	XC-50	609 m	3046 m	BXTGDCC	0.65% Cu	tourmaline	400	7.51	4.63
							tourmaline		8.28	5.4
							tourmaline		7.73	4.85
492	DL-57	XC-40	86 m	4021 m	BXTGDCC	1.27% Cu	specularite	400	0.88	8.45
							specularite		-0.21	9.54
VIIG50d	DL-03	XC-50	58 m	4064 m	BXTGDCC	13.85% Cu	quartz	552.2	11.11	9.52
230b	DL-64	XC-50	25 m	4048 m	BT-BXTGDCC	2.88% Cu	quartz	372.9	14.66	9.97
							quartz		13.41	8.72
							quartz		14.11	9.42
524	DL-71	XC-70	99.5 m	4032 m	BXTGDCC	2.75% Cu	quartz	577	12.39	11.08
							quartz		12.83	11.52
							quartz		12.58	11.27
224b	TSS-22	XC-50	501 m	3153 m	BXTGDCC	0.73% Cu	quartz	498	9.7	7.39
							quartz		10.61	8.3
							quartz		10.23	7.92
226a	TSS-22	XC-50	730 m	2925 m	GDCC(T)	1.54% Cu	quartz	505.7	10.43	8.23
							quartz		10.51	8.31

grade) ranges between 10.65 and 10.72‰ (n=2). $\delta^{18}O_{fluid}$ compositions were calculated using the quartz-water fractionation equation generated by Matsuhisa et al. (1979) in combination with highest homogenisation temperatures of hypersaline fluid inclusions from quartz in the samples used (Table 4.12). The calculated $\delta^{18}O_{fluid}$ composition for sample 240e ranges between 5.76 and 6.38‰ and sample 246k ranges between 8.70 and 8.77‰ (Fig. 4.31). A histogram showing the total dataset of oxygen isotope fluid compositions of quartz, tourmaline and specularite for Río Blanco and Sur-Sur are shown in Figure 4.32.

Sur-Sur

A total of eight samples were chosen for oxygen isotope analysis in the mineralised Sur-Sur Tourmaline Breccia. Of the eight samples, five contained quartz cement; two contained tourmaline and one contained specularite (Table 4.12). These samples were collected over a 1.1 km vertical depth interval in the Tourmaline Breccia, through both high and low-grade zones (Table 4.12). Measured $\delta^{18}O_{mineral}$ values range between 9.7 and 14.66‰ (n=12) for quartz, 7.51 to 9.02‰ (n=6) for tourmaline and -0.21 and 0.88‰ (n=2) for specularite (Table 4.12).

Oxygen isotope fluid compositions for quartz, tourmaline and specularite were derived using fractionation calculations of these minerals with water from Matsuhisa et al. (1979), Kotzer et al.

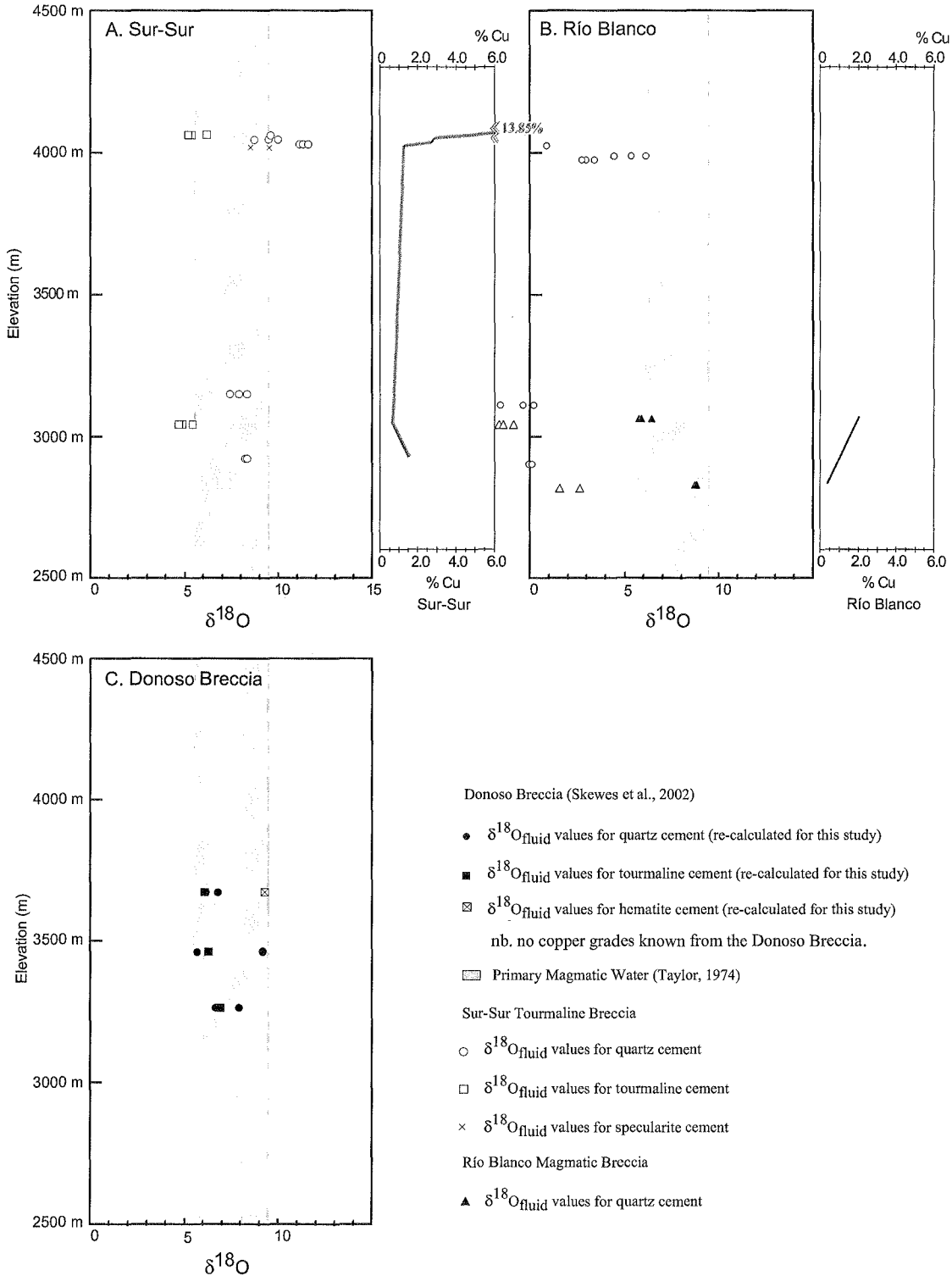

Figure 4.31. Oxygen isotope fluid values for quartz from the Río Blanco Magmatic Breccia and quartz, tourmaline and specularite from the Sur-Sur Tourmaline Breccia (this study), and quartz, tourmaline and hematite from the Los Bronces Donoso Breccia (Skewes et al., 2002). Copper grades for the individual samples are also plotted for the vertical section. The grey shaded area is the boundary of primary magmatic water as defined by Taylor (1974).

(1993) and Zheng and Simon (1991), respectively. Temperature estimates were obtained from maximum homogenisation temperatures of hypersaline fluid inclusions in quartz. However, for tourmaline and specularite, temperature estimates are less well constrained due to a lack of hypersaline fluid inclusions in these minerals. Both tourmaline and specularite cemented the Tourmaline Breccia void space before quartz precipitation and main-stage mineralisation. Consequently, a temperature of 400°C has been estimated for mineral deposition. This temperature has been chosen because Fournier (1999) estimated it to be that of steam and brine at the brittle-ductile transition, and it therefore should be an approximation of fluid temperature for the superheated gas in the breccia column immediately after brecciation. In addition, the maximum homogenisation temperature of a hypersaline fluid inclusion measured in another sample in the Tourmaline Breccia was 402.6°C (sample 62b; Section 4.3 - 'Fluid Inclusions').

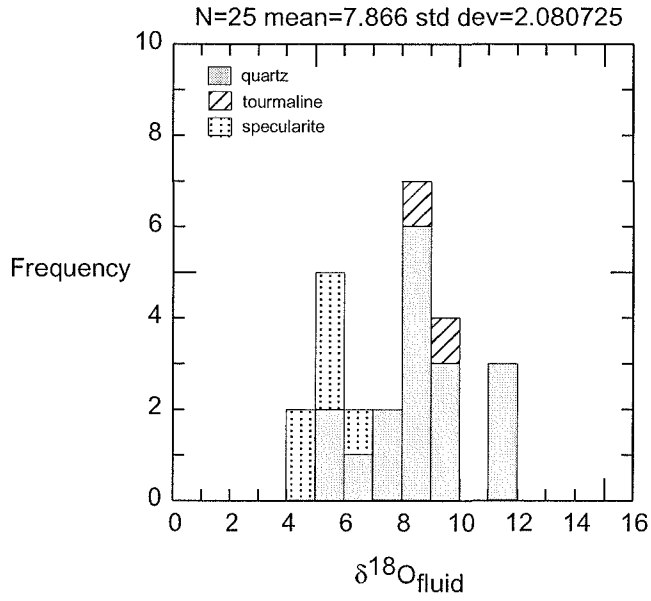

Figure 4.32. Histogram of calculated oxygen isotope fluid values for quartz, tourmaline and specularite from this study.

Calculated $\delta^{18}O_{fluid}$ compositions for quartz cement in the Tourmaline Breccia are from 7.39 to 11.52‰. $\delta^{18}O_{fluid}$ compositions for tourmaline cement in the Tourmaline Breccia range between 4.63 and 6.14‰, and between 8.45 and 9.54‰ for specularite (Table 4.12). These fluid compositions and those from the Donoso Breccia (Los Bronces) are plotted against depth and copper grade in Figure 4.31. The fluid compositions for the Donoso Breccia (Skewes et al., 2002) were recalculated using the same fractionation equations used in this study for consistency, i.e. quartz-water, tourmaline-water and hematite-water fractionation equations of Matsuhisa et al. (1979), Kotzer et al. (1993) and Zheng and Simon (1991), respectively.

Above 4000 m elevation in the Tourmaline Breccia, a dramatic increase in copper grade occurs (Fig. 4.31). This increase in copper grade is coincident with the greatest range of oxygen isotope fluid compositions from all three minerals analysed (5.14-11.52‰).

4.4.5 Discussion

The oxygen isotope data from breccia cement minerals in the Río Blanco Magmatic Breccia and Sur-Sur Tourmaline Breccia are consistent with a dominantly magmatic fluid source. These results agree with previous work by Kusakabe et al. (1984; 1990), Holmgren et al. (1988) and Skewes et al. (2002) that the mineralising fluids in the Río Blanco-Los Bronces ore deposit complex are dominantly magmatic in origin in the potassic and phyllic alteration assemblages.

The study by Kusakabe et al. (1984; 1990) is limited by the poor temperature constraints obtained from sulfur isotope geothermometry using co-existing sulfide and sulfate minerals. This approach is problematic because textural evidence from the current study show that sulfide and sulfate minerals in the Río Blanco system did not co-precipitate (e.g. Figs. 3.5c-f and 3.9a-b). Therefore the $\delta^{18}O_{fluid}$ compositions generated by Kusakabe et al. (1984; 1990) at Río Blanco are poorly constrained. Recalculation of the Kusakabe et al. (1984; 1990) dataset using the appropriate fractionation factors and an error of ±100°C indicates that a meteoric water component of up to 25% could have been present during mineralisation and alteration along an inferred mixing trendline with Los Bronces snow (Fig. 4.30). At the Lepanto Far South East deposit, such mixing trends are defined by vapour (e.g. alunite) and brine (e.g. biotite) mineral species and indicate a maximum proportion of 20-30% local meteoric water (Hedenquist et al., 1998).

Through the exposed vertical interval of the Sur-Sur Tourmaline Breccia, there is a change upwards from tightly clustered $\delta^{18}O_{fluid}$ compositions to more scattered in the higher altitude part of the breccia column (>4000 m elevation). This is coincident with high copper grades and may be due to mixing with another water source, whether it be igneous rock-equilibrated meteoric water or a magmatically-derived vapour phase. Irrespective of possible mixing, the O/D data supports a predominance of magmatic-hydrothermal fluids in the mineralised breccias at Río Blanco.

4.5 Sulfur Isotopes

4.5.1 Introduction

Sulfur isotope geochemistry has greatly improved our understanding of ore deposit genesis and has helped in the development of both ore deposit and exploration models (e.g. Talyor, 1986, Ohmoto and Goldhaber, 1997). The analysis of sulfur isotopes can provide information about;

- The source(s) of sulfur
- Physico-chemical conditions at the site of mineral deposition;
- Temperature of mineral deposition;
- Chemical composition and evolution of mineralising fluids;
- Mechanisms of sulfide mineral deposition.

In conjunction with a favourable structural architecture, effective chemical processes are required for high-grade ore deposition. If fluids evolve down steep physico-chemical gradients along their flow paths, then high-grade ore can be precipitated. Base metal solubilities in hydrothermal fluids are determined by the prevailing temperature, pH, redox, pressure, salinity and activity of H_2S. Changes in these extensive variables can occur through physical processes such as fault rupturing, water-rock interaction, phase separation and/or mixing with other fluids that have contrasting chemistries and/or temperatures.

Economic geologists commonly combine petrographic studies with stable isotopic analyses to understand fluid evolution in hydrothermal systems. The sulfur isotopic compositions of sulfide minerals can vary due to changes in the prevailing physico-chemical conditions, particularly redox, when the mineralising fluid is oxidised $m SO_4 = m H_2S$ (Ohmoto and Goldhaber, 1997). Limited fractionation can also occur due to temperature changes, and variable sulfide $\delta^{34}S$ compositions may result when two or more isotopically distinct sulfur sources are mixed (Ohmoto and Rye, 1979; Ohmoto and Goldhaber, 1997). In porphyry copper systems, sulfide minerals typically have near-zero $\delta^{34}S$ values (Ohmoto and Rye, 1979), although strongly negative $\delta^{34}S$ values have been reported from porphyry systems associated with oxidising hydrothermal fluids (e.g., Goonumbla, Heithersay and Walshe, 1995). For more details concerning sulfur isotope geochemistry, refer to Jensen (1959), Fauré (1977), Valley et al. (1986), Ohmoto and Rye (1979), Ohmoto (1986), Taylor (1987), Kyser (1987) and Ohmoto and Goldhaber (1997).

4.5.2 Previous work

The sulfur isotope systematics of the El Teniente and Río Blanco deposits were investigated between 1979 and 1983 in a collaborative program between the Geological Society of Japan and CODELCO-Chile. The objective of this research was to clarify the origin of the hydrothermal fluids that were responsible for mineralisation and associated alteration at El Teniente and Río Blanco. Results were presented in Kusakabe et al. (1984) and Kusakabe et al. (1990). They collected samples from the Río Blanco sector and classified them on the basis of their alteration assemblage, which Kusakabe et al. (1984) referred to as the 'potassic-zone', 'potassic-propylitic transitional zone', 'potassic-zone with quartz-sericite alteration', 'quartz-sericite alteration zone', 'brecciated zone' and a 'sericite zone within the Dacite Porphyry'. Sulfur isotope analyses were

performed on chalcopyrite, pyrite and anhydrite mineral separates from vein assemblages with no paragenetic constraints provided. Data from Kusakabe et al. (1984) are summarised in Table 4.13.

Table 4.13. Table showing $\delta^{34}S$ isotope compositions generated on anhydrite, chalcopyrite and pyrite in different alteration zones in the Río Blanco sector. Modified from Kusakabe et al. (1984).

Sample information			$\delta^{34}S$ (‰)		
No.	DDH	Site (m)	Anhy	Cpy	Py
Potassic zone					
1	228	99.85	12.1		
2	478.05	12	-1.3	-1	
3	467.16	-3.9			
11	230	502.5	11	-0.4	
Potassic-propylitic transitional zone					
4	234	161	11.5	-3.5	
12	225	499.4	-2.8		
17	233	450.1	-0.7	-0.8	
Potassic zone with quartz-sericite alteration					
8	230	387	11.8	-2.1	
9	375.1	12	-2.9	-1.6	
10	371.9	11.9	-2.1		
16	233	129.4	10.6	-2.1	
22	166A	361.2	12.2	-1.6	-1.1
23	150.1	12.2	-2.5		
Quartz-sericite alteration zone					
5	234	353.2	13.4	-1.4	
20	231	251.2	-0.7		
21	433.1	-0.7			
Brecciated zone					
13	189	9.9	11.8	0	
18	231	59.6	11.5	-2.4	
19	54.4	12.6	-2.5		
n		14	16	6	
mean		11.9	-1.9	-1.1	
range	2.8	3.9	0.9		
std. dev.	0.7	1.11	0.3		

Kusakabe et al. (1984) found that the $\delta^{34}S$ values of anhydrite show insignificant variation through different alteration zones in the Río Blanco system (11 to 13.4 ‰). However, $\delta^{34}S$ sulfide compositions revealed greater degrees of variation in the potassic zone (-0.4 to -3.9 ‰) and propylitic zone (-0.7 to -3.5 ‰) and less variation between compositions in the quartz-sericite zone (-0.7 to -2.9 ‰; Table 4.13).

Kusakabe et al. (1984) used sulfur isotope geothermometry (e.g. Ohmoto and Rye, 1979, Ohmoto and Lasaga, 1982) to calculate temperatures based on the isotopic compositions of co-existing anhydrite and chalcopyrite (Fig. 4.33). Calculated temperatures are highest and $\Delta\delta^{34}S$ values are lowest for samples from the potassic zone. The potassic-propylitic assemblage has the lowest temperatures and highest $\Delta\delta^{34}S$ values. Kusakabe et al. (1984) suggested that temperatures decreased systematically outward from the potassic-zone. Kusakabe et al. (1984) estimated a bulk sulfur composition of +7.6 ‰ for Río Blanco.

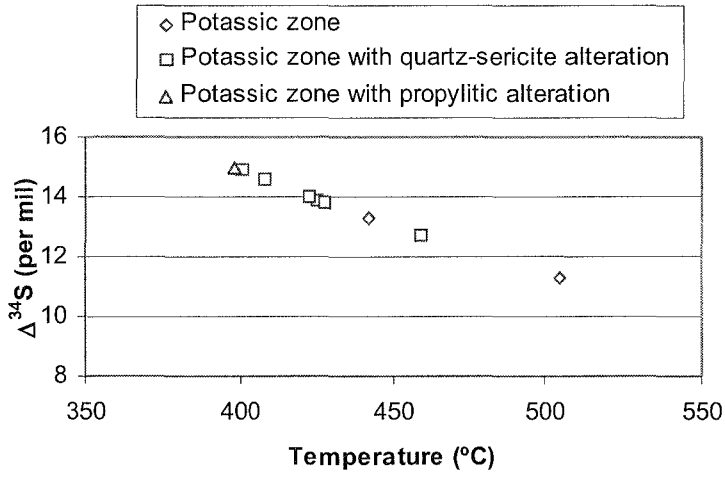

Figure 4.33. Calculated temperatures versus the $\delta^{34}S$ for co-existing sulfide-sulfate pairs through different alteration zones at Río Blanco. Data from Kusakabe et al. (1984).

A limited number of sulfur isotope analyses of sulfides and sulfates were obtained by Holmgren et al. (1988) from three of the Los Bronces breccias. The sulfide $\delta^{34}S$ values are between -4.8 and -0.49 ‰ (Table 4.14; Fig. 4.34). The most negative value was collected from the highest altitude sample (3,946 m asl) in the Infiernillo Breccia. Anhydrite compositions varied between 9.90 and 17.84 ‰ (Table 4.14; Fig. 4.34).

Table 4.14. Sulfur isotope data from Los Bronces breccias (Holmgren et al., 1988).

sample	mineral	drillhole	elevation (m asl)	lithology	$\delta^{34}S$
1	pyrite	GG 10.5	3,946	Infiernillo Breccia	-4.81
2	pyrite	J-4.5	3,754	Donoso Breccia	-1.18
3	anhydrite	H-5.5	3,462	Donoso Breccia	9.90
4	chalcopyrite	H-5.5	3,462	Donoso Breccia	-0.79
5	pyrite	H-5.5	3,462	Donoso Breccia	-1.61
6	chalcopyrite	H-5.5	3,269	Donoso Breccia	-1.13
7	pyrite	H-5.5	3,269	Donoso Breccia	-1.30
8	pyrite	C-12.0	3,774	quartz monzonite	-0.18
9	anhydrite	D-6.5	3,228	Central Breccia	17.14
10	chalcopyrite	D-6.5	3,228	Central Breccia	-0.97
11	pyrite	D-6.5	3,228	Central Breccia	-0.47

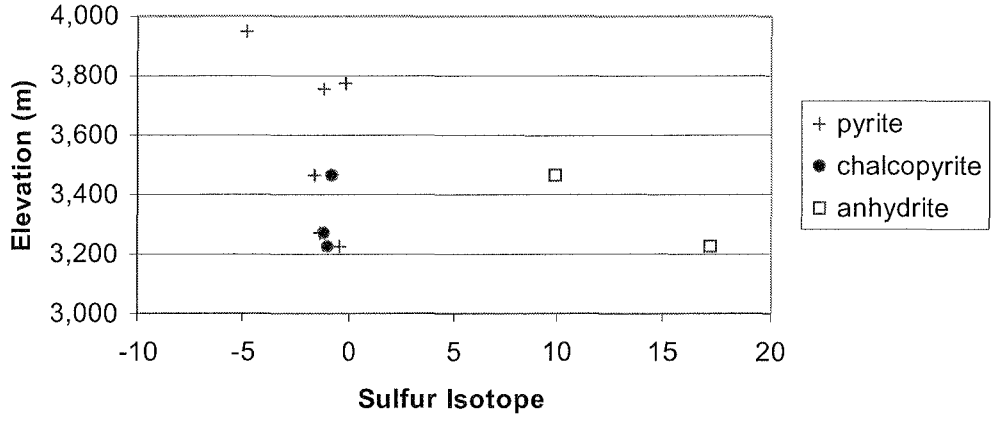

Figure 4.34. Sulfur isotope compositions of sulfide and sulfate minerals plotted against depth in Los Bronces breccias (Holmgren et al., 1988).

4.5.3 This study

This sulfur isotope investigation aims to obtain information about the prevailing physico-chemical conditions during sulfide deposition, to constrain how the compositions of the mineralising fluids evolved both spatially and temporally and to determine if isotopic variations correlate with high-grade copper zones in the breccia cements at Río Blanco and Sur-Sur. Specifically, sulfide and sulfate minerals were collected and analysed to evaluate:

- The sulfur isotope composition of the hydrothermal fluids within discrete, well-constrained paragenetic stages;
- The source(s) of sulfur for each paragenetic stage;
- The temperatures of mineral deposition;
- Whether any sulfur isotope zonation occurs spatially within the breccias; and
- Whether any insights into ore forming process can be obtained from this data.

Sulfide and sulfate minerals analysed include chalcopyrite, pyrite, bornite, molybdenite, anhydrite and gypsum. Samples chosen for this analysis were collected from two sections in the Sur-Sur sector (section XC-50SS and longitudinal section D-D' through the Tourmaline Breccia) and one section through the Río Blanco sector (XC-130RB). It should be noted that during this study, no coexisting sulfide/sulfate or sulfide/sulfide minerals were observed.

4.5.4 Methods

The sulfur isotope compositions of sulfides have been determined using conventional (hand-drill) techniques for coarse-grained sulfides (Robinson and Kusakabe, 1975), and the laser ablation method for fine-grained sulfides (100-300 μm; Huston et al., 1993). Conventional sulfur isotope analyses were performed on drilled sulfide mineral separates. These separates were combusted with excess Cu_2O in vacuo to produce SO_2 (Robinson and Kusakabe, 1975), and the sulfur gas separated to determine the $^{34}S/^{32}S$ ratios. An analytical uncertainty of ±0.1‰ is estimated from internal standards of homogeneous galena from Broken Hill ($\delta^{34}S$ = 3.4‰) and Rosebery ($\delta^{34}S$ = 12.4‰) run with an SO_2 reference gas of $\delta^{34}S$ approximately equal to CDT. These internal standards were calibrated against international sphalerite standards IAEA NZ1 ($\delta^{34}S$ = 1.83‰) and NBS ($\delta^{34}S$ = 4.34‰). The results are expressed in standard δ per mil (‰) notation relative to the Canyon Diablo Troilite (CDT), and were calculated using the following formula:

$$\delta^{34}S_{sample} = \frac{[(^{34}S/^{32}S)_{sample} - (^{34}S/^{32}S)_{standard}]*1000‰}{(^{34}S/^{32}S)_{standard}}$$

Laser ablation analysis of sulfur isotopes were performed according to the procedure outlined in

Huston et al. (1993) using an 18W Quantronix 117 Nd:YAG laser in an oxidising atmosphere (at 25 torr oxygen pressure). Polished wafers with dimensions of 10 mm x 10 mm and 150-200 μm thick that contained sulfide grains greater than 70 μm wide were prepared for analysis. Ablation pits ranged in size between 100 μm and 300 μm, and generally only one laser blast for 1-3 seconds was required per analysis. The analytical uncertainty for the conventional technique is estimated to be ±0.2 per mil (‰). The precision of laser ablation is roughly twice that of the conventional technique (Huston et al., 1993). Duplicate analyses obtained from the same sample in this study confirmed this.

Conventional and laser ablation sulfur isotope ratio measurements were undertaken using a VG Micromass 602D mass spectrometer and a VG Sira 10 mass spectrometer, respectively. Both instruments are located in the Central Science Laboratory, University of Tasmania under the supervision of Mr Keith Harris.

4.5.5 Results

Sulfur isotope analyses were undertaken on one hundred and eighty-three sulfide and twenty-seven sulfate samples from Río Blanco and Sur-Sur sectors in the ore deposit. The statistics for these results are shown on Table 4.15 and histogram on Figure 4.35. A total of sixty-nine sulfide and fourteen sulfate samples were analysed from Río Blanco (Table 4.16). One hundred and fourteen sulfide and seven sulfate samples were analysed from Sur-Sur (Table 4.17). The sulfur isotope results have been plotted and contoured on one cross-section through Río Blanco (cross section XC-130RB - Figures 4.38; 4.39 below) and one cross and one longitudinal section through Sur-Sur (cross section XC-50 and longitudinal section D-D' - Figures 4.42; 4.43; 4.44; 4.45).

Table 4.15. Sulfide and sulfate sulfur isotope results for Río Blanco and Sur-Sur.

Total sulfides			
n	**Mean $\delta^{34}S$ ‰**	**Range $\delta^{34}S$ ‰**	**Std Dev.**
183	-0.70	-4.12 to +3.34	1.35
Total sulfates			
n	**Mean $\delta^{34}S$ ‰**	**Range $\delta^{34}S$ ‰**	**Std Dev.**
27	12.38	10.07 to 17.86	1.73

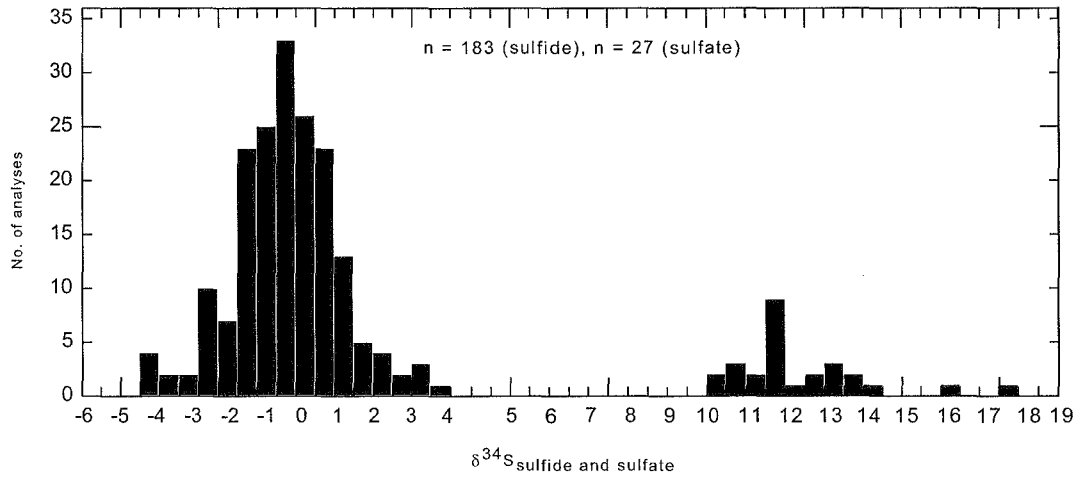

Figure 4.35. Total combined sulfide and sulfate histogram for Río Blanco and Sur-Sur from this study.

Río Blanco

Río Blanco Sulfides

Sixty-nine $\delta^{34}S$ compositions were measured from sulfides collected from three main paragenetic stages in the Río Blanco sector. These are: (i) stage 2 sulfide veins (biotite alteration halo); (ii) stage 3 Río Blanco Magmatic Breccia sulfide cement; and (iii) stage 8 sulfide veins (quartz-sericite alteration halo). Fourteen sulfate analyses were obtained from the Río Blanco samples (stage 3, stage 8 and stage 9 D veins). Sulfur isotope data for Río Blanco samples are listed in Table 4.16, Appendix G2 and illustrated in Figure 4.36 and 4.37.

Table 4.16. Summary of sulfur isotope data for sulfides and sulfates from Río Blanco.

Sulfides	**n**	**Mean $\delta^{34}S$ ‰**	**Range $\delta^{34}S$ ‰**	**Std. Dev.**
Stage 2 veins	6	+0.88	-1.14 to +1.92	1.11
Stage 3 cement	41	-0.23	-2.38 to +2.64	0.92
Stage 8 veins	22	-0.38	-3.94 to +3.34	1.35
Total	**69**	**-0.18**	**-3.94 to +3.34**	**1.12**
Sulfates	**n**	**Mean $\delta^{34}S$ ‰**	**Range $\delta^{34}S$ ‰**	**Std. Dev.**
Stage 3 cement	11	13.27	10.07 to 17.86	2.23
Stage 8 veins	2	12.6	12.39 to 12.81	0.29
Stage 9 veins	1	11.84	11.84	
Total	**14**	**13.07**	**10.07 to 17.86**	**2.01**

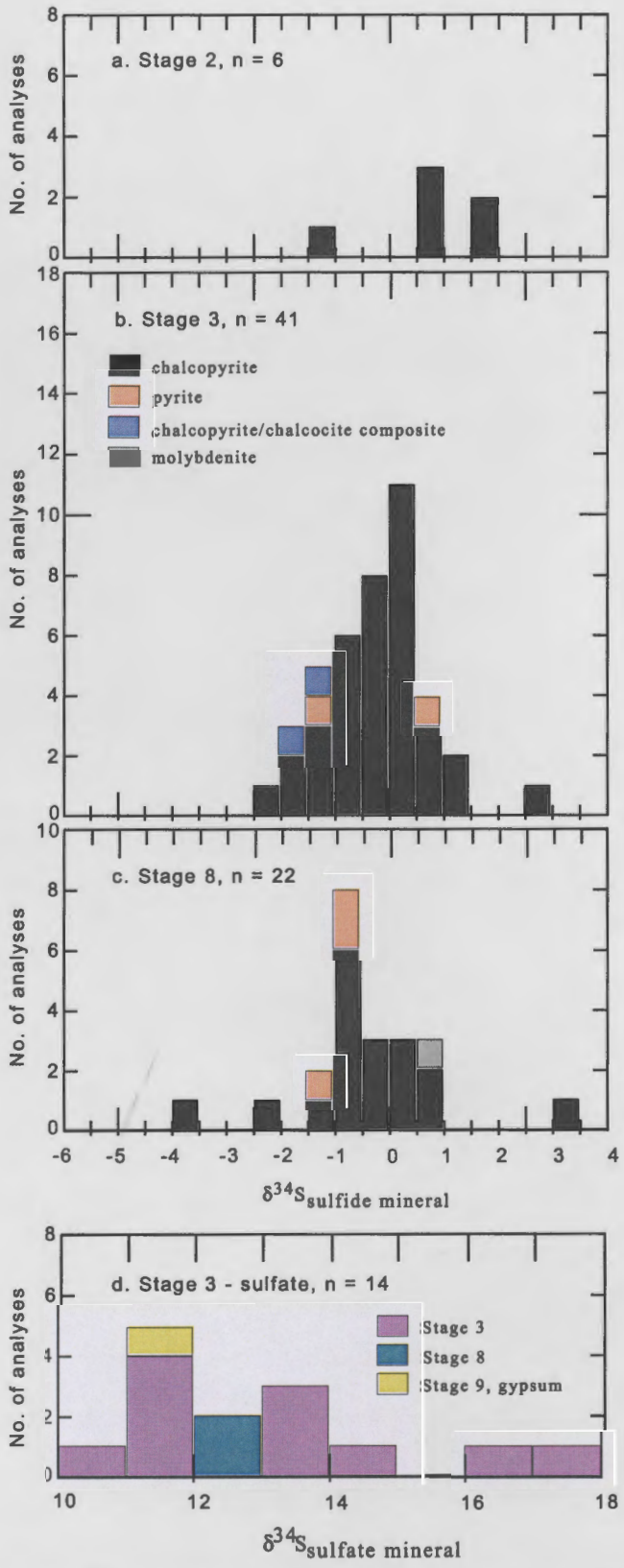

Figure 4.36. Histograms showing the sulfur isotope composition of sulfide and sulfate minerals with paragenetic constraint from Río Blanco: a. Sulfur isotope compositions for stage 2 sulfide veins; b. Sulfur isotope compositions for stage 3 sulfide cement from the Río Blanco Magmatic Breccia; c. Sulfur isotope compositions for stage 8 sulfide veins and; d. Sulfur isotope compositions for sulfate minerals (anhydrite and gypsum) separated from stage 3 cement and stage 8 veins.

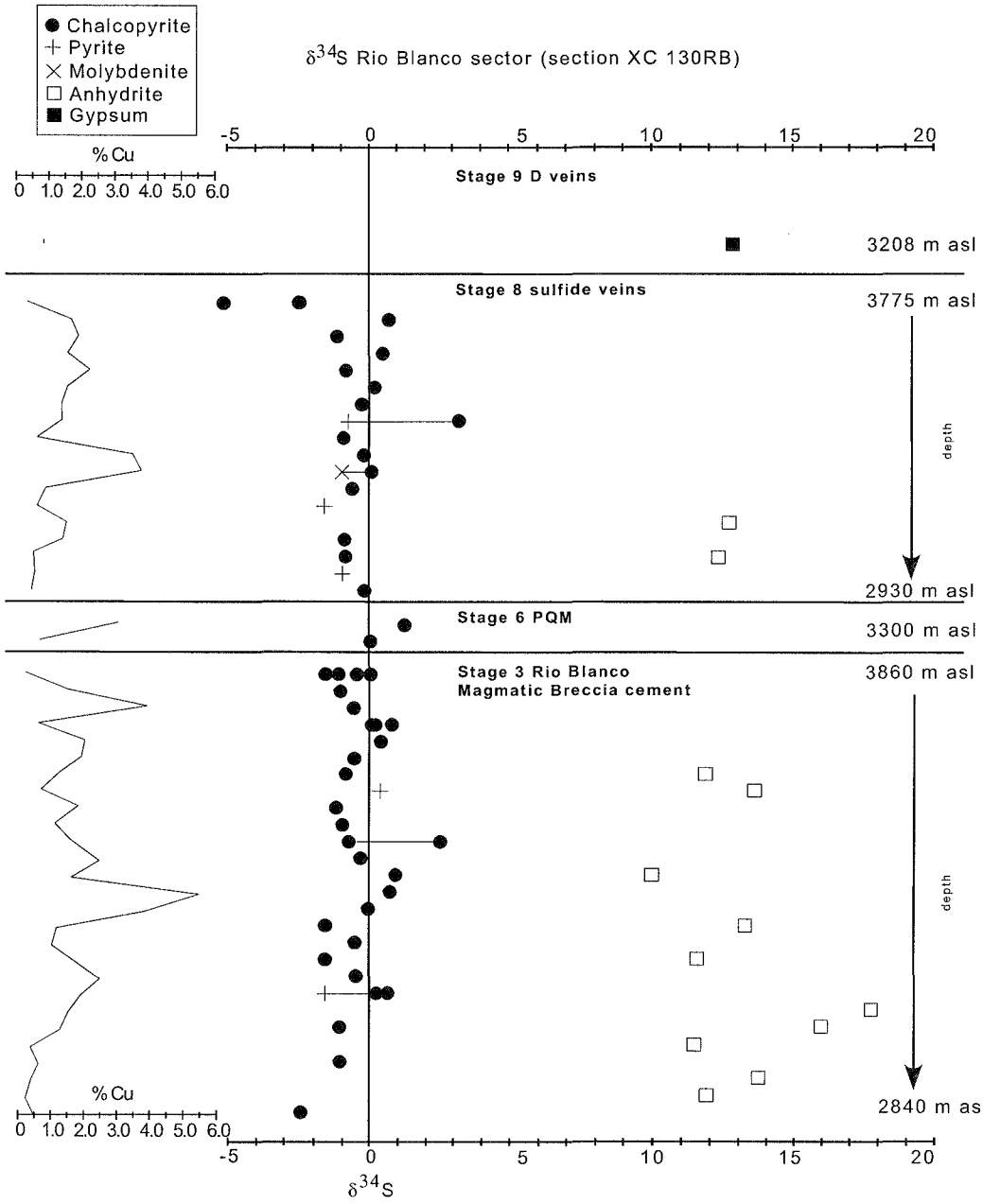

Figure 4.37. Sulfide and sulfate sulfur isotope results compared with copper grade and depth for samples collected in the Río Blanco sector (section XC-130RB). Stage 2 veins were not collected from this section.

Stage 2: sulfide veins

Three hydrothermal events pre-dated the main stage of mineralisation (Magmatic Breccia) in the Río Blanco sector. Only one of these (Stage 2b; Fig. 3.1) contained sulfide grains suitable for analysis by the laser ablation method. A total of six sulfur isotope analyses were obtained from two samples of stage 2, sulfide veins collected deep in the Don Luis sector. The sulfur isotope values for chalcopyrite from these samples are between -1.14‰ and +1.92‰, with a mean of +0.88‰ (Table 4.16; Appendix G2).

Stage 3: Magmatic Breccia sulfide cement

The formation of the Magmatic Breccia coincided with the main phase of mineralisation in the Río Blanco sector. Forty-one sulfur isotope analyses were obtained from chalcopyrite (39) and pyrite (2) grains from the breccia cement. Of the forty-one analyses, thirty-four (24 conventional, 10 laser) were collected from two adjacent sections (XC-125 and 135, spaced 30 m apart) and have been plotted onto one composite section (XC-130 RB). The remaining seven conventional analyses are from samples collected deep in the Don Luis sector, on section XC-275. The $\delta^{34}S$ values range between -2.38‰ and +2.64‰, with a mean of -0.23‰. The results for sulfide cement from section XC-130RB are contoured in Figures 4.38 and 4.39. The contoured image of section XC-130RB shows more negative $\delta^{34}S$ values at depth.

Stage 6: Quartz Monzonite Porphyry

The Quartz Monzonite Porphyry (PQM) in the Río Blanco sector crosscuts the Magmatic Breccia. Two sulfur isotope analyses (one conventional and one laser ablation) were obtained from disseminated chalcopyrite contained within the altered porphyry groundmass (+0.06 and +1.38 ‰, respectively; Fig. 4.37).

Stage 8: sulfide veins

Sulfide veins with quartz-sericite alteration halos crosscut the stage 3 Magmatic Breccia and stage 6 PQM in the Río Blanco sector. Twenty-two sulfur isotope values were generated from chalcopyrite (18), pyrite (3) and molybdenite (1). The $\delta^{34}S$ values range between -3.94‰ and +3.34‰, with a mean value of -0.38‰ (Table 4.16). The more negative $\delta^{34}S$ values occur in the uppermost level of section XC-130RB (Figs. 4.37 and 4.39).

Río Blanco Sulfates

As described in subsection 3.5.2, only rocks below the "gypsum line", a weathered (secondary) interface at approximately 3400 m elevation in the Río Blanco sector contains anhydrite. Above this interface, gypsum is the only sulfate mineral present. Thirteen sulfate analyses; eleven from stage 3 anhydrite cement, two from stage 8 veins and one from a gypsum-bearing stage 9 vein were generated in the Río Blanco sector.

Stage 3: Magmatic Breccia sulfate cement

Eleven $\delta^{34}S$ compositions of anhydrite from Magmatic Breccia cement were analysed on section

XC-130RB. Values range between 10.07‰ and 17.86‰, with a mean composition of 13.09‰. Two anomalously high $\delta^{34}S$ sulfate values within the Río Blanco Magmatic Breccia cement (DDH 450, 95-158 m; 240b, 241b) correlate spatially to zones of depleted $\delta^{34}S$ sulfide values (Figure 4.37).

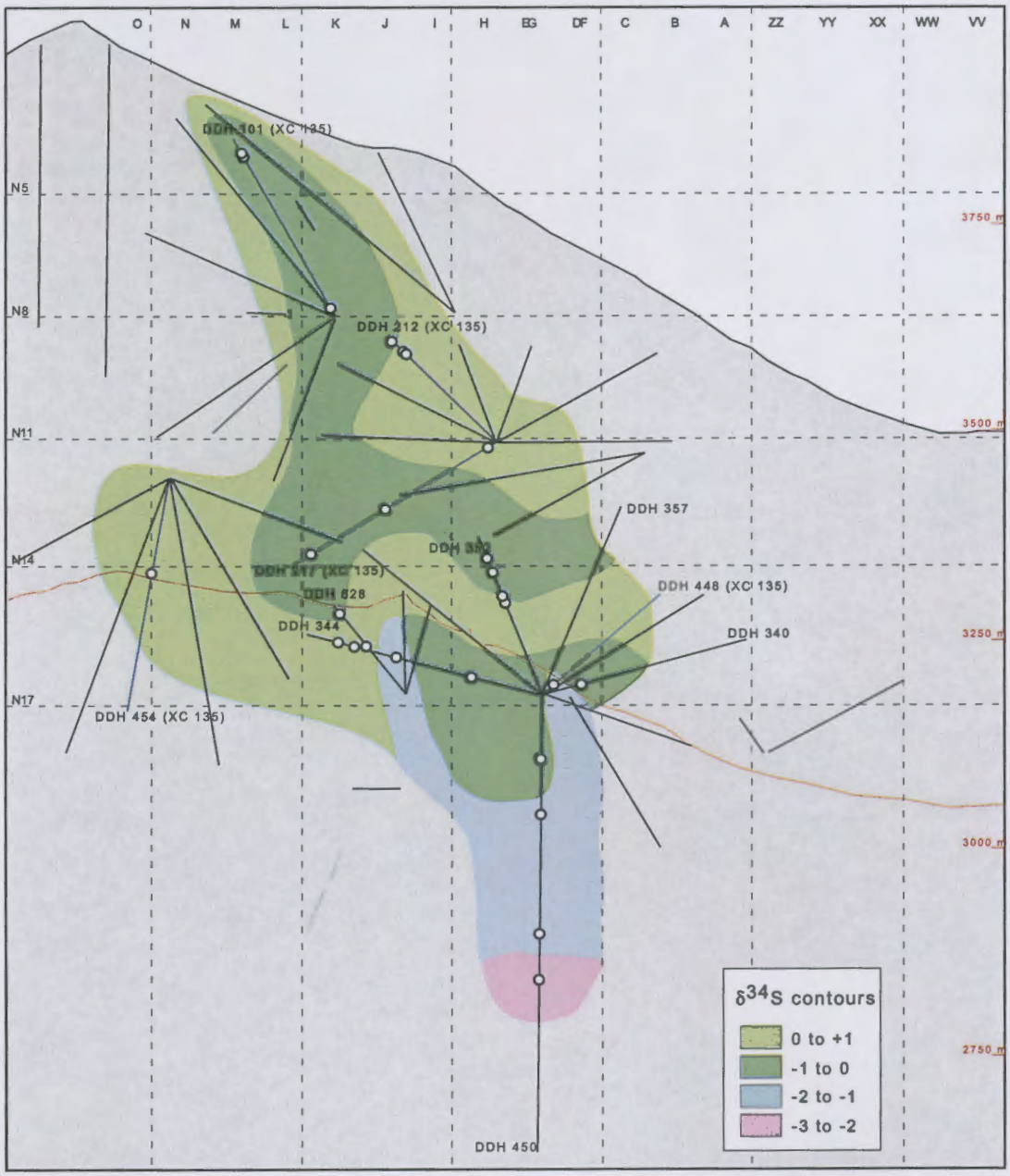

Figure 4.38. Contoured distribution of sulfur isotope values for stage 3 sulfide cement from the Río Blanco Magmatic Breccia on section XC-130RB. Sample locations are indicated by white circles. The trace of this section is shown on Figure 3.14, and copper grades shown on Figure 3.17d.

Stage 8: Anhydrite veins

Three analyses of sulfate minerals (two anhydrite, one gypsum) were performed on samples with veins that have crosscut the Río Blanco Magmatic Breccia cement. These sulfate veins are parage-

netically coeval with the quartz sericite sulfide veins. The results range between 10.12‰ and 12.81‰, with a mean value of 11.69‰. The data for sulfate veins in the Río Blanco sector are shown on Table 4.16 and Figure 4.36.

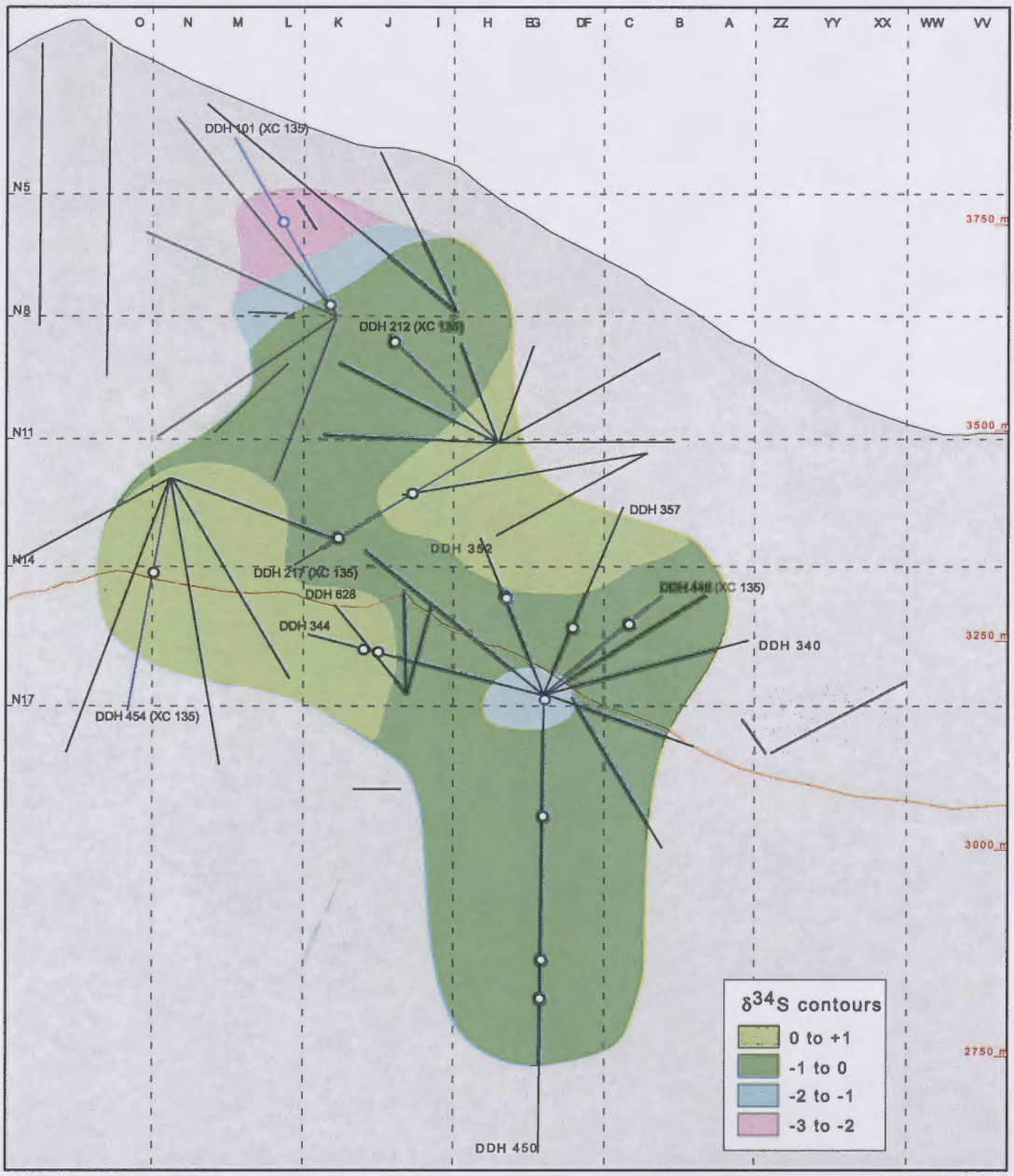

Figure 4.39. Contoured distribution of sulfur isotope compositions for Río Blanco stage 8 veins on section XC-130RB. Sample locations are indicated by white circles. The trace of this section is shown on Figure 3.14, and copper grades shown on Figure 3.17d.

Sur-Sur

In this study, one hundred and fourteen sulfur isotope analyses have been completed on sulfides from three paragenetic stages in the Sur-Sur sector: (i) stage 3 Tourmaline Breccia sulfide cement; (ii) stage 8 sulfide veins (quartz-sericite alteration halo) and; (iii) stage 9 D veins (quartz-sericite

alteration halo; Table 4.17; Figs. 4.40 and 4.41). In addition, seven $\delta^{34}S$-sulfur isotope analyses were obtained from stage 3 Tourmaline Breccia sulfate cement (Table 4.17). The total dataset for section XC-50 is presented on Figure 4.40, and the complete dataset for Sur-Sur listed in Appendix G3. The sulfur isotope results have been plotted and contoured on cross section XC-50 and longitudinal section D-D' in Sur-Sur (Figs. 4.42-4.45).

Table 4.17. Summary of sulfur isotope data for sulfides and sulfates from Sur-Sur.

Sulfides - Sur-Sur	**n**	**Mean $\delta^{34}S$ ‰**	**Range $\delta^{34}S$ ‰**	**Std dev.**
Stage 3 cement	72	-1.14	-4.12 to +2.65	1.46
Stage 8 veins	27	-0.94	-4.05 to +2.54	1.22
Stage 9 veins	15	-0.36	-1.69 to +1.06	0.77
Total	**114**	**-0.99**	**-4.12 to +2.65**	**1.35**

Sulfates - Sur-Sur	**n**	**Mean $\delta^{34}S$ ‰**	**Range $\delta^{34}S$ ‰**	
Stage 3 cement	7	12.21	11.15 to 13.39	0.85

Stage 3: Tourmaline Breccia sulfide cement

The Tourmaline Breccia cement contains the bulk of the copper ore in the Sur-Sur sector. Sulfur isotope compositions were determined on seventy-two main-stage sulfide samples hosted within the Tourmaline Breccia cement. The analyses were performed on chalcopyrite (48), pyrite (20), bornite (1) and chalcopyrite/chalcocite composites (3). Results range from -4.12 to +2.65‰ with a mean value of -1.14‰ (Table 4.17; Fig. 4.40). Sulfide and sulfate sulfur isotope compositions are plotted against copper grade and depth in Figure 4.41. Sulfur isotope contours of Tourmaline Breccia sulfide cement in section XC-50 and longitudinal section D-D' can be observed on Figures 4.42 and 4.43, respectively.

When the main-stage sulfur isotope results are plotted spatially, the most negative $\delta^{34}S$ sulfide values are located at high altitude (>4000 m elevation) in the Tourmaline Breccia (Figs. 4.41-4.43). At these high altitudes, chalcopyrite grains are partially replaced by chalcocite. To confirm that supergene processes have not affected the sulfur isotope compositions, the laser ablation method was used to analyse adjacent chalcopyrite and chalcocite grains. The results from the laser ablation analyses of individual chalcopyrite and chalcocite grains indicate no significant difference from the conventional results for composite chalcopyrite/ chalcocite grains (Fig. 4.40; Appendix G2). Therefore, the low $\delta^{34}S$ values at high altitude in the Tourmaline Breccia are a hypogene phenomena. As for chalcopyrite, pyrite $\delta^{34}S$ sulfide values also decrease upwards through the breccia to more negative values above 4000 m elevation (Fig. 4.41). These results support the notion that isotopic fractionation upwards through the breccia column caused depletion of ^{34}S in the sulfide

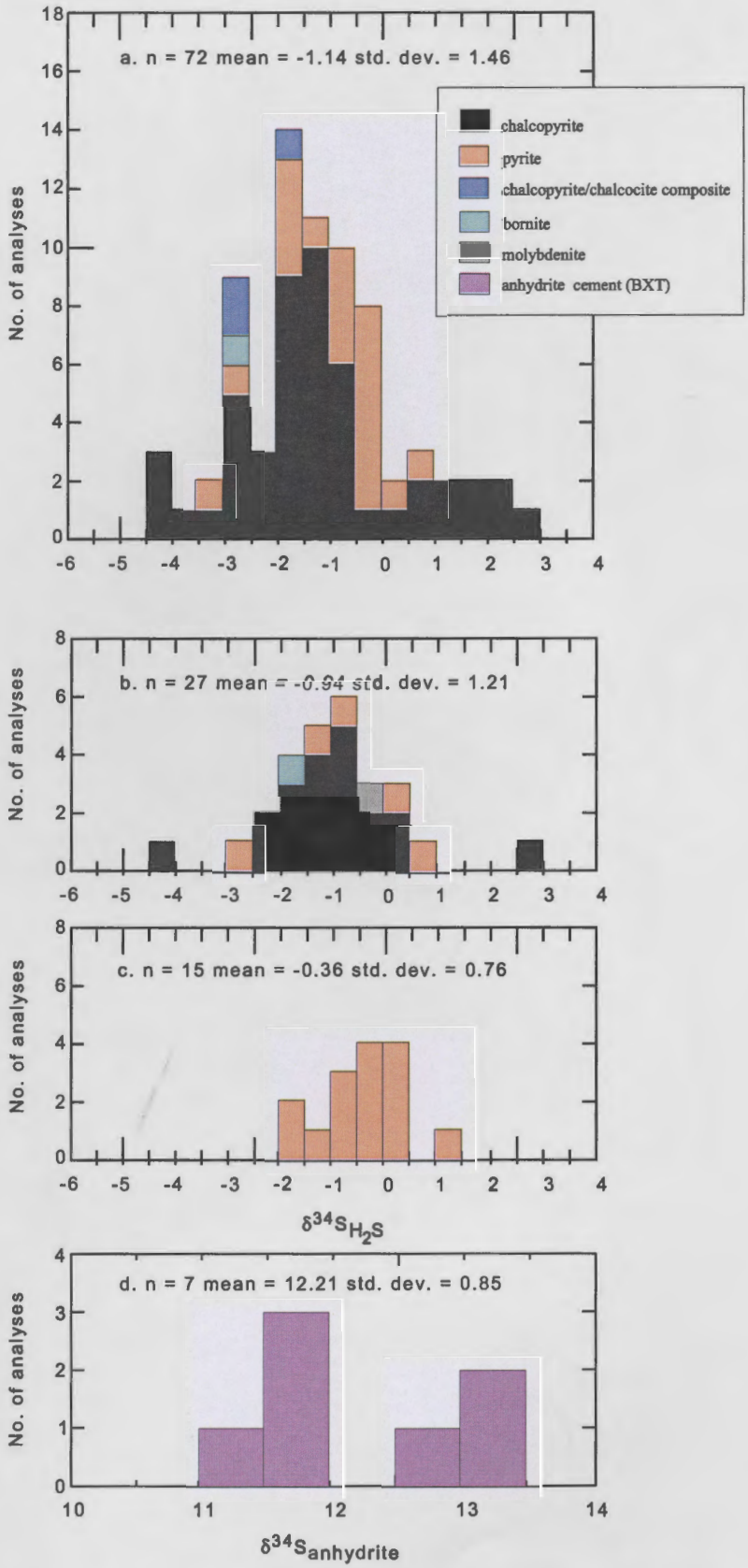

Figure 4.40. Histograms showing the sulfur isotope composition of sulfide and sulfate minerals from Sur-Sur: a. Sulfur isotope compositions for stage 3 Tourmaline Breccia sulfide cement; b. Sulfur isotope compositions for stage 8 sulfide veins that crosscut the Tourmaline Breccia; c. Sulfur isotope compositions for stage 9 D veins; and d. Sulfur isotope compositions for stage 3 anhydrite cement.

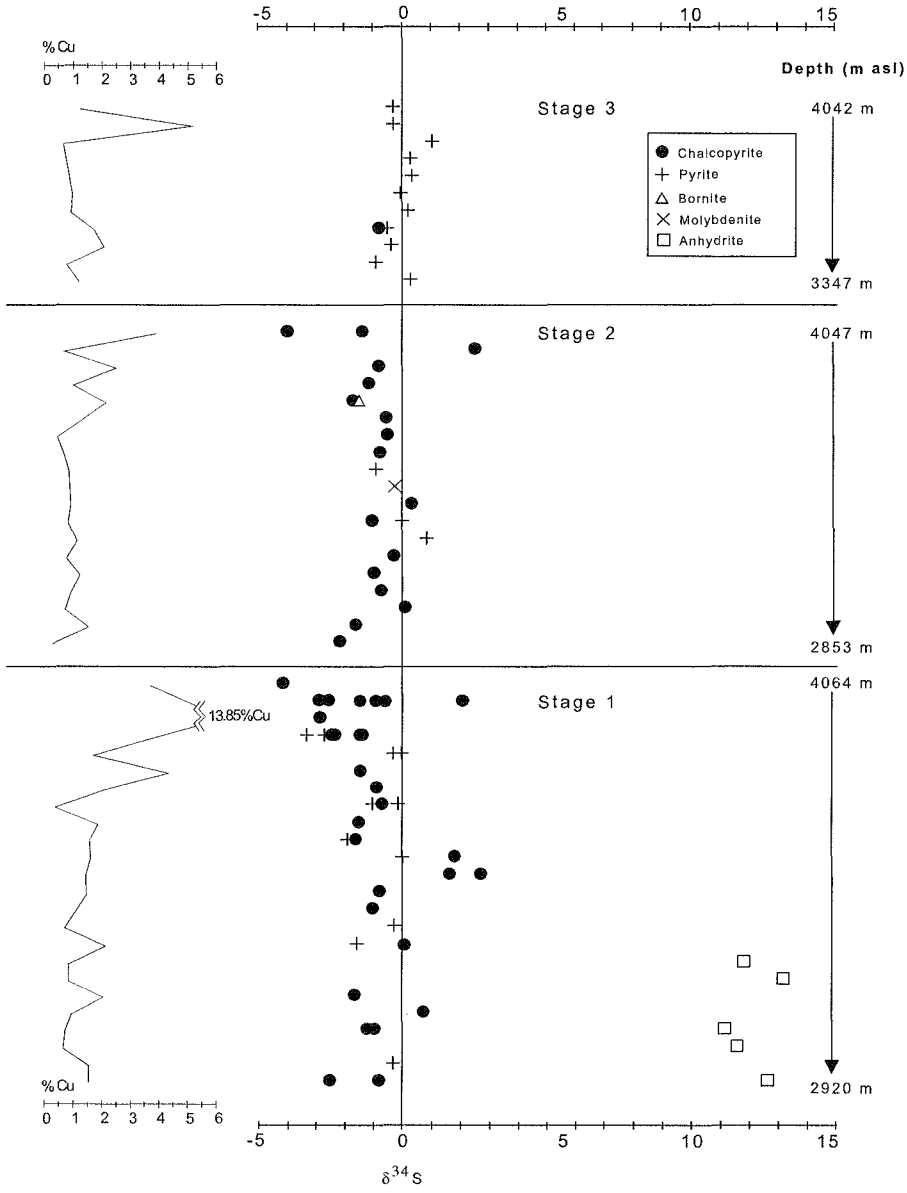

Figure 4.41. Sulfide and sulfate sulfur isotope results plotted with copper grade and depth for samples collected from cross section XC-50 Sur-Sur.

minerals.

Apart from the most negative sulfur isotope values occurring at shallow depths in the system, cross section XC-50 contains discrete zones within the rock column where more negative $\delta^{34}S$ values correlate to zones of higher copper grades (Fig. 4.41). The deepest of these zones occurs at 736 m in drillhole TSS-22 where a discrete, isolated high-grade (1.5-2.0% Cu) zone coincides with $\delta^{34}S$-sulfide values of -1 to -2‰ (Figs. 4.41 and 4.42). Another sample with $\delta^{34}S$ depletion, midway up through the breccia in drill hole TSS-22 (133 m) also correlates to a discrete high-grade zone (2.07% Cu; Fig. 4.42).

Stage 8: Sulfide veins

Sulfur isotope compositions were determined for twenty-seven sulfide samples taken from stage 8 veins that have crosscut the Tourmaline Breccia at Sur-Sur. These analyses were performed on chalcopyrite (20), pyrite (5), bornite (1) and molybdenite (1; Figs. 4.40 and 4.41), and results range between -4.05‰ and +2.54‰, with a mean composition of -0.94 (Table 4.17). The more negative compositions are located at high elevations in the Sur-Sur Tourmaline Breccia, as is the case for the stage 3 sulfide cement. In addition, more negative values are also located both to the north and south, along strike of the Sur-Sur Tourmaline Breccia and in the deepest drillhole in cross section XC-50 (Fig. 4.44).

Stage 9: D veins

Sulfur isotope compositions were measured from fifteen pyrite samples collected from stage 9 veins at Sur-Sur. The results range between -1.69‰ and +1.06‰, with a mean composition of -0.36‰ (Table 4.17; Fig. 4.40). The most negative compositions are located to the north and south, along strike of the Tourmaline Breccia, distal from the main mineralised system. Stage 9 veins contain gypsum and traces of anhydrite and chalcopyrite in addition to abundant pyrite. The anhydrite and chalcopyrite were not abundant enough for sulfur isotopic analyses of mineral pairs. Pyrite grains analysed from stage 9 veins have $\delta^{34}S$ values close to 0‰ (Table 4.17; Figs. 4.40-4.42) indicating limited sulfur fractionation at this late vein stage.

Stage 3: Sulfate cement

Anhydrite is preserved below the 'gypsum line' at 3600 m elevation in cross section XC-50, Sur-Sur. Above this interface, gypsum is the only sulfate mineral present. Sulfur isotope results of seven anhydrite samples collected at elevations below 3600 m from the Tourmaline Breccia cement have $\delta^{34}S$ values between 11.15‰ and 13.39‰, with a mean composition of 12.21‰ (Table 4.17; Figs. 4.40 and 4.41).

Sulfur isotopes and copper grades

To determine whether any relationships exist between $\delta^{34}S$ values and copper grades, these two parameters have been plotted together for the Río Blanco sector and the Sur-Sur sector (Fig. 4.46). In the Río Blanco sector, increasing $\delta^{34}S$ values correlate broadly with increasing copper grades (Fig. 4.46). The opposite is the case in the Sur-Sur sector, where elevated copper grades correspond with more negative sulfur isotope compositions of sulfide minerals (Fig. 4.46).

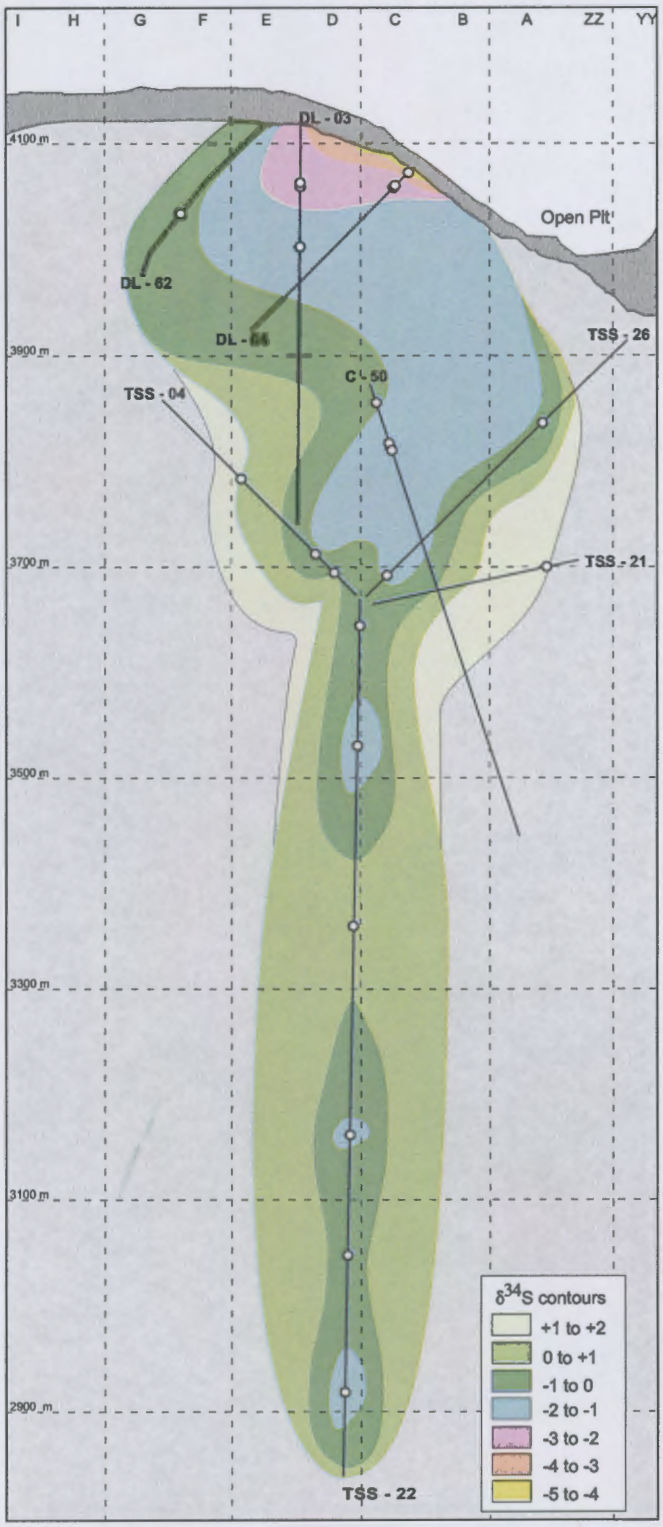

Figure 4.42. Contoured distribution of sulfur isotope compositions of stage 3 Tourmaline Breccia sulfide cement on cross section XC-50, Sur-Sur. Sample locations are indicated by white circles. The trace of this section is shown on Figure 3.14, and copper grades shown on Figure 3.19d.

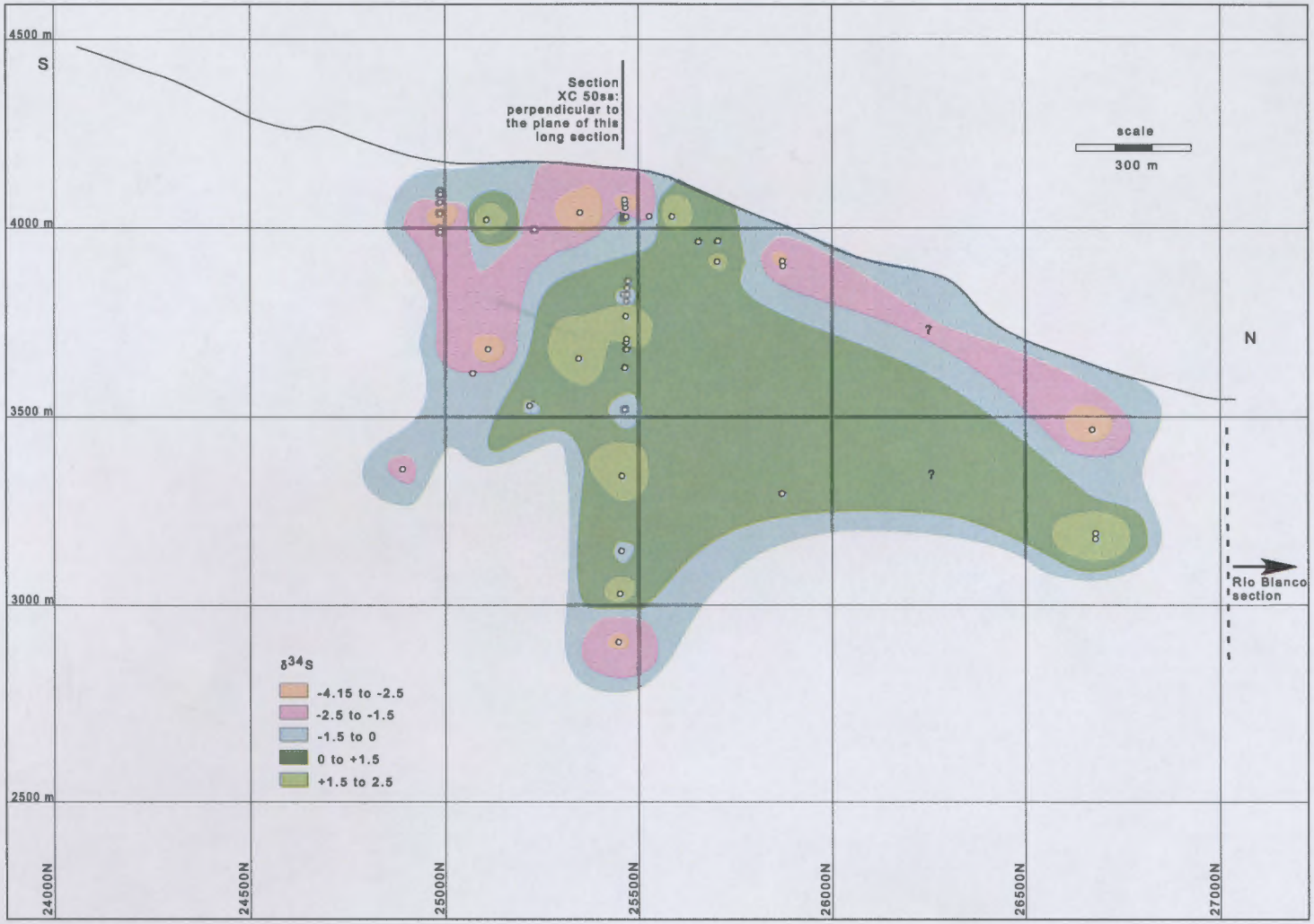

Figure 4.43. Contoured distribution of sulfur isotope compositions of stage 3 Tourmaline Breccia sulfide cement on longitudinal cross section D-D'. Sample locations are indicated by white circles. The trace of this section is shown on Figure 3.14.

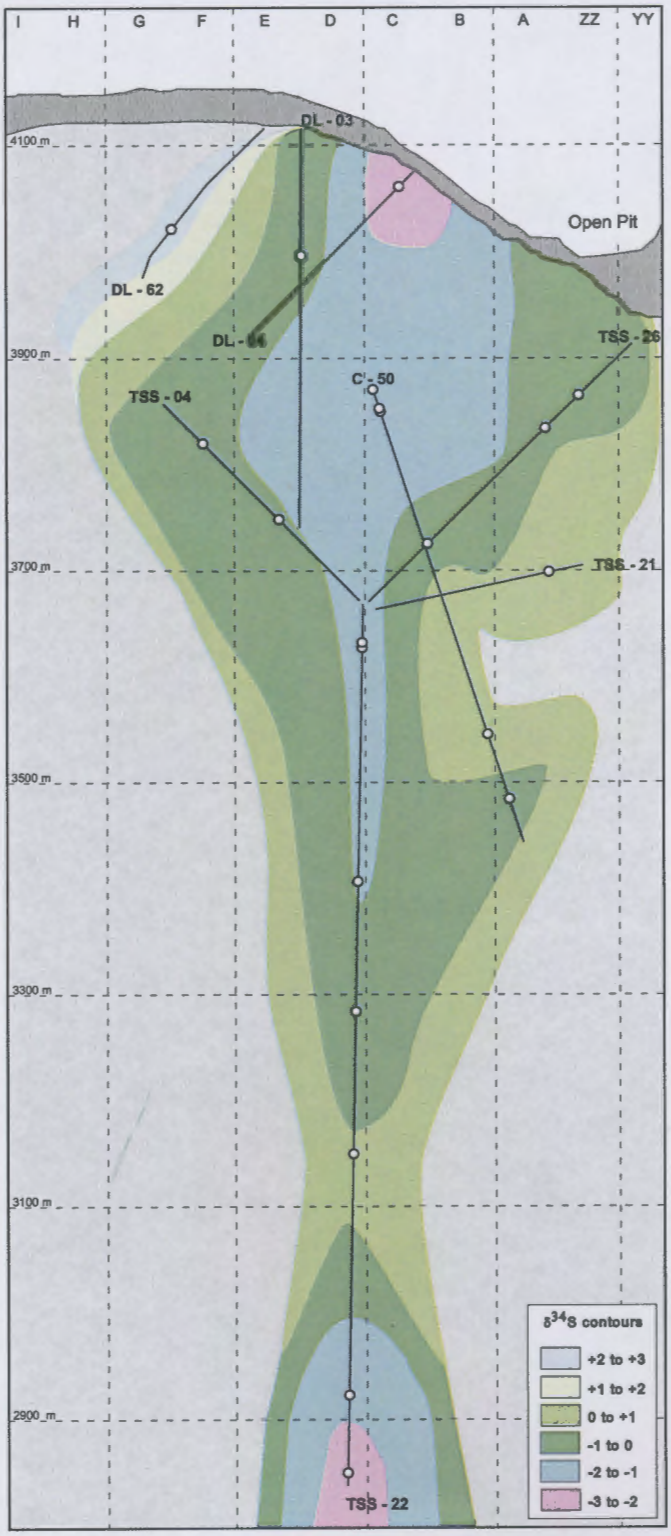

Figure 4.44. Contoured distribution of sulfur isotope compositions of stage 8 sulfide veins from cross section XC-50, Sur-Sur. Sample locations are indicated by white circles. The trace of this section is shown on Figure 3.14, and copper grades shown on Figure 3.19d.

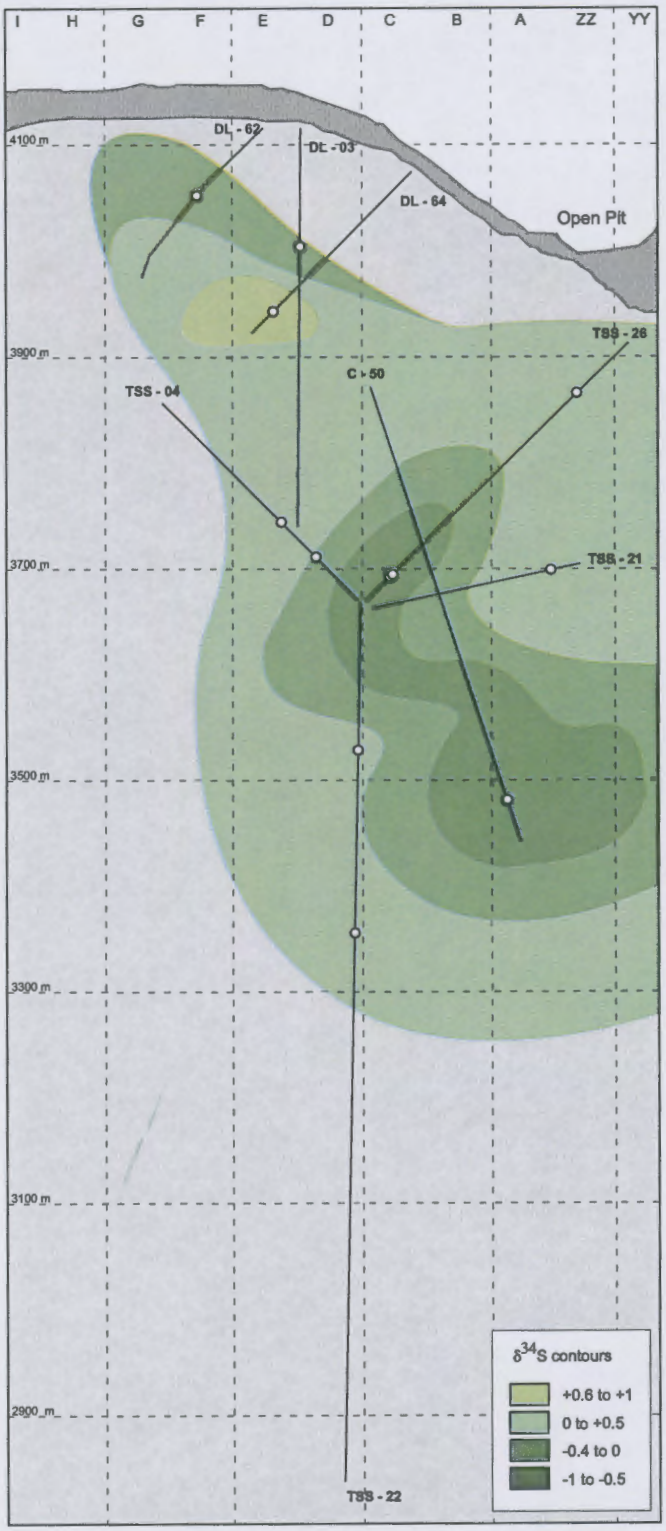

Figure 4.45. Contoured distribution of sulfur isotope compositions of stage 9 D veins from cross section XC-50, Sur-Sur. Sample locations are indicated by white circles. The trace of this section is shown on Figure 3.14, and copper grades shown on Figure 3.19d.

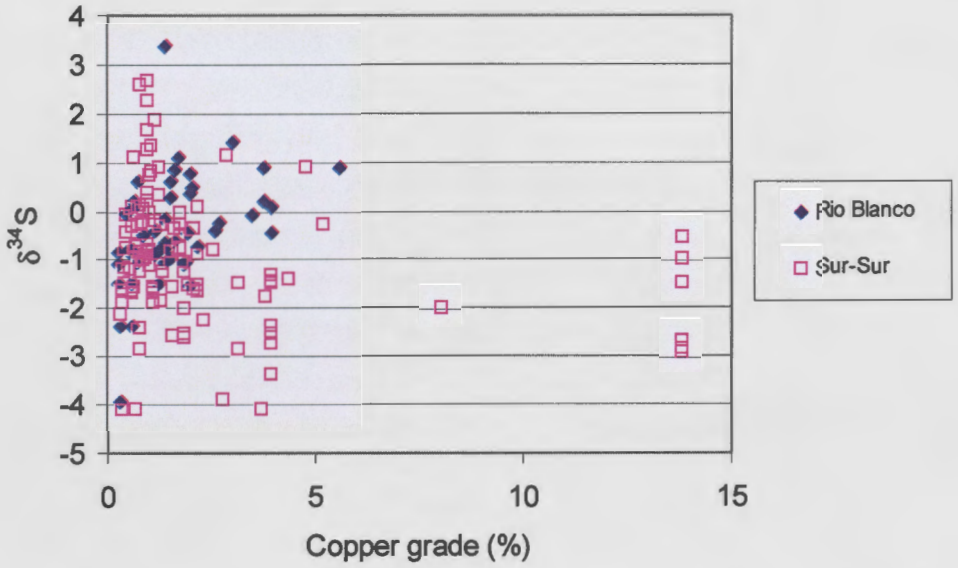

Figure 4.46. Graphical representation showing $\delta^{34}S$ values plotted against copper grade in the Río Blanco and Sur-Sur sectors.

4.5.6 Discussion

Spatial variations in the ratio of $\delta^{34}S/\delta^{32}S$ in sulfide minerals may relate to the degree of isotopic fractionation that the mineralising fluid undergoes during transport, and/or mixing of two isotopically distinct sulfur reservoirs. The fractionation of sulfur in high temperature magmatic-hydrothermal systems is controlled by changes in temperature and/or redox conditions (Ohmoto and Rye, 1979). The definition of oxidised and reduced hydrothermal fluids used here follows the conventions of Lydon (1983) and Cooke and Simmons (2000), whereby "oxidised" fluids contain high concentrations of sulfate species rather than sulfide-bearing species. Conversely, "reduced" fluids are those that contain greater concentrations of reduced, aqueous sulfur-bearing species (e.g. aqueous sulfide) rather than sulfate.

Significant fractionation of sulfur by temperature can only occur when a hydrothermal fluid contains appreciable amounts of both oxidised and reduced sulfur species [i.e. $R > 0.1$; where R is the mole ratio of sulfate to sulfide ($m\Sigma SO_4/m\Sigma H_2S$; Ohmoto and Goldhaber 1997). For example, cooling of a fluid with $m\Sigma SO_4/m\Sigma H_2S = 1$ from temperatures of 350° to 200°C can cause a decrease in $\delta^{34}S_{sulfide}$ and an increase in $\delta^{34}S_{sulfate}$ of about 8‰, if the $m\Sigma SO_4/m\Sigma H_2S$ ratio and equilibrium between them are maintained (Ohmoto and Goldhaber, 1997). In general, $\delta^{34}S$ values of vein sulfates that precipitate from a cooling, H_2S-predominant fluid ($R < 0.5$) will increase significantly with decreasing temperature. They will be much higher than for the original igneous sulfate value, whereas $\delta^{34}S$ values for the coexisting sulfides will only decrease slightly, remaining close to the

original bulk sulfur composition (Rye, 1993). In contrast, if the cooling fluid is sulfate-predominant (R > 0.5), sulfide $\delta^{34}S$ values will become increasingly negative whereas the sulfate mineral values will only increase marginally (Rye, 1993). I-type magmas (such as those associated with porphyry copper deposits) typically produce more oxidising hydrothermal fluids (R > ~0.01) than their more reduced S-type counterparts (R < ~0.01; Ohmoto and Goldhaber, 1997).The magnitude of changes in the $m\Sigma SO_2/m\Sigma H_2S$ ratio of a fluid during cooling (or heating) depends on the concentration ratios of H, O and S in the fluid, and also on the open or closed state of the system with respect to sulfur (Ohmoto and Goldhaber, 1997). In a closed system, water sourced from a crystallising magma should maintain a constant R-value during cooling. If the system is open, the ratio of oxidised to reduced sulfur species in a fluid may be changed by reactions with wall-rocks, such as by reaction with Fe^{2+}- or Fe^{3+}-bearing minerals, by precipitation of sulfide or sulfate minerals, or by phase separation of a fluid (Ohmoto and Goldhaber, 1997). If equilibrium between oxidised and reduced species is maintained in this open system, an increase in the ratio of oxidised to reduced species (i.e. oxidation) will cause the $\delta^{34}S$ values of the individual fluid species to decrease. On the other hand, reduction of the fluid may cause the δ values of the species to increase (Ohmoto and Goldhaber, 1997).

Under oxidising (sulfate-predominant) conditions, $\delta^{34}S$ is preferentially taken up in sulfate minerals (e.g. anhydrite). Co-precipitating sulfide minerals will scavenge available $\delta^{32}S$, resulting in progressively lower $\delta^{34}S$ values for sulfides (Ohmoto and Goldhaber, 1997). This process was first documented by Gavelin et al. (1960), who reported that the six most negative sulfide sulfur isotope compositions in a hydrothermal system from Cornwall were taken from samples containing barite. The general reaction can be seen below;

$$H_2S^{34} + S^{32}O_4^{2-} <=> H_2S^{32} + S^{34}O_4^{2-} \qquad \text{(Jensen, 1959)}$$
$$\text{(reduced)} \qquad \text{(oxidized)}$$

Rye (1993) reported spatial variations in $\delta^{34}S$-sulfide values from the high sulfidation gold deposit at Summitville, Colorado. Near-zero $\delta^{34}S$-sulfide values occurred at depth within the South Mountain Porphyry, whereas more negative $\delta^{34}S$-sulfide values occurred at higher elevations within the system. The $\delta^{34}S$ data for co-existing vein sulfides and sulfates require that the hydrothermal fluids were sulfide-dominant and proposed to have followed a reducing path after exsolution from an oxidised magma (Rye, 1993). Consequently, it is possible for a trend to negative $\delta^{34}S$-sulfide values to be produced by both oxidising and reducing hydrothermal fluids, provided that R > ~0.1. It is the magnitude of the negative shift in $\delta^{34}S$-sulfide values that reflects whether the fluid is oxidised (R > 0.5) or reduced (R < 0.5).

Río Blanco

Stage 2 sulfides

Stage 2 veins have $\delta^{34}S$ values tightly constrained around 0‰. These early veins are interpreted to be magmatic-hydrothermal in origin. There is no evidence for sulfur isotope fractionation in the limited data set from this vein stage.

Stage 3 sulfides

Sulfides contained in the Río Blanco Magmatic Breccia cement have more negative $\delta^{34}S$ values at depth within the system (Figs. 4.37 and 4.38). Through the Río Blanco sector, the sulfur isotopic compositions of sulfide minerals vary by approximately 5‰, with no obvious spatial zonation in the sulfur isotope data. Given the near-zero values and geological relationships, a predominantly magmatic-hydrothermal origin for the sulfur is inferred, with variations most likely a product of fluctuations in the prevailing physico-chemical conditions (especially temperature) during ore deposition.

Two anomalously positive $\delta^{34}S$-sulfate values occur within the Río Blanco Magmatic Breccia cement ($\delta^{34}S$ = 17.86‰; 16.05‰). These correlate to zones of high-grade ore and negative $\delta^{34}S$ sulfide values (Fig. 4.37). Because ^{34}S isotope preferentially sequesters into anhydrite, this can result in depletion of ^{34}S in sulfide minerals (chalcopyrite). These limited data imply that conditions at this locality were either cooler and/or more oxidised than in the main part of the mineralised zone at Río Blanco. Based on Rye (1993), the spread of $\delta^{34}S$ values on Figure 37 of sulfide and sulfate minerals suggests that the mineralising fluid at Río Blanco was reducing (H_2S-predominant), with fractionation of ^{34}S in sulfates caused by scavenging of the limited amount of ^{34}S by anhydrite.

Stage 8 sulfides

The $\delta^{34}S$ sulfide values obtained from the stage 8 sulfide veins that crosscut the Magmatic Breccia do not differ significantly from sulfide values measured from stage 3 Río Blanco Magmatic Breccia. The more negative $\delta^{34}S$ values from one sample at a shallow level in the Río Blanco system could be due to localised fractionation of sulfur due to interaction with an oxidised fluid, remobilisation of Magmatic Breccia cement or to deposition from a lower temperature solution (Figs. 4.37 and 4.39). Based on near-zero data, these veins are interpreted to be magmatic-hydro-

thermal in origin.

Sur-Sur

Stage 3 sulfides

At deep levels in the Sur-Sur Tourmaline Breccia, relatively homogeneous and near-zero values for $\delta^{34}S$ are preserved. These are consistent with data from Río Blanco which have been interpreted to indicate sulfide deposition at near-constant temperature under reducing conditions ($H_2S_{(aq)}$-predominant; co-precipitated with magnetite).

Distinctly negative sulfur isotope compositions (-2 to -4‰) have been obtained for chalcopyrite and pyrite at high altitudes in the Sur-Sur Tourmaline Breccia (Figs. 4.41-4.43). The deeper levels also contain discrete zones with more negative $\delta^{34}S$-sulfide values and elevated copper grades (Figs. 4.41 and 4.42). This spatial zonation of sulfide mineral isotopic compositions suggests either a significant decrease in temperature occurred and/or oxidising conditions prevailed at higher elevations in the breccia body and also locally at depth. The shallow-level zone of negative sulfur isotopic compositions corresponds with the highest copper grades in the Sur-Sur Tourmaline Breccia, and occurs between 3700 and 4100 m elevation on cross-section XC-50. The high copper grades at shallow depths in Sur-Sur location are due in part to supergene enrichment, because chalcopyrite grains have been partially replaced by chalcocite. Laser ablation analyses of adjacent supergene chalcocite and hypogene chalcopyrite grains has returned similar negative $\delta^{34}S$-sulfide results for both minerals (Appendix G3), indicating that supergene processes did not affect the isotopic compositions of the sulfides.

In combination with high copper grades, the negative $\delta^{34}S$-sulfide compositions at shallow levels also correspond to elevated specularite:magnetite ratios in the Tourmaline Breccia cement. The current paragenetic study (Section 3) has shown that specularite precipitated prior to the main stage of mineralisation in the Tourmaline Breccia. The presence of specularite is interpreted to indicates that an oxidised (hematite-stable) fluid was present, at least in the upper parts of the brecciated rock column, prior to the main phase of mineralisation. In contrast, because the main-stage copper-bearing sulfides co-precipitated with magnetite, a more reduced fluid must have deposited them. The observed paragenetic sequence therefore either provides mineralogical evidence for (i) temporal evolution of one fluid from more oxidising to more reducing conditions with time, or (ii) two fluids with contrasting redox potentials occurring, and possibly interacting, within the breccia column. Consequently, it is necessary to model whether the observed spatial array of $\delta^{34}S$-sulfide compositions at Sur-Sur could be produced simply by cooling-induced sulfur isotopic fractionation from a reduced fluid (case i) or by deposition of shallow-level sulfides from an oxidised

sulfur reservoir (case ii). These two scenarios are modelled at the end of the discussion section.

Stage 8 veins

The contoured distribution of δ^{34}S-sulfide values obtained from stage 8 sulfide veins closely resembles the δ^{34}S zonation detected from stage 3 sulfide cement. This is due either to: (1) sulfur being locally scavenged and recycled from sulfides deposited during the initial brecciation event; or (2) similar processes operated during stages 3 and 8 in the breccia column.

The overprinting of stage 8 in veins onto stage 8 breccia cement is permissive of local sulfide recycling. Negative δ^{34}S-sulfide values also occur in stage 8 veins at the deepest zone in the Tourmaline Breccia (Fig. 4.44) indicating that local isotopic fractionation has occurred.

Stage 9 D veins

The contoured distribution of δ^{34}S values for stage 9 veins bears no resemblance to either of the preceding mineralisation events at Sur-Sur (Fig. 4.45). The data have all been obtained from pyrite and have values close to 0‰. Stage 9 veins are the last sulfide-bearing stage to have been deposited. The tightly constrained sulfur isotope data are interpreted to have been generated from a reduced magmatic-hydrothermal fluid that underwent no significant isotopic fractionation at Sur-Sur.

Isotopic Modelling

In order to model sulfur isotope fractionation at Sur-Sur, it is necessary to assume a bulk sulfur isotopic composition of the mineralising fluid. For the purposes of this discussion, an initial bulk sulfur value of +1 per mil has been assumed. Note, however, that this assumption cannot be validated using coexisting sulfide and sulfate isotopic compositions due to the petrographic evidence for textural disequilibrium between chalcopyrite and anhydrite (Fig. 3.5c-f). Other choices of bulk isotopic compositions of the mineralising fluid together with different choices of R-values can produce similar results to those listed below. In other words, the modelling results presented here are non-unique solutions. They are merely discussed in order to demonstrate whether isotopic models for sulfide deposition at Sur-Sur are valid theoretically – they do not prove whether these processes actually occurred.

Case 1: Sulfide deposition from a cooling, reduced hydrothermal fluid

Closed-system Rayleigh fractionation of sulfide and sulfate isotopic compositions has been modelled for the Sur-Sur mineralising fluid using fractionation factors and equations listed in Ohmoto

and Goldhaber (1997). For a bulk sulfur composition of +1 per mil, ranges of chalcopyrite and anhydrite compositions similar to those measured from Sur-Sur are predicted to precipitate from a reduced fluid (R = 0.25) that undergoes cooling from approximately 450° to 300°C (Fig. 4.47). This range of temperatures is consistent with the bulk of the fluid inclusion data generated from Sur-Sur (Fig. 4.17b, g, l).

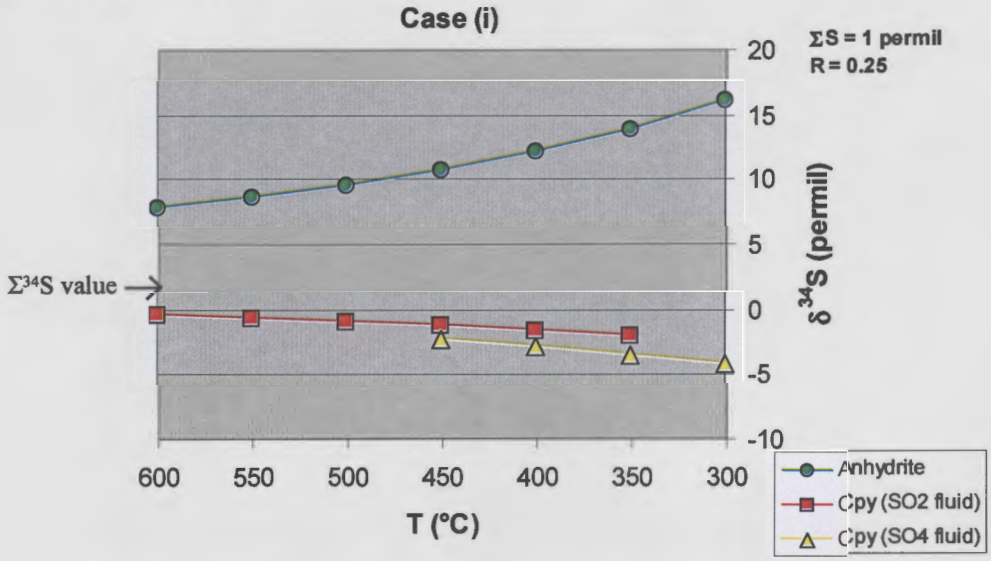

Figure 4.47. Calculated sulfate-sulfide equilibria as a function of temperature (°C) versus $\delta^{34}S$ assuming co-precipitated sulfate-sulfide, a total sulfur content of 1 per mil and an $m\Sigma SO_4/m\Sigma H_2S$ value of 0.25 (i.e. reduced, H_2S-predominant fluid). Two curves for chalcopyrite compositions are shown: chalcopyrite compositions precipitated from an SO_2-bearing fluid and chalcopyrite precipitated from an SO_4-bearing fluid (Ohmoto and Goldhaber, 1997). $SO_{2\,(g)}$ undergoes disproportionation to aqueous sulfate at approximately 400°C, but kinetics may inhibit the onset of this transition in natural systems. Hence, some overlap of temperatures has been plotted for the two curves.

Figure 4.47 shows that in theory, the observed array of $\delta^{34}S$ compositions of sulfide and sulfate minerals at Sur-Sur (e.g. -4.12 to +17.86 per mil) can be produced by precipitation from a cooling, reduced magmatic-hydrothermal fluid. However, the observed spatial array of sulfide data at Sur-Sur includes a transition upwards from -1 to -5 per mil over a vertical interval of ~100m (Fig. 4.42). This shift in isotopic compositions would require approximately 150°C of cooling over a very narrow vertical window of mineralisation (~100m). Such enormous temperature gradients are rare in hydrothermal systems. They are known to occur at the very tops of boiling geothermal systems (e.g., Henley, 1985) and where submarine vent fluids exhale onto the sea floor (e.g., Franklin, 1983). They are unlikely to be produced by conductive cooling within the Earth. Immediately below the paleosurface, boiling can cause cooling by approximately 100°C over 100m, but temperature changes due to boiling at greater depths are much less extreme (e.g. Henley, 1985). The most likely way to produce such a large temperature change in the subsurface over a narrow spatial interval is via fluid mixing, consistent with the observed salinity arrays from the fluid inclusion study.

Case 2: Sulfide deposition from a shallow, oxidised fluid reservoir

In shallow crustal settings, exsolution of hydrothermal fluids from a crystallising magma can result in the generation of large volumes of gases (including oxidising components such as $SO_{2\,(g)}$ and acidic components such as $HCl_{(g)}$) and smaller volumes of dense, saline brine (Henley and McNabb, 1978; Burnham, 1979; Bodnar et al., 1985). Magmatic-hydrothermal breccias provide an environment whereby fractionation of sulfur could occur readily within the breccia column, with SO_2 partitioning preferentially into a buoyant gas phase, and H_2S into a residual brine. During breccia formation, the gas phase could physically separate from the brine and ascend through the breccia column, producing a shallow crustal fluid reservoir rich in SO_2 or SO_4^{2-} (either through condensation into meteoric water or through magmatic gas disproportionation; Rye, 1993). The density contrasts between the brine and vapour are such that the dense brine should remain near the magmatic source, unless driven upwards by pressure differentials (tectonic or magmatic), an upsurge in brine generation or by magma resurgence.

Could the negative sulfur isotope compositions of sulfides at Sur-Sur be the product of sulfide deposition from an oxidised (sulfate-predominant) fluid, distinct from the reduced mineralising brine that produced the sulfides with near-zero $\delta^{34}S$ values throughout most of the breccia column? This scenario has been tested by assuming that SO_2 gas physically separated from the deep-level mineralising brine, and has been trapped at the top of the breccia column. In this case, the oxidised fluid is assumed to have a bulk sulfur isotopic composition of +11.15‰ (the lowest $\delta^{34}S$-sulfate value measured from the Sur-Sur tourmaline breccia cement; Table 4.17). Assuming that the fluid in this scenario is highly oxidising (R = 0.9), the range of sulfide sulfur isotopic compositions predicted to form at temperatures of 450°-300°C are comparable with those observed at shallow levels in the Sur-Sur breccia (Fig. 4.48). In this case, extreme temperature gradients are again required. Such gradients may have occurred if the SO_2-bearing magmatic gas condensed into lower temperature meteoric groundwater at the top of the breccia body.

Fluid Sources and Ore-Forming Processes

The $\delta^{34}S$ compositions of sulfide and sulfate minerals in the Río Blanco system are consistent with a reduced (H_2S-predominant) composition and magmatic-hydrothermal source for the bulk of the mineralising fluids. However, while the sulfide $\delta^{34}S$ compositions in the breccia cement at Sur-Sur can be explained in terms of cooling-induced isotopic fractionation from reduced magmatic-hydrothermal fluids, their spatial distribution cannot. The results of numerical modelling of sulfide isotopic compositions imply that fluid mixing is required to explain the spatial array of $\delta^{34}S$ compositions, possibly through mixing-induced cooling of the magmatic-hydrothermal brine, and/or via condensation of SO_2-rich magmatic gases into a shallow groundwater reservoir at the top of the breccia column. These hypotheses are given further consideration in Section 5.

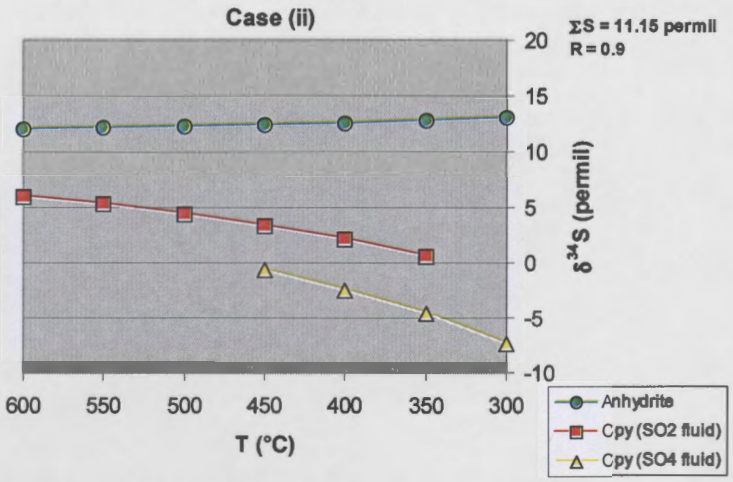

Figure 4.48. Calculated sulfate-sulfide equilibria as a function temperature (°C) versus $\delta^{34}S$ assuming co-precipitated sulfate-sulfide, a total sulfur content of 11.15 per mil and an $m\Sigma SO_4/m\Sigma H_2S$ value of 0.9 (i.e. oxidised, SO_2-predominant fluid). As for Figure 4.47, two curves for chalcopyrite compositions are shown: chalcopyrite compositions precipitated from an SO_2-bearing fluid and chalcopyrite precipitated from an SO_4-bearing fluid (Ohmoto and Goldhaber, 1997).

Section 5 – Synthesis and Genetic Model

5.1 Introduction

This section synthesises and discusses information presented in the previous sections and reviews aspects of ore genesis in breccia-related porphyry copper deposits. The objective is to develop a genetic model for the formation of mineralised breccias at Río Blanco. Although many features of the geology, mineralisation, alteration and fluid chemistry at Río Blanco are comparable with 'typical' porphyry copper deposits, Río Blanco is distinctive in that most of the resource occurs as breccia cement rather than as mineralised stockwork veins. While breccias are common in many porphyry systems (e.g., Bryner, 1971; Sillitoe, 1985), only a comparatively small proportion of them are mineralised. Río Blanco-Los Bronces is by far the largest known example of breccia-hosted mineralisation in a porphyry copper setting. It provides an unrivalled opportunity to understand the processes important for generating a Behemothian (Clark, 1995), breccia-hosted copper resource.

5.2 Previous genetic models for Río Blanco-Los Bronces

5.2.1 Los Bronces

Warnaars et al. (1985) presented a schematic model for the temporal evolution of Los Bronces (Fig. 5.1). The vertical axis represents the relative intensity of hydrothermal activity and the horizontal axis represents time (Ma). Their major findings were that:

- Hydrothermal mineralisation and alteration occurred during the last cooling phase of the eastern part of the San Francisco Batholith.
- The breccias formed over a short period of time in response to pressure build-up during a retrograde phase of the hydrothermal system, which originally produced weak stockwork-hosted ore.
- Within the porphyry system, pyrite was the first sulfide mineral formed, followed by chalcopyrite, bornite, and later molybdenite. Subsequent short-lived but substantial pulses of brecciation localised new deposition of quartz, tourmaline, sulfides and specularite.
- Late, post-breccia mineralised faults and veins containing specularite, enargite, sulfosalts, chalcopyrite, sphalerite and galena in a gangue of quartz, barite, and siderite formed during the

youngest phases of mineralisation.

- Hydrothermal activity was cut-off by and disrupted by the post-mineral dacite and rhyolite of La Copa.

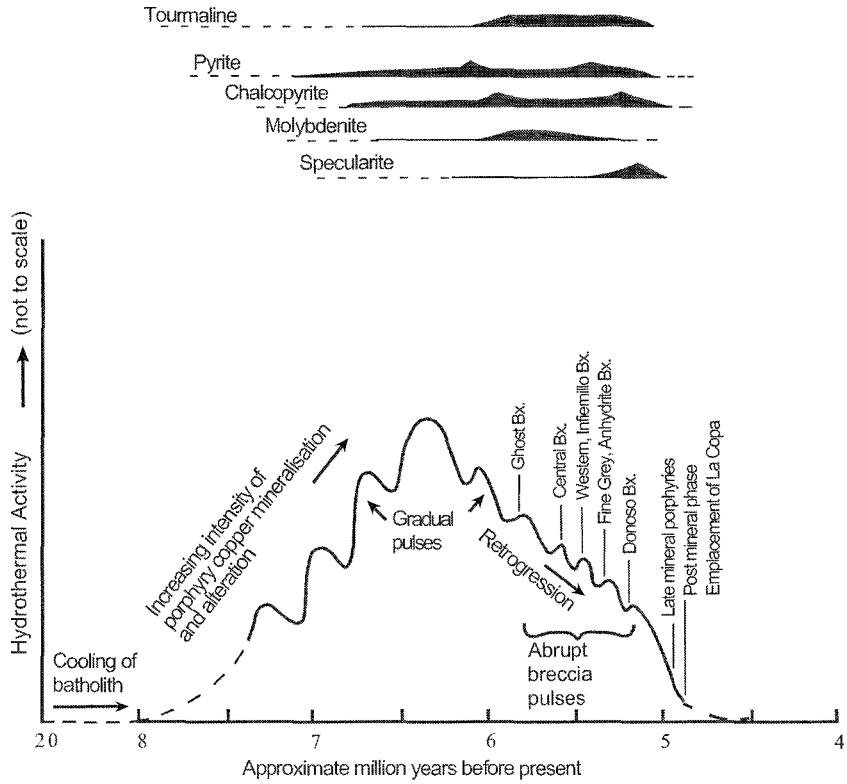

Figure 5.1. Schematic representation of hydrothermal events during the formation of the Los Bronces breccias (from Warnaars et al., 1985).

5.2.2 Río Blanco

Vargas et al. (1999) produced a schematic model showing zonal relationships in the Sur-Sur and La Americana sectors (Fig. 5.2). This model is based on relationships observed over a large area that have been superimposed onto a symmetrical, two-dimensional cross-section. Despite the simplicity of this model for such a complex system, it is useful because it illustrates important mineral zonation in the ore deposit. Key features include a specularite alteration halo that extends gradationally out from the Tourmaline Breccia, and a biotite-cemented breccia that extends downwards from the Tourmaline Breccia. Pyrite abundances increase upwards through the Tourmaline Breccia column, and pyrite:chalcopyrite ratios increase outwards to the margin of the orebody, where chalcopyrite disappears from the breccia cement assemblage (Vargas et al., 1999). Vargas et al. (1999) suggested that magmatic fluids were responsible for initial shattering of the rock column and mineralisation of the breccias. They argued that a certain amount of meteoric water must have mixed with the magmatic-hydrothermal fluids based on work by Holmgren et al. (1988). Vargas et

al. (1999) speculated that mixing with groundwaters may have been responsible for the huge volume and complex reworking of the breccias, and for the apparently large fluctuations in temperature, pressure, oxygen fugacity and salinity. They based these arguments on the presence of magnetite, hematite and anhydrite in varying abundances within the breccias.

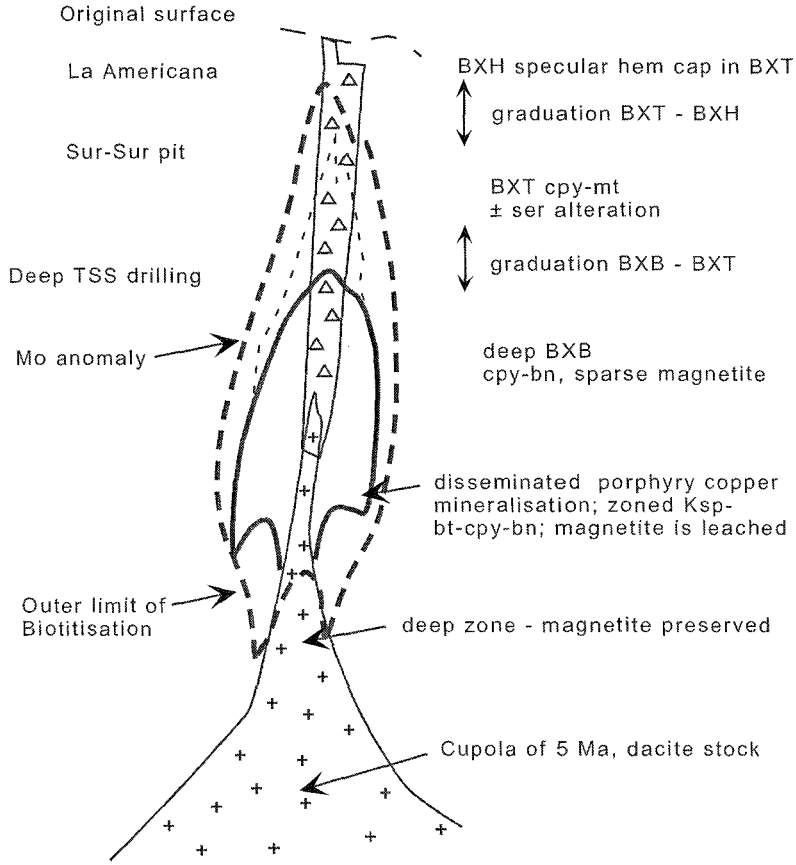

Figure 5.2. Schematic model of zonal patterns related to ore-bearing tourmaline breccias in the Río Blanco - Los Bronces district. BXT = Tourmaline Breccia; BXB =Biotite Breccia; BXH = Hematite Breccia (from Vargas et al., 1999).

5.3 Geodynamics and Architecture

The following points are key elements of the regional architecture and geodynamic setting relevant to ore formation at Río Blanco.

- In the vicinity of the Río Blanco-Los Bronces ore deposit, Farellones Formation volcanism is dated between 18.6 and 16.6 Ma. The youngest of these dates is interpreted to mark the end of volcanism and arc extension. Kay et al. (1991) argue the termination of volcanic activity in central Chile is associated with quiescent sub crustal conditions due to slab underplating. Cessation of volcanism over 10 million years prior to ore formation shows that the model for porphyry ore formation within a coeval stratovolcano (e.g., Sillitoe, 1973) is not relevant to Río

Blanco.

- Cessation of volcanic activity is attributed to a change from extensional to compressional tectonics between ~20 and 16 Ma. This initiated plutonism in central Chile, resulting in the emplacement of the multi-phase San Francisco Batholith between 20.1 and 5.2 Ma.
- Kay et al. (1991) proposed that the crust in central Chile thickened from ~35-40 km in the late Oligocene to ~55-65 km in the late Miocene, attributable to ductile deformation in the lower crust accompanying magmatism under a compressional tectonic regime. Crustal thickening caused a change in the mineralogy of crustal residues for central Chile igneous rocks from a hydrous amphibole-garnet-plagioclase assemblage to an almost anhydrous plagioclase-poor garnet granulite assemblage, which may have increased fluid flux from the lower crust (Kay et al., 1999). Evidence from Sr isotopes also supports crustal thickening in central Chile, where early Miocene (~20 Ma) back-arc alkaline basalts have relatively low $^{87}Sr/^{86}Sr$ ratios (~0.7036) and high Nd (+4.5) compared to the central Chile calc-alkaline magmatic rocks, suggesting that the younger rocks were intruded through and associated with progressively thicker crust (Kay et al., 1991).
- The Río Blanco-Los Bronces ore deposit formed during the final stages of formation of the San Francisco Batholith, between 7.4 and 5.2 Ma (Serrano et al., 1996). The prevailing tectonic regime at this time was still compressional (Skarmeta et al., 2000).
- Localized zones of back-arc extension and/or dilation were present in Central Chile until 5 Ma, when volcanism in the region completely terminated over the flat slab zone (Kay and Mpodozis, 2002).
- The architecture of the crust in central Chile seems to have been controlled largely by tectonic activity related to the subduction of the Juan Fernandez Ridge, which produced a flat slab zone beneath central Chile in the Miocene (Fig. 1.6). Hollings et al. (submitted) argue that crustal thickening and deformation and giant Cu-Mo porphyry formation in central Chile is associated with the south-directed migration of the steep-to-flat flexure of the downgoing slab.
- At the district scale, the Río Blanco and Río San Francisco Faults were active as extensional faults until the Miocene. They were inverted into high angle reverse faults by shortening (Skarmeta et al., 2000).
- Skarmeta et al. (2000) interpreted the Río Blanco Fault as an east dipping, high angle reverse fault and the San Francisco Fault as a west-dipping, high angle reverse fault (Fig. 2.13). Consequently, Río Blanco is inferred to have formed in a horst, as illustrated schematically in Figure 5.3.
- The Río Blanco and San Francisco Faults are also interpreted to have been pull-apart structures (Skarmeta et al., 2000), facilitating dilation, and allowing fluids and magmas to be localised within the Río Blanco-Los Bronces area.
- Although the Río Blanco-Los Bronces ore deposit formed during Pliocene shortening, it is

possible that oblique stresses related to the subduction of the Juan Fernandez Ridge in central Chile could have caused oblique transpression along N-S faults. This may have produced the NE- and NW- trending fault arrays that are preserved in rocks associated with the Río Blanco-Los Bronces ore deposit. These faults were active up until approximately 4 Ma and interacted with the N-S faults to produce dilational jogs that allowed fluids and magmas to be focussed at Río Blanco-Los Bronces.

- The breccias, porphyries and subvolcanic rocks that comprise the Río Blanco ore deposit intruded the southeastern portion of the San Francisco Batholith, and also the overlying volcanic and volcaniclastic rocks of the Farellones Formation. Erosion has removed the Farellones Formation cover sequence at Sur-Sur, however, in the Río Blanco sector, the volcanic and volcaniclastic cover rocks have possibly been preserved as a downfaulted block. Longitudinal section E-E' shows the contact of the overlying Farellones Formation with granodiorite of the San Francisco Batholith (Fig. 2.4). Hydrothermal biotite and chalcopyrite (Figs. 3.15a, b and 3.16c, d) are less abundant above the contact between the granodiorite and the overlying volcanic and volcaniclastic rocks. The distribution of the Magmatic Breccia cement minerals in section E-E' therefore is controlled by the host rock compositions (Fig. 2.4). It may be that the overlying volcanic and volcaniclastic rocks (Farellones Formation) acted as a barrier to fluid flow and confined the hydrothermal fluids within the Río Blanco system, helping to propagate repeated cycles of brecciation and cementation by hydrothermal minerals.
- Uplift and erosion continued through the evolution of the ore deposit complex, culminating in the emplacement of the Don Luis Porphyry, Dacite Chimney and La Copa Rhyolite after mineralisation ceased. The youngest of these units (La Copa Rhyolite) contains an extrusive facies, making a return to minor volcanism in the late Pliocene (3.9 Ma) and also marking the late Pliocene paleosurface.

5.4 Brecciation and Fluid Exsolution Processes

The bulk of the ore at Río Blanco-Los Bronces occurs as breccia cement. It is therefore necessary to review briefly the types of processes that can produce breccias in porphyry systems. In general, breccias in porphyry copper deposits can form by magmatic, tectonic and/or hydrothermal processes. Brecciation in these environments can be essentially instantaneous. It can produce rock flour breccias such as diatremes (phreatomagmatic breccias) or fault breccias. It can also produce mineralised magmatic-hydrothermal breccias that contain ore minerals as cements (e.g. Sillitoe, 1985). The following sections review the three main categories of breccias that may occur in porphyry environments.

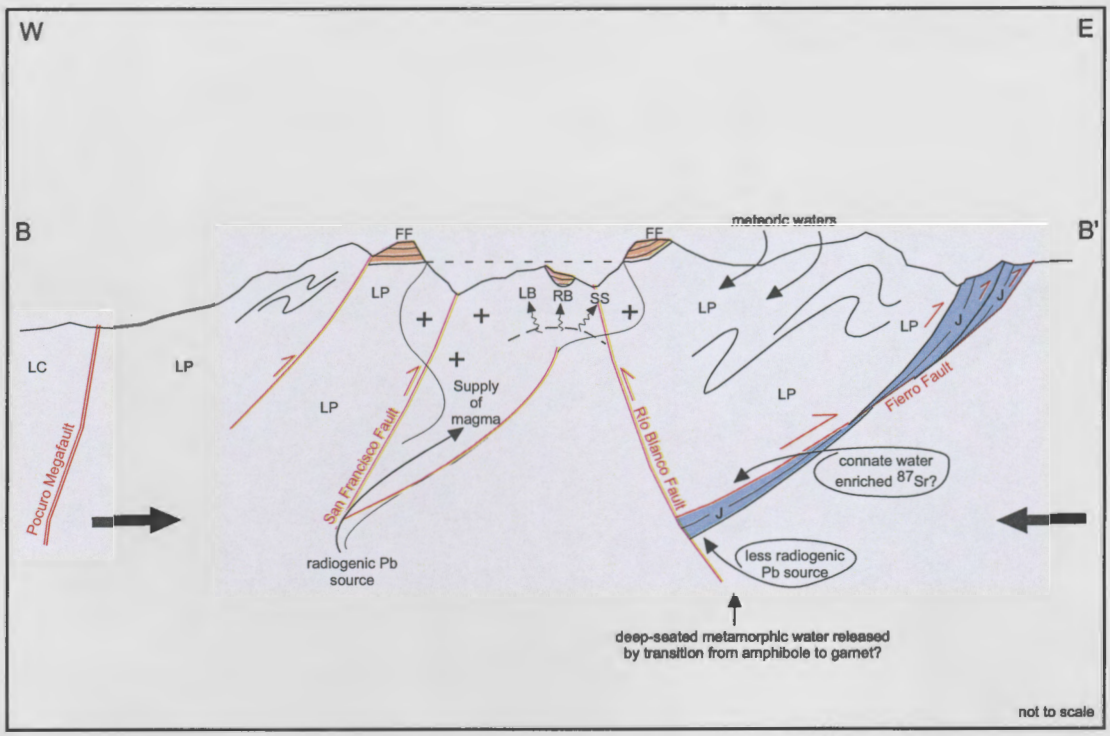

Figure 5.3. Schematic, interpretive cartoon illustrating the architecture at Río Blanco-Los Bronces based on the current study, Skarmeta et al. (2000) and cross-section B-B' in Figure 1.2. FF = Farellones Formation, J = Jurassic sediments and evaporates, LB = Los Bronces, LC = Las Chilcas Formation, LP = Los Pelambres Formation, RB = Río Blanco, SS = Sur-Sur, + = San Francisco Batholith.

5.4.1 Tectonic Breccias

Sibson (1986) argued that implosive brecciation is associated with the sudden creation of void space and fluid pressure differentials at dilational fault jogs during earthquake rupture and fault propagation. Dilational breccias are particularly favourable sites for hydrothermal mineral deposition and form transitory low-pressure channels for the rapid passage of hydrothermal fluids. High flux fluid flow has also been suggested to occur through the production of a fault-fracture mesh involving extensional and extensional shear fractures above pre-existing faults that have been reactivated during shortening (Sibson, 2000). This can result in the most extreme fault valve action and generate permeable pathways for rising hydrothermal fluids along steep reverse faults. Activation of the mesh occurs from fluid pressure build-up preceding each episode of reverse fault slip (Sibson, 2000). Closely spaced fracture networks, whether stockwork or breccia form, most effectively when the rocks overlying a magma chamber retain tensile behaviour. This is followed by post-failure high-flux discharge along the faults. Between successive slip increments, the fault regains cohesive strength by the precipitation of hydrothermal cements within the mesh (Sibson, 2000). The incipient weakness of rocks in tension increases their failure potential when exposed to pressure gradients generated by an underlying magma chamber.

The Sur-Sur Tourmaline Breccia is thought to be (in part) tectonic, having probably formed partly in response to fault movements. This is discussed further in Section 5.4.3.

5.4.2 Phreatomagmatic breccias

Phreatomagmatic breccias (including maar-diatreme complexes) can form when cool groundwaters interact explosively with subsurface magmas (Sillitoe, 1985). Part of the process of formation for these breccias is that they vent, resulting in loss of volatile constituents to the atmosphere. This explains in part why many phreatomagmatic breccias are unmineralised and form prior to, or after, mineralisation in porphyry environments (Sillitoe, 1985). Some of these breccias are mineralised within their coarse clastic marginal facies, where metalliferous fluids have been able to permeate through parts of the breccia (e.g. El Teniente). The main facies within these large breccia pipes are typically matrix-supported, contain rock flour and are comparatively impermeable, causing them to only be weakly altered and unmineralised (Sillitoe, 1985).

One phase of the La Copa Rhyolite complex has been reported to be a 'diatreme' (i.e. phreatomagmatic breccia; Serrano et al., 1996). However, it is not associated with mineralisation in the ore deposit. The unmineralised rock flour breccias (BXTO, BXMN and BXTTO) that occur adjacent to (and which formed after) the Sur-Sur Tourmaline Breccia are supported by a rock flour matrix and could be phreatomagmatic or tectonic in origin. More work is required to fully assess the origin of these unmineralised breccias at Río Blanco.

5.4.3 Magmatic-Hydrothermal Breccias

Burnham (1985) proposed that magmatic-hydrothermal breccias in subvolcanic environments formed by the sequential release of mechanical energy from moderately hydrous magmas (~2-4 wt. % H_2O) through the process of decompression and subsequent aqueous fluid exsolution. Although decompression is considered to be the main energy source for breccia formation, phase separation can play an important role in propagating the active front of fragmentation, especially in shallow crustal environments due to steam expansion (Burnham, 1985).

Magmatic-hydrothermal breccia formation is a two-stage process. Initial breaking of the rock column may be caused by hydrostatic pressures exceeding the combined lithostatic load and the tensile strength of the rock (Burnham, 1985) and/or by fault rupturing due to tectonism. After brecciation, upwelling magmatic-hydrothermal fluids cement the broken rock (clasts). Evidence for these fluids are preserved as brine (type ii) and vapour-rich (type iii) fluid inclusions in the breccia cement.

Processes of phase separation in porphyry environments has been reviewed by workers such as Burnham (1985), Bodnar et al. (1985) and Fournier (1999). Metals can be partitioned from the melt into the aqueous phases. Many authors argue that the metals are carried as metal chloride

complexes within the dense brines in porphyry copper systems, and that most of the metals readily partition into this aqueous fluid rather than into the silicate melt (Holland, 1972; Kilinc and Burnham, 1972; Henley and McNabb, 1978; Candela, 1984; Candela and Holland, 1986; Candela, 1989; Candela and Piccoli, 1995).

To generate porphyry-style mineralisation, the source magma must be saturated with respect to volatiles. Furthermore, those volatiles must separate physically from the melt and migrate by convection to the apical regions of the magma chamber, where they can pond beneath the crystallising carapace (Henley and McNabb, 1978; Burnham, 1979; Candela, 1991; Shinohara and Kazahaya, 1995). Burnham (1985) proposed that the mass fraction of H_2O in the initial melt is considered to be the most important factor in the formation of hydrothermal breccias in porphyry systems. The mass fraction of water in the initial melt must be 0.02 to 0.04 at liquidus temperatures to release sufficient energy for breccia formation (Burnham, 1985). The formation of volatiles in a magma chamber at shallow depths occurs as a sequential process (Burnham, 1997). At first, volatile exsolution may occur by a process known as second boiling, where the crystallisation of anhydrous minerals from the magma results in an overall increase in the proportion of volatiles remaining in the melt. This process is also responsible for generating sufficient mechanical energy to produce fracture failure to depths of 4-5 km (Burnham, 1985).

Second boiling is enhanced by decompression (first boiling) of the magma chamber as it ascends upwards through the crust. This causes expansion of the uncrystallised fluid and release of dissolved, low-density volatile constituents (Burnham, 1979, Candela, 1991). Decompression can be triggered by brittle failure if the hydrostatic pressure associated with the accumulation of volatiles in the apical regions of a magma chamber exceeds the lithostatic load and the tensile strength of the confining rocks (Henley and McNabb, 1978; Burnham, 1985).

Aqueous phase separation in porphyry copper systems can generate dense, high salinity fluids (brines) and low-density gases. According to Henley and McNabb (1978), the metal-bearing brine (40-60 wt. % NaCl equivalent) remains in and around the apical regions of the crystallising magma due to its high density where it may produce potassic alteration and associated stockwork mineralisation (low fluid pressures) or magmatic-hydrothermal breccias (high fluid pressures). The low-density gas phase is buoyant and migrates upwards from the same intrusion. Phase separation is considered to occur at the interface between lithostatic and hydrostatic pressure conditions at the brittle-ductile transition at temperatures as high as 370-400°C for silicic rocks in tectonically active regions (Fig. 5.4; Fournier, 1991; Fournier, 1999). In the temperature range of 350-425°C, the aqueous solubilities of silicates and oxides such as quartz, decrease markedly as pressure decreases at constant temperature (Fournier, 1985). Thus, gangue precipitation is particularly likely in this temperature range, where there are relatively steep pressure gradients (Fournier,

1991).

The change in confining pressure from lithostatic to hydrostatic by decompression induces fracturing and volatile release into the overlying rocks. The low-density fluid (gas) continues to be released in batches, and migrates upward through the vertical rock column propagating the fracture front until its energy dissipates. The low-density gas mixture that separates from the denser, metal-carrying brine is considered to be composed mainly of magmatic water (juvenile H_2O; Henley and McNabb, 1978). However, other components such as SO_2, CO_2 and HCl are also likely to be present (Henley and McNabb, 1978). Allman-Ward et al. (1982) documented that tourmaline breccias at Wheal Remfrey formed as a consequence of disruption and fluidisation by a boron-rich fluid undergoing decompression. The volume of tourmaline breccia preserved at Río Blanco is an indication that boron was a major component of at least one aqueous phase. Wolf and London (1997) argue that B_2O_3 is partitioned into the gas phase from crystallising magmas.

Porphyry copper deposits typically contain a stockwork of closely spaced, crosscutting veins that form an orebody centred on a porphyry stock (Lowell and Guilbert, 1970). In contrast, the Río Blanco-Los Bronces deposit consists of multiple bodies of breccia (mineralised and unmineralised) that were emplaced over approximately one million years, with the bulk of the resource contained within the first two magmatic-hydrothermal breccia bodies formed (Río Blanco and Sur-Sur). Rapid magmatic gas generation and expansion drives magmatic-hydrothermal brecciation. Stockwork veining will form when energy release is lower, either due to smaller volumes or lower rates of gas exsolution that result in less dense fracturing in porphyry copper environments (Fournier, 1999). Once fractures in the overlying rock column are cemented with newly precipitated minerals, the system essentially seals itself and the whole process can be repeated in a multiphase system.

The Río Blanco Magmatic Breccia has characteristics typical of a magmatic-hydrothermal breccia. The geometry of the Magmatic Breccia suggests no obvious correlation to faults. The Magmatic Breccia contains a partially recrystallised rock flour matrix and is also cemented by large quantities of hydrothermal minerals. The cements contain high temperature coexisting hypersaline and low-density gas-rich fluid inclusions, consistent with magmatic-hydrothermal fluids sourced from a crystallising magma. The processes involving fluid exsolution described above are inferred to have been responsible for the formation of this breccia.

The Sur-Sur Tourmaline Breccia has characteristics of both tectonic and magmatic-hydrothermal breccias. Even though no cataclastite has been observed, the Tourmaline Breccia is a 3 km long body aligned along the southward continuation of the Río Blanco Fault, and a tectonic component to its formation is suspected (Figs. 2.8, 2.9 and 2.11). The Tourmaline Breccia is generally clast-supported and is cemented by a large quantity of hydrothermal mineral cement with small quantities

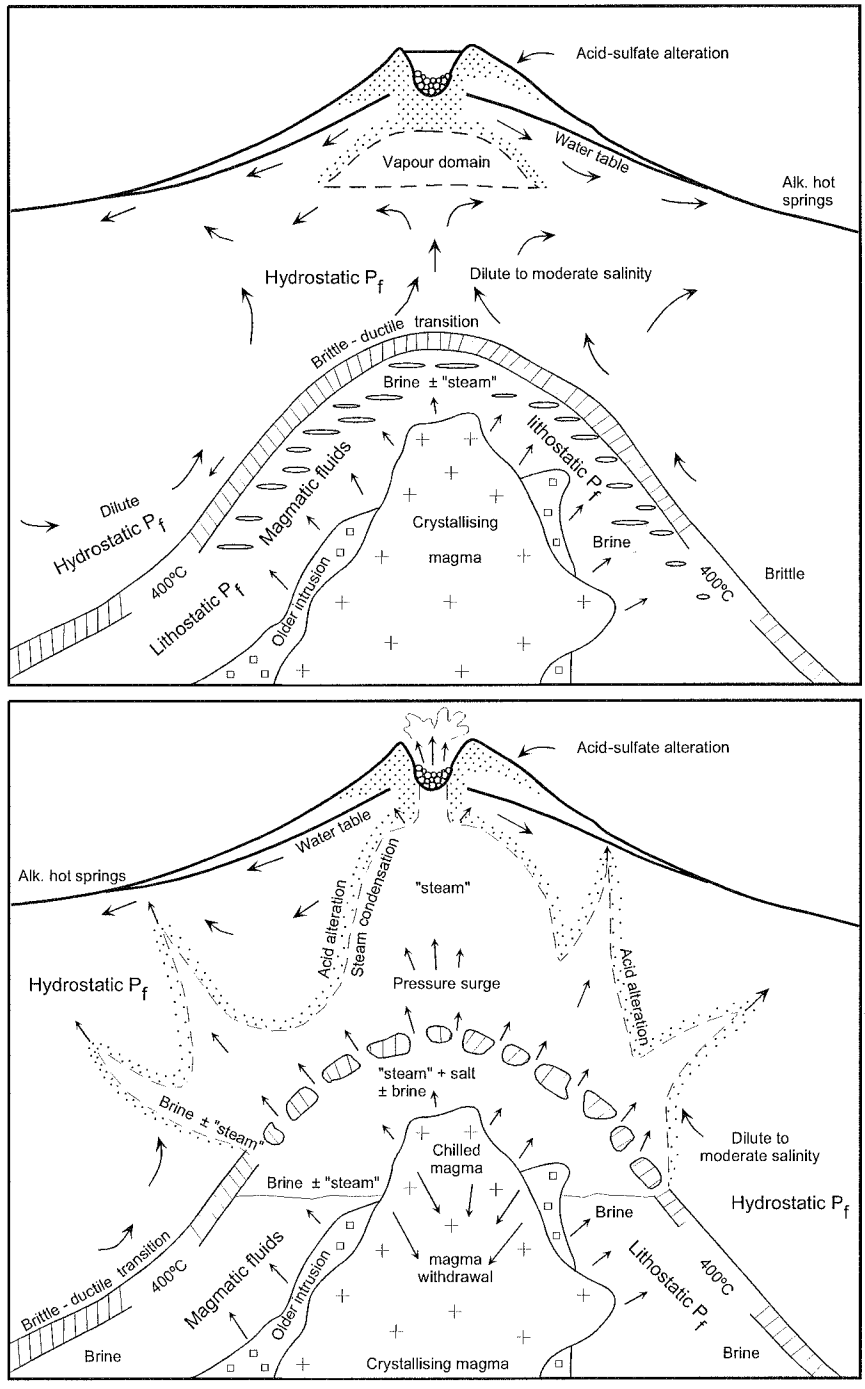

Figure 5.4. Schematic model of the transition from magmatic to epithermal conditions in a subvolcanic environment where the tops of plutons are in the range of 1 to 3 km. a) The brittle to plastic transition occurs at about 370° to 400°C and dilute, dominantly meteoric water circulates at hydrostatic pressure in brittle rock while highly saline, dominantly magmatic fluid at lithostatic pressure accumulates in plastic rock. b) Episodic and temporary breaching of a normally self-sealed zone allows magmatic fluid to escape into the overlying hydrothermal system (Fournier, 1999). Note that Fournier (1999) speculates that fluid exsolution occurs together with volcanic fumarole activity.

of rock flour. The cements contain hypersaline brines and gases, consistent with a magmatic-hydrothermal origin for the mineralising fluids. The quantity of cement varies along strike of the Tourmaline Breccia. Where small quantities of cement occur, the breccia is a crackle breccia and copper grades are low. The high fracture density distribution along section D-D' at Sur-Sur corresponds to zones of high fluid fluxes, as indicated by the presence of ore-grade zones along strike of the Tourmaline Breccia (e.g. Fig. 2.9). This spatial association of high-grade zones and intense fracturing is interpreted to indicate that a tectonic trigger must have been important for brecciation at Sur-Sur, even though catastrophic magmatic-hydrothermal brecciation has destroyed any cataclasite and/or gouge zones that may have formed initially in the breccia body. A schematic model for breccia emplacement at Sur-Sur is illustrated on Figure 5.5.

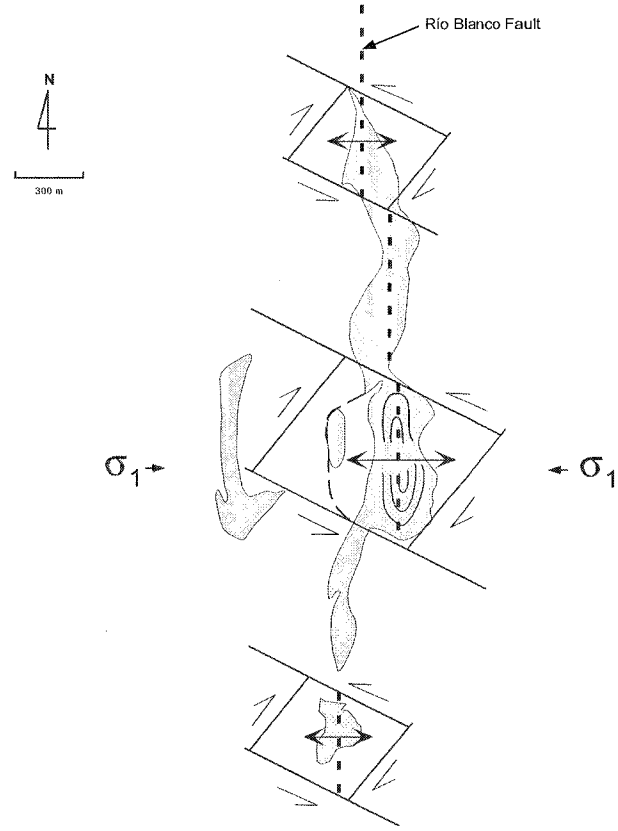

Figure 5.5. Schematic model encompassing dilation in zones of high fracture density and hydrothermal fluid flow in the Sur-Sur Tourmaline Breccia.

In addition to the magmatic-hydrothermal and tectonic triggers for brecciation at Río Blanco, it is possible that climatic triggers may have also been involved. Crustal thickening most likely continued to elevate the central Chilean Andes throughout the formation of the Río Blanco-Los Bronces

system, resulting in progressive exhumation of the ore system. Given the current climate and altitude, it is likely that glaciers covered the region during the late Miocene, helping to promote rapid erosion. If the palaeo-climate was similar to today, seasonal dumps of snow and ice probably covered the mountain ranges during winter months until the warmer summer months melted the ice. Glacial moraines would have developed and scoured large volumes of rock and sediment from the Río Blanco Fault, ultimately producing the north-south trending, up to 1 km deep valley preserved today (Fig. 5.6). The Río Blanco valleys are U-shaped, contain striations and have smooth valley walls. Erosion by ice, and/or seasonal melting of ice may have contributed to fault rupture and/or hydrothermal explosions, due to cyclic changes in lithostatic load above the site of ore deposition. It is possible that the pressure changes caused by glacial erosion and retreat may have been sufficient to trigger some sub-surface brecciation events during the formation of the hydrothermal system. A modern example of phreatic brecciation triggered by draining of a glacially dammed lake has been documented from Yellowstone National Park, USA (Muffler et al., 1971).

5.5 Fluid Reservoirs

As for most porphyry copper systems, Río Blanco contains abundant evidence for the involvement of magmatic-hydrothermal fluids in ore (and breccia) formation. However, the geochemical datasets presented in Section 4 cannot be explained solely by magmatic-hydrothermal brines and gases liberated from crystallising magmas. This section highlights the datasets that appear to require external fluid involvement, possibly combined with back-reaction of two magmatically-derived fluids, in order to fully explain their characteristics.

5.5.1 Stable isotopes and fluid inclusions

Oxygen and deuterium isotope studies of breccia cement minerals at Río Blanco-Los Bronces suggest that the fluids circulating during breccia formation were of magmatic derivation, with little evidence for a meteoric component. No oxygen/deuterium isotope evidence is available to argue that the pre-ore oxide stage minerals (e.g. tourmaline and specularite) were precipitated by external waters. Instead, the water was predominantly sourced from a magmatic reservoir. Increased acidity related to $HCl_{(g)}$ dissociation and/or $SO_{2(g)}$ disproportionation is considered to be responsible for the transition from biotite to phyllic alteration at Río Blanco-Los Bronces, rather than an influx of external water. A minor component of meteoric water was detected in propylitic-altered samples analysed by Kusakabe et al. (1984; 1990).

The sulfur isotope data collected in this study indicate that the sulfur in sulfide and sulfate miner-

Figure 5.6. Photograph taken from La Americana towards the north up the Río Blanco glacial valley. The Sur-Sur open pit is in the mid-foreground and the glacier to the top right of the photo is Cerro Negro. The foreground elevation is at ~4500 m, and the northern flank of the Río Blanco valley is at ~2000 m elevation.

als is magmatically-derived. However, distinctly negative sulfur isotope values obtained for chalcopyrite at high altitude (>3700 m asl) in the Sur-Sur Tourmaline Breccia correlate with zones of high copper grade, abundant specularite (or anhydrite at depth) and vuggy textures in the breccia matrix (Figs. 3.19d, 3.21a, 2.23a, 4.42 and 4.43). The transition from near-zero to -4‰ values of $\delta^{34}S$ occurs over a 100 m vertical interval. This fractionation is inferred to have been produced by mixing-induced cooling at the top of the Sur-Sur system, coincident with the development of widespread specularite cement (Section 3.4.3).

Type i, ii and iii fluid inclusions indicate the presence of low salinity water, a hypersaline brine and a gas phase in the mineralised breccia bodies. The large range of salinity data presented in Section 4.3 is interpreted to indicate fluid mixing between low salinity liquid (and/or gas?) with hypersaline brine. The abundance of liquid-rich fluid inclusions suggests there was a large quantity of low salinity water in the system, however, the source of this water is not clear. Two sources can be suggested, (i) from the magma chamber; or (2) an external water, be it meteoric groundwater, connate water from the underlying sedimentary successions, or metamorphic water from the lower crust. None of the fluids involved in this process are parent fluids, all are daughter fluids derived from some magmatic fluid and a possible external fluid supplied water (see below).

5.5.2 Radiogenic isotopes

The early anhydrite and tourmaline breccia cement in the Magmatic and Tourmaline Breccias are enriched in $^{87}Sr/^{86}Sr$ relative to the immediate host rocks in the ore deposit (Fig. 4.5). The enrichment is only recorded in the $^{87}Sr/^{86}Sr$ data; in contrast the ε_{Nd} signature is the same in both the gangue and the host rocks. This trend towards elevated $^{87}Sr/^{86}Sr$ and constant ε_{Nd} has previously been recorded for sedimentary and volcanic rocks that have interacted with seawater (Rollinson, 1993). The only rocks in the district that have had exposure to seawater (prior to uplift of the Andes) are the Jurassic and Cretaceous Formations including Yeso Principal, the San José, Cristo Redentor and the base of the Los Pelambres Formation. Stratigraphic reconstruction that accommodates thrusting in the district places these sedimentary rocks beneath the Río Blanco-Los Bronces ore deposit (Figs. 1.2 and 5.3), and they may be the source of the enriched Sr values in the anhydrite.

The sulfide breccia cement at Río Blanco has a similar Pb isotope signature to the regional rocks of the Southern Volcanic Zone. In contrast, the early breccia cement minerals (anhydrite) have a less radiogenic Pb isotope signature than the sulfide ores and host rocks (Fig. 4.6). Although the limited oxygen/deuterium isotope data obtained to date indicate that most of the water in the Río Blanco hydrothermal system is of magmatic derivation, a component of water in the breccias must be exotic, in that it needed to have interacted with older rock formations to produce the Pb and Sr

isotope systematics of the anhydrite and tourmaline. The external Pb source had a less radiogenic isotopic signature, comparable to the Precordilleran basement and Precordillera of central Chile (Fig. 4.6).

There is an apparent conundrum in the stable and radiogenic isotope data, in that the anhydrite contains magmatic S, and it also contains Pb and Sr (and, by inference, Ca?) derived at least partly from external reservoirs. This situation could be explained by SO_2-bearing magmatic gases flushing upwards through the breccia column, and condensing into and reacting with an external water containing exotic Pb, Sr and possibly Ca (Ca could also have been sourced locally by leaching of plagioclase during phyllic alteration). Mixing-induced reaction of oxidised S with Ca caused anhydrite deposition. This occurred prior to flushing of the breccia column by magmatic brine and deposition of main stage sulfide mineralisation. This two-stage process is consistent with the textural evidence for replacement of oxide-stage anhydrite by main stage sulfides (e.g., Fig. 3.5c-f).

The Pb isotope compositions of sulfides from the mineralised breccia cements indicate a well-homogenised source, probably from the parent magma chamber. This is not to say that the sulfide Pb was not exposed to other Pb sources upon ascent. However, the volume of Pb in the magma chamber was so great that external sources of Pb had no, or very little influence on the overall magmatic Pb signature (Fig. 4.6).

In terms of external fluid reservoirs, the most important finding in this study is the radiogenic isotope compositions of the anhydrite. The anhydrite cement contains no hypersaline fluid inclusions. It has enriched $^{87}Sr/^{86}Sr$ and less radiogenic Pb isotopic compositions compared to the host rocks and sulfide minerals. It is concluded that the fluid that deposited the early anhydrite in the breccia cement must have been sourced at least in part from outside the magmatic-hydrothermal system. It may be that the source of this external water was the lower crust. Kay et al. (1999) argued that crustal thickening caused the wholesale breakdown of amphibole to garnet in central Chile, and this would have released a low salinity aqueous fluid (Fig. 2.15). It is possible (but cannot be proven with the available data) that this hypothesised metamorphic fluid could have less radiogenic Pb isotopes and higher $^{87}Sr/^{86}Sr$ values, and may have been involved in the precipitation of early breccia cements, prior to sulfide precipitation at Río Blanco. Meteoric and connate sources also cannot be discounted at this stage. More work is required to evaluate the source of the exotic Pb and Sr contained within anhydrite at Río Blanco.

Figure 5.3 illustrates one possible architecture that could account for the data generated by the current study, the structural mapping of Skarmeta et al. (2000) and the regional geology (Fig. 1.2). This schematic model illustrates the possible role of basement faults (such as the Río Blanco Fault) in channelling external fluids to explain the anomalous radiogenic isotope data. The base-

ment faults are considered to be reactivated normal faults that were inverted during Miocene shortening. This shortening resulted in crustal thickening and thrust faulting. Architectural reconstruction of Jurassic to Cretaceous marine sediments and volcanic rocks to the east of the ore deposit places these rocks in a location beneath Río Blanco. Inversion and reactivation of the Río Blanco Fault may have tapped deeply-derived metamorphic waters such as those proposed by Kay et al. (1999) or connate fluids contained within the Jurassic-Cretaceous sedimentary and volcanic rocks. Alternatively, it could have caused infiltration of these units by shallowly-derived meteoric water. Any of these processes could explain the Sr enrichment in anhydrite at Río Blanco. However, the Pb isotope data is probably best explained by Kay et al.'s (1999) deep-seated metamorphic fluids (Fig. 5.3).

5.6 Ore depositional processes

Fluids need to undergo drastic changes in chemical potential along their flow paths in order to precipitate high-grade ore. The fluid inclusion data from Río Blanco and Sur-Sur show evidence for high temperature phase separation of magmatic-hydrothermal gases and brines, and this process may have caused precipitation of at least some of the sulfides in the mineralised breccias. Given that most of the ore resides as breccia cement in relict pore spaces, water-rock interaction is not thought to have been an important process for ore deposition. Conductive cooling is also considered to be an unlikely process of ore formation, as thermal gradients need to be very steep to induce high-grade sulfide ore deposition (Drummond and Ohmoto, 1985).

As discussed in the previous section, fluid mixing has been inferred as the most likely mechanism to explain the stable and radiogenic isotopic compositions of anhydrite at Río Blanco. With regards ore deposition, the highest-grade ore zone in the Sur-Sur Tourmaline Breccia coincides with a mineralogical transition from deep-level magnetite to shallow-level specularite, and with a domain of sulfide minerals that have distinctly negative $\delta^{34}S$ values. Ore deposition in this zone is inferred to be a product of fluid mixing, which is believed to have caused dramatic cooling and oxidation of the mineralising brine (Section 4.5). Similar iron oxide zonation of magnetite at depth to specularite at shallower levels has been observed at the Candelaria Cu-Au deposit, Chile (Marschik and Fontbote, 2001). This Fe-oxide transition also corresponds to a shift towards lower $\delta^{34}S$ values up section in the Santos and Socarvon Rampa mines and is interpreted to reflect oxidation of the ore fluid (Marschik and Fontbote, 2001).

Specularite and anhydrite are indicators of oxidised fluid conditions ($mSO_4 = mH_2S_{(aq)}$), whereas magnetite forms under relatively reduced conditions ($mH_2S = mSO_4$; e.g. Cooke and Simmons, 2000). The vertical zonation and paragenesis of specularite and magnetite in the Sur-Sur Tourma-

line Breccia is inferred to be a product of the mixing-induced reaction of two magmatic-hydrothermal fluids derived from the parent magma by phase separation. These fluids are inferred to have physically separated at the base of the breccia column due to density contrasts and then back-reacted with each other higher up within the Sur-Sur breccia body. The deep-level biotite-cemented breccia and the domain where chalcopyrite and magnetite co-exist in the tourmaline breccia (below 4000 m) are inferred to be domains where a reduced (H_2S-predominant) fluid prevailed (most likely, the magmatic-hydrothermal brine). In contrast, based on the observed mineralogy, the specularite zone at high elevations (above 4000 m) in the Tourmaline Breccia is inferred to have contained predominantly oxidised fluid (suspected to be a hybrid water that formed when magmatic gas condensed into the externally sourced, exotic Pb-bearing water). The transitional zone between 3500 m and 4000 m elevation where pre-ore oxide stage specularite is pseudomorphed by magnetite is a zone of overlap between these two contrasting fluid types. This is interpreted to be the main zone of mixing, where the reduced mineralising brine has interacted with the oxidised hybrid fluid. It seems likely that the actual mixing zone would have fluxed up and down at any given point in time, depending on the rate of upwelling of brine and down-welling of hybrid water. Evidence for this is provided by the extreme salinity array preserved in fluid inclusions throughout the vertical interval of breccia-hosted mineralisation. It is suggested that mixing produced an effective thermo-chemical gradient that precipitated copper out of the fluid phase to produce high-grade chalcopyrite zones between 3500 and 4000 m in the Tourmaline Breccia. A similar, but less obvious scenario has been recorded in the Río Blanco Magmatic Breccia, where the same gradient from magnetite-dominance at depth to specularite at the highest altitudes is observed, however, a lack of spatial data cannot confirm or reject if this feature has affected the grade distribution in the Río Blanco Magmatic Breccia.

The transition upwards from potassic and phyllic alteration in the Sur-Sur Tourmaline Breccia probably relates to acidity generated by the magmatically-derived SO_2-bearing gas. Acidity could have been generated by $HCl_{(g)}$ dissociation and/or SO_2 disproportionation. The sub-magmatic hydrolysis of SO_2 could have been the source of sulfide sulfur for chalcopyrite and bornite with distinctly negative $\delta^{34}S$ values in the high-grade ore zone at Sur-Sur.

The subtle sulfur isotope zonation at Sur-Sur supports the hypothesis that a thermochemical gradient existed at the top of the breccia body. The redox conditions for mineral assemblages in the Sur-Sur Tourmaline Breccia has been portrayed using a phase diagram constrained by the log activity of H_2S and the log activity of fO_2, a temperature of 400°C and a pressure of 500 bars (Fig. 5.7). Pre-ore oxide stage specularite is represented by point #1. The reduced mineralising fluid that co-precipitated chalcopyrite and magnetite is represented by #2. It is possible that mixing of fluid #1 with fluid #2 would initially produce a fluid with an intermediate composition (#3), apparently coincident with high-grade ore deposition at Sur-Sur. Continued interaction with fluid #1 into

fluid #3 evolved the hybrid fluid to point #4, which is recorded in mineral assemblages at the highest elevations in the Tourmaline Breccia where only pyrite, specularite and tourmaline have cemented the breccia. Overall, the equilibration of high temperature, saline and reduced mineralising brine with cooler, dilute, oxidised water and/or gas decreased temperatures and a_{Cu+} due to chalcopyrite deposition and drove the sulfide stability from chalcopyrite to pyrite (Fig. 5.7).

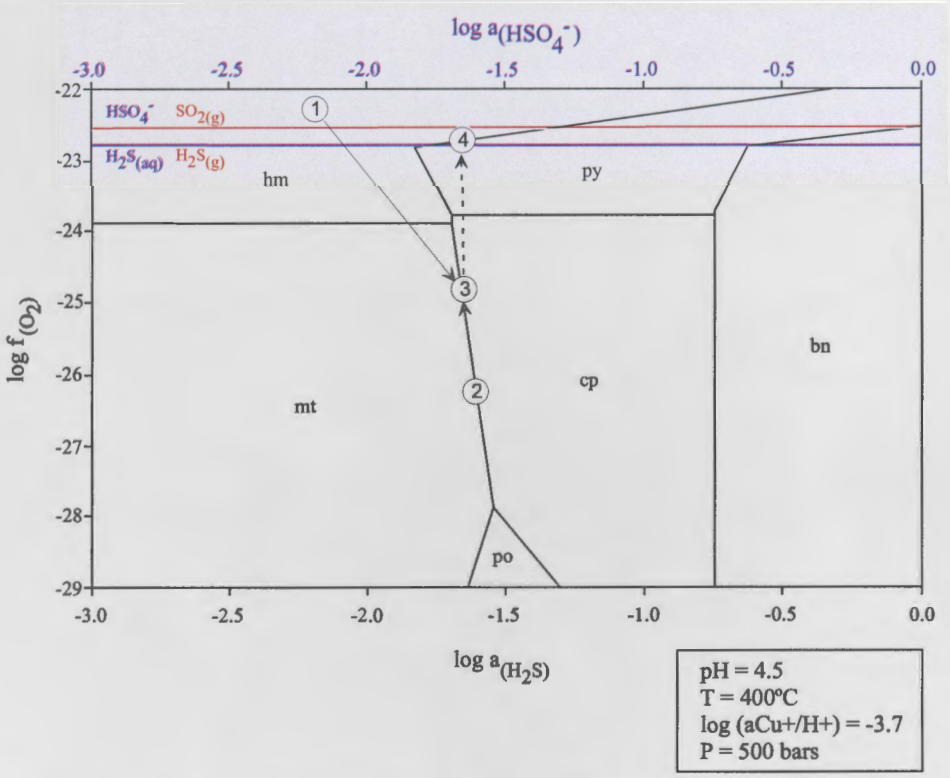

Figure 5.7. Phase diagram showing the log activity of H_2S, the log activity of fO_2, the log activity of HSO_4^-, a log activity of Cu+/H+ of -3.7, a pH of 4.5, at a temperature of 400°C and a pressure of 500 bars.

In summary, high-grade ore deposition at Sur-Sur appears to have involved back-reaction of two magmatic-hydrothermal fluids (gas and brine). The external water inferred to be the source of exotic Pb and Sr in anhydrite could have been involved in this process, in that it may have been the fluid into which magmatic gas condensed within the breccia body, producing a hybrid, acidic, oxidised low salinity water that precipitated anhydrite, tourmaline and specularite cement. It would have also altered rock clasts to a quartz-sericite±tourmaline assemblage, prior to the main-stage mineralisation event, which involved mixing of the hybrid water with the brine, at least at shallow levels in the breccia body. Mixing-induced cooling of the brine outstripped the competing effects of oxidation to allow high-grade ore deposition at the top of the Sur-Sur breccia. Mechanisms of ore deposition in the Río Blanco Magmatic Breccia remain uncertain, due to the lack of obvious mineralogical and/or isotopic gradients coincident with high-grade ore zones.

Based on the available geological and geochemical evidence, the Río Blanco-Los Bronces system is considered to be a variation on the porphyry copper theme. Ore deposition in porphyry copper

deposits remains poorly understood, despite several decades of voluminous research on this class of hydrothermal ore deposit. At Río Blanco and Sur-Sur, there is evidence for a complete interplay of fluid mixing, phase separation, oxidation-reduction and water-rock interaction during the formation of the mineralised biotite and tourmaline-cemented breccias. The combination of these processes has led to ore deposition over more than a one kilometre vertical interval of breccia-hosted mineralisation.

5.7 A Genetic Model for Río Blanco

The geological evolution of the Río Blanco ore deposit is described sequentially below, and illustrated schematically in Figures 5.8-5.12.

5.7.1 Stages 1 and 2: Magnetite-actinolite alteration and potassic stockwork veins

After the emplacement of the San Francisco Batholith into the Los Pelambres and Farellones Formations, an initial phase of diffuse hydrothermal alteration produced the stage 1 magnetite-actinolite alteration assemblage. The origin of stage 1 fluids is unknown, although a high temperature is inferred from the mineral assemblage. Similarly, the exact distribution of stage 1 assemblage is not known, however it was described by Serrano et al. (1996) to surround the potassic alteration zone of the deposit, and was inferred to form at a depth between 3 and >6 km.

Stage 1 was followed by stage 2, a weakly mineralised stockwork of sulfide-bearing quartz-biotite veins with biotite alteration halos that are localised at depth mainly in the Río Blanco and Don Luis sectors (Fig. 5.8). Stage 2 veins crosscut the magnetite-actinolite alteration and are localised mainly between the Río Blanco and Don Luis sectors (Fig. 5.8). The stockwork veins are the precursor to the extensive, strongly-mineralised biotite and tourmaline-cemented breccias that host the bulk of the ore at Río Blanco.

5.7.2 Stage 3: Brecciation and mineralisation

The Magmatic Breccia crosscuts the stage 2 veins and hosts most of the ore in the Río Blanco to Don Luis sectors. $^{40}Ar/^{39}Ar$ age spectra of hydrothermal biotite and K-feldspar indicate a final cooling age between 4.78 and 4.2 Ma for the Magmatic Breccia. Transitionally upward and outward from the Magmatic Breccia is the mineralised Tourmaline Breccia, which utilised the Río Blanco Fault in the Sur-Sur sector. Final cooling of the Tourmaline Breccia has been dated at 5.42 ± 0.09 to 4.78 ± 0.04 Ma by Ar-Ar of whole rock sericite and biotite cement, respectively. These

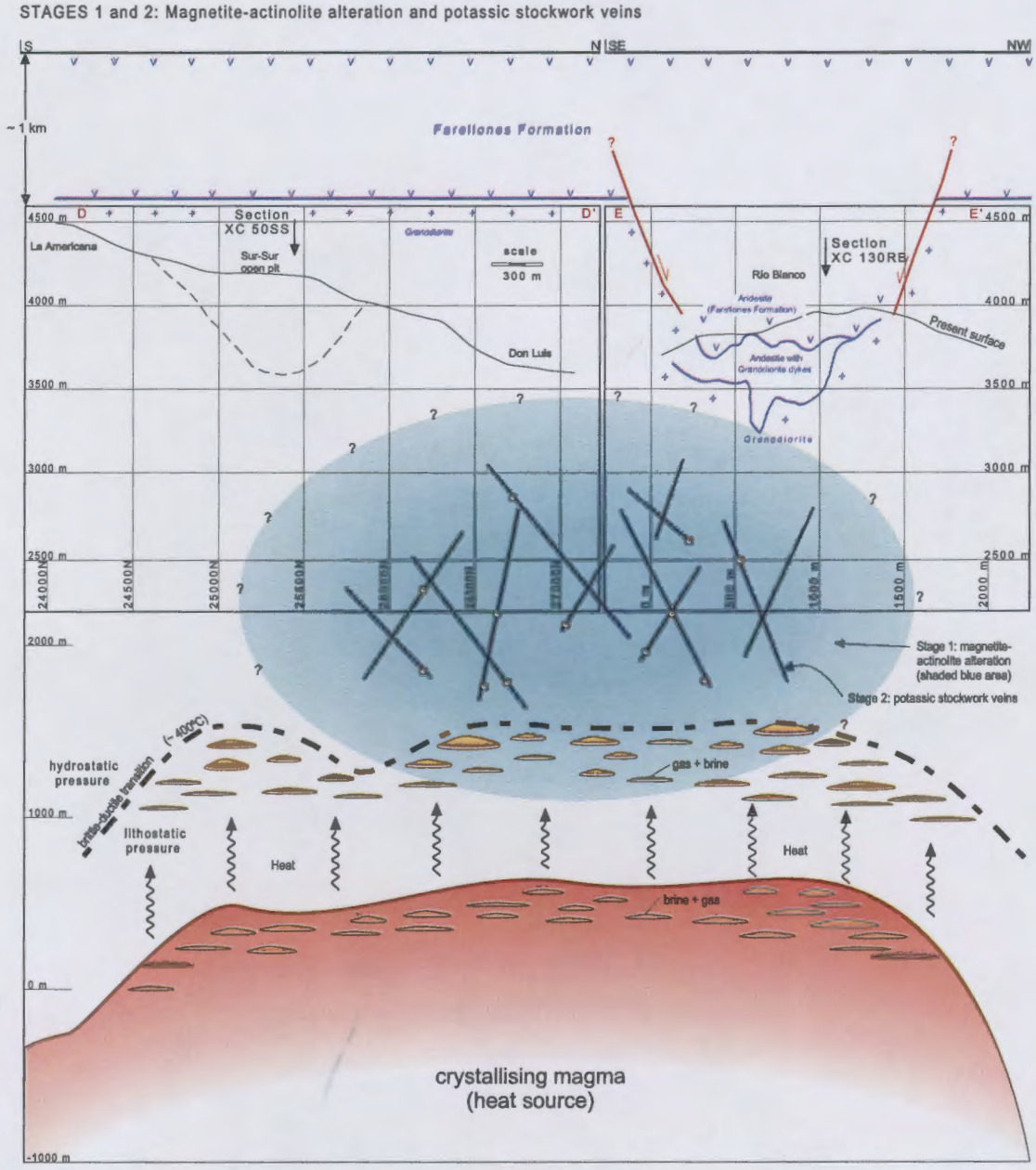

Figure 5.8. Schematic diagram showing paragenetic stages 1 and 2 at Río Blanco. This schematic diagram is based on geological relationships along longitudinal sections D-D' and E-E' through the La Americana, Sur-Sur, Don Luis and Río Blanco sectors (section lines shown in Fig. 3.15). An inferred crystallising magma chamber is shown at depth with a carapace of dissolved gas and brine below the brittle-ductile transition (400°C) as presented in Fournier (1999). The host rock geology (andesite and granodiorite) is shown as blue lines, symbols and text. The present-day topographic surface is marked as a sub-horizontal black line between 3500 and 4500 m elevation. Two inferred normal faults are included in the Río Blanco sector to accommodate the present position of the 'roof pendant'. The outline of the Sur-Sur open pit is shown as a dashed line. The vertical depth of the brittle-ductile transition below the palaeo-surface is estimated at 4 km based on the model of Fournier (1999). Early, diffuse magnetite-actinolite (stage 1) alteration is cross cut by stage 2a and 2b potassic stockwork veins.

two early breccias are host to the orebody at Río Blanco. Tourmaline Breccias equivalent to the Sur-Sur Tourmaline Breccia but with more complex geometries host copper ore at Los Bronces (Warnaars et al., 1985)

Magmatically derived high temperature, high salinity hydrothermal brines produced biotite alteration in the Río Blanco Magmatic Breccia and at deep levels in the Sur-Sur Tourmaline Breccia (Figs. 5.9 and 5.10). The biotite-cemented breccias in the Río Blanco to Don Luis sectors are strongly mineralised, whereas the biotite-cemented breccias at the base of the Sur-Sur Tourmaline Breccia are weakly mineralised. Based on the available isotopic and fluid inclusion evidence, the fluids that produced sericite alteration in the main body of the Sur-Sur Tourmaline Breccia were also predominantly of magmatic-hydrothermal derivation.

The Río Blanco Magmatic Breccia and Sur-Sur Tourmaline Breccia both consist of clasts set in a fine, broken, altered rock flour matrix with variable amounts of hydrothermal cement including biotite, tourmaline, sulfides, sulfate, specularite, magnetite and quartz. Formation of the magmatic-hydrothermal breccias is interpreted to have occurred via the mechanisms discussed by Henley and McNabb (1978), Burnham (1985) and Fournier (1999). Breccia formation required decompression of the system resulting in catastrophic brittle failure and the separation of a low-density gas phase and brine from a supercritical fluid within the cupola of a deep-level crystallising magma (Fig. 5.9). Gas expansion propagated the brecciation upward through the overlying rock column in the hydrostatic domain, probably aided by tectonic dilation. Physical separation of low-density gas from the dense brine during upflow would have been driven by density contrasts.

It is hypothesised that magmatic gases (a mixture of H_2O, SO_2, HCl and possibly B_2O_3; Wolf and London, 1997) would have been the first fluid phase to flux upwards through the magmatic-hydrothermal breccias at Río Blanco after fragmentation (Fig. 5.9). The gas could have carried brine droplets as aerosols up through the breccia, as has been hypothesised for White Island volcano (Hedenquist et al., 1993). Populations of co-existing vapour-rich and hypersaline fluid inclusions with similar homogenisation temperatures indicate that gases continued to flush through the breccia when the brine up welled and permeated through the void space. This may explain the presence of opaque daughter minerals (e.g. chalcopyrite, hematite) in many vapour-rich fluid inclusions in the Río Blanco Magmatic Breccia quartz cement.

The biotite-cemented breccias in the Don Luis and Sur-Sur sectors have no obvious upper lithologic barrier (possibly due to erosion) that would have confined the rising hydrothermal fluids. Instead, the transition upwards to sericite alteration may relate to some as yet unrecognised structural seal, or due to a decrease in confining pressures and/or temperatures. At the upper limit of the biotite alteration zone, condensation of magmatically- derived gas into external waters of uncertain derivation produced hybrid, acidic, SO_2-rich waters. Magmatic-hydrothermal brines perme-

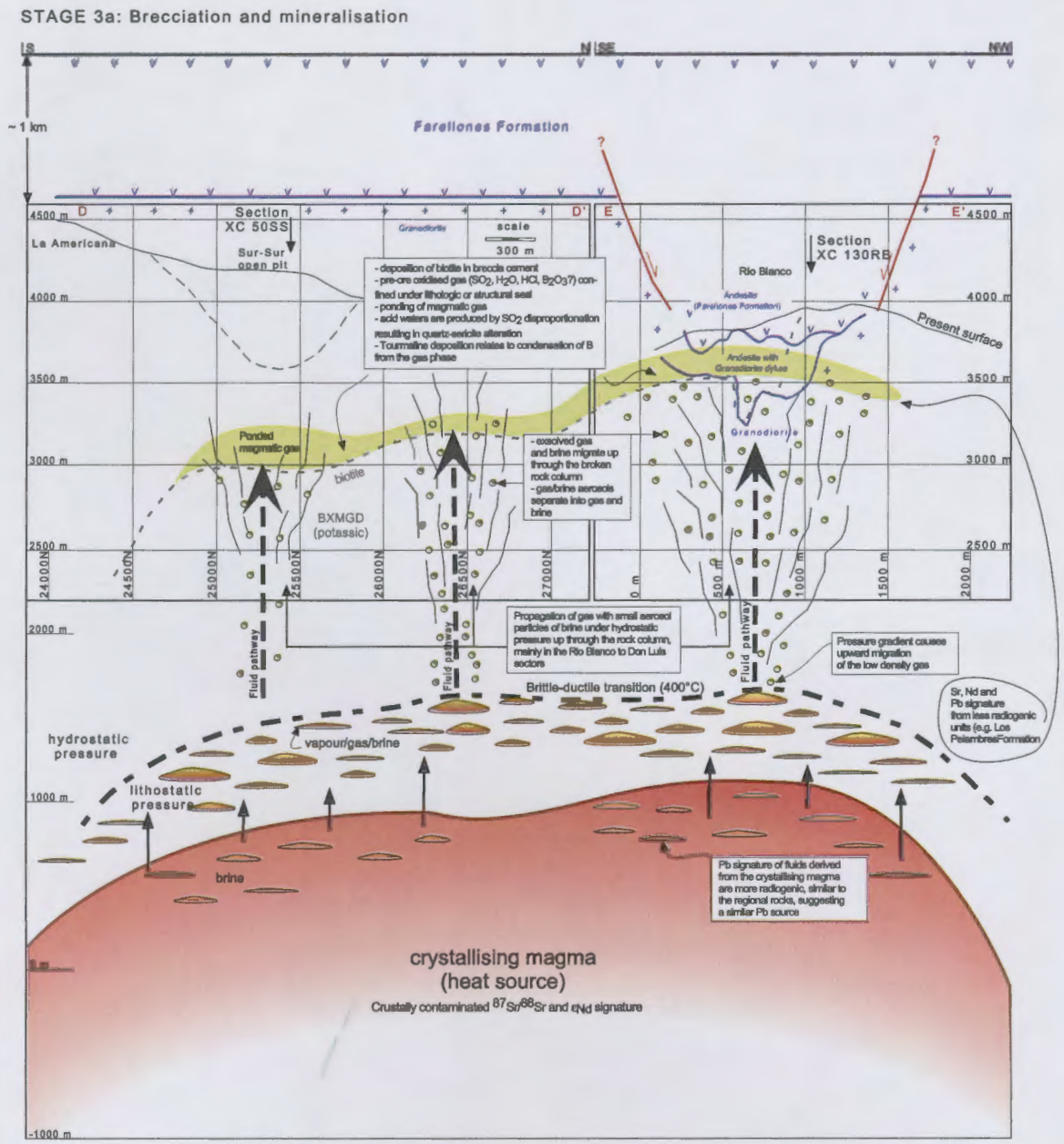

Figure 5.9. Schematic diagram showing stage 3 of the Río Blanco paragenesis. For details, see caption of Fig. 5.8. Accumulation of dissolved gases and brine occurred in the carapace above the magma chamber. Pressure gradients across the brittle-ductile transition trigger the exsolution of a low-density gas phase, possibly together with aerosol particles of dense brine. These migrate upwards into the overlying rock column, with steam expansion driving fracturing of the rock column. Hydrothermal phases cement void space and replace rock flour matrix with biotite. Gas may have been trapped at the biotite/quartz-sericite altered interface producing an SO_2 –rich fluid reservoir either through condensation into meteoric groundwater or through disproportionation. This oxidised fluid contained SO_2, H_2O, HCl and B_2O_3 and began to react with the breccia clasts, resulting in the deposition of tourmaline and associated quartz-sericite alteration at shallow levels. The oxidised fluid also precipitated specularite (and anhydrite at depth) cement in the void space. The fractured and partially cemented rock column was then permeated with the dense brine resulting in the co-precipitation of main-stage chalcopyrite and magnetite cement. The yellow circles are exsolved hydrothermal gas and brine.

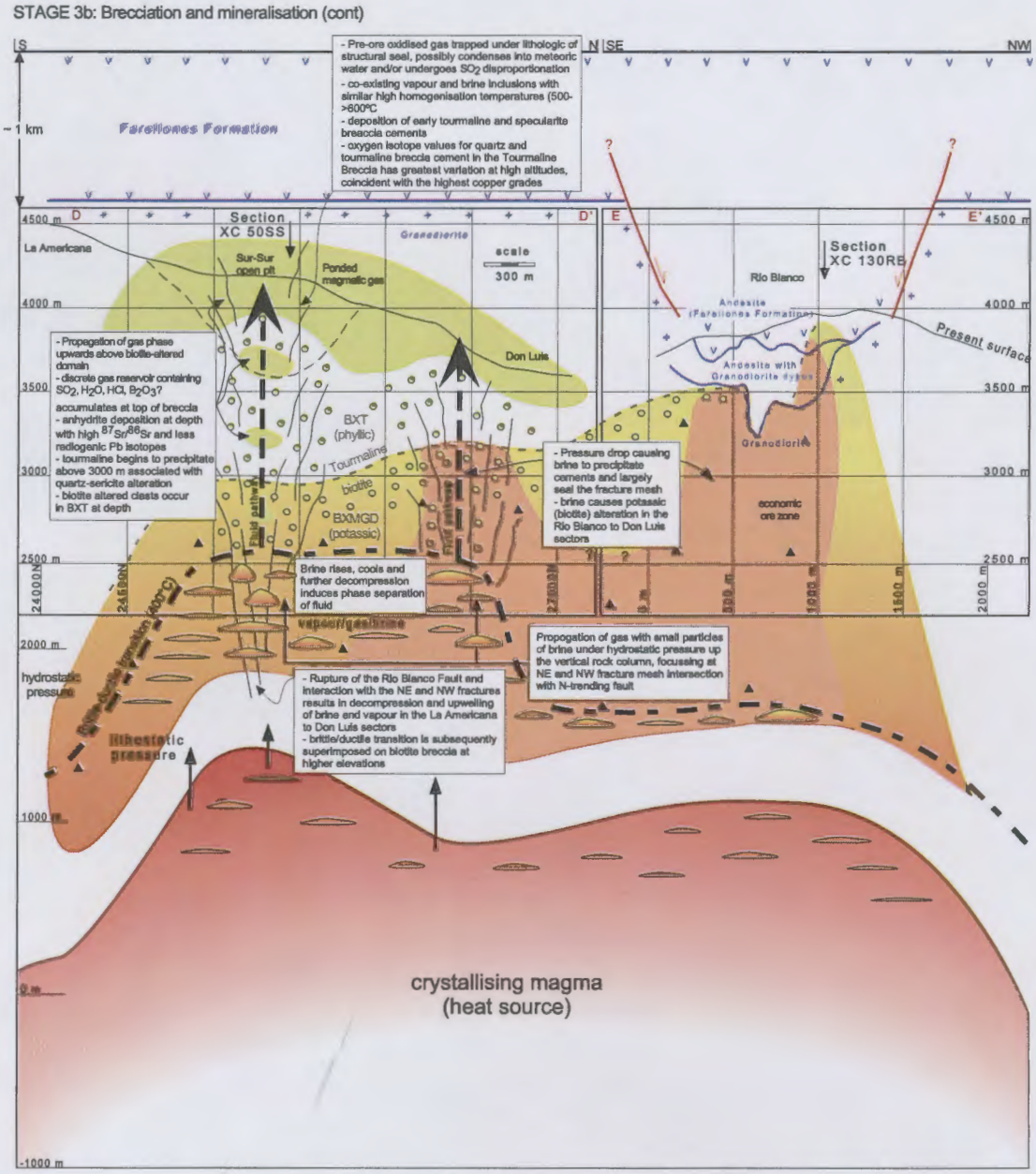

Figure 5.10. Schematic diagram showing continued evolution of paragenetic stage 3 after Fig. 5.9. For details of this section, see caption of Fig. 5.8. After sealing of the Magmatic Breccia by hydrothermal cements, activation of the Río Blanco Fault tapped the crystallising magma at depth. The subsequent increase in temperature and pressure in combination with further release brine and dissolved gases caused tourmaline deposition associated with quartz-sericite alteration in the Sur-Sur Tourmaline Breccia. Superimposition of this new phase of brecciation caused the entrainment of biotite alteration into clasts at the base of the Tourmaline Breccia. The Tourmaline Breccia is aligned along strike of the Río Blanco Fault, however the brecciation and abundance of hydrothermal minerals along its strike increases where NE and NW fractures that cross cut the Tourmaline Breccia intensify, suggesting these fractures were also active during brecciation, and produced greater permeability for rising hydrothermal fluids. Brecciation of the overlying rock column along strike of the Río Blanco Fault was propagated by gas expansion until enough energy had been dissipated to cause cessation of brecciation. Early, oxidised mineral cements begin to precipitate, producing tourmaline, anhydrite and specularite at higher levels.

ated the broken rock column at Río Blanco, resulting in mineralisation, biotite alteration of clasts and rock flour matrix and final cementation of the Magmatic Breccia (Fig. 5.10).

Sealing of the Magmatic Breccia coupled with reactivation of the Río Blanco Fault caused a migration of the locus of hydrothermal activity to the Sur-Sur sector. Fault-related decompression is the most likely trigger for formation of the 3 km long Tourmaline Breccia body. While the Sur-Sur Tourmaline Breccia has undergone brittle deformation, deep in the Don Sector, Magmatic Breccia that occurs immediately to the north of the Sur-Sur Tourmaline Breccia (along strike of the Río Blanco Fault) has undergone brittle-ductile deformation (Fig. 3.2f). Dilation caused by the intersection of the NE and NW fracture arrays with the N-trending Río Blanco Fault in the La Americana, Sur-Sur and Don Luis sectors provided loci for hydrothermal fluid flow and high-grade ore deposition. Elsewhere, along strike of the Tourmaline Breccia, low-grade or barren sections occur, which are inferred to be domains of restricted fluid flow.

The transition from biotite-cemented breccia at depth to tourmaline-cemented breccia above 3000 to 3500 m in the Sur-Sur Tourmaline Breccia also marks a transition between potassic and phyllic alteration. In thin section, the transitional zone (~100 m depth) contains discrete domains characterised by hydrothermal biotite or tourmaline. Where these domains overlap, textural relationships between biotite and tourmaline appear to be non-destructive, although the distribution of tourmaline appears to have been superimposed over that of hydrothermal biotite (Fig. 3.8c). This relationship is repeated at the deposit scale, where a mineral zonation is observed from deep-level biotite upwards to tourmaline associated with phyllic alteration (Figs. 3.16a, b, c, d and 3.21a, b). Three parameters are inferred to have caused the switch from biotite to tourmaline precipitation: 1) decrease in Fe-Mg content of the fluid (Fig. 4.1), 2) increased acidity of the fluid (Fig. 4.2), and 3) decrease in temperature. All of these changes would promote tourmaline deposition. Mechanisms that can induce B_2O_3 saturation of a magmatic-hydrothermal fluid have been discussed by Wolf and London (1997). They demonstrated that as magmas crystallise, the Fe-Mg content of the melt decreases, and the B_2O_3 content increases until biotite-tourmaline equilibria are attained. This feature is consistent with the biotite and tourmaline Fe-Mg plots in Figure 4.2.

The increase in acidity of the fluids at the biotite-tourmaline transition is inferred to relate to dissociation of HCl and SO_2 in magmatically-derived gas that fluxed through the breccia column (Fig. 5.11). The acidity of the fluids in the Tourmaline Breccia appears to have increased at high altitudes (~4000 m) where tourmaline cement contains greater quantities of Al and granodiorite clasts are leached of Al-bearing minerals. Al is more soluble when exposed to acid fluids, and when the granodiorite clasts were leached, the fluid that was to precipitate the tourmaline became saturated with Al, resulting in tourmaline mineral growth. Nonetheless, acidity did not increase beyond muscovite stability into the clay-stability field, as no argillic or advanced argillic minerals

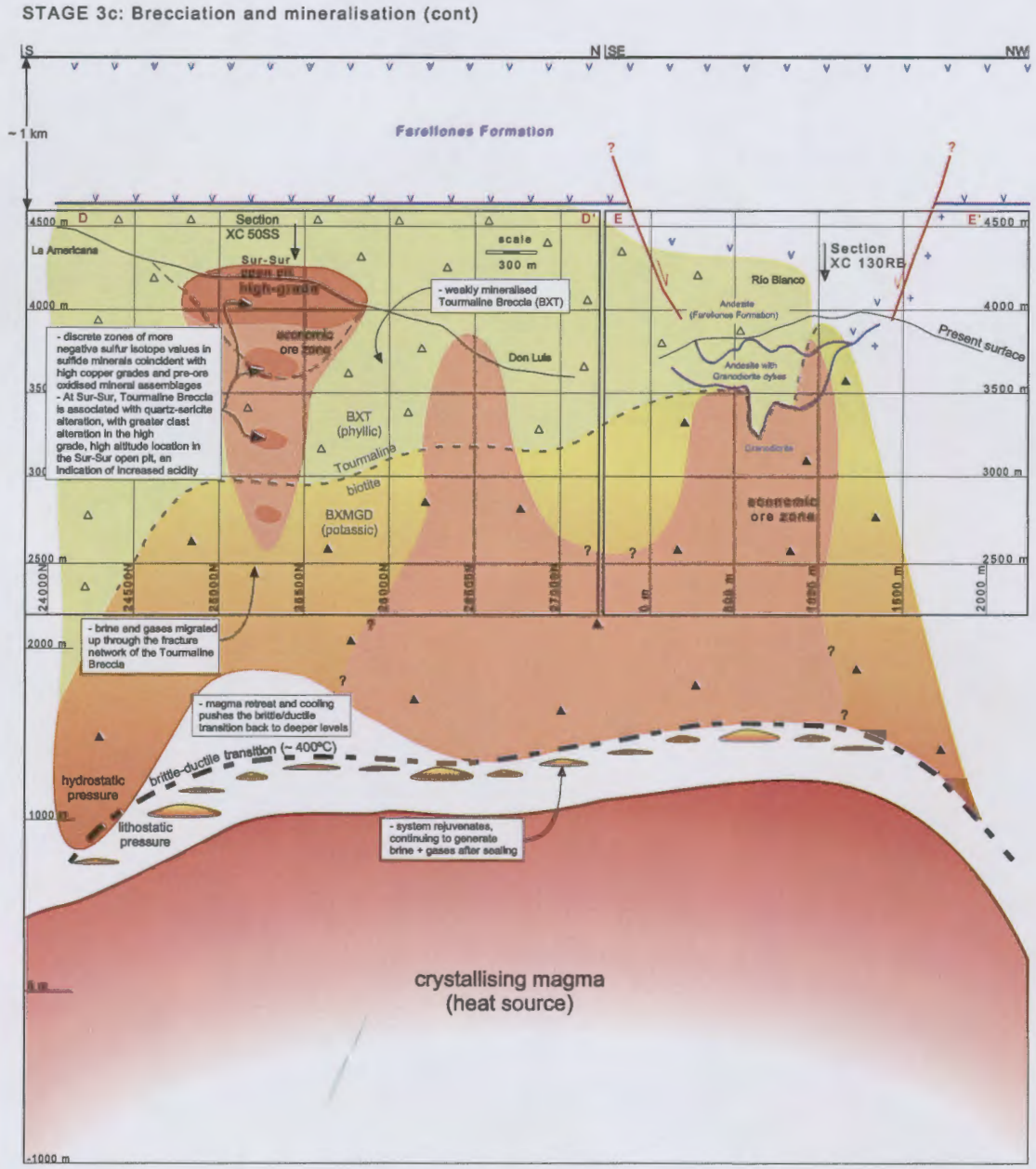

Figure 5.11. Schematic diagram showing continued evolution of stage 3 (after Figs. 5.9 and 5.10). For details of this section see caption of Fig. 5.8. After fracturing of the rock column above the Magmatic Breccia in the Sur-Sur sector and partial cementation of the fractures by tourmaline, anhydrite and specularite, the reduced brine (chalcopyrite-magnetite stable) migrated upwards from the carapace of the crystallising magma, precipitating stage 3 sulfide ore. The negative sulfur isotope values at high elevation (above 4000 m) in Sur-Sur mark a domain of dramatic temperature decrease. After the Tourmaline Breccia was thoroughly cemented, the system was sealed once again, the brittle-ductile transition retreats to deeper levels and dissolved gases and brine reaccumulate at depth. This temperature decrease is most likely caused by fluid mixing.

occur in the Sur-Sur breccia. A domain of advanced argillic alteration is preserved at high altitudes (>5000 m) on the flanks of the ridge to the east of Sur-Sur (R. Vargas, pers comm., 2000). This domain of advanced argillic alteration may be the upward continuation of the acidic alteration zone at Sur-Sur.

5.7.3 Stages 4-9: Porphyry emplacement, phyllic stockwork veins and La Copa complex

The mineralised biotite and tourmaline-cemented breccias are cross cut by a series of quartz-sericite altered porphyry stocks (PF, PQM and PDL; Fig 5.12). The PQM has been dated between 5.2 ± 0.3 to 5.2 ± 0.01 Ma, and the PDL formed between 4.9 ± 0.1 and 3.9 ± 0.7 Ma (Serrano et al., 1996). These porphyries generated a weak stockwork of sulfide-bearing veins with quartz-sericite alteration halos. It is not clear whether they added new copper and molybdenite, or remobilised pre-existing sulfides from the breccias. The Feldspar porphyry appears to be closely related temporally and spatially to the Tourmaline Breccia in the Don Luis sector, based on the observed alignment of feldspar phenocrysts in the Feldspar Porphyry at the sheared contact with the Tourmaline Breccia. Ductile fabrics have not been observed at the other contacts between the breccias and porphyry stocks or dykes.

The contoured distribution of $\delta^{34}S$-sulfide values in section XC-50SS obtained from stage 8 sulfide veins closely resembles the distribution for the sulfide cement of main-stage mineralisation. This is due either to: 1) sulfur being locally recycled from sulfides deposited during the initial brecciation event; or 2) similar hydrothermal processes operated during this vein event within the breccia column.

The final components to be emplaced in the ore deposit are the Dacite Chimney and the La Copa Rhyolite complex, both of which are unmineralised and in places appears to have removed part of the copper resource associated with the breccias. The age of the Dacite Chimney is between 4.9 ± 0.2 and 4.8 ± 0.2 Ma, and the age of the La Copa Ryholite is between 4.9 ± 0.2 and 3.9 ± 0.1 Ma (Serrano et al., 1996). The post-mineral porphyries had sufficient residence times in the upper crust to evolve compositionally, leading to enrichment in $^{87}Sr/^{86}Sr$ and depletion in ε_{Nd}. Weak phyllic alteration of these units indicates minor late-stage hydrothermal activity.

5.8 Recommendations for future work

A number of unresolved questions remain, that will require additional detailed analytical work to resolve. These include;

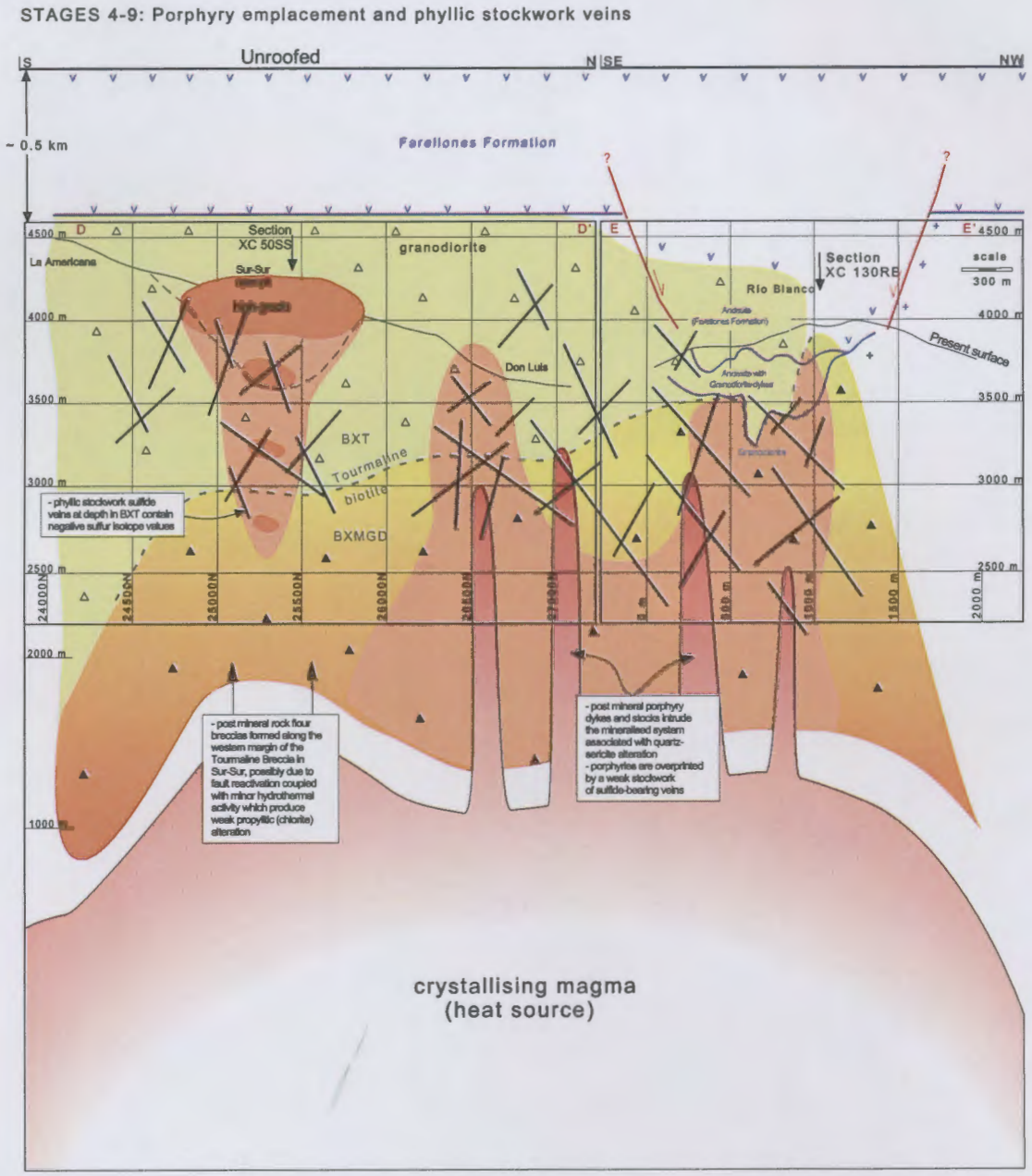

Figure 5.12. Schematic diagram showing paragenetic stages 4 to 9. For details of this section see caption of Fig. 5.8. After the emplacement of the two mineralised breccias (BXMGD and BXT) a series of porphyry stocks (PF, PQM and PDL), mainly in the Río Blanco and Don Luis sectors, intruded the system and drove a stockwork of molybdenite and chalcopyrite veins associated with quartz-sericite alteration. In the Sur-Sur sector, a series of weakly mineralised rock flour breccias (Castellana, Monolito and Paloma) formed on the western side of and adjacent to the Tourmaline Breccia. The final components to enter the system are the sub volcanic Dacite Chimney and the La Copa Ryholite, not shown on this diagram.

- Additional sulfur isotope data from the propylitic zone outside the main mineralised system would be useful to provide better constraints on the nature of any sulfur isotope fractionation and/ or to test whether external sulfur reservoirs mixed with the magmatic reservoir.
- It would be useful to obtain hydrogen isotope data in addition to the oxygen isotope data from breccia cement minerals and fluid inclusions to better quantify the possible amount of meteoric, connate and/or metamorphic water associated with ore formation and alteration.
- Further PIXE and ICPMS work on well-constrained fluid inclusion samples would be useful to determine compositions and proportions of certain elements in the breccia cement quartz, e.g. boron and copper contents in vapour-rich fluid inclusions.
- Detailed $^{40}Ar/^{39}Ar$ geochronology of pure sericite and Re-Os geochronology of molybdenite from the Sur-Sur Tourmaline Breccia would help to determine the age of the Tourmaline Breccia relative to the biotite-cemented Magmatic Breccia. U-Pb shrimp geochronology could better constrain the and the late porphyry intrusions.
- A comprehensive structural study in the immediate vicinity of the Río Blanco-Los Bronces ore deposit, with the specific aim of investigating syn-mineral structures to relate the structural architecture with brecciation in more detail.
- Analysis of more rock and mineral samples for radiogenic isotopes (Pb, Sr and Nd) to provide greater constraints on fluid sources and genesis. The Sr and Pb isotopic compositions of the early magnetite-actinolite alteration assemblage would be of particular interest for testing hypotheses of external fluid involvement.
- A detailed investigation of contact relationships between the Feldspar Porphyry and the Tourmaline Breccia in the Don Luis sector. This would help to resolve crucial timing and genetic issues with regards the porphyry intrusions and magmatic-hydrothermal breccias.
- Cathode luminescence of fluid inclusion samples to test paragenetic relationships between individual flincs in individual quartz grains.

REFERENCES

Allman-Ward, P., Halls, C., Rankin, A. and Bristow, C.M., 1982, An intrusive hydrothermal breccia body at Wheal Remfry in the western part of the St Austell Granite Pluton, Cornwall, England: in A.M. Evans, ed., Metallisation associated with acid magmatism, John Wiley and Sons Ltd.

Alvarez, N.D., 1999, Geología distrito-Andina, 1:10000 escala mapa de geología, Vice presidencia de exploraciones y asociaciones mineras gerencia de exploraciones, CODELCO-Chile.

Anglo American website: http://www.angloamerican.co.uk/press/2002/02052002.asp

Antoine, A.C., 1976, Mapa de distribución de la alteración hidrotermal en el área Andina – Disputada, Santiago, Instituto de Investigaciones Geológicas.

Atkinson, W.W., Souviron, A., Vehrs, T.I. and Faunes, A.G., 1996, Geology and mineral zoning of the Los Pelambres porphyry copper deposit, Chile: in F. Camus, R.H. Sillitoe, R. Peterson, eds, Andean copper deposits: new discoveries, mineralisation, styles and metallogeny, Society of economic geologists special publication no. 5, p. 131-155.

Audétat, A., Günther, D. and Heinrich, C.A., 1998, Formation of a magmatic-hydrothermal ore deposit: insights with LA-ICP-MS analysis of fluid inclusions, Science, v. 279, no. 5359, p.2091-2094.

Baksi, A.K., Archibald, D.A. and Farrar, E., 1996, Intercalibration of $^{40}Ar/^{39}Ar$ dating standards, Chemical Geology, 129, p. 307-324.

Barreiro, B.A., 1984, Lead isotopes and Andean magma genesis: in R.S. Harmon and B.A. Barreiro, eds, Andean Magmatism – chemical and isotopic constraints, Shiva Press, Bristol, p. 21-30.

Barton, M.D. and Johnson, D. A., 1996, Evaporitic-source model for igneous-related Fe-oxide-(REE-Cu-Au-U) mineralisation: Geology, v. 24, no. 3, p. 259-262.

Blondel, J.R., 1980, Porfido de composición granodioritica de la mina Río Blanco. Unpublished memoria de titulo, Departamento de Geología y geofísica, Santiago, Universidad de Chile, 88p

Bodnar, R.J., Burnham, C.W. and Sterner, S.M., 1985, Synthetic inclusions in natural quartz, III, Determination of phase equilibrium properties in the system H_2O-NaCl to 1000°C and 1500 bars, Geochimica et Cosmochimica Acta, 49, p.1861-1873.

Bodnar, R.J., Sterner, S.M. and Hall, D.L., 1989, SALTY: A fortran program to calculate the compositions of fluid inclusions in the system NaCl-KCl-H_2O, Computers and Geosciences, 15, p.14-41.

Bonatti, E., Harrison, C.G.A, Fisher, D.E., Honnorez, J., Schilling, J.G, Stipp, J.J., Zentilli, M., 1977, Easter volcanic chain (Southeast Pacific): a mantle hot line, Journal of Geophysical Research, 82, 17, p. 2457-2478.

Bottinga, Y. and Javoy, M., 1973, Comments on oxygen isotope geothermometry, Earth and Planetary Science Letters, v. 20, p. 250-265.

Bowman, J.R., Parry, W.T., Kropp, W.P. and Kruer, S.A., 1987, Chemical and isotopic evolution of hydrothermal solutions at Bingham, Utah, Economic Geology, v. 82, p. 395-428.

Bryner, L., 1970, Ore deposits of the Philippines; an introduction to their geology, Economic Geology and the Bulletin of the Society of Economic Geologists, v.64, no.6, p.644-666.

Burnham, C.W., 1979, Magmas and hydrothermal fluids: in H. L. Barnes, ed., Geochemistry of hydrothermal ore deposits, 2nd edition, John Wiley & Sons, Inc., p. 71-136.

Burnham, C.W. and Ohmoto, H., 1980, Late-stage processes of felsic magmatism, Mining geology special issue, no. 8, p.1-11.

Burnham, C.W., 1985, Energy release in subvolcanic environments: implications for breccia formation, Economic Geology, v. 80, p. 1515-1522.

Burnham, C.W., 1997, Magmas and hydrothermal fluids: in Barnes, H.L., ed., Geochemistry of hydrothermal ore deposits, 2nd edition, New York, John Wiley and Sons, Inc, p. 63-123.

Cahill, T. and Isacks, B.L., 1985, Shape of the subducted Nazca Plate: in American Geophysical Union spring meeting, Eos, Transactions, American Geophysical Union, 66, 18, p. 299-1985.

Camus, F., 1976, Geology of the El Teniente orebody with emphasis on wall-rock alteration, Economic Geology, v. 70, no. 8, p. 1341-1372.

Camus, F., 2002, The Andean porphyry systems: in Cooke, D.R., and Pongratz, J., eds., Giant ore deposits characteristics, genesis and exploration, CODES Special Publication No. 4, University of Tasmania.

Candela, P.A., 1984, A partitioning model for the rare earth elements and other polyvalent, chloride complexed metals in melt-vapour systems: in Anonymous, ed., Geological Society of America, 97th Annual meeting, Reno, Nevada, U.S.A., 462p.

Candela, P.A. and Holland, H.D., 1986, A mass transfer model for Cu and Mo in magmatic hydrothermal systems: the origin of porphyry-type ore deposits, Economic Geology, v. 81, p. 1-19.

Candela, P.A., 1989, Magmatic ore forming fluids: thermodynamic and mass transfer calculations of metal concentrations: in Whitney, J.A. and Naldrett, A.E., eds., Ore deposition associated with magmas: Reviews in Economic Geology, 4, p. 203-221.

Candela, P.A., 1991, Physics of aqueous phase evolution in plutonic environments, American Mineralogist, v. 76, p. 1081-1091.

Candela, P.A. and Piccoli, P.M., 1995, Model ore-metal partitioning from melts into vapour and vapour/brine mixtures: in Thompson, J.F.H., ed., Magmas, fluids and ore deposits: short course series (Mineralogical Association of Canada), 23, Victoria, B.C., p. 101-127.

Castelli, J. C., 1999, Geología de exploración básica generativa entre Andina y el Río Colorado 1:50000: Santiago, CODELCO - Chile.

Chiba, H., Kusakabe, M., Hirano, S.I., Matsuo, S. and Shigeyuki, S., 1981, Oxygen isotope fractionation factors between anhydrite and water from 100 to 500°C, Earth and Planetary Science Letters, 53, p. 55-62.

Charrier, R., Baeza, O., Elgueta, S., Flynn, J.J., Gans, P., Kay, S.M., Muñoz, N., Wyss, A.R. and Zurita, E., 2002, Evidence for Cenozoic extensional basin development and tectonic inversion south of the flat-slab segment, southern central Andes, Chile (33°-36°S), Journal of South American Earth Sciences, 15, p. 117-139.

Clark, A.H., 1995, Giant ore Deposits – II: Controls on the scale of orogenic magmatic - hydrothermal mineralisation, Department of Geological sciences, Queens University, Kingston, Ontario.

Clayton, R.N. and Mayeda, T.K., 1963, The use of bromine pentafluoride in the extraction of oxygen from oxides and silicates for isotopic analysis. Geochimica et Cosmochimica Acta 27, p. 43-52.

Contreras, A. and Vargas, R., 1994, Geología de superficie Los Bronces- Río Blanco, escala 1:1000, Compañía Minera Disputada de Las Condes y CODELCO Chile – División Andina unpublished map.

Cooke, D.R. and Simmons, S.F., Characteristics and genesis of epithermal gold deposits, Reviews in Economic Geology, 13, p.221-244.

Craig, H., 1961, Isotopic variations in meteoric water, Science, 133, p. 1702-1703.

Dalrymple, G.B., Alexander, Jr., E.C., Lanphere, M.A. and Kraker, G.P., 1981, Irradiation of samples for $^{40}Ar/^{39}Ar$ dating using the Geological Survey TRIGA Reactor, U.S. Geological Survey, Professional Paper 1176, 55p.

Davidson, J.P., Harmon, R.S. and Wörner, G., 1991, The source of central Andean magmas; some considerations: in Harmon, R.S. and Rapela. C.W., eds., Andean magmatism and its tectonic setting: Boulder, Colorado, Geological Society of America Special Paper 265.

Davidson, J.P., 1996, Deciphering mantle and crustal signatures in subduction zone magmatism, American Geophysical Union Monograph 96, p. 251-262.

Davidson, P. and Kamenetsky, V. S., 2001, Immiscibility and continuous melt-fluid evolution within the Río Blanco porphyry system, Chile: Evidence from inclusions in magmatic quartz, Economic Geology, v. 96, p. 1921-1929.

Davies, A.G.S., Cooke, D.R. and Gemmell, B.J., 2000, Breccias associated with epithermal and porphyry systems – towards a systematic approach to their description and interpretation: in Louis A. Bucci and John L. Mair, eds, Gold in 2000 – short course poster session extended abstract volume, p. 98-103.

Deer W.A., Howie, R.A. and Zussman, J., 1992, An introduction to rock forming minerals, Longman group Ltd, London, 528p.

Dilles, J.H., Tomlinson, A.J., Martin, M.W. and Blanco, N., 1997, El Abra and Fortuna Complexes: a porphyry copper batholith sinistrally displaced by the Falla Oeste, 8th Congresso Geologico Chileno, Antofagasta, p. 1883-1887.

Doe, B.R. and Zartman, R.E., 1979, Plumbotectonics I, the Phanerozoic: in H.L. Barnes, ed., Geochemistry of hydrothermal ore deposits, 2nd edition: New York, Wiley Interscience, p. 22-70.

Drake, R. E., Charrier, R., Thiele, R., Munizaga, F., Padilla, H. and Vergara M., 1982, Distribucion

y edades K/Ar de volcanitas post-Neocomianas en la Cordillera Principal entre 32 y 36 degrees: Implicaciones estratigraphicas y tectonicas para el meso-cenozioco de Chile central, III congreso geologico chileno, Concepcion, Chile.

Drummond, S.E. and Ohmoto, H., 1985, Chemical evolution and mineral deposition in boiling hydrothermal systems, Economic Geology, v. 80, no. 1, p.126-147.

Elburg, M. and Foden, J., 1998, Sources for magmatism in central Sulawesi: geochemical and Sr-Nd-Pb isotopic constraints, Chemical Geology, v. 156, no.1-4, p.67-93.

Farmer, G.L. and DePaolo, D.J., 1983, Origin of Mesozoic and Tertiary granite in the western United States and implications for pre-Mesozoic crustal structure; 1, Nd and Sr isotopic studies in the geocline of the northern great basin, Journal of Geophysical Research, v. 88, p. 3379-3401.

Farmer, G.L. and DePaolo, D.J., 1987, Nd and Sr isotope study of hydrothermally altered granite at San Manuel, Arizona: implications for element migration paths during the formation of porphyry copper ore deposits, Economic Geology, v. 82, p. 1142-1151.

Fauré, G., 1977, Principles of isotope geology: John Wiley and Sons, New York, 456p.

Fleck, R.J., Sutter, J.F. and Elliot, D.H., 1977, Interpretation of discordant 40Ar/39Ar age spectra of Mesozoic tholeiites from Antarctica, Geochimica et Cosmochimica Acta, v. 41, p. 15-32.

Foden, J., Mawby, J., Kelley, S., Turner, S. and Bruce, D., 1995, Metamorphic events in the eastern Arunta Inlier, pt. 2, Nd-Sr-Ar isotopic constraints, Precambrian Research, v. 71, p. 207-227.

Fournier, R.O., 1985, The behaviour of silica in hydrothermal solutions, Reviews in Economic Geology, v. 2, p. 45-61.

Fournier, R.O., 1987, Conceptual models of brine evolution in magmatic-hydrothermal systems, U.S. Geological Survey Professional Paper 1350, v. 2, p. 45-61.

Fournier, R.O., 1991, The transition from hydrostatic to greater than hydrostatic fluid pressure in presently active continental hydrothermal systems in crystalline rock, Geophysical research letters, 18, 5, p. 955-958.

Fournier, R.O., 1999, Hydrothermal processes related to movement of fluid from plastic into brittle rock in the magmatic-epithermal environment, Economic Geology, v. 94, 8, p. 1193-1211.

Franklin, J.M., 1983, Future directions of mineral deposit research in Canada, - Canadian Geoscience Council, Report: 1983-1, 184p.

Frikken, P.H., 2001, Geology of the Río Blanco-Los Bronces breccia-hosted Cu-Mo deposit: in D.R. Cooke and P. Hollings, eds., Field guide: Geology, tectonics and giant porphyry Cu-Mo deposits of central and northern Chile: AMIRA P511-Giant Ore Deposits, Chilean field meeting, p. 129-160.

Frikken, P.H., 2002, Río Blanco – District to deposit scale: in D. Cooke, J.L. Walshe and P. Hollings, eds., Chilean Atlas VOLUME 1: Giant porphyry deposits of the Andean Fold Belt - AMIRA P511.

Frikken, P.H., Cooke, D.R., Walshe, J.L., Skarmeta, J., Serrano, L. and Vargas, R., 2002, Sulfur

isotope and mineral zonation in the Sur-Sur breccia complex, Río Blanco Cu-Mo deposit, Chile – Implications for ore genesis, Chilean Atlas VOLUME 2: Giant porphyry deposits of the Andean Fold Belt - AMIRA P511.

Frutos, J., 1990, Statabound ore deposits in the Andes: in L. Fontbote, G.C. Amstutz, M. Cardozo, E. Cedillo, J. Frutos, eds, The Andes Cordillera: A synthesis of the geologic evolution, Springer-verlag Berlin Heidelberg.

Gana, P. and Wall, R., 1996, Del Cretácico superior Terciario, en el borde occidental de la cordillera principal, al sur de la cuesta Chacabuco, Chile central (33°- 33°30'S): Santiago, Servicio Nacional de Geología y Minera.

Gavelin, S., Parwel, A. and Ryhage, R., 1960, Sulfur isotope fractionation in sulfide mineralization, Economic Geology, v. 55, p. 510-530.

Goerne, G.V., Franz, G. and Heinrich, W., 2001, Synthesis of tourmaline solid solutions in the system Na_2O-MgO-Al_2O_3-SiO_2-B_2O_3-H_2O-HCl and the distribution of Na between tourmaline and fluid at 300 to 700 degrees C and 200 Mpa, Contributions to Mineralogy and Petrology, 141, p. 160-173.

Gustafson, L.B. and Hunt, J.P., 1975, The porphyry copper deposit at El Salvador, Chile, Economic Geology and the Bulletin of the society of economic geologists, v. 70, no. 5, p. 857-912.

Gutscher, M.A., Maury, R., Eissen, J.P. and Bourden, E., 2000, Can slab melting be caused by flat subduction?, Geology, v. 28, p. 535-538.

Hall, C.M., 1981, The application of K/Ar and $^{40}Ar/^{39}Ar$ methods to the dating of recent volcanics and the Laschamp event, Unpublished PhD thesis, University of Toronto, Toronto, Canada, 186 p.

Hanus, V. and Vanek, J., 1978, Morphology of the Andean Wadati-Benioff zone, andesitic volcanism, and tectonic features of the Nazca Plate, Tectonophysics, 44, 1-4, p. 65-77.

Hashke, M.R., Scheuber, E., Günther, A. and Reutter, K.J., 2002, Evolutionary cycles during the Andean orogeny: repeated slab breakoff and flat subduction?, Terra Nova, 14, p. 49-55.

Hedenquist, J.W., Simmons, S.F., Giggenbach, W.F. and Eldridge, S.C., 1993, White Island, New Zealand, volcanic-hydrothermal system represents the geochemical environment of high-sulfidation Cu and Au ore deposition, Geology (Boulder), v. 21, no. 8, p.731-734.

Hedenquist, J.W., Arribas, A., Jr., and Reynolds, T.J., 1998, Evolution of an intrusion-centred hydrothermal system: Far Southeast-Lepanto porphyry and epithermal Cu-Au deposits, Philippines, Economic Geology, v. 93, p. 373-404.

Hedenquist, J.W. and Richards, J.P., 1998, The influence of geochemical techniques on the development of genetic models for porphyry copper deposits: in J.P. Richards and P.B. Larson, eds, Techniques in hydrothermal ore deposits geology, Reviews in Economic Geology, v. 10, p. 235-256.

Heinrich, C.A., Ryan, C.G., Mernagh, T.P. and Eadington, P.J., 1992, Segregation of ore metals between magmatic brine and vapour – a fluid inclusion study using PIXE microanalysis, Economic Geology, v. 87, p.1566-1583.

Heithersay, P.S., and Walshe, J.L., 1995, Endeavour 26 North: A porphyry copper-gold deposit in the late Ordovician shoshonitic Goonumbla Volcanic Complex, New South Wales, Australia, Economic Geology, v. 90, p. 1506-1532.

Henley, R.W. and McNabb, A., 1978, Magmatic vapour plumes and groundwater interaction in porphyry copper emplacement, Economic Geology, v. 73, p. 1-20.

Henley, R.W., 1985, The geothermal framework of epithermal deposits: in B.R. Berger and P.M. Bethke, eds., Geology and geochemistry of epithermal systems, Reviews in Economic Geology, v. 2, p.25-44.

Henry, D.J. and Guidotti, C.V., 1985, Tourmaline as a petrographic indicator mineral: an example from the staurolite-grade metapelites of NW Maine, American Mineralogist, v. 70, p. 1-15.

Henry, D.J. and Guidotti, C.V., 2002, Titanium in biotite from metapelitic rocks; temperature effects, crystal-chemical controls, and petrologic applications, American Mineralogist, v. 87, no.4, p.375-382.

Hildreth, W. and Moorbath, S., 1988, Crustal contributions to arc magmatism in the Andes of central Chile, Contributions to Mineralogy and Petrology, v. 98, p. 455-498.

Holland, H.D., 1972, Granites, solution and base metal deposits, Economic Geology, v. 67, p. 281-301.

Hollings, P., 2001. The lithogeochemical framework of central Chile. AMIRA Project P511 – Hydrothermal Systems, 10th Sponsors Meeting Confidential Report, August 2001, p. 40-84 (unpublished).

Hollings, P. and Frikken, P., 2001. Whole rock geochemistry of the 'roof pendant' andesites and Don Luis Porphyry, Río Blanco. AMIRA Project P511 – Hydrothermal Systems, 10th Sponsors Meeting Confidential Report, August 2001, 276-282 (unpublished).

Hollings, P. and Cooke, D.R. 2002, Regional Geochemistry of Tertiary volcanic rocks in central Chile: implications for tectonic setting and ore deposit genesis, Chilean Atlas VOLUME 2: Giant porphyry deposits of the Andean Fold Belt - AMIRA P511.

Hollings, P., Frikken, P.H. and Cannell, J., 2002, Central Chile regional scale – geology and lithogeochemistry: in D. Cooke, J.L. Walshe and P. Hollings, eds., Chilean Atlas VOLUME 1: Giant porphyry deposits of the Andean Fold Belt - AMIRA P511.

Hollings, P., Cooke, D. and Clark, A., Regional geochemistry of Tertiary volcanic rocks in central Chile: Implications for tectonic setting and ore deposit genesis, submitted to Economic Geology.

Holmgren, C., Marti, M., Skewes, M.A., Schneider, A. and Harmon, R., 1988, Análisis isotópicos y de inclusiones fluidas en el yacimiento Los Bronces, Chile central: in Congreso Geológico Chileno, no. 5, Actas, v. 1, p. B299-B314.

Horita, J., Cole, D.R. and Weslowski, 1995, The activity-composition relationship of oxygen and hydrogen isotopes in aqueous salt solutions: III. Vapour-liquid water equilibration of NaCl solutions to 350°C, Geochimica et Cosmochimica Acta, v. 59, p. 1139-1151.

Huston, D.L., Power, M. and Large, R.R., 1993, Laser ablation analysis of sulfur isotopes: An

analytical technique now available in Australia: in second national meeting of the specialist group in economic geology, Armidale, Geological Society of Australia, p. 30-31.

Jensen, M.L., 1959, Sulfur isotopes and hydrothermal mineral deposits, Economic Geology, v. 54, p. 374-394.

Jordan, T.E., Isacks, B.L., Allmendinger, R.W., Brewer, J.A., Ramos, V.A., Ando, C.J., 1983, Andean tectonics related to geometry of subducted Nazca Plate, Geological Society of America Bulletin, 94, 3, p. 341-361.

Jordan, T.E., Allmendinger, R.W., Damanti, J. and Drake, R., 1993, Chronology of motion in a complete thrust belt: the Precordillera, 30-31°S, Andes mountains, Journal of Geology, 101, p.133-156.

Kay, S.M., Maksaev, V. Moscoso, R. Mpodozis, C., Nasi, C., 1987, Probing the evolving Andean lithosphere: mid-late Tertiary magmatism in Chile (29°-30°30') over the modern zone of subhorizontal subduction, Journal of Geophysical Research, B, Solid Earth and Planets, 92, 7, p. 6173-6189.

Kay, S.M., Maksaev, V., Moscoso, R. Mpodozis, C. Nasi, C., Gordillo, C.E., 1988, Tertiary Andean magmatism in Chile and Argentina between 28°S and 33°S; correlation of magmatic chemistry with a changing Benioff zone, Journal of South American Earth Sciences, 1, 1, p. 21-38.

Kay, S.M., Mpodozis, C., Ramos, V.A. and Munizaga, F., 1991, Magma source variations for mid-late Tertiary magmatic rocks associated with a shallowing subduction zone and a thickening crust in the central Andes (28-33°S), Geological Society of America, special paper 265, p.113-137.

Kay, R.W. and Kay, S.M., 1993, Delamination and delamination magmatism, Tectonophysics, v. 219, p. 177-189.

Kay, S. M. and Kurtz, A.C., 1995, Magmatic and tectonic characterisation of the El Teniente region: CODELCO - Chile, Division El Teniente, 180p.

Kay, S.M. and Ambruzzi, J.M., 1996, Magmatic evidence for Neogene lithospheric evolution of the central Andean "flat slab" between 30-32 degrees south, Tectonophysics, 259, p. 15-28.

Kay, S.M., Mpodozis, C. and Coira, B., 1999, Neogene magmatism, tectonism and mineral deposits of the central Andes: in B.J. Skinner, ed., Geology and ore deposits of the central Andes, Society of Economic Geologists, Special Publication no. 7, p. 7-59.

Kay, S.M., Mpodozis, C. and Coira, B., 1999, Geology and ore deposits of the central Andes: in B.J. Skinner, ed, Society of Economic Geologists Special Publication no. 7, p. 27-59.

Kay, S.M. and Mpodozis, C., 2002, Magmatism as a probe to the Neogene shallowing of the Nazca plate beneath the modern Chilean flat-slab, Journal of South American Earth Sciences, v. 15, p. 39-57.

Keith, J.D., 2000, Does eruption preclude or enhance the possibility of mineralization in porphyry systems?, Abstracts with Programs, Geological Society of America, v. 32, no. 7, p. A110.

Kesler, S.E., Jones, L.M. and Walker, R.L., 1975, Intrusive rocks associated with porphyry copper mineralisation in island arc areas, Economic Geology, v. 70, p. 515-526.

Kilinc, I.A. and Burnham, C.W., 1972, Partitioning of chloride between a silicate melt and coexisting aqueous phase from 2 to 8 kilobars, Economic Geology, v. 67, p. 231-235.

Klohn, C., 1960, Geología de la cordillera de los Andes de Chile central, provincias de Santiago, O'Higgins, Colchagua y Curico: Santiago, Instituto de Investigaciones Geológicas, boletín no. 8, 95p.

Kotzer, T.G., Kyser, T.K., King, R.W. and Kerrich, R., 1993, An empirical oxygen- and hydrogen-isotope geothermometer for quartz-tourmaline and tourmaline-water, Geochimica et Cosmochimica Acta, 57, p. 3421-3426.

Kusakabe, M., Nakagawa, S., Hori, M., Matsihisa, Y., Ojeda, J.M. and Serrano, L., 1984, Oxygen and Sulphur isotopic compositions of quartz, anhydrite, and sulphide minerals from the El Teniente and Río Blanco porphyry copper deposits, Chile, Bulletin of the Geological Survey of Japan, v. 35, 11, p. 583-614.

Kusakabe, M., Hori, M., Yukihhiro, M., 1990, Primary mineralization-alteration of the El Teniente and Río Blanco porphyry copper deposits, Chile: Stable isotopes, fluid inclusions and Mg^{2+}/Fe^{2+}/Fe^{3+} ratios in hydrothermal biotite: in Stable isotopes and fluid processes in mineralization, H.K. Herbert and S.E. Ho, eds, the University of Western Australia, publication no. 2, p. 244-259.

Kyser, T.K., 1987, Short course in stable isotope geochemistry of low temperature fluids, Mineralogical association of Canada, v. 13, 452 p.

Lavenu, A. and Cembrano, J., 1999, Compressional- and Transpressional- stress pattern for Pliocene and Quaternary brittle deformation in fore arc and intra arc zones (Andes of central and southern Chile), Journal of Structural Geology, v. 21, p. 1669-1691.

Levi, B., Vergara, M., Nystrom, J.O. and Henriquez, F., 1988, Low-grade metamorphic facies series in the Mesozoic-Cenozoic volcanic sequences of central Chile: a re-appraisal and some applications, Anais do VII Congresso Latino-Americano de Geologia, Belem, Para 1, p. 243-251.

Lindsay, D.D., Zentilli, M. and Rojas De La Rivera, J., 1995, Evolution of an active ductile to brittle shear system controlling mineralisation at the Chuquicamata porphyry copper deposit, northern Chile, International geology review, v. 37, p. 945-958.

Lopez, L. and Vergara, M., 1982, Geoquimica Y petrogénesis de rocas granodioriticas asociadas con el yacimiento cuprífero Río Blanco-Los Bronces, Revista Geológica de Chile, 15, p. 59-70.

Lowell, D.J. and Guilbert, J.M., 1970, Lateral and vertical alteration-mineralisation zoning in porphyry ore deposits, Economic geology and the Bulletin of the society of economic geologists, v. 65, no. 4., p. 373-408.

Lydon, J.W., 1983, Chemical processes controlling the origin and deposition of sediment-hosted stratiform lead-zinc deposits, Mineralogical Association of Canada Short Course Handbook, 8, p. 175-250.

Marschik, R. and Fontbote, L., 2001, The Candelaria-Punta del cobre iron oxide Cu-Au (-Zn-Ag) deposits, Chile, Economic Geology, v. 96, 8, p. 1977-1826.

Mathur, R., Ruiz, J., Titley, S., Gibbins, S. and Margotomo, W., 2000a, Different crust sources for Au-rich and Au-poor ores of the Grasberg Cu-Au porphyry deposit, Earth and Planetary Science Letters, v. 183, p. 7-14.

Matsuhisa, Y., Goldsmith, J.R. and Clayton, R.N., 1979, Oxygen isotopic fractionation in the system quartz-albite-anorthite-water, Geochimica et Cosmochimica Acta, 43, p. 1131-1140.

McClay, K., Skarmeta, J., and Bertens, A., 2002, Structural controls on porphyry copper deposits in northern Chile: new models and implications for Cu-Mo mineralisation in subduction orogens: in Abstract Volume, S. Vearncombe, ed., Applied structural geology for mineral exploration and mining, International Symposium, Australian Institute of Geoscientists, Kalgoorlie, Western Australia.

McDougall, I. and Harrison, T.M., 1988, Geochronology and Thermochronology by the $^{40}Ar/^{39}Ar$ Method, Oxford University Press, N.Y., 212 p.

McMahon, T.P., 1994, Pliocene intrusions in the Gunung Bijih (Ertsberg) mining district, Irian Jaya, Indonesia; major- and trace-element chemistry, International Geology Review, v. 36, no. 10, p. 925-946.

Morgan, D. and London, G.B., 1989, Vapor-undersaturated experiments with Macusani glass + H (sub 2) 0 at 200 MPa, and the internal differentiation of granitic pegmatites, Contributions to Mineralogy and Petrology, v. 2, 1, p. 1-17.

Muffler, L.J.P., White, D.E. and Truesdell, A.H., 1971, Hydrothermal explosion craters in Yellowstone National Park, Geological Society of America Bulletin, v. 82, p. 723-740.

Munizaga, F., 1994, Ar-Ar ages of igneous rocks and breccias at Río Blanco-Los Bronces, CODELCO – Chile, Santiago, Unpublished report, 2p.

Muntean, J.L. and Einaudi, M.T., 2001, Porphyry-epithermal transition: Maricunga Belt, northern Chile, Economic Geology, v. 96, p. 743-772.

Nash, J.T., 1975, Fluid inclusion studies of vein, pipe, and replacement deposits, northwestern San Juan Mountains, Colorado, Economic Geology, v. 70, no. 8, p.1448-1462.

Norton, D.I. and Cathles, L.M., 1973, Breccia pipes - Products of exsolved vapour from magmas, Economic Geology, v. 68, p. 540-546.

Nyström, J.O., Parada, M.A. and Vergara, M.A., 1993, Sr-Nd isotope compositions of Cretaceous to Miocene volcanic rocks in central Chile: A trend towards a MORB signature and a reversal with time, second ISAG, Oxford, UK, p. 411-414.

Ohmoto, H. and Lasaga, A.C., 1982, Kinetics of reactions between aqueous sulfates and sulfides in hydrothermal systems, Geochimica et Cosmochimca Acta, 46, p. 1727-1745.

Ohmoto, H. and Rye, R.O., 1979, Isotopes of sulfur and carbon: in Geochemistry of hydrothermal ore deposits, H. L. Barnes, ed, John Wiley & Sons, Inc.

Ohmoto, H., 1986, Stable isotope geochemistry of ore deposits: in J.W. Valley, H.P. Taylor and J.R. O'Neil, eds, stable isotopes in high temperature geological processes, Mineralogical society of America, v. 16, p. 491-560.

Ohmoto, H. and Goldhaber, M.B., 1997, Sulfur and Carbon isotopes: in Geochemistry of hydrothermal ore deposits, 3rd edition, H.L. Barnes, ed, John Wiley & Sons, Inc.

Onstott, T.C. and Peacock, M.W., 1987, Argon retentivity of hornblendes: A field experiment in a slowly cooled metamorphic terrane, Geochimica et Cosmochimica Acta, 51, p. 2891-2904.

Pardo-casas, F. and Molnar, P., 1987, Relative motion of the Naca (Farellon) and South American plates since late cretaceous time, Tectonics, v. 6, 3, p. 233-248.

Potter, R.W.I, Clynne, M.A. and Brown, D.L., 1978, Freezing point depression of aqueous sodium chloride solutions, Economic Geology, v. 73, p. 284-285.

Puig, A., 1988, Geologic and metallogenic significance of the isotopic composition of lead in galenas of the Chilean Andes, Economic Geology and the Bulletin of the Society of Economic Geologists, v. 83, 4, p. 843-858.

Quirt, S., Clark, A.H., Farrar, E., and Sillitoe, R.H., 1971, Potassium-argon ages of porphyry copper deposits in northern and central Chile, Geological Society of America, Abstracts with Programs, v. 3, p. 676-677.

Rae, A., 2002, Alteration systematics and mineralising potential of the Palinpinon geothermal field, Negros Island, Philippines, Unpublished PhD thesis.

Ramos, V.R., 1995, Field guide to the geology of the precordillera fold and thrust belt (central Andes): Andean Thrust Tectonics.

Ramsey, J.G., 1967, Folding and fracturing of rocks: McGraw-Hill, New York, 568p.

Richards, J.P., Boyce, A.J. and Pringle, M.S., 2001, Geological evolution of the Escondida area, Northern Chile: A model for spatial and temporal localisation of porphyry copper mineralisation, Economic Geology, v. 96, 2, p. 271-305.

Rivano S., Godoy, E, Vergara, M and Villarroel. R., 1990, Redefinición de la Formación Farellones en la cordillera de los Andes de Chile central (32°-34°S), Revista Geológica de Chile, 17, p. 205-214.

Rivano, S., Sepulveda, S., Boric, R. and Espineira, D., 1993, Carta de Geológica de Chile, Hojas Quillota y Portillo, regiones de Valpariaso y Coquimbo, V región, Servicio Nacional de Geología de Chile, no. 73, 1:250000.

Rivano, S., 1995, Notes for Carta Geológica de Chile, Hojas Quillota y Portillo, regiones de Valpariaso y Coquimbo, V región, Servicio Nacional de Geología de Chile, no. 73, 202p.

Robinson, B.W. and Kusakabe, M., 1975, Quantitative preparation of sulfur dioxide, for $^{34}S/^{32}S$ analyses, from sulfides by combustion with cuprous oxide, Analytical Chemistry, v. 47, p. 1179-1181.

Roddick, J.C., 1983, High precision intercalibration of $^{40}Ar/^{39}Ar$ standards. Geochimica et Cosmochimica Acta, 47, p. 887-898.

Roedder, E., 1984, Fluid inclusions: Chelsea, Michigan, Mineralogical Society of America, 644p.

Rojas, A., 1985, Geología y petrogénesis del porfido Don Luis en el yacimiento Río Blanco, División Andina, CODELCO – Chile, Unpublished memoria de titulo, Departamento de Geología y geofísica, Santiago, Universidad de Chile, 109p.

Rollinson, H., 1993, Using Geochemical Data: Evaluation, Presentation, Interpretation, Longman Group UK Limited, 352p.

Ruiz, C., Aguirre, L. and Corvalan, J., 1965, Geología y yacimientos metalíferos de Chile, Inst. Invest. Geol., Santiago, Chile.

Rye, R.O., 1993, The evolution of magmatic fluids in the epithermal environment: the stable isotope perspective, Economic Geology, v. 88, p. 733-753.

Serrano, L., Vargas, R., Stambuk, V., Aguilar, C., Galeb, M., Holmgren, C., Contreras, A., Godoy, S., Vela, I., Skewes, A.M. and Stern, C.R., 1996, The late Miocene to early Pliocene Río Blanco-Los Bronces copper deposit, central Chilean Andes: in F. Camus, R.H. Sillitoe, R. Peterson, eds., Andean copper deposits: new discoveries, mineralisation, styles and metallogeny, Society of Economic Geologists, special publication 5, p.119-130.

Sheppard, S.M.F., Nielsen, R.L. and Taylor, H.P., Jr., 1969, Oxygen and hydrogen isotope ratios of clay minerals from porphyry copper deposits, Economic Geology, v. 64, p. 755-777.

Sheppard, S.M.F., Nielsen, R.L. and Taylor, H.P., Jr., 1971, Hydrogen and oxygen isotope ratios in minerals from porphyry copper deposits, Economic Geology, v. 66, p. 515-542.

Sheppard, S.M.F. and Gustafson, L.B., 1976, Oxygen and Hydrogen isotopes in the porphyry copper deposit at El Salvador, Chile, Economic Geology, v. 71, p. 1549-1559.

Shinohara, H. and Kazahaya, K., 1995, Degassing processes related to magma chamber crystallisation: in Thompson, J.F.H., ed., Magmas, fluids and ore deposits: short course series (Mineralogical Association of Canada), 23, Victoria, B.C., p. 47-70.

Sibson, R.H., 1986, Brecciation processes in fault zones: inferences from earthquake rupturing, Pure Applied Geophysics, v. 124, p. 159 – 174.

Sibson, R.H., 2000, A brittle failure mode plot defining conditions for high flux flow, Economic Geology, v. 95, p. 41-48.

Sillitoe, R.H., 1973, The tops and bottoms of porphyry copper deposits, Economic Geology, v. 68, p. 799-815.

Sillitoe, R.H., 1985, Ore-related breccias in volcanoplutonic arcs, Economic Geology and the Bulletin of the Society of Economic Geologists, v.80, no.6, p.1467-1514.

Skarmeta, J., Castelli, J.C., Alvarez, N.D., Adriasol, A., and Lopez, G., 2000, Control Estructural de la mineralización en Andina: CODELCO-central, Santiago, Chile.

Skewes, M.A. and Holmgren, C., 1993, Solevantamiento andino, erosión y emplazamiento de brechas mineralizadas en el deposito de cobre porfídico Los Bronces, chile central (33°S): aplicación de geothermometria de inclusiones fluidas, Revista geológica de chile, 20, 1, p. 71-83.

Skewes, A. and Stern, C.R., 1994, Tectonic trigger for the formation of late Miocene Cu-rich breccia pipes in the Andes of central Chile, Geology, Geological Society of America, Boulder,

CO, United States, 22, 6, p.551-554.

Skewes, A.M. and Stern, C.R., 1994, Geochemistry of igneous rocks and magmatic/hydrothermal breccias at Río Blanco-Los Bronces, unpublished report to CODELCO, 16p.

Skewes, A.M. and Stern, C.R., 1996, Late Miocene mineralised breccias in the Andes of central Chile: Sr and Nd isotopic evidence for multiple magmatic sources: in F. Camus, R.H. Sillitoe, R. Peterson, eds, Andean copper deposits: new discoveries, mineralisation, styles and metallogeny, Society of economic geologists special publication no. 5, p. 119-130.

Skewes, M.A., 1996, Termometría de inclusiones fluidas en matriz de brechas de La Americana y Sur-Sur, Río Blanco, unpublished Codelco report.

Skewes, M.A., Holmgren, C. and Stern, C.R., 2002, The Donoso copper-rich, tourmaline-bearing breccia pipe in central Chile: petrologic, fluid inclusion and stable isotope evidence for an origin from magmatic fluids, Mineralium Deposita, Springer-verlag.

Spröhnle, C., 1988, Geología de los sectores Sur-Sur y Don Luis del yacimiento Río Blanco, División Andina, CODELCO – Chile, Unpublished memoria de titulo, Departamento de geología y geofísica, Santiago, Universidad de Chile, 177p.

Stambuk, V., Serrrano, L. and Vargas, R., 1985, Geología del sector Sur-Sur, yacimiento Río Blanco: Congreso Geológico Chileno, 4th, Antofagasta, Actas, v. 2, p. 383-404.

Stambuk, V., Aguilar, C., Blondel, J., Galeb, M., Serrano, L., Vargas, R., 1988, Geología del yacimiento Río Blanco, Superintendencia de Geología, CODELCO-Chile, División Andina, 69p.

Stambuk, V., Aguilar, C., Blondel, J., Galeb, M., Serrano, L., Vargas, R., 1993, The Río Blanco porphyry copper and hydrothermal breccia deposit, central Chile: Superintendencia de Geologia, CODELCO-Chile, Division Andina, 30p.

Steiger, R.H. and Jager, E., 1977, Subcommission on geochronology: Convention on the use of decay constants in geo- and cosmo-chronology, Earth and Planetary Science Letters, v. 36, p. 359-362.

Stern, C.R., 1989, Pliocene to present migration of the volcanic front, Andean southern volcanic zone, Revista Geologica de Chile, v. 16, 2, p. 145-162.

Stern, C.R. and Skewes, M.A., 1993, Petrochemistry of igneous rocks at Río Blanco-Los Bronces: a diagnostic report, CODELCO-Chile.

Stern, C.R. and Skewes, M.A., 1995, Miocene to present magmatic evolution at the northern end of the Andean southern volcanic zone, central chile, Revista geologica de chile, v. 22, 2, p. 261-272.

Suzuoki, T. and Epstein, S., 1976, Hydrogen isotope fractionation between OH-bearing minerals and water Geochimica et Cosmochimica Acta, 40, 10, p. 1229-1240.

Taylor, B.E., 1986, Magmatic volatiles: isotopic variation of C, H and S: in J.W. Valley, H.P. Taylor, J.R. O'Neil, eds., Stable isotopes in high temperature geological processes, Reviews in Mineralogy, v. 16, p. 185-219.

Taylor, B.E., 1987, Stable isotope geochemistry of ore forming fluids: in Short Course in Stable

Isotope Geochemistry of Low Temperature Fluids, T.K. Kyser, ed, Saskatoon: Mineralogical Association of Canada, v. 13, p. 337-445.

Taylor, H.P., Jr., 1974, The application of oxygen and hydrogen isotope studies to problems of hydrothermal alteration and ore deposition, Economic Geology, v. 69, p. 843-883.

Taylor, H.P., Jr., 1997, Oxygen and hydrogen isotope relationships in hydrothermal mineral deposits: in H.L. Barnes, ed., Geochemistry of hydrothermal ore deposits, 3rd edition, New York, John Wiley, p. 229-302.

Thiele, R., 1980, Hoja Santiago, Región Metropolitana: Instituto de Investigaciones Geológicas, Carta geología de Chile, 39, 51p.

Thiele, R., Beccar, I., Levi, B., Nystrom, J.O. and Vergara, M., 1991, Tertiary Andean volcanism in a caldera-graben setting, Geologische Rundschau v. 80, 1, p. 179-186.

Tilton, G.R., 1979, Isotopic studies of Cenozoic Andean calc-alkaline rocks, Year Book - Carnegie Institution of Washington, 78, p. 298-303.

Titley, S.R. and Beane, R.E., 1981, Porphyry copper deposits, Part 1: Geologic settings, petrology, and tectogenesis, Economic Geology, 75th Anniversary Volume, p. 214-235.

Toro, J.C, 1986, Cuerpos subvolcanicos asociados a zonas de alteración hidrotermal en la alta cordillera de Chile central, Unpublished Memoria de Titulo, Departamento de Geociencias, Antofagasta, Universidad del Norte, 174p.

Tosdal, R.M., 1995, Pb isotopic constraints on reconstructions of eastern North America and western South America, Abstracts with Programs - Geological Society of America, v.27, no.6, p.398.

Tosdal, R.M. and Munizaga, F., 1996, Basement influences on ore deposits in the Chilean Andes (30-34°S), Abstracts with programs, Geological Society of America, 28, 7, 154p.

Tosdal, R.M., Wooden, J.L. and Bouse, R.M., 1999, Pb isotopes, ore deposits and metallogenic terranes: in D.D. Lambert and J. Ruiz, eds, Reviews in Economic Geology: Application of radiogenic isotopes to ore deposit research and exploration, v. 12, 199p.

Valley, J.W., Taylor, H.P. and O'Neill, J.R., 1986, Stable isotopes in high temperature geological processes, Reviews in Mineralogy, Mineralogical Society of America, v. 16, 570p.

Vargas, R., Gustafson, L.B., Vukasovic, M, Tidy, E. and Skewes, A., 1999, Ore Breccias in the Río Blanco-Los Bronces porphyry copper deposit, Chile: in B.J. Skinner, ed., Geology and Ore Deposits of the Central Andes, Society of Economic Geologists, special publication 7, p. 281-297.

Vergara, M. and Drake, R., 1978, Edades potasio-argon y su implicancia en la geología regional de Chile central, Comunicaciones, 23, p.1-11.

Vergara, M. and Drake, R., 1979, Eventos magmáticos platónicos en Los Andes de Chile central. Actas II Congreso Geológico Chileno, Tomo I, p. F19-F30.

Vergara, M. and Latorre J., 1984, El Complejo volcánico Pliocenico de Río Blanco, Santiago, Revista Geológica de Chile, v. 22, p. 49-60.

Vergara, M., Charrier, R., Munizaga, F., Rivano, S, Sepulveda, P., Thiele, R. and Drake, R., 1988, Miocene volcanism in the central Chilean Andes (31°30'S-34°35'S), Journal of South American Earth Sciences, v. 1, 2, p. 199-209.

Vergara, M., Levi, B., Nyström, J.O. and Cancino, A., 1995, Jurassic to early Cretaceous island arc volcanism, extension, and subsidence in the coast range of central Chile, Geological society of America – bulletin, 107, 12, p. 1427-1440.

Von Huene, R., Corvalan, J., Flueh, E.R., Hinz, K., Korstgard, J., Ranero, C.R., Weinrebe, W. and the CONDOR scientists, 1997, Tectonic control of the subducting Juan Fernandez Ridge on the Andean margin near Valparaiso, Chile, Tectonics, v. 16, 3, p. 474-488.

Walshe, J.L., Halley, S.W., Anderson, J.A. and Harrold, B.P., 1996, The interplay of groundwater and magmatic fluids in the formation of the cassiterite-sulfide deposits of western Tasmania, Ore Geology Reviews, 10, p. 367-387.

Warnaars, F.W., Holmgren, C.D. and Barassi, S., 1985, Porphyry copper and tourmaline breccias at Río Blanco-Los Bronces, Chile, Economic Geology, v. 80, p.1544-1565.

Watanabe, Y. and Hedenquist, J.W., 2001, Mineralogic and stable isotope zonation at the surface over the El Salvador porphyry copper deposit, Chile, Economic Geology, v. 96, p. 1775-1797.

Wolf, M.B. and London, D., 1997, Boron in granitic magmas: stability of tourmaline in equilibrium with biotite and cordierite, Contributions to Mineralogy and Petrology, v. 130, p. 12-30.

Yañez, G., Cembrano, J., Pardo, M., Ranero, C. and Selles, D., 2002, The Challenger-Juan Fernandez-Maipo major tectonic transition of the Nazca-Andean subduction system at 33°-34°S: geodynamic evidence and implications, Journal of South American Earth Sciences, 15, p. 23-38.

Warnaars, F.W., Holmgren, C.D. and Barassi, S., 1985, Porphyry copper and tourmaline breccias at Río Blanco-Los Bronces, Chile, Economic Geology, v. 80, p. 1544-1565.

Wilson, M., 1989, Igneous Petrogenesis, Unwin Hyman, London.

York, D., 1969, Least squares fitting of a straight line with correlated errors, Earth and Planetary Science Letters, 5, p. 320-324.

Yu, Z., Robinson, P. and McGoldrick, P., 2001, An evaluation of methods for the for the chemical decomposition of geological materials for trace element determination using ICP-MS, Geostandards Newsletter: The Journal of Geostandards and Geoanalysis, v. 25, no. 2-3, p. 199-217.

Zartman, R.E. and Haines, S.M., 1988, The plumbotectonic model for lead isotope systematics among major terrestrial reservoirs: a case for bi-directional transport, Geochimica et Cosmochimica Acta, v. 52, p. 1327-1339.

Zentilli, M., Doe, B., Hedge, C.E., Alvarez, C.E., Tidy, E. and Daroca, J.A., 1988, Isótopos de plomo en yacimientos de tipo porfído cuprífero comparados con otros depósitos metalíferos en los Andes del norte de Chile y Argentian: Congreso Geológico Chileno, 5th, Santiago, Augusto 8-12, Actas, p. B331-369.

Zheng, Y. F. and Simon, K., 1991, Oxygen isotope fractionation in hematite and magnetite: A theoretical calculation and application to geothermometry of metamorphic iron-formations, European Journal of Mineralogy, 3, p. 877-886.

List of Appendices

Appendix A: Drillholes logged, partially logged and sampled from the three sectors.

Rio Blanco sector	L	S
DDH-101		
DDH-125		
DDH-192		
DDH-212		
DDH-217		
DDH-219		
DDH-238		
DDH-244		
DDH-248		
DDH-260		
DDH-268		
DDH-272		
DDH-330		
DDH-340		
DDH-344		
DDH-352		
DDH-353		
DDH-357		
DDH-358		
DDH-372		
DDH-378		
DDH-380		
DDH-389		
DDH-402		
DDH-406		
DDH-422		
DDH-429		
DDH-439		
DDH-448		
DDH-450		
DDH-454		
DDH-471		
DDH-480		
DDH-492		
DDH-513		
DDH-557		
DDH-566		
DDH-576		
DDH-580		
DDH-593		
DDH-628		

Don Luis sector	L	S
DDH-638		
DDH-652		
DDH-723		
DDH-730		
DDH-733		
DDH-734		
DDH-737		
DDH-738		
DL-148		
DL-48		
DL-85		
DL-94		

Sur-Sur sector	L	S
C-50		
DDH-555		
DDH-560		
DDH-E40		
DL-03		
DL-138		
DL-139.1		
DL-16		
DL-46A		
DL-53		
DL-57		
DL-62		
DL-64		
DL-71		
DL-79A		
DL-87		
E20-A		
TSS-04		
TSS-12		
TSS-13		
TSS-16		
TSS-21		
TSS-22		
TSS-23		
TSS-26		
TSS-28		
TSS-29		
TSS-36		

L = logged, S = sampled

Appendix B1: Major and trace element data for Río Blanco samples. CA3 and CA13 from Hollings (2001)

						La Americana													
	Andesite roof pendant					Deep		Shallow		Don Luis Porphyry						Feldspar porphyry			
Sample	**231**	**235**	**138C**	**AN2b**	**AN4**	**AN1A**	**AN1C**	**CA3**	**CA13**	**234**	**280**	**291**	**59916**	**59917**	**ST4A**	**O1PF1**	**O1PF3**	**O1PF11**	**ST1D**
Section		XC 195	XC 135	Laura	XC 235	110-180	110-180			Monolito	XC 275	XC 275	XC 315	XC 030	XC 215	XC 345	XC 275	XC 245	XC 235
DDH	La Union		217	area	330	23	TSS23			Mountain	734	734	DL-94	560	380	733	734	738	576
Elevation	surface	3250	3433	surface	3304	3293	3293	surface	surface	surface	2899	2842	3472	3735	3265	2930	2771	3199	3259
Easting	24080	23310	23484	24500	23842	24482	24482	382664	382806	24100	24704	24758	24301	24365	24121	24277	24825	24609	24408
Northing	27090	27520	27331	26300	26836	24623	24623	632879	632826	25840	26843	26828	26538	25582	27126	26347	26804	27174	27134
Lithology	andesite	andesite	andesite	andesite	andesite	andesite	andesite	basalt	andesite	PDL	PDL	PDL	PDL	PDL	PDL/ PQM	PF	PF	PF	PF
SiO2	55.52	58.41	56.20	55.58	56.61	55.47	58.39	52.99	56.04	68.63	70.16	69.26	70.17	68.89	74.08	69.02	69.69	69.08	67.77
TiO2	0.95	0.91	0.89	0.98	0.90	0.79	0.81	1.07	1.01	0.33	0.22	0.34	0.24	0.31	0.20	0.28	0.37	0.29	0.37
Al2O3	17.66	17.78	17.71	20.15	18.09	21.42	17.88	18.94	17.69	16.54	16.00	17.09	16.52	15.53	14.15	16.52	16.09	16.86	17.10
Fe2O3	12.79	7.61	10.44	7.15	10.94	7.92	10.30	8.84	7.85	2.18	1.09	1.75	5.27	8.68	1.50	1.48	2.15	2.91	2.10
MnO	0.03	0.07	0.05	0.12	0.02	0.02	0.03	0.26	0.33	0.05	0.02	0.01	0.01	0.04	0.08	0.01	0.00	0.01	0.01
MgO	4.01	3.44	3.69	3.19	3.74	3.19	2.98	4.85	4.43	0.85	0.56	0.98	0.57	0.87	0.40	0.83	1.17	0.90	0.95
CaO	1.93	4.70	0.41	6.39	2.97	1.38	2.07	7.37	5.65	2.03	2.28	1.32	1.01	0.37	1.52	2.01	1.66	2.69	2.69
K2O	4.54	3.71	8.92	1.63	5.06	5.88	4.90	1.44	2.25	3.70	4.07	1.29	3.88	4.97	6.17	3.99	1.08	3.03	2.90
Na2O	2.32	3.08	1.44	4.53	1.41	3.70	2.41	3.94	4.50	5.54	5.49	7.79	2.25	0.21	1.81	5.74	7.64	4.12	5.96
P2O5	0.27	0.27	0.25	0.27	0.25	0.23	0.23	0.30	0.27	0.14	0.09	0.16	0.10	0.13	0.08	0.11	0.13	0.11	0.15
Mg#	0.41	0.50	0.44	0.50	0.43	0.47	0.39	0.55	0.55	0.46	0.53	0.55	0.19	0.18	0.37	0.55	0.55	0.40	0.50
Ti	5634	5399	5296	5885	5397	4707	4815	6410	6020	2004	1303	2028	1394	1850	1190	1657	2200	1742	2206
P	1181	1175	1064	1192	1084	1021	1015	1289	1163	619	407	671	415	557	365	491	578	498	669
Cr	94	57	89	56	86	30	51	42.05	135.68	5	4	6	3	7	3	3	6	8	9
Ni	39	42	42	38	39	28	30	45.52	68.96	4	2	6	4	9	2	8	3	4	6
Rb	246	172	262	48	230	254	251	47	55	99	85	56	107	196	157	47	100	83	69
Sr	188	456	92	735	165	155	156	644	740	537	486	326	113	29	194	573	562	372	671
Ba	396	389	1300	413	538	337	482	431.8	602.1	1030	776	209	508	349	954	791	718	182	772
Sc	21.25	19.05	18.99	20.14	21.21	12.79	16.38	21.9	19.2	2.23	2.79	4.00	2.43	4.36	2.72	2.97	4.28	4.05	3.68
V	178.37	175.27	161.45	159.18	194.76	127.59	168.68	225.2	184.4	39.80	28.15	51.67	32.87	52.35	26.65	40.03	50.97	64.95	55.40
Nb	6.23	5.59	4.77	6.07	5.80	4.89	4.23	4.58	4.92	3.75	2.48	1.85	1.16	2.98	1.99	2.35	2.14	2.08	2.15
Zr	171.93	185.31	85.19	190.75	159.27	119.38	140.57	114.5	170.6	123.06	103.30	99.14	100.00	102.35	98.33	115.90	98.48	101.78	118.58
Th	8.17	11.39		6.07	5.59	6.24	5.81	2.95	5.74	3.34	3.73	4.82	4.12	3.62	2.82	2.97	2.96	3.63	3.48
Y	12.87	15.01	13.30	13.36	13.76	8.94	12.26	15.9	15.8	3.95	3.73	2.87	2.11	3.09	3.45	3.69	3.77	3.74	3.99
La	21.76	19.51	17.57	25.40	22.25	20.33	18.81	17.18	17.01	11.14	10.61	20.10	12.21	12.13	10.24	14.49	9.74	16.60	14.41
Ce	42.91	43.95	34.68	45.23	36.89	34.32	36.46	36.33	39.55	29.42	26.08	42.09	24.84	25.69	33.18	31.23	23.50	34.34	32.92
Nd	19.26	22.21	16.65	22.77	18.01	17.37	19.55	17.92	19.57	13.37	11.64	16.76	8.51	12.93	10.34	14.38	11.26	15.04	14.72
Cu	3678	2174	5382	49	3932	1768	1268	137.06	287.23	15	3830	5434	6025	122	1881	6143	1835	1021	1431
Zn	37	66	77	133	68	47	33	77.80	34.43	76	12	24	18	50	210	33	24	21	20

Appendix B2: Previous major and trace element data from Río Blanco.

Rock type	Early and middle Miocene host rocks Andesite		Quartz monzonites			Granodiorites			Magmatic Breccia	Late Miocene and early Pliocene porphyritic rocks quartz monzonite, latite, dacite and rhyolite						
sample	An1*	An2*	LB-1#	LB-2#	LB-8#	LB-3*	GDRB*	LB-7*	RBBxMag†	PQM*	LB-12#	LBL†	PDL*	LB-11*	LB-10*	ChDac*
age (Ma)	>16	>16	20.1-15.9	11.3		18.5	11.7	8.6	7.3	5.2	5.2	5.1	4.9	4.9	4.8	4.8
SiO_2	62.1	56.2	59.9	65.3	69.61	60.5	65.6	63.06	64	66.1	66.13	71.2	68.7	69.5	67.8	70.9
TiO_2	0.28	0.78	0.78	0.46		0.65	0.45		0.35	0.13	0.4	0.26	0.14			0.13
Al_2O_3	16.1	16.9	17.1	15.8	14.2	16.8	16.2	15.4	15.1	15.6	16.4	17.6	15.7	15.5	15.7	15.2
Fe_2O_3	5.4	4.7	1.4	1.2	1.25	2.08	1.6	3.65	2.4	1.57	3.77	1.2	1.1	0.63	0.83	2.2
FeO	2.5	4.6	4.28	2.41	1.42	3	2.6	1.41	1.8	2.63	1.1	0.17	0.59	0.91	0.83	0.59
MnO			0.11	0.08	0.05	0.09		0.08			0.011			0.02	0.11	
MgO	1.8	4.7	2.44	1.53	0.95	3.05	2.6	3.43	2.6	1.59	3.28	0.39	0.48	0.41	0.33	0.36
CaO	0.32	5.3	4.24	3.04	1.58	5.42	3.3	1.74	2.3	2.1	0.12	0.21	0.73	1.75	2.52	0.33
K_2O	6.6	2.9	3.16	3.55	3.23	2.22	3.2	2.95	6.3	3.95	4.9	5.5	4.8	2.43	2.57	5.2
Na_2O	2.1	3.1	4.72	4.68	4.26	4.6	4.48	4.24	3.49	5.4	0.11	0.14	4.7	4.76	4.38	3.63
LOI	2.5	0.9				0.25	0.1	0.27	2.3	0.9		2.9	2	0.85	1.67	1.5
Total	99.7	100.8				98.86	100.3	96.23	100.64	99.97		99.57	98.94	97.04	97.07	100.04
Rb	151	158				41.5	90.2	37.7	160	42.4		130	112	29.8	66.7	192
Sr	136	392				677	450	730	219	650		12	358	903	703	173
Cs	5.1	4.1				2.7	3.6	5	3.5	2.7		1	1.4	14.1	11.6	3.6
Ba	480	422				535	512	545	775	560		228	864	745	708	967
Sc	9.6	10.8				13.3	6.3	12.8	6.7	2.1		3.3	2.3	2.3	1.9	2
Hf	4.8	5.2				3.4	4.3	2.3	5.6	3		3.8	3.3	2.3	3.2	2.9
Th	9.6	8.5				5	12	3.3	6.9	4.3		2.7	4.1	2.8	2.6	4.2
U	3.6	4.2				5.6	3.5	5	3.4	1.2		1.9	1.8	2.2	1.6	2.2
La	17.9	21.1				14.2	17.1	15	17.4	12		14.1	16.4	13.3	12.3	11.8
Ce	34.4	38.1				28.6	31.1	27.9	34.2	20.6		23.8	27.9	28.6	26.1	25.5
Nd	14.9	18.2				18.7	16.4	20.8	17	7.73		10	14.6	13	13.4	10.4
Sm	2.82	3.56				3.53	2.52	4.06	2.99	1.18		1.82	1.98	2.2	2.25	1.45
Eu	0.78	0.94				0.92	0.67	1.05	0.65	0.42		0.41	0.52	0.58	0.48	0.5
Tb	0.3	0.38				0.31	0.28	0.37	0.28	0.12		0.11	0.13	0.25	0.24	0.13
Yb	1.25	1.45				1.85	1.08	1.43	1.04	0.48		0.42	0.39	0.59	0.45	0.56
Lu	0.2	0.22				0.29	0.14	0.11	0.14	0.05		0.06	0.05	0.09	0.05	0.06

Previous whole rock analyses. * = Serrano et al. (1996), # = Warnaars et al. (1985) and † = Skewes and Stern (1994).

Appendix C1: Electron microprobe data for hydrothermal biotite

Label	219dhydbiot 1	219dhydbiot 2	219dhydbiot 3	219dhydbiot 4	219dhydrobt 5	223ahydbiot 6	223ahydbiot 7	223ahydbiot 8	223ahydbiot 11	222ehydbiot 12	222ehydbiot 13	222ehydbiot 14	222ehydbiot 15	222ehydbiot 16
SiO2	40.68	37.77	38.51	38.55	38.32	38.29	43.34	36.2	40.08	37.38	36.73	39.89	43.27	38.69
TiO2	2.1	2.42	2.21	2.47	2.2	1.64	1.52	1.62	1.19	1.76	1.18	1.64	0.88	1.9
Al2O3	16.08	16.27	16.11	15.99	16.32	17.76	17.17	18.06	20.08	17.15	18.47	18.57	26.28	17.63
Cr2O3	0.01	0	0	0.04	0.04	0.02	0.03	0.05	0	0	0.02	0	0.01	0.03
FeO	13.48	14.77	14.36	14.41	14.26	14.75	13.03	15.35	11.67	15.8	15.67	14.08	8.74	14.89
V2O3	0.14	0.15	0.06	0.1	0.14	0.05	0.1	0.07	0.05	0.03	0.04	0.1	0.14	0.07
ZnO	0.08	0	0.07	0	0.09	0.06	0.06	0	0.17	0	0	0	0.12	0
MnO	0.12	0.12	0.09	0.1	0.09	0.11	0.12	0.19	0.22	0.1	0.16	0.09	0.05	0.15
MgO	14.28	13.84	14.36	14.33	14.21	12.26	10.81	12.84	8.81	12.49	12.93	11.76	6.13	12.55
CaO	0.15	0.08	0.06	0.06	0.02	0.02	0.05	0.02	0.07	0.02	0.01	0.05	0.02	0.01
Na2O	0.21	0.14	0.2	0.19	0.15	0.15	0.11	0.2	0.06	0.04	0.04	0.09	0.16	0.06
K2O	9.13	10	9.78	9.89	9.91	10.01	9.4	9.76	9.63	10.1	10.21	10.21	9.94	10.13
BaO	0	0	0	0	0	0	0	0	0	0	0	0	0.03	0
Rb2O	-	-	-	-	-	-	-	-	-	-	-	-	-	-
Cs2O	-	-	-	-	-	-	-	-	-	-	-	-	-	-
SrO	0	0	0	0	0	0	0	0	0	0	0	0	0	0
NiO	0	0	0	0.09	0	0.02	0	0.02	0	0.01	0.02	0	0	0
CuO	0	0	0	0	0	0.05	0.18	0.04	0.03	0	0.04	0	0	0.06
F	1.16	1	1.09	1.03	1.16	1.1	1.07	0.77	0.91	1.42	1.24	1.32	0.67	1.43
Cl	0.17	0.1	0.13	0.13	0.11	0.18	0.11	0.19	0.12	0.07	0.06	0.07	0.04	0.06
H2O(c)	3.55	3.53	3.51	3.55	3.48	3.46	3.63	3.56	3.55	3.29	3.4	3.48	3.97	3.38
O=F	0.49	0.42	0.46	0.43	0.49	0.47	0.45	0.32	0.38	0.6	0.52	0.56	0.28	0.6
O=Cl	0.04	0.02	0.03	0.03	0.02	0.04	0.03	0.04	0.03	0.01	0.01	0.02	0.01	0.01
Sum Ox%	100.81	99.76	100.08	100.47	99.99	99.43	100.26	98.55	96.22	99.05	99.69	100.79	100.15	100.41
Si	5.887	5.621	5.688	5.677	5.667	5.696	6.235	5.473	5.998	5.625	5.494	5.803	6.04	5.698
Ti	0.229	0.271	0.246	0.274	0.245	0.183	0.165	0.184	0.133	0.2	0.133	0.18	0.093	0.211
Al/Al IV	2.113	2.379	2.312	2.323	2.333	2.304	1.765	2.527	2.002	2.375	2.506	2.197	1.96	2.302
Al VI	0.629	0.475	0.493	0.453	0.512	0.81	1.146	0.691	1.54	0.666	0.75	0.986	2.363	0.758
Cr	0.001	0	0	0.005	0.004	0.002	0.003	0.006	0	0.001	0.003	0.001	0.001	0.004
Fe2+	1.631	1.839	1.773	1.774	1.764	1.835	1.567	1.941	1.46	1.989	1.96	1.713	1.021	1.834
V	0.016	0.018	0.007	0.012	0.017	0.006	0.012	0.009	0.006	0.004	0.005	0.011	0.016	0.008
Zn	0.008	0	0.008	0	0.009	0.007	0.007	0	0.019	0	0	0	0.012	0
Mn2+	0.015	0.015	0.012	0.012	0.011	0.014	0.015	0.024	0.027	0.012	0.02	0.012	0.005	0.018
Mg	3.081	3.071	3.162	3.147	3.133	2.719	2.317	2.892	1.964	2.802	2.883	2.55	1.276	2.756
Ca	0.023	0.013	0.009	0.01	0.003	0.004	0.007	0.003	0.012	0.003	0.001	0.007	0.003	0.001
Na	0.059	0.04	0.059	0.053	0.044	0.042	0.031	0.059	0.019	0.012	0.012	0.024	0.042	0.016
K	1.686	1.899	1.843	1.858	1.87	1.899	1.725	1.882	1.839	1.938	1.949	1.895	1.77	1.904
Ba	0	0	0	0	0	0	0	0	0	0	0	0	0.002	0
Rb	-	-	-	-	-	-	-	-	-	-	-	-	-	-
Cs	-	-	-	-	-	-	-	-	-	-	-	-	-	-
Sr	0	0	0	0	0	0	0	0	0	0	0	0	0	0
Ni	0	0	0	0.01	0	0.003	0	0.002	0	0.001	0.003	0	0	0
Cu	0	0	0	0	0	0.006	0.02	0.004	0.004	0	0.004	0	0	0.006
F	0.53	0.472	0.508	0.48	0.543	0.52	0.485	0.367	0.43	0.677	0.587	0.609	0.294	0.666
Cl	0.041	0.026	0.033	0.034	0.028	0.046	0.027	0.048	0.03	0.017	0.016	0.017	0.008	0.015
OH	3.428	3.502	3.459	3.486	3.429	3.434	3.488	3.585	3.541	3.306	3.397	3.373	3.698	3.32
Sum Cat#	19.377	19.641	19.611	19.608	19.612	19.53	19.015	19.697	19.023	19.628	19.722	19.38	18.603	19.516
XMg	0.654	0.626	0.641	0.639	0.64	0.597	0.597	0.598	0.574	0.585	0.595	0.598	0.556	0.6
Oct	5.594	5.671	5.694	5.675	5.679	5.573	5.22	5.74	5.145	5.671	5.751	5.441	4.771	5.581
Int	1.768	1.952	1.91	1.921	1.917	1.945	1.764	1.944	1.869	1.953	1.962	1.927	1.816	1.921

Appendix C1 (cont).

All elemental analyses were performed on carbon coated polished thin sections using a Cameca SX50 electron microprobe at the University of Tasmania's Central Science Laboratory using:

- Beam Current: 25nA
- Acceleration Voltage: 15kV
- Atomic percentages for hydrothermal biotite calculated on the basis of 22 oxygen and 4 OH, F, Cl.

Appendix C2: Electron microprobe data for tourmaline cement

	62bcoarseTm	62bcoarsTmrim	62bcoarseTm	62bcoarseTm	62bcoarseTm	223afineblueTm	223acoarsbrTm	223acoarsbrTm	223afineblueTm	222ehydbt-Tm	222eblueTm	222eblueTm	222eblueTmnee
Label	1	2	3	4	5	6	7	8	9	10	11	12	13
SiO2	36.305	37.482	35.857	36.434	36.401	35.251	35.171	34.430	36.511	35.064	34.353	34.708	34.628
TiO2	0.238	0.142	0.540	0.348	0.368	0.264	0.375	0.509	0.244	0.497	0.693	0.606	1.807
Al2O3	32.042	33.816	29.624	29.676	33.256	29.337	27.562	28.093	32.824	34.914	34.834	34.867	21.632
Cr2O3	0.000	0.013	0.011	0.018	0.000	0.004	0.006	0.000	0.020	0.000	0.024	0.000	0.024
FeO	9.114	4.419	10.733	9.591	7.392	12.315	13.572	14.163	8.498	9.319	9.374	8.849	16.807
MnO	0.000	0.042	0.000	0.000	0.000	0.016	0.022	0.065	0.036	0.000	0.014	0.019	0.000
MgO	6.889	8.591	6.892	7.571	6.942	6.124	6.352	6.010	6.423	4.785	4.874	4.804	7.690
CaO	0.176	0.063	0.231	0.148	0.132	0.748	0.805	1.192	0.384	0.484	0.699	0.449	1.505
V2O3	0.113	0.000	0.000	0.000	0.000	0.007	0.000	0.000	0.000	0.000	0.000	0.000	0.000
Na2O	2.670	2.201	2.671	2.571	2.705	2.239	2.405	2.056	2.227	2.328	2.285	2.257	2.039
K2O	0.039	0.014	0.031	0.033	0.042	0.055	0.062	0.033	0.046	0.048	0.045	0.046	0.138
B2O3	12.235	13.011	13.279	13.414	12.587	13.414	13.424	13.094	12.578	12.467	12.698	13.177	13.569
ZnO	0.019	0.087	0.059	0.000	0.000	0.000	0.004	0.023	0.036	0.000	0.000	0.000	0.002
CuO	0.037	0.000	0.039	0.020	0.000	0.027	0.000	0.030	0.049	0.000	0.000	0.056	0.000
NiO	0.030	0.033	0.014	0.035	0.003	0.032	0.000	0.057	0.054	0.005	0.000	0.024	0.000
F	0.083	0.075	0.011	0.135	0.172	0.153	0.153	0.215	0.054	0.075	0.103	0.119	0.156
Cl	0.011	0.013	0.011	0.006	0.000	0.016	0.088	0.029	0.016	0.012	0.004	0.020	0.003
Sum Ox%	100.000	100.000	100.000	100.000	100.000	100.000	100.000	100.000	100.000	100.000	100.000	100.000	100.000
Cations													
Si	5.340	5.513	5.274	5.359	5.354	5.293	5.281	5.170	5.482	5.265	5.158	5.211	5.199
Ti	0.027	0.016	0.060	0.039	0.041	0.030	0.042	0.057	0.028	0.056	0.078	0.068	0.204
Al	5.589	5.898	5.167	5.176	5.800	5.192	4.878	4.972	5.809	6.179	6.165	6.171	3.828
Cr	0.000	0.001	0.001	0.002	0.000	0.000	0.001	0.000	0.002	0.000	0.003	0.000	0.003
Fe	1.128	0.547	1.328	1.187	0.915	1.546	1.704	1.778	1.067	1.170	1.177	1.111	2.110
Mn	0.000	0.005	0.000	0.000	0.000	0.002	0.003	0.008	0.005	0.000	0.002	0.002	0.000
Mg	1.520	1.895	1.521	1.671	1.532	1.371	1.422	1.346	1.438	1.071	1.091	1.075	1.722
Ca	0.028	0.010	0.037	0.024	0.021	0.120	0.129	0.192	0.062	0.078	0.112	0.072	0.242
V	0.013	0.000	0.000	0.000	0.000	0.001	0.000	0.000	0.000	0.000	0.000	0.000	0.000
Na	0.766	0.631	0.766	0.738	0.776	0.652	0.700	0.599	0.648	0.678	0.665	0.657	0.594
K	0.007	0.003	0.006	0.006	0.008	0.010	0.012	0.006	0.009	0.009	0.009	0.009	0.026
B	3.124	3.323	3.391	3.425	3.214	3.476	3.478	3.393	3.259	3.230	3.290	3.414	3.516
Zn	0.002	0.009	0.006	0.000	0.000	0.000	0.000	0.003	0.004	0.000	0.000	0.000	0.000
Cu	0.004	0.000	0.004	0.002	0.000	0.003	0.000	0.003	0.006	0.000	0.000	0.006	0.000
Ni	0.004	0.004	0.002	0.004	0.000	0.004	0.000	0.007	0.007	0.001	0.000	0.003	0.000
Sum cations	17.551	17.856	17.563	17.632	17.662	17.700	17.651	17.534	17.825	17.737	17.750	17.801	17.445
for calc only	0.041	0.042	0.040	0.040	0.041	0.041	0.040	0.040	0.042	0.042	0.042	0.042	0.038
AlAl	35.706	41.434	28.919	28.862	40.669	28.049	21.880	22.824	39.742	46.762	46.205	47.671	-0.047
Al50Fe50	27.387	13.114	33.141	29.549	22.184	38.137	42.585	43.934	25.670	27.794	27.917	26.593	55.100
Al50 Mg50	36.906	45.452	37.940	41.589	37.147	33.814	35.534	33.242	34.588	25.444	25.878	25.736	44.947
Ca-Fe(tot)-Mg													
Ca	1.042	0.407	1.267	0.817	0.846	3.961	3.975	5.785	2.407	3.359	4.722	3.199	5.943
Fe(tot)	42.153	22.300	46.034	41.199	37.074	50.905	52.346	53.634	41.574	50.453	49.444	49.193	51.801
Mg	56.805	77.292	52.700	57.985	62.080	45.134	43.679	40.581	56.019	46.187	45.834	47.608	42.256

Appendix C2: Electron microprobe data for tourmaline cement

Label	222eblueTmnee 14	222eblueTmnee 15	SS_tm 16	SS_tm 17	SS_tm 18	SS_tm 19	SS_tm 20	SS_tm 21
SiO2	37.366	34.117	35.699	35.200	34.826	36.366	37.146	34.920
TiO2	0.565	1.144	0.413	0.327	0.907	0.395	0.182	0.467
Al2O3	30.510	21.029	30.869	26.707	32.921	32.064	34.687	30.496
Cr2O3	0.051	0.005	0.003	0.022	0.052	0.038	0.046	0.031
FeO	8.896	18.605	12.167	14.658	14.438	8.247	3.586	16.842
MnO	0.000	0.046	0.003	0.000	0.024	0.000	0.000	0.013
MgO	6.403	7.070	5.052	6.367	2.245	7.046	8.533	2.055
CaO	0.225	1.821	0.410	1.161	0.314	0.275	0.223	0.401
V2O3	0.000	0.000	0.000	0.000	0.000	0.000	0.052	0.000
Na2O	2.314	1.842	2.356	2.114	1.856	2.342	2.041	2.069
K2O	0.772	0.133	0.027	0.020	0.026	0.023	0.008	0.006
B2O3	12.660	14.089	12.846	13.233	12.276	13.172	13.320	12.635
ZnO	0.000	0.000	0.085	0.017	0.084	0.000	0.137	0.025
CuO	0.032	0.017						
NiO	0.014	0.000	0.000	0.054	0.005	0.000	0.000	0.003
F	0.193	0.084	0.071	0.113	0.021	0.033	0.032	0.035
Cl	0.000	0.000	0.000	0.006	0.005	0.000	0.008	0.002
Sum Ox%	100.000	100.000	100.000	100.000	100.000	100.000	100.000	100.000
Cations								
Si	5.610	5.122	5.293	5.219	5.164	5.392	5.508	5.178
Ti	0.064	0.129	0.046	0.036	0.101	0.044	0.020	0.052
Al	5.400	3.722	5.395	4.668	5.754	5.604	6.062	5.330
Cr	0.006	0.001	0.000	0.003	0.006	0.004	0.005	0.004
Fe	1.117	2.336	1.509	1.818	1.790	1.023	0.445	2.089
Mn	0.000	0.006	0.000	0.000	0.003	0.000	0.000	0.002
Mg	1.433	1.583	1.117	1.408	0.496	1.558	1.887	0.454
Ca	0.036	0.293	0.065	0.184	0.050	0.044	0.035	0.064
V	0.000	0.000	0.000	0.000	0.000	0.000	0.006	0.000
Na	0.674	0.536	0.677	0.608	0.534	0.673	0.587	0.595
K	0.148	0.026	0.005	0.004	0.005	0.004	0.001	0.001
B	3.280	3.651	3.287	3.386	3.141	3.370	3.408	3.233
Zn	0.000	0.000	0.009	0.002	0.009	0.000	0.015	0.003
Cu	0.004	0.002	0.000	0.000	0.000	0.000	0.000	0.000
Ni	0.002	0.000	0.000	0.006	0.001	0.000	0.000	0.000
Sum cations	17.773	17.406	17.405	17.342	17.054	17.717	17.980	17.004
for calc only	0.040	0.038	0.040	0.039	0.040	0.041	0.042	0.039
AlAl	35.838	-2.584	34.524	18.271	43.117	36.943	44.450	35.399
Al50Fe50	28.102	61.154	37.623	46.058	44.536	24.991	10.596	53.058
Al50 Mg50	36.060	41.430	27.853	35.671	12.347	38.066	44.954	11.543
Ca-Fe(tot)-Mg								
Ca	1.396	6.954	2.420	5.408	2.134	1.665	1.495	2.444
Fe(tot)	43.187	55.468	56.070	53.307	76.623	38.973	18.789	80.124
Mg	55.417	37.578	41.510	41.285	21.243	59.362	79.716	17.432

Appendix C2 (cont)

All elemental analyses were performed on carbon coated polished thin sections using a Cameca SX50 electron microprobe at the University of Tasmania's Central Science Laboratory using:

- Beam Current: 25nA
- Acceleration Voltage: 15kV

The number of cations in the chemical structure of tourmaline were calculated based on the model in Deer et al. (1992).

Appendix D: Radiogenic isotopes analytical methods

Appendix D1: $^{40}Ar/^{39}Ar$ Analytical Methods

Mineral separates and flux-monitors (standards) are wrapped in Al-foil and the resulting disks are stacked vertically into a 11.5 cm long and 2.0 cm diameter container, and then irradiated with fast neutrons in position 5C of the McMaster Nuclear Reactor (Hamilton, Ontario) for a duration of 10 hours appropriate for the expected age of the sample. Groups of flux monitors (typically 12 in total) are located at ca. 1 cm intervals along the irradiation container and J-values for individual samples are determined by second-order polynomial interpolation between replicate analyses of splits for each postion in the capsule. Typically, J-values are between ca. 0.003 and 0.03 and vary by <10% over the length of the capsule. No attempt is made to monitor horizontal flux gradients as these are considered to be minor in the core of the reactor.

For total fusion of monitors and step-heating using a laser, the samples are mounted in an aluminum sample-holder, beneath the sapphire view-port of a small, bakeable, stainless-steel chamber connected to an ultra-high vacuum purification system. An 8W Lexel 3500 continuous argon-ion laser is used. For total-fusion dating the beam is sharply focused; for step-heating the laser beam is defocused to cover the entire sample. Heating periods are ca. 3 minutes at increasing power settings (0.25 to 7 W). The evolved gas, after purification using an SAES C50 getter (ca. 5 minutes), is admitted to an on-line, MAP 216 mass spectrometer, with a Baur-Signer source and an electron multiplier (set to a gain of 100 over the Faraday). Blanks, measured routinely, are subtracted from the subsequent sample gas-fractions. The extraction blanks are typically <10 x 10-13, <0.5 x 10-13, <0.5 x 10-13, and <0.5 x 10-13 cm-3 STP for masses 40, 39, 37, and 36, respectively.

Measured argon-isotope peak heights are extrapolated to zero-time, normalized to the $^{40}Ar/^{36}Ar$ atmospheric ratio (295.5) using measured values of atmospheric argon, and corrected for neutron-induced ^{40}Ar from potassium, ^{39}Ar and ^{36}Ar from calcium (using production ratios of Onstott and Peacock, 1987), and ^{36}Ar from chlorine (Roddick, 1983). Dates and errors are calculated using formulae given by Dalrymple et al. (1981), and the constants recommended by Steiger and Jager (1977). Isotope correlation analysis used the formulae and error propagation of Hall (1981) and the regression of York (1969). Errors shown in the tables and on the age spectra and isotope correlation diagrams represent the analytical precision at 2å, assuming that the errors in the ages of the flux monitors are zero. This is suitable for comparing within-spectrum variation and determining which steps form a plateau (McDougall and Harrison, 1988, p, 89). A conservative estimate of this error in the J-value is 0.5% and can be added for inter-sample comparison. The dates and J-values for the intralaboratory standard (e.g., MAC-83 biotite at 24.36 Ma) are referenced to TCR sanidine at 28.0 Ma (Baksi et al., 1996) for young samples and to Hb3Gr hornblende at 1071 Ma for old samples.

Appendix D2: Analytical procedure for Sr and Nd isotopes

"The long-term reproducibility of the complete analytical procedure is measured by the analysis of an in-house standard; the standard deviation is 43 ppm for $^{87}Sr/^{86}Sr$ and 58 ppm for $^{143}Nd/^{144}Nd$. Machine performance is monitored by the analyses of international standards".

"In preparation for analysis, Sr was loaded onto a single Ta filaments, and Nd onto a double Ta-Re filaments. All samples were run as metals. Analysis of was performed on a Finnigan MAT 261 single collector mass spectrometer at the University of Adelaide. All Sr and Nd ratios are normalised to $^{86}Sr/^{88}Sr=0.1194$ and $^{146}Nd/^{144}Nd=0.7129$. During the course of the study the La Jolla Nd-standard was 0.511836 ± 15 (2ó error on all the means of >500 eleven scan data blocks), and the SRM-987 Sr-standard was 0.710155 ± 20 (2ó). The total procedural Sr and Nd blanks were 1.1 and 0.2 ng/g, respectively, which in general is negligible by comparison with the typical >500 ng of Sr and Nd dissolved and analysed".

Appendix D3: Analytical procedure for Pb isotopes

"For Pb isotopic analyses approximately 100 mg of ground sample was leached for 10 minutes in hot 6 M HCl to remove possible contamination. The samples were dissolved in a mixture of HF and HNO_3 and fluorides were converted to chlorides by dry-down with HCl. The sample was redissolved in 0.6 M HBr and Pb was separated from all other elements with Dowex 1-X8 anion exchange resin. Part of the sample was loaded with high purity Si gel mixed with HNO_3; the amount of sample loaded was dependant on the Pb content of the sample. The aim was to obtain a =1 V beam on ^{208}Pb when the sample was run at 1150°C on a Finnigan MAT 261 TIMS housed at the Department of Geology and Geophysics at the University of Adelaide. Pb isotopic compositions were measured in dynamic mode, with a total of 8 s counting time on each peak. A fractionation correction of 0.12% per amu was applied. Estimated errors are 0.007 for $^{206}Pb/^{204}Pb$, 0.009 for $^{207}Pb/^{204}Pb$ and 0.030 for $^{208}Pb/^{204}Pb$ based on repeated measurements of the NBS981 standard. Blanks are approximately 300 pg".

Procedures outlined here are from Foden et al. (1995) and Elburg and Foden (1998).

Appendix E1: Río Blanco microthermometric data

Río Blanco sector																
sample	DDH	section	location	lithology	Cu grade	stage	% of type i:ii:iii	sample	Type	froze at	Te	Tm	Th (liq)	Th (vap)	Th (salt)	salinity	Td
Pre breccia, potassic stockwork veins																	
259	DDH-734	XC-275	611 m	BXMGDCC	0.65	2 x qtz V. (biot.)	q.v.(1)	259ia	ia			-3.7		256.8		5.994	
							49:37:14	259ib	ia			-4.4		213.4		7.011	
								259ic	ia			-2.3		336.5		3.852	
								259id	ia			-4.4		338		7.011	
								259iia	iic					287	500	56.3	
								259iib	iia					242.8	252	34.8	
								259iic	iia-b					220.5	323.5	39.6	
								259iid	iia-b					292.6	216.4	32.7	
							q.v.(2)	259ia	ia			-4.4		397.4		7.011	
							39:46:15	259ib	ia			-1.7		367.9		2.888	
								259ic	ia			-3.7		387.2		5.994	
								259id	ib			-9.2		393.3		13.104	
								259iia	iia					319.5	271.6	36	
								259iib	iia					250.6	302.7	38.1	
								259iic	iia					265.8	258.1	35.1	
								259iid	iia					217.4	313.1	38.1	
								259iie	iia-b					372.5	500	56.3	
								259iif	iia					267.1	302.1	38.1	
								259iig	iia					156.3	209.6	32.4	
268a	DDH-734	XC-275	342 m	DIOR (GDCC)	0.6	qtz V (biot)	51:26:23	268aia	ib	-53.9		-3.6		216.4		5.846	
								268aib	ia	-52.6		-3.7		378.4		5.994	
								268aic	ia	-41.6		-3.5		365.6		5.697	
								268aid	ia			-0.6		367		1.047	
								268aie	ia	-53.7		-4.7		404.8		9.308	
								268aif	ib	-69.1		-18.6		318.8		21.941	
								268aig	ia	-48.1		-3		378.1		4.942	
								268aiia	iia					265	214.3	32.6	
								268aiib	iic					275.9	366.3	43.1	
								268aiic	iia					305.3	392.9	45.4	
								268aiid	iic					270.9	304.1	38.2	
								268aiiia	iii	-37.9		-5.3	303.5			8.267	
Río Blanco Magmatic Breccia quartz cement																	
252d	DDH-448	XC-135	14 m	GDRB	1.9	qtz, anhy cement	type i to type iii	252dia	ia	-51.3		-1.5		191.1		2.561	
							20:01	252dib	ia	-47.3		-1		320.7		1.728	
								252dic	ia	-47.4		-0.8		354		1.389	
								252did	ia	-65	-26.7	-12.2		383.6		16.239	
								252diiia	iii	-51.9	-23.1	-5.3	445.9			8.267	
								252diiib	iii	-64.2		-12.2	566.2			16.239	
								252diiic	iii	-68.8		-14.5	492.1			18.357	
246k	DDH-450	XC-125	347 m	BXMGD	0.39	qtz cement	40:28:32	246kia	ia	-59.9	-46	-9.4		194.9		13.327	
								246kib	ia	-43.8	-27.8	-1		327.1		1.728	
								246kic	ib	-77.5	-33.7	-22.1		405		24.104	
								246kid	ib	-88.5	-28.4	-24.9		401.3		25.932	
								246kie	ib	-76.1	-28.9	20.7		419.7		23.15	
								246kif	ib	-40.4		-5.2		324.9		8.13	
								246kiia	iic					281.9	504	56.8	
								246kiib	iic					279.3	458.2	51.8	
								246kiic	iic					523.4	514.8	58	
								246kiid	iic					318.5	356.1	42.2	
								246kiie	iic					303.1	478.8	54	
								246kiif	iic					423.5	300.5	38	
								246kiig	iic					260.7	333.5	40.4	
								246kiih	iic					331.3	299.2	37.9	

Appendix E1: Río Blanco microthermometric data

sample	DDH	section	location	lithology	Cu grade	stage	% of type i:ii:iii	sample	Type	froze at	Te	Tm	Th (liq)	Th (vap)	Th (salt)	salinity	Td
								246kiiia	iii		-69.8	-7.1	356.5			10.616	
								246kiiib	iii		-48.3	-22.7				24.503	581.6
								246kiiic	iii			-0.1	401.7			0.177	
245p	DDH-450	XC-125	290 m	BXMGD	0.74	qtz cement	50:30:20	245pia	ia	-53.9	-32.6	-18.4		337.4		21.499	
								245pib	ia	-52.4	-23.6	-17.1		411.9		20.505	
								245pic	ia	-50.3	-33	-15		317.7		18.789	
								245pid	ib	-46.7	-19.2	-1.7		472.6		2.888	
								245pie	ia	-46	-32.2	-13		321		17	
								245piia	iia					417.9	268.8	35.8	
								245piib	iic					280.8	284.4	36.8	
						anhy cement		245piic	iic					226.7	354.6	42.1	
						anhy cement		245piid	iic					356.1	402.4	46.3	
								245piie	iic					453.9	308.7	38.5	
								245piif	iic					292.4	301	38	
								245piig	iia					278.3	337.5	40.7	
								245piiia	iii	-39.3		-9.9		425.7		13.877	
								245piiib	iii	-43.3	-23.1	-10.3	472.8			14.307	
								245piiic	iii	-42.2	-21.9	-6.4	459.3			9.728	
240e	DDH-450	XC-125	115 m	BXMGD + D.V.	1.46	qtz cement	45:08:47	240eia	ia	-55.5	-43.5	-9.5		280.7		13.438	
								240eib	ia	-56.1	-37.2	-13.1		427.4		17.094	
								240eic	ia	-45		2.3		395.3		3.852	
								240eid	ia	-46.4		0.7		399.6		1.218	
								240eie	ib		-32.2	-21		449.2		23.358	
								240eif	ia			0.6		405.3		1.047	
								240eiia	iia					421.2	427.3	48.6	
								240eiib	iia					313			395.1
								240eiiia	iii			-1.3	428.2			2.23	
								240eiiib	iii	-50.5		-1.3	423.2			2.23	
133b	DDH-217	XC-135	37 m	An	2.5	qtz cement	28:32:40	133bia	ib	-66.4		-21.5		600		23.3	
								133bib	ia	-51.9	-24	-10.1		308.8		14.043	
								133bic	ib	-37.1		-5.2		340.3		8.13	
								133bid	ib	-70.7		-19.2		478.7		22.087	
								133bie	ia	-65.5	-37.7	-17.3		533.8		20.661	
								133biia	iic					362.5	325.9	39.8	
								133biib	iic					240.4	425.1	48.4	
								133biic	iia					349.5	270.5	35.9	
								133biid	iic					555.6	255	34.9	
								133biie	iia					600	276.8	36.3	
								133biif	iic					432.6	282	36.7	
								133biig	iic					426.9	378.9	44.2	
								133biiia	iii	-44.7		-5.4	456.1			8.403	
								133biiib	iii	-65.9	-46.5	-13.9	600			17.826	
								133biiic	iii	-47.6		-0.3	600			0.527	
								133biiid	iii	-53.4		-9.1	473.6			12.991	
								133biiie	iii	-54.7		-20.7	478.6			23.15	
								133biiif	iii	-42.5	-33.2	-5.8	436.9			8.941	
354	DDH-101	XC-125	245 m	An	1.64	qtz cement	10:45:45	354ia	ia	-53.8	-43.4	-13.5		352.7		17.463	
								354ib	ia	-49.7		-4		369.6		6.434	
								354iia	iia					272.5	435.6	49.5	
								354iib	iia					489.2	337.4	40.7	
								354iic	iic					364.3	570.4	64.8	
								354iid	iia					275.7	213.2	32.6	
								354iie	iia					237.7	437.2	49.6	
								354iif	iia					288	267	35.7	
								354iig	iic					311.1	600	68.7	

Appendix E1: Río Blanco microthermometric data

sample	DDH	section	location	lithology	Cu grade	stage	% of type i:ii:iii	sample	Type	froze at	Te	Tm	Th (liq)	Th (vap)	Th (salt)	salinity	Td
								354iih	iic					256.6	546	61.7	
								354iii	iic					424.9	548.5	62.1	
								354iij	iic					600	534.7	60.4	
								354iik	iic					551.5	568.1	64.5	
								354iil	iic					240.6	535.5	60.5	
								354iim	iic					530.4	266.4	35.7	
								354iiia	iii	-59.5		-8.9	505.8			12.764	
								354iiib	iii	-43.1		-12.4	365.4			16.432	
								354iiiac	iii	-94.8		-54.8	600				
								354iiid	iii			-7.1	466.7			10.616	
373	DDH-454	XC-135	111 m	GDRB	0.73	anhy cement	53:35:12	373ia	ia	-48.7	-25.2	-1.7		237.7		2.888	
								373ib	ia	-49.3	-29	-4.9		371.6		7.715	
								373ic	ia	-49.4		-2.8		306.4		4.634	
								373ic2	ib			1.7		376.2		2.888	
								373iiia	iii	-60.9	-38	-10				13.985	516.2
373	DDH-454	XC-135	111 m	GDRB	0.73	qtz cement	53:35:12	373id	ia	-60.1	-40	-11.9		315.9		15.945	
								373ie	ia	-57.6	-34	-4.6		402.1		7.295	
								373if	ia	-55.6		-9.6		438.6		13.549	
								373iia	iia					333.8	269.6	35.9	
								373iib	iic					294.4	254.7	34.9	
								373iiia	iii	-49.1		-7.9		446		11.595	
								373iiib	iii	-38.5		1.2	327.8			2.063	
								373iiic	iii	-43.7		0.8	383.9			1.389	
240b	DDH-450	XC-125	95-115 m	BXMGD	2.92	anhy cement	68:12:20	240bia	ib	-56.9	-38.4	-21.6				23.3	478.7
								240bib	ia	-48.1	-36.2	-18.2		426.1		21.349	
								240bic	ib	-46.3		-5.7		492.6		8.807	
								240bid	ia			0		384.2		0	
								240bie	ia	-32.2		0.4		311.2		0.701	
								240bif	ia	-50.7		-7.9		436.2		11.595	
								240biia	iic					327	175.5	30.7	
								240biib	iic					316	297.5	37.7	
								240biic	iic					342.9	198.4	31.8	
								240biid	iic					308.7	211.1	32.5	
								240biiia	iii	-47.5		-4.2	467.5			6.724	
								240biiib	iii			-3.1	365.7			5.094	
								240biiic	iii	-64.6		-4.8	456.6			7.576	
155	DDH-344	XC-125	85 m	GDRB	1.18	qtz cement	57:27:16	155ia	ia	-39.9		-1		310.7		1.728	
								155ib	ia	-47.1		-4.7		429.9		7.436	
								155ic	ib	-42.6		0		391.5		0	
								155id	ia	-59.6	-19.8	-11.1		465.4		15.142	
								155ie	ia			-1.6		415.9		2.725	
								155if	ia	-53.7		-4.9		413.5		7.715	
								155ig	ia	-27.7		-0.3		425.2		0.527	
								155iia	iic					255.4	328.6	40	
								155iib	iic					301.2	326.2	39.8	
								155iic	iic					359.3	372.3	43.6	
								155iid	iic					323.4	315.9	39.1	
								155iiia	iii	-44.3		-0.9	362.6			1.559	
								155iiib	iii	-50.2		4	391.3			6.434	
								155iiic	iii	-38.5		10.9	477.1			14.936	
								155iiid	iii			1.5	397.2			2.561	
								155iiie	iii	-42.4		-1.4		410.2		2.396	
160a	DDH-344	XC-125	178 m	BXMGD(An)	1.28	qtz cement	64:33:03	160aia	ib	-52.1		-2.3		411.8		3.852	
								160aib	ia	-87.5		7.5		390.7		11.11	
								160aic	ia	-58.2		-5.5		393.2		8.538	

Appendix E1: Río Blanco microthermometric data

sample	DDH	section	location	lithology	Cu grade	stage	% of type i:ii:iii	sample	Type	froze at	Te	Tm	Th (liq)	Th (vap)	Th (salt)	salinity
								160aid	ib	-51		-1				1.728
								160aiia	iic					325.9	248.2	34.5
								160aiib	iic					404.2	284.9	36.9
								160aiic	iia					349.3	229.8	33.5
								160aiid	iia					344.8	284.8	36.9
								160aiiia	iii	-38.5		2.6	410.7			4.324
								160aiiib	iii	-53.4	-22.3	-2.5	431.5			4.167
								160aiiic	iii	-49.2		-0.5	400.9			0.874
								160aiiid	iii	-46.9		1.4	391.9			2.396
								160aiiie	iii	-51		0	402.2			0
284	DDH-734	XC-275	439 m	GDCC	0.95	qtz, anhy cement	80:14:06	284ia	ia	-35.4		2.8		292.3		4.634
								284ib	ia	-52.9		-3		296.1		4.942
								284ic	ia	-60.6		-6.8		391.6		10.329
								284id	ib	-41.9		1.3		388.6		2.23
								284ie	ia	-69.4	-29.3	-5.5		374.8		8.538
								284if	ia	-47.4	-19.1	-3.1				5.094
								284iia	iic					297.4	322.3	39.5
								284iib	iib					352.5	222	33
								284iic	iia					340.1	394.4	45.5
								284iid	iic					389.8	211.3	32.5
								284iiia	iii	-35.6		0.9		399		1.559
								284iiib	iii	-45.1		2.2	393.8			3.694
Feldspar Porphyry																
296	DDH-734	XC-275	485.3 m	PF	0.7	qtz eyes	74:21:05	296ia	ia	-36.4		-1.5		216		2.561
								296ib	ia	-39.8		-1.8		190.7		3.051
								296ic	ia	-48.3		-3.5		360		5.697
								296id	ia	-47.3	-23.8	-2.7		374.5		4.479
								296ie	ia	-49.1	-21.4	-3.6		389		5.846
								296if	ia	-56.9	-37.7	-7.8		362.3		11.475
								296ig	ib		-34.6	-7.2		373.2		10.741
								296iia	iic					256	387.9	45
								296iib	iic					363.5	378.8	44.2
								296iic	iic					283.6	384.2	44.6
								296iid	iic					289.9	438.1	49.7
								296iie	iic					335.6	406.7	46.7
								296iif	iic					326	348.2	41.6
								296iig	iic					335.7	442.8	50.2
Quartz Monzonite Porphyry																
247c	DDH-352	XC-125	0-16 m	PQM	0.68	qtz eyes	42:18:40	247cia	ia	-55	-22.5	-6.7		465		10.112
								247cib	ia			1.5				2.561
								247cie	ib	-72.2	-32.1	17.8		422.4		21.046
								247cif	ia	-52.9	-29.8	-10.1		497.5		14.093
								247ciia	iic					307.6	331.6	40.3
								247ciib	iib					309	247.8	34.5
								247ciic	iic					329.1	352.2	41.9
								247ciid	iic					429.5	265.9	35.6
								247ciiia	iii	-54.4	-33.3	-6.1	459.3			9.337
239j	DDH-450	XC-125	80 m	PQM	1.5	qtz eyes		239jiia	iic					341.9	261	35.3
molybdenite rimmed quartz stockwork veins (quartz-sericite alteration halo)																
245f	DDH-450	XC-125	277 m	BXMGD	0.46	Moly rimmed Qtz	85:00:15	245fia	ia	-36		-3.8		311.8		6.141

Appendix E1: Río Blanco microthermometric data

sample	DDH	section	location	lithology	Cu grade	stage	% of type i:ii:iii	sample	Type	froze at	Te	Tm	Th (liq)	Th (vap)	Th (salt)	salinity	Td
								245fig	ia	-36	-14.2	-2.8		296		4.634	
								245fih	ia			-1.6		337		2.725	
								245fii	ia	-49	-21.1	-7.3		320.6		10.865	
								245fij	ia	-44	-27.3	-4.2		298.9		6.724	
								245fik	ia	-41		0		292.6		0	
								245fiiia	iii		-20.6	-2.2	402.3			3.694	
								245fiiib	iii	-40	-27.7	-2.9	388.9			4.788	
								245fiiic	iii		-24.1	-4.1				6.579	425
268b	DDH-734	XC-275	342 m	DIOR (GDCC)	0.6	biot haloed stockwork vein reactivated by a moly rimmed qtz V.	88:06:06	268bia	ia	-51.3	-25.2	-5.8		407.9		8.941	
								268bib	ia	-53.6	-19.2	-0.9		400		1.559	
								268bic	ia	-59	-51.5	-11.6		401.7		15.648	
								268bid	ia			-2.3		428.8		3.852	
								268bie	ia	-42.6		-0.5		307.7		0.874	
								268bif	ib	-57.1	-39.7	-19		330.1		21.941	
								268big	ia	-59.5	-24	-7.4		403.6		10.988	
								268biia	iic					328.2	207.6	32.3	
								268biib	iia					341.2	320	39.4	
								268biic	iic					368.6	277.5	36.4	
								268biid	iia					339.5	210.4	32.4	
								268biie	iic					360.4	284.1	36.8	
								268biif	iic					268	343.3	41.2	
								268biiia	iii			0	402.8			0	
								268biiib	iii	-58.3	-21.8	-11.1	472.6			15.142	
								268biiic	iii	-46.8		-3.4	444.7			5.547	
								268biiid	iii	-54.6		-4.9	424.8			7.715	
								268biiie	iii			1.3	433.9			2.23	
quartz/sulfide stockwork veins (quartz-sericite alteration halo)																	
352	DDH-101	XC-125	243.5 m	GDRB	1.54	qtz/cpy v	45:10:45	352ia	ia			2.2		355.1		3.694	
								352ib	ia	-58.2		-12.4		349.3		16.432	
								352iia	iic					311	363.9	42.9	
								352iib	iia					319.5	244.3	34.3	
								352iic	iia					298.6	383.4	44.6	
								352iiia	iii	-49		1.2	421.1			2.063	
								352iiib	iii	-58.3		-3.5	443.1			5.697	
237c	DDH-450	XC-125	6 m	PQM	0.56	qtz/cpy v	23:04:73	237cia	ia	-36		-1.6		332		2.725	
								237cib	ia	-46		-9.1		275.2		12.991	
								237cic	ia	-30.8		1.6		266		2.725	
								237cid	ib	-70.9		-23.1		361.2		24.766	
								237cie	ia	-48.2		0		288.4		0	
								237ciia	iic					290.5	230.8	33.5	
								237ciib	iia					311.6	237.3	33.9	
								237ciic	iic					246.2	302.7	38.1	
								237ciiia	iii	-68.7		-3.2		404.4		5.246	
								237ciiib	iii	-48.7		-2.7	428.2			4.479	
								237ciiic	iii	-49.3		-6		468.9		9.206	
								237ciiid	iii	-40.8		-2	422.4			3.374	
377	DDH-454	XC-135	116 m	GDRB	0.86	qtz/cpy/mt v	46:31:23	377ia	ia	-43.5	-25	-8.5		391.7		12.303	
								377ib	ia	-34.9		-0.5		384.5		0.874	
								377ic	ia	-44.3		-1.2		379.4		2.063	
								377id	ia	-40.3	-32.5	-6.5		435.2		9.856	
								377ie	ia	-39.1	-27.4	-5.6		348.9		8.673	
								377iia	iic					342.1	154.9	29.9	
								377iib	iic					267.5	317.3	39.2	
								377iic	iic					279.6	273.5	36.1	
								377iid	iic					334.4	167.8	30.4	

Appendix E1: Río Blanco microthermometric data

sample	DDH	section	location	lithology	Cu grade	stage	% of type i:ii:iii	sample	Type	froze at	Te	Tm	Th (liq)	Th (vap)	Th (salt)	salinity	Td
								377iie	iic					275.2	238.1	33.9	
								377iif	iic					255	293.9	37.5	
								377iiia	iii	-43.5		-1		395		1.728	
								377iiib	iii	-46.8		-2	407.3			3.374	
								377iiic	iii	-46.1		-5.3	417.5			8.267	
								377iiid	iii	-26.8		0.4	418.2			0.701	
247c	DDH-352	XC-125	0-16 m	PQM	0.68	qtz/cpy v	11:58:31	247cic	ib	-83.8		0.5		266.6		0.874	
								247cid	ia	-43.8		1.8		275.4		3.051	
								247ciie	iic					258.9	279.6	36.5	
								247ciif	iia					336.9	305.3	38.3	
								247ciig	iic					317.3	375.1	43.8	
239j	DDH-450	XC-125	80 m	PQM	1.5	qtz/cpy v	70:15:15	239jia	ia	-67.3	-34.7	-17.7		302.6		20.97	
								239jib	ib	-65.7	-49.6	-23.3		316.8		23.3	
								239jiib	iia					294.4	287.1	37	
								239jiic	iic					458.6	172.9	30.6	
								239jiiia	iii	-34.2		6.6	373.2			9.985	
								239jiiib	iii	-51.9		-5.3	500			8.267	
late stage "D" - pyrite rich veins (quartz-sericite alteration halo)																	
274	DDH-734	XC-275	359.9 m	GDCC	1	"D" v	95:01:04	274ia	ia	-50.9		-7.4		313.5		10.988	
								274ib	ia	-36.3		-2.5		237		4.167	
								274ic	ia	-48.2		-2.5		250.1		4.167	
								274id	ia	-48		-2.8		185		4.634	
								274ie	ia	-48.9		-3.4		194.7		5.547	
								274if	ia	-51.5		-5.5		347.5		8.538	
								274ig	ia	-46.3		-2.8		301.6		4.634	
								274ih	ia	-47.7	-38.5	-3		326.8		4.942	
								274ii	ia	-41.6		-2.9		303.3		4.788	
								274ij	ia	-39.6		-3.1		285.4		5.094	
								274ik	ia	-50		-2.6		267.7		4.324	
								274il	ia	-47.2	-11.4	-2.2		324.6		3.694	
								274iia	iic					160	210.5	32.4	
								274iiia	iii	-34.5		-0.8		418		1.389	

Appendix E2: Sur-Sur microthermometric data

Sur-Sur sector

sample	DDH	section	location	lithology	Cu grade	stage	% of type i:ii:iii	sample	Type	froze at	Te	Tm	Th (liq)	Th (vap)	Th (salt)	salinity	Td
Pre breccia, potassic stockwork veins																	
189a	DL-03	XC-50	132 m	BXTGDCC	2.52	qtz v. (biot)	33:23:44	189aia	ib	-33.7		-0.9		350.5		1.559	
								189aib	ia	-33.9		-0.3		299.2		0.527	
								189aic	ia	-74.9		-28.6		258		28.288	
								189aid	ia	-59.8	-45	-0.4		271.8		0.701	
								189aie	ia	-63.1	-29.3	-15.9		367.5		19.543	
								189aif	ia			-48.7		280		46.616	
								189aig	ia		-32.9	1.8		269.6		3.051	
								189aih	ia	-44.6	-24.7	-9.6		309.9		13.549	
								189aiia	iia					240.3	397.8	45.9	
								189aiib	iia-b					209.1	362.1	42.7	
								189aiic	iia					232.3	299.9	37.9	
								189aiid	iia					163.3	437.3	49.6	
								189aiie	iia					215.2	226.8	33.3	
								189aiif	iia					246.9	183.3	31.1	
								189aiig	iia					220.5	299.1	37.9	
								189aiih	iia					153.2	429.8	48.9	
								189aiiia	iii	-61.5		-20.3				22.872	478.2
								189aiiib	iii				440.4				
								189aiiic	iii				446.9				
								189aiiid	iii	-58.5		-11.8	522.8			15.847	
								189aiiie	iii			-4.7	431.4			7.436	
								189aiiif	iii	-36.9		-10.5	438.6			14.519	
								189aiiig	iii			-4.2	440.3			6.724	
218c	TSS-22	XC-50	802 m	BXMGDCC	0.3	qtz v. (biot)	74:16:10	218cia	ia					220.7			
								218cib	ia					374.7			
								218cic	ia					190.6			
								218ciia	iic					247	311.1	38.7	
						GDCC - qtz		218cigda	ia			-7.9		368.8		11.595	
								218cigdb	ia					281.4			
								218cigdc	ia			-13.3		376.2		17.28	
								218ciigda	iic					197.4	230.3	33.5	
								218ciigdb	iic			-20.6		306.5		23.081	
								218ciigdc	iic			-23.4		215.8		24.963	
								218ciigdd	iic					310.7	183.9	31.1	
								218ciigde	iic					248.4	377.4	44	
Tourmaline Breccia quartz cement																	
221b	TSS-22	XC-50	28 m	BXTGDCC	2.15	qtz cement	Primary-30:35:35	221bia	ia			11.9		330.9		15.945	
							second-70:8:22	221bib	ia			-16.2		244.6		19.788	
								221bic	ia			-11		329.2		15.039	
								221bid	ia			-20.5		390.4		23.011	
								221biia	iic					278.6	416.3	47.6	
								221biib	iic					288.3	267.2	35.7	
								221biic	iic			15		295.5	255	34.9	
								221biid	iic					233.5	412.2	47.2	
								221biie	iic					251.8	357.8	42.4	
								221biif	iic			-25.4		309.3	137.1	29.2	
123a	E20-A	0	170 m	BXTGDCC	0.2	qtz cement	32:36:32	123aia	ia			-4		302.9		6.434	
								123aib	ia			-9.1		433.5		12.991	
								123aic	ia			-2.8		312.3		4.634	
								123aid	ia			-9.9		376.3		13.877	
								123aie	ia			-25		341		25.996	
								123aif	ia			-9.3		318.9		13.216	
								123aig	ia			-6		375.8		9.206	

Appendix E2: Sur-Sur microthermometric data

sample	DDH	section	location	lithology	Cu grade	stage	% of type i:ii:iii	sample	Type	froze at	Te	Tm	Th (liq)	Th (vap)	Th (salt)	salinity	Td
								123aiia	iia					242.2	411.2	47.1	
								123aiib	iia					255.4	330	40.1	
								123aiic	iia-b					278.7	92-450	50.9	
								123aiid	iia					372.5	290.3	37.2	
								123aiie	iia-b					431.3	332.5	40.3	
								123aiif	iib					306.3	193.8	31.6	
								123aiig	iia					479	477.3	53.8	
								123aiih	iia-b					269	332.4	40.3	
								123aiii	iia-b					495.1	193.5	31.6	
								123aiij	iia-b					295.9	310.4	38.7	
62b	TSS-22	XC-50	736 m	BXTGDCC	1.54	qtz cement	22:30:48	62bia	ia			-3.2		242.1		5.246	
								62bib	ia			-5.5		362.4		8.538	
								62bic	ia			-0.2		374.5		0.352	
								62bid	ia			0		385.1		0	
								62bie	ia			-18.9		415.2		21.868	
								62bif	ia			-3.5		305.8		5.697	
								62big	ia					372			
								62bih	ia	-59	-26	-18.8		427.2		21.795	
								62biia	iia-b					313.2	214.6	32.6	
								62biib	iia-b					250.6	334.7	40.5	
								62biic	iia-b					310.1	297.8	37.8	
								62biid	iia-b					305.5	345.3	41.3	
								62biie	iia-b					279.9	372.4	43.6	
								62biif	iia-b					293.2	333.7	40.4	
								62biig	iia-b					265.1	365.4	43	
								62biih	iia-b					302.3	285.3	36.9	
								62biii	iia-b					337.9	394.9	45.6	
								62biij	iia-b					402.1	377.7	44.1	
								62biik	iia					347.9	320.4	39.4	
								62biil	iia					270.7	350.4	41.8	
								62biim	iia					365.6	286.3	37	
								62biin	iia					330.1	371.8	43.5	
								62biio	iia					289.6	340.1	40.9	
								62biip	iia					348.8	315.4	39	
								62biiq	iia					321.1	345.3	41.3	
								62biir	iia					252.2	306.5	38.4	
								62biis	iia						494.5	55.7	
								62biit	iia						505.7	57	
								62biiu	iia						449.9	50.9	
								62biiv	ii					452.6	469.9	53	
								62biiia	iii			-1.7		390.5		2.888	
224b	TSS-22	XC-50	500-510 m	BXTGDCC	0.73	qtz cement	9:24:67'	224bia	ia	-53.3	-46.2	-5.1		359.1		7.992	
								224bib	ia	-33	-22.2	-0.7		377.1		1.218	
								224bic	ia	-64.9		-15		374.4		18.789	
								224bid	ia	-47.9		-3.8		365.9		6.141	
								224bie	ia			-3.8		299.8		6.141	
								224bif	ia	-39.5	-36	-9.4		306.9		13.327	
								224big	ia	-50.2	-10.9	-4.3		371.2		6.867	
								224bih	ia	-72.3	-38.4	-23.5		333.6		25.028	
								224bil	ia			-14.9		428.6		18.703	
								224biia	iia					297.2	249.6	34.6	
								224biib	iia-b					288	324.8	39.7	
								224biic	iia					357.8	316.7	39.1	
								224biid	iia					323.2	328.1	40	
								224biie	iia					264.8	391	45.2	

Appendix E2: Sur-Sur microthermometric data

sample	DDH	section	location	lithology	Cu grade	stage	% of type i:ii:iii	sample	Type	froze at	Te	Tm	Th (liq)	Th (vap)	Th (salt)	salinity	Td
								224biif	iia					260.8	357.4	42.3	
								224biig	iia					498	430.7	49	
								224biih	iia					437	412.1	47.2	
								224biil	iia					406.6	453.4	51.3	
								224biij	iia					336.9	281.6	36.7	
								224biik	iia					242.8	420.4	48	
								224biil	iia					256.8	441.8	50.1	
								224biim	iia					324.8	328.1	40	
								224biin	iia					297.6	366.5	43.1	
								224biiia	iii	-43.4		-0.8	397.5			1.389	
								224biiib	iii	-36		-4.9		427.3		7.715	
								224biiic	iii	-47.1	-23.6	-10.3	505.6			14.307	505.6
223b	TSS-22	XC-50	300-310 m	BXTGDCC	0.96	qtz cement	14:29:57	223bia	ia			-0.5		357.3		0.874	
								223bib	ia			-2.9		350.3		4.788	
								223bic	ia			-16.3		376.7		19.869	
								223bid	ia					411.8			
								223bie	ia			-6		314.8		9.206	
								223bif	ia			-18.8		305.2		21.795	
								223big	ia			-5.3		369		8.267	
								223biia	iia					269.3	406	46.6	
								223biib	iia-b			-36.3		328.2	262-291	37.3	
								223biic	iia					291.7	303.1	38.1	
								223biid	iia					271.7	448.2	50.7	
								223biie	iia-b					313.9	179.1	30.9	
								223biif	iia					240.6	362.1	42.7	
								223biig	iia-b					305.5	210.7	32.4	
								223biih	iia-b					252.1	412.2	47.2	
								223biii	iia					294.7	267.3	35.7	
								223biij	iia					256.9	346.6	41.4	
								223biik	iia					258.4	345.2	41.3	
								223biil	iia					259.8	343.6	41.2	
								223biim	iia					256.9	416.9	47.6	
								223biin	iia					321.9	242.9	34.2	
								223biio	iia					232.6	396.4	45.7	
222f	TSS-22	XC-50	130-140 m	BXTGDCC	2.07	qtz cement	6:38:56	222fia	ia			-20.6		417.8		23.081	
								222fib	ia			-9.6		444.6		13.549	
								222fic	ia					331.1			
								222fid	ia			-12.3		411.7		16.336	
								222fie	ia			-10.3		382.9		14.307	
								222fif	ia					351.5			
								222fig	ia			-6.2		373.4		9.468	
								222fih	ia			-4		336.4		6.434	
								222fii	ia			-9.9		403.4		13.877	
								222fij	ia			-3.9		375.2		6.288	
								222fik	ia			-19.2		351		22.087	
								222fiia	iia-b					305.1	215.6	32.7	
								222fiib	iia					231.1	383.5	44.6	
								222fiic	iia-b					431.6	320.1	39.4	
								222fiid	iia					301.5	223.1	33.1	
								222fiie	iia-b					255.5	329.1	40.1	
								222fiif	iia					270.5	301.3	38	
								222fiig	iia					244.1	361.5	42.7	
								222fiih	iia					274.2	317.8	39.2	
								222fiii	iia					257.7	329.8	40.1	
								222fiij	iia-b					337.9	130.8	29	

Appendix E2: Sur-Sur microthermometric data

sample	DDH	section	location	lithology	Cu grade	stage	% of type i:ii:iii	sample	Type	froze at	Te	Tm	Th (liq)	Th (vap)	Th (salt)	salinity	Td
								222fiik	iia-b					286.8	255	34.9	
								222fiil	iia					256.4	288.2	37.1	
								222fiim	iia-b					317.3	169.4	30.5	
								222fiin	iia-b			-47.9		357.9	180-197	31.8	
								222fiio	iia					304.1	136.7	29.2	
228f	TSS-4	XC-50	50-60 m	BXTGDCC	0.96	qtz cement	10:42:48	228fia	ia			-6.1		324.7		9.337	
								228fib	ia	-53.8	-49.2	-18.6		341.2		21.647	
								228fic	ia	-38.5		-4		412.2		6.434	
								228fid	ia	-75.1				309.5			
								228fie	ia	-63.7	-29.9	-23.6		372.9		25.093	
								228fif	ia	-82.8	-37.9	-8.7		370.5		12.535	
								228fig	ia	-58.1	-26.6	-9.8		446		13.768	
								228fih	ia	-65.6	-32.5	-15.4		371		19.127	
								228fii	ia	-45.4		-2.7		357.6		4.479	
								228fij	ia	-58.8	-32.7	-14.7		341		18.531	
								228fik	ia	-70.7	-26	-17.2		424.7		20.583	
								228fiia	iia					310.7	250.8	34.7	
								228fiib	iia					290.3	226.6	33.3	
								228fiic	iia					281.3	302.3	38.1	
								228fiid	iia					321.7	173.1	30.6	
								228fiie	iia					277.1	357.4	42.3	
								228fiif	iia					273.4	159.4	30.1	
								228fiig	iia					242.2	374.7	43.8	
								228fiih	iia					134.8	265.6	35.6	
								228fiii	iia					235.1	311	38.7	
								228fiij	iia					233.2	429.9	48.9	
								228fiik	iia					252.1	547	61.9	
								228fiiia	iii	-70.4		-17.6	452.4		144.9	20.893	
101a	C-50	XC-50	26 m	BXTGDCC	1.36	qtz cement	17:36:47	101aia	ia	-42	-29.8	-8.9		389		12.764	
								101aib	ia		-44.5	-23		299.4		24.701	
								101aic	ib		-49.9	-12.8		316.7		16.813	
								101aid	ia		-24	-11.8		392.6		15.847	
								101aie	ia	-76.3	-39.3	-21.1		433.7		23.426	
								101aif	ia	-45	-41.7	-5.9		426.9		9.074	
								101aig	ia			-3.1		375.2		5.094	
								101aih	ia	-67.1	-41.3			389.5			
								101aiia	ii					322.6	137.5	29.2	
								101aiib	ii					295.7	210	32.4	
								101aiic	ii					252.4	226.4	33.3	
								101aiid	iia					294.2	267.3	35.7	
								101aiie	iia	-70	-52.3	18.3		432	211.9	32.5	
								101aiif	iia					301.1	332.8	40.4	
								101aiig	iia					240	338.1	40.8	
								101aiih	iia					260.7	238.3	34	
								101aiiia	iii			-4.3	499.7			6.867	
								101aiiib	iii	-71	-41.5	-9.4	534			13.327	
								101aiiic	iii	-43.1	-32.3	-9.4	500			13.327	
LGS50	DL-64	XC-50	192-200m	BXTGDCC	0.6	qtz cement	20:31:49	lsg50ia	ia			0		328		0	
								lsg50ib	ia			-7.2		336.1		10.741	
								lsg50ic	ia					402.3			
								lsg50id	ia					351.7			
								lsg50ie	ia			-15.5		362.3		19.211	
								lsg50iia	iia					271.3	294.9	37.6	
								lsg50iib	iia-b					265	370	43.4	
								lsg50iic	iib-a					310.1	103-481	54.2	

Appendix E2: Sur-Sur microthermometric data

sample	DDH	section	location	lithology	Cu grade	stage	% of type i:ii:iii	sample	Type	froze at	Te	Tm	Th (liq)	Th (vap)	Th (salt)	salinity	Td
								lsg50iid	iib-a					267.6	183-218	32.8	
								lsg50iie	iib					338.4	179.5	30.9	
								lsg50iif	iia					375.3	462.4	52.2	
								lsg50iig	iia-b						228.5	33.4	
								lsg50iih	iia-b					295.4	373.5	43.7	
								lsg50iii	iia-b					302.5	144.4	29.5	
								lsg50iij	iia					253.1	373.1	43.7	
								lsg50iik	iia-b					380.1	371	43.5	
								lsg50iiia	iii			-0.2	497.5			0.352	
								lsg50iiib	iii				408.7				
230b	DL-64	XC-50	20-30 m	BT-BXTGDCC	3.91	qtz cement	24:20:56	230bia	ia					195.2			
								230bib	ia					401.7			
								230bic	ia					379.1			
								230bid	ia	-72				421.2			
								230bie	ia	-48		-11.6		389.3		15.648	
								230bif	ia					308.4			
								230big	ia	-41		-5.4		342.9		8.403	
								230biia	iia-b					261.2	167.1	30.4	
								230biib	iia-b					245.8	322.3	39.5	
								230biic	iia-b					265.8	288.9	37.1	
								230biid	iia-b					241.5	340.1	40.9	
								230biie	iia-b					257.3	221.4	33	
								230biif	iia-b					291.3	372.9	43.6	
								230biig	iia-b			-23.7		276.8		25.158	
								230biih	iia-b					322	288.1	37.1	
								230biiia	iii			-11.7		406.8		15.747	
190	DL-03	XC-50	139 m	BXTGDCC	2.52	qtz cement	41:42:17	190ia	ia	-88.6	-44.1	-0.3		425.4		0.527	
								190ib	ia	-61.6	-27.4	-9.6		376.1		13.549	
								190ic	ia	-63	-53.5	-14.8		386.4		18.617	
								190id	ia	-45.8		-3		332		4.942	
								190ie	ia	-54.5		-9.5		290.8		13.438	
								190if	ia	-42.5		-2.9		370.2		4.788	
								190ig	ia	-47.7	-30.1	-5		326.6		7.854	
								190ih	ia	-46.1	-34.1	-17.3		344.3		20.661	
								190ii	ia			-0.4		379.5		0.701	
								190iia	iia					240.7	291.2	37.3	
								190iib	iia					242.2	498.8	56.2	
								190iic	iia					269.8	268.6	35.8	
								190iid	iia					240.1	308.1	38.5	
								190iie	iia					240.9	391.5	45.3	
								190iif	iia					261.7	321.6	39.5	
								190iig	iia					265.3			427.4
								190iih	iia					277.2	292.4	37.4	
								190iii	iia					445.6	324.1	39.7	
								190iij	iia					257.1	325.7	39.8	
								190iik	iia					268.9	166.1	30.3	
								190iil	iia					231.5	378.2	44.1	
								190iim	iia					301.1	166.3	30.3	
								190iin	iia,b					256.4	350.5	41.8	
								190iio	iia,b					258.1	394.4	45.5	
								190iip	iia					290.3	256	35	
								190iiq	iia					453.2	234.4	33.7	
								190iir	iia					330.4	328.7	40	
								190iis	iia					307.7	188.3	31.3	
								190iit	iia					263.5	417.5	47.7	

Appendix E2: Sur-Sur microthermometric data

sample	DDH	section	location	lithology	Cu grade	stage	% of type i:ii:iii	sample	Type	froze at	Te	Tm	Th (liq)	Th (vap)	Th (salt)	salinity	Td
								190iiia	iii			1.3	393.1			2.23	
								190iiib	iii	-34.9		1.2	370.2			2.063	
VHG50a	DL-03	XC-50	56 m	BXTGDCC	13.85	qtz cement	24:32:44	vhgaia	ia			-6.7		394		10.112	
								vhgaib	ia	-74.1	-44.2	0.1		309.5		0.117	
								vhgaic	ia	-58.6		-10		320.9		13.985	
								vhgaid	ia					256.8			
								vhgaie	ia	-49.3		-15.1		345.1		18.874	
								vhgaiia	iia					222.7	361	42.6	
								vhgaiib	iia					219.7	338.2	40.8	
								vhgaiic	iia					256.9	233.2	33.7	
								vhgaiid	iia					248.1	298.4	37.8	
								vhgaiie	iia					238.1	287.8	37.1	
								vhgaiif	iia					263.4	302.3	38.1	
								vhgaiig	iia					269.8	209.2	32.4	
								vhgaiiia	iii		-48.6		>550				
VHG50d	DL-03	XC-50	58 m	BXTGDCC	9.93	qtz cement		vhgdia	ia	-84.5	-32.1		>600		115		
								ib	ia	-86.3	-58.6			303.9			
								ic	ib	-52.2		-4.2		344.2		6.724	
								iia	iic					163.4	346.7	41.5	
								iib	iic					231.3	419.8	47.9	
								iic	iic					269.9	327.7	40	
								iid	ii					229.9	332.4	40.3	
								iie	iic					275.5	163.9	30.2	
								iif	iia					337.1	156.4	35	
								iig	iia					282.5	262	35.4	
								iih	iic					>600	375.4	43.9	
								iii	iic					>600	417.4	47.7	
								iij	iic					516.1	328.4	40	
								iik	iic					275.2	552.2	62.5	
								iil	iia					306.3			
								iim	iic					201.6	235.4	33.8	
								iin	iic					229.1			363
								iiia	iii	-71.6		-15.8	>600			19.46	
490	DL-57	XC-40	85 m	BXTGDCC	2.46	qtz cement	37:23:40	490ia	ia	-41.7	-24.7	-6.1		334.2		9.337	
								490ib	ia	-65.6	-50.4	-20.6		304.3		23.081	
								490ic	ia	-47.7	-33.5	-1.1		360.5		1.896	
								490iia	iia					213.8	288.3	37.1	
								490iib	iic					390.4	446.7	50.6	
								490iic	iic					253	324.6	39.7	
								490iid	iia					314.7			490.9
								490iie	iia					202.4	332.1	40.3	
								490iif	iia					259.6	244.2	34.3	
								490iig	iia					298.8	288.4	37.1	
								490iih	iic					242	438.9	49.8	
								490iii	iia					578.9	338.9	40.8	
								490iiia	iii				400.3				
								490iiib	iii	-75.4		-0.4	390.5			0.701	
								490iiic	iii	-53.8		-12.6	425			16.624	
								490iiid	iii				352.5				
								490iiie	iii	-70.1		-23	>400			24.701	
524	DL-71	XC-70	99.5 m	BXTGDCC	2.75	qtz cement	51:05:44	524ia	ia			-1.9		311.1		3.213	
								524ib	ia	-37.8	-28	-3		364.8		4.942	
								524ic	ia	-43.5	2.8	20		440.9		22.66	
								524id	ia	-36.7	-20.8	0		338.9		0	
								524ie	ia	-36.8	-30.4	-5.8		354.1		8.941	

Appendix E2: Sur-Sur microthermometric data

sample	DDH	section	location	lithology	Cu grade	stage	% of type i:ii:iii	sample	Type	froze at	Te	Tm	Th (liq)	Th (vap)	Th (salt)	salinity	Td
								524iia	iic					260.8	>600	>68.7	
								524iib	iia					386.3	354	42.1	
								524iic	iic					353.7	238.9	34	
								524iid	iia					337.8	240.3	34.1	
								524iie	iia						380.4	44.3	565.9
								524iif	iic					308.3	363.1	42.8	
								524iig	iic					577.5	439.3	49.8	
								524iiia	iii				396.9				
								524iiib	iii				464				
								524iiic	iii				>600		526.7	59.4	
								524iiid	iii	-66.7	-46.3	-16.1	458.6			19.706	
								524iiie	iii			-9.4	446.4			13.327	
								524iiif	iii			-6.3	450.2			9.598	
quartz/sulfide stockwork veins (quartz-sericite alteration halo)																	
218b	TSS-22	XC-50	802 m	BXMGDCC	0.3	qtz v.	66:16:18	218bia	ia			-4.8		258.3		7.576	
								218bib	ib			-18.1		378.2		21.274	
								218bic	ia			-8.3		415.6		12.069	
								218bid	ia			-8.5		403		12.303	
								218bie	ia			-23.4		386.2		24.963	
								218bif	ia			-5.6				8.673	
								218biia	iia					296.4	409	46.9	
								218biib	iia					214.6	211.5	32.5	
								218biic	iia					432.9	264.4	35.5	
								218biid	iia					348.5	281.2	36.6	
								218biie	iia					311.8	316.2	39.1	
								218biif	iia					244.2	362.7	42.8	
								218biig	iia					265.2	379.9	44.3	
								218biih	iia					273.7	428.9	48.8	
								218biii	iia					303.1	387	44.9	
								218biij	iia					310.5	436	49.5	
								218biik	iia					299.2	378.3	44.1	
								218biil	iia					285.3	400.2	46.1	
								218biiia	iii			-2.6	393.4			4.324	
								218biiib	iii			-6.8		416.3		10.239	
46	TSS-22	XC-50	37 m	BXTGDCC	0.86	qtz v.	43:07:50	46ia	ia			-3.6		390		5.846	
								46ib	ia			-6.6		368.7		9.985	
								46ic	ia			-5.8		393.6		8.941	
								46id	ia			0.2		367.1		0.352	
								46ie	ia			-0.4		377.7		0.701	
								46if	ia			9.8		416.8		13.768	
								46iia	iia					264.3	317.4	39.2	
								46iib	iia					269.7	314.5	39	
								46iic	iia					255.7	308.2	38.5	
								46iid	iia-b					250.2	409.4	46.9	
								46iie	iia-b					297.9	247.8	34.5	
								46iif	iia-b					357.9	270.1	35.9	
								46iig	iia					289.4	248.4	34.5	
								46iih	iia					271.1	323.1	39.6	
								46iiia	iii			-1.5		394.4		2.561	
39a	TSS-26	XC-50	335 m	GDCC	0.6	qtz v.		39aia	ib			-8.2		393.6		11.952	
								39aib	ia	-40.1		-1.9		347.6		3.213	
								39aiia	iia					302.6	204.4	32.1	
								39aiib	iia					414.6	345.6	41.4	
								39aiiia	iii	-36.6		1.8	406.6			3.051	
59b	TSS-22	XC-50	380 m	BXTGDCC	0.94	qtz v.	24:17:59	59bia	ia	-36.4		-3.1		391.8		5.094	

Appendix E2: Sur-Sur microthermometric data

sample	DDH	section	location	lithology	Cu grade	stage	% of type i:ii:iii	sample	Type	froze at	Te	Tm	Th (liq)	Th (vap)	Th (salt)	salinity	Td
								59bib	ia	-54	-24	-13.9		378.4		17.826	
								59bic	ia	-38.8		-4		235.9		6.434	
								59bid	ia	-43	-23.4	-5.8		371.2		8.941	
								59biia	iia					230.9	268.4	35.8	
								59biib	iia					289.4	327.1	39.9	
								59biic	iia					278.9	267.2	35.7	
								59biid	iia					317.5	169.8	30.5	
								59biie	iia					262.4	391.7	45.3	
								59biif	iia						268.6	35.8	
								59biig	iia					310.5	291.1	37.3	
7	TSS-4	XC-50	155 m	BTBXTGDCC	1.11	qtz v.	14:38:48	7ia	ia	-45.9	-22.9	-8.9		407		12.764	
								7ib	ib	-41.5	-30.8	18.8		378.8			
								7ic	ia	-37.9	-23.9	-10.2		458.5		14.2	
								7id	ia	-46.4	-16	-4		369.6		6.434	
								7ie	ia	-48.2		0.6		378.2		1.047	
								7if	ia	-55	-29.1	-18.3		395.2		21.424	
								7ig	ia	-48.8	-26.2	-5.5	555.2			8.538	
								7ih	ia	-57.7	-39.2	-17.2		385.3		20.583	
								7ii	ia	-44.1		-1.3		363.6		2.23	
								7ij	ia	-44.1		-3.6		395		5.846	
								7iia	iia					330.8	169.5	30.5	
								7iib	iia					258.5	334.3	40.5	
								7iic	iia					285.1	238.3	34	
								7iid	iia					288.1	210.4	32.4	
								7iie	iia					232.5	285.2	36.9	
								7iif	iia					249	435.4	49.4	
								7iig	iia					270.6	274.4	36.2	
								7iih	iia					322.8	464.4	52.4	
								7iii	iia					283.5	303.7	38.2	
								7iij	iia					272	361.2	42.6	
								7iik	iia					442.4	439.2	49.8	
								7iil	iia					272.7	356.6	42.3	
								7iim	iia					307.6	455.5	51.5	
								7iin	iia					462.7	473.6	53.4	
								7iio	iia					327.2	281.9	36.7	
								7iip	iia					264.3	339.9	40.9	
								7iiq	iia					366.9	483.7	54.5	

Tourmaline Breccia tourmaline cement

sample	DDH	section	location	lithology	Cu grade	stage	% of type i:ii:iii	sample	Type	froze at	Te	Tm	Th (liq)	Th (vap)	Th (salt)	salinity	Td
62b	TSS-22	XC-50	736 m	BXTGDCC	1.54	Tm cement	i, iic	62bia	ia					389.7			
								62bib	ib				-22.7	301.6		24.503	
								62biia	iic					402.6	303.9	38.2	
								62biib	iic						263.3	35.5	
								62biic	iic		-62.2	-50.8	-26.7	240.7	217.6	32.8	
								62biid	iic		-54	-41.3	-31.7	148.1	250.2	34.7	
223a	TSS-22	XC-50	300-310 m	BXTGDCC	0.96	Tm cement	I	223aia	ia		-49.2		4.9			7.715	
								223aib	ia		-46		-3.3	284		5.397	
								223aic	ia		-48.8		-7.7	240.3		11.354	
7	TSS-4	XC-50	155 m	BTBXTGDCC	1.11	Tm cement	I	7ia	ib		-64		-19.9	235.4		22.589	
								7ib	ia		-52.6		-12.8	200		16.813	
								7ic	ia		-45.9		-4.4	218.4		7.011	
								7id	ia		-47.3		-1.5	188.9		2.561	
VHG50d	DL-03	XC-50	58 m	BXTGDCC	9.93	Tm cement	I	vhg50dia	ib		-59.7		-9.4	220.6		13.327	
								vhg50dib	ib			-62.4	12.9	191.3		16.907	
								vhg50dic	ib		-49.3	-30.6	-12	301.9		16.044	

Appendix E2: Sur-Sur microthermometric data

sample	DDH	section	location	lithology	Cu grade	stage	% of type i:ii:iii	sample	Type	froze at	Te	Tm	Th (liq)	Th (vap)	Th (salt)	salinity	Td
								vhg50did	ia		-50.9	-33.6	-5	140.5		7.854	
225c	TSS-22	XC-50	609 m	BXTGDCC				225cia	ia		-53.8		-10.1	445.2		14.093	
								225cib	ia		-48.5		0.7	191.9		1.218	
								225cic	ia				-2.3	225.7		3.852	
								225cid	ia		-48.9		-1.7	186.3		2.888	
								225cie	ia		-48.9		-1.7	156.2		2.888	
								225cif	ia		-48.3		-1.9	156.4		3.213	

Appendix E3: PIXE data

Inclusion sample	K conc.(ppm)	e_K error	mdl_K mdl	Ca conc.(ppm)	e_Ca error	mdl_Ca mdl	Ti conc.(ppm)	e_Ti error	mdl_Ti mdl
PF218B-1A-E_115432	12651	1277.9	919.99	2706	328.52	432.42	3304.6	334.82	203.53
PF218B-1B-E_115433	18105	2117.7	1725.3	3610.3	497.33	731.53	3024.7	352.47	322.48
PF218B-1C-E_115434	12597	3715.1	8730	3873.1	1389.4	3474.9	6775.2	851.84	1401.4
PF221B-1A-E_115435	9382.7	997.76	756.77	1214.8	189.97	380.72	0.00E+00	0.00E+00	0.00E+00
PF221B-1B-E_115436	2811	742.57	1935.6	1020.1	352.24	973.73	0.00E+00	0.00E+00	0.00E+00
PF221B-1C-B_115437	9857.8	909.12	550.42	1193.1	144.45	259.56	107.5	73.231	129.27
PF230B-1A-E_115454	35381	6190.7	9132.6	8910.7	1193.7	2635.2	588.79	542.87	849.03
PF230B-2A-E_115455	2442.7	264.98	540.8	178.15	116.93	306.44	0.00E+00	0.00E+00	0.00E+00
PF46-1A-E_115456	13239	1265.9	2113.9	1703.7	358.23	833.74	76.401	189.03	388.53

Inclusion sample	Mn conc.(ppm)	e_Mn error	mdl_Mn mdl	Fe conc.(ppm)	e_Fe error	mdl_Fe mdl	Cu conc.(ppm)	e_Cu error	mdl_Cu mdl
PF218B-1A-E_115432	854.19	61.637	51.911	6478.1	223.81	43.18	1105.3	49.189	53.595
PF218B-1B-E_115433	1484.2	96.736	79.825	10434	422.01	65.432	170.5	32.699	80.431
PF218B-1C-E_115434	2828.3	219.13	346.24	18683	752.8	283.47	57.572	127.17	323.35
PF221B-1A-E_115435	574.9	32.246	45.103	105.97	17.701	37.017	21.353	14.649	38.107
PF221B-1B-E_115436	1231.4	87.712	109.11	1453.7	83.899	89.605	53.613	35.145	89.675
PF221B-1C-B_115437	1144.2	71.356	37.363	10916	379.33	32.346	2382.3	86.505	47.668
PF230B-1A-E_115454	3762.3	243.25	195.18	52561	1572.5	159.54	1551.3	90.485	193.17
PF230B-2A-E_115455	2311.6	120.35	52.938	1669.3	90.313	47.669	57.92	22.383	50.317
PF46-1A-E_115456	1593.4	112.15	100.06	29238	1064.9	83.347	100.2	41.419	105.7

Inclusion sample	Zn conc.(ppm)	e_Zn error	mdl_Zn mdl	As conc.(ppm)	e_As error	mdl_As mdl	Br conc.(ppm)	e_Br error	mdl_Br mdl
PF218B-1A-E_115432	364.3	22.208	40.258	49.214	30.32	51.124	75.136	19.281	41.33
PF218B-1B-E_115433	452.14	27.149	56.375	143.31	35.451	74.646	88.286	33.866	69.656
PF218B-1C-E_115434	547.26	107.51	216.42	300.28	119.29	262.26	6.7518	110.2	277.3
PF221B-1A-E_115435	104.94	18.554	35.48	67.476	28.79	40.216	40.249	16.364	36.274
PF221B-1B-E_115436	467.02	42.426	83.402	92.525	44.802	99.803	68.08	39.828	83.674
PF221B-1C-B_115437	397.02	16.069	33.348	809.79	72.987	46.263	486.42	42.356	39.862
PF230B-1A-E_115454	1115.9	86.104	137.01	1101.6	123.13	157.8	588.82	116.31	137.02
PF230B-2A-E_115455	331.26	22.229	45.326	55.796	34.818	68.969	61.68	22.909	49.5
PF46-1A-E_115456	669.89	36.825	78.461	621.56	86.797	98.522	432.02	49.864	85.443

mdl = minimum detection limit

Inclusion sample	Rb conc.(ppm)	e_Rb error	mdl_Rb mdl	Sr conc.(ppm)	e_Sr error	mdl_Sr mdl	Pb conc.(ppm)	e_Pb error	mdl_Pb mdl
PF218B-1A-E_115432	73.538	23.426	51.298	8.9573	20.606	52.782	179.81	78.311	148.45
PF218B-1B-E_115433	154.53	42.055	89.45	27.984	38.961	97.774	54.023	89.982	225.96
PF218B-1C-E_115434	0.00E+00	0.00E+00	0.00E+00	0.00E+00	0.00E+00	0.00E+00	0.00E+00	0.00E+00	0.00E+00
PF221B-1A-E_115435	44.542	18.834	41.62	36.781	20.053	41.627	2.235	71.048	119.62
PF221B-1B-E_115436	0.00E+00	0.00E+00	0.00E+00	0.00E+00	0.00E+00	0.00E+00	52.482	115.41	294.18
PF221B-1C-B_115437	211.05	29.915	46.313	90.08	20.992	45.801	234.54	208.74	199.52
PF230B-1A-E_115454	597.7	118.84	172.13	616.26	102.81	178.88	397.96	308.95	604.36
PF230B-2A-E_115455	0.00E+00	0.00E+00	0.00E+00	0.00E+00	0.00E+00	0.00E+00	358.4	91.181	206.27
PF46-1A-E_115456	128.56	44.538	89.325	81.409	40.193	80.808	295.61	217.93	355.16

Appendix F1: Oxygen isotope analytical methods

Silicates and Oxides (BrF5)

Carbon dioxide for oxygen isotope analysis is prepared using the method described by Clayton and Mayeda (1963). In preparation of the line, waste products are frozen into a stainless steel waste trap and the bombs "baked out" (heated to reaction temperature empty, under vacuum) for one hour in readiness for further samples.

When loading the sample, 8-10 mgs of powdered sample is weighed into delivery probes and loaded into nickel reaction vessels ("bombs", 255mm long, 19 mm od, 12mm id), under a back flush of ultra-high purity argon. The bombs and manifold are evacuated, firstly by a rough pump, then by a high vacuum pump, an aliquot of bromine pentafluoride frozen into the bombs using liquid nitrogen (LN) and the bombs heated to 550°C (650°C for resistant minerals) for 14 hours.

When extracting the sample, the resultant oxygen is pulsed over a hot carbon filament (30A, 50-70V, platinum electrodes to catalyse the reaction), the carbon dioxide collected as generated (using LN), the yield measured and the gas collected for isotopic measurement.

Standards

Yield Correction
Yield (mmole/mg) = (P(torr)-0.8095) * 16.64
weight(mgs) * 0.8221

Delta Correction
δSMOW = 1.04 * draw +37.06

Appendix F2: O/D Fractionation equations

Summary of O isotope fractionation equations used in this study

Mineral-water fractionation equation	Temperature range	Reference
$10^3 ln\ \alpha_{quartz\text{-}water} = 3.34 \times 10^6/T^2 - 3.31$	200 – 500°C	Matsuhisa et al. (1979)
$10^3 ln\ \alpha_{anhydrite\text{-}water} = 3.21 \times 10^6/T^2 - 4.72$	100 – 550°C	Chiba et al. (1981)
$10^3 ln\ \alpha_{tourmaline\text{-}water} = -14.3 \times 10^3/T + 8.51 \times 10^6/T^2 - 0.94 \times 10^9/T^3 + 0.08 \times 10^{12}/T^4 + 8.04$	300 - 600°C	Kotzer et al. (1993)
$10^3 ln\ \alpha_{hematite\text{-}water} = 2.69 \times 10^6/T^2 - 12.82 \times 10^3/T + 3.78$	0 - 1200°C	Zheng and Simon (1991)

Summary of D isotope fractionation equations used in this study

Mineral-water fractionation equation	Temperature range	Reference
$10^3 ln\ \alpha_{tourmaline\text{-}water} = -27.2 \pm 4.4\ (10^6/T^2) + 28.1 \pm 9.8$	300 - 600°C	Kotzer et al. (1993)
$10^3 ln\ \alpha_{biotite\text{-}water} = 0.4\ (10^6/T^2) - 3.1$	500 - 800°C	Bottinga and Javoy (1973)
$10^3 ln\ \alpha_{muscovite\text{-}illite\text{-}water} = 0.4\ (10^6/T^2) - 3.1$	0 - 700°C	Sheppard and Gilg (1996)

T = temperature in K.

Appendix G: Sulfur isotope data

Appendix G1:

Appendix I1: List of acronyms
AN - Andesite
GDRB - Río Blanco Granodiorite
GDCC - Cascada Granodiorite
BXMGD - Magmatic Breccia
BXMGDRB - Río Blanco Magmatic Breccia
BXMGDCC - Cascada Magmatic Breccia
BXAN - Magmatic Breccia with andesite clasts
BXT - Tourmaline Breccia (5-15% tourmaline)
BT - Tourmaline Breccia (<5% tourmaline)
BXTT - Tourmaline Breccia (>15% tourmaline)
BXTO - Castellana Breccia (TO; tobaceo = fine grained and granular)
BXMN - Monolito Breccia (Monolito is a topographic feature near the mine)
BXTTO - Paloma Breccia
DIOR - Diorite
PF - Feldspar Porphyry
PQM - Quartz Monzonite Porphyry
PDL - Don Luis Porphyry
CHDAC - Dacite Chimney
CHRIOL - La Copa Rhyolite
qtz - quartz
tm - tourmaline
bt - biotite
V - vein
cpy - chalcopyrite
bn - bornite
cov - covellite
py - pyrite
mo - molybdenite
anhy - anhydrite
chl - chlorite
spec - specularite
mt - magnetite
sid - siderite
gyp - gypsum
k-spar - k feldspar
D - D vein
diss. - disseminated
q/s - quartz-sericite alteration
sil - silicic alteration
Ma - Million years ago (Mega atoms)
R - rock sample
TS - thin section
PTS - polished thin section
Fi - fluid inclusion analysis
Si - sulfur isotope analysis, LA - laser ablation, C - conventional drilled
Oi - oxygen isotope analysis
Bt chem - biotite mineral chemistry
Tm chem - tourmaline mineral chemistry
WR - wholerock analysis
Sr - strontium isotope analysis
Nd - neodymium isotope analysis
Pb - lead isotope analysis
op - overprinted by
bx - breccia

Appendix G2: Río Blanco sulfur isotope data

Rio Blanco

Sample No.	Section	DDH	Location	Sulf.	%Cu	Cpy:Py	Rock Type	Matrix	Clasts	$\delta^{34}S$ (wrt CDT)	Method
Sulfides											
285	XC 275	DDH 734	447 m	cpy	1.30%	7 3	GDCC	bt matrix. cpy/anhy/qtz V. (bt), pre-breccia vein	No clasts	0.89	LA
285	XC 275	DDH 734	447 m	cpy	1.30%	7 3	GDCC	bt matrix. cpy/anhy/qtz V. (bt), pre-breccia vein	No clasts	-1.14	LA
285	XC 275	DDH 734	447 m	cpy	1.30%	7 3	GDCC	bt matrix. cpy/anhy/qtz V. (bt), pre-breccia vein	No clasts	0.75	LA
325	XC 275	DDH 734	618.2 m	cpy	1.60%	8 2	BXMGDCC	no matrix. anyh/qtz/cpy V (V1) op by cpy/bt V. (bt - V1), pre-breccia vein	No clasts	1.91	LA
325	XC 275	DDH 734	618.2 m	cpy	1.60%	8 2	BXMGDCC	no matrix. anyh/qtz/cpy V (V1) op by cpy/bt V. (bt - V?), pre-breccia vein	No clasts	0.97	LA
325	XC 275	DDH 734	618.2 m	cpy	1.60%	8 2	BXMGDCC	no matrix. anyh/qtz/cpy V (V1) op by cpy/bt V. (bt - V2), pre-breccia vein	No clasts	1.92	LA
245n	XC 125	DDH 450	290 m	py	0.74%	8 2	BXMGD	cpy cement	no clasts	-1.05	C
148	XC 135	DDH 217	246 m	cpy	3.04%	10 0	PQM	no matrix. diss. cpy brought in with PQM intrusion?	No clasts	1.38	LA
350	XC 125	DDH 101	242 m	cpy	0.27%	1 9	AN	no matrix. diss. cpy	No clasts	0.09	LA
363	XC 135	DDH 212	156 m	cpy	1.03%	7 3	BXAN	pseudo matrix. sulfides. cpy cement	No clasts	0.87	LA
363	XC 135	DDH 212	156 m	cpy	1.03%	7 3	BXAN	pseudo matrix. sulfides. cpy cement	No clasts	0.33	LA
239f	XC 125	DDH 450	76 m	cpy/py	2.01%	8 2	BXMGDRB	3% bt matrix. cpy cement	2-3 cm, diffuse clast boundaries, sub-rounded	0.73	LA
239f	XC 125	DDH 450	76 m	cpy/py	2.01%	8 2	BXMGDRB	3% bt matrix. cpy cement	2-3 cm, diffuse clast boundaries, sub-rounded	0.35	LA
239f	XC 125	DDH 450	76 m	cpy/py	2.01%	8 2	BXMGDRB	3% bt matrix. py cement	2-3 cm, diffuse clast boundaries, sub-rounded	-1.54	LA
250b	XC 125	DDH 352	120 m	cpy	1.63%	8 2	BXMGDRB	no matrix. cpy cement	Intense biot. Alt. No Clasts	2.64	LA
130a	XC-135	DDH-217	6 m	cpy	2.05%	9 1	An	cement/diss. cpy, spec., mt	0.1 - 7 cm clasts	0.48	C
140	XC-135	DDH-217	158 m	cpy	1.96%	7 3	BXAN/GD	cpy cement, bt, tm?, mt	0.3 - 4 cm clasts, angular - rounded	-0.44	C
155	XC-125	DDH-344	85 m	cpy	1.18%	8 2	GDRB	cpy cement, mt + diss blebs sulfide and mt.		-0.43	C
160a	XC-125	DDH-344	178 m	cpy	1.28%	9 1	BXMGD(An)	cement/diss? cpy, anhy, mt	assimilated clasts of An, dior up to 5 cm	-1.52	C
166a	XC-125	DDH-344	234 m	cpy	3.96%	7 3	BXMGD	cpy cement, anhy, bt	0.1 - 15 cm clasts	0.05	C
167c	XC-125	DDH-344	253 m	cpy	5.60%	10 0	BXMGD(An)	cement/diss. cpy, tm.	0.2 - 5 cm clasts	0.88	C
179a	XC-125	DDH-340	43 m	cpy	2.63%	9 1	BXMGD(t)	cpy cement, tm, bt	0.1 - 4 cm clasts	-0.4	C
246j	XC-125	DDH-450	343 m	cpy	0.63%	8 2	BXMGD	cement/diss? cpy, mt, anhy.	No visable clasts	-2.38	C
241b	XC-125	DDH-450	128-158 m	cpy	1.39%	9 1	BXMGD	cpy cement, anhy. mt.	No visable clasts	-1.05	C
250b	XC-125	DDH-352	120 m	cpy	1.63%	8 2	BXMGD/An?	cement/diss? cpy	No visable clasts	-0.64	C
251b	XC-125	DDH-352	160 m	cpy	1.17%	8 2	BXAN	cpy cement, mt	0.2 - 5 cm clasts	-0.89	C
251h	XC-125	DDH-352	176 m	cpy	1.88%	8 2	BXAN	cpy cement, qtz, vuggy	up to 20 cm clasts	-1.12	C
252d	XC-135	DDH-448	14 m	cpy	1.90%	7 3	GDRB	cement/diss.? cpy, anhy., k-sp, mt, qtz	No visable clasts	-1.05	C
253d	XC-135	DDH-448	138 m	cpy	0.65%	7 3	PQM	clumps of cpy in PQM + k-spar? alteration	No visable clasts	0.06	C
335	XC-125	DDH-628	66 m	cpy	1.74%	8 2	BXMGD	cpy cement, anhy, mo, qtz	No visable clasts	1.06	C

Appendix G2: Río Blanco sulfur isotope data

Sample No.	Section	DDH	Location	Sulf.	%Cu	Cpy:Py	Rock Type	Matrix	Clasts	$\delta^{34}S$ (wrt CDT)	Method
341	XC-125	DDH-628	108 m	cpy	2.72%	9 1	BXMGD	cpy cement, bt, BXMGD	2 - 10 cm clasts	-0.25	C
344	XC-125	DDH-101	12 m	cpy	1.54%	8 2	GDRB	diss. cpy, py,	No visable clasts	-0.97	C
350	XC-125	DDH-101	242 m	cpy	0.27%	1 9	GDRB	cement/diss. cpy, cc?	No visable clasts	-0.38	C
363	XC-125	DDH-212	156 m	cpy	0.65%	7 3	BXAN	cpy cement, qtz	No visable clasts	0.18	C
365	XC-125	DDH-212	176.2 m	cpy	3.97%	9 1	BXAN	cpy cement, mt, spec.	pseudo Bx	-0.47	C
264	XC-275	DDH-734	328.8 m	cpy	1.75%	8 2	GDCC	cement/diss? cpy, mt, qtz, mo, anhy.	1 - 8 cm clasts	-0.3	C
275	XC-275	DDH-734	364.5 m	cpy	1.30%	6 4	GDCC	cement/diss? cpy + anhy traces in drilled sample	No visable clasts	0.07	C
277	XC-275	DDH-734	366.6 m	cpy	1.30%	6 4	DIOR (GDCC)	cpy cement	0.3 - 6 cm clasts	-0.59	C
279	XC-275	DDH-734	386 m	cpy	1.55%	6 4	GDCC	cpy cement, mt, chl.	5 - 10 cm clasts	0.2	C
284	XC-275	DDH-734	439 m	cpy	1.35%	8 2	GDCC	cpy cement, qtz, anhy; green blebs	0.5 - 3 cm clasts, Diss mag. in clasts	0.25	C
303	XC-275	DDH-734	519.23 m	cpy	1.50%	8 2	BXMGDCC	cpy cement, bt, qtz	pseudo Bx	0.11	C
319	XC-275	DDH-734	549 m	cpy	1.53%	8 2	BXMGDCC	cpy cement, bt, qtz, green blebs	pseudo Bx	-0.04	C
374	XC-135	DDH-454	111 m	py	0.73%	7 3	GDRB	py cement, anhy, cpy, qtz, mo V. (reactivation?)	No visable clasts	0.58	C
147a	XC-135	DDH-217	226 m	cpy	1.30%	10 0	GDRB	diss cpy and anhy clumps	No visable clasts	-0.78	C
243f	XC-125	DDH-450	190-210 m	cpy	0.53%	7 3	PQM	cpy cement in anhy bx	0.3 - 10 cm clasts	-0.81	C
350	XC 125	DDH 101	242 m	cpy,cc	0.27%	1 9	AN	no matrix. diss. cpy rimmed by cc	No clasts	-1.09	LA
350	XC 125	DDH 101	242 m	cpy,cc	0.27%	1 9	AN	no matrix. diss. cpy rimmed by cc	No clasts	-1.51	LA
293	XC 275	DDH 734	476.5 m	py			GDCC	no matrix. S.V. - cpy (q/s)	no clasts	-0.56	C
246f	XC 124	DDH 450	326 m	py	0.57%	8 2	PQM	S.V. (white q/s)	no clasts	-0.85	C
348	XC 125	DDH 101	145 m	cpy	0.31%	8 2	GDRB	no Matrix. S.V.-cpy (q/s)	No clasts	-2.38	LA
237a	XC 125	DDH 450	4 m	py	0.61%	2 8	PQM	no Matrix. S.V. -py, cpy (White q/s)	No Clasts	-1.5	LA
250d	XC 125	DDH 352	124 m	cpy/py	1.38%	8 2	BXMGDRB	no matrix. S.V.-cpy (q/s)	no clasts	3.34	LA
250d	XC 125	DDH 352	124 m	cpy/py	1.38%	8 2	BXMGDRB	no matrix. S.V.-py (q/s)	no clasts	-0.65	LA
170b	XC-125	DDH-357	85 m	cpy	3.49%	10 0	GDRB	S.V.-cpy, principal hydrothermal vein	No visable clasts	-0.09	C
241j	XC-125	DDH-450	128-158 m	cpy	1.39%		PQM	S.V.- cpy, principal hydrothermal vein	No visable clasts	-0.79	C
244h	XC-125	DDH-450	235-260 m	cpy	0.48%	8 2	PQM	S.V.-cpy, py, qtz, wide, vertical (white q/s)	No visable clasts	-0.04	C
376	XC-135	DDH-454	116 m	cpy	1.53%	7 3	GDRB	S.V.-cpy, anhy V. (q/s) with coarse, euhedral py	No visable clasts	0.28	C
250e	XC-125	DDH-352	125 m	cpy	1.38%	8 2	BXMGD	S.V. - cpy (blue), cpy + py traces,	pseudo bx	-0.18	C
162	XC-125	DDH-344	204.5 m	cpy	0.87%	9 1	BXMGD	S.V. -cpy./qtz/anhy/mo, sid V. (reactivated)	No visable clasts	-0.52	C
253c	XC-135	DDH-448	126 m	cpy	0.61%	7 3	PQM	S.V. -cpy, mt, spec, qtz	No visable clasts	-0.83	C
366	XC-125	DDH-212	176.6 m	cpy	1.87%	10 0	BXAN	S.V.-cpy (q/s)	No visable clasts	-1.06	C
165a	XC-125	DDH-344	224 m	cpy	3.78%	8 2	BXMGD	S. V., cpy	No visable clasts	0.19	C
165a	XC-125	DDH-344	224 m	moly	3.78%	8 2	BXMGD	S. V., mo	No visable clasts	0.88	C
345	XC-125	DDH-101	14 m	cpy	1.64%	8 2	GDRB	S.V.-cpy, bn, qtz (q/s)	No visable clasts	0.81	C
139a	XC-135	DDH-217	126 m	cpy	1.53%	8 2	An	S. V. - cpy + diss. high grade An.	No visable clasts	0.6	C

Appendix G2: Río Blanco sulfur isotope data

Sample No.	Section	DDH	Location	Sulf.	%Cu	Cpy:Py	Rock Type	Matrix	Clasts	$\delta^{34}S$ (wrt CDT)	Method
147c	XC-135	DDH-217	227 m	cpy	2.21%	10 0	GDRB	S. V. - cpy (q/s)	No visable clasts	-0.75	C
256	XC-275	DDH-734	422 m	cpy	1.30%	6 4	GDCC	S.V. -cpy, anhy V. reactivated with cpy, mo along edges	No visable clasts	-0.55	C
308	XC-275	DDH-734	529.6 m	cpy	1.65%	8 2	PF	S.V. - cpy (q/s)	No visable clasts	0.04	C
348	XC 125	DDH 101	145 m	cpy	0.31%	8 2	GDRB	no matrix. S.V.-cpy (q/s)	No clasts	-3.94	LA
Sulfates											
240b	XC 125	DDH 450	95-115 m	Anhy	1.63%	8 4	BXMGDRB	2%. anhy. anhy cement	No real clasts	17.86	C
373	XC 135	DDH 454	111 m	Anhy	0.73%	7 3	GDRB	3-10% matrix. anhy, cpy, mt, spec, mo?. anhy cement	0.5-10 cm. Sub-angular, low transport	13.64	C
147a	XC 135	DDH 217	226 m	Anhy	1.30%	10 0	GDRB	3-5% matrix. anhy cement + cpy. no bt in matrix	rock intact, no real clasts	11.91	C
160a	XC 125	DDH 344	178 m	Anhy	1.10%	9 1	BXMGD(An)	3-5% matrix. anhy cement + cpy. Assimilated An clasts in GD	1-15 cm, angular, low transport	13.31	C
241b	XC 125	DDH 450	128-158 m	Anhy	1.49%	9 1	BXMGD	5-10%. anhy cement, cpy, mt, chl.	1-5 cm. Angular, low transport	16.05	C
244a	XC 125	DDH 450	235-260 m	Anhy	0.50%	8 2	PQM	3-5%. anhy cement (coarse)	0.1-5 cm. Angular	11.49	C
246c	XC 125	DDH 450	322 m	Anhy	0.49%	8 2	BXMGD	1%. anhy cement. small amount of anhy, hydrothermal? bt.	10 cm or more	13.78	C
246h	XC 125	DDH 450	334 m	Anhy	0.34%	8 2	BXMGD	3%. anhy cement, chl. altered from bt matrix.	10 cm or more	11.96	C
252d	XC 135	DDH 448	14 m	Anhy	1.90%	7 3	BXMGD	3%. anhy cement, bt, cpy.	>10 cm	11.62	C
335	XC 125	DDH 628	66 m	Anhy	1.74%	8 2	BXMGD	5-7%. anhy cement, cpy	1- 5 cm, sub-angular	10.07	C
443	XC 155	DDH 439	7 m	Anhy	2.05%	8 2	GDRB	5-7 %. anhy cement, tm.	0.3 - 5 cm. angular	14.28	C
243f	XC 125	DDH 450	190-210 m	Anhy	0.48%	7 3	PQM	3-5%. anhy v, cpy.	0.5-5 cm, Angluar	12.39	C
239j	XC 125	DDH 450	80 m	Anhy	1.50%	6 4	PQM	anhy V. assimilated An clasts in PQM	None	12.81	C
247e	XC 125	DDH 352	13 m	Gyp	0.85%	3 7		gyp in D vein or later		11.84	C

Appendix G3: Sur-Sur sulfur isotope data

Sur-Sur

Sample No.	section	DDH	Location	Sulf.	%Cu	Cpy:Py	Rock Type	Matrix	Clasts	$\delta^{34}S$ (wrt CDT)	Method
Sulfides											
70 - 1	XC 50	DL 62	132 m	py	1.73%	6 4	BXT GDCC	20 - 30%, py cement, tm	5 mm - 3 cm, angular to sub-rounded, mod - strongly sericiticised	-0.28	C
70 - 2	XC 50	DL 62	132 m	py	1.73%	6 4	BXT GDCC	20%, py cement, tm	5 mm - 4 cm, angular to sub-rounded	-0.06	C
2	XC 50	TSS 4	31 m	py	0.72%	4 6	BXT GDCC	20 - 30%, py cement, tm, mt	5 mm - 5 cm, angular, weak to mod. sericitisation	-0.29	C
100e	XC 50	C 50	24 m	cpy	2.13%	7 3	BXT GDCC	20 - 30 %, cpy cement, tm, qtz	<5 mm - 7cm, angular	-0.9	C
101d	XC 50	C 50	43 m	cpy	1.90%	7 3	BXT GDCC	20 - 30%, cpy cement, tm, chl	3 mm - 5 cm, angular to sub-angular, q/s alteration	-1.53	C
102a	XC 50	C 50	60 m	cpy	1.08%	6 4	BXT GDCC	5 - 10%, cpy cement, mt, py, spec, tm		-1.62	C
102a	XC 50	C 50	60 m	py	1.08%	6 4	BXT GDCC	6 - 10%, cpy cement, mt, py, spec, tm		-1.91	C
186a	XC 50	DL 03	118 m	cpy	4.36%	8 2	BXTGDCC	20%, cpy cement, tm	1 - 5 cm wide, sub-rounded	-1.44	C
210a	XC 50	TSS 26	30 m	cpy		5 5	BXTGDCC	10%, cpy cement, mt, qtz, py, mo	3 - 10 cm, jig-saw fit	-1.02	C
222e	XC 50	TSS 22	133 m	cpy	2.07%	7 3	BXTGDCC	5%, cpy cement, mt	1 - 7 cm, jig-saw fit	-1.64	C
225d	XC 50	TSS 22	611 m	py	1.60%	7 3	BXTGDCC	>5%, py cement, bt, anhy, cpy	0.5 - 10 cm, jig-saw fit	-0.36	C
228c	XC 50	TSS 4	50-60 m	cpy	0.96%	5 5	BXTGDCC	15%, cpy cement, tm, mt, py	0.2 - 5 cm, angular to rounded, localised transport, pervasive mt alteration	-0.81	C
230c	XC 50	DL 64	20-30 m	cpy	3.91%	6 4	BT-BXT	10%, cpy cement, tm, bn	<10 cm, jigsaw fit	-2.38	C
VHG50c	XC 50	DL 03	57.8 m	cpy	13.85%	10 0	BXTGDCC	70%, cpy cement, cc		-2.67	C
VHG50d	XC 50	DL 03	58 m	cpy	13.85%	10 0	BXTGDCC	45%, cpy cement, tm, cc, qtz	2 mm - 2 cm, angular to sub-angular, q/s and tm alteration	-2.84	C
7	XC 50	TSS 4	155 m	cpy	1.11%	6 4	BXTGDCC	10%, cpy cement, tm	0.2 -10 cm, sub-angular, transported	1.82	LA
33	XC 50	TSS 26	238 m	py		7 3	BT GDCC	5 -10%, cpy cement, tm	0.2 -10 cm, subangular, transported	-1.02	LA
33	XC 50	TSS 26	238 m	cpy		7 3	BT GDCC	5 -10%, cpy cement, tm	0.2 -10 cm, subangular, transported	-0.73	LA
220b	XC 50	TSS 22	26 m	cpy	2.15%	8 2	BXTGDCC	15%, cpy cement, tm	0.5 - 5 cm, jigsaw fit	0.05	LA
223a	XC 50	TSS 22	300-310 m	cpy	0.96%	7 3	BXTGDCC	5-10%, cpy cement, tm, mt	0.2 - 7cm, sub-rounded, transported	0.71	LA
224a	XC 50	TSS 22	500 m	cpy	0.73%	7 3	BXTGDCC	10-15%, cpy cement, tm, anhy	0.2 - 4 cm, sub-rounded, transported	-1.25	LA
224a	XC 50	TSS 22	500 m	cpy	0.73%	7 3	BXTGDCC	10-15%, cpy cement, tm, anhy	0.2 - 4 cm, sub-rounded, transported	-1.03	LA
226b	XC 50	TSS 22	730-740 m	cpy	1.54%	8 2	GDCC(T)	<1%, cpy cement, bn		-0.82	LA
227c	XC 50	TSS 21	140-150 m	cpy	0.94%	5 5	BXTGDCC	40%, cpy cement, tm, py, sid, qtz	2 - 4 cm	2.65	LA
227c	XC 50	TSS 21	140-150 m	cpy	0.94%	5 5	BXTGDCC	40%, cpy cement, tm, py, sid, qtz	2 - 4 cm	1.61	LA
VHG50c	XC 50	DL 03	57.8 m	cpy	13.85%	10 0	BXTGDCC	70%, cpy cement, cc		2.03	LA
VHG50c	XC 50	DL 03	57.8 m	cpy	13.85%	10 0	BXTGDCC	70%, cpy cement, cc		-0.97	LA
VHG50c	XC 50	DL 03	57.8 m	cpy	13.85%	10 0	BXTGDCC	70%, cpy cement, cc		-1.45	LA

Appendix G3: Sur-Sur sulfur isotope data

Sample No.	Section	DDH	Location	Sulf.	%Cu	Cpy:Py	Rock Type	Matrix	Clasts	$\delta^{34}S$ (wrt CDT)	Method
VHG50c	XC 50	DL 03	57.8 m	cpy	13.85%	10 0	BXTGDCC	70%, cpy cement, cc		-0.55	LA
230c	XC 50	DL 64	20-30 m	cc	3.91%	6 4	BT-BXT	10%, cc, cpy cement, tm, bn, py	<10 cm, jigsaw fit	-2.54	LA
230c	XC 50	DL 64	20-30 m	cc	3.91%	6 4	BT-BXT	10%, cc, cpy cement, tm, bn, py	<10 cm, jigsaw fit	-1.51	LA
230c	XC 50	DL 64	20-30 m	py	3.91%	6 4	BT-BXT	10%, py cement, cc, tm, bn, cpy	<10 cm, jigsaw fit	-3.39	LA
230c	XC 50	DL 64	20-30 m	cpy	3.91%	6 4	BT-BXT	10%, cpy cement, cc, tm, bn, py	<10 cm, jigsaw fit	-1.47	LA
230c	XC 50	DL 64	20-30 m	py	3.91%	6 4	BT-BXT	10%, py cement, cc, tm, bn, cpy	<10 cm, jigsaw fit	-2.74	LA
VHG50c	XC 50	DL 03	57.8 m	cc	13.85%	10 0	BXTGDCC	70%, cc, cpy cement		-2.9	LA
33	XC 50	TSS 26	238 m	py	0.40%	7 3	BT GDCC	<5%, cement/diss py, tm	5 - 10 cm, angular	-0.79	LA
33	XC 50	TSS 26	238 m	py	0.40%	7 3	BT GDCC	<5%, cement/diss py, tm	5 - 10 cm, angular	-0.11	LA
7	XC 50	TSS 4	155 m	py	1.11%	6 4	BXTGDCC	10%, cpy cement, tm	0.2 - 10 cm, sub-angular, transported	-0.22	LA
220b	XC 50	TSS 22	26 m	py	2.15%	8 2	BXTGDCC	15%, cpy cement, tm	0.5 - 5 cm, jigsaw fit	-1.66	LA
226b	XC 50	TSS 22	730-740 m	cpy	1.54%	8 2	GDCC(T)	<1%, cpy cement, bn		-2.57	LA
78	XC 130	DL 138	96 m	cpy	1.83%	6 4	BT GDCC	5-7%, cement/diss cpy, py, qtz, tm, vuggy	1 - 4 cm, angular, q/s to sil alteration	-2.54	C
80	XC 130	DL 138	102 m	py	0.57%	3 7	BT GDCC	5%, cement/diss cpy, py, qtz, tm, vuggy	5mm - 4 cm, angular to sub-angular, q/s alteration	0.08	C
82	XC 130	DL 138	128 m	py	0.88%	3 7	BXTT GDCC	70+%, py cement, tm, py	2 mm - 2 cm, sub-rounded to rounded, q/s alteration	-0.98	C
94	XC 130	DL 139.1	123 m	cpy	0.65%	3 7	BT GDCC	10-15%, cpy cement, tm, vuggy	3 mm to 10 cm, angular, chl, k-spar, sericite alteration	-4.12	C
95	XC 130	DL 139.1	170 m	py	3.11%	6 4	GDCC	5-15%, py cement, spec, cpy, bn, tm	5 mm - 6 cm, angular to sub-angular	-1.52	C
95	XC 130	DL 139.1	170 m	bn	3.11%	6 4	GDCC	5-15%, bn cement, spec, py, cpy, tm	5 mm - 6 cm, angular to sub-angular	-2.89	C
96	XC 130	DL 139.1	184 m	cpy	2.30%	7 3	BXT GDCC	20-30%, cpy cement, tm, chl	2 mm - 5 cm, angular, q/s and chl alteration	-2.26	C
98b	XC 130	DL 139.1	300 m	cpy	0.33%	7 3	BXTT GDCC	60%, cpy cement	3 mm - 1 cm, sub-rounded, silicified and sericitised	-4.11	C
104c	110-180	TSS 36	62 m	cpy	1.09%	9 1	BXT GDCC	10-20%, cpy cement, mt, tm, vuggy	5 mm - 5 cm, angular, q/s alteration	-1.58	C
104c	110-180	TSS 36	62 m	cpy	1.09%	9 1	BXT GDCC	10-20%, cpy cement, mt, tm, vuggy	5 mm - 5 cm, angular, q/s alteration	-1.71	C
121a	XC 0	E 20 A	20 m	py	0.67%	5 5	BXT GDCC	20-25%, py cement, tm, cpy	3mm - 4 cm, angular, sil and q/s alteration	-0.7	C
126c	XC 455 E	DL 16	16 m	cpy	0.75%	5 5	GDCC (T)	5-7%, cpy cement, mt, py, chl, vuggy	1 - 5 cm, angular	-2.87	C
127a	XC 455 E	DL 16	25 m	py	0.63%	5 5	GDCC (T)	5-10%, py cement, tm, py, cov, vuggy	3 mm - 20 cm, angular, k-spar, sericite, plagioclase, chl	-1.6	C
484	XC 40	DDH E 40	110.5 m	cpy	1.84%	7 2	BXTGDCC	10%, cpy cement, tm, cpy, cov	0.2 - 15 cm, jigsaw fit	-1.25	C
492	XC 40	DL 57	86 m	cpy	1.27%	8 2	BXTGDCC	20-25%, cpy cement, spec, cpy, bn, py, vuggy	0.2 - 5 cm, clasts are angular	-1.86	C
504	XC 90	DL 79A	178 m	cpy	8.06%	9 1	BXTGDCC	25-30%, cpy cement, tm	0.2 - 6 cm, sub-rounded, transported	-1.97	C
508	XC 110	TSS 29	84.1 m	cpy		9 1	BXTGDCC	30%, cpy cement, mt, tm, py, qtz.	0.2 - 5 cm, sub-rounded, transported	-3.14	C
523	XC 70	DL 71	98 m	cpy	2.75%	9 1	BXTGDCC	25-30%, cpy cement, mt, qtz, py	1 - 5 cm, sub-angular, low transport	-3.91	C

Appendix G3: Sur-Sur sulfur isotope data

Sample No.	Section	DDH	Location	Sulf.	%Cu	Cpy:Py	Rock Type	Matrix	Clasts	$\delta^{34}S$ (wrt CDT)	Method
500a	XC 90	TSS 12	118 m	cpy	3.77%	9 1	BXTGDCC	30-40%, cpy cement, anhy, mt	0.5 - 7 cm, sub-angular, jigsaw fit	-1.8	C
516	XC 110	DL 87	146 m	cpy	0.95%	3 7	BTGDCC	2%, cpy cement, tm, vuggy	0.2 - 10cm, jig-saw fit, angular	2.25	LA
516	XC 110	DL 87	146 m	py	0.95%	3 7	BTGDCC	2%, py cement, tm, vuggy	0.2 - 10cm, jig-saw fit, angular	-0.86	LA
522	XC 70	TSS 28	4 m	cpy	2.83%	3 7	BXTGDCC	3%, cpy cement, tm, qtz	0.2 - 5 cm, obscured clast margins	1.11	LA
530	XC 30	DL 53	50 m	cpy	1.03%	6 4	BXTGDCC	10%, cpy cement, tm, py, spec	0.2 -10 cm, jigsaw fit and localised transport zones	1.32	LA
530	XC 30	DL 53	50 m	py	1.03%	6 4	BXTGDCC	10%, py cement, tm, cpy, spec	0.2 - 10 cm, jigsaw fit to localised transport zones	0.77	LA
538	XC 315E	DL 85	142 m	cpy	0.75%	5 5	GDCC	15-20%, cpy cement, tm, py	0.5 - 10 cm, sub-rounded, low transport	-2.42	LA
541	XC 315E	DL 85	427 m	cpy	4.75%	9 1	BXMGD	Pervasive bt alteration, diss cpy		0.86	LA
191b	XC 10	DL 46A	80 m	cpy	0.39%	2 4	BXTGDCC	10%, cpy cement, tm, py	0.2 - 5cm, jigsaw fit to localised transport zones	-1.18	LA
195b	XC 10	DL 46A	158 m	py	0.54%	2 8	BXTGDCC	5%, py cement, tm, cpy	0.2 - 20 cm, sub-angular, low transport	-0.33	LA
206d	XC 455E	DL 16	610 m	cpy	1.84%	6 4	BXTGDCC	10%, cpy cement, tm, qtz, sid, gyp		-1.08	C
545	XC 315E	DL 85	424 m	cpy	1.29%	9 1	BXMGD	30%, cpy cement, anhy, bt		-1.28	C
115a	110-180	TSS 36	441 m	cpy	0.56%	8 2	BXMN/BXTO	30%, cpy cement, anhy, bt	0.1 - 10 cm	-1.68	C
01BXT12	XC 90	TSS 12	116 m	cpy	3.77%	9 1	BXTGDCC	30%, cpy cement, anhy		-0.05	C
33	XC 50	TSS-26	238 m	cpy	0.40%	7 3	BT GDCC	<5%, s.v. cpy, py, qtz (q/s/sil)	5 - 10 cm, angular	-0.44	C
46	XC 50	TSS-22	37 m	cpy	0.86%	7 3	BXT GDCC	5-15%, s.v. cpy, tm, anhy, cov, chl, sid (sil/q/s)	5 mm to 15 cm, angular to sub-rounded, mod - strongly sericitised	-1.02	C
46	XC 50	TSS-22	37 m	py	0.86%	7 3	BXT GDCC	5-15%, s.v. py, tm, anhy, cov, chl, sid (sil/q/s)	5 mm to 15 cm, angular to sub-rounded, mod - strongly sericitised	0.01	C
57b	XC 50	TSS-22	258 m	cpy	1.23%	6 4	BT GDCC	<5%, s.v. cpy, qtz, anhy (sil/q/s)	>10 cm, diss cpy, sid, q/s alteration	-0.95	C
59b	XC 50	TSS-22	380 m	cpy	0.94%	6 4	BXT GDCC	<5-10%, s.v. cpy, qtz, tm (sil/q/s/chl)	>10 cm, angular, sil alteration	-0.69	C
62b	XC 50	TSS-22	736 m	cpy	1.54%	8 2	BXT GDCC	10%, s.v. cpy, cov, py, tm, qtz, vug infill (sil/q/s)	no visable clasts, q/s alteration with diss cpy	-1.58	C
101a	XC 50	C-50	26 m	cpy	2.13%	7 3	BXT GDCC	30-40%, s.v. cpy, tm, mt, qtz, bn (sil)	<5 mm - 3 cm	-1.67	C
101a	XC 50	C-50	26 m	bn	2.13%	7 3	BXT GDCC	30-40%, s.v. bn, tm, mt, qtz, cpy (sil)	<5 mm - 3 cm	-1.53	C
24	XC 50	TSS 26	81 m	mo		2 8	BTGDCC	mo/qtz vein (q/s)	no visable clasts	-0.24	C
218d	XC 50	TSS 22	802 m	cpy	0.30%	8 2	BXMGDCC	5%, s.v.-cpy, anhy (q/s)		-2.16	C
100b	XC 50	C-50	4 m	cpy	1%	5 5	BXT GDCC	10-15%, s.v.-cpy, tm, qtz (q/s)	<5 mm - 7 cm, angular to sub-rounded, q/s alteration	-1.14	C
12	XC 50	TSS 4	211 m	cpy	0.64%	2 8	PF	no matrix, s.v.-cpy, py (q/s)	no visable clasts	-0.75	LA
208e	XC 50	C 50	412 m	cpy	0.79%	7 3	BXTGDCC	no matrix, s.v.-cpy, py (q/s)		-0.27	LA
209d	XC 50	C 50	350 m	py	1.21%	7 3	BXTGDCC	no matrix, s.v.-cpy, py, anhy (q/s)	pervasive chl	0.86	LA
212b	XC 50	TSS 26	279 m	cpy		4 6	BXTGDCC	no matrix, s.v.-cpy, py, qtz (q/s)		-0.54	LA
224e	XC 50	TSS 22	508 m	cpy	0.73%	7 3	BXTGDCC	2%, s.v.-cpy, tm (q/s)	0.4 - 7 cm, sub-angular	0.12	LA

Appendix G3: Sur-Sur sulfur isotope data

Sample No.	Section	DDH	Location	Sulf.	%Cu	Cpy:Py	Rock Type	Matrix	Clasts	$\delta^{34}S$ (wrt CDT)	Method
227a	XC 50	TSS 21	140-150 m	cpy	0.94%	6 4	BXTGDCC	no matrix, s.v.-cpy, qtz (q/s)		0.34	LA
229c	XC 50	TSS 4	100-110 m	py	0.94%	6 4	BXTGDCC	10-15%, s.v.-py, tm, cpy (q/s)	0.2 - 7 cm, mt altered, sub-rounded, localised transport	-0.87	LA
230a	XC 50	DL 64	20-30 m	cpy	3.91%	6 4	BT-BXT	<1%, s.v.-cpy, vuggy (q/s)		-1.35	LA
74b	XC 50	DL 62	152 m	cpy	0.73%	5 5	BXMN	30%, s.v. cpy, py (q/s)	0.2 - 3 cm, sub-rounded, transported	2.54	LA
230a	XC 50	DL 64	20-30 m	cpy	3.91%	6 4	BT-BXT	<1%, s.v. cpy, vuggy (q/s)		-4.05	LA
188a	XC 50	DL 03	132 m	cpy	2.52%	7 3	BXTGDCC	20%, s.v. cpy, tm, py (q/s)	0.2 - 30 cm, sub-angular, transported	-0.82	LA
121c	XC 0	E 20-A	69 m	cpy	0.39%	4 6	GDCC (T)	<5%, s.v. cpy, tm, cov (sil/q/s)	5 - 10 cm, angular, k-spar, q/s, chl alteration	-1.49	C
127b	XC 455 E	DL-16	54 m	py	1.80%	9 1	GDCC	10%, s.v. cpy, py (q/s)		-2.61	C
127b	XC 455 E	DL-16	54 m	cpy	1.80%	9 1	GDCC	10%, s.v. cpy, py (q/s)		-2.03	C
199	XC 10	TSS 16	110 m	cpy	0.35%	4 6	BTGDCC	no matrix, s.v. cpy, py, bn (q/s)		-1.92	LA
197b	XC 10	TSS 16	69 m	py	0.53%	7 3	GDCC	no matrix, s.v. py, cpy (q/s)		-1.21	LA
20a	XC 50	TSS 26	33 m	py	1.75%	5 5	BXT GDCC	<5-15%, D vein py, cpy, qtz	<2 cm, rounded to sub-angular, clast size increases away from mineralised zone	-0.52	C
20a	XC 50	TSS 26	33 m	py	1.75%	5 5	BXT GDCC	<5-15%, D vein py, cpy, qtz	<2 cm, rounded to sub-angular, clast size increases away from mineralised zone	-0.79	C
69b	XC 50	DL 62	117 m	cpy	1.27%	3 7	BXT GDCC	<50%, D vein cpy, py, qtz, tm	3 mm to 7 cm, angular, mod. to strongly sericitised	-0.3	C
LGS50	XC 50	DL 64	192-200 m	py	0.60%	2 8	BXT GDCC	5-7%, D vein py, cpy, tm	5 mm - 4 cm, angular, jig-saw fit, q/s alteration	1.06	C
187	XC 50	DL 03	123 m	py	5.18%	9 1	BXTGDCC	10 - 15%, D vein py, tm., qtz	<30 cm	-0.28	C
208a	XC 50	C 50	412 m	py	0.79%	7 3	BXTGDCC	no matrix, D vein py	no visable clasts	-0.88	C
212a	XC 50	TSS 26	279 m	py		4 6	BXTGDCC	no matrix, D vein py	no visable clasts	0.32	C
222g	XC 50	TSS 22	137 m	py	2.07%	7 3	BXTGDCC	no matrix, D vein py	no visable clasts	-0.37	C
223e	XC 50	TSS 22	307 m	py	1.20%	6 4	BXTGDCC	no matrix, D vein py	no visable clasts	0.31	C
227b	XC 50	TSS 21	146 m	py	0.94%	5 5	BXTGDCC	no matrix, D vein py	no visable clasts	0.2	C
228a	XC 50	TSS 4	50-60 m	py	0.96%	5 5	BXTGDCC	3%, D vein py, tm	0.2 - 30 cm	-0.05	C
229b	XC 50	TSS 4	100 m	py	0.94%	6 4	BXTGDCC	10%, D vein py, tm	0.2 - 5 cm, angular, transported.	0.35	C
79	XC 130	DL 138	102 m	py	0.57%	3 7	BT GDCC	5%, D vein py, tm, cpy	2 - 6 cm, angular to sub-angular, q/s alteration	-1.69	C
HGS130a	XC 130	DL 139.1	295.1 m	py	1.27%	6 4	BXT GDCC	40%, D vein py, tm	2 mm - 4 cm, sub-rounded, sericitised	-1.09	C
194c	XC 10	DL 46A	148 m	py	0.35%	2 8	BTGDCC	3-5%, D vein py, tm, qtz	0.5 - 7 cm, jigsaw fit	-1.63	C
Sulfates											
45	XC 50	TSS 22	34 m	Anhy	0.86	7 3	BXTGDCC	35%, matrix anhy, cpy, tm	5 mm - 5 cm, angular to sub-rounded, diss cpy, q/s/chl alteration	11.81	C
46	XC 50	TSS 22	37 m	Anhy	0.86	7 3	BXTGDCC	30%, matrix anhy, tm, qtz, cpy, py	5 mm - 10 cm, angular to sub-angular, q/s alteration	13.17	C

Appendix G3: Sur-Sur sulfur isotope data

Sample No.	Section	DDH	Location	Sulf.	%Cu	Cpy:Py	Rock Type	Matrix	Clasts	$\delta^{34}S$ (wrt CDT)	Method
60c	XC 50	TSS 22	578 m	Anhy	0.69	7 3	BXTGDCC	15-20%, matrix anhy, tm, cpy	1 - 7 cm, sub-rounded, q/s/chl alteration	11.56	C
62b	XC 50	TSS 22	736 m	Anhy	1.54	8 2	BXTGDCC	5%, matrix anhy, tm, cpy, qtz	5 - 10 cm, sub-angular	12.6	C
224a	XC 50	TSS 22	500-510 m	Anhy			BXTGDCC	10-15%, matrix anhy, tm, cpy	0.2 - 4 cm, sub-rounded, transported	11.15	C
500b	XC 90	TSS 12	118 m	Anhy			BXTGDCC	30-40%, matrix anhy, cpy, mt	0.5 - 7 cm, sub-angular, semi jigsaw fit	13.39	C
01BXT12	XC 90	TSS 12	116 m	Anhy	3.77%	9 1	BXTGDCC	30%, matrix anhy, cpy	0.5 - 7 cm, sub-angular	11.77	C

Appendix H: Rock catalogue (refer to Appendix G1 for acronyms)

UTAS #	Sample #	Northing	Easting	altitude (m)	Section	DDH	Depth	Lithology	description	Analysis Done
150753	2	24000-28000	23000-25000	2500-4500 m	XC 50	TSS 4	31 m	BTBXTGDCC	sulfide V. (cpy)	Si
150754	3	24000-28000	23000-25000	2500-4500 m	XC-50	TSS-4	57 m	BXTT		TS
150755	7	24000-28000	23000-25000	2500-4500 m	XC-50	TSS-4	155 m	BTBXTGDCC	Qtz V.	PTS, Fi qtz, Fi Tm, Si
150756	12	24000-28000	23000-25000	2500-4500 m	XC 50	TSS 4	211 m	PF	Qtz V., sulfideV. (q/s)	Si
150757	21	24000-28000	23000-25000	2500-4500 m	XC-50	TSS-26	36 m	BXT	Tm./sulfide/mt. V O.P.by D sulfide/Sid. V.	PTS
150758	24	24000-28000	23000-25000	2500-4500 m	XC 50	TSS 26	81 m	BT	Qtz V. + sulfide (mo,cpy,bm)	Si
150759	28	24000-28000	23000-25000	2500-4500 m	XC-50	TSS-26	180 m	GDCC		TS
150760	33	24000-28000	23000-25000	2500-4500 m	XC 50	TSS 26	238 m	GDCC (BXT?)	Tm./ Qtz/sulfide V.	Si
150761	45	24000-28000	23000-25000	2500-4500 m	XC 50	TSS 22	34 m	BXTGDCC	anhy cement, sulfide	Si
150762	46	24000-28000	23000-25000	2500-4500 m	XC-50	TSS-22	37 m	BXTGDCC	sulfide/Qtz/Anhy. V. (irregular margin), 2 cm	PTS, Fi qtz, Si
150763	49	24000-28000	23000-25000	2500-4500 m	XC-50	TSS-22	84 m	BXTGDCC	BXTGDCC, Clast zonation	TS
150764	70	24000-28000	23000-25000	2500-4500 m	XC 50	DL 62	132 m	BTGDCC?	sulfide cement., py	Si
150765	78	24000-28000	23000-25000	2500-4500 m	XC-130	DL-138	96 m	BTGDCC	sulfide cement.	Si
150766	79	24000-28000	23000-25000	2500-4500 m	XC 130	DL 138	102 m	BTGDCC	sulfide/Qtz V., sulfide cement.	Si
150767	80	24000-28000	23000-25000	2500-4500 m	XC 130	DL 138	102 m	BTGDCC	BTGDCC (Jigsaw fit texture)	Si
150768	82	24000-28000	23000-25000	2500-4500 m	XC 130	DL 138	128 m	BXTGDCC	sulfide cement.	Si
150769	84	24000-28000	23000-25000	2500-4500 m	XC-130	DL-138	149 m	BXTTO		TS
150770	85	24000-28000	23000-25000	2500-4500 m	XC-130	DL-138	152 m	BXTO	Different clast types present	TS
150771	90	24000-28000	23000-25000	2500-4500 m	XC-130	DL-138	294 m	BXMN		TS
150772	94	24000-28000	23000-25000	2500-4500 m	XC-130	DL-139.1	123 m	BTGDCC		PTS, Si
150773	95	24000-28000	23000-25000	2500-4500 m	XC-130	DL-139.1	170 m	GDCC		PTS, Si
150774	96	24000-28000	23000-25000	2500-4500 m	XC 130	DL 139.1	184 m	GDCC	sulfide cement., Qtz, Chl	Si
150775	134	24000-28000	23000-25000	2500-4500 m	XC-135	DDH-217	50 m	An		TS
150776	140	24000-28000	23000-25000	2500-4500 m	XC-135	DDH-217	158 m	BXAN/GD	sulfide cement. + mt	Si
150777	148	24000-28000	23000-25000	2500-4500 m	XC 135	DDH 217	246 m	PQM	Qtz/mo/sulfideV.	Si
150778	155	24000-28000	23000-25000	2500-4500 m	XC-125	DDH-344	85 m	GDRB	sulfide cement., mt + Diss blebs sulfide and mt.	Fi qtz, Si
150779	157	24000-28000	23000-25000	2500-4500 m	XC-125	DDH-344	136 m	BXMGD(T)	BXMGD(T)	TS
150780	161	24000-28000	23000-25000	2500-4500 m	XC-125	DDH-344	198 m	BXMGD(An)	Matrix and clast? + An, Anhy,Mo	TS
150781	162	24000-28000	23000-25000	2500-4500 m	XC-125	DDH-344	204.5 m	BXMGD	sulfide/Qtz/Anhy/mo V.	Si
150782	171	24000-28000	23000-25000	2500-4500 m	XC-125	DDH-357	2 m	BXMGD	Biot Matrix, sulfide V.	TS
150783	183	24000-28000	23000-25000	2500-4500 m	XC-125	DDH-340	157 m	PQM	Brecciated PQM with Biot matrix	TS
150784	187	24000-28000	23000-25000	2500-4500 m	XC 50	DL 03	123 m	BXTGDCC	D V. (py rich)	Si
150785	190	24000-28000	23000-25000	2500-4500 m	XC-50	DL-03	139 m	BXTGDCC	qtz cement	Fi qtz
150786	199	24000-28000	23000-25000	2500-4500 m	XC-010	TSS-16	110 m	BXTGDCC	sulfideV.	PTS, Si
150787	231	24000-28000	23000-25000	2500-4500 m	La Union	roof pendant	Surface	An	Roof pendant Andesite from La Union, abundant sulfides	TS, WR
150788	234	24000-28000	23000-25000	2500-4500 m		Monolito Mountain	surface	PDL		TS, WR
150789	235	24000-28000	23000-25000	2500-4500 m	XC 195	N-16		An		TS, WR
150790	256	24000-28000	23000-25000	2500-4500 m	XC-275	DDH-734	422 m	GDCC	Wide Anhy V. Reactivated with cpy, mo	Si
150791	257	24000-28000	23000-25000	2500-4500 m	XC-275	DDH-734	491 m	PF	mo rimmed Qtz V.(Q/S) op by thin mo V.; sulfide.,Qtz, Anhy. V.(Q/S); K'spar phenocryst	PTS
150792	258	24000-28000	23000-25000	2500-4500 m	XC-275	DDH-734	546 m	BXMGDCC	op. Relationships of Qtz V. (biot.); cpy, qtz,anhy. V.(biot.) op by qtz.,cpy V (Q/S)	PTS
150793	259	24000-28000	23000-25000	2500-4500 m	XC-275	DDH-734	611 m	BXMGDCC		Fi qtz
150794	261	24000-28000	23000-25000	2500-4500 m	XC-275	DDH-734	304 m	GDCC		PTS
150795	264	24000-28000	23000-25000	2500-4500 m	XC-275	DDH-734	328.8 m	GDCC	V. but poss. Matrix with cpy, mt.,Qtz, mo, Anhy.	PTS, Si
150796	266	24000-28000	23000-25000	2500-4500 m	XC-275	DDH-734	337.9 m	DIOR (GDCC)	Early Qtz V. Op by thin sulfide,Qtz V. (biot)	PTS
150797	269	24000-28000	23000-25000	2500-4500 m	XC-275	DDH-734	347 m	DIOR (GDCC)		PTS
150798	270	24000-28000	23000-25000	2500-4500 m	XC-275	DDH-734	347.9 m	DIOR (GDCC)	Anhy, Qtz., cpy V. (biot) op by thin sulfideV. (biot)	PTS
150799	272	24000-28000	23000-25000	2500-4500 m	XC-275	DDH-734	350 m	DIOR (GDCC)	mt./Act. Alt. Op by Thin Biot. V.	PTS
150800	273	24000-28000	23000-25000	2500-4500 m	XC-275	DDH-734	353.2 m	DIOR (GDCC)	BXMGDCC; preferred biot. Elongation truncated by Matrix, original fabric disrupted by Bx	TS

Appendix H: Rock catalogue (refer to Appendix G1 for acronyms)

UTAS #	Sample #	Northing	Easting	altitude (m)	Section	DDH	Depth	Lithology	description	Analysis Done
150801	274	24000-28000	23000-25000	2500-4500 m	XC-275	DDH-734	359.9 m	GDCC	D V. (py, qtz, sid., gyp?)	PTS, Fi qtz
150802	275	24000-28000	23000-25000	2500-4500 m	XC-275	DDH-734	364.5 m	GDCC	anhy cement.; sulfideV.-cpy (Q/S)	Si
150803	276	24000-28000	23000-25000	2500-4500 m	XC-275	DDH-734	364.5 m	GDCC/BXMGD	Contact; porphyroclasts; matrix; ductile flow; Qtz., Anhy., cpy V. (biot); thin sulfideV.-cpy (Q/S)	TS
150804	277	24000-28000	23000-25000	2500-4500 m	XC-275	DDH-734	366.6 m	DIOR (GDCC)	sulfideV.-cpy (Q/S) ; sulfide cement. - cpy	Si
150805	279	24000-28000	23000-25000	2500-4500 m	XC-275	DDH-734	386 m	GDCC	Matrix mt., cpy, chl.	Si
150806	280	24000-28000	23000-25000	2500-4500 m	XC-275	DDH-734	392 m	PDL	sulfideV. (Q/S) Qtz eyes	PTS, TS, WR
150807	281	24000-28000	23000-25000	2500-4500 m	XC-275	DDH-734	395 m	GDCC	Gyp.,Sid. V. (late)	PTS
150808	282	24000-28000	23000-25000	2500-4500 m	XC-275	DDH-734	411 m	GDCC	thin parallel biot. V's; Matrix biot., thin sulfideV. (biot); thin sulfideV. (Q/S)	PTS
150809	283	24000-28000	23000-25000	2500-4500 m	XC-275	DDH-734	419.8 m	GDCC	biot alteration; thin mo V. (Q/S)	PTS
150810	284	24000-28000	23000-25000	2500-4500 m	XC-275	DDH-734	439 m	GDCC	green blebs; Qtz matrix; Anhy. Matrix; cpy matrix	Fi qtz, Si
150811	285	24000-28000	23000-25000	2500-4500 m	XC 275	DDH 734	447 m	GDCC	anhy cement, chl, qtz	Si
150812	291	24000-28000	23000-25000	2500-4500 m	XC-275	DDH-734	470.4 m	PDL	biotite books	TS, WR
150813	293	24000-28000	23000-25000	2500-4500 m	XC-275	DDH-734	476.5 m	GDCC	sulfideV.-cpy (Q/S)	PTS, Si
150814	294	24000-28000	23000-25000	2500-4500 m	XC-275	DDH-734	477 m	GDCC	Biot. Bx, biot Vein OP relationship	PTS
150815	295	24000-28000	23000-25000	2500-4500 m	XC-275	DDH-734	484 m	GDCC	Green blebs surrounding a Qtz V., Qtz V. OP Rel.	PTS
150816	296	24000-28000	23000-25000	2500-4500 m	XC-275	DDH-734	485.3 m	PF	Typical PF	PTS, Fi qtz
150817	301	24000-28000	23000-25000	2500-4500 m	XC-275	DDH-734	508.4 m	PF?		PTS
150818	303	24000-28000	23000-25000	2500-4500 m	XC-275	DDH-734	519.23 m	BXMGDCC	cpy cement	Si
150819	307	24000-28000	23000-25000	2500-4500 m	XC-275	DDH-734	528 m	BXMGDCC/PF	Contact, PF op by thin sulfide/Qtz V.(biot)	PTS
150820	308	24000-28000	23000-25000	2500-4500 m	XC-275	DDH-734	529.6 m	PF	mo rimmed Qtz V.(Q/S) op by sulfideV. (Q/S)	Si
150821	313	24000-28000	23000-25000	2500-4500 m	XC-275	DDH-734	528.7 m	BXMGDCC	Biot bx + rock flour?	TS
150822	319	24000-28000	23000-25000	2500-4500 m	XC-275	DDH-734	549 m	BXMGDCC	cpy cement, green blebs	Si
150823	320	24000-28000	23000-25000	2500-4500 m	XC-275	DDH-734	584 m	PDL	Large unaltered biot books, mo rimmed Qtz V.(Q/S) op by thin sulfideV. (Q/S)	PTS, TS
150824	323	24000-28000	23000-25000	2500-4500 m	XC-275	DDH-734	609.5 m	BXMGDCC	Biot Bx. (ductile) truncated by a later phase of biot Bx.	PTS
150825	325	24000-28000	23000-25000	2500-4500 m	XC-275	DDH-734	618.2 m	BXMGDCC	Anhy/Qtz V (white halo?) the brittle failure of this vein indicates compression	PTS, Si
150826	332	24000-28000	23000-25000	2500-4500 m	XC-275	DDH-734	628 m	BXMGDCC	Brn/Py/mo V. (Q/S)	PTS
150827	333	24000-28000	23000-25000	2500-4500 m	XC-275	DDH-734	628.1 m	BXMGDCC	different clast types in deformed matrix	TS
150828	335	24000-28000	23000-25000	2500-4500 m	XC-125	DDH-628	66 m	BXMGD	anhy cement, Cpy, mo	Si
150829	341	24000-28000	23000-25000	2500-4500 m	XC-125	DDH-628	108 m	BXMGD?	cpy cement, BXMGD	Si
150830	344	24000-28000	23000-25000	2500-4500 m	XC-125	DDH-101	12 m	GDRB	Diss. Cpy, Py,	Si
150831	345	24000-28000	23000-25000	2500-4500 m	XC-125	DDH-101	14 m	GDRB	sulfideV.-Cpy, Brn, Qtz (Q/S)	Si
150832	348	24000-28000	23000-25000	2500-4500 m	XC-125	DDH-101	145 m	GDRB	sulfideV-cpy (Q/S)	PTS, Si
150833	350	24000-28000	23000-25000	2500-4500 m	XC-125	DDH-101	242 m	GDRB	Diss. Cpy, chalcocite?	Si (x6)
150834	352	24000-28000	23000-25000	2500-4500 m	XC-125	DDH-101	243.5 m	GDRB	Qtz/Cpy V., Qtz Brn. V	Fi qtz
150835	354	24000-28000	23000-25000	2500-4500 m	XC-125	DDH-101	245 m	GDRB	qtz cement and py	PTS, Fi qtz
150836	363	24000-28000	23000-25000	2500-4500 m	XC 135	DDH 212	156 m	BXAN	cpy cement + Qtz	Si
150837	365	24000-28000	23000-25000	2500-4500 m	XC-125	DDH-212	176.2 m	BXAN	cpy cement, mt., Spec.	Si
150838	366	24000-28000	23000-25000	2500-4500 m	XC-125	DDH-212	176.6 m	BXAN	sulfideV.-Cpy (Q/S)	Si
150839	373	24000-28000	23000-25000	2500-4500 m	XC-135	DDH-454	111 m	GDRB	Anhy Bx., minor Spec. Cpy, Py, Chl	Fi qtz, Si
150840	374	24000-28000	23000-25000	2500-4500 m	XC-135	DDH-454	111 m	GDRB	mo V. + other minerals (reactivation?)	Si
150841	376	24000-28000	23000-25000	2500-4500 m	XC-135	DDH-454	116 m	GDRB	sulfideV.-Cpy V. with coarse, euhedral Py intergrown	PTS, Si
150842	377	24000-28000	23000-25000	2500-4500 m	XC-135	DDH-454	116 m	GDRB	mt/Cpy V. + Qtz and Anhy., mt. Is replaced by Spec	Fi qtz
150843	390	24000-28000	23000-25000	2500-4500 m	XC-085	DDH-566	161 m	BXMGD	Bx. - is it rock flour?	PTS
150844	443	24000-28000	23000-25000	2500-4500 m	XC 155	DDH 439	7 m	GDRB	anhy cement, Cpy	Si
150845	450	24000-28000	23000-25000	2500-4500 m	XC-195	DDH-372	14.3 m	?	Rock flour Bx? 20 cm	PTS

Appendix H: Rock catalogue (refer to Appendix G1 for acronyms)

UTAS #	Sample #	Northing	Easting	altitude (m)	Section	DDH	Depth	Lithology	description	Analysis Done
150846	484	24000-28000	23000-25000	2500-4500 m	XC 40	DDH E 40	110.5 m	BXT	cpy cement	Si
150847	490	24000-28000	23000-25000	2500-4500 m	XC-40	DL-57	85 m	BXTGDCC	qtz cement	Fi qtz
150848	491	24000-28000	23000-25000	2500-4500 m	DL-57	XC-40	86 m	BXT	Pre BXT Qtz V.	PTS
150849	492	24000-28000	23000-25000	2500-4500 m	XC 40	DL 57	86 m	BXT	Matrix Spec, cpy, py; shows paragenesis of matrix minerals	Si
150850	493	24000-28000	23000-25000	2500-4500 m	XC-90	TSS-12	110 m	BXT	preferential tm ppt on the a certain side of clasts	PTS
150851	500	24000-28000	23000-25000	2500-4500 m	XC 90	TSS 12	118 m	BXT	cpy cement, mt., Anhy	Si
150852	504	24000-28000	23000-25000	2500-4500 m	XC 90	DL 79A	178 m	BXT	cpy cement	Si
150853	508	24000-28000	23000-25000	2500-4500 m	XC 110	TSS 29	84.1 m	BXT	cpy cement	Si
150854	516	24000-28000	23000-25000	2500-4500 m	XC 110	DL 87	146 m	BTGDCC	cpy cement	Si
150855	522	24000-28000	23000-25000	2500-4500 m	XC 70	TSS 28	4 m	BXT	cpy cement	Si
150856	523	24000-28000	23000-25000	2500-4500 m	XC-70	DL-71	98 m	BXT	cpy cement, mt., Qtz	PTS, Si
150857	524	24000-28000	23000-25000	2500-4500 m	XC-70	DL-71	99.5 m	BXTGDCC	sulfideV.-Cpy (Q/S), qtz cement	Fi qtz
150858	530	24000-28000	23000-25000	2500-4500 m	XC-30	DL-53	50 m	BXT	cpy cement, Py, mt	PTS, Si
150859	538	24000-28000	23000-25000	2500-4500 m	XC-315E	DL-85	142 m	GDCC	cpy cement, Py	PTS, Si
150860	541	24000-28000	23000-25000	2500-4500 m	XC 315E	DL 85	427 m	BXMGD	cpy cement, Anhy	Si
150861	545	24000-28000	23000-25000	2500-4500 m	XC 315E	DL 85	424 m	BXMGD	Pseudo Bx, anhy cement, Cpy	Si
150862	546	24000-28000	23000-25000	2500-4500 m	XC-325	DDH-737	49 m	BXMGD	Biot. Bx	PTS
150863	547	24000-28000	23000-25000	2500-4500 m	XC-325	DDH-737	87 m	BXMGD/BXT	BXMGD/BXT?	PTS
150864	548	24000-28000	23000-25000	2500-4500 m	XC-325	DDH-737	96 m	BXT	BXT	TS
150865	MiR9901	24000-28000	23000-25000	2500-4500 m	XC-035	DDH-513	134 m	CHRIOL	Western edge of CHRIOL	Photo
150866	Mid9907	24000-28000	23000-25000	2500-4500 m	XC-155	DDH-555	250 m	CHDAC	East side of CHDAC, Nivel 17	Photo
150867	59916	24000-28000	23000-25000	2500-4500 m	XC 315	DL-94	221 m	PDL	Shallow, PDL/PQM	TS, WR
150868	59917	24000-28000	23000-25000	2500-4500 m	XC 030	DDH-560	258 m	PDL	Mid-level - East side of PDL, PDL/PQM	TS, WR
150869	01BXT12	24000-28000	23000-25000	2500-4500 m	XC 90	TSS 12	116 m	BXT	coarse anhy in cpy cement	Si , Sr/Nd, Pb
150870	01BXTLU	24000-28000	23000-25000	2500-4500 m	La Union open pit	Surface		BXT	abundant spec and py	PTS
150871	100b	24000-28000	23000-25000	2500-4500 m	XC 50	C-50	4 m	BXTGDCC	sulfide cement. (Brn./Cpy)	Si
150872	100d	24000-28000	23000-25000	2500-4500 m	XC-50	C-50	21 m	BXTGDCC	BXTGDCC, Diss sulfide	TS
150873	100e	24000-28000	23000-25000	2500-4500 m	XC 50	C 50	24 m	BXTGDCC	BXTGDCC, sulfide cement.	Si
150874	101a	24000-28000	23000-25000	2500-4500 m	XC-50	C-50	26 m	BXTGDCC	qtz cement, sulfide, mt.	Fi qtz, Si
150875	101d	24000-28000	23000-25000	2500-4500 m	XC 50	C 50	43 m	BXTGDCC	sulfide cement. + Chl.	Si
150876	102a	24000-28000	23000-25000	2500-4500 m	XC 50	C 50	60 m	BXTGDCC	Matrix mt. and sulfide	Si
150877	104c	24000-28000	23000-25000	2500-4500 m	XC 110-180	TSS 36	62 m	BXTGDCC	sulfide cement., Chl, Qtz V.	Si
150878	106b	24000-28000	23000-25000	2500-4500 m	XC 110-180	TSS-36	134 m	BXMN	BXMN (+ BXT clasts etc)	TS
150879	115a	24000-28000	23000-25000	2500-4500 m	XC 110-180	TSS 36	441 m	BXMN/BXTO	anhy cement, sulfide	Si
150880	121a	24000-28000	23000-25000	2500-4500 m	XC 0	E 20 A	20 m	GDCC(T)	sulfide cement.	Si
150881	121c	24000-28000	23000-25000	2500-4500 m	XC 0	E 20-A	69 m	GDCC(T)	sulfide cement.	Si
150882	122b	24000-28000	23000-25000	2500-4500 m	XC 0	E20-A	75 m	GDCC(T)	GDCC	PTS
150883	123a	24000-28000	23000-25000	2500-4500 m	XC 0	E20-A	170 m	BXTGDCC	qtz cement/mt	Fi qtz
150884	126c	24000-28000	23000-25000	2500-4500 m	XC 455 E	DL 16	16 m	GDCC	sulfide cement. (in minor Bx zone) and mt.	Si
150885	127a	24000-28000	23000-25000	2500-4500 m	XC 455 E	DL 16	25 m	GDCC	sulfide cement. (in minor Bx zone)	Si
150886	127b	24000-28000	23000-25000	2500-4500 m	XC 455 E	DL-16	54 m	GDCC	qtz cement, mt, sulfide	Si
150887	129c	24000-28000	23000-25000	2500-4500 m	XC-135	DDH-217	4 m	An	?Tm phenocrysts in An?	PTS
150888	130a	24000-28000	23000-25000	2500-4500 m	XC-135	DDH-217	6 m	An	HIGH GRADE An (sulfide,Spec.,mt.- Dissulfide and Matrix)	Si
150889	132b	24000-28000	23000-25000	2500-4500 m	XC-135	DDH-217	27 m	An	GDRB clast (or dyke?) in An	TS
150890	133b	24000-28000	23000-25000	2500-4500 m	XC-135	DDH-217	37 m	An	Qtz	Fi qtz
150891	138c	24000-28000	23000-25000	2500-4500 m	XC 135	DDH-217	107 m	An	Medium level roof pendant	WR, TS
150892	139a	24000-28000	23000-25000	2500-4500 m	XC-135	DDH-217	126 m	An	HIGH GRADE An, sulfide V. + Dissulfide	Si
150893	147a	24000-28000	23000-25000	2500-4500 m	XC-135	DDH-217	226 m	GDRB		Si
150894	147c	24000-28000	23000-25000	2500-4500 m	XC-135	DDH-217	227 m	GDRB	sulfide V.	Si
150895	160a	24000-28000	23000-25000	2500-4500 m	XC-125	DDH-344	178 m	BXMGD(An)	anhy cement + sulfide	Fi qtz, Si
150896	164a	24000-28000	23000-25000	2500-4500 m	XC-125	DDH-344	210 m	PQM		TS

Appendix H: Rock catalogue (refer to Appendix G1 for acronyms)

UTAS #	Sample #	Northing	Easting	altitude (m)	Section	DDH	Depth	Lithology	description	Analysis Done
150897	165a	24000-28000	23000-25000	2500-4500 m	XC-125	DDH-344	224 m	BXMGD	mo/sulfide V., abundant mo	Si
150898	165b	24000-28000	23000-25000	2500-4500 m	XC-125	DDH-344	226 m	BXMGD	An clast in An clast? + Anhy, sulfide	TS
150899	166a	24000-28000	23000-25000	2500-4500 m	XC-125	DDH-344	234 m	BXMGD	HIGH GRADE BXMGD, sulfide cement.	Si
150900	167c	24000-28000	23000-25000	2500-4500 m	XC-125	DDH-344	253 m	BXMGD(An)	HIGH GRADE BXMGD(An),sulfide cement.	Si
150901	170b	24000-28000	23000-25000	2500-4500 m	XC-125	DDH-357	85 m	GDRB	HIGH GRADE GDRB (3.49% Cu)	Si
150902	179a	24000-28000	23000-25000	2500-4500 m	XC-125	DDH-340	43 m	BXMGD	sulfide cement.	Si
150903	180a	24000-28000	23000-25000	2500-4500 m	XC-125	DDH-340	70 m	BXMGD	BXMGD with Biotite matrix	TS
150904	186a	24000-28000	23000-25000	2500-4500 m	XC 50	DL 03	118 m	BXTGDCC	cpy cement	Si
150905	188a	24000-28000	23000-25000	2500-4500 m	XC 50	DL 03	132 m	BXTGDCC	sulfideV. , cpy cement	Si
150906	189a	24000-28000	23000-25000	2500-4500 m	XC-50	DL-03	132 m	BXTGDCC	Pre-Bx Qtz V.	Fi qtz
150907	191b	24000-28000	23000-25000	2500-4500 m	XC 10	DL 46A	80 m	BXTGDCC	cpy cement	Si
150908	194c	24000-28000	23000-25000	2500-4500 m	XC 10	DL 46A	148 m	BXTGDCC	D V. (py rich) & sulfide cement. (py)	Si
150909	195b	24000-28000	23000-25000	2500-4500 m	XC 10	DL 46A	158 m	BXTGDCC	cpy cement? (Vein?)	Si
150910	197b	24000-28000	23000-25000	2500-4500 m	XC 10	TSS 16	70 m	BXTGDCC	sulfideV.	Si
150911	19b	24000-28000	23000-25000	2500-4500 m	XC-50	TSS-26	17 m	BTGDCC		TS
150912	206d	24000-28000	23000-25000	2500-4500 m	XC 455E	DL 16	610 m	BXTGDCC	sulfide cement.?, coarse Tm., Qtz	Si
150913	208a	24000-28000	23000-25000	2500-4500 m	XC 50	C 50	412 m	BXTGDCC	D V. (py)	Si
150914	208e	24000-28000	23000-25000	2500-4500 m	XC 50	C 50	412 m	BXTGDCC	sulfideV.	Si
150915	209d	24000-28000	23000-25000	2500-4500 m	XC 50	C 50	350 m	BXTGDCC	D V. With Anhy.	Si
150916	20a	24000-28000	23000-25000	2500-4500 m	XC 50	TSS 26	33 m	BTGDCC	sulfide V.	Si
150917	210a	24000-28000	23000-25000	2500-4500 m	XC 50	TSS 26	30 m	BXTGDCC	sulfide cement (cpy), mt. & Qtz	Si
150918	212a	24000-28000	23000-25000	2500-4500 m	XC 50	TSS 26	279 m	BXTGDCC	D V.	Si
150919	212b	24000-28000	23000-25000	2500-4500 m	XC 50	TSS 26	279 m	BXTGDCC	sulfideV.	Si
150920	215a	24000-28000	23000-25000	2500-4500 m	XC-50	TSS-22	782 m	BXT/BXMGDCC		TS
150921	218b	24000-28000	23000-25000	2500-4500 m	XC-50	TSS-22	802 m	BXMGDCC	Qtz V. (4 cm wide) + Anhy.	Fi qtz
150922	218c	24000-28000	23000-25000	2500-4500 m	XC-50	TSS-22	802 m	BXMGDCC	sulfideV.	Fi qtz
150923	218d	24000-28000	23000-25000	2500-4500 m	XC 50	TSS 22	802 m	BXMGDCC	sulfideV.	Si
150924	219a	24000-28000	23000-25000	2500-4500 m	XC-50	TSS-22	816 m	BXMGDCC		TS
150925	219d	24000-28000	23000-25000	2500-4500 m	XC-50	TSS-22	816 m	BXMGDCC	BXMGDCC, thin parallel biot V	TS, bt chem
150926	220b	24000-28000	23000-25000	2500-4500 m	XC 50	TSS 22	26 m	BXTGDCC	sulfide cement. (cpy)	Si
150927	221b	24000-28000	23000-25000	2500-4500 m	XC-50	TSS-22	28 m	BXTGDCC	qtz cement	Fi qtz
150928	222e	24000-28000	23000-25000	2500-4500 m	XC-50	TSS-22	133 m	BXTGDCC	sulfide cement. (cpy)	PTS, Si, bt chem, tm chem
150929	222f	24000-28000	23000-25000	2500-4500 m	XC-50	TSS-22	130-140 m	BXTGDCC	qtz cement	Fi qtz
150930	222g	24000-28000	23000-25000	2500-4500 m	XC 50	TSS 22	137 m	BXTGDCC	D V. (py)	Si
150931	223a	24000-28000	23000-25000	2500-4500 m	XC-50	TSS-22	300-310 m	BXTGDCC	sulfide cement. (cpy)	PTS, Fi Tm, Si, bt chem, tm chem
150932	223b	24000-28000	23000-25000	2500-4500 m	XC-50	TSS-22	300-310 m	BXTGDCC	qtz cement	Fi qtz
150933	223e	24000-28000	23000-25000	2500-4500 m	XC 50	TSS 22	307 m	BXTGDCC	D V.	Si
150934	224a	24000-28000	23000-25000	2500-4500 m	XC 50	TSS 22	500 m	BXTGDCC	anhy cement. + Cpy (equilib.)	Si
150935	224b	24000-28000	23000-25000	2500-4500 m	XC-50	TSS-22	500-510 m	BXTGDCC	qtz cement	Fi qtz, O isotopes
150936	224e	24000-28000	23000-25000	2500-4500 m	XC 50	TSS 22	508 m	BXTGDCC	sulfideV. (are abundant here!)	Si
150937	225c	24000-28000	23000-25000	2500-4500 m	XC-50	TSS-22	609 m	BXTGDCC	Tm cement (coarse), 0.65% Cu	Fi Tm, O isotopes, Sr/Nd
150938	225d	24000-28000	23000-25000	2500-4500 m	XC 50	TSS 22	611 m	BXTGDCC	anhy cement. + py	Si
150939	226a	24000-28000	23000-25000	2500-4500 m	XC 50	TSS 22	730-740 m	GDCC(T)	qtz cement, 1.54% Cu	O isotopes
150940	226b	24000-28000	23000-25000	2500-4500 m	XC 50	TSS 22	730-740 m	GDCC(T)	sulfide cement. (Cpy), 1.54% Cu	Si
150941	227a	24000-28000	23000-25000	2500-4500 m	XC 50	TSS 21	140-150 m	GDCC	sulfideV. (cpy)	Si
150942	227b	24000-28000	23000-25000	2500-4500 m	XC 50	TSS 21	146 m	GDCC	D V. (py)	Si
150943	227c	24000-28000	23000-25000	2500-4500 m	XC-50	TSS-21	140-150 m	GDCC	sulfide cement. (py?)	PTS, Si
150944	228a	24000-28000	23000-25000	2500-4500 m	XC 50	TSS 4	50-60 m	BXTGDCC	D V. (py)	Si
150945	228c	24000-28000	23000-25000	2500-4500 m	XC 50	TSS 4	50-60 m	BXTGDCC	MatrixS (cpy)	Si
150946	228f	24000-28000	23000-25000	2500-4500 m	XC-50	TSS-4	50-60 m	BXTGDCC	qtz cement	Fi qtz
150947	229b	24000-28000	23000-25000	2500-4500 m	XC 50	TSS 4	100 m	BXTGDCC	D V. (py)	Si
150948	229c	24000-28000	23000-25000	2500-4500 m	XC 50	TSS 4	100-110 m	BXTGDCC	sulfideV. (cpy, py)	Si
150949	230a	24000-28000	23000-25000	2500-4500 m	XC 50	DL 64	20-30 m	BT-BXTGDCC	sulfideV.	Si
150950	230b	24000-28000	23000-25000	2500-4500 m	XC-50	DL-64	20-30 m	BT-BXTGDCC	qtz cement	Fi qtz, O isotopes
150951	230c	24000-28000	23000-25000	2500-4500 m	XC-50	DL-64	20-30 m	BT-BXTGDCC	sulfide cement. (cpy)	Si

UTAS #	Sample #	Northing	Easting	altitude (m)	Section	DDH	Depth	Lithology	description	Analysis Done
150952	237a	24000-28000	23000-25000	2500-4500 m	XC-125	DDH-450	4 m	PQM	sulfideV. (white Q/S) & sulfideV. (blue Q/S)	PTS, Si
150953	237c	24000-28000	23000-25000	2500-4500 m	XC-125	DDH-450	6 m	PQM	sulfideV. (blue Q/S) & Qtz V. (Blue Q/S)	Fi qtz
150954	239e	24000-28000	23000-25000	2500-4500 m	XC 125	DDH-450	74 m	BXMGD	Silicic altered clasts of GD in BXMGD	photo
150955	239f	24000-28000	23000-25000	2500-4500 m	XC-125	DDH-450	76 m	BXMGD	sulfide cement (cpy) & Qtz	PTS, Si
150956	239j	24000-28000	23000-25000	2500-4500 m	XC-125	DDH-450	80 m	PQM	Anhy V., assim. Clast, sulfideV. (white), sulfideV. (blue)	Fi qtz, Si
150957	240b	24000-28000	23000-25000	2500-4500 m	XC-125	DDH-450	102 m	BXMGD	anhy cement.(2.92% Cu)	Fi qtz, Si, Sr/Nd, Pb
150958	240e	24000-28000	23000-25000	2500-4500 m	XC-125	DDH-450	115 m	BXMGD	qtz cement, D V. (py)	Fi qtz, O isotopes
150959	241b	24000-28000	23000-25000	2500-4500 m	XC-125	DDH-450	136 m	BXMGD	sulfide cement (cpy) & Anhy.	Si
150960	241j	24000-28000	23000-25000	2500-4500 m	XC-125	DDH-450	128-158 m	PQM	sulfideV. (cpy)	Si
150961	243f	24000-28000	23000-25000	2500-4500 m	XC-125	DDH-450	190-210 m	PQM	anhy cement.? (PQM)	Si
150962	244a	24000-28000	23000-25000	2500-4500 m	XC 125	DDH 450	235-260 m	PQM	anhy cement. (PQM)	Si
150963	244h	24000-28000	23000-25000	2500-4500 m	XC-125	DDH-450	235-260 m	PQM	wide, vertical sulfideV. - cpy (white)	Si
150964	245b	24000-28000	23000-25000	2500-4500 m	XC-125	DDH-450	264 m	BXMGD		TS
150965	245f	24000-28000	23000-25000	2500-4500 m	XC-125	DDH-450	277 m	BXMGD	mo rimmed Qtz V.	Fi qtz
150966	245i	24000-28000	23000-25000	2500-4500 m	XC-125	DDH-450	282 m	BXMGD	sulfideV. (white) op. by sulfideV. (blue)	PTS
150967	245n	24000-28000	23000-25000	2500-4500 m	XC 125	DDH 450	290 m	BXMGD	sulfide cement. (cpy + Anhy.)	Si
150968	245p	24000-28000	23000-25000	2500-4500 m	XC-125	DDH-450	290 m	BXMGD	qtz cement	Fi qtz
150969	246c	24000-28000	23000-25000	2500-4500 m	XC 125	DDH 450	322 m	BXMGD	mo. Rimmed Qtz V. & Thick Qtz V. (early or Late?)	Si
150970	246f	24000-28000	23000-25000	2500-4500 m	XC 124	DDH 450	326 m	PQM	sulfideV. (white) & Early Qtz V.	Si
150971	246h	24000-28000	23000-25000	2500-4500 m	XC 125	DDH 450	334 m	BXMGD	anhy cement. (0.38% Cu)	Si, Sr/Nd, Pb
150972	246j	24000-28000	23000-25000	2500-4500 m	XC-125	DDH-450	343 m	BXMGD	sulfide cement. (cpy) + mt. + Anhy.	Si
150973	246k	24000-28000	23000-25000	2500-4500 m	XC-125	DDH-450	347 m	BXMGD	qtz cement, 0.39% Cu	Fi qtz, O isotopes
150974	247c	24000-28000	23000-25000	2500-4500 m	XC-125	DDH-352	0-16 m	PQM	early Qtz V. Op by Late Qtz V.	Fi qtz
150975	247e	24000-28000	23000-25000	2500-4500 m	XC 125	DDH 352	13 m	PQM	Py, cpy, spec, gyp. V.	Si
150976	250b	24000-28000	23000-25000	2500-4500 m	XC 125	DDH 352	120 m	BXMGD	sulfide cement. (cpy)	Si
150977	250d	24000-28000	23000-25000	2500-4500 m	XC 125	DDH 352	124 m	BXMGD	sulfideV. (white)	Si
150978	250e	24000-28000	23000-25000	2500-4500 m	XC-125	DDH-352	125 m	BXMGD	sulfideV. (blue)	Si
150979	251b	24000-28000	23000-25000	2500-4500 m	XC-125	DDH-352	160 m	BXAN	mt., cpy cement	Si
150980	251d	24000-28000	23000-25000	2500-4500 m	XC-125	DDH-352	160.5 m	BXAN	sulfideV. (blue)	photo
150981	251h	24000-28000	23000-25000	2500-4500 m	XC-125	DDH-352	176 m	BXAN	sulfide cement. (cpy)	Si
150982	252d	24000-28000	23000-25000	2500-4500 m	XC-135	DDH-448	14 m	GDRB	anhy cement., cpy	Fi qtz, Si
150983	253c	24000-28000	23000-25000	2500-4500 m	XC-135	DDH-448	126 m	PQM	sulfide, mt., Spec V	Si
150984	253d	24000-28000	23000-25000	2500-4500 m	XC-135	DDH-448	138 m	PQM	Clump of cpy in PQM + alteration	Si
150985	268a	24000-28000	23000-25000	2500-4500 m	XC-275	DDH-734	342 m	DIOR (GDCC)	shearing relationship mo rimmed Qtz V. (bio/chl); thin sulfideV.-cpy (Q/S); Qtz., Anhy., cpy V (biot)	Fi qtz
150986	31b	24000-28000	23000-25000	2500-4500 m	XC-50	TSS-26	211 m	GDCC	sulfide V., mt in GDCC	PTS
150987	34c	24000-28000	23000-25000	2500-4500 m	XC-50	TSS-26	265 m	GDCC	Qtz, mo rimmed qtz V + cpy	PTS
150988	39a	24000-28000	23000-25000	2500-4500 m	XC-50	TSS-26	335 m	GDCC	Pink Qtz V. OP. by sulfide V., Epi in GDCC, possulfide Reactivated	Fi qtz
150989	43c	24000-28000	23000-25000	2500-4500 m	XC-50	TSS-22	6 m	BXTGDCC	sulfideV.(D-Type, 2 cm wide)	PTS
150990	52a	24000-28000	23000-25000	2500-4500 m	XC-50	TSS-22	130 m	BXTGDCC	mt V. (deep)	PTS
150991	55a	24000-28000	23000-25000	2500-4500 m	XC-50	TSS-22	217 m	BXTGDCC	Tm(1) V. O.P. by Tm(2) flooding	PTS
150992	57b	24000-28000	23000-25000	2500-4500 m	XC 50	TSS-22	258 m	BXTGDCC	sulfide cement., (Dissulfideaggregates)	Si
150993	59b	24000-28000	23000-25000	2500-4500 m	XC-50	TSS-22	380 m	BXTGDCC	Qtz V. + sulfide cement.	Fi qtz, Si
150994	60c	24000-28000	23000-25000	2500-4500 m	XC 50	TSS 22	578 m	BXTGDCC	Anhy in Tm matrix (0.69%Cu)	Si, Sr/Nd, Pb
150995	61b	24000-28000	23000-25000	2500-4500 m	XC-50	TSS-22	635 m	BXTGDCC	sulfide/Qtz V. (GDCC)	PTS
150996	62b	24000-28000	23000-25000	2500-4500 m	XC-50	TSS-22	736 m	BXTGDCC	sulfide cement. + Anhy, sulfide/Tm/Qtz V.	PTS, Fi qtz, Fi Tm, tm chem, Si
150997	62d	24000-28000	23000-25000	2500-4500 m	XC-50	TSS-22	752 m	BXTGDCC	sulfide/Qtz V.	PTS
150998	62f	24000-28000	23000-25000	2500-4500 m	XC-50	TSS-22	803 m	BXTGDCC	Qtz/sulfide V.	PTS
150999	66b	24000-28000	23000-25000	2500-4500 m	XC-50	DL-62	65.5 m	BXTTO	BXT clast in BXTTO, Tm.	TS
151000	69b	24000-28000	23000-25000	2500-4500 m	XC 50	DL 62	117 m	BTGDCC	sulfide cement., py	Si
151001	74b	24000-28000	23000-25000	2500-4500 m	XC-50	DL-62	152 m	BXTTOMN	sulfide V. (or BXMN)	PTS, Si

Appendix H: Rock catalogue (refer to Appendix G1 for acronyms)

UTAS #	Sample #	Northing	Easting	altitude (m)	Section	DDH	Depth	Lithology	description	Analysis Done
151002	77b	24000-28000	23000-25000	2500-4500 m	XC-50	DL-62	211 m	BXMN	BXMN	TS
151003	77c	24000-28000	23000-25000	2500-4500 m	XC-50	DL-62	212 m	BXMN	PDL, PF clasts?	TS
151004	98b	24000-28000	23000-25000	2500-4500 m	XC 130	DL 139.1	300 m	BXTTGDCC	sulfide cement.	Si
151005	An1a	24000-28000	23000-25000	2500-4500 m	110-180	TSS-23	609 m	An	Andesite discrimination	WR, TS
151006	An1b	24000-28000	23000-25000	2500-4500 m	110-180	TSS-23	609 m	An	Andesite discrimination	TS
151007	An1c	24000-28000	23000-25000	2500-4500 m	110-180	TSS-23	609 m	An	Andesite discrimination	WR, TS
151008	An2	24000-28000	23000-25000	2500-4500 m	XC-225	DDH-272	190 m	An	Andesite discrimination	TS
151009	An2b	24000-28000	23000-25000	2500-4500 m		Laura area	surface	An	Andesite discrimination	WR, TS
151010	An3	24000-28000	23000-25000	2500-4500 m				An	Andesite discrimination	TS
151011	An4	24000-28000	23000-25000	2500-4500 m	XC 235	DDH-330	334 m	An	Andesite discrimination	TS, WR
151012	HGS130a	24000-28000	23000-25000	2500-4500 m	XC 130	DL 139.1	295.1 m	BXTGDCC	high grade	Si
151013	HGS50	24000-28000	23000-25000	2500-4500 m	XC-50	DL-64	0-14 m	BXTGDCC	high grade	PTS
151014	LGS50	24000-28000	23000-25000	2500-4500 m	XC-50	DL-64	192-200m	BXTGDCC	low grade	Fi qtz, Si
151015	O1PF1	24000-28000	23000-25000	2500-4500 m	XC 345	DDH-733	343.5 m	PF	PF discrimination	TS, WR
151016	O1PF11	24000-28000	23000-25000	2500-4500 m	XC 245	DDH-738	276.5 m	PF	PF discrimination	TS, WR
151017	O1PF3	24000-28000	23000-25000	2500-4500 m	XC 275	DDH-734	465 m	PF	PF discrimination	TS, WR
151018	O1PF5	24000-28000	23000-25000	2500-4500 m	XC 275	734	485.4 m	PF	PF discrimination	TS
151019	SS Open pit	24000-28000	23000-25000	2500-4500 m		Pit sample		BXTGDCC	leached clasts and coarse tourmaline	PTS, tm chem, Sr/Nd
151020	St1c	24000-28000	23000-25000	2500-4500 m	XC-235	DDH-576	105 m	PF	clear contact. PF has a darker colour to PQM.	TS
151021	St1d	24000-28000	23000-25000	2500-4500 m	XC 235	DDH-576	109 m	PF	Contact of PQM/PDL. Contact is not preserved and the difference	PTS, TS, WR
151022	St4a	24000-28000	23000-25000	2500-4500 m	XC 215	DDH-380	320 m	PDL/PQM	porphyry discrimination	TS, WR
151023	St5a	24000-28000	23000-25000	2500-4500 m	XC-125	DDH-344	15 m	PQM	porphyry discrimination	TS
151024	St6b	24000-28000	23000-25000	2500-4500 m	XC-145	DDH-358	24 m	PQM	porphyry discrimination	TS
151025	St8c	24000-28000	23000-25000	2500-4500 m	XC-315	DDH-652	220 m	PDL	porphyry discrimination	TS
151026	St8d	24000-28000	23000-25000	2500-4500 m	XC-315	DDH-652	220 m	PDL	porphyry discrimination	TS
151027	St8f	24000-28000	23000-25000	2500-4500 m	XC-315	DDH-652	221 m	PDL	porphyry discrimination	TS
151028	St9b	24000-28000	23000-25000	2500-4500 m	XC-295	DDH-638	44 m	PDL	porphyry discrimination	TS
151029	VHG50a	24000-28000	23000-25000	2500-4500 m	XC-50	DL-03	56 m	BXTGDCC	v high grade, shallow	Fi qtz, O isotopes
151030	VHG50c	24000-28000	23000-25000	2500-4500 m	XC 50	DL 03	57.8 m	BXTGDCC	v high grade, shallow	PTS, Si
151031	VHG50d	24000-28000	23000-25000	2500-4500 m	XC 50	DL 03	58 m	BXTGDCC	v high grade, shallow	PTS, Si, Fi qtz, Fi tm, O isotopes